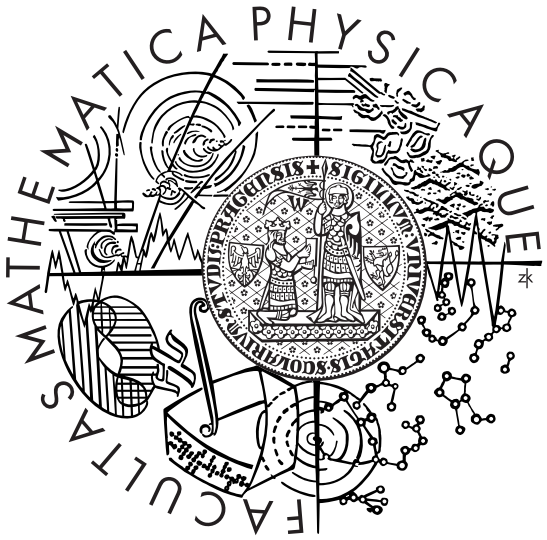
Charles University Prague
Faculty of Mathematics and Physics



a thesis submitted for the degree of
Philosophiae Doctor

Surface Wave Analysis and Inversion Application to the Bohemian Massif

by

Petr Kolínský

Supervisor: RNDr. Johana Brokešová, CSc.
Consultant: RNDr. Jiří Málek, PhD.

Department of Geophysics
Faculty of Mathematics and Physics
Charles University Prague
V Holešovičkách 2
180 00 Praha 8
Czech Republic

Prague 2010

CHARLES UNIVERSITY PRAGUE

faculty of mathematics and physics



Contents

Contents 5

Acknowledgements 7

Statement 7

List of supporting grant projects 8

Abstract 9

Abstrakt (česká verze) 11

Introduction 13
Surface waves . . . 13
Motivation . . . 15
Outline of the thesis . . . 16

Part I: Theory 19

Chapter 1: Surface wave analysis 21
1.1 Background research of surface wave analysis methods . . . 21
1.2 Multiple filtering method . . . 39
1.3 Illustrative description of the method . . . 41
1.4 Formally exact description of the method . . . 51
1.5 Instrumental time correction . . . 55
1.6 Seismograms, velocigrams or accelerograms? . . . 57
1.7 Tests of the multiple filtering method . . . 68

Chapter 2: Surface wave inversion methods 73
2.1 Overview of the inversion methods . . . 73
2.2 Isometric method description . . . 75
2.3 Application of the isometric method for dispersion curve inversion . . . 76
2.4 Inversion tests . . . 78

Part II: Applications 81

Chapter 3: Application A: Uppermost crust shear wave velocities 83
3.1 Dealing with the topic . . . 83
3.2 **The Western Bohemia uppermost crust shear wave velocities from Love wave dispersion** (original paper) . . . 83
3.2.1 Abstract . . . 83
3.2.2 Introduction . . . 84
3.2.3 Group velocity analysis . . . 85
3.2.4 Inversion for shear wave velocities . . . 86
3.2.5 Forward computations . . . 88
3.2.6 Test of the multiple filtering . . . 89
3.2.7 Test of the inversion . . . 89
3.2.8 Data . . . 93
3.2.9 Results . . . 93
3.2.10 Discussion and conclusion . . . 98
3.2.11 Acknowledgements . . . 99
3.2.12 References . . . 99
3.3 Additional remarks to the paper . . . 101

Chapter 4: Application B: Rayleigh wave tomography 103
4.1 Dealing with the topic . . . 103
4.2 **The Western Bohemia uppermost crust Rayleigh wave tomography** (original paper) . . . 104
4.2.1 Abstract . . . 104
4.2.2 Introduction . . . 105
4.2.3 Group velocity analysis . . . 107

4.2.4 Group velocity tomography . . . 109
4.2.5 Data . . . 110
4.2.6 Tomographic images . . . 110
4.2.7 Discussion and conclusion . . . 113
4.2.8 Acknowledgements . . . 116
4.2.9 References . . . 116
4.3 Smoothing and resolution of the tomography . . . 117

Chapter 5: Application C: Phase velocity and crustal structure 121
5.1 Dealing with the topic . . . 121
5.2 **Shear wave crustal velocity model of the Western Bohemian Massif from Love wave phase velocity dispersion** (original paper) . . . 121
5.2.1 Abstract . . . 121
5.2.2 Introduction . . . 122
5.2.3 Data . . . 125
5.2.4 Love wave analysis . . . 126
5.2.5 Phase velocity measurement . . . 127
5.2.6 Backazimuth correction . . . 128
5.2.7 Inversion . . . 128
5.2.8 Synthetic tests of the analysis and inversion . . . 130
5.2.9 Results . . . 132
5.2.10 Discussion . . . 136
5.2.11 Conclusion . . . 139
5.2.12 Acknowledgements . . . 140
5.2.13 References . . . 140
5.3 What is not included in the paper . . . 142

Part III: Software 149

Chapter 6: The SVAL program 151
6.1 History of the program . . . 151
6.2 Basic characteristic . . . 152
6.3 How it looks . . . 154
6.4 File inputs . . . 157
6.5 Keyboard inputs . . . 161
6.6 File outputs . . . 176
6.7 Outputs displayed in the auxiliary window . . . 191
6.8 Outputs displayed in the main window . . . 192
6.9 Outputs displayed in the frequency domain window . . . 196
6.10 Outputs displayed in the inversion window . . . 198
6.11 Working with the SVAL program – analysis . . . 199
6.12 Examples of analysis . . . 213
6.13 Working with the SVAL program – inversion . . . 220
6.14 Examples of inversion . . . 224

Chapter 7: The PhaseCorr program 231
7.1 About the program . . . 231
7.2 How it looks . . . 231
7.3 File inputs . . . 231
7.4 Keyboard inputs . . . 233
7.5 File outputs . . . 236
7.6 Displayed outputs . . . 236
7.7 Working with the PhaseCorr program . . . 238

Conclusion 247
Resume . . . 247
Outlooks . . . 248
Epilogue . . . 249

Appendix: Explanatory dictionary 251

References 253

Acknowledgements

I would like to thank all my colleagues from the Department of Seismology, Institute of Rock Structure and Mechanics, Academy of Sciences of the Czech Republic, for friendly atmosphere and help with all the seismology. Jan Valenta has been helping me with Linux peculiarities and other software problems. Renata Gaždová has found many bugs in my programs. Gratitude to all the staff of Department of Geophysics, Faculty of Mathematics and Physics, Charles University in Prague, for their suggestive help during my PhD studies. Jiří Zahradník inspired me with his questions and comments during seismic seminar meetings. Oldřich Novotný helped me much by providing his matrix method computation program.

Many thanks to MicroSeismic, Inc., Houston, Texas, USA, where I spent the most rewarding months at the end of my studies. Leo Eisner has my gratitude for inviting me to Texas and Peter M. Duncan for giving me the opportunity to learn how seismic service company works.

I am grateful to my supervisor Johana Brokešová and my consultant Jiří Málek for their patience and tolerance. Johana Brokešová and Jiří Málek are also co-authors of the papers used in my thesis.

Statement

I hereby declare that I have elaborated this thesis on my own and that the references include all sources of information I have exploited. All the work presented in this thesis is based on my original work, unless otherwise mentioned. It is not substantially the same as any work that has been, or is being submitted to any other university for any degree, diploma or any other qualification. I agree with lending and free distribution of this thesis.

Prague, August 30, 2010

Petr Kolínský

List of supporting grant projects

During my studies, I was supported by the following grant projects:

- *Nature of seismicity in the Hronov-Poříčí fault area*, Czech Science Foundation, No. 205/09/1244, 2009 – 2013.
- *Physical study of objects and processes in the solar system and in astrophysics*, research plan of the Faculty of Mathematics and Physics, Charles University in Prague, No. MSM0021620860, 2007 – 2013.
- *Research into the properties of geomaterials, development of methods of their ecological exploitation and interpretation of geodynamic processes*, research plan of the Institute of Rock Structure and Mechanics, No. A VOZ30460519, 2005 – 2011.
- *Upper crustal model of the Ohře Rift and its vicinity*, Grant Agency of the Academy of Sciences of the Czech Republic, No. A300460602, 2006 – 2010.
- *Propagation of seismic surface waves in the Trans-European suture zone*, Grant Agency of the Academy of Sciences of the Czech Republic, No. A300460705, 2007 – 2009.
- *Earthquake swarms in the western part of the Bohemian Massif and their link with crustal fluids*, Czech Science Foundation, No. 205/06/1780, 2006 – 2008.
- *Hydrogeological effects of seismicity in the Hronov-Poříčí fault zone area*, Czech Science Foundation, No. 205/05/H020, 2005 – 2008.
- *International seismic experiment PASSEQ – Passive seismic experiment in Trans-European suture zone*, 2006 – 2007.
- *SLICE – Seismic lithospheric investigation of Central Europe*, Ministry of Environment of the Czech Republic, No. VaV/630/3/02, 2002 – 2005.
- *Seismic velocity model in the vicinity of Eger rift from dispersion of surface waves*, starting grant of the Grant Agency of the Academy of Sciences of the Czech Republic, No. Z3046908-I039, 2004.
- *Geodynamical processes in the upper part of Earth's crust affecting the environment and ecological utilization of raw materials*, research plan of the Institute of Rock Structure and Mechanics, No. AV0Z3046908, 1999 – 2004.
- *Study of the upper crustal structure on the territory of Bohemia using seismic waves from quarry blasts*, Czech Science Foundation, No. 205/01/0481, 2001 – 2003.

Abstract

title:	Surface Wave Analysis and Inversion Application to the Bohemian Massif
author:	Mgr. Petr Kolínský, DiS.
author's e-mail address:	kolinsky@irsm.cas.cz
departments:	Department of Geophysics Faculty of Mathematics and Physics Charles University Prague V Holešovičkách 2, Praha 8 – 180 00, Czech Republic and Department of Seismology Institute of Rock Structure and Mechanics, v.v.i. Academy of Sciences of the Czech Republic V Holešovičkách 41, Praha 8 – 182 09, Czech Republic
supervisor:	RNDr. Johana Brokešová, CSc.
supervisor's e-mail address:	johana.brokesova@mff.cuni.cz
consultant:	RNDr. Jiří Málek, PhD.
consultant's e-mail address:	malek@irsm.cas.cz
keywords:	*surface waves, group velocity, phase velocity, frequency-time analysis, multiple filtering, tomography, inversion problems, Earth crust structure, Bohemian Massif*

An overview of surface wave analysis methods as well as of inversion techniques is given. Special attention is paid to the multiple filtering method for dispersion curve estimation, which is described by two different ways in detail. The isometric method is used for dispersion curve inversion and its description and tests are presented.

Described methods are further used in applications. The applications show examples of surface wave analysis and inversion for 1D and 2D crustal structure. The analysis of Love waves generated by quarry blasts and measured at short epicentral distances from 5 to 50 km and their inversion for uppermost crustal structure down to a depth of 3 km is given with results benchmarked by the synthetic waveform computation. An example of 2D surface wave tomography based on Rayleigh waves for Western Bohemia region is given in comparison to previous studies of the area. Phase velocities measured across the Bohemian Massif using the records of Aegean Sea earthquakes are presented with their inversion for crust and upper mantle 1D shear wave velocity distribution. A new method for estimating the true backazimuths of surface wave propagation for different wavelengths is presented.

The methods used in applications are compiled in a software newly developed during the author's PhD studies. The interactive SVAL program is a universal tool for surface wave dispersion estimation in an arbitrary frequency band and also for dispersion curve inversion to 1D structure. All functions of the program are described; all handlers and tools for filtering the records and for inverting the dispersion curves are discussed; examples are given and instructions for use are added. Color screenshots of the SVAL program windows help to understand the program functionality better. All input and output files are described and examples of them are given. For phase velocity estimation based on the results of the SVAL program analysis, the PhaseCorr program was developed and it is also described with all the necessary tools for estimating phase velocities between two stations at the same seismic profile.

Abstrakt

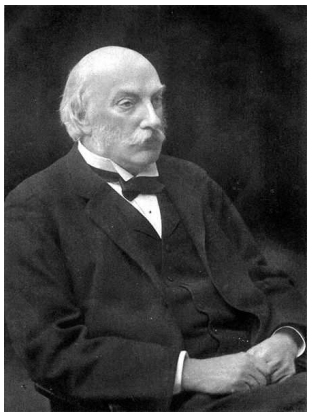
česká verze

název:	Analýza a inverze povrchových vln Aplikace na Český masiv
autor:	Mgr. Petr Kolínský, DiS.
e-mailová adresa autora:	kolinsky@irsm.cas.cz
pracoviště:	Katedra geofyziky Matematicko-fyzikální fakulta Karlova univerzita v Praze V Holešovičkách 2, Praha 8 – 180 00 a Oddělení seismologie Ústav struktury a mechaniky hornin, v.v.i. Akademie věd České republiky V Holešovičkách 41, Praha 8 – 182 09
školitelka:	RNDr. Johana Brokešová, CSc.
e-mailová adresa školitelky:	johana.brokesova@mff.cuni.cz
konzultant:	RNDr. Jiří Málek, PhD.
e-mailová adresa konzultanta:	malek@irsm.cas.cz
klíčová slova:	*povrchové vlny, grupová rychlost, fázová rychlost, frekvenčně-časová analýza, mnohokanálová filtrace, tomografie, obrácené úlohy, struktura zemské kůry, Český masiv*

V práci je podán přehled metod analýzy povrchových vln a také přehled řešení obrácených úloh. Zvláštní pozornost je věnována metodě mnohokanálové filtrace pro určování disperzních křivek. Tato metoda je detailně popsána dvěma různými způsoby. Pro inverzi disperzních křivek je používána isometrická metoda, jejíž popis a testy jsou v práci uvedeny.

Popsané metody jsou dále použity v aplikacích. Tyto aplikace podávají příklady analýzy povrchových vln a inverze na 1D a 2D strukturu kůry. Je ukázána analýza Loveových vln generovaných lomovými odpaly a měřených v krátkých epicentrálních vzdálenostech od 5 do 50 km. Je provedena jejich inverze na strukturu svrchní kůry do hloubky 3 km. Výsledky jsou ověřeny výpočtem syntetických vlnových obrazů. Je uveden příklad 2D tomografie západních Čech založené na Rayleighových vlnách a provedeno srovnání s předešlými výzkumy této oblasti. Ukázány jsou také fázové rychlosti měřené v Českém masivu na záznamech zemětřesení z Egejského moře a jejich inverze na 1D rozložení rychlostí střižných vln v kůře a svrchním plášti. Je také uvedena nová metoda pro určování skutečných směrů příchodů povrchových vln pro různé vlnové délky.

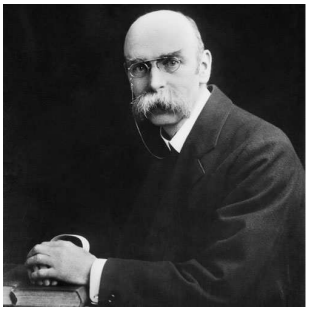
Metody použité v aplikacích jsou zpracovány do nově vyvinutých programů sestavených během autorova doktorského studia. Je popsán interaktivní program SVAL, což je všestranný nástroj pro určování disperze povrchových vln v libovolném frekvenčním oboru a také pro inverzi disperzních křivek na 1D strukturu. Jsou popsány všechny funkce programu, všechna nastavení a nástroje pro filtraci záznamů a pro invertování disperzních křivek. Jsou uvedeny příklady a návod k použití. Barevné obrázky oken programu SVAL pomáhají lépe pochopit fungování programu. Jsou popsány všechny vstupní a výstupní soubory a uvedeny jejich příklady. Program PhaseCorr je sestaven pro určování fázových rychlostí. Pracuje s výsledky analýzy programu SVAL. Program PhaseCorr je také popsán se všemi potřebnými nástroji pro určování fázových rychlostí mezi dvěma stanicemi na jednom seismickém profilu.



"It is not improbable that the surface waves here investigated play an important part in earthquakes, and in the collision of elastic solids."

John William Strutt, 3rd Baron Rayleigh

Rayleigh, J. W. S., 1885: On waves propagating along the plane surface of an elastic solid, *Proc. London Math. Soc.*, 17, 4–11, citation from page 11. Reprinted in: Rayleigh, J. W. S., 1900: Scientific papers, *Cambridge University Press*, Vol. II. 1881–1887, 626 pp. Citation from page 447.



"The hypothesis of a discontinuity of structure of the earth, at a depth which is small compared with the radius, has been shown to lead to important results in regard to the earlier phases of the main shock – the phases which are characterized by a preponderance of horizontal movement at right angles to the direction of propagation."

Augustus Edward Hough Love

Love, A. E. H., 1911: Some problems of geodynamics, *Cambridge University Press*, Cambridge, 180 pp, citation from page 165, paragraph 182.

Introduction

We give a short overview of three aspects of the thesis here in the *Introduction*. Section *Surface waves* gives a brief summary of the possible problems of surface wave analysis and inversion. This PhD thesis deals with some of them. It does not resolve all of them – it was not the intention at all. The thesis concerns some of the analysis and inversion goals and tries to solve them in detail, as described in the following chapters. Section *Motivation* contains the ideas and approaches to the work and section *Outline of the thesis* introduces the way how the thesis is built using the original papers, newly written parts, software and examples and how these elements are joined together to present compact work.

Surface waves

The fine deep internal structure of the Earth is often obtained from studies of seismic body waves. As opposed to that, surface waves can give us averaged information about the mean upper Earth structure between the source and our seismic stations, or between two or more seismic stations only. Presented thesis deals with surface wave structural seismology. All the theory, applications and software described in the thesis is particularly intended for the estimation of distribution of seismic velocities in the Earth crust and upper mantle. We present several methods of velocity distribution estimation from surface waves measurements, newly developed software and examples of applications. We use surface waves as a special tool for imaging the Earth interior.

As seismology has made significant progress in the last decades, new pieces of knowledge are found in both the methods of analysis and hence in the understanding of the earthquake behavior and wave propagation. The need of better knowledge of the Earth crust emerges not only as a natural wish to understand what is the globe made from, but also as a logical implication of all the progress of other geophysical branches. As we are able to determine the source mechanisms, we have to know the structure better to predict the ground motion. As we can detect microearthquakes with new and sensitive seismic stations, we need more detailed images of the seismic velocities to locate the events properly. As we can analyze long period ground motion, we are looking for 2D or 3D distribution of seismic velocity heterogeneities to explain wave propagation in regional scale. As we can detect short-period surface waves from quarry blasts, we are looking for detailed velocity structure of the uppermost parts of the Earth crust to understand the subsurface geology in local scale. Surface waves, as a special sort of seismic waves of all wavelengths, may give us new information of the target region or they can complement our knowledge obtained by other seismological or generally geophysical means.

Years ago surface waves were considered to be the "big" waves in the records of regional or teleseismic events. One may find an explanation that surface waves are the largest waves in the records, larger than body waves and that they are of 20 s period and longer. Of course, none of this is true. When one starts to deal with surface waves, this is a natural practice to learn about this phenomenon using this simple approach and there is nothing wrong about it. However, it is not the whole truth at the same time.

As shown in the next chapters, we may find the surface waves of periods as long as hundreds of seconds and as short as 0.03 s ($\approx$ 30 Hz). Estimating the dispersion of waves recorded at a distance of thousands of kilometers and using broadband instruments, we usually find the waves of periods as long as 200 s (Ewing and Press, 1954; Nafe and Brune, 1960; Nakanishi and Anderson, 1982; Mitra et al., 2006). From the records obtained by short-period geophones during shallow seismic refraction survey, we are able to detect surface waves in the range of 0.03 to 0.2 s (Forbriger, 2003a and 2003b; Xia et al., 2004). And there is no doubt that if we recorded high frequency records in the laboratory experiments, we would find surface waves of wavelengths even shorter (Park et al., 1998).

The amplitudes of surface waves are diverse as well. Looking at the records of shallow Greek earthquakes (Kolínský et al., 2010) at the distance of 1500 km, we see the surface waves to be of amplitudes much higher then the body waves at the first glance. Great epicentral distance, longer paths of body waves, higher attenuation of shorter frequencies and a good opportunity for surface waves to evolve, result in their dominance in the records. However, analyzing some of the records from quarry blasts, we do not see any surface waves at all (Kolínský and Brokešová, 2007 and 2008). Close epicentral distance, high

frequency content, small magnitude of the source, not enough time for waves to interfere and create the surface waves, complicated uppermost crust structure resulting in many reflections and conversions will make the records full of body waves. But it does not mean the surface waves disappear somewhere. They are in the records and using a proper technique, they may be found, their dispersion may be estimated and the velocity structure of their paths revealed.

We do not want to present the entire description of the surface waves theory here, but one thing to be kept in mind whenever talking about this phenomenon should be mentioned. Surface waves may be considered by two – at the first sight – completely different approaches. The first one considers the surface waves and their modes to be a result of interference of traveling waves, the second one regards the surface waves as a higher-frequency approximation of standing waves – the Earth normal modes, see Widmer-Schnidrig and Laske (2007). These approaches are, of course, valid also for body waves, but dealing with surface waves we are close to the opportunity to use both approaches together.

Traveling waves: Considering the radiation of P and S waves from the source, having the heterogeneous model of the Earth with a free surface at the top, having a theory of reflection, total reflection, conversion, interference and superposition of both types of body waves, surface waves appear as an additional phase built up by P and S wave interference in certain distance from the source and they propagate along the Earth surface or along any sharp discontinuity inside the Earth (Rayleigh, 1885; Love, 1911; Haskell, 1953; Harkrider and Anderson, 1962, Toksöz and Ben-Menahem, 1963; Montagner and Jobert, 1983). These waves propagate along geometrical great circle source – station paths in 1D velocity models (Nakanishi and Anderson, 1983), their trajectories bend in 3D models (Laske, 1995). We consider them propagating from the source with dispersive velocity, different wavelengths and periods. They can reflect and scatter (Pollitz, 1994), attenuate (Romanowicz, 1995), convert, focus and defocus (Lay and Kanamori, 1985). They are influenced by heterogeneity and anisotropy (Tanimoto and Anderson, 1985).

Standing waves: On the other hand, we have a theory of the free oscillations of the Earth (Benioff et al., 1961; Brune, 1964; Alsop, 1964). Any wave of any frequency may be considered as a mode of free oscillation. As we go to the long period part of the surface wave spectrum, we are closer to the fundamental oscillations of the Earth.

These two approaches resemble the well known wave/particle duality in nuclear physics. We do not mean this comparison in any physical sense. We would only like to emphasize that any of two different approaches, both valid at the same time, may be used when the situation is better described by one of them. Usually, when talking about surface waves, we do not specify which approach we use. And – of course – we use both approaches at the same time. When talking about higher modes of surface waves, we may have both the interference theory of superposition of body waves to let the higher modes evolve, or the finite proportions of the globe to explain the surface wave modes as higher modes of the free oscillations.

We have mentioned that surface waves can be found in nearly all records and the diversity of their use originates from this fact. When looking for universal properties of the Earth crust and mantle, we use teleseismic records with surface waves around 30 – 300 s. These waves could not resolve the Earth crust in detail, we may consider the crust as a homogeneous layer and try to find out the depth of low velocity asthenosphere and estimate seismic velocities of upper mantle (Kuo et al, 1962; Gupta et al., 1977; Silveira et al., 1998; Yoshida and Suetsugu, 2004; Khan et al., 2009). When describing the Earth crust in a regional scale, we use the waves of period from 5 to 60 s recorded from the source at the depths around 5 – 30 km and at the distance of 500 – 2000 km. These waves can give us information about the layering of the crust and also about the depth of the Moho discontinuity (McEvilly, 1964; Noponen, 1966; Novotný et al., 2001; Delorey et al., 2007). Such studies are found in great number in papers from the last decades.

Surface waves from local earthquakes may be used for detailed resolution of upper crust using the periods between 1 to 20 s (Chávez-García et al., 1995; He et al., 2004). Quarry blasts are used to estimate the few kilometers of the uppermost crust in epicentral distances up to tens of kilometers processing even shorter surface waves of periods around 1 s (Gaždová et al., 2008; Kolínský and Brokešová, 2007). This research is not so common, however, nearly the same approach as that for the teleseismic or regional studies can be used for it.

In shallow seismic or in gas and oil prospection, surface waves are not commonly in practical use. Many prospection companies deal with one component vertical geophones only and hence even the shear waves are not measured and used regularly (Kolínský et al., 2009). Surface waves in seismic prospection can give us additional information about the uppermost meters of the medium which is not traced by body waves and which is – at the same time – crucial for estimating the statics and geophone corrections (Gabriels et al., 1987; Xia et al., 2004).

Surface waves are, as a complex phenomenon, influenced by many physical properties of the medium which they propagate through. The heterogeneity in vertical direction and the free surface are responsible for the dispersion of surface waves. The heterogeneity in horizontal direction is responsible for bending of

the paths of the waves and for the occurrence of Love and Rayleigh waves on both radial and transverse components. Surface wave focus and defocus and their amplitudes are strongly influenced by heterogeneity along their paths. Anisotropy causes that both Love and Rayleigh waves are found at all three components of a record. It is also responsible for sometimes striking discrepancies between the velocities of Rayleigh waves measured at vertical and radial components (Maupin, 2002). Joint inversion of both Love and Rayleigh waves in isotropic medium is usually impossible. Surface waves also reflect from sharp vertical discontinuities, they refract along faults and suture zones (Its and Lee, 1993; Meier et al., 1997). Properties of waveforms are strongly influenced while the surface waves cross the oceanic/continental boundary (Gregersen and Alsop, 1976; Drake and Bolt, 1980). They interfere among themselves, they convert from one type to the other (Maupin, 2007). Different wavelengths of the waves are sensitive not only to different depths, but also to different lateral extent – we talk about influence zones of the surface waves for given period (Yoshizawa and Kennett, 2002). To distinguish between fundamental and higher mode is sometimes hard work and to estimate the number of higher modes is usually even impossible (Gabriels et al., 1987; Zhang and Chan, 2003; Beucler et al., 2003).

All these complexities of surface waves has lead to developing of many techniques of their measurement, analysis and inversion. The basic approach to measure surface waves is to look at records in the frequency and time domains at the same time. We have several techniques of frequency-time analysis (Kocaoglu and Long, 1993; Kristeková, 2006), we may filter the records in time or frequency domain, we may use wavelet transforms, distributions and other techniques. Some of them have better resolution than others, but are more costly when using computers, some of them are more intuitive for use, some of them are outdated, but good for explaining the basic properties of the analysis. Using the frequency-time analysis, we always fight the uncertainty principle and we deal with all the problems of signal sampling, filtration, smoothing and truncating.

When inverting the information obtained by surface wave analysis, we have the possibility to make an inversion of the dispersion curve for 1D velocity distribution with depth (Plešinger et al., 1991; Novotný et al., 1995 and 1997), or to use the approaches of surface wave tomography to get 2D images for certain periods of surface waves in the target region (Ritzwoller and Levshin, 1998; Barmin et al., 2001; Villaseñor et al., 2001). The final step is the three-stage approach, when artificially computed local dispersion curves are inverted for the 3D velocity distribution using 2D tomographic images for different wavelengths emerging as a result of 1D dispersion curve analysis (Kennett and Yoshizawa, 2002).

Considering the finite wavelengths of different periods of surface waves, the method of diffraction tomography was developed (Ritzwoller at al., 2002; Levshin et al., 2005). To invert the surface waves for the velocity distribution using the whole waveforms is not a common procedure now, but in principle, it is possible (Snieder, 1988a and 1988b). Methods of inverting the frequency-time representation of record (Forbriger, 2003a and 2003b) have been developed. We can compare separated surface wavegroups with those computed by forward modeling using the structural model obtained by the dispersion curve inversion (Kolínský and Brokešová, 2007).

Motivation

Looking at geophysical journals in the past years, we see a clear trend to publish studies dealing with huge amount of data processed by automatic routines. In seismology it means to use many records from real or virtual broadband station networks, to process thousands of arrival times, to estimate statistical quantities concerning the data quality, errors and reliability. Surface waves studies also follow this tendency. Automatic dispersion curve estimation allows to use hundreds and thousands of records for surface wave measurement, to average many data to get stable results, to provide a tomography from tens of stations. This approach is logical and defensible.

However, the basic understanding of the elementary physical properties of the surface wave measurement and processing is sometimes missing there. If we processed thousands of records by completely automatic procedures, we would need strong constrains to get reliable dispersion curves. We use a priori conditions to get rid of the "wrong" measurements without the knowledge why these measurements are "wrong". If we do not look at all the data we have measured by the analyst's eye, we cannot be sure our computers have done all the job properly.

There are two reasons why we do not keep the automatic way in our research, or – at least – we do not follow it all the time. Firstly, we would like to concentrate our effort to small datasets with detailed analysis and clear understanding of what had happened right in this record of the given event. Secondly, we are limited by our station and computer equipment and our team dealing with surface waves is smaller compared to the foreign universities. So, by the fact we are not able to provide global or regional studies based on years of records from the stations from all over the world, which may seem to be a disadvantage disqualifying us from the latest trends. We try to keep the advantage of our research by providing detailed analysis of peculiar records from our stations with the aim to small scale research,

short station distances and local events. We use reliable methods, broadband stations and we keep an eye on the latest proceedings in surface wave studies to help us concentrate the effort on problems which have not been solved yet.

The SVAL program, described in this thesis, is intended to process the data record by record with interactive analyst intervention. There is also an option to process the data automatically. However, we are aware of the limits of automatic processing and we do not produce the dispersion curves automatically, since for the dispersion curve compilation, the seismologist personal work is unavoidable. We use the automatic procedures only to estimate the propagation times of surface wavegroups with no assumption where is the "right" dispersion curve. For simple envelope maxima arrival time estimating (see Chapter 1), the analyst work may be spared since the computer is able to do the job properly.

Another goal of the methods developed and described in the presented thesis is to process any records from any source. Studies dealing with a priori assumptions and providing automatic estimation of dispersion curves are properly working when we process the records which the assumptions were made for.

The goal during my PhD studies was to develop a universal tool to process any records from earthquakes of any epicentral distance, the records of any sampling frequency, of any period range and from any instrument. We aimed to develop a procedure which is easily adjustable for all the options we may encounter.

One of the main advantages of presented software is that we get rid of the very restrictive assumption that surface waves have the highest amplitudes in the records. We are able to find surface waves also in records where they have much smaller amplitudes than body waves. We need to analyze records of such a different origin as are the M = 8.3 Kuril Islands earthquake measured by STS2 instrument at the distance of 8.500 km and with sampling frequency of 10 Hz or quarry blasts with magnitude less then 0.0, measured by 1 Hz Lennartz geophone at the distance of 15 km with the sampling frequency of 250 Hz. And the natural way to be able to do this is – to have NO a priori assumptions concerning the results at all.

Another problem one encounters when reading all the papers analyzing surface waves is the amount of methods of processing the data. As a beginner, I was amazed by the fact that the same thing may be done using so many procedures. Moving window filtering in the time domain, multiple filtering in frequency domain, distributions, wavelets... and modifications of all of them. Already during my master studies, I recognized that the power of providing a reliable result is not relying on the use of the latest and most complicated technique with the most impressive name. I support the idea to use the simplest methods with clear and intuitive physical implications and with easily adjustable parameters to be able to understand all the steps, to check them and to accommodate the routines to the needs of the actual record. It does not matter that the base of the technique is 40 years old. Keep in mind that *old* does not always mean *outdated*. So there is no need to think up a new method, it is often sufficient to use properly the ones that have already been invented.

All the above mentioned problems, goals, challenges and implications have their sense only when used with interesting datasets to resolve the structure of some appealing region. In our case, this is the Bohemian Massif, geologically diverse area of Variscan age in Central Europe. Bohemian Massif as a whole, or its parts such as the Western Bohemia region, have been of special interest of geologists and geophysicist for decades. Also surface wave measurements across the Bohemian Massif were provided in the past, but currently no systematic effort to study Bohemian Massif by surface waves is pursued. More than 20 permanent broadband stations are deployed in the Czech Republic and hence the opportunities for group velocity measurements and relative phase velocity estimation from regional and teleseismic events as well as smaller area investigation using quarry blasts are abundant. Surface wave measurements and studies can complement well the ongoing effort to understand the area's Earth crust and upper mantle as well as to estimate the origin of seismic swarms in the Western Bohemia region. Surface waves can provide better constrains for upper parts of the seismic velocity distributions. In case of the Bohemian Massif and teleseismic events, "upper" means crust and upper mantle. In case of quarry blasts, "upper" means the uppermost few kilometers below the surface.

Outline of the thesis

The thesis is written as a self-consistent text. Three generally basic segments of each seismological work – theory, software and measurements with results – are presented in three parts of the text. Part I (Chapters 1 and 2) – *Theory* – describes the theory of surface wave analysis and inversion. It is neither a complete list of procedures nor a detailed description of the techniques, however, the multiple filtering technique is described here closely. Part II (Chapters 3 – 5) – *Applications* – presents three papers with results of surface wave surveys made in the Bohemian Massif. Part III (Chapters 6 and 7) – *Software* – contains detailed descriptions of the SVAL and the PhaseCorr programs.

The thesis follows the way of surface wave studies from seismogram measurements to the velocity distribution estimation. It describes the theoretical background of the measurements and analysis of dispersion curves, the tools and software for processing and the inversion procedure implemented directly in the computer program. We are able to analyze the group velocity dispersion curve and determine the 1D velocity model of the structure. In addition to this, we can also provide phase velocity measurement using two stations. Having either group or phase velocity dispersion curves, we provide surface wave tomography. The application of Rayleigh wave tomography in Chapter 4 was done using the software provided by prof. Tatiana B. Yanovskaya.

The thesis is based on five papers:

- **Kolínský, P., 2004**: Surface wave dispersion curves of Eurasian earthquakes: the SVAL program, *Acta Geodyn. Geomater.*, 1 (134), 165–185.
- **Kolínský, P., 2005**: Seismic velocity model in the vicinity of Eger Rift from dispersion of surface waves, Final report about the Internal start project of the Grant Agency of the Academy of Sciences of the Czech Republic, *Acta Research Reports*, 14, 67–71.
- **Kolínský, P. and Brokešová, J., 2007**: The Western Bohemia uppermost crust shear wave velocities from Love wave dispersion, *Journal of Seismology*, 11, 101–120.
- **Kolínský, P. and Brokešová, J., 2008**: The Western Bohemia uppermost crust Rayleigh wave tomography, *Acta Geodyn. Geomater.*, 5 (149), 5–17.
- **Kolínský, P., Málek, J. and Brokešová, J., 2010**: Shear wave crustal velocity model of the western Bohemian Massif from Love wave phase velocity dispersion, *Journal of Seismology*, in press.

I use two approaches how the papers are implemented in the thesis. Two of them (Kolínský, 2004 and Kolínský, 2005) are disjointed in the text of Part I (Chapters 1 and 2). We do not refer to these papers because the text of the thesis is just based on the previous work and almost no paragraphs or even sentences were kept unchanged from the original papers. Most of the text of Part I is written originally for the thesis.

Three remaining papers (Kolínský and Brokešová 2007, 2008 and Kolínský et al., 2010) are completely included in the thesis. Chapter 3 (Kolínský and Brokešová, 2007), Chapter 4 (Kolínský and Brokešová, 2008) and Chapter 5 (Kolínský et al., 2010) contain all the text, figures, tables and references of the respective papers. The text of the three papers is exactly the same as has been published in the journals, however, the numbering of sections, figures and tables is set according to the thesis and may differ from the numbering originally published. Each figure taken from the papers has its original number given in parenthesis in its caption – this concerns not only the figures from the three fully cited papers but also the figures from Kolínský (2004) and one figure from the Master thesis Kolínský (2003). In Part I, the captions of previously published figures are adjusted for the thesis. However, in Part II, the original captions of all figures are used for all three papers cited there.

The original text of the three cited papers is clearly marked in the text of the thesis – the beginning and the end of each citation is indicated to distinguish the text of the papers from the text written newly for the thesis.

The three fully cited papers in Chapters 3 – 5 are supplemented by additional remarks and figures concerning some of the issues solved during the elaboration of the papers.

The paper by Kolínský and Brokešová (2007) has two parts. It concerns both methodology as well as real data processing. Theoretical sections describe the analysis of surface waves and inversion of dispersion curves. Both analysis and inversion techniques are supplemented by tests. The paper is completely incorporated in Part II – *Applications* – of the thesis, Chapter 3 (Application A).

The paper by Kolínský and Brokešová (2008) concerns the analysis of surface waves from quarry blasts in Western Bohemia. The paper by Kolínský and Brokešová (2007) deals with Love waves, however, the paper by Kolínský and Brokešová (2008) is based on Rayleigh waves. All the text of this paper is completely incorporated in Part II – *Applications* – of the thesis, Chapter 4 (Application B), and supplemented by additional tests of resolution and other remarks. All details concerning this chapter elaboration are introduced at the beginning of the chapter.

The text of the paper by Kolínský et al. (2010, in press), which has been accepted for publication in the Journal of Seismology, is incorporated in Part II – *Applications* – of the thesis, Chapter 5 (Application C). Introduction to this chapter contains a description of issues concerning the elaboration of the topic.

Part III (Chapters 6 and 7) is written newly for the thesis. The topic of Chapter 6 is the same as the topic of Kolínský (2005), however, the description of the SVAL program is completely redesigned and expanded. Chapter 7 is a new description of the previously unpublished PhaseCorr program.

All the work with surface waves was accompanied by permanent development and debugging of the SVAL program (Chapter 6). In the last few years, the program has been tested and used by other

colleagues from the Department of Seismology, Institute of Rock Structure and Mechanics, Academy of Sciences of the Czech Republic. This thesis should serve also as a detailed manual and tutorial to the SVAL program. Other smaller software pieces were also written and one of them – the PhaseCorr program – is also described in this thesis (Chapter 7).

After Part III – *Software*, the *Appendix* follows. The need of an explanatory dictionary emerged few years ago, when I had a seminar lecture at the Department of Geophysics. I have printed a dictionary similar to the one presented here in the thesis to keep in mind the basic terms of surface wave topic. Since then, we added several terms and explanations.

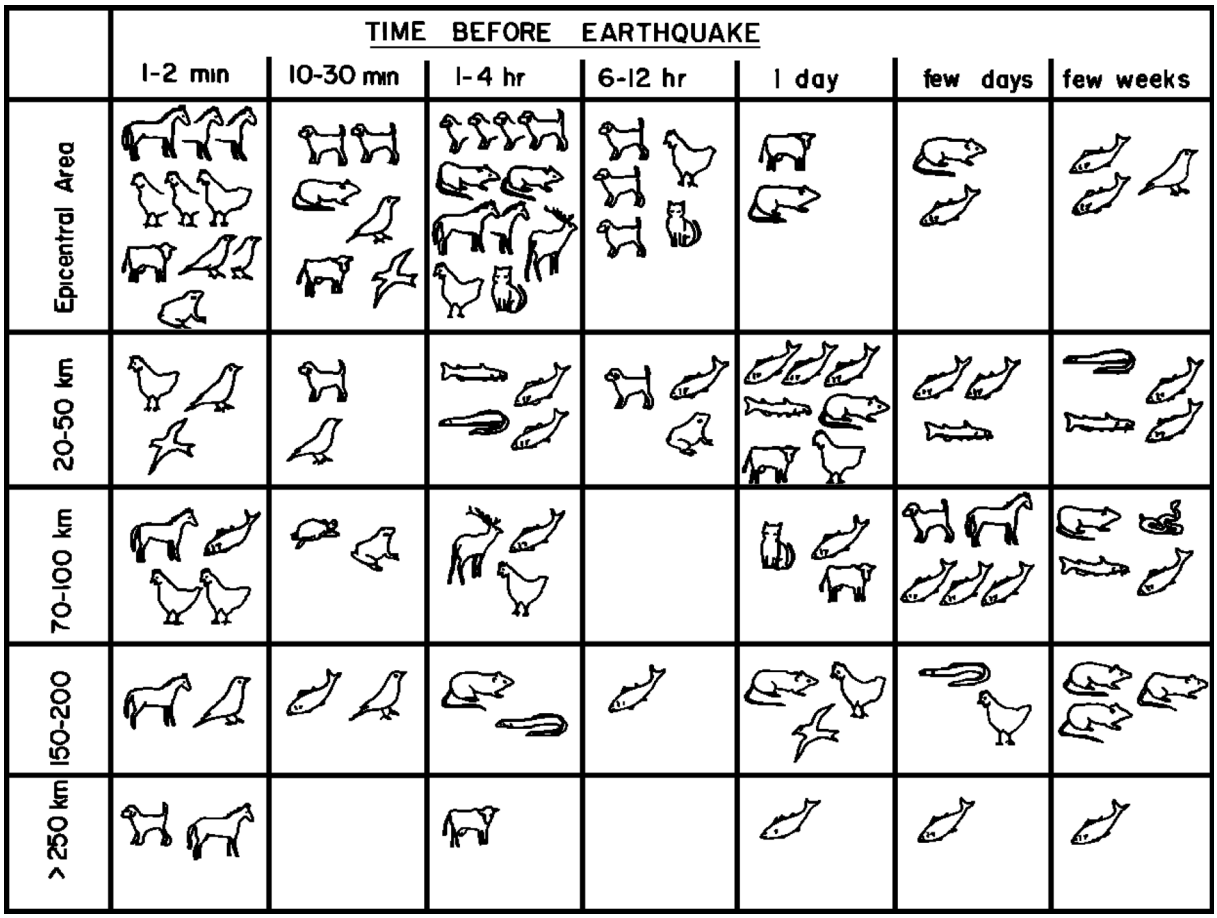
At the end of the thesis, *References* are listed. These are the references taken from the three papers included in Part II – *Applications* – as well as other papers and books mentioned in the rest of the text. They are alphabetically ordered without a notice which paper they originally belonged to. Many of them also belong to several papers at the same time. The way how the papers are referenced in the text is kept coherent throughout the thesis, regardless of the fact the text is taken from the papers or that it is originally written for the thesis.

Attached is CD-ROM with the software executable files and also all source codes. Examples given in Chapter 6 are also copied at the disk with data files needed for practicing them. The disk contains also the text of the thesis in several formats as well as the LaTeX source file and all the figures in *.eps file format. The *readme.txt* file provides information about the disc arrangement.



Part I: Theory





Distribution of animal behavior incidents according to the distance from the epicenter and the time before the main shock of 36 different earthquakes in Europe, Asia, North America and South America. Symbols indicate reports on the following animals: catfish, eels, other fish, frogs, snakes, turtles, sea birds, chickens, other birds, dogs, cats, deer, horses, cows, rats, and mice. Data are nonsystematic and collected from many sources.

Figure reprinted from: Buskirk, R. E., Frohlich, C. and Latham, G. V., 1981: *Unusual animal behavior before earthquakes: A review of possible sensory mechanisms*, Reviews of Geophysics and Space Physics, 19, 247–270, Fig. 1, page 249. Printed with permission kindly provided by Dr. Ruth E. Buskirk.

Chapter 1

Surface wave analysis

1.1 Background research of surface wave analysis methods

In next pages, we give an overview of papers and studies concerning surface wave measurement and analysis. We do not consider this text to be complete in a manner that it includes all the works – there are hundreds of papers dealing with the problem and it is not possible to list them all. However, we present this overview to be complete in a way that it mentions all the features, physical properties and problems concerning surface wave generation, propagation, observation and analysis. An overview of inversion methods for obtaining the structural parameters from surface waves is given in Section 2.1.

Historical remarks (1885 – 1911)

The term *surface waves* was used for the first time by Rayleigh (1885). Using the wave equation he deduced that when a free surface is present above a homogeneous halfspace, a wave with an eliptical particle motion, amplitude decreasing with depth and velocity slower than the shear wave velocity propagates along the surface. Rayleigh did not observe these waves, his paper was a pure physical prediction.

After fifteen years, Oldham (1900) mentioned the work of Rayleigh again. He pointed out that the first two observed phases (so-called *preliminary tremors*) in seismograms could be the longitudinal and shear waves (called *condensational* and *distortional waves* by Oldham) and he also hypothesized that the *large waves* may have been those mentioned by Rayleigh in 1885. However, some discrepancies were observed – the ratio of amplitudes measured at vertical and radial components did not match the one predicted by Rayleigh. Oldham observed also a transverse motion which was not predicted by Rayleigh and so doubts about the basis of the *large waves* persisted. Oldham (1900) also cited the sentence from Rayleigh (1885), which is used as a motto of the presented thesis, saying that the surface waves may have played an important role in earthquakes.

Rayleigh could not predict the transverse surface wave assuming only the homogeneous halfspace, but Oldham observed the transverse motion. These facts were set together by Love (1911), who explained that if the Earth had been covered by a *crust* with physical properties different form those beneath it, the transverse *large waves* would have been explained (see also the motto of the presented thesis). Rayleigh had a simple assumption about the medium complexity and hence predicted only the Rayleigh waves. As opposed to that, Love, who observed the transverse waves, predicted the presence of the Earth crust trying to explain the observed phenomenon. His concept does not match our understanding of the Earth crust exactly. He used the term "crust" in quotation marks since it was only a parable in his book. Love did not use the term *surface waves* at all, instead, he apply the terms *superficial waves* when discussing the physics of the phenomenon and *main shock* or *principal portion* when referencing to the observed wavegroups. He also mentioned the *group velocity* and *wave velocity* (today called *phase velocity*) for the first time. Love (1911) also discussed the basics of the dispersion. He determined the properties of Rayleigh waves propagating in the layer above the halfspace and stated that in this case, Rayleigh waves revealed the dispersion too. Other historical remarks may be found in Dziewonski and Romanowicz (2007).

Early surface wave observations (1934 – 1972)

Since 1930s, surface waves have been observed and described. No advanced computational techniques were invented till the end of 1960s. However, with the first data analysis, also the first attempts to use surface waves for structure estimation were provided.

Carder (1934) use a huge amount of records collected from 1910 and studied nearly 400 events from all over the world. He pointed out the basics of surface waves and he tried to develop the theory of Love waves using more layers. He noticed the differences in propagation of surface waves across continental and oceanic paths. In the Pacific Ocean, he described paths with different wave velocities. He hypothesized some conclusions which would not be assumed as exactly right today, however, his 78-pages work has to be reminded as one of the first to describe the surface wave observations with implications for global structural features.

As opposed to Carder, who studied many earthquake records at one station, Wilson (1940) concentrated at just one event which occurred in South Atlantic and was recorded at 93 stations. Theoretical dispersion curves for Love waves were computed using one or two layers above the halfspace and compared with measurements. Wilson found that the oceanic crust is similar for all oceans and that the surface waves propagated faster in the oceanic structure in comparison with the continental one at given depth. The thickness of the continental crust was estimated to be 30 – 40 km. A similar study was carried out by De Lisle (1941) – in contrary to the Wilson's study, Rayleigh waves were investigated. De Lisle used the earthquake from North Pacific and estimated the Pacific Ocean crust to be 10 km thick.

All latter studies measured the dispersion by reading the time and period of a dominant wave in the seismogram. Compiling many records, they were able to determine a dispersion curve. Wilson and Baykal (1948) proposed another approach – they tried to read several successive waves from the single seismogram. They again used theoretical dispersion curves to be compared with the measured ones. They proposed refractions effects at the ocean-continental boundary observing the difference between the oceanic and continental velocities. The method of estimating the dispersion from the whole wavetrain was further developed in the paper by Ewing and Press (1952). Arrival times of peaks and troughs were read and periods were estimated from the time differences. Group velocity was then estimated for each period. An effect of the water layer on Rayleigh waves was discussed and an occurrence of longer wavetrains at more distant stations revealed.

New surface wave related phenomena were discussed by Evernden (1953 and 1954). He explained the polarization anomalies by different arrival azimuths, he described "packets" of waves in some records and suggested it is due to multipathing (although he did not use this term). He also revealed that the coda is not only a dispersion phenomenon, but that it also occurs due to scattering and refraction. Evernden (1954) also used the tripartite method – the direction of arrival and phase velocity of the wave was measured using stations in a triangular net, assuming plane wave propagation. Similar approach to estimate the backazimuth would be today found when processing the data from seismic arrays. The data of Evernden (1954) were used by Press (1957) to estimate the crustal thickness in the San Francisco Bay region.

In the 50's, the surface waves were intensively studied by many authors. A significant step forward was made when Thomson (1950) and Haskell (1953) introduced their matrices for dispersion curve computation. It was possible to determine theoretical curves for an arbitrary number of layers and researchers were not further limited by one or two layers over a halfspace only. The modified matrix method (Proskuryakova et al., 1981) based on Thomson-Haskell approach is used for the forward computation during the inversion problem solution in the proposed thesis.

Ewing and Press (1954) progressed with measuring Rayleigh waves of 1 to 7 minutes with the aim to reveal properties of the mantle. They processed dispersion curves for several wavegroup passages around the Earth ($R_2 - R_7$). As they obtained a good agreement between various passages and various events, they concluded that such long waves were not influenced by the different crust of the continents and oceans since no refraction and scattering effects were observed. For comparison, theoretical dispersion curves were computed using the method of Haskell (1953), however, only one layer above the halfspace was considered.

Studies using a comparison of measured dispersion with the theoretical one computed using one or two layers above a halfspace continued in papers by Berckhemer (1956) (East Atlantic Ocean) and Press et al. (1956) (Africa).

The main effort was still aimed to the observation and measurement. Olivier and Ewing (1957) observed higher modes of Rayleigh waves for the first time. They discussed the discrepancies of the measured dispersion and particle motion with respect to theoretical predictions given in previous studies. Surprisingly, they did not observe higher modes of Love waves.

One of the first attempts not only to observe the surface waves, but also to synthesize the seismograms, was made by Brune et al. (1960). They related the phase of given spectral components in the origin with the phase velocity along the path and the actual phase measured in the record. If two of the quantities are known, the third one can be computed. They present examples of phase velocity estimation for several events as well as they computed a synthetic seismogram (called *reconstructed* in the paper) for one event using the known velocities. Another example was given by Satô (1960), who used Fourier transform to compute synthetic seismograms (called *numerically reproduced*) using the known phase velocity dispersion

curve. He tested this approach in a laboratory experiment and compared the measured and synthesized seismograms. Fourier transform has been used many times since that paper was published to analyze the phase velocity dispersion in further studies.

Long period Rayleigh waves were observed by Nafe and Brune (1960). They used the two-station method to measure phase velocities between periods of 100 to 400 s of R_3 and R_5 with discussing the uncertainty of dispersion curve estimation using different choice of crest identification. The same problem persists also in our measurement (see Chapter 5) and examples at the end of Chapter 7. Nafe and Brune (1960) solved this uncertainty by comparing measurement from several events at several pairs of stations. The right dispersion curve should agree for all of them. Similar approach – the a priori information about the phase velocity – is used also for the phase velocity determination in this thesis.

The New York-Pennsylvania area was studied by Oliver et al. (1961) using the tripartite method. Rayleigh wave phase velocities were used in combination with the refraction data to reveal layered crustal structure with the low velocity sedimentary layer at the top. The thickness of the crust was determined to be 37 km.

The polar phase shift was introduced both theoretically and experimentally by Brune et al. (1961). They found that when surface wave passed a pole region (180° or 360°), its phase was shifted by $\pi/2$ due to the Earth's circular spherical surface. Thus, when traveling the whole circle, the phase was shifted by π in advance to the original phase. The study suggested to correct the previous phase velocity measurements where waves crossing the epicentral or antipodal regions were used. The great Chilean earthquake of May 22, 1960, provided data to test the theoretical prediction of spherical harmonic wave behavior with respect to normal modes of the Earth.

Long period Rayleigh waves up to 1000 s were observed and matched with the free spheroidal oscillations of the Earth by Brune et al. (1961) using the data of the same Chilean event. Phase and group velocities of both Rayleigh and Love waves between 60 – 700 s were measured using the peak and trough technique and an equivalence of record analysis in terms of standing and progressive waves was shown. The paper presented a synthesis of surface wave and normal mode theories and provided an observational evidence and incorporation of both approaches. Source mechanism of the Chilean earthquake was also verified by the surface wave measurement in the study.

A development of computer facilities enabled to use the matrices of Haskel (1953) for effective dispersion curve computation. Oliver and Dorman (1961) studied oceanic surface waves of period 6 – 8 s. The dispersion curves were very steep in this range and long nearly sinusoidal wavetrains were hence observed. Observed velocities were compared with the theoretical ones computed in models of up to four layers over the halfspace and introducing not only the effect of water layer, but also an influence of the sediments at the bottom of the oceans. The Thomson-Haskell matrices were further reformulated and programmed for transversely isotropic layers by Harkrider and Anderson (1962). They supposed that observed discrepancies between Rayleigh and Love waves may have been explained by anisotropy. Their program could compute dispersion curves for up to 200 layer over a halfspace.

Application of the above mentioned approaches was provided by Kuo et al. (1962). They observed Rayleigh waves in the period range of 20 – 140 s. They used group velocity estimation applying the peak and trough technique as well as determination of phase velocities using one station method assuming the initial phase in the origin and two-station correlation method without a need to assume any initial phase. Only qualitative discussion of the structure was proposed in this paper.

The previously known effect of Earth's rotation on standing waves (normal modes) was extended to show the effect on traveling surface waves by Backus (1962). Love waves were found not to be much affected, but Rayleigh waves making several orbits around the Earth were estimated to change its azimuth of arrival to the station significantly due to the Earth's rotation. It was proposed that these effects could be observed only for periods of hundreds of seconds which are not influenced by the crustal structure. However, this paper consisted of theoretical deductions only and no observations were proposed at all.

A comprehensive paper by Oliver (1962) presented figures compiling at that time known observations of Rayleigh and Love phase and group velocity dispersion curves for continental and oceanic structure in the period range 2 – 3000 s. Phase velocity dispersion curves were marked with points corresponding to free oscillations and so the paper matched surface waves and normal modes together considering them as two different approaches using standing and traveling waves to observe the same features of Earth's motion.

In an innovative study, Dorman and Ewing (1962) presented the numerical inversion procedure to invert the phase velocity dispersion data. Brune and Dorman (1963) not only observed the phase velocities of Love waves in the continental crust of the Canadian shield, but they also complemented fundamental mode surface wave phase measurement with higher mode group velocity dispersion and body waves travel times. They used the inversion technique formulated by Dorman and Ewing (1962) to invert the dispersion data to layered crust and upper mantle velocities down to the depth of 380 km beneath the Canadian shield. Brune and Dorman (1963) found out that as two layers were not sufficient to resolve

inflections of the dispersion curves, three layers would be enough for inverting the periods shorter than 40 s. They also found a low velocity channel in the upper mantle. Theoretical seismograms computed using the phase velocity and the method based on Fourier transform were shown. The latter two studies were prepared at the same time and mutually referred each other. A review of inversion techniques is given in Section 2.1.

The Fourier transform-based phase velocity estimation and least-squares inversion method were further used, for example, in the study of McEvilly (1964), who found that it is not possible to fit the data for both Rayleigh and Love waves by an isotropic model, similarly as it had been proposed by Harkrider and Anderson (1962). Anisotropy suggested by McEvilly was that S_V velocities were 8% lower than S_H. Partial derivatives of Love and Rayleigh wave phase velocities were studied by McEvilly (1964) and conclusions for sensitivity of different layers for both types of waves were presented. Shorter periods and narrower range of them were sensitive for given layer in case of Rayleigh waves.

Surface waves measured by Brune et al. (1963) from both nuclear explosions and earthquakes led to a result that from explosions, the amplitudes of surface waves are much smaller then from earthquakes. Authors studied also radiation patterns and set a new formula for surface wave magnitude M_S. This determination of M_S was based not on the classical 20 s-period wave observation, but instead, on estimating the area under surface wave envelope on the seismogram taking into account the whole spectrum of surface waves observed. Similar results for significantly smaller radiation of surface waves from explosions than from earthquakes of comparable magnitude were also observed by Liebermann et al. (1966) and Liebermann and Pomeroy (1969), who used the discrepancy to distinguish between earthquakes and nuclear explosions.

Toksöz and Ben-Menahem (1963) studied surface waves between 50 – 400 s. Fourier analysis with the polar phase shift introduced was used to estimate dispersion curves from two successive passages of odd or even orders. Thus Toksöz and Ben-Menahem eliminated the uncertainty of the unknown initial phase in the source. They found that phase velocities along similar paths are in agreement, but velocities measured along different paths differed more than to be explained by measurement errors. They deduced that not only the oceanic – continental paths discrepancies existed, but lateral variations of upper mantle beneath both continents and oceans must be present. Toksöz and Ben-Menahem (1963) also discussed the advantages and disadvantages of Fourier transform-based phase velocity determination and compared the errors with those made when using the older direct time domain methods. They mentioned that the use of the Fourier transform method was especially suitable for periods where the group velocity dispersion curve was flat and the record was pulse-like and did not allow for the direct peak and trough estimation.

Attenuation of the mantle was described by Anderson and Archambeau (1964). They pointed out advantages of determining the Q from surface waves than from body waves – the amplitudes of surface waves were much better estimated. Observed variations of Q with period was attributed only to the variation of Q with depth. The authors hypothesized that Q of the material of the Earth was period independent.

Pilant and Knopoff (1964) observed and discussed the "beating" of surface waves. Such anomalies of the dispersive waveforms occurred as an interference phenomena of two waves similar in the frequency content and emerged, for example, as a consequence of two consecutive events which occurred nearly simultaneously in time as a multiple earthquakes.

Greek earthquakes recorded in Finland provided the opportunity for Noponen (1966) to estimate the phase velocities across the south and north part of the Baltic shield using two two-station pairs. Phase velocities were measured by the Fourier transform method and the curves contained significant oscillation. Noponen smoothed these oscillations, however, he did not explain them successfully. He suggested instrumental errors and he excluded the effect of propagation paths since the structure from Greece to Findland is purely continental and no refractions are probable. A comparison of the dispersion curves for Baltic and Canadian shields was provided with discussing the differences. During our phase velocity measurement (Chapter 5) we obtain similar undulations as Noponen (1966) and their origin still remains a bit unclear.

Another study dealing with phase velocities in Europe was made by Knopoff et al. (1966), who investigated the crust and upper mantle beneath the Alps. They used several tripartite arrays and estimated the depth of the Moho discontinuity as well as a shear wave low velocity zone (4.2 km/s) between the depths of 80 – 220 km. They also regionalized the structure for discrete areas covered by the station network and gave the propagation vectors of arriving waves with respect to period for each event. Similarly we estimate the backazimuths in Chapter 5 of this thesis. Tripartite method was further upgraded by Knopoff et al. (1967). They supposed multipartite arrays and estimated the possibilities to reveal lateral heterogeneity of the region in case the propagation direction coincided with some of the legs of the array. If the propagation vector lay in the direction of one of the leg of the tripartite array, phase velocity between the two corresponding stations could be determined accurately. When using the quadrilateral array, and when the propagation vector coincided with the diagonal of such array,

qualitative conclusions about the lateral heterogeneity beneath the array may have been deduced. When the waves propagated along two of the legs in quadrilateral array, two different phase velocities may have been quantitatively determined and the heterogeneity could be described.

An unusual study of Harkrider and Anderson (1966) used surface waves to compute the energy carried by given period or by selected period range. They also estimated the partitioning of energy among the various surface wave modes.

A paper by Toksöz and Anderson (1966) dealing with long period surface waves revealed the distinction between shield and tectonic areas concerning the upper mantle as well as it found an evidence for discontinuities in the depths of 350 and 700 km. The authors measured the phase velocities by two successive passages of the same wave train.

Behavior of surface waves at continental margins was studies by Knopoff and Mal (1967), by Capon (1970) and later by Gregersen and Alsop (1976) and Drake and Bolt (1980). Knopoff and Mal (1967) estimated the effect of inclined Moho on the phases of surface waves. Backscattering and other features were discussed in pure theoretical and deductive manner and no observational examples were given. Capon (1970) studied multipathing of surface waves using the data from Large Aperture Seismic Array (LASA) located in the United States. He found that almost all actual propagation paths could be associated with reflections and refractions at the continental margins and the others may have been deviated by other tectonic features. Gregersen and Alsop (1976) also calculated amplitude ratios of incident and transmitted Love waves across the continent-ocean boundary and tried to compare the numerical results with observation across the continental margin in California. The most discussed phenomenon was the conversion of fundamental mode to higher modes when the crustal thickness changes abruptly. Due to this conversion, energy was spread out and as dominant only the periods for Love waves of 30 s and longer remained, since they were not sensitive to the crustal structure. Drake and Bolt (1980) computed synthetic phase velocities of Love waves incident at the continental margins by the finite element method.

Fundamental and higher mode interference was described by Thatcher and Brune (1969). They found that due to this interference, anomalous velocities of Love waves may have been observed since the fundamental mode was contaminated with the higher modes. They suggested that the discrepancy between the Rayleigh and Love wave dispersion data, observed by many of the above listed studies, and often explained by the anisotropy, may have been not due to anisotropy but rather due to the mode interference. They pointed out the fact that the overlapping of group velocity dispersion curves for fundamental and higher modes is critical for certain period ranges in standard Earth's models, but phase velocity dispersion curves may have stayed separated enough to be distinguished. This applied especially for Love waves since the higher modes of them were excited by the source with much more energy than in the case of Rayleigh waves. Authors also stated that the interference of the modes can, however, produce fluctuations in apparent observed Love wave phase velocity curves. Such fluctuations are also observed in Chapter 5 of this thesis, but since no beating wave packets are present in the time domain of records of the Greek earthquakes, the fluctuations are probably not caused by the mode interference. Thatcher and Brune (1969) also concluded that this anomalous Love wave phase velocities were observed mainly for oceanic paths and for periods longer than 60 s. Neither the path type nor the period range is the case of our study in Chapter 5.

Excitation of Love waves by explosive sources was discussed by Aki and Tsai (1972). They gave a detailed overview of possible model how the S_H waves could originate during the explosions and they presented several evidences that the most probable was the triggering model of a stress release. They observed usually similar amplitudes of Rayleigh waves from repeated explosions, however, the amplitudes of Love waves differed significantly explosion from explosion. In the present thesis, Chapter 3, we present a study (Kolínský and Brokešová, 2007) based on measuring the Love waves generated by quarry blasts. We do not consider the source mechanisms in our paper, but Aki and Tsai (1972) gave possible explanations. However, Love waves observed in the paper by Kolínský and Brokešová (2007) did not emerge as a result of tectonic release – much more probable was that they originated as a result of non-uniform explosion radiation pattern and wave type conversion in the vicinity of the source.

Frequency-time representation and simple models (1969 – 2007)

Until the end of the 60's, surface wave studies had been using the above mentioned analysis methods with only light modifications. In many papers, the disadvantages of the techniques were mentioned and complicated computational problems were postponed with a notice that it would be solved when the methods and computational facilities were available. For example, Toksöz and Ben-Menahem (1963) were aware of the limitations when using the Fourier transform to determine the phases from the record spectra and they explicitly stated the problems.

A major step forward was made when the frequency-time analysis of records was introduced. Dziewonski et al. (1969) described the *multiple filtering technique*, provided tests and a comparison of it with

the previously used peak and trough technique. They establish the frequency-time representation of amplitudes depending on both frequency and time together, what we call a spectrogram today. The Gaussian filters were used for the first time in the latter work and their width was proportional to the central frequency. Landisman at al. (1969) introduced the *moving window technique* for computing the frequency-time representation. Moving window technique is complementary method equivalent to the multiple filtering.

The data analysis of the proposed PhD. thesis uses the multiple filtering technique described by Dziewonski et al. (1969) and separate sections are introduced later in this chapter to describe both the basics of the method as well as the modifications made by the author of the thesis. Further development, improvements and resolving power of the frequency-time analysis was proposed by Levshin et al. (1972).

Based on the frequency-time representation, a method for group velocity measurement avoiding the errors given by the finite filter width was developed by Dziewonski et al. (1972). It was called the *residual dispersion measurement* method. The errors of group velocity determination were large when the dispersion curve was steep. The authors transformed the observed seismograms in such a manner that the group velocity was changing very little with the period. A unit amplitude spectrum of a synthetic seismogram with the theoretical assumed dispersion was computed. The observed seismogram was then correlated with the synthetic one in the spectral domain what produced the differential dispersion curve. Thus, the group velocity dispersion of the observed seismogram was determined. The method worked when the difference between the assumed and observed dispersion was small, however, it was no problem to iterate the steps to achieve the proper dispersion curve determination even in case they did not have any a-priori assumption at the beginning.

Technical details of the frequency-time analysis, width of the filters used for the multiple filtering and the *time variable filtering* proposed for isolation of the dispersed wavetrains from records were discussed by Cara (1973). The time variable filtering is used in its modified version in the proposed PhD thesis for computing the separated wavegroups using the truncated harmonic components of the original record. These separated wavegroups are used to emphasize the mode belonging to the determined dispersion curve when compared with the original seismogram, see next chapters.

Further suggestions to the multiple filtering were made by Canitez (1977), who proposed the *optimal filtering*. His filters had a different shape than the Gaussian filters used in the previous studies. Today, by the term *optimal filtering*, we mean even the Gaussian filters, whose widths are controlled not only by the central frequency, but also by an additional adjustable parameter, as described in the next section of this thesis.

The phase-matched filters were introduced by Herrin and Goforth (1977) to resolve the distinct modes in complicated records where several surface wavegroups came at the same time. These nearly simultaneous arrivals may have been caused, for example, by multipathing or by reflection of surface waves. The phase-matched filtering is similar to the residual dispersion measurement by Dziewonski et al. (1972). Herrin and Goforth (1977) set a theoretical dispersion, computed a synthetic spectrum of the corresponding synthetic record and iteratively matched the phases of this spectrum to the phases of the spectrum of the observed seismogram. When the phases were matched, the amplitudes produced by the correlation of the synthetic and observed spectra were strongly amplified at the time where the recorded surface wave at the given period had its strongest arrival.

Nyman and Landisman (1977) suggested *display-equalized filters* for the frequency-time analysis as a modification of the Gaussian filters. The coefficient controlling the widths of the filters was not depending only on the central period of the filter, but both on the period and group velocity. The resolution of the spectrogram was thus *equalized in display* of the time and frequency axis. Improved time variable filtering was also introduced in the latter work.

Together with the new analysis methods development, the observation of the surface waves continued. Stephens and Isacks (1977) described the properties of S_n arrivals using the theory of normal modes and Love waves in the oceanic structure. Gupta et al. (1977) analyzed records of long period surface waves across the stations in Southeast Asia from the earthquake which occurred near the New Hebrides Islands. Interstation phase velocities were determined using the *impulse response method* for waves as long as several minutes. The *impulse response* was estimated as an inverse Fourier transform of the Fourier transform of the signal at the farther station divided by the Fourier transform of the signal at the nearer station. The upper mantle shear wave low velocity zone was revealed and conclusions concerning the tectonic origin of the region were discussed. Pěč and Novotný (1977) interpreted the L_g and S_a waves as a first higher mode of Love waves.

Wong (1982) studied an effect of topography on the diffraction of Rayleigh waves. Mode conversion from compressional to shear waves and wave amplification were discussed. Similar study was performed by Snieder (1986), who introduced the linearized scattering theory to describe 3D surface wave phase velocity variations caused by topography. He concluded that for fundamental modes of periods between 15 and 30 s, the phase velocity perturbation are of the order of 1% for a mountain 1000 m high. The

topography did not affect phase velocities of higher modes considerably. As a second result, he emphasized the scattering of surface waves itself and proposed to use the theory for studying the surface wave reflections at continental margins. Snider (1988a) further used the scattering theory to analyze regional and teleseismic records of surface waves. His approach was demonstrated on modeling the effect of scattering from earthquakes in Greece and surface wave propagating across Europe with heterogeneities presented by the Alps, Teisseyre-Tornquist zone and the edge of north Africa. Direct and scattered synthetics were compared and the coda emerging due to the scattering was discussed. The later arrivals of surface waves were strongly increased by the scatterers. Snieder (1988b) then used the theory to study the structure beneath Europe and the Mediterranean. Effects of the topography, especially the amplitude amplification, were recently considered also by Savage (2004). The paper gave the theory as well as its demonstration using two real examples of Rayleigh wave amplification caused by mountain ridges in California.

Frequency-time analysis applied to many records at the same time from receivers along a profile was designed by McMechan and Yedlin (1981). They transformed the time-offset representation of the geophone line records to the time-slowness representation. Such a procedure was called slant-stacking. Than, this slant-stack was transformed to the frequency-slowness representation, what was a Fourier transform of the previous time-slowness diagram. Maxima of such a frequency-time distribution indicated the dispersion curve along the receiver line. Such a representation is kind of a spectrogram, but as an input for the transform, many records were used instead of single seismogram which had been used traditionally.

With higher observational and analysis accuracy, the theory of error estimation becomes important. Feng and Teng (1983) tested several implementation of the frequency-time representations (constant relative bandwidth Gaussian multiple filters, display-equalized filters and others). They provided an error analysis of the techniques and proposed a new *matched-filter frequency-time analysis* based on modification of the residual dispersion measurement. The new technique was based on the knowledge of the problems concerning the older methods and was tested as well. Wielandt and Schenk (1983) studied the error of estimation of the signal phase using the Fourier spectra. They studied both the moving window and multiple filtering techniques and approximated the phase error using the Taylor expansion. They concluded that the error may have been significant for periods over 240 s and that it is larger when smaller number of periods are used in the time domain during the filtration. The *frequency variable filters* were proposed by Russell et al. (1988) to improve the resolution accuracy of filtration in the frequency domain. Their filters combined the advantages of both time variable filters and phase matched filters developed in older studies.

The *Gaussian beam method*, developed by Keller and Streifer (1971) and Deschamps (1971), was applied for forward modeling of surface waves by Yomogida and Aki (1985). Laterally heterogeneous structure was used for the computation and hence it would be possible to use the method for observing structural anomalies by inverting the observed waveforms using this forward computation method.

When both group and phase velocity dispersion curves were available, their mutual relation could be used for smoothing the curves using polynomial expansion functions as presented by Dean (1986). Such a simultaneous analysis resulted in decreased errors of surface wave dispersion determination.

Surface waves concerned not only regional and global scales, they were used also as a prospection tool. Gabriels et al. (1987) provided an experiment with 288 geophones line deployed in sediments and measured Rayleigh waves generated by an impact source. Using the f-k analysis they identified six higher modes of surface waves and obtained a layered structure down to the depth of 50 m.

Murphy and Shan (1988) studied the local structure conditions influencing Rayleigh waves induced by the atmospheric explosions. They found out that amplitude, dominant frequency and duration of the wavegroups are strongly influenced by to geology beneath the station. Synthetic records were modeled and it was found that when the velocity contrast between the two upper layers increases, the wavetrain becomes longer. When the shear wave velocity decreases in the first layer, the amplitude of the surface wavegroup becomes higher. They also stated an important experimental relation connecting the depth of the first significant discontinuity, the shear wave velocity above this discontinuity and the site characteristic frequency of the observed group velocity. When the shear wave velocity is around the value of 2.3 km/s, then the depth in kilometers corresponds to the period of the Airy phase in seconds. The effects of sedimentary layer on surface wave propagation were studied by Yamanaka et al. (1989). Multiple filtering analysis was used to process the seismograms from western Nagano earthquake, 1984, and the trapping of surface waves in low-velocity upper layers was confirmed. The authors used the structure known from 2D seismic surveys and modeled the surface waves by finite difference method.

A comprehensive book concerning all the knowledge about surface waves summarizing the theory up to date edited by Keilis-Borok (1989) presented chapters devoted to main topics of surface wave measurement and analysis. The basics of the theory of propagation of surface waves in vertically inhomogeneous media as well as in the media of weak lateral inhomogeneity was given. Matrix method and ray tracing



were explained as a computational tools for theoretical dispersion curves determination. The chapter describing the observation of surface waves is of particular interest and the paragraphs concerning the frequency-time analysis by Levshin et al. (1989) proposed several important methods of increasing the accuracy of the multiple filtering technique. The most important was the instantaneous period estimation, which solved the problem with asymmetric spectrum weighted by the symmetric Gaussian filter. As the product of the latter two functions was again asymmetric, the prevailing frequency of the filtered spectra did not correspond to the central frequency of the filter. The central frequency could not be used to plot the group velocity in the period-velocity diagram, instead, the instantaneous period computed as an arctangent of the ratio of imaginary and real parts of the analytical signal corresponding to each filtered quasimonochromatic component was proposed to be used. The quasimonochromatic signals were obtained as an inverse Fourier transform of the filtered spectra. This approach is used in all dispersion curve estimations throughout the presented PhD thesis.

Dispersion curves of group velocity obtained by the two-station method and measured beneath Hawai'i were compared with the age-dependent dispersion curves for the ocean lithosphere by Woods et al. (1991). The implications for lithospheric thickness suggested that the Hawai'ian swell is rather older than formerly predicted.

Surface wave propagation and its peculiarities across Eurasia were studied by Levshin et al. (1992). Group velocities as well as differential phase velocities were determined for 35 events for period range of 15 – 300 s. Polarization was analyzed and the anomalies were explained by scattering and refraction due to lateral inhomogeneities and boundaries. The theory of multiple filtering was again referenced there and the dependence of the filter widths on period was studied to provide an accurate frequency-time analysis. Similar relation between the filter width coefficient and central period is used also in the presented PhD thesis. Another study dealing with polarization anomalies of surface waves was published by Levshin et al. (1994). They provided many measurements of waves propagating across Eurasia, confirmed the systematic anomalies of paths deviations and the reproducibility of these measurements. The use of such smooth varying polarization anomalies and their dependence on frequency was proposed to be useful for structural studies. Kocaoglu and Long (1993) summarized the properties of frequency-time analysis methods for estimation of group velocities, discussing mainly the moving window and multiple filtering techniques. They also mentioned the *moving window autoregressive spectral estimation*, the *Wigner distribution* and the *Choi-Williams distribution* and their advantages and disadvantages with respect to the classical techniques.

Wielandt (1993) mentioned the fundamental difference between the phase velocity of the wave and the phase velocity of the medium in which the wave propagates. In case of plane wave, this difference vanished. However, in real cases, the two phase velocities should be noticed and Wielandt gave a relation between them. The same was valid also for the wavenumber. The conversion from one to the other required the knowledge of the local amplitude derivation in space. Geometry of the wavefield influencing the discrepancy was discussed and station locations to reveal the true phase velocity were proposed. However, in reality, we almost never have six stations close to each other to use the designed geometry. Wielandt also mentioned that in case of interference of similar waves from different direction, he obtained a wavefield, which may have been explained by lateral inhomogeneity despite the fact that the interference occurred in the homogeneous medium. This paper called in question all the two-station method measurements and the phase velocity estimations which did not take this effect into account, what was the case of almost all of them. However, even in later works, the author of this thesis did not find any remarks to this problem. The only exception is the paper by Sebe et al. (2009), who mentioned the work of Wielandt (1993) with the remark that in their case, the waves are of a planar shape and the problems mentioned by Wielandt (1993) did not affect their results.

The behavior of surface waves beneath the Mexico City was given by Chávez-García et al. (1995). Strong ground motion from the $M_s = 8.1$ earthquake, September 1985, was analyzed to confirm the structure beneath the central Mexico. The amplification of the surface waves at the edges of sedimentary basin was revealed by observing short period phase velocities of surface waves generated by refraction experiment. Das and Nolet (1995) presented a waveform-fitting method to estimate the Moho depth using computation of many surface wave modes for regional earthquakes in the period range 12.5 – 125 s.

A novel *multitaper dual-frequency method* to analyze the dispersive records was proposed by Mellors at al. (1998). Many advantages were described in the paper concerning the correct phase estimation, higher modes and multipathing identification. However, the benefits of the technique are disputable and this method was not used widely in later works, probably also due to the computational complexity. A different approach to surface waves in laboratory conditions was designed by Park et al. (1998), who described a method for estimation of multimode dispersion curves from a shot gather that may have been useful in near surface seismic prospecting. Frequency-wavenumber analysis of surface waves was studied by Foti et al. (2000) with respect to shallow seismic engineering using hundreds of geophones.

In the 90's, the question of errors of group velocity determination using the multiple filtering again



arose and Shapiro and Singh (1999) provided a procedure for its correction. The authors mentioned especially the problem with the estimation of the period of the given filter for strongly decreasing amplitudes of long periods. The paper concerned the same problem as described by Levshin et al. (1989). The actual period of the filtered spectra does not match the central frequency. In this thesis, we use the instantaneous period estimation suggested by Levshin et al (1989). Shapiro and Singh (1999) proposed another approach using the *centroid frequency* which was suitable when several frequency-time spectrograms were stacked and the instantaneous period estimation was not possible.

A textbook by Novotný (1999) explained a basic theory of dispersive surface wave propagation as well as analytical matrix method computation based on modified Haskell's approach and published earlier by Proskuryakova et al. (1981).

Raykova and Nikolova (2000) used the multiple filtering technique to estimate group velocities of Rayleigh waves crossing the Balkan Peninsula. Many 1D shear wave velocity models for individual paths were estimated. Raykova and Nikolova (2003) proposed a similar study using both Rayleigh and Love waves and including the anisotropy into account. Shear wave velocities determined using Love wave dispersion curves revealed higher values than those obtained using Rayleigh waves. The anisotropy was estimated to reach 12% and the discrepancy between Love and Rayleigh waves was also assigned to lateral heterogeneity.

Isse at al. (2000) measured phase vleocities across the Philippine Sea by the two station method. Many paths were used, Fresnel zones estimated and the difference of spectral phases used to measure the phase velocities. A-priori estimates of long-period velocities were used to select the proper number of wavelengths between the two stations for each measurement. Love wave group velocities from events in Turkey, 1999, were measured in western Greece and inverted for layered models of the crust by Novotný et al. (2001).

A method for estimating the shear wave velocities for shallow oil prospection from marine multicomponent records was presented by Ritzwoller and Levshin (2002). Fundamental and higher modes together with P and S wave traveltimes were used to determine shear wave velocity as well as v_p/v_s ratio of upper 100 m.

A special *roller-coaster algorithm* was developed for higher mode phase velocity estimation by Beucler et al. (2003). This was an inversion technique which compared the recorded and synthetic seismogram spectra and minimized the misfit function between them at two steps – first, it found a large scale variation over the model space and then it looked for the solution in the local variations of the misfit function. The problems of higher modes were also discussed by Zhang and Chan (2003) who studied the effects of dispersion curve sampling, frequency range, misidentified mode number and cross-mode data mixing on the inverted shear wave velocity results.

An extensive study of higher modes in shallow seismic was given by Forbriger (2003a and 2003b). He described a method for estimating the velocity of higher modes of short period surface waves by stacking the spectrograms shifted with the velocity of searched mode. He showed that it was difficult to distinguish between many higher modes and he proposed a method to invert the whole spectrogram with eliminating the need to separate the distinct modes. A summary of surface waves use in the near surface seismic prospecting and their properties, measurement and higher modes problems were presented by Xia et al. (2004).

Baker and Stevens (2004) proposed a new method for computing the polarization of surface waves and its accuracy estimates. It was useful for associating the records with the events since it allowed to find the true backazimuths of propagation. Wijk and Levshin (2004) mentioned that effects of scatterers were frequency dependent and hence, each scatterer worked as a source of dispersion which may have been confused with a layered-structure dispersion and wrong estimate might have been done if the effects of scattering had not been taken into account.

Mitra at al. (2006) used the classical two-station technique for measuring phase velocities of Rayleigh waves. They used the *transfer function method*, when the seismogram at the farther station was expressed as a convolution of the seismogram at the nearer station with a filter describing the properties of the interstation structure. Hence, the dispersion curves were not measured directly, but they were a product of the inversion. They measured three events records using several station pairs and as a result, they obtained one dispersion curve characterizing the South Indian Shield. This curve was then inverted for the shear wave velocity down to the depth of 400 km.

Multiple filtering was used for group velocity dispersion curve measurement by Wang et al. (2006). The analysis was then refined using the phase-matched filtering. The paper was based on observation of surface waves in coastal plain of Taiwan from one of the aftershocks ($M = 6.2$) of the Chi-Chi earthquake, 1999. Surface waves were found to be of the highest amplitudes in the middle of the plain, what was explained by the interference of the propagating surface waves and surface waves generated by a conversion from P and S waves in the edges of the plain. The location of the strongest surface wave motion was period dependent and did not depend on specific local geological conditions. Again, the multiple filtering

was used by López-Pineda et al. (2007) for measuring the surface waves in Baja California and Mexico. Shear wave structure and crustal thickness were estimated with implications for tectonic origin of the region.

Forward modeling of teleseismic surface waves around the period of 150 s was provided by Ferreira and Woodhouse (2007) in order to study the effects of the source and propagation and station conditions. Different structural models with geometrical propagation along great circles or with refraction at lateral heterogeneities were shown. For the phase anomalies, the propagation terms were the most important for both Love and Rayleigh waves. In case of amplitudes, for Rayleigh waves, the source and propagations terms were both significant, however, local station conditions had no considerable effect on Rayleigh wave amplitudes. For the Love waves, only the term of propagation was dominant and both the source and stations effects were negligible. Love waves exhibited larger azimuthal variations from the great circle than Rayleigh waves. The authors concluded that the phase anomalies of surface waves could be explained by laterally inhomogeneous structure. However, they were not able to interpret the amplitude variations either using the 1D PREM or the 3D tomographic structures.

Theoretical and comprehensive overview of all possible techniques for frequency-time representation was given in the work by Kristeková (2006). Her thesis gave an introduction of the dispersive signals, their analysis, decomposition and synthesis, uncertainty principle and other phenomena of the signal processing. The methods of moving window, wavelet transformations, Wigner distribution and several other techniques of estimating the properties in the frequency and time domains together were introduced and compared. A modified *matching pursuit decomposition method* was developed. Although the work contained many techniques and examples, the reliability of their use remained uncertain due to complicated numerical solutions or even theoretical disadvantages of the particular approaches.

For the frequency-time representation of the dispersive signals, the classical method of multiple filtering unambiguously prevails in the literature concerning surface waves.

Mode coupling in 3D anisotropic structures (1998 – 2007)

Anisotropy and heterogeneity play an important role in measuring and modeling surface waves since the mode coupling occurs. By mode coupling, an interaction between the same frequency of the fundamental and higher modes of both Love and Rayleigh waves is understand.

Kobayashi and Nakanishi (1998) observed Rayleigh-to-Love wave conversion at Japanese records of events from Oregon and California, U. S. Quasi-Love waves were observed at the vertical components of the records and distinquished from the refracted Love waves at the radial components. From the apparent group velocity differences, the origin of quasi-Love waves was localized to be around the Aleutian and Kuril trench. It was hypothesized that the conversion occurred due to the lateral heterogeneity or due to the lateral variations of azimuthal anisotropy.

Maupin (2001) studied theoretically the refraction and scattering of surface waves in heterogeneous structures. Illustrative figures explaining what happened when surface waves came, for example, to a vertically oriented cylinder of a diameter of 36 km with different properties than the surrounding medium, were given. Due to the anisotropy, the polarization of Love and Rayleigh waves was deviated and hence one type of the waves was converted to the other. Theoretical examples using realistic values of anisotropy and heterogeneity of the mantle were used for computing the wavefield (amplitude and phase) maps. The paper concluded that in isotropic medium, heterogeneities influenced amplitudes and phases of the surface waves. In anisotropic medium, also the polarization was changed.

Another paper by Maupin (2002) tried to solve the question, why the structure inverted using Love waves was generally faster than the one inverted from Rayleigh waves. Anisotropy played a role, however, the discrepancy was much bigger than the anisotropy could cause. Possible explanation was that it was due to the heterogeneity, which influenced both types of waves in a different way and hence, apparently, Love waves propagated faster in the same medium than Rayleigh waves. Synthetic examples were given and the small changes of phases were demonstrated. The variation of observed amplitudes, however, was much larger. Even weak heterogeneity in the scale of hundreds of kilometers could cause an increase or decrease of amplitudes 3 to 6 times. The mutual influencing of modes of Love and Rayleigh waves and their coupling did not seem to be significant in terms of phase velocity variations. The study concluded that the Love-Rayleigh discrepancy in the order of several percent could not be explained by weak heterogeneities and it was necessary to look for other explanation.

Application of the above mentioned theoretical approaches was used to infer the anisotropy beneath the Kerguelen hot spot by Pettersen and Maupin (2002). Polarization anomalies of Rayleigh waves could not be explained by either off-great circle propagation or by heterogeneities in the vicinity of the hot spot. Earthquakes which occurred in the Indian ocean were selected to ensure purely oceanic paths and Rayleigh waves on transverse component were searched using the frequency-time analysis. A comparison of Rayleigh waves on transverse and radial components was plotted with respect to azimuth of propagation and special direction of significant anomaly was revealed. Station in front of the hot spot revealed no

polarization anomaly and station behind it did, so, the anomaly had to emerge right beneath the hot spot. The anisotropy was the only possible explanation for the observed polarization discrepancies.

A comprehensive theory was given in Maupin (2007). The book gave an explanation of synthetic seismograms computation using mode coupling theory. In the homogeneous medium, surface waves were given by decoupled vertical and horizontal components. In the heterogeneous medium, the modes were coupled. Two basic approaches were described: The first one was based on local 1D sensitivity kernels describing the coupling along the surface wave paths. The other approach relied on having a reference model and local perturbations were introduced. Refraction, reflection and mode conversion on sharp discontinuities was studied. The difficulty emerged due to the different velocity of each mode. When one mode was converted to the other, the angles of reflection and refraction differed too. Examples based on continental margins mode conversion were also mentioned and theoretically explained. The effect of these discontinuities was much stronger considering Love waves, which were converted to a set of higher modes, while Rayleigh waves crossed the margins without any significant conversion. Focusing and defocusing effects on amplitudes of surface waves propagating in 3D structures were also mentioned.

These approaches explained theoretically the physics of the mode coupling, which had been observed and discussed in last decades. It also tried to propose a method for computing synthetics for possible inversion of the observed wavefields. However, the necessity of broadband seismic arrays emerged since by single station, the needed properties of surface waves could not be inferred.

Surface waves, source mechanisms and nuclear explosions (1981 – 2006)

Application of surface waves as a tool for source mechanism estimation was proposed by Romanowicz (1981), who studied shallow earthquakes in Central Asia, determined their depths and mechanisms and found regionalized phase velocity variations between the sources and stations. Bukchin (1995) used teleseismic surface wave amplitude spectra to reveal the moment tensor of the Georgian earthquake, 1991. Much later, Lasserre et al. (2001) determined the source parameters of the Tibetan earthquakes, 1995 and 1996, using similar method. Together with the P wave polarization, the method enabled to estimate the source mechanisms of smaller earthquakes than it was possible using only the body waves.

The general behavior of surface waves propagating in complicated structures was studied by Langston (1989). He used the records of underground nuclear explosions in the western United States and he revealed the scattering effects, attenuation and resultant exponential decay of coda from the Rayleigh waves of periods 5 and 10 s. Three mutually incompatible but possible models of coda behavior were proposed: first, Rayleigh waves were attenuated by the single scatterers, second, anelastic attenuation was possible and third, the energy of Rayleigh waves was converted into the body waves at the scatterers. Nuclear explosions as a source of surface waves were also studied by Levshin and Ritzwoller (1995) and compared with records of earthquakes from the same region to discuss to the problem of discriminating between the two. The authors revealed that the group velocities from earthquakes and explosions agreed well, however, the spectral amplitudes differed considerable since earthquake record spectra contained longer periods than the spectra of records obtained from explosions. Higher modes were not observed from explosions but they were measured at records from earthquakes. The authors also stated that large Love waves were generated by the nuclear explosions at Lop Nor test site, what indicated a significant tectonic release.

Another study processing the data from earthquakes and nuclear explosions near the Lop Nor test site in China, was the paper by Bukchin et al. (2001). Moment tensors were estimated for several earthquakes and explosions using the amplitude spectra of surface waves and the difference in the ratio between the isotropic and nonisotropic component of the moment tensor was used to discriminate between the tectonic and explosive sources. An automated detection algorithm for surface waves of range between 8 – 40 s was developed by Levshin and Ritzwoller (2001), who used a-priori information of group velocities in Asia and then allowed the procedure to scan the records for extracting small amplitude surface waves. The algorithm was tested again using the earthquakes and nuclear explosions near the Chinese Lop Nor test site and was intended as a tool for automatic identification of small surface wavegroups that could indicate nuclear explosions. Phase-matched or anti-dispersion filters were used to compress the signal, then the records were cleaned from noise and again redispersed by applying the inverse of the phase-matched filter.

Rupture directivity of the great Alaskan earthquake of November 3, 2002, was observed by Velasco et al. (2002) in terms of significant amplitude anomalies of Love waves. Dominant Love waves were observed as far as 3000 km from the epicenter along a great circle parallel to the Denali fault and a triggering effect on smaller events, which occurred right at the time when the surface waves from the Alaska propagated across their epicenters, was evidenced. Ammon et al. (2006) described a method for rapid estimation of the source parameters of the great earthquakes using only few surface wave measurements and their directivity effects. The advantage of the method was that it could be used fast during tens of minutes after the earthquake and hence it could provide information about potential tsunami warning. The technique was demonstrated using records of Rayleigh waves from the 2004 Sumatra-Andaman earthquake.

To detect short period Rayleigh waves in the range around 2.0 s, an automatic procedure was developed by Tibuleac and Britton (2006). It was aimed at the recognition of smaller shallow events, explosions and mining activities. The innovation was that the surface waves were not searched after the events had been found by some other detection method, but the algorithm worked in an opposite manner. The continuous record was scanned and the Rayleigh wavegroups were identified without the knowledge of the particular events. Polarization analysis, backazimuth estimation and event localization were also implemented.

Similarly, Ekström (2006) also suggested that surface waves may have been used for detection and location of earthquakes. He proposed an idea that since the noise was low in the period range of 30 – 500 s, even small surface waves from weak events could be recognized. A hypothesis that some of the earthquakes may have had such unusual source properties that we are not able to detect them using standard body-wave procedures was set and a method for detecting them using the surface waves was presented. A-priori information about 2D phase velocity distribution was needed for the location of events. The method was applied to 11 years of data and 93 % of events contained in standard catalogues were revealed. When constraining the results for events shallower than 70 km, even 98 % were found. What was more important, the method was able to found more than 1000 events which had not been included in standard catalogues. It worked for events with magnitude > 4.6.

Surface waves combined with other observables (2004 – 2010)

Qualitatively new approach was demonstrated by Shapiro et al. (2004), who constrained the structure of the Canadian Shield using the surface waves and thermodynamic observables such as heat flow and the temperature of the upper mantle. Yoshida and Suetsugu (2004) studied the Pitcairn hot spot using the phase velocities of Rayleigh waves to prove the hypothesis that the lithosphere is thinned by the hot spot heating. Two-station method was used for determination of the phase velocities. It is another example of the use of surface waves in connection with thermal properties of the Earth, however, as opposed to Shapiro et al. (2004), who used the thermal observables to constrain the inversion, Yoshida and Suetsugu (2004) used the surface waves to reveal the thermal properties and the lithospheric thickness of the hot spot. Khan et al. (2009) determined mantle thermal state and anisotropic structure using observations of fundamental and higher modes of surface waves in global scale.

Low-frequency tremors were correlated with surface waves by Miyazawa and Brodsky (2008). Envelopes of the tremors coincided with envelopes of Rayleigh waves. Hypothesis of the tremors being triggered by passing surface waves was proposed and demonstrated by observing the surface waves and tremors after the 2004 Sumatra-Andaman earthquake. The same great earthquake was observed by the high-rate GPS station in North America and Love wave dispersion curves were estimated from the absolute displacement by Davis and Smalley (2009). Another great event, the 2008 Wenchuan earthquake, Sichuan, China, served as a source of observations of water level changes caused not only by Rayleigh waves, what had been already described, but also by shear and Love waves as far as 2000 km away, as described by Wang et al. (2009).

Combination of receiver functions and surface wave dispersion measurement becomes an efficient tool how to constrain both the average velocity information with smoothly varying parameters (dispersion measurement) and sharp velocity contrasts (receiver functions) for the crust in the same time. Lawrence and Wiens (2004) used receiver function in a joint inversion with Rayleigh wave phase velocities. Their inversion was more unique and needed less a priori constrains than separate inversion of only one of the observables. Both the structural velocities as well as interfaces were determined successfully and the method was than applied to the data yielding a regional model of Patagonia. Similar study was performed by Chang et al. (2004) who determined the crustal structure of southern Korea and by An and Assumpção (2004) who studied the structure beneath the Paraná Basin, Brazil. Surface wave tomography and receiver functions were than used by Juliá et al. (2008) also to determine the structure of the Paraná Basin. P wave receiver functions and Rayleigh wave group velocities were jointly inverted by Julia et al. (2009) to recover the crust and upper mantle structure of the Indian shield. Dispersion curves were used to constrain the background absolute values of the shear wave velocities and receiver function measurement provided detailed variations of the resultant models.

Surface wave dispersion measurement and tomographic maps were inverted jointly with the data from gravity measurements for the central Asia sedimentary basins to constrain the shear wave velocity distribution by Maceira and Ammon (2009).

Rotational seismology started to play its role in the surface wave analysis as well. Kurrle et al. (2010) showed that since for plane waves, the horizontal phase velocity could be determined as a ratio between the rotation rate around the vertical axis and the transverse acceleration, Love wave fundamental mode could be detected and its phase velocity dispersion curve revealed by measurement of these quantities. The method was confirmed both by synthetic experiment as well as real measurement. The determined phase velocity dispersion curve contained information about the local structure beneath the station, however, direct inversion of the curve to the structural properties did not seem to be feasible due to the higher modes contamination.

Surface wave tomography (1982 – 2009)

Surface wave tomography dominates the literature concerning the long period observations and global Earth models in last three decades. Generally, all the methods are based on measuring 1D characteristic along the surface wave paths and on following assemblage of the information in 2D and 3D models.

The first method estimating the 1D characteristic along the surface wave path relies on measuring group or phase velocity dispersion curves, complemented by finite frequency effects and influence zones in advanced studies. Then, these path-averaged group or phase velocities are inverted into 2D velocity maps. Local dispersion curves can be extracted if many maps for many periods are computed. These local dispersion curves could be inverted into 1D shear wave structure. Hence, a 3D image of the Earth structure could be estimated.

The second method again produces averaged characteristic along the source-receiver path, but in this case, waveforms of surface waves including higher modes are directly inverted into 1D shear wave velocity model along the path. Then, these shear wave models are assembled into 3D image of the crust and upper mantle.

The surface wave tomography with 2D distribution of velocities was proposed, for example, by Ditmar and Yanovskaya (1987) and by Yanovskaya and Ditmar (1990). No regionalization was implemented, instead, basis functions were used as an approximation of the ray geometry to represent a distribution of velocities in 2D plane. The basis functions were set on a-priori assumptions and they also respected the ray coverage so that the results was not dependent on them and was fully given by the velocities measured along the rays. Yanovskaya et al. (1998) applied the method for tomography of the Black Sea. 111 paths for Rayleigh waves and 114 paths for Love waves were used. The 2D maps were than used for compiling local dispersion curves, which were further inverted into 1D shear wave velocity models. These models were then assembled into two 2D structural profiles crossing the region. Structural inversion was made separately for Love and Rayleigh and from the discrepancy, the anisotropy of about 9% was estimated.

Similar approach with computing the 2D maps on a sphere was provided by Yanovskaya et al. (2000) who covered the whole Eurasia with a resolution of $10^o \times 10^o$. Yanovkaya and Kozhevnikov (2003) studied also the broad region of Asia. 2D maps were than inverted for 1D local structures. In Chapter 4, we use the method described in the latter papers and the software provided by prof. Tatiana B. Yanovskaya which uses the procedures. The procedure does not use any a priori regionalization of the studied area, the resolution depend only on the ray coverage. 2D distribution of velocities is determined in a grid of nodes, with an error estimate for each node. As the number of nodes is set higher, the velocity in each node is determined by lower number of raypaths and hence the error is higher. This approach differs from the tomography inversions procedures used by some other authors. A summary of the method and detailed discussion with implication for the Iberian peninsula surface wave tomography were given by Sabadell et al. (1997).

Another possibility how to set an inversion of larger areas is to use spherical harmonic expansions. One of the first attempts to determine a global distribution of surface waves group velocities was provided by Nakanishi and Anderson (1982). They observed Rayleigh waves of periods between 100 and 300 s. The measured velocities were expressed in terms of spherical harmonics with no assumptions of regionalization of the Earth. Woodhouse and Dziewonski (1984) proposed global models of velocity distribution based on transverse isotropic approach with inverting waveforms (not only the surface waves) of many events into spherical harmonics. Montagner and Tanimoto (1990) used a tomographic method to determine the azimuthal anisotropy in the global scale using squares of size of $20^o \times 20^o$. Further, Montagner and Tanimoto (1991) used spherical harmonics and they also involved the azimuthal anisotropy into account to provide a global tomographic model of the upper mantle using thousands of surface wave records. Spherical harmonics were also used by Durek et al. (1993) to constrain global attenuation using the surface wave amplitudes. A similar study was made by Romanowicz (1995), who also estimated global attenuation distribution using an inversion without any a priori regionalization.

Phase velocities of Rayleigh waves, measured using the single station method, were used to reveal the upper mantle structure of Tibet by Bourjot and Romanowicz (1992). A lateral resolution of heterogeneities at the scale of 300 km was achieved with no a priori assumptions. Global phase velocity distribution was studied by Ekström et al. (1997). Again, single station phase velocity method was implemented using the phase-matched filters and residual dispersion minimization. Spherical harmonics up to the degree 40 were than used for inversion. Muyzert and Snieder (1996) studied the effects of the source mechanism on single-station phase velocity observations and pointed out that a good source model was requested when using this method.

Laske and Masters (1996) provided global phase velocity distribution maps and they added also amplitude and polarization data into inversion, because former studies had mutually disagreed and new constrains had to be found. Spherical harmonics were again used as a base for the inversion. Similarly, Trampert and Woodhouse (1996) also presented global phase velocities. Their resolution of heterogeneites between 500 and 850 km was achieved by adding more major arc velocity measurements. As the pre-

vious studies, Zhang and Lay (1996) also implemented spherical harmonics, however, they used hybrid parametrization and performed a block model inversion to recover the phase velocity distribution around the globe. Tens of thousands seismograms were processed.

Regional study of the Indian Ocean was proposed by Debayle and Lévêque (1997). Their tomography is not based on dispersion measurement. The 1D path averaged velocities were estimated using the waveform inversion designed to match the seismograms including higher modes. Records of events with close epicenters were clustered and the same propagation paths were then assumed. A good correlation of the results with tectonic features in the region was observed. Another regional study was made by Lebedev at al. (1997), who estimated the upper mantle structure beneath the Philippine Sea using also the waveform inversion including body and surface waves. In the latter study, no velocity maps were computed, the seismograms were directly inverted into 1D average shear wave velocity model along each path. Then, a 3D model was assembled. High-velocity subductions and low-velocity volcanic regions were revealed.

Meier et al. (1997) proposed a new method which took into account the scattering of surface waves. Mode conversion was considered and Fresnel zones for surface waves were computed. This *diffraction tomography* was demonstrated on the data from the Philippine Sea.

En extensive Eurasian surface wave tomographic study was published by Ritzwoller and Levshin (1998). The approach of Yanovskaya and Ditmar (1990) was used with no a priori parametrization of the studied area. Maps of group velocities of broad period range from 20 to 200 s were provided, checkerboard tests were made and comparison with former studies presented. Central Asia tectonics was described by Levshin et al. (1997) using the same approach. Curtis et al. (1998) were also interested in Eurasia tectonics, but they used the phase velocity measurements to provide the tomographic study. Another important difference to former studies was that they used triangular cell geometry and resolved the phase velocity for each cell. Similar approach with squared blocks was used for the preliminary Western Bohemia tomography, as described in the introduction to Chapter 4.

Regional surface wave anisotropic tomographic studies continued by describing the Atlantic Ocean by Silveira et al. (1998), by Silveira and Stutzmann (2002), and by revealing the tectonic features beneath Tibet by Griot et al. (1998). Vdovin et al. (1999) presented group velocity maps of both Love and Rayleigh wave covering South America and surrounding oceans. Feng et al. (2004) studied also South American continent estimating a 3D model of the lithosphere by inverting the group velocity (multiple filtering) maps into shear wave velocity structure. Debayle and Kennett (2000) constructed maps of Australia using waveform inversion. 1D models were obtained for each path and than the vertical shear wave velocity maps for several depths were computed taking anisotropy into account.

As the resolution of tomographic images increased, possible systematic errors were further revealed. Levshin et al. (1999) pointed out that the source group time, i. e. the delay of long period radiation due to the source mechanism, was not negligible for periods longer than 75 s. Yoshizawa et al. (1999) studied the resolving power of polarization data. They recognized that polarization anomalies were able to detect smaller heterogeneities more precisely than velocity measurements itself. Spherical harmonic expansion was used to invert phase velocities and polarization data to compare both results. A discussion of the conclusions with respect do former studies, especially with Laske and Masters (1996), was also given.

Spetzler et al. (2001) discussed the limits of ray theory when constructing tomographic maps of higher structural details. They noticed that increasing the path coverage would not increase the resolution since it reached a fundamental limitations of the simple great circle approximation. They proposed to include finite frequency effects into inversion. Spetzler et al. (2002) further developed the scattering theory and used it while constructing tomographic global phase velocity maps. The comparison with former great-circle maps showed a good agreement for heterogeneities comparable with surface wavelengths, however, to reveal smaller structural anomalies, the finite frequency approach had to be involved.

Tanimoto (2003) proposed a method to estimate the finite-frequency dependence of the surface wave along its geometrical ray path. It was represented by an ellipse which width depended on the wavelength and which was set between the source and the station. Lateral spread of the wave inside the ellipse was described by Gaussian distribution perpendicular to this path. This approach was based on simple geometrical assumption and was valid for laterally homogeneous medium only. Finite-frequency effects were also described by Yoshizawa and Kennett (2002b) and *influence zones* of surface waves were introduced as a 1/3 of the first Fresnel zone. The latter approach was more general than the one given by Tanimoto (2003) and could be applicable also for laterally heterogeneous medium.

Yoshizawa and Kennett (2002a) proposed a complicated path-averaged dispersion estimation using waveform inversion and combining many records along similar paths. Nonuniqueness was discussed in the paper with respect to construction of tomographic images. A very complete summary of all new and advanced techniques in surface wave tomography was presented in the thesis by Yoshizawa (2002). Further, the *three-stage approach* (1D path-specific dispersion + 2D phase velocity maps + 3D shear wave structure inversion) was used by Yoshizawa and Kennett (2004) for estimating the tomography of

the Australia region. Ray bending, off-great circle propagation, finite frequency effects and multimode dispersion were incorporated. An overview of tomographic methods, different parameterizations and an application of the *partitioned waveform inversion* to the North America upper mantle was given by Lee and Frederiksen (2005). Asymmetric off-great circle sensitivity kernels were used. Finite-frequency surface wave anisotropic tomography including wavefront healing and reaching the global scale was made by Zhou et al. (2006).

Sieminski et al. (2004) compared tomography with finite frequency effects and scattering taken into account with classical ray theory and pointed out that the disadvantages of the simple ray approach could be counterbalanced by the dense ray coverage and physically based regularization of the inversion problem.

Barmin et al. (2001) summarized the method of constructing the tomographic maps using the dispersion estimation along the ray paths and than nearly linearly inverting them into the 2D group or phase velocity distribution. They discussed regularization, smoothing and effects of anisotropy, which could be also retrieved by this method. Similar resume was given also by Kennett and Yoshizawa (2002). Shapiro and Ritzwoller (2002) extended the approach by Monte-Carlo inversion for 3D shear wave velocities. The method of Barmin et al. (2001) was used by Levshin et al. (2001) to image the Arctic crust and upper mantle. To complement the group velocities, P_n and S_n waves were added. Ritzwoller et al. (2001) than described also the structure beneath Antarctica what did Danesi and Morelli (2001) as well. Not only the group velocity maps, but also the inversion for 3D shear wave velocity model was presented in both latter works. The work continued further by estimating the phase and group velocity maps for Eurasia by Villaseñor et al. (2001). For joint inversion of both Love and Rayleigh wave dispersion maps, the transverse isotropy of the upper mantle was assumed.

Fundamental mode phase velocities and normal mode splitting measurements were used by Beghein et al. (2002) to estimate both shear and compressional wave velocities of the mantle using the neighborhood algorithm with a discussion of the resolution and error estimates.

Further development of the diffraction tomography was proposed by Ritzwoller et al. (2002). Effects of finite frequencies were incorporated, diffraction and scattering was considered. *Wavefront healing* was described as a phenomenon occurring after the wave was diffracted. As it propagated further from the point of diffraction, the wavefront was again getting its initial shape. Differences with respect to Gaussian tomography, which took into account width of the rays along the paths but without scattering, were emphasized. Levshin et al. (2005) proposed the use of major-arc dispersion measurement for the global diffraction tomography what improved the ray coverage especially in the southern hemisphere where the minor-arc measurements were lacking due to the low station deployment.

A study concerning small region of Yunnan province, China, was made by Zheng et al. (2004). Two-station method was used to measure phase velocities along paths crossing the region and obtained values were inverted into tomographic maps by the method of Yanovskaya and Ditmar (1990) using the periods from 4 to 15 s. Not only the maps but also 2D cross sections of shear wave velocity across several profiles in the region were presented. Similar methods were also used in the thesis by Raykova (2005) who estimated 3D structure of the Balkan Peninsula with a resolution of $(1^\circ \times 1^\circ)$. The thesis continued by the paper of Raykova and Nikolova (2007), who provided a tomographic study of southeastern Europe with estimating the shear wave velocities of the crust and discussing the depth of the Moho. Raykova and Panza (2006) focused on inversion of local dispersion curves into the shear wave velocity structure in the Carpathians. The Aegean Sea was studied by Karagianni et al. (2002) using the data from a large experiment which took place in Greece, 1997. Bourova et al. (2005) measured only few paths of both Love and Rayleigh waves across the Aegean Sea with estimating the two-station phase velocities. Corrections of the true propagation paths were incorporated using the array approach. For each path, the dispersion measurement was provided for several events and hence, an error estimate was possible. Inversion for shear wave velocity structure was given. Tomographic maps of all the papers mentioned in this paragraph were determined by the method of Ditmar and Yanovskaya (1987) and Yanovskaya and Ditmar (1990), see also Chapter 4.

The Mediterranean region was described by Marone et al. (2004) with Love-Rayleigh discrepancy observed and anisotropy estimated. Pontevivo and Panza (2002) focused on smaller area of the region providing tomographic study of Italy. Guidarelli et al. (2002) used the tomographic maps and resulting velocity models of even smaller area in Italy to determine moment tensors of local earthquakes. Similar application was proposed also by Chimera et al. (2003) concerning another Italian region as well.

Much broader continental-scale study by Kobayashi and Zhao (2004) concerned the Antarctic region covering not only the continent itself, but also all the surrounding oceans. Multiple filtering was used to measure group velocities in the range 20 – 150 s, and the method of Barmin et al. (2001) was used for the tomography. Conclusions describing the possible tectonic origins of the area were made.

Multiple resolution tomography was used by Boschi et al. (2004) to reveal the structure beneath the Mediterranean. It allowed to parametrize the region of interest, where the data coverage was good, much

more densely than the global model, where the raypath coverage was poorer. Inverting also the global structure, even with lower resolution, the local measurements in the region of interest were not influenced by unknown effects of the structure outside of the region and teleseismic events could be used for such a study. Okabe et al. (2004) used similar approach for southeast Asia. They measured phase velocities by comparing the spectra of observed seismograms with those obtained from synthetics computed for the PREM model. The phase velocity perturbations along the paths were then inverted into 2D maps. The resolution blocks of homogeneous velocity were smaller in the center of the region ($5^o \times 5^o$) and larger toward the edges of the area ($15^o \times 15^o$). In each block, the local dispersion curve was inverted into 1D shear wave velocity model and hence a 3D structure was revealed.

West et al. (2004) proposed a method for joint tomographic inversion using both surface and body waves at the same time.

Crustal higher modes were used for tomographic inversion by Levshin et al. (2005), what extended the former use of mantle higher modes. The latter study presented higher modes measurement in the period range 7 – 18 s across Central Asia. First overtones tomographic maps were inverted into shear wave velocities what reduced the uncertainty of the models obtained by the fundamental modes only and improved the vertical resolution.

Regional studies continued by Yao et al. (2005), who provided the tomography of China, Tibet and Mongolia with discussing the results in comparison with the work by Shapiro and Ritzwoller (2002) since some discrepancies occurred. Vuan et al. (2005) studied the west Antarctica region. Levshin et al. (2007) used enormous amount of surface wave data from last several decades to construct tomographic maps across the European Arctic. Feng et al. (2007) combined dispersion measurements with waveform inversion, with the data from refraction experiments and with the depths of Moho given by receiver functions technique to construct a model of South America continent. South Pacific Ocean was studied by Weeraratne et al. (2007) who tested the models of intraplate volcanic ridges origin using ocean-bottom seismometers. Implications for geodynamic models were discussed with respect to revealed low velocity anomalies using the surface waves.

Study of the local conditions beneath the Baltic Sea in the area of approximately 1×1 km was performed by Kugler et. al (2007). They used a three-stage approach to constructs a 3D model of the sea bottom from measuring the dispersion of Scholte waves (generalized Rayleigh waves traveling along the interface between the sediment and the water) in the frequency range of 2 – 20 Hz, generated by airgun shots in the water and recorded by ocean bottom seismometers as well as buried geophones.

Zhang et al. (2007) estimated 1D model of the Gulf of California which revealed significant low velocity zone around the depth of 70 km. Tomographic maps with azimuthal anisotropy were then computed and compared with the tectonics of the region. Area of similar size was described by Delorey et al. (2007), who studied the structure beneath the Reykjanes Ridge near Iceland. Not only the phase and group velocities, but also the amplitudes were used in the tomographic inversion. The inversion used forward modeling of wavegroups at certain periods and their comparison with the measured ones. An interaction of the Icelandic hot spot with the ridge was confirmed. Another hot spot study was given by Villagómez et al. (2007) who proposed 3D structure beneath Galápagos Islands. Two plane wave approximation was used to account for the multipathing, polarization analysis was performed, isotropic and anisotropic models were presented. Velocities were determined with unrealistically low errors. Velocity distribution was used for temperature estimation and detailed chemical mantle composition what seems to be too hypothetic. Caribbean-South American plate boundary was comprehensively described by Miller et al. (2009). Tomography allowed to reveal the regional tectonic setting including fault systems and subduction zones.

Tape et al. (2007) proposed to use the *adjoint method* for the inversion. The finite-frequency tomography was constructed using sensitivity kernels which were computed by both the observed wavefield propagating from the source to the receiver and theoretical adjoint wavefield propagating in the opposite direction. The paper was purely methodological, a 3D reference model was used to compute synthetic "observed" seismograms and 3D model was searched by the proposed method.

The relation between global crustal parameters and the surface wave data were studied by Meier et al. (2007). Surface wave phase and group velocity maps were inverted for density functions of crustal thickness and averaged shear wave velocity. Implications for the resolving ability of certain periods were given.

Spectral amplitudes, phases, wavefronts and other detailed observations and measurements were provided by Pollitz (2008) using the data from the USArray. As opposed to the complicated amplitude patterns, the phases of the observed surface wavefronts were smooth. Finite-frequency multiplane tomography resulted in Rayleigh wave phase velocity maps across western U. S. as well as 3D shear wave velocity distribution in the region.

Surface wave array analysis (1993 – 2007)

Array techniques concerns not only the body waves, but also the surface wave measurements use the advantage of simultaneous observation of the seismic motion at networks with an aperture comparable with the wavelengths of interest.

Alsina et al. (1993) used the array technique to estimate the wavefronts of teleseismic events incident on the Iberian Peninsula. Obtained values were compared with phase velocities computed for the great circle propagation paths. In the period range 16 – 100 s, the deviations were up to 8° what represented a velocity error up to 1%.

Stange and Friederich (1993) proposed a method for estimating structural properties of the crust and upper mantle using a network of 9 stations while inverting the teleseismic records. This method overcame some of the disadvantages of the two-station technique for estimating the phase velocities. The records from nine stations were inverted together. In the first approximation, the assumption of plane waves was introduced, then the two-plane wave approximation was used what explained the observed variations better. Backazimuths of propagation, phases as well as amplitudes of the surface waves were inverted. The technique was then applied to anisotropic structural parameters as well, however, the reduction of residua was not significantly better.

The theory of inverting both the structural parameters as well as the backazimuths of propagation of surface waves was further developed by Friederich and Wielandt (1995). Only synthetic data were used in the study and complicated parametrization of the structure and properties of the waveforms were used. Friederich (1998) then inverted the obtained wavefields into a 3D vertical shear wave velocities of the upper mantle for southern Germany with examples of other regions analysis. Forward scattering theory and also backscattering was introduced to explain not only the properties beneath the array, but also to cover the heterogeneities influencing the propagation of surface waves outside the network. However, fundamental trade-off between the properties of the incoming wavefield and the properties of the structure beneath the array influencing the wavefiled persisted.

Freybourger et al. (2001) and Saltzer (2002) used an array of stations in Southern Africa to estimate path-averaged models between sources of the events and the stations as well as a 1D anisotropic model beneath the array.

The two plane wave method described by Forsyth and Li (2005) was used to resolve lateral variations and anisotropy of the phase velocities under the array as well as the backazimuths of propagation of two multipathed plane waves. The discussion of the two plane wave approach and its reliability was also given in the latter work.

Although a 1D structural model was obtained by Hwang and Yu (2005), they also used an array of stations to measure phase velocities beneath Taiwan. Plane waves were considered as propagating across the array and simple geometrical approach was used to determine phase velocity dispersion curves. This enabled to use long-period surface waves for local study and to estimate the shear wave velocity down to the depth of 200 km.

A study aimed at the tectonic and petrological context of the crust using the Rayleigh waves was published by Chen et al. (2007), who studied the Slave craton in the northwestern Canadian shield. The array approach with two-plane wave approximation was used to invert phase velocities of the surface waves, which were further inverted for the structure.

Array techniques and f-k analysis were used to determine phase velocities of short period Love waves beneath Bucharest for seismic hazard estimation by Sebe et al. (2009). To extract the dispersion curves, the signals were deconvolved with a reference dispersion. Thus the fundamental mode was concentrated to a short time window and the noise and other wavegroup signals were removed by tapering. Structural properties down to the depth of 2 km were determined.

Ambient noise tomography (2003 – 2010)

In the last decade, ambient seismic noise became an important and qualitatively new observation quantity to provide both large scale as well as local tomographic images of the Earth interior.

Generation of microseisms and their localization was described, among others, by Essen at al. (2003). Ocean wave measurements were correlated with broadband seismic measurements in northern and central Europe. The source of the microseisms was localized to be controlled by the ocean wave amplitudes near the coast of Norway. Implications for structural studies based on measuring the ambient seismic noise were proposed by Shapiro and Campillo (2004), who correlated seismic records of several days at several pairs of stations in the U. S. As a result, they obtained dispersive Rayleigh wavetrains. Dispersion measurement using the noise correlations was compared with traditional technique of analyzing the surface waves generated by earthquakes by Shapiro et al. (2005). They used a record of an event which had occurred near another seismic station and they estimated the dispersion curve using the classical measurement. The two stations were then used for ambient noise correlation with the same result. Using many pairs of stations, tomographic images of the Californian structure were then determined. Similar computations

were provided also by Sabra et al. (2005a and 2005b) who again computed many station-pairs correlations in Southern California and then determined the tomographic maps of the region. Possibilities of noise correlations across the Pacific Ocean were discussed by Lin et al. (2006).

Attention was paid to the source location of the noise. Shapiro et al. (2006) determined the source of the strong 26 s microseism to be in the Gulf of Guinea.

Kang and Shin (2006) used short period Rayleigh waves of the range 2 – 4 s to estimate maps of group velocities in the southern Korea. Comparison with the local geology gave a good agreement. Another application using short period surface waves was that proposed by Brenguier et al. (2007) who inverted the 2D tomographic maps into a 3-D shear wave velocity structure beneath the volcano at La Réunion island. Similarly, low velocity zones were revealed beneath the Okmok volcano, Aleutian, Alaska, by Masterlak et al. (2010) using the ambient noise tomography. Larger scale tomography of the Europe was made by Yang et al. (2007). Since the seasonal variations of the velocities determined from the correlations computed from the 3-months data emerged, very long time series (whole year) were then correlated. The discussion of the method reliability was presented with the notice that only the stations which are more distant then three times the wavelength could be used for correlations.

A summary of the method with detailed description of the particular steps was given by Bensen et al. (2007). The authors provided general cookbook with real examples of measurement. Normalization in the time domain by running average was performed, spectral whitening to suppress the 7.5 and 15 s microseisms was applied and the 26 s spectral peak from the Gulf of Guinea was decreased by a special filter. Then, all pairs of stations were used for cross-correlations, however, after that, only the pairs with a meaningful results were used further. Dispersion curves were determined using the classical multiple filtering method. Station distance with respect to the wavelength was also discussed.

New Zealand tomography using the ambient seismic noise was provided by Lin et al. (2007). Another regions were than studied by the same technique, for example, the Iberian Peninsula, by Villaseñor et al. (2007). Icelandic tomography was provided by Gudmundsson et al. (2007) with a remark that better ambient noise was measured in winter, when more storms were occurring near the island. Tomographic maps of the western U. S. were estimated by Moschetti and Ritzwoller (2007). Lin et al. (2008) studied the same region, however, both Rayleigh and Love waves were used to produce the tomographic images. Yang et al. (2008) made a combination of ambient noise and earthquake tomography to reveal the structure of the uppermost mantle beneath the same region. The whole North America was mapped by Bensen et al. (2008) and by Liang and Langston (2009). Southern Africa phase velocity maps from ambient noise by Yang et al. (2008) were compared with maps obtained from teleseismic tomography. Similarly, teleseismic tomography of the western U. S. was proposed by Yang and Ritzwoller (2008) and the maps were compared with those obtained by ambient noise tomography. In places where the raypath coverage of the teleseismic tomography was good, the maps agreed well. Zheng et al. (2008) estimated the Rayleigh group velocity maps of China with clear correlation to surface geology.

The development of the ambient noise methods continued further. High frequency surface waves were theoretically studied by Gouédard et al. (2007) by ambient noise simulations in complex shallow structures. Another theoretical problems of the ambient noise tomography were discussed by Yang and Ritzwoller (2008), who pointed out that to provide reliable results, the noise sources have to be located homogeneously around the region of interest. The source locations as well as the origins of the noise were studied. As a result, the interaction of the water waves at the coastal regions were identified as a noise sources and the possible sources in the deep oceans were rejected. However, the waves at the coastal regions depended on storms occurring in the middle of the oceans. The discrepancy between inhomogeneous distribution of the noise sources along the coast with the ambient noise tomography reliability supported by homogeneous noise propagation was commented. Synthetic test was provided with an implication showing that it was enough to have partly random noise source distribution to provide proper tomography. When the poor cross correlations were obtained, such measurement must have been rejected.

Nishida et al. (2008) showed that the background Love waves may have been excited as well as Rayleigh waves and that the sources must have been other than vertical pressure loading, as supposed formerly. In the most recent study, Fukao et al. (2010) showed that background Love and Rayleigh waves (*Earth's hum* or *Earth's background free oscillations*) of the period range 50 – 200 s were generated by infragravity waves of the oceans which were coupled with the ocean bottom topography.

As a contrary to other regions, where the noise was dominated by the fundamental mode, in New Zealand, the Rayleigh waves contained also higher mode, as revealed by Brooks et al. (2009).

Hobiger et al. (2009) presented a technique to calculate Rayleigh wave ellipticity from the ambient noise using single station. It allowed to estimate the local structure using only a few minutes of the noise recording. When using array of stations, the azimuths and prograde and retrograde motions could be analyzed.

Ekström et al. (2009) proposed another method of phase velocity dispersion curve computation using

Bessel function approximation of the measured spectra. An advantage of this approach with respect to the previous ones was that it avoided the limitation given by short interstation distances with respect to wavelengths. Baig et al. (2009) proposed a method to denoise the seismic noise cross correlations to provide more accurate measurement. Using the technique, even the changes of velocities with time could be observed, what was especially useful for volcano monitoring. Another attitude was proposed by Lin et al. (2009) – each station was considered as an effective source of the noise and then the other stations were used to recover the wavefronts of the propagating noise. Both phase velocity variations and propagation azimuth were estimated.

Most recently, ambient noise tomography of southeast Australia was performed by Arroucau et al. (2010) using data from temporary arrays with dense coverage rolling across the area under investigation. Periods from 2.5 to 20 s were used with the lateral resolution of the maps reaching 40 km.

Surface wave studies in the Bohemian Massif and neighboring regions (1977 – 2010)

One of the first studies revealing the structure of the small area in the Central European region was made by Holub (1977). Short period surface waves from blasts were observed in Western Carpathians and their properties were described. Plešinger (1979) gave the characteristics of the Kašperské hory (KHC, Southern Bohemia) station and discussed an idea of several surface wave profiles crossing the Bohemian Massif for structural properties determination. Novotný (1983) proposed theoretical dispersion curves for the KHC and Ksiaz (KSP, Poland) profile. This forward modeling was based on structural results obtained by former deep seismic sounding experiments.

Surface wave measurements were then performed along profile KHC-KSP by Wielandt et al. (1987) who used the standard two-station phase velocity method. Both Love and Rayleigh waves from 10 to 100 s were used. Ten earthquakes from Japan and the Atlantic Ocean were observed to cover the profile by waves propagating from both sides. Measured dispersion curves were averaged to obtain one smooth curve which was further inverted into shear wave velocity model. Love and Rayleigh wave dispersion curves were inverted separately and two distinct models resulted. The conclusion was that it was not possible to describe the region with isotropic and reasonably smooth shear wave velocity model.

Plešinger et al. (1991) gave the crustal velocity estimation for profile KHC-Moxa (MOX, Germany). Novotný et al. (1995 and 1997) continued with surface wave dispersion measurements along longer profiles in the same direction as profile KHC-KSP estimating the 1D structure in broader region outside of the Bohemian Massif. Deep seismic sounding experiments produced surface waves which were observed and interpreted by Holub and Novotný (1997) for the Western Carpathians area. Novotný et al. (2005) estimated 1D structure of the uppermost crust in the Moravo-Silesian region and Western Carpathians inverting the dispersion curves from blasts. Malinowski (2005) used the CELEBRATION experiment data for the analysis of short-period Rayleigh waves and estimated the crustal structure for the upper 2 km along one of the CELEBRATION profiles.

In the proposed thesis, the three papers (Kolínský and Brokešová, 2007 and 2008 and Kolínský et al., 2010) dealing with surface waves in the Bohemian Massif are presented. An overview of the Bohemian Massif seismic experiments and studies is also given in Chapters 3 – 5.

1.2 Multiple filtering method

In the next paragraphs we explain why the multiple filtering method is a suitable tool for frequency-time analysis. We compare it with the technique of moving window.

Frequency-time representation is a 3D depiction of a distribution of energy in dependence both on time and frequency of the record. In this representation, frequency and time axis are theoretically equivalent. However, it does matter how the representation is computed. Two basic and equivalent methods of computing the frequency-time representation are "the technique of moving window" and "the multiple filtering technique". Both are based on the Fourier transform and both work in similar manner in the respective domain.

Moving window technique filters the signal in the time domain. The time signal is weighted and only a part of it is selected in a close vicinity of given central time. Then this small part of the whole signal is transformed to the frequency domain. This selecting procedure is repeated for many central times, many Fourier transforms are made and many spectra are obtained. Then the spectra are aligned side by side one to another along the time axis representing the central times. We use 2D frequency-time base of the plot while the spectral amplitudes are shown in the third dimension along the third axis. In fact, instead of the complex spectra, the modulus of the spectra is depicted (amplitude spectra), what represents the energy carried by the signal at each time for each frequency. Such a 3D representation is called "spectrogram".

In case of the multiple filtering method, all the steps are done in the other domain. First, the Fourier spectrum of the whole record is computed. Then for many central frequencies, only limited part of the

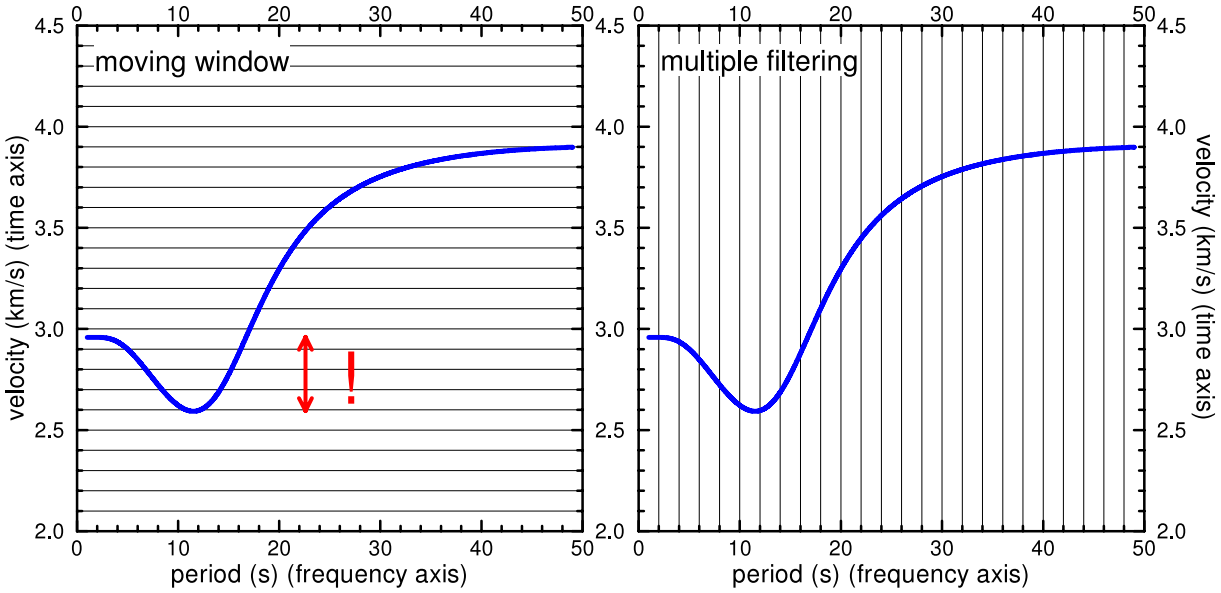


Figure 1.1: Comparison of frequency-time plane slicing. On the left panel, the moving window technique assembles the spectrogram by slices parallel to the frequency axis. For each central time, separate spectrum is given. On the right panel, the multiple filtering assembles the spectrogram by slices parallel to the time axis. A separate time signal for each central frequency is used. Blue curve is the synthetic Rayleigh wave group velocity dispersion curve computed for the PREM (Dziewonski and Anderson, 1981).

spectrum close to the given frequency is selected. These weighted spectra are transformed back to the time domain and a set of harmonic signals is obtained. They are plotted side by side along the frequency axis of the frequency-time representation. Instead of harmonic signals itself, their envelopes (moduli of analytical signals corresponding to these harmonic signals) are used. Envelopes directly represent the energy carried by the respective harmonic signal.

Spectrograms created by moving window and multiple filtering techniques are equivalent. However, there are some peculiarities showing us that the multiple filtering method is more suitable for analyzing dispersed surface wave records.

As we stated, the two methods are equivalent theoretically. However, the multiple filtering has some advantages compared to the moving window technique. The first practical difference may be seen in the fact that we measure our records in the time domain and not in the frequency one. It seems to be much more straightforward to filter the records directly in the time domain and after that to transform them in the frequency domain – to use the moving window technique. However, one additional Fourier transform is not so costly to get the advantage of the multiple filtering in the frequency domain. As we transform the filtered spectra back, we obtain a set of monochromatic signals in the time domain. And it is much more suitable to check them in the time domain and to compare them with the original records. We can look one by one at the harmonic components of the record and directly see when the wave of given period comes. This comparison would not be possible while using the moving window technique.

The frequency-time analysis of surface waves is used to estimate the dispersion curve. The dispersion curve is the dependence of the propagation time of wave envelope of given period on that period. As it is shown in Fig. 1.1, the classical group velocity dispersion curve is a function $t = t(f)$. In other words, the propagation time t depends on frequency f. In our case, the group velocity U depends on period T, we have $U = U(T)$. We use the time t and velocity U equivalently in following text as well as we do it for frequency f and period T. These pairs of quantities are only reciprocal values one of the other and no special consequences imply while using one or the other.

While looking at the shape of the group velocity dispersion curve in Fig. 1.1 we see that because the curve has a minimum and hence it is not monotonic, the dependencies reversed to the latter are not functional. The period is not a function of velocity, $T \neq T(U)$. These trivial facts are important when comparing both methods of frequency-time computation. A disadvantage of using the moving window technique for surface wave dispersion estimation is the fact that by the moving window technique, we "slice" the spectrogram parallel to the frequency axis. So, for each central time, the method is able estimate the dispersion point only for one frequency. However, in Fig. 1.1 we see that for velocities between 2.6 and 3.0 km/s we have two dispersion points at two distinct frequencies for each arrival time (velocity). By the multiple filtering method, we "slice" the spectrogram in the right way parallel to the time axis and we have no problem to find out all the dispersion points because for each period only one velocity has to be looked for.

In fact, using the multiple filtering technique, we also seek several dispersion points for each period. These different dispersion points belong to the different modes of surface waves. We try to identify all of them in our spectrogram and after that we compile the dispersion curve from some of the dispersion points according to the criterion of continuity of the curve, see next section for detailed explanation. Thus, in principle, there is no problem to find more than one functional value for given variable. The advantage of multiple filtering technique is not the fact we look for one or more values for one period, but the fact that this technique is able to clearly find out the extremes of the curve. The minimum of the dispersion curve in Fig. 1.1 is called Airy phase and it is located around the period of 12 s. As it is clear from the figure, it is much more easier to estimate the shape and location of this minimum using the proper "slicing" of the spectrogram by the multiple filtering technique then using the moving window one. In the case of monotonously dispersed signals, this problem vanishes.

By the multiple filtering technique, it is more difficult to estimate steeper dispersion curves. It may be a problem in the case of higher modes because their dispersion curves are typically very steep (velocity changes rapidly with period) for certain period ranges. In the case of such a steep dispersion curve, the moving window technique could give more appropriate results exactly in the same manner as the multiple filtering gives better results for the flat portion of the curves (extremes).

Other methods of frequency-time analysis mentioned in literature such as moving window autoregressive analysis or frequency-time distributions (Kocaoglu and Long, 1993) are adjusted to give higher resolution of energy distribution, which is not limited by the uncertainty principle of the Fourier transformation (for explanation of this feature, see Section 1.4). There are many problems with processing the records while using these sophisticated techniques. For example, the method of estimation of autoregressive parameters in the case of the moving window autoregressive analysis and the presence of cross terms in the case of the frequency-time distribution methods cause many difficulties. The multiple filtering technique gives better resolution than we actually need to estimate the dispersion curves. It can be proved by the sufficiently high resolution of computed spectrograms and reasonably smooth dispersion curves throughout the thesis.

In my opinion, there is not a strong need to use more complicated methods of frequency-time analysis then the multiple filtering technique. The most difficult aim and the main goal are not to reach high resolution of frequency-time representation but to interpret the ridges and to draw the continuous dispersion curves. I encounter many problems with the dispersion curve estimation, higher modes identification, dispersion splitting due to multipathing and recognizing other dispersion curve related phenomena and I was never limited by the resolution of the spectrograms. The difficulties with the inversion of dispersion curves also mitigate the need for higher resolution of the analysis. I would not be able to use any more precisely determined dispersion curves in my inversion anyway. Hence I think that the multiple filtering method has a good use for its simplicity, easy controlling and suitable comparison of filtered harmonic signals in the time domain.

1.3 Illustrative description of the method

In this section, a description of the multiple filtering method is given. As an intention, we do not use any equations, expressions or mathematical symbols to introduce the technique. This is just to propose the basic idea how the multiple filtering works. This section is supplemented by figures explaining the steps of the process. For exact and formal explanation of the method, see the next Section 1.4 and also Section 3.2.3.

general approach

Here we give and overview of the whole process, which is schematically shown in flow chart in Fig. 1.2. Consider a particular component of an earthquake record, for example see Fig. 1.3. First of all the complex Fourier spectrum of the record is computed. In Fig. 1.4 the power spectrum is depicted by bold black line. After that the complex spectrum is filtered. It means that both real and imaginary parts of the spectrum are multiplied by a set of weighting functions, as depicted in Fig. 1.4 for the power spectrum. For weighting, smooth Gaussian functions are used. Toward higher frequencies, the width of the filters in the frequency domain broadens to ensure more accurate resolution in the time domain, which is needed to represent narrower signals of shorter periods. This filtering is done for selected central frequencies (periods). By the weighting, we obtain many spectra shown by colored rugged lines in Fig. 1.4. All these filtered spectra are transformed back to the time domain. We obtain a set of nearly monochromatic time functions – for each period of filtering we get one corresponding signal in the time domain as shown in Fig. 1.5 by thin solid oscillating lines. Envelopes of each of the signals are computed, see thin solid black slowly changing lines in Fig. 1.5.

Than we use a procedure for selecting the proper wavegroup from each signal. Local maxima of each envelope are found and according to the mutual relationships of arrival times of these maxima, one of

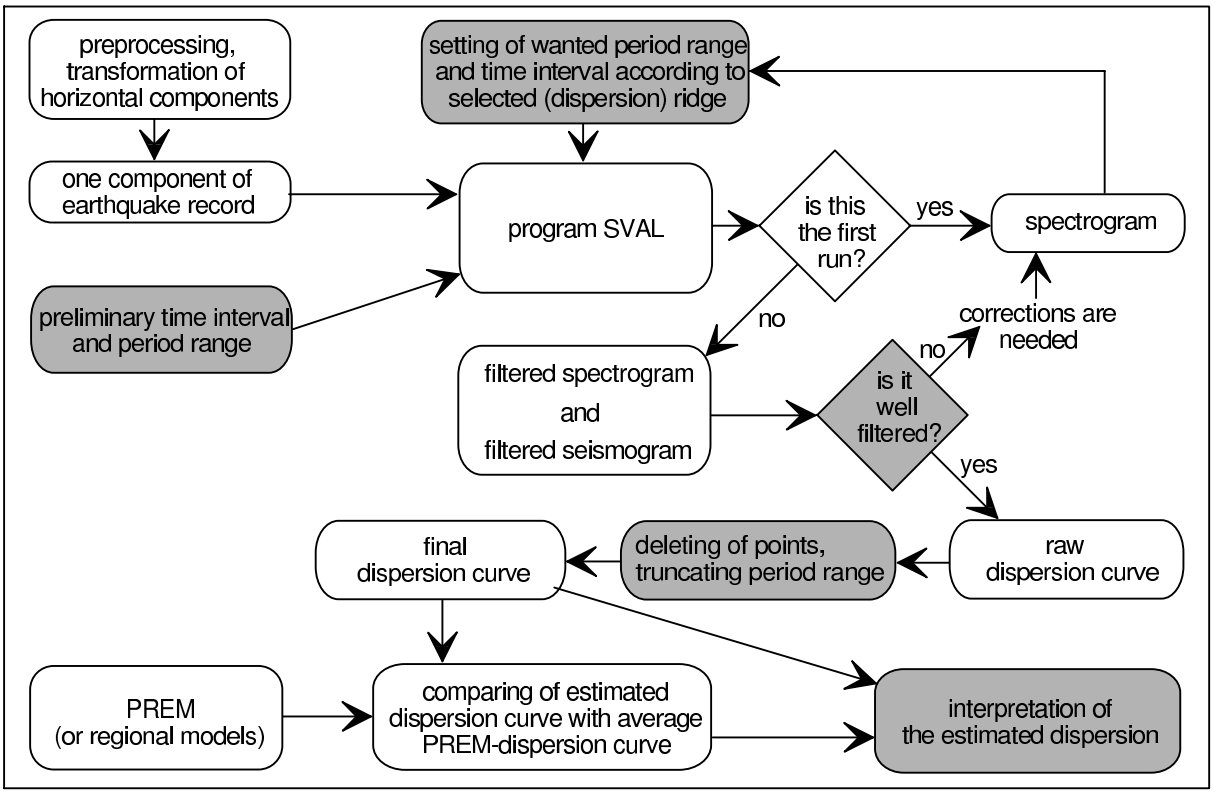


Figure 1.2: (*Fig. 4 in Kolínský, 2004*) The flow chart shows the process of computing the dispersion curves. Greyfilled frames represent the steps where human intervention has to be made.

the local maxima at each signal is selected to represent a point at a smooth curve linking all the selected times. Such a curve representing the arrival times of the wavegroups depending on period is the *dispersion curve* and the procedure for its selecting is using a *criterion of continuity*.

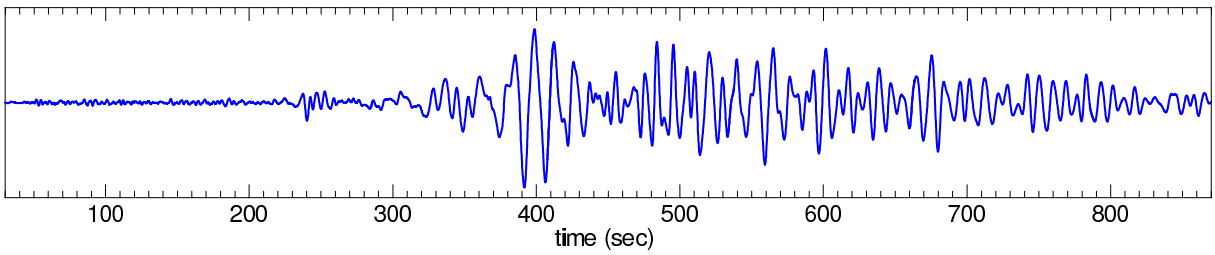


Figure 1.3: Example of a broadband record of transverse component (shear waves, Love waves) of earthquake in Turkey, February 3, 2002, origin time: 07:11:28.41 UTC, epicentral coordinates: 38.57° N and 31.27° E, depth: 5 km, $M_w = 6.5$, epicentral distance to the Praha seismic station: 1846 km.

In Fig. 1.5 we see that each of the signals contains several maxima. For longer periods, usually, it is easier to find the desired wavegroup corresponding for example to the fundamental mode. For shorter periods, the number of wavegroups in each signal increases and we have to carefully select one of them. The criterion of continuity works in such a way that at first, we find the wavegroup for longer periods. Then, we proceed filter by filter toward shorter periods and we look for the local maximum of the next signal to be as close in time to the maximum of the preceding signal as possible regardless of its amplitude. Fig. 1.5 shows the selected wavegroups by bold dashed lines. For longer periods, the fundamental wavegroups were found as the highest maxima of each signal. However, when selecting the highest maxima of the signals for shorter periods, we obtain unreasonable result since other wavegroups exceed the amplitudes of the fundamental mode for shorter periods. This is the reason why we do not use the criterion of the highest amplitude but instead, we apply the criterion of continuity of the dispersion curve.

After selecting the dispersion curve, we truncate all signals around the selected maxima to keep only the desired wavegroups, see bold dashed lines in Fig. 1.5. All the rest of the time signals is deleted and the edges of each wanted wavegroup are smoothed by cosine window. We truncate also the corresponding envelopes of these wavegroups, see Fig. 1.5 – bold solid lines. The procedure of truncating the quasimonochromatic signals is explained in Fig. 1.6.

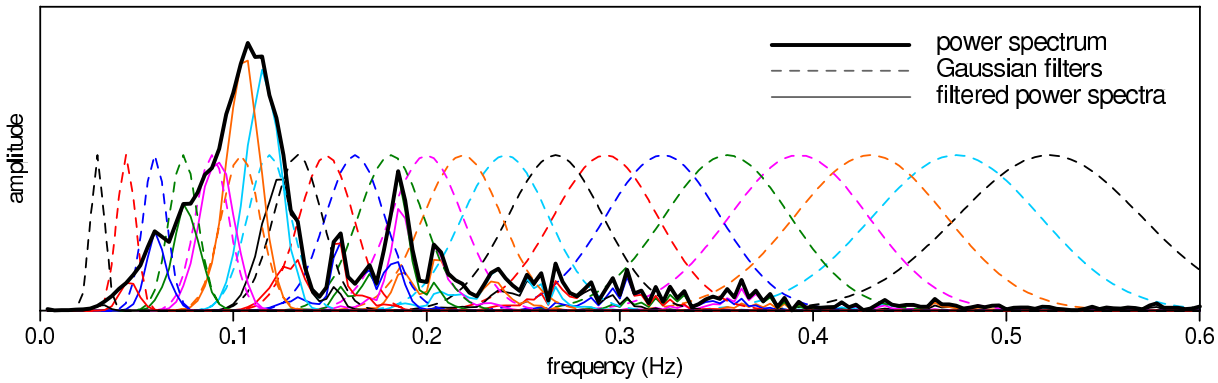


Figure 1.4: (*Fig. 1 in Kolínský, 2004; colored*) The use of the Gaussian filters as a tool of the multiple filtering technique. Amplitude spectrum of an earthquake record from the previous figure is drawn (black bold solid line). Gaussian filters (colored dashed lines) used for weighting the spectrum are shown. The spectra obtained by the filtering are also drawn (colored solid lines). Each filter and its corresponding filtered spectrum have the same color. The frequency step is bigger and the filters are broader toward high frequencies. The amplitudes of the raw spectrum and Gaussian filters are mutually not in the scale.

The original whole envelopes are used to create the complete spectrogram. Ordering one envelope side by side according to the periods of corresponding time signals, we obtain a 3D depiction of the energy contained in the original record with respect both to time and frequency. Example of such spectrogram is given in Fig. 1.7. Each of the envelopes is shown in different color. The same feature is shown also in a map view in Fig. 1.8. In the panel **A** of the figure, we see the spectrogram. Color scale represents the amplitude of the envelopes.

Selected local maxima of the spectrogram forming the dispersion curve are shown by light green line in Fig. 1.7. Each selected maximum is emphasized by black dot.

Another example of resultant dispersion curve is shown in Fig. 1.8, panel **D**. Again, according to the found dispersion curve, the harmonic signals and their envelopes are truncated and we may create truncated spectrogram as shown in Fig. 1.8, panel **E**.

Truncated harmonic signals may be used for creating the separated dispersed wavegroup. This dispersed wavegroup is a product of the analysis and is used to compare the mode corresponding to the found dispersion curve with the original seismogram. The truncated harmonic components are simply summed up as it is schematically shown in Fig. 1.9. The resulted separated surface wavegroups compared to original record are shown in Fig. 1.10. Fundamental and first higher mode of Love waves as well as Rayleigh wave and other wavegroups are shown there. By a green line, we show also shear waves, which are not dispersed but the process of their separated wavegroup computation is the same as in the case of surface waves.

Fig. 1.11 presents a schematic view of selecting the desired modes from the spectrogram. Finally, Fig. 1.12 shows, how the results are presented in a comprehensive manner: all three components of the record are processed, several dispersive ridges are found, dispersion curves are estimated and compared with the synthetic dispersion curves for the fundamental and first higher modes of both Love and Rayleigh waves.

Now, we will describe the method in detail.

flow chart

Fig. 1.2 shows a flow chart of the whole process described above. First, we can do any preprocessing of the records and we also need to rotate the horizontal components to the transverse and radial ones. We set preliminary interval of velocities (time) and period range. Then we run the procedure for computing the frequency-time analysis (the SVAL program in our case) for the first time. We check the complete spectrogram and we set a new velocity and period ranges for the desired dispersion ridge. We run the procedure again. We obtain the separated seismogram as well as the truncated spectrogram. We compare the separated surface wavegroup with the original record and we check if we targeted the desired wavegroup. If we are not satisfied with the results, we change the period and velocity ranges and repeat the procedure again. If we are satisfied, we can draw a dispersion curve corresponding to the selected ridge. We check, if the dispersion curve follows a continuous ridge across the spectrogram. The current version of the SVAL program enables also to add some dispersion points by clicking on them directly in the program's window. Once we have the dispersion curve, we can compare it with other curves. The flow chart made for the paper Kolínský (2004) describes the comparison with dispersion curve of the PREM model and regional dispersion curve computed for the Bohemian Massif.

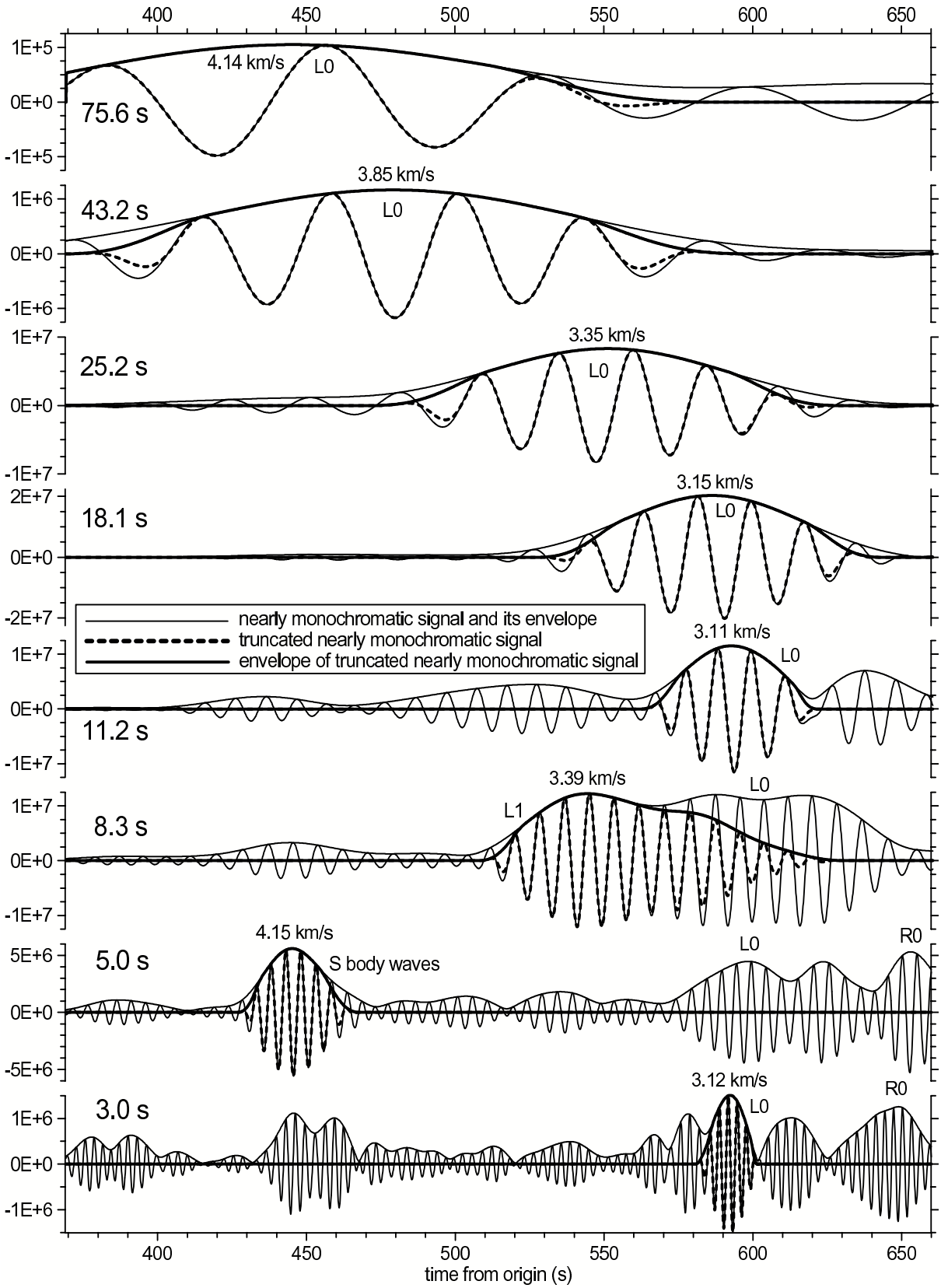


Figure 1.5: (*Fig. 2 in Kolínský, 2004*) Thin solid lines represent real parts of nearly monochromatic complex signals and their envelopes. Bold solid lines represent truncated and smoothed envelopes and bold dashed lines the truncated and smoothed real parts of the nearly monochromatic signals. Eight filters were selected for this figure from more than hundred filters used during the processing. The figure illustrates, how the maximal amplitude criterion may lead to unwanted results. At the period of 3.0 s, the fundamental mode was properly found. However, for 5.0 s, the S wave and for 8.3 s, the first higher mode of Love wave is found. The desired fundamental mode is only leaking into the selected wavegroup for the 8.3 s filter. For longer periods, again the desired fundamental mode is found. For periods 5.0 and 8.3 s the filtered nearly monochromatic signal contain wavegroups with amplitudes exceeding the amplitudes of the fundamental mode. Group velocities of the selected wavegroups are marked. Notice that the amplitude scale differs for each plot.

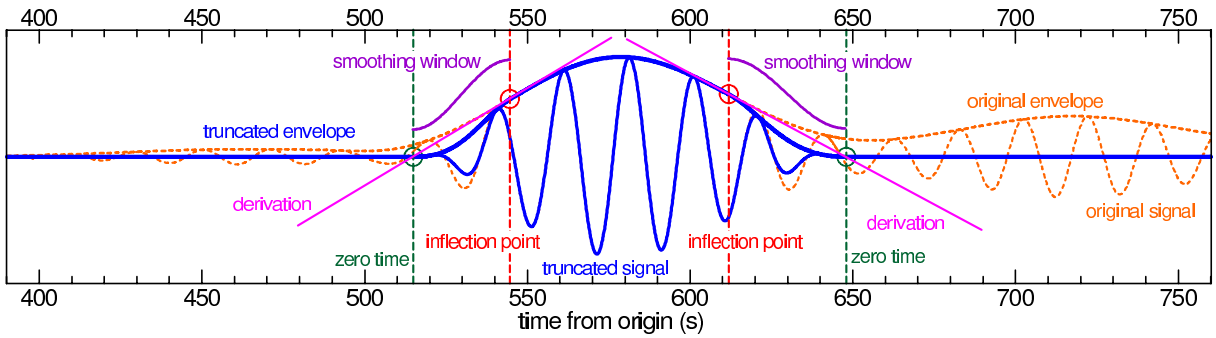


Figure 1.6: Procedure for truncating the quasimonochromatic signals. For this example, the 20 s period wave of the Turkish earthquake spectrum was used.

Now we will comment some steps of the analysis in details. These details are based on the text of the paper Kolínský (2004). Some of the features of our procedures were updated from the time when the paper was published. It concerns especially the compiling of the dispersion curve by using the criterion of continuity.

dispersion ridge

Now we will proceed with the idea how the proper dispersion ridge is found. Fig. 1.11 shows a schematic diagram of the process of zooming at the proper ridge. First of all, we compute the spectrogram for the whole record. By changing the time and frequency windows of the computation, we can zoom at the previously identified part of the spectrogram. It helps us to concentrate all the filtering, truncating

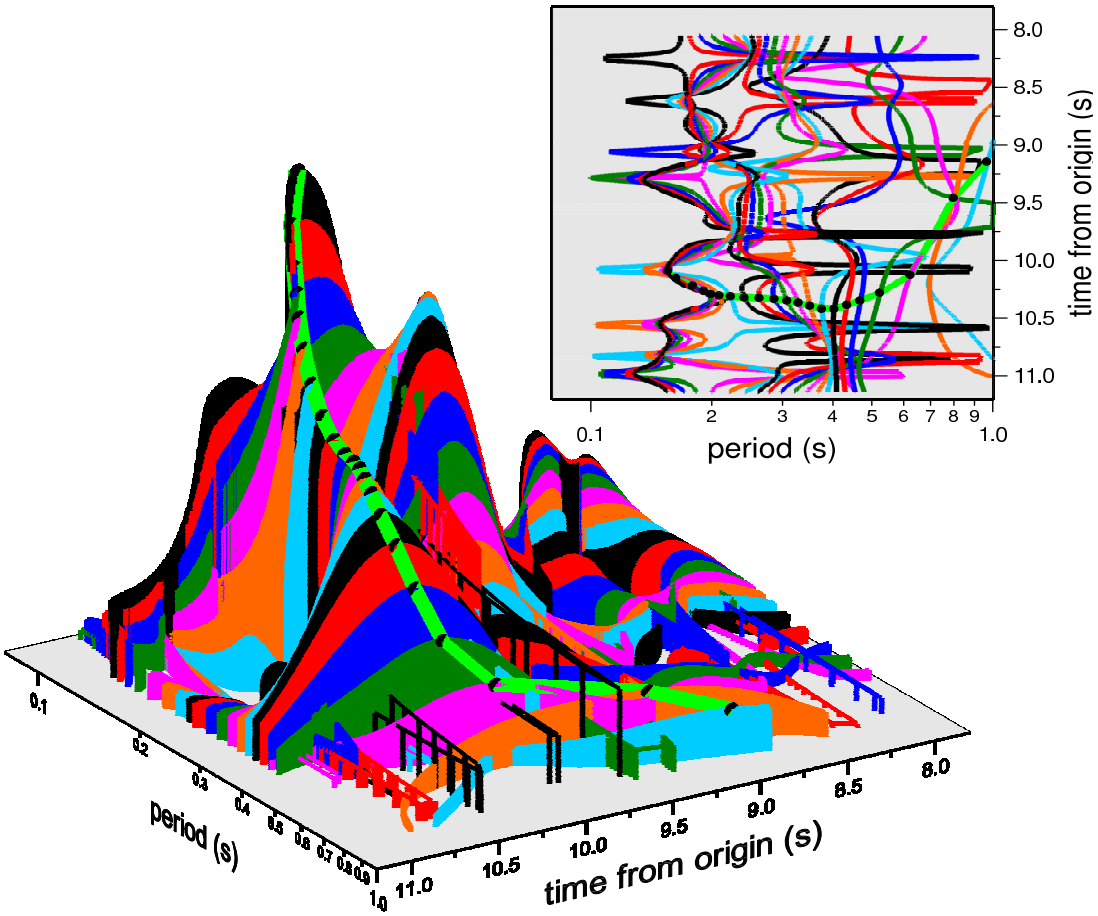


Figure 1.7: 3D view of the spectrogram. Instead of a smooth plane covering the envelopes of the quasimonochromatic signals, each "slice" of the spectrogram is visible in this depiction. A 2D map view of the 3D spectrogram is also depicted in the upper right corner of the figure to demonstrate the variations of each quasimonochromatic signal in the period-velocity plane. Corresponding "slices" have the same color in both plots. Bold light green line with black dots shows the dispersion curve in both 2D and 3D depictions.

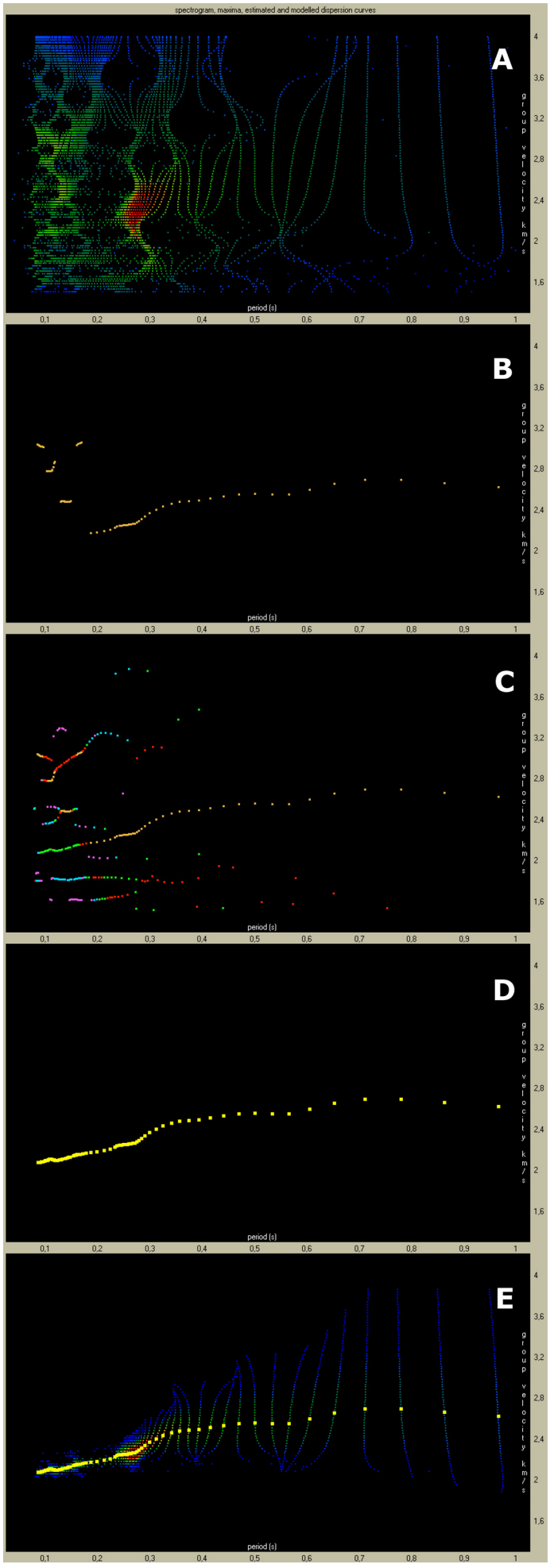


Figure 1.8: Five steps of the frequency-time analysis. This figure expands the map-view plot from Fig. 1.7 and describes, how the dispersion curve is compiled using the local envelope maxima.

A: Spectrogram of the record is computed. Red is the highest amplitude, blue is the lowest one.

B: For each filter, its absolute envelope maximum is found and plotted by light brown color. Only a part of the desired dispersion curve is formed by the propagation times of these maxima and on the other hand, some of the shorter-period maxima belong apparently to other modes.

C: All other local envelope maxima are found and plotted for each filtered signal. The highest maximum is drawn by light brown color as in panel B, the second highest maximum by red color, the third one by green, fourth one by blue and the fifth maximum by purple color. These lower maxima complement the ridges implicated by the highest maxima from panel B.

D: According to the criterion of continuity, the fundamental dispersion curve is compiled using all available maxima regardless of their amplitudes. In the example, the first to fourth maxima are used for final dispersion curve compilation.

E: Fundamental dispersion ridge is cut from the spectrogram along the found dispersion curve. The edges of the truncated spectrogram are smoothed. As the dispersion curve reaches longer periods, the fundamental mode wavegroups corresponding to these periods are also broader what results in wider truncated spectrogram.

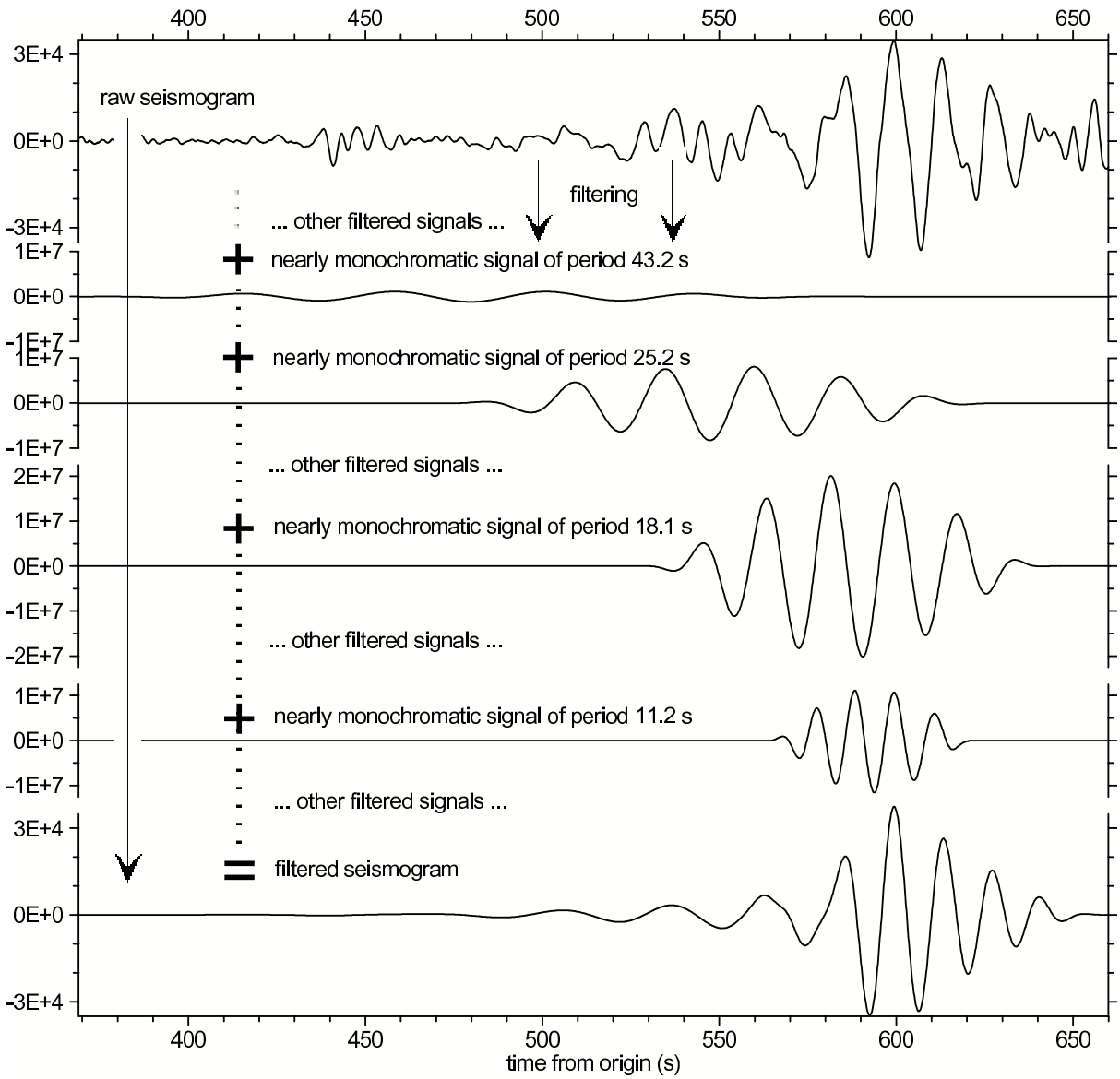


Figure 1.9: (*Fig. 3 in Kolínský, 2004*) Four truncated and smoothed real parts of nearly monochromatic signals are used to show, how the separated seismogram is computed. A hundred of filters in the period range from 11.0 to 105.0 s was used for summing up the separated seismogram. Only eight of them are presented in Fig. 1.5 (dashed lines) and only four of them in this figure. The original raw seismogram is drawn in the uppermost plot and the resulted separated fundamental mode wavegroup in the lowermost one. Vertical scales of the middle four plots are the same for comparison of the relative amplitudes of all four nearly monochromatic signals.

and dispersion curve compilation to the restricted area and these processes are not spoiled by unwanted wavegroups of the original complete spectrogram. Instead of time we use velocity for selecting the range on the time axis. This is more convenient because we have some a priori knowledge of surface wave velocities we may expect and hence we can use these assumptions even for the first spectrogram computation. The velocity range gives us the opportunity to fit the proper time window for the first trial regardless of the epicentral distance and wave propagation time. Instead of frequencies we use periods what has the advantage of more suitable values for surface waves of longer periods (55 s instead of 0.0182 Hz). Also the scale of the period axis may be conveniently selected as the logarithmic one.

Fig. 1.11 relates directly to Fig. 1.10. The local spectrograms of fundamental and higher mode of Love waves, as well as the wavegroup corresponding to the coda and shear waves are marked in the complete spectrogram by solid black rectangles in Fig. 1.11. Corresponding four truncated spectrograms are shown in upper and right part of the figure. The wavegroups corresponding to these four selected spectrograms are presented by colored lines in Fig. 1.10.

Generally, we may look only for the highest maxima of the envelope at each signal to find the arrival time of the wavegroup. However, this simple procedure cause problems as we see in short-period plots of Fig. 1.5. The required mode does not have to necessarily have the highest amplitudes in the given

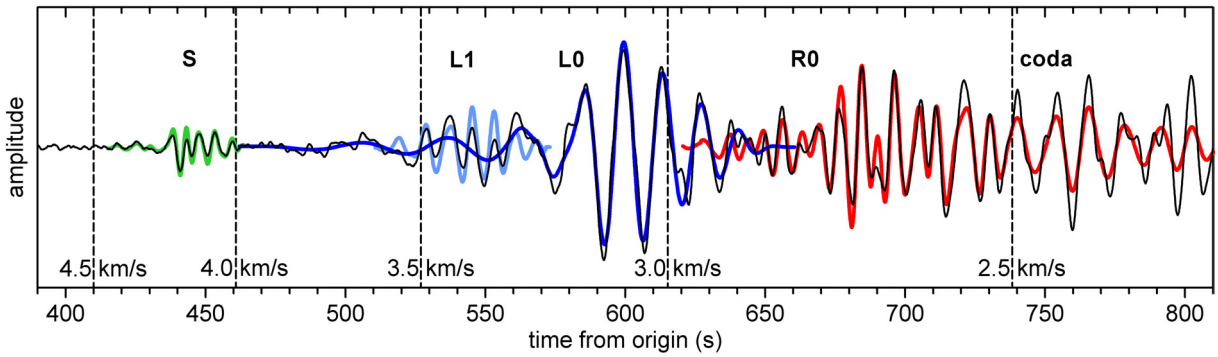


Figure 1.10: (*Fig. 7 in Kolínský, 2004*) Four selected ridges are used to create the corresponding separated seismograms. Three dispersed surface wave modes (L_0 – dark blue line, L_1 – light blue line, R_0 and coda – red line) and also body S-waves (green line) are shown. The first higher mode of Love wave L_1 is clearly visible within the long periods of Love fundamental mode L_0. The original seismogram is drawn by thin solid black line. Five points of the group velocity are marked.

harmonic component. When looking for the fundamental mode of surface wave, using regional event records, the longer periods would probably have the highest amplitudes, however, as seen in Fig. 1.5, the analysis of short periods would suffer of not-recognizing the fundamental mode at the shorter periods where the body waves or higher modes dominate. Using only the criterion of the highest amplitudes, we would limit our analysis only to the longer periods. In case of more complicated records as, for example, quarry blast records described later in the presented thesis, the criterion of the highest amplitude does not work at all since all the surface waves are hidden in the noise and consecutive body wave arrivals.

Criterion of continuity overcomes these problems. It is enough to set one dispersion point located at the desired mode and the program finds the smoothest dispersion ridge containing the given point. If even this procedure fails, we can select the dispersion points by mouse-clicking on the computer screen.

Fig. 1.8 shows the procedure for selecting the proper ridge using the criterion of continuity. Panel **A** is the original spectrogram. In panel **B** we see the highest maxima of each of the envelopes. These maxima correspond to the arrival times of the energy carried by each of the wave at the wavegroup with the highest amplitude. But because the surface waves we are looking for are not necessarily of the highest amplitudes in the record, we look also for other lower local maxima in each harmonic component, as shown in Fig. 1.8, panel **C**. Different maxima orders are depicted by different colors. Then we compile the resultant dispersion curve using any of the previously found maxima according to the criterion of continuity and regardless of their amplitude, as shown in panel **D**. When the dispersion curve is found, we plot and check also the corresponding truncated spectrogram, as depicted in Fig. 1.8, panel **E**.

Let us continue with the example in Figs. 1.10 and 1.11. As we selected the main dispersion ridge of fundamental mode of Love waves, we can continue by selecting other smaller ridges. In Fig. 1.11 a filtration of the wavegroup corresponding to the first higher mode of Love waves L_1 is presented. It is well visible in Fig. 1.10 that the original seismogram contains two different components: in the same time interval of 510 – 570 s, the waves of periods about 30 – 50 s of fundamental mode (dark blue) and periods about 6 – 11 s of the first higher mode (light blue) are present. The other solid black rectangle in Fig. 1.11 shows a shear wavegroup. It does not reveal any dispersion of velocities but the procedure of its selection works exactly in the same manner as for the dispersive surface wavegroups. The separated seismogram, drawn in Fig. 1.10 by green line, clearly shows this shear wavegroup in context of other features of the original signal.

width of the filters

Since the filters in the frequency domain are of finite width and hence the corresponding time signals are not exactly harmonic but they contain broader range of frequencies, as we go along each of the signals, the instantaneous period of it for each time is varying. Fig. 1.7 represents an example where very wide filters were used and hence each of the time signals contains a broader part of the original spectrum. This is the reason why the period of each of the envelopes varies so much. In the upper right corner of the figure we see a map view of the same spectrogram where the color lines show the same envelopes – we see that they are of complicated shapes.

In Fig. 1.7, also a dispersion curve is drawn by bold green line – it is depicted both in the 3D view as well as in the map view of the spectrogram. Black dots are the dispersion points. At each of the envelope, one dispersion point was found and the curve made by connecting these points is the dispersion curve. We see that at least in the middle part of the curve, the envelopes are monochromatic in the close vicinity of the dispersion curve. Since we do not need to know the instantaneous periods along the whole

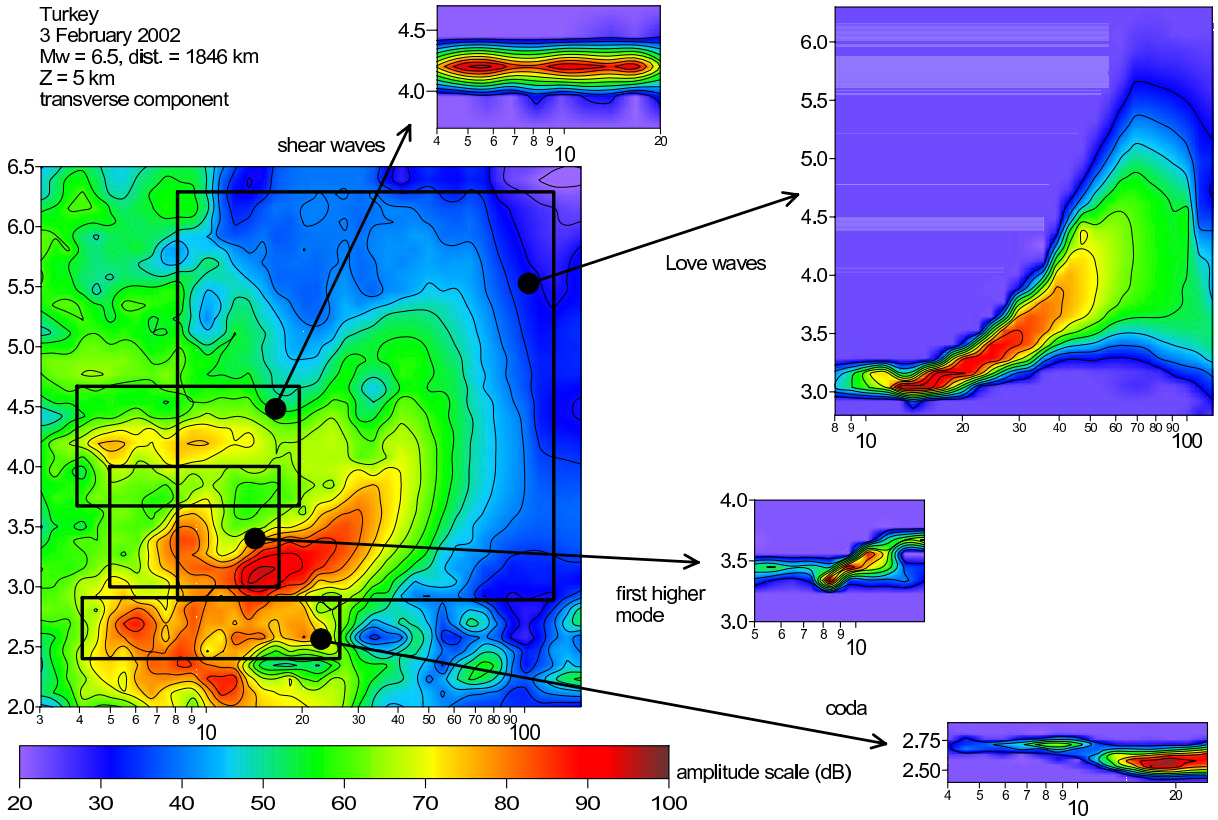


Figure 1.11: (*Fig. 6 in Kolínský, 2004; modified*) Spectrogram of the transverse component of the Turkish earthquake record is shown. This is another possible depiction of Figs. 1.7 and 1.8 **A**. The four rectangles represent a selection of three dispersive surface wave modes (L_0, L_1 and coda) and one non-dispersive ridge of body S-wave. The energy contours spacing is 5 dB for the whole spectrogram and 10 dB for the four separated spectrograms.

harmonic signals, we may be satisfied with the results even when the signals are nearly monochromatic only for restricted time interval around the the envelope maxima. The estimation of the instantaneous period does not work for low amplitudes and hence we can see striking variations in the instantaneous periods estimated along some of the guasimonochromatic signals in times where their amplitudes are too low.

Fig. 1.8 shows a spectrogram with much more monochromatic signals. In panel **E** of Fig. 1.8, we see that the signals are nearly monochromatic for the longer periods while they are a bit blurred for the shorter ones. It means that the filter width is set properly for the longer periods, while the filters for the shorter periods are too broad in the frequency domain.

The method of setting the different filter widths for different periods is described in Section 1.4. Examples are also given in Section 6.11 and in Fig. 6.12.

analytical signal

The filtering is applied for the positive frequencies of the spectrum; the negative ones are not used in further processing. Using only the positive frequencies is the way to obtain an analytic signal corresponding to the original record. If we make an inverse Fourier transform of the whole spectra, we get, of course, the same real time signal. If we make an inverse FT only of the positive part of the spectra, multiplied by the factor of two, we get a complex time signal – the analytical signal. The real part of the analytical signal equals the original real signal and the imaginary part represents the Hilbert transform of the original signal. Modulus of the analytical signal given as a square root of the sum of squares of real and imaginary parts of it represents an envelope of the original record.

By making an inverse Fourier transform of each of the filtered spectra (positive frequencies only), we obtain a set of nearly monochromatic complex signals of selected frequencies. By computing the modulus of each of it, we obtain an envelopes of the nearly monochromatic signals. Each of these envelopes represents a distribution of energy carried by a wave of a given period.

In fact, the time-domain signals are not exactly monochromatic because the filters have finite widths in the frequency domain, as we mentioned in preceding paragraphs. Regardless of the fact at which period the given signal was filtered, the instantaneous frequency along the whole filtered quasimonochromatic signal is computed using the derivative of the instantaneous phase, which is given as an arctan of the

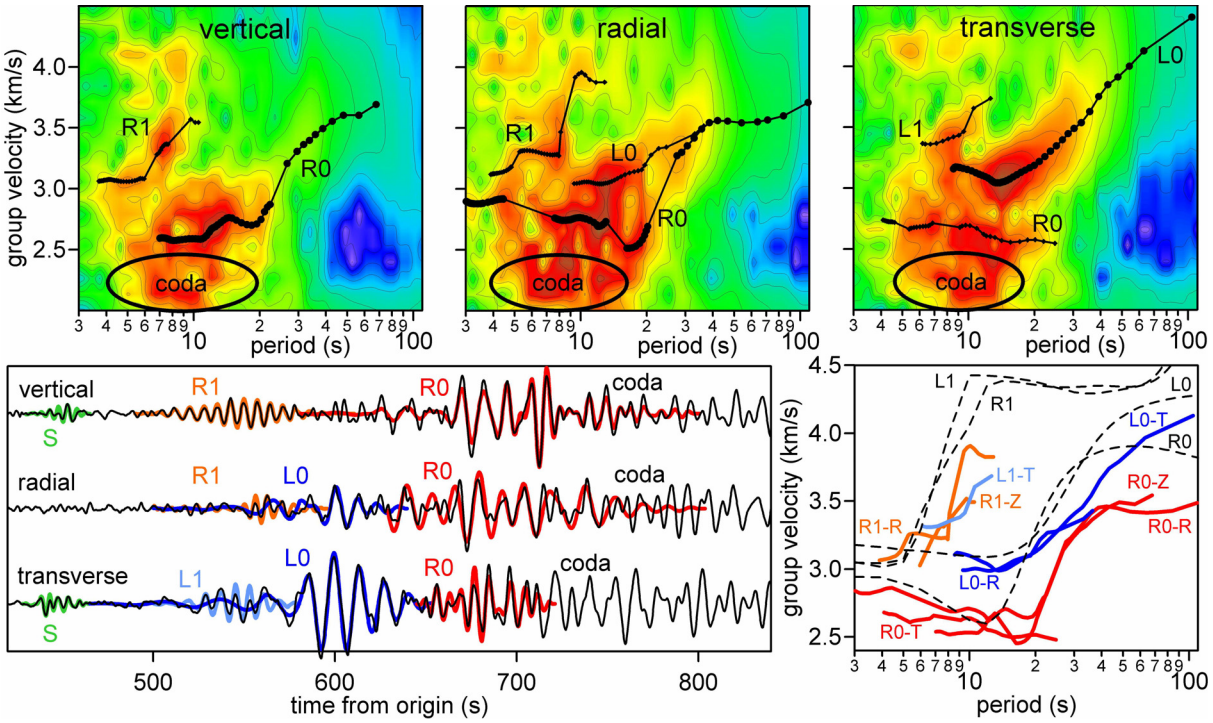


Figure 1.12: (*Fig. 8 in Kolínský, 2004*) Surface wave analysis of three-component record of the earthquake in Turkey, February 3, 2002, origin time: 07:11:28.41 UTC, epicentral coordinates: 38.57° N and 31.27° E, depth: 5 km, $M_w = 6.5$, epicentral distance to the Praha seismic station: 1846 km. The same color amplitude scale as in Fig. 1.11 is used for imaging all spectrograms. The energy contours spacing is 5 dB.

ratio between imaginary and real part of the analytical signal. Hence, the analytical signal is used two times in our computation – for computing the envelope of the quasimonochromatic time signal as well as for estimation the instantaneous period of the signal.

separated dispersed wavegroup

To create a separated seismogram containing only the waves of selected mode, we need to select the proper ridge as it is shown on the right side of Fig. 1.11. The procedure selects a broader part of the spectrogram along the estimated dispersion curve – the whole dispersion ridge. The detailed scheme of the procedure is depicted in Fig. 1.6. The procedure uses the maximum of each nearly monochromatic signal envelope (bold orange dashed line) and finds the two nearest inflection points of the envelope (red circles, red dashed lines). One of these points is before the envelope maximum and the other behind it. By a linear extrapolation using the derivation of the inflection points (pink lines), two zero points are found (dark green circles, dark green dashed lines). The signal envelope (bold orange dashed line) between the two inflection points is kept, both parts of the envelope between the inflection and zero points are smoothed by the cosine window (violet line) to the zero amplitude and the rest of the original envelope is truncated. It results in a truncated envelope (bold blue line). This process is applied not only to the signal envelopes but also on the nearly monochromatic signals themselves (thin orange dashed line). The same time values of inflection and zero points found at the signal envelope are used for the corresponding signal and the truncated signal is produced (thin blue line in Fig. 1.6). Examples of this selection are shown in Fig. 1.5 – bold dashed lines are the truncated and smoothed nearly monochromatic signals and bold solid lines are their corresponding envelopes.

The truncated and smoothed real parts of nearly monochromatic signals are summed up and they create the separated seismogram. Process of the summing of the separated seismogram is shown in Fig. 1.9. The uppermost plot represents the original seismogram. Than, the next four plots show examples of the harmonic components with selected and truncated fundamental mode wavegroups. Actually, a hundred of filters was used during the processing, but only four of them are depicted in the figure. The lowermost plot of Fig. 1.9 represents the resultant separated fundamental mode wavegroup obtained by the summation of the properly truncated harmonic components. The fundamental mode wavegroup, depicted in the lowermost plot of Fig. 1.9, is then shown in Fig. 1.10 by dark blue color in comparison with the original seismogram, which is also shown in the uppermost plot of Fig. 1.9.

When comparing the separated dispersive wavegroup with the original seismogram, we see what part of the original signal belongs to a selected wavegroup, see Fig. 1.10. By consecutive filtering of different modes, we can even separate the wavegroups coming at the same time with different frequency content

and compare the different modes mutually. As an example, see L_1 and L_0 modes in Fig. 1.10.

truncated spectrogram

By using truncated and smoothed envelopes we create a separated (or truncated) spectrogram. According to it, we check our assumption concerning the selection of the desired dispersion ridge from the original spectrogram. Examples of four truncated spectrograms are given in the right hand side of Fig. 1.11. Similarly as Fig. 1.10 allows to compare the original and selected wavegroup in the time domain, Fig. 1.11 compares the original and separated spectrograms in the frequency-time representation. Both depictions are equivalent and both are used to check if the desired dispersion curve and ridge were selected and filtered properly. The black solid rectangles in Fig. 1.11 show the areas of the original frequency-time plane which were used to filter out the wanted modes. By limiting the ranges of time and period we help the procedure to aim the processing at the requested ridge.

period range

This parameter can be set arbitrarily, but only a specified range has a physical meaning. In case of surface waves of distant earthquakes we do not study the periods shorter than 2 s and so there is no question of Nyquist frequency in case of sampling rate of 10 Hz, for example. The length of the longest period, which can be found, depends on the length of the studied part of the record. The procedure checks whether the maximum period that should be estimated is not longer than half of the length of the selected record interval. It is possible to look for even longer periods but we cannot estimate the envelope of such periods well and therefore the maximum of energy is less accurately resolved.

When processing short period surface waves from shallow seismic survey, we have to deal with limited sampling rate. The procedure is set to allow the shortest period of filtration to be four times the sampling time interval to estimate the envelope of such a wave properly.

time interval

This parameter is coupled with the period range. The time interval is the most important value to be changed for the selection of a dispersion ridge. To select the given dispersion ridge, we are sometimes forced to reduce the time interval (to zoom at the proper ridge) and therefore we obtain a less accurate group velocity for longer periods (envelopes are not well-defined or longer waves do not fit the short time window). In fact, the estimation of dispersion belonging to the given ridge is more critical in shorter periods. The overtones, coda and body waves have shorter periods than the fundamental mode of surface waves. Longer periods are usually well visible and the long-period parts of different modes do not overlap. After introducing the criterion of continuity for the dispersion curve compilation, reducing the time interval for selecting the desired dispersion ridge is not so critical, however, sometimes we still need to use it.

1.4 Formally exact description of the method

After the illustrative characterization of the method from the previous section, we now introduce a formal description of the multiple filtering. We follow the general explanation given in Kolínský (2004). Similar expressions are to be found also in Kocaoglu and Long (1993) and in Dobeš (1981). For the most complete and formal description of the multiple filtering technique, refer to Chapter 3, Section 3.2.3, where the paper Kolínský and Brokešová (2007) is cited.

Let us compare the multiple filtering technique with the technique of moving window. It gives a general view of the filtration both in frequency and time domains. The frequency-time representation can be defined in the form of an integral $S(F,T)$ in the time domain as

$$S(F,T) = \int_{-\infty}^{\infty} g(t)k(F,T,t)dt, \tag{1.1}$$

where t is time and $g(t)$ represents signal in the time domain (earthquake record). F is frequency and $k(F,T,t)$ is a complex kernel. That is why the integral $S(F,T)$ is also complex. While t is the variable of the time signal $g(t)$, symbol T denotes the time variable of the resultant frequency-time representation $S(F,T)$. In the same manner, symbol F denotes the frequency variable of $S(F,T)$ while symbol f represents the variable of the Fourier spectrum $G(f)$ corresponding to the time signal $g(t)$. The variables T and F also represent "central time" and "central frequency" of filters in time and frequency domains, respectively, as we will see later. We set the dependence of the kernel on the variables t and T to be

$$k(F,T,t) = k(F,T-t) \tag{1.2}$$

so that we can write the integral 1.1 as

$$S(F,T) = \int_{-\infty}^{\infty} g(t)k(F,T-t)dt. \tag{1.3}$$

For each fixed frequency F this expression represents convolution of signal $g(T)$ with the kernel $k(F,T)$

$$S(F,T) = g(T) * k(F,T). \tag{1.4}$$

In the frequency domain, this convolution transforms into multiplication. The kernel $k(F,T,t)$ can be understood as an impulse response of a filter. If we choose the kernel in form

$$k(F,T-t) = w(T-t).e^{-i2\pi Ft}, \tag{1.5}$$

we can write the integral (1.3) by formula

$$S(F,T) = \int_{-\infty}^{\infty} g(t)w(T-t)e^{-i2\pi Ft}dt. \tag{1.6}$$

The function $w(T-t)$ may be a narrow symmetric window centered at time T. For fixed T, the signal g(t) is weighted by the function $w(T-t)$. It means that function $w(T-t)$ selects only a small part of the original signal $g(t)$. Then we make a Fourier transform of this selected part of signal for given T. For different T, function $w(T-t)$ slides along the signal $g(t)$ and for each time T it weights the original signal again. Many consecutive Fourier transforms for each T are made. This method of computing a frequency-time representation is called "the moving-window technique".

Since the convolution in the time domain corresponds to the multiplying of the spectra in the frequency domain, we obtain the same integral $S(F,T)$ as an inverse Fourier transform

$$S(F,T) = \int_{-\infty}^{\infty} G(f)K(F,T,f)e^{iT2\pi f}df; \tag{1.7}$$

where $G(f)$ is a spectrum of the signal $g(t)$ and $K(F,T,f)$ is a spectrum of the impulse response $k(F,T,t)$. In other words, $K(f)$ is a Fourier transform of $k(t)$ for fixed F and fixed T. We can understand $K(F,T,f)$ as a transfer function of the filter. If we have the kernel

$$K(F,T,f) = W(F-f), \tag{1.8}$$

the integral $S(F,T)$ can be written as

$$S(F,T) = \int_{-\infty}^{\infty} G(f)W(F-f)e^{iT2\pi f}df. \tag{1.9}$$

Note that in the definition (1.8), there is no T variable on the right side of the equation and hence the kernel $K(F,T,f) = K(F,f)$ in the frequency domain does not depend on T. The signal spectrum $G(f)$ is weighted by the filtering function $W(F-f)$ and then the result is transformed back to the time domain. The weighting function $W(F-f)$ is centered to the frequency F. For each frequency F it selects only the part of the spectrum $G(f)$ near this frequency and the resulted weighted spectrum is transformed back to the time domain. We can do this for many central frequencies F and hence this method is called "the multiple filtering technique".

We define the spectrogram $P(F,T)$ as the squared modulus of complex integral $S(F,T)$:

$$P(F,T) = |S(F,T)|^2. \tag{1.10}$$

The frequency-time representation $P(F,T)$ displays a distribution of energy of signal both in time and frequency domain.

The results of moving-window and multiple filtering techniques are equivalent theoretically, but there can be some numerical differences.

In addition to the previous paragraphs, we would like to make remarks to the shape of the filters, to the uncertainty principle and to the width of the filters and its controlling. We use the Gaussian filters in the frequency domain when performing the multiple filtering. A symmetric window of the form of equation (1.8) looks, for example, like

$$W(F-f) = e^{-\alpha\frac{(F-f)^2}{F^2}}, \tag{1.11}$$

where α is a coefficient controlling the width of the filter and will be discussed later. These filters have a disadvantage of their infinite length, what is overcome by truncating the filters for low values of their amplitude. On the other hand, they have one very beneficial property. As the Fourier transform of a Gaussian function is again a Gaussian function, using the Gaussian functions as filters in the frequency

domain (as well as in the time domain in case of moving window technique) we achieve the best resolution in both domains together. Resolution of the filtering in the frequency domain is given by the width of the analysis window $W(F-f)$ while the resolution in the time domain is given by the width of the analysis window $w(T-t)$ as imply the equations (1.9) and (1.6), respectively.

The uncertainty principle is a general property of the Fourier transform. The localization of energy in the spectrogram is influenced by the width of the filters in case of the multiple filtering technique as well as in the case of the moving window technique. We cannot achieve arbitrary resolution in both frequency and time domains. If we use shorter time window to improve localization in the time domain, we obtain broader local spectrum in the frequency domain. When using narrow filter in frequency domain, we obtain worse resolution in time.

The uncertainty principle is expressed simply as

$$\Delta t \Delta f \geq \frac{1}{4\pi}, \tag{1.12}$$

where Δt and Δf represents the time and frequency dispersion, respectively. In our notation it reads:

$$\Delta\left[w(T-t)\right] \,.\, \Delta\left[W(F-f)\right] \geq \frac{1}{4\pi}. \tag{1.13}$$

If we use the Gaussian frequency window as a weighting function in the simplest shape of

$$W(F-f) = e^{(F-f)^2}, \tag{1.14}$$

we achieve the equality in expression (1.13) and therefore the smallest time and frequency dispersions. The impulse response (an inverse Fourier transform of the frequency-domain weighting function) is also a Gaussian function.

During the frequency-time analysis, the widths of the filters are set specifically according to the properties of the signal and according to the required resolution in respective domains. We do not necessarily need to have the best resolution in both domains together, sometimes, we look for better resolution in one of the domains to analyze the properties in that domain in detail. In our procedure, the scaling factor α can be easily changed and hence we can adjust the resolution of the frequency-time representation.

Let us discuss in detail the controlling of the width of the filters. When using the weighting function as

$$W(F-f) = e^{-\alpha(F-f)^2}, \tag{1.15}$$

the process of such filtering is called "the constant resolution filtering". The filter bandwidth controlled by $(F-f)$ is constant for all central frequencies F and is scaled by coefficient α constantly for all frequencies. The drawback of this filtering is that we cannot approach low central frequencies F. To get the well defined spectrogram, we need to keep the width of the filter $(F-f)$ smaller than the central frequency $(F-f) < F$. This condition is not fulfilled for low central frequencies F. For $F \to 0$ the weighting function covers too broad part of a spectrum to localize the energy well.

To improve this, we can use "the constant relative resolution filtering" (Dziewonski et al., 1969). The filtering function is given by equation (1.11). For the lower central frequencies F, the absolute value of filter width is narrower but the relative width of the filters given by $(F-f)/F$ remains constant. For $F \to 0$ the width of filters decreases to keep the resolution of energy constant in the frequency domain.

Now, let us discuss the parameter α. It is possible to change the width of the filters by increasing or decreasing this parameter. If the parameter α is constant for all the used central frequencies, we talk about "the homogeneous filtering". If the parameter $\alpha(F)$ varies with the central frequency, it is called "the optimal filtering". By increasing the parameter α toward low frequencies, we intensify the effect of the constant relative resolution filtering and by decreasing α we reduce this effect. When α is increased, it makes the filters narrower, if it is decreased, filters are broader.

In all our computations, we use the constant relative resolution optimal Gaussian filtering as a tool of the multiple filtering technique. The weighting function (filter) reads:

$$W(F-f) = e^{-\alpha(F)\frac{(F-f)^2}{F^2}}. \tag{1.16}$$

For controlling the coefficient α, we use a linear dependence on the central period T given as

$$\alpha(T) = a + b.T. \tag{1.17}$$

Period $T = 1/F$ is used instead of frequency F. Parameters a (absolute coefficient of the linear function) and b (slope of the linear function) can be changed during our analysis and so we can set them

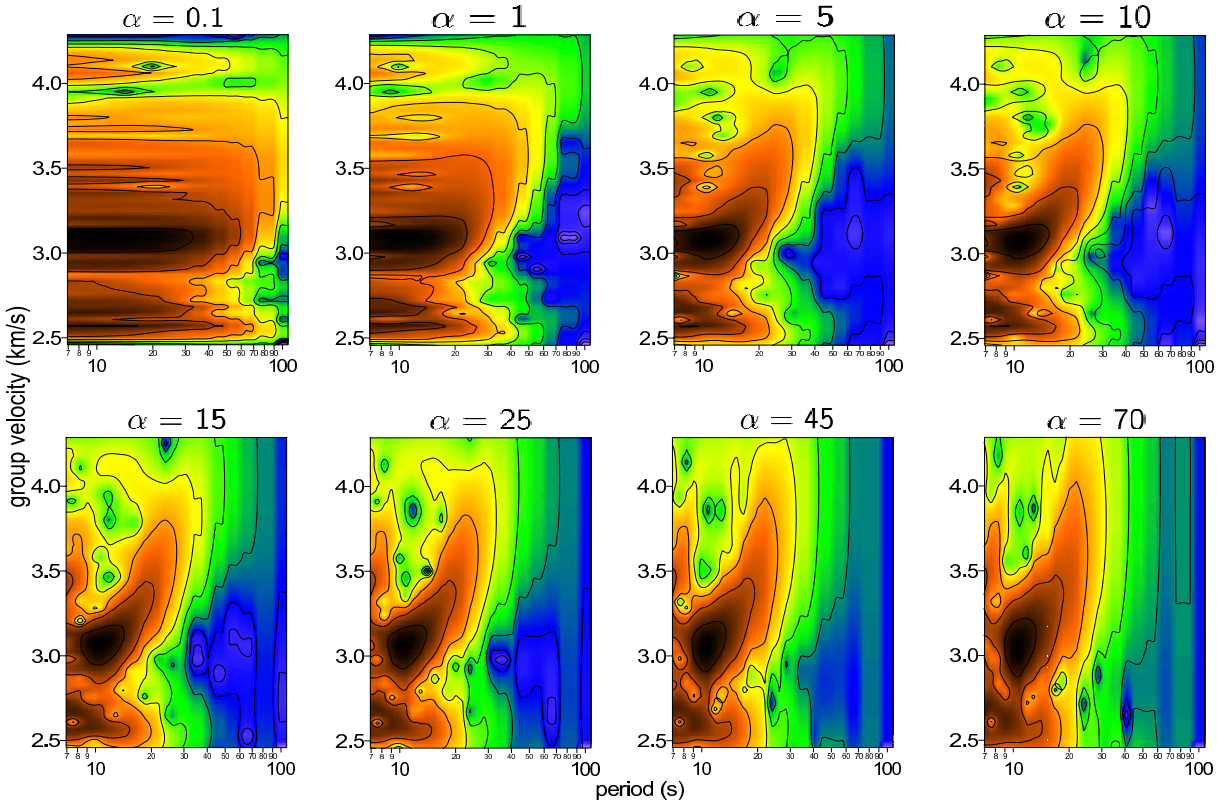


Figure 1.13: (*Fig. 5 in Kolínský, 2004 and Fig. 4.14 in Kolínský, 2003; modified*) Comparison of spectrograms computed for eight different values of the α coefficient and hence for eight different widths of the filters. In each plot, the α coefficient is constant in the whole period range. All other parameters of filtration remains the same. For $\alpha = 5$, the spectrogram is estimated well for long periods and for $\alpha = 45$, it is estimated well for short periods. According to these spectrograms, the optimal linear dependence of coefficient α on the central period T was set. The energy contours spacing is 7 dB.

to values leading to the best results of filtration. The slope b is negative in the equation (1.17) and so coefficient α is reduced for longer central periods T in our procedures.

Coefficient α is set experimentally to give smooth dispersion ridge. Its value depends on the properties of the record. Noise and frequency content of the record are the factors influencing the coefficient setting.

An example, how different coefficients α change the spectrogram, is shown in Fig. 1.13. In the example, α does not depend on the period – it has the same value along all the spectrum. In each of the eight panels, this value is different. We see that for example for the value $\alpha = 5$ or $\alpha = 10$ the dispersion ridge is well pronounced for longer periods but it is blurred for shorter ones. For shorter periods, α has too low value. It means, the filters are too broad and the filtering has low resolution in the frequency domain. We see that the spectrogram has nearly the same amplitudes between the periods 7 – 20 s and hence we cannot resolve the energy content in this period range.

For the values $\alpha = 45$ and $\alpha = 70$, the dispersion ridge in the spectrogram become well pronounced for shorter periods, but it is blurred for the longer ones. Again – α has now sufficiently high value for the shorter periods, but it is too high for the longer ones. The filters for longer periods are too narrow and so the resolution of the filtering is low in the time domain. We see that the spectrogram for longer periods remains nearly constant while moving along the time (velocity) axis. Generally, we use the relation 1.17 of α coefficient to give higher α for shorter periods and lower α for longer ones. Hence, b is negative.

Now we give a remark to the number of filters. Using large number of filters in the given frequency range means that the energy distribution in the frequency-time representation is multiplied and we do not see actual energy distribution for given time and frequency. The filters overlap each other by significant amount of their width. Sometimes also filters of other shapes are used in the multiple filtering. For example using cosine filters, we may easily adjust the distance between neighboring central frequencies so that the sum of the normalized filters will be equal to 1 and hence we get the distribution of energy undistorted. Since we do not need the energy distribution for our measurements to be kept accurate, we use large number of the filters. The filters of the Gaussian shape are implemented for their simplicity and natural physical properties of resolution both in frequency and time domains respectively. We take advantage of dense filter distribution to recover more dispersion points in our analysis. Of course, the density of filter distribution along the frequency axis in spectral domain is also adjustable in our computation.

1.5 Instrumental time correction

When processing any seismic data, instrumental transfer function has to be applied to obtain the proper amplitude and phase independent of the instrument used. However, using the arrival times of body waves measured by short-period geophones, the correction is almost never applied. As opposed to that, for surface wave analysis, the instrumental characteristic is a crucial tool to reveal the true properties of records. Each instrument distorts different periods by different way and since the properties of the signal changing with period is exactly the matter we are dealing with when processing dispersed surface wave records, we need to know the characteristic of the instrument to correct the records.

Instrumental transfer function is usually given by the poles and zeros. Using these, we obtain a complex function given as a ratio of two polynomials. The absolute value of this complex function gives us information how the amplitudes are distorted by the seismograph, the phase of the function tells us how the original phases of the record are shifted. The transfer function is given in spectral domain and its application is straightforward – we divide the spectrum of the measured record by the transfer function of the used instrument and we get corrected spectrum which corresponds to the signal as if it was measured with the instrument not influencing the record in any way.

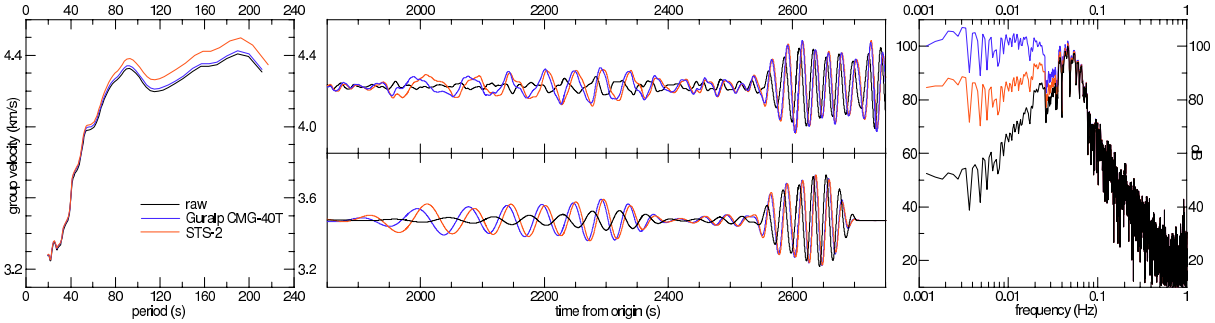


Figure 1.14: Instrumental transfer function influencing dispersion curve, record, separated surface wavegroup and spectrum. The same colors in each of the four plots represent the same instrumental correction applied. Black is the original record, blue is the record corrected as if it was measured by Guralp CMG-40T and red is the record corrected as if measured by STS-2.

Fig. 1.14 demonstrates the correction. We present a record of the transverse component of M = 8.3 earthquake, which occurred near the Kurile Islands on November 15, 2006, origin time: 11:14:16 UTC, epicentral coordinates: 46.607° N and 153.23° E. The record was obtained at the Háje station (HAJ), part of the Příbram array, Czech Republic. Epicentral distance is 8635 km. By black color, the original record as it was measured, is depicted in the upper-middle plot. The lower-middle plot shows the separated surface wavegroup estimated by the multiple filtering technique. Corresponding dispersion curve is shown in the left plot and corresponding spectrum in the right plot. The same color for the same raw/corrected quantities is used in all four panels. The blue color at all four plots corresponds to the record, surface wavegroup, dispersion and spectrum, as it should look like when corrected for the influence of the instrument Guralp CMG-40T. This is the broadband seismograph actually used and hence, the blue lines shows the real quantities independent of the instrument. To emphasize the influence of different kinds of instruments, we add also another correction. The red color shows, how the record would look, if it was measured by the STS-2 seismometer.

We see that since the STS-2 instrument has a flat characteristic up to 120 s, the restoration of the longer period amplitude is not so strong as it must be when using the Guralp seismometer with a flat characteristic up to only 30 s. Since the amplitudes of long periods (> 30 s) are much more distorted by the Guralp, its correction has to increase the corresponding part of the spectrum more than in case of the STS-2. In other words, the STS-2-corrected amplitude spectrum differs from the original less than the Guralp-corrected. However, concerning the phases, the situation is opposite. The phase characteristic of the STS-2 is stronger than the one for Guralp and hence the dispersion curve corrected for the STS-2 seismometer differs from the original one more than the one corrected for the Guralp.

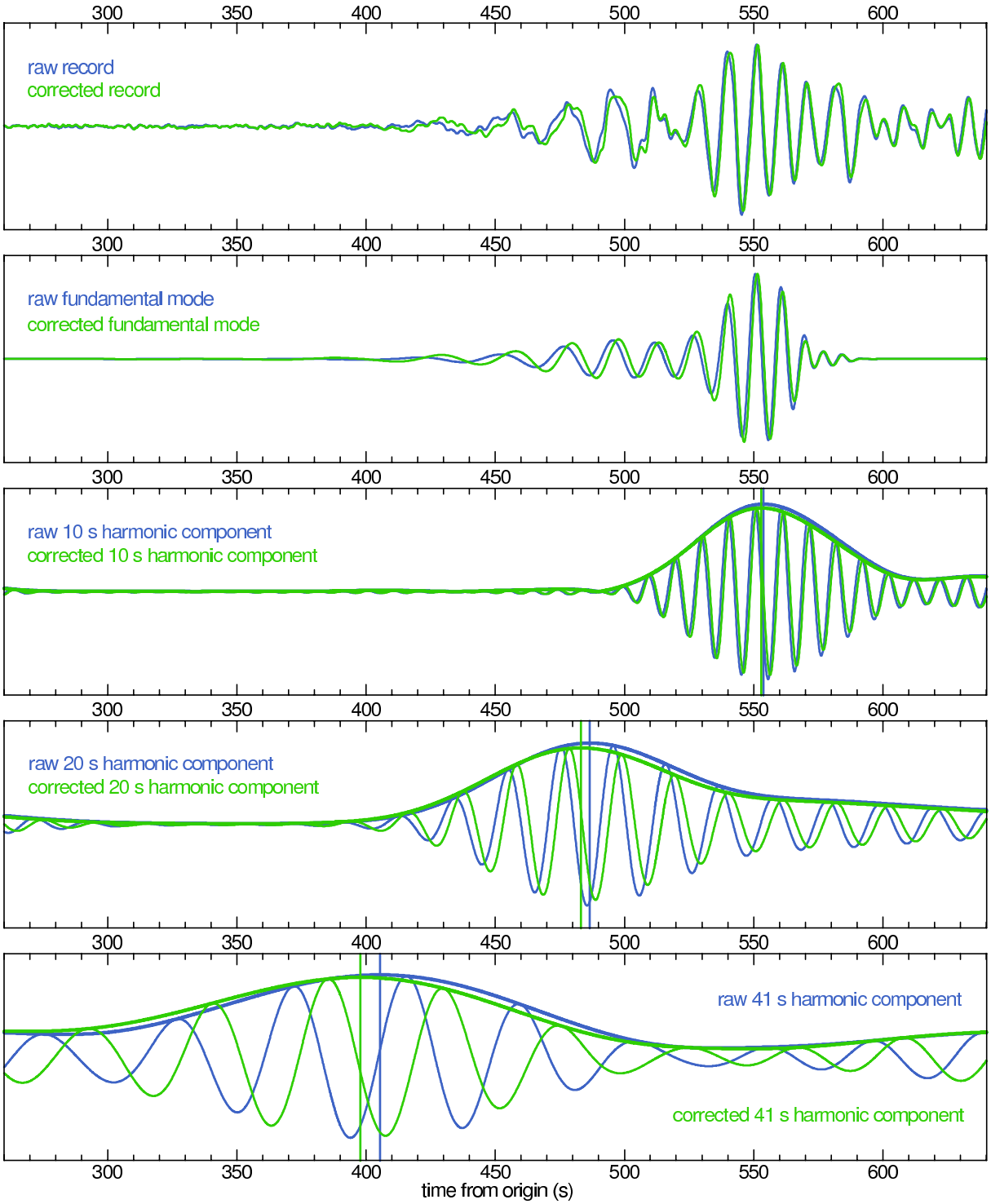


Figure 1.15: Phases are shifted toward later times and hence the phase velocities of corrected record are slower than those determined from the raw record. In the contrary, maxima of the envelopes are shifted toward smaller times and so the group velocities of the corrected record are higher than those determined from the raw record.

However, the influence of the phase characteristic on the group velocity is not straightforward. Group velocities are estimated using the envelopes of the harmonic components and the quantity which the phase characteristic is concerning is the phase of the underlying (carrying) wave beneath that envelope. Generally, the instrument cause a shift of the phase of the harmonic component. It looks like the whole harmonic signal is shifted in time by certain time interval. But together with the phases, which are shifted, the amplitudes are also restored. It causes that the envelope of the "shifted" harmonic signal does not shift in the same manner. It can be shifted less, more and even in the opposite direction.

This is illustrated in Fig. 1.15. We use a record of radial component of the Aegean Sea earthquake from October 5, 2005, origin time: 21:40:04.09, epicentral coordinates: 38.15° N and 26.75° E, recorded at the seismic station Tábor (TBR), Czech Republic. Epicentral distance is 1582 km. In the first panel,

the raw record is depicted by blue line and the instrument corrected record by green line. We see that the whole corrected record is shifted toward later times. In the second panel, separated fundamental mode of Rayleigh waves is presented, again both for the raw and corrected record. The last three panels shows harmonic components of the used record at 10, 20 and 41 s. We again see the phases of the components to be shifted toward later times. The vertical lines in the last three panels depict the maxima of the respective envelopes. The colors used for this time marks are the same as for the respective signals. As opposed to the phases, the maxima of the corrected envelopes are shifted toward lower times.

We conclude that it is not possible to use the time shifts given by the phase correction for restoration of the group velocities.

1.6 Seismograms, velocigrams or accelerograms?

Estimating the group velocity dispersion curve from any type of record gives the same results. Using the multiple filtering technique, we look for maxima of the envelopes of harmonic components of the original signal. These components are obtained using inverse Fourier transform of a filtered spectrum, which is filtered by the Gaussian filter. The envelope of the signal in the time domain is thus also a Gaussian-like. Such a signal is called Gabor's signal – the sinusoidal carrier wave is modulated by the Gaussian function. The Gaussian-like shape of the harmonic components of surface waves in the time domain is, however, not artificially caused by the filtration. It is a natural property of the waveforms, as mentioned, for example, in Widmer-Schnidrig and Laske (2007). Hence we may represent our harmonic components of dispersed surface wave by the Gabor's signals. The natural Gaussian-like envelopes of the surface wavegroups also justify the use of the Gaussian filters in the frequency domain.

Let us inspect, how the envelope of such a signal behave when the signal is differentiated. We assume a time signal $s(t)$, according to, for example, Červený (2001), which will be considered as a synthetic *seismogram* in next paragraphs, i.e., it represents a theoretical ground displacement

$$s(t) \quad = \quad \underbrace{sin(\omega_c t)}_{carrying\ wave} \quad . \overbrace{e^{-\alpha\omega_c(t-t_c)^2}}^{modulation} , \tag{1.18}$$

where t is time, α is the coefficient controlling the width of the wavegroup, ω_c is the angular frequency of the harmonic component, i. e., the frequency of the carrying wave, and t_c is the time, where the wavegroup is centered, i. e., the time of the maximum of the wavegroup envelope. In the following examples, we consider the values of the used quantities to be

$$\begin{aligned} t &\in (0; 300)\ \mathrm{s} \\ t_c &= 150\,\mathrm{s} \\ \omega_c &= 2\pi f_c\ , \text{ where} \\ f_c &= 0.05\,\mathrm{Hz}\ \text{(the period of the wave is 20 s)} \\ \alpha &= 0.003\ \ \text{(or 0.03 is some examples)} \\ \text{sampling frequency} &= 10\,\mathrm{Hz}\ . \end{aligned}$$

Using the given quantities, the carrying wave, the envelope and the resultant synthetic seismogram $s(t)$ is depicted in Fig. 1.16.

Intuitively, we see that the envelope of the given signal $s(t)$ exactly matches the modulation function $e^{-\alpha\omega_c(t-t_c)}$. It is not surprising, since the envelope of the carrying wave $sin(\omega_c t)$ is 1 and the envelope of the modulation function is the modulation function itself. After multiplication of the carrying wave by

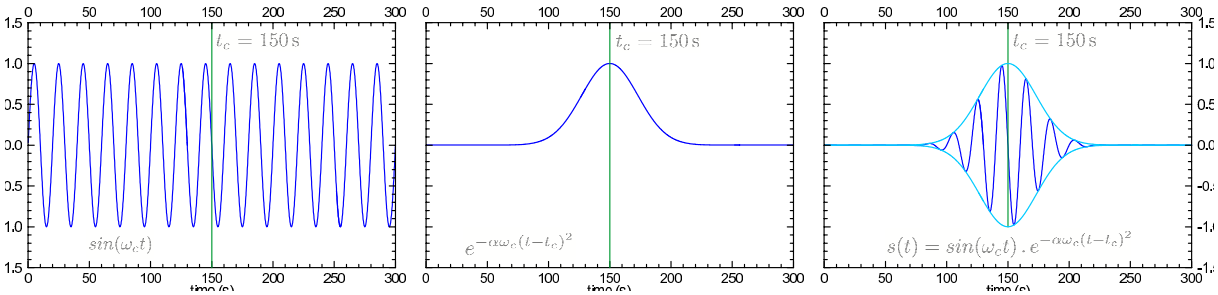


Figure 1.16: Carrying sinusoidal wave modulated by the Gaussian function produces Gabor's signal centered at time t_c.

the modulation function, the envelope equals the modulation function. However, this is true only when the carrying wave has a constant envelope.

We denote the derivative of the $s(t)$ as $v(t)$. It will represent a synthetic *velocigram* in the following examples, i. e., a theoretical ground velocity. The relation is

$$v(t) \quad = \quad s'(t) \tag{1.19}$$

and in case of our Gabor's signal it gives

$$v(t) \quad = \quad \underbrace{[cos(\omega_c t) - 2\alpha\,(t - t_c)\,sin(\omega_c t)]}_{carrying\ wave} \,.\, \overbrace{\omega_c\, e^{-\alpha\omega_c (t-t_c)^2}}^{modulation} \quad . \tag{1.20}$$

The synthetic velocigram $v(t)$ given by the latter expression is depicted in Fig. 1.17.

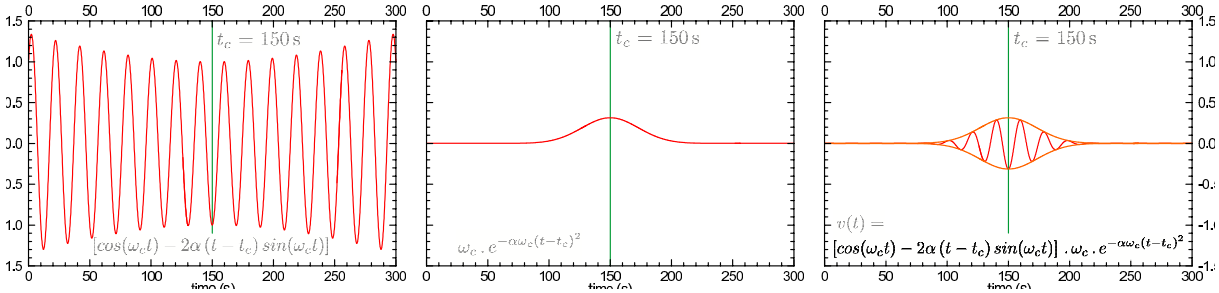


Figure 1.17: By derivation of the signal from the previous Fig. 1.16, we obtain a carrying wave with varying period modulated by modified Gaussian function but centered at the same time t_c.

We see that the carrying wave of $v(t)$ is given by a sum of *sin* and *cos* functions, however, its envelope is not constant now. It is important that even the envelope of the carrying wave is not constant, it is still centered at time t_c. Both the *sin* and *cos* functions have their envelopes constant and the only non-constant factor is the $t - t_c$ which is symmetric to t_c. The modulation factor of $v(t)$ also differs from the modulation of $s(t)$, the difference is the amplitude factor ω_c. However, the modulation of $v(t)$ is still centered at t_c. So, the envelope of the $v(t)$, given as a product of the envelope of the carrying wave and the modulation function, must be also centered at t_c as it was in the case of the envelope of $s(t)$. Both envelopes drawn together are presented in Fig. 1.18.

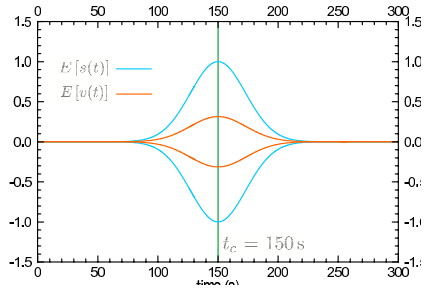


Figure 1.18: Comparison of envelopes of the signals from Figs. 1.16 and 1.17. Their shape differs, the position in time is the same.

This is what we wanted to prove – the maximum of the envelope of the velocigram $v(t)$ is found at the same time t_c as is the maximum of the envelope of the seismogram $s(t)$. Hence it does not make any difference if we estimate the group propagation time from the record of ground displacement or from the record of ground velocity when the ground displacement is represented by the Gabor's signal.

Let us examine the shape of both envelopes more precisely. The envelope $E\,[f(t)]$ of a given real function $f(t)$ is defined as a modulus of the analytical signal $A\,[f(t)]$ of that function as

$$E\,[f(t)] \quad = \quad |A\,[f(t)]| \tag{1.21}$$

and the analytical signal is computed as

$$A\,[f(t)] \quad = \quad f(t) - i\,H\,[f(t)] \quad , \tag{1.22}$$

where $H\left[f(t)\right]$ is the Hilbert transform of $f(t)$. Because the Hilbert transform

$$H\left[sin(\omega_c t)\right] \quad = \quad cos(\omega_c t)\ , \tag{1.23}$$

the envelope of the carrying wave of $s(t)$ is

$$E\left[sin(\omega_c t)\right] \quad = \quad |sin(\omega_c t) - i\ cos(\omega_c t)| \quad = \quad \sqrt{sin^2(\omega_c t) + cos^2(\omega_c t)} \quad = \quad 1\ . \tag{1.24}$$

It may be shown that the envelope of the product of two functions is the envelope of one of the functions multiplied by an absolute value of the other function

$$E\left[f(t)g(t)\right] \quad = \quad E\left[f(t)\right]\ |g(t)|\ . \tag{1.25}$$

To prove this, we need the Bedrosian's theorem (Bedrosian, 1962), which tells that

$$H\left[f(t)g(t)\right] \quad = \quad H\left[f(t)\right]\ g(t)\ , \tag{1.26}$$

in other words that the Hilbert transform of a product of two functions is the Hilbert transform of one of them multiplied by the other. This theorem is valid for functions from $L^2(-\infty;+\infty)$ with detached spectra, what means that one of the spectrum is non-zero for frequencies distinct from those where the other spectrum is non-zero so that $F\left[f(t)\right](\omega) = 0$ for $|\omega| > \omega_a$ and $F\left[g(t)\right](\omega) = 0$ for $|\omega| < \omega_a$ for certain frequency ω_a. Considering the Gaussian function as effectively non-zero for a finite frequency range, the spectra are detached in case of harmonic carrying waves and Gaussian modulation factors when at least approximately three periods of the carrying waves are squeezed beneath the modulation factor. In the left panel of Fig. 1.19, synthetic signals $s(t)$ and $v(t)$ are shown using the quantities listed above ($\alpha = 0.003$). Signals for narrower modulation factor $\alpha = 0.015$, with the mutually osculating spectra, are shown in the middle panel of Fig. 1.19.

In the following text, we derive an expression for the envelope of the synthetic velocigram $v(t)$ with respect to the original synthetic seismogram $s(t)$. The red envelopes in Fig. 1.19 have already been computed using this expression. For shorter Gabor's signals, the validity of the expressions deduced below is limited. The limitation can be demonstrated by the synthetic velocigram envelopes (orange) in Fig. 1.19. As long as these (orange) envelopes are well matched to the signals $v(t)$ (red), the relation between the envelopes of $v(t)$ and $s(t)$ is valid. By modeling signals and their envelopes for other widths of the modulation factors, we found out that the expression is still valid also for partly overlapping spectra, as shown in the right panel of Fig. 1.19 for $\alpha = 0.100$. Hence we see that since we typically find four and more periods within the modulation function during surface wave measurements, we are not constrained by the validity limitations of this deduction.

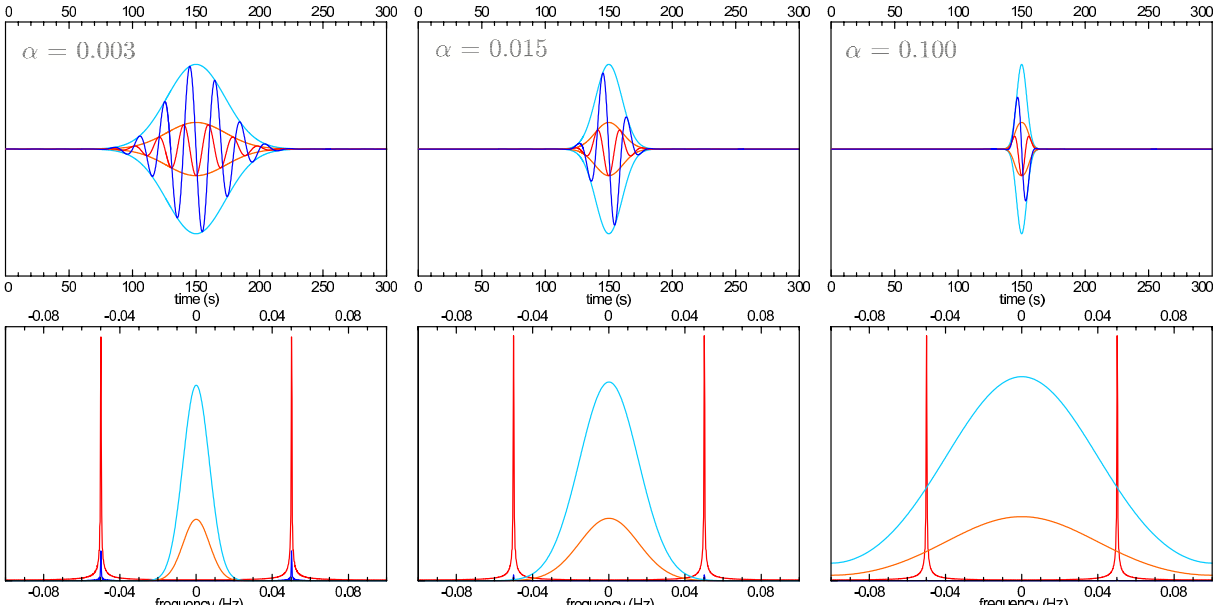


Figure 1.19: Synthetic seismograms $s(t)$ (dark blue) and velocigrams $v(t)$ (red) with their envelopes (light blue and orange) and spectra of the carrying waves and the modulation functions of $s(t)$ and $v(t)$ for three different α coefficients. Spectra of the modulation functions (light blue and orange) have their respective height and the spectra of the carrying functions (dark blue and red) also have their respective height. However, the mutual heights of the carrying waves and modulation functions are not in scale. Notice the tiny spectra of carrying wave of $s(t)$ (dark blue), which are smaller for bigger α coefficients. They are almost invisible in the right plot compared with the red spectra of the carrying wave of $v(t)$.

Using the Bedrosian's theorem, the envelope of the product of $f(t)$ and $g(t)$ is

$$\begin{aligned} E\left[f(t)g(t)\right] &= \left|A\left[f(t)g(t)\right]\right| = \\ &= \sqrt{f^2(t)g^2(t) + H^2\left[f(t)g(t)\right]} = \\ &= \sqrt{f^2(t)g^2(t) + H^2\left[f(t)\right]g^2(t)} = \\ &= \sqrt{f^2(t) + H^2\left[f(t)\right]}\sqrt{g^2(t)} = \\ &= E\left[f(t)\right]\left|g(t)\right| \qquad \text{q.e.d.} \end{aligned} \tag{1.28}$$

Assuming that $f(t)$ is the carrying wave with envelope equaled to 1, see equation (1.24), and $g(t)$ is the modulation factor, we see that the envelope of the seismogram $s(t)$ is

$$E\left[s(t)\right] = e^{-\alpha\omega_c(t-t_c)^2}\,, \tag{1.28}$$

and so it does equal the modulation factor as expected. It means that the dark blue modulation factor (middle plot of Fig. 1.16) equals the light blue envelope (right plot of Fig. 1.16).

The envelope of the velocigram $v(t)$ is a bit more complicated to investigate. From equation (1.20) we see that the modulation factor of $v(t)$ differs only by the amplitude scaling from the modulation of $s(t)$, however, the carrying wave $[cos(\omega_c t) - 2\alpha\,(t-t_c)\,sin(\omega_c t)]$ has non-constant envelope, in other words, it already has its own modulation. To determine the envelope of the whole $v(t)$, we need to estimate the envelope of the carrying wave of $v(t)$ and after that to simply multiply it by the modulation factor as in the case of $s(t)$. The Hilbert transform of sum of two functions is the sum of the two Hilbert transforms of those functions, so

$$H\left[f(t)+g(t)\right] = H\left[f(t)\right] + H\left[g(t)\right]\,. \tag{1.29}$$

To shorten the next expressions, substitute

$$\underbrace{cos(\omega_c t)}_{f(t)} - \underbrace{2\alpha\,(t-t_c)}_{h(t)}\,\underbrace{sin(\omega_c t)}_{k(t)}\,.$$

Then the envelope of the carrying wave is

$$\begin{aligned} E[f(t)-h(t)k(t)] &= \left|A\left[f(t)-h(t)k(t)\right]\right| = \\ &= \sqrt{\left[f(t)-h(t)k(t)\right]^2 + H^2\left[f(t)-h(t)k(t)\right]} = \\ &= \sqrt{f^2(t) - 2f(t)h(t)k(t) + h^2(t)k^2(t) + H^2[f(t)] - 2H[f(t)]\,H[h(t)k(t)] + H^2[h(t)k(t)]}. \end{aligned}$$

By only rearranging the terms we have

$$E[f(t)-h(t)k(t)] = \sqrt{\underbrace{f^2(t)+H^2[f(t)]}_{E^2[f(t)]} + \underbrace{h^2(t)k^2(t)+H^2[h(t)k(t)]}_{E^2[h(t)k(t)]} - 2f(t)h(t)k(t) - 2H[f(t)]\,H[h(t)k(t)]}.$$

Using the Bedrosian's theorem we get

$$E\left[f(t)-h(t)k(t)\right] = \sqrt{E^2\left[f(t)\right] + E^2\left[h(t)k(t)\right] - 2f(t)h(t)k(t) - 2H\left[f(t)\right]H\left[k(t)\right]h(t)}\,.$$

Substituting back the functions for $f(t)$, $h(t)$ and $k(t)$ we see that the last two terms under the square root vanish, since

$$f(t)h(t)k(t) + H[f(t)]\,H[k(t)]\,h(t) = [cos(\omega_c t)2\alpha\,(t-t_c)sin(\omega_c t)] - [sin(\omega_c t)2\alpha\,(t-t_c)cos(\omega_c t)] = 0.$$

Hence, under the square root we have

$$E\left[f(t)-h(t)k(t)\right] = \sqrt{E^2\left[cos(\omega_c t)\right] + E^2\left[2\alpha\,(t-t_c)sin(\omega_c t)\right]}\,,$$

what gives, after using the equation (1.25)

$$E\left[f(t)-h(t)k(t)\right] = \sqrt{E^2\left[cos(\omega_c t)\right] + E^2\left[sin(\omega_c t)\right](2\alpha\,(t-t_c))^2} = \sqrt{1+(2\alpha\,(t-t_c))^2}\,. \tag{1.30}$$

As we know the envelope of the carrying wave of the $v(t)$ to be given by equation (1.30), we see that the envelope of the whole $v(t)$ is

$$E\left[v(t)\right] = \sqrt{1+(2\alpha\,(t-t_c))^2}\;\omega_c\,e^{-\alpha\omega_c(t-t_c)^2}\,. \tag{1.31}$$

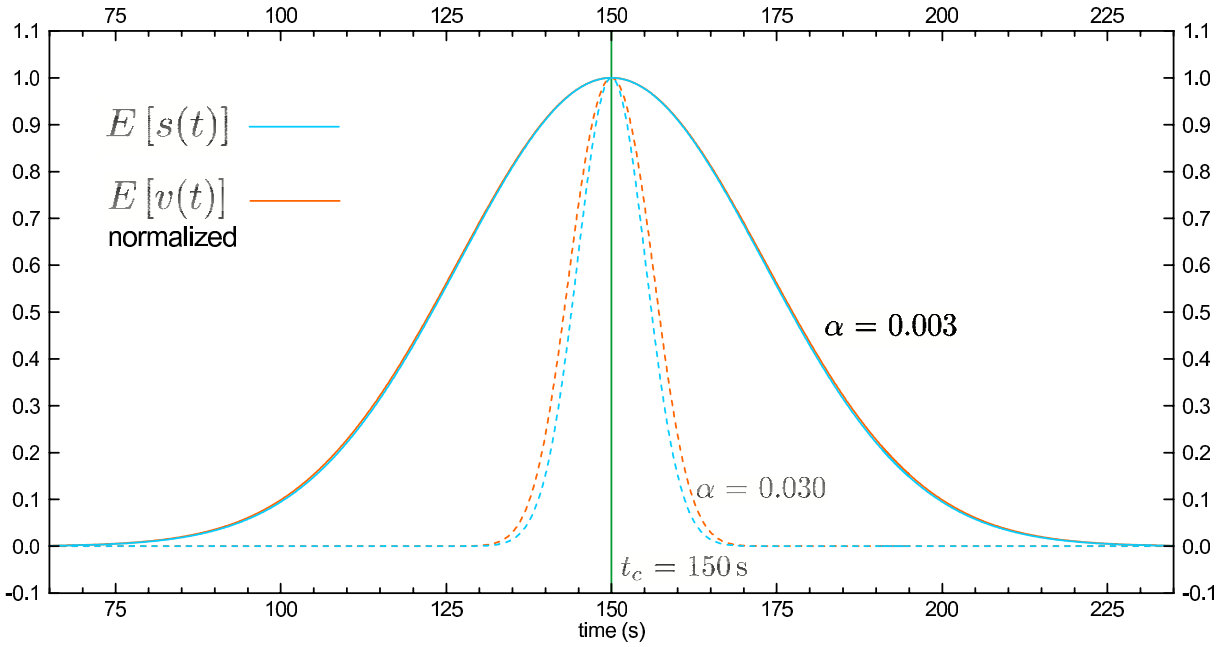


Figure 1.20: Normalized envelopes from Fig. 1.18 for $\alpha = 0.003$ with comparison of envelopes for signals with coefficient $\alpha = 0.03$. All four envelopes are normalized to have the same height.

This envelope differs from the modulation factor of the $v(t)$ and hence, the orange envelope (right plot of Fig. 1.17) differs from the red modulation factor (middle plot of Fig. 1.17), despite the fact they seem to be nearly the same. Comparing the envelopes of $s(t)$ (eq. 1.28) and $v(t)$ (eq. 1.31) we get

$$E\,[v(t)] \quad = \quad E\,[s(t)]\,.\left[\sqrt{1+(2\alpha\,(t-t_c))^2}\;\omega_c\right]\;. \tag{1.32}$$

To emphasize the difference of both envelopes, we omit the amplitude scaling factor ω_c for a while and so we normalize both envelopes to the same height. Drawing them together we get the comparison in Fig. 1.20.

The figure shows that the orange envelope of $v(t)$ is a bit wider than the envelope of $s(t)$. In Fig. 1.20, envelopes of both $s(t)$ and $v(t)$ are shown for two different α coefficients. As the α coefficient is bigger, the envelopes are narrower and the difference between them is emphasized. It reveals the other difference between the signal and its derivative – as the envelope of $v(t)$ is wider then the envelope of $s(t)$, the spectrum $F\,[v(t)]$ is narrower than is the spectrum $F\,[s(t)]$. In addition, $F\,[v(t)]$ is shifted to higher frequencies then $F\,[s(t)]$. The comparison of both spectra is given in Fig. 1.21.

We depict the spectra for the two α coefficients to emphasize the different widths between $F\,[v(t)]$ and $F\,[s(t)]$. We see, for $\alpha = 0.003$ that while the light blue spectrum of $s(t)$ has its maximum at

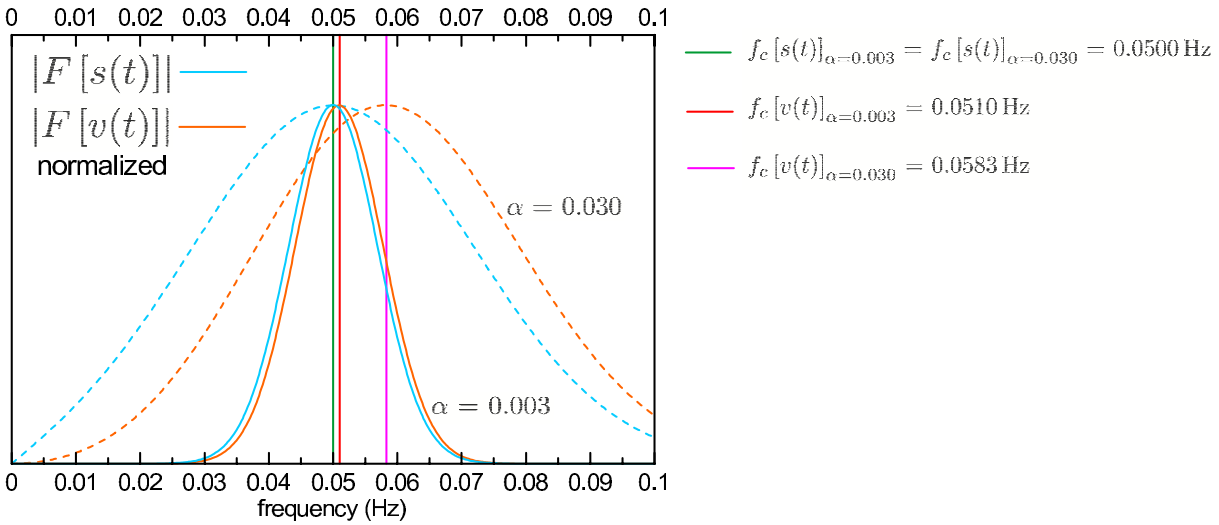


Figure 1.21: Fourier amplitude spectra of the signals from Figs. 1.16 and 1.17 for $\alpha = 0.003$ (solid lines) and $\alpha = 0.03$ (dashed lines). Central frequencies f_c are marked.

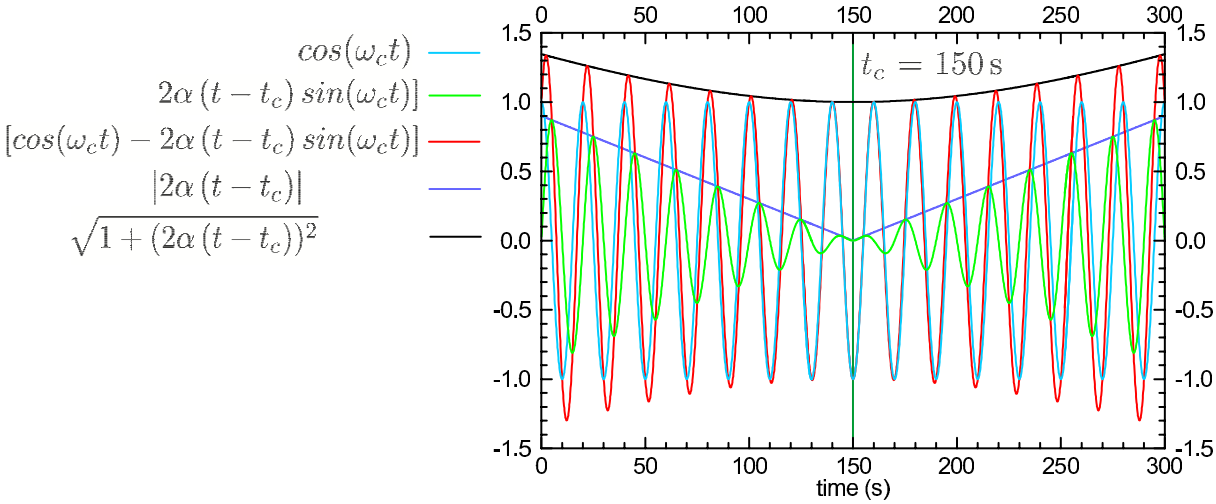


Figure 1.22: Decomposition of the carrying wave of velocigram $v(t)$ from Fig. 1.17. Two harmonic components with constant period produce wave with varying period since the sin is modulated by linear function.

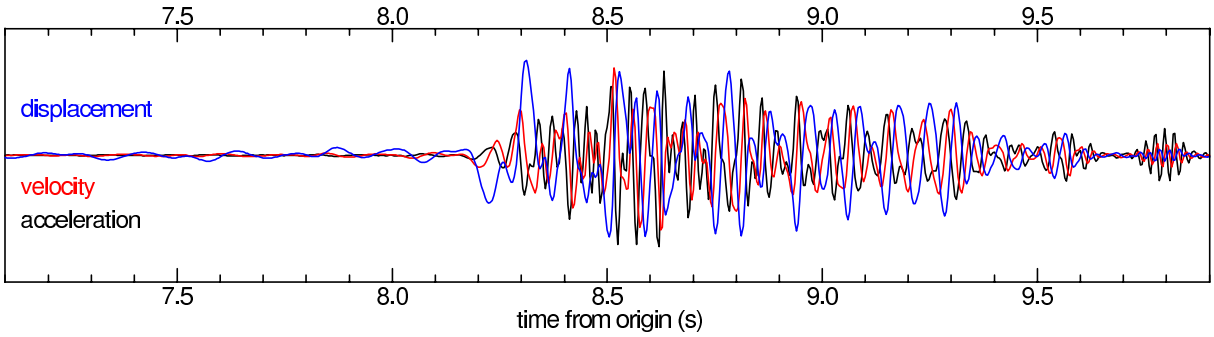


Figure 1.23: Synthetics of the ground displacement, velocity and acceleration corresponding to the single 1D structural model.

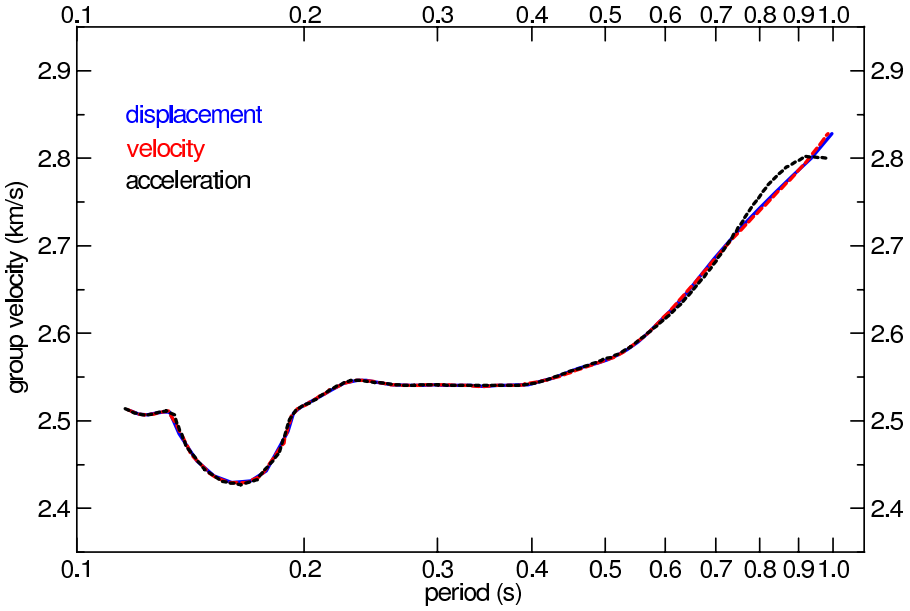


Figure 1.24: Synthetic data. Dispersion curves determined by the multiple filtering technique are the same regardless of the used record type.

$f_c = 0.050\,\mathrm{Hz}$, (green) what corresponds to the frequency of the carrying wave $\omega_c = 2\pi f_c$ in the term $sin(\omega_c t)$, the orange spectrum of $v(t)$ has its maximum at the frequency of $0.051\,\mathrm{Hz}$ (red). For $\alpha = 0.03$, the f_c for $s(t)$ remains the same, and for $v(t)$ it is shifted to $0.0583\,\mathrm{Hz}$ (violet). As the α is bigger, the spectrum is broader and the difference between the spectra of $s(t)$ and $v(t)$ is larger.

The higher frequency content may be demonstrated when looking at the carrying wave of the $v(t)$ decomposed to its particular terms as depicted in Fig. 1.22.

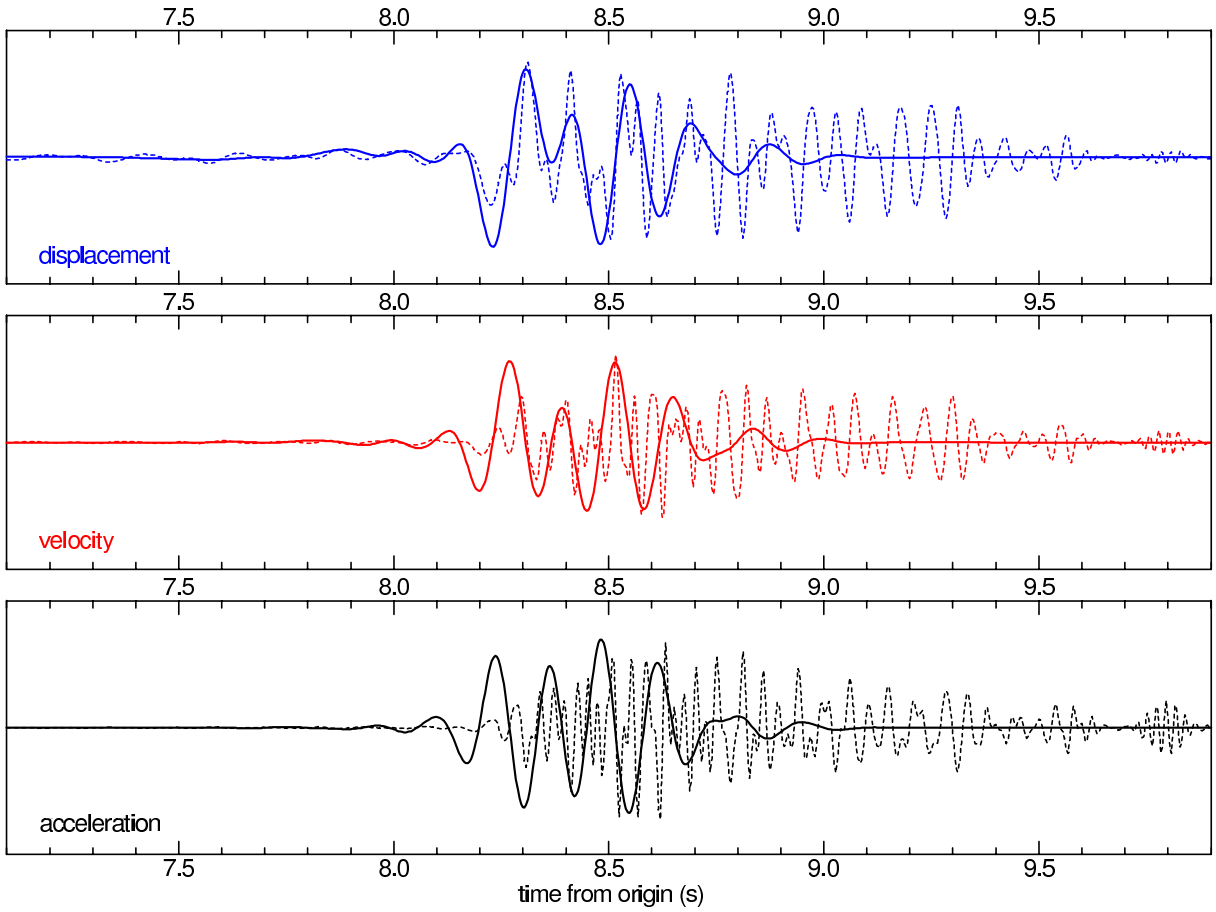


Figure 1.25: Separated fundamental mode surface wavegroups (solid lines) in comparison with respective synthetic records from Fig. 1.23 (dashed lines). Displacement, velocity and acceleration waveforms are shown.

Summing the *cos* (light blue) with modulated *sin* (light green) we obtain the carrying wave with higher frequency (red) than was the frequency $\omega_c t$ of the *cos* and *sin*, respectively. However, in the time t_c, where the contribution of $sin(\omega_c t)$ is zero, the instantaneous frequency of the carrying wave exactly equals f_c. Thus, the instantaneous frequency of the $v(t)$ beneath the maximum of its envelope is exactly the same as the instantaneous frequency of $s(t)$.

We see that although the seismogram $s(t)$ and its derivative, the velocigram $v(t)$, have different carrying waves (which differ both on amplitude and on phase) and although they have different envelopes (varying on amplitude and on frequency content), the time of the maximum of their envelopes is the same and the instantaneous frequency at the time of this maximum is also the same for both signals.

These results are demonstrated using a synthetic example. We consider a 1D velocity model of uppermost crust down to the depth of 3 km, which was determined from short period surface wave measurement at station Trojmezí in the Western Bohemia region from the record of blast in quarry Libá, see Chapter 3. Synthetic records were computed using the discrete wavenumber method (DWN) (Bouchon, 1981).

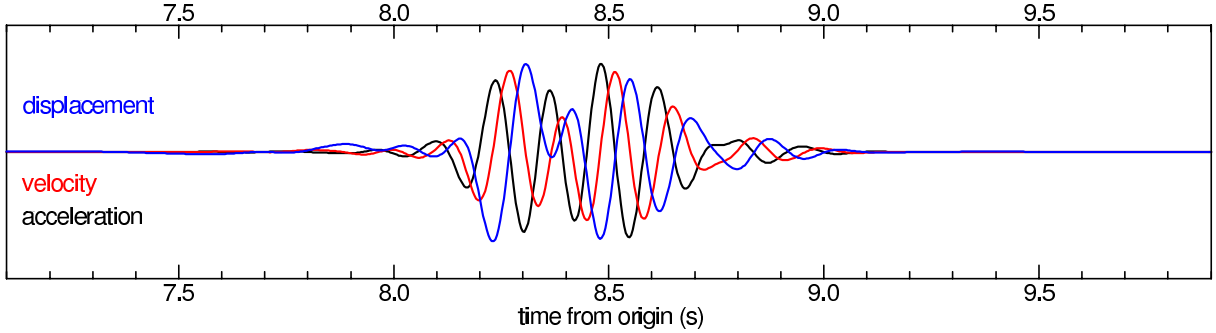


Figure 1.26: Fundamental modes separated using displacement, velocity and acceleration synthetic records from Fig. 1.25 in mutual comparison.

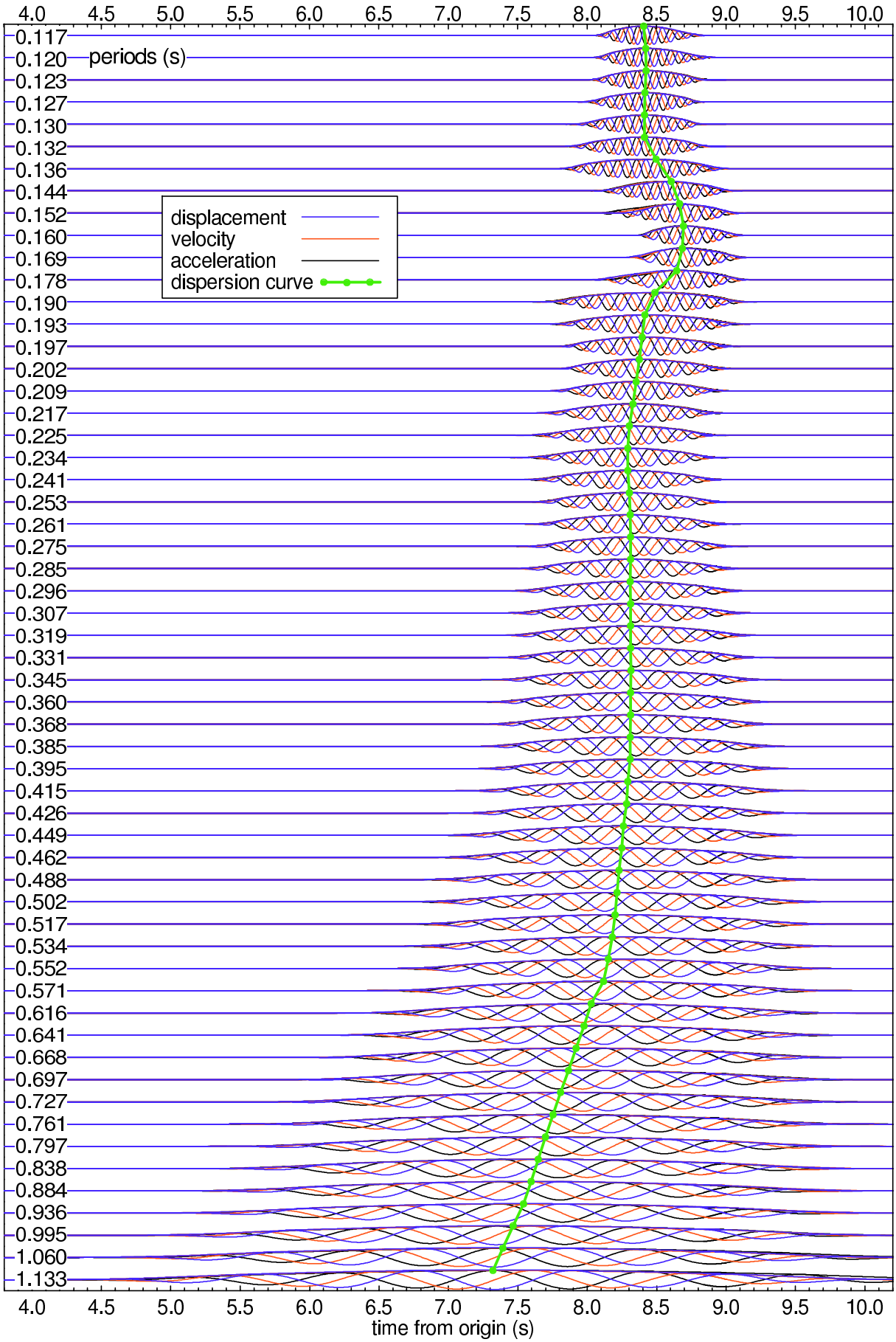


Figure 1.27: Harmonic components of the synthetic records presented at previous figures. Displacement, velocity and acceleration wavegroups are shown by different colors. The envelopes of all three component types are given for each period and the dispersion curve matching the envelope maxima determined for ground displacement is shown (green). The maxima of all three component types are at the same time for all periods.

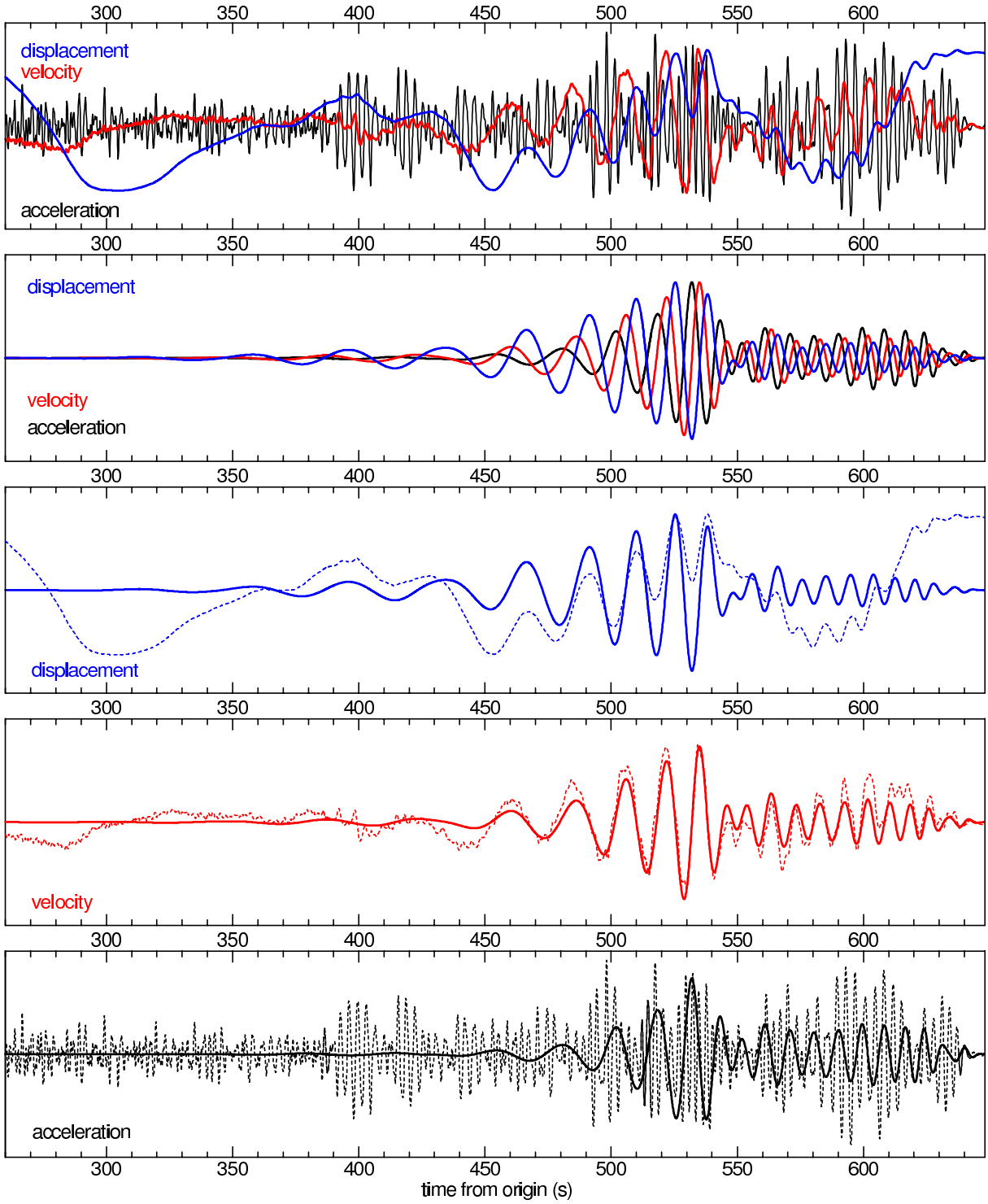


Figure 1.28: Transverse component of a real ground velocity record of the Aegean Sea earthquake measured at station HAJ is presented by the red line in the uppermost plot. Corresponding ground displacement is depicted by blue line and corresponding ground acceleration by black line. The second panel compares separated fundamental modes of Love waves obtained by processing independently all three record types from the uppermost plot. Last three panels shows comparisons of displacement, velocity and acceleration records with their respective separated fundamental modes.

For the single structural model, synthetic ground displacement, velocity and acceleration were computed, see Fig. 1.23. The particular synthetics are mutually distinctively different. Amplitudes are normalized to have approximately the same height.

All three synthetics were used for surface wave dispersion curve determination using the multiple filtering technique. The same width of filters in the frequency domain and the same time window of records were used for all three synthetics. The resultant dispersion curves are shown in Fig. 1.24. The dominant frequency of the records in Fig. 1.23 is between 10 – 20 Hz, however, we estimated the dispersion curves in the range from 0.11 s to 1.0 s. The longer wavelengths are much lower than the dominant portion

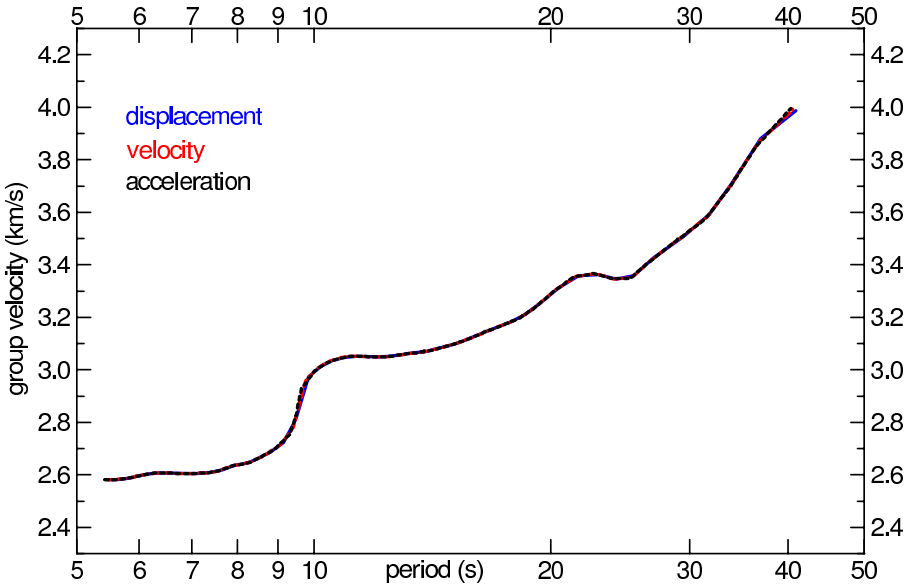


Figure 1.29: Real data. Dispersion curve determined from records of displacement, velocity and acceleration. All three dispersion curves are the same.

of the records, but the dispersion curves are clearly estimated in the broad period range. We see that all three curves are the same regardless of the fact they were estimated from three various records. Since the longer periods are further reduced in the velocity and acceleration synthetics, the longer-period part of the accelerogram-based dispersion curve slightly differs from the curves estimated from seismogram and velocigram.

Separated wavegroups corresponding to the fundamental modes with dispersion curves given in Fig. 1.24 are plotted in Fig. 1.25 by solid bold lines. In the background, the original synthetics from Fig. 1.23 are shown by thin dashed lines. The color setting is kept the same in all the figures. We clearly see the effect of longer period amplitude decay at the beginning of the main wavegroup and shorter period amplification at the end of the wavegroups as we proceed by the derivation from the displacement to the velocity and acceleration synthetics. The three separated fundamental modes are mutually different.

All three separated surface wavegroups from Fig. 1.25 are shown together in Fig. 1.26. In this figure, we notice the approximate $\pi/2$ shift in the phases of the velocigram with respect to the seismogram and of accelerogram with respect to the velocigram, as the latter is a derivative of the previous and the derivative of a harmonic component is similar to the original but shifted by a quarter of period in time.

In the last figure of this example, Fig. 1.27, all normalized harmonic components which were used to determine the dispersion curves in Fig. 1.24, are shown for 57 filters with respective instantaneous periods of the envelope maxima. Again, the displacement components are blue, the velocity components are red and the acceleration ones are black. The respective three envelopes are drawn for each filter. We see that the carrying harmonic components of ground velocity are shifted in time by quarter of period ($\pi/2$) with respect to displacement. The acceleration components are shifted by π, what represents a shift of half of the period with respect to the displacement components. Hence, the acceleration phases have reversed polarity with respect to the displacement phases. Despite these facts, the maxima of the envelopes are at the same time for all three record types at each period and hence the green dispersion curve connecting all 57 components in Fig. 1.27 is the only one for all three synthetic records.

Another test of the dispersion curve invariance with respect to the record type is given using the transverse component of the Aegean Sea earthquake (Greece) measured at station Háje (HAJ) in the Czech Republic. The earthquake occurred on October 17, 2005, origin time: 05:45:16.0, epicenter coordinates: 38.13° N and 26.50° E. The epicentral distance is 1622 km and sampling rate is 10 Hz. This second test is given here to verify the idea of group velocity dispersion curve invariance using completely different type of record in comparison with the first test. The epicentral distance, frequency content, propagation times and velocities are different from those used in the first test. In contrast to the first test which was based on synthetic records, this second test uses real measured data.

The record was measured by the Guralp CMG 40T instrument, which records the ground velocity. We apply the instrumental transfer function on the raw data and it produces an instrument-independent record of ground velocity, which is depicted by red color in Fig. 1.28. The instrumental transfer function is given by a set of poles an zeros. We add one zero located at the origin of the complex plane to the transfer function, what produces a new transfer function which is equal to the original one multiplied by the $i\omega$ term. Since the multiplication by the term $i\omega$ in the frequency domain corresponds to the derivation in the time domain, and since the spectrum of the raw velocity record is divided by the transfer function,

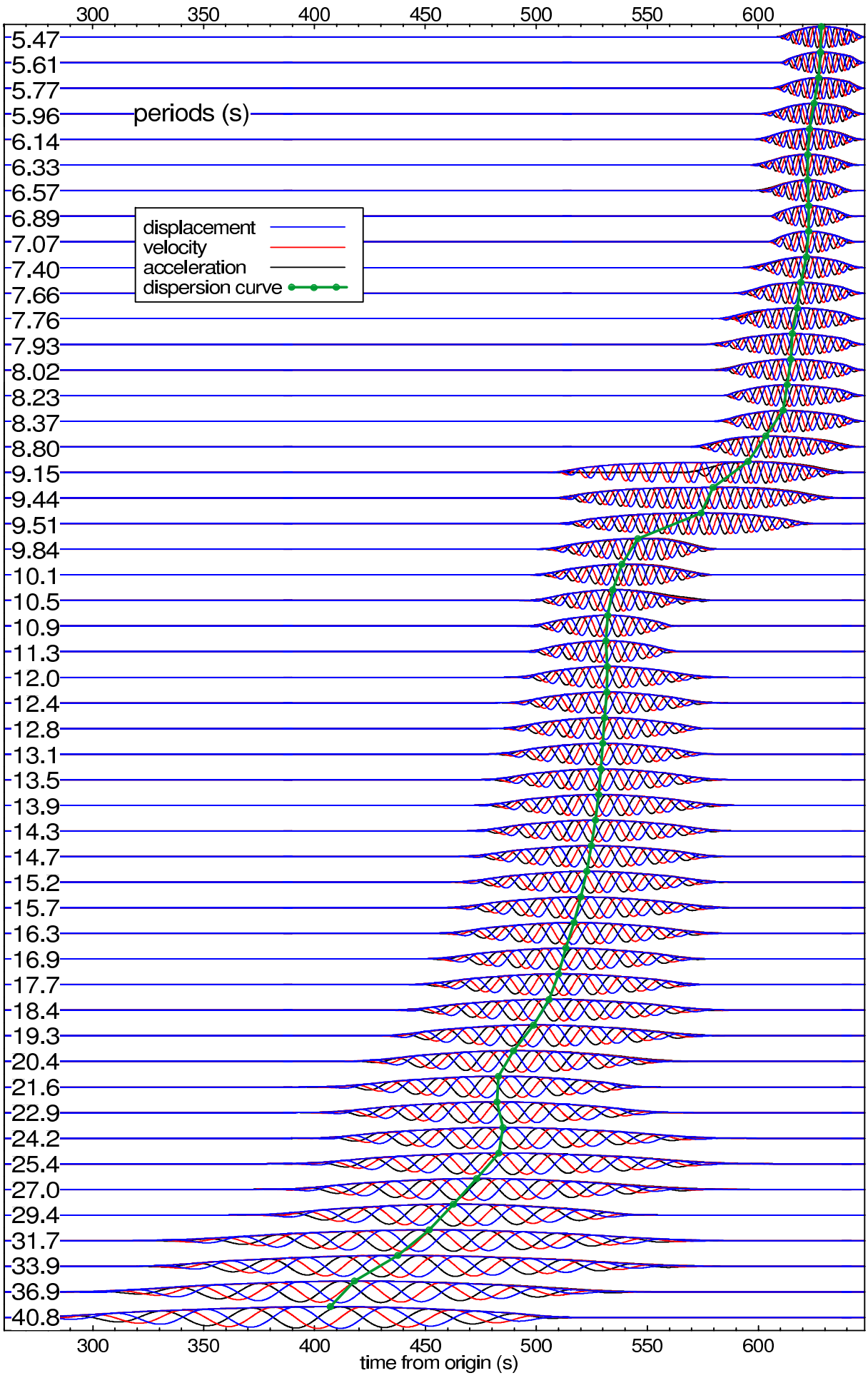


Figure 1.30: The same as in Fig. 1.27 but for real record of the Aegean Sea earthquake measured at station HAJ.

effectively, we integrate the velocity record and hence we obtain a record of ground displacement. It is depicted by blue color in Fig. 1.28. Similarly, we delete one zero from the set of zeros of the original transfer function and we obtain a derivative of the velocigram – an accelerogram – see black lines in Fig. 1.28.

Fig. 1.28, uppermost plot, shows the three records. We see that the long periods are strongly amplified in the displacement record (blue) with respect to the original velocity record (red). On the other hand, the acceleration record (black) contains a dominate portion of high frequencies in comparison with the velocigram.

We process the three records by the same manner as in the previous example. We use the same parameter setting during the multiple filtering for all three signals and we obtain three dispersion curves shown in Fig. 1.29. Despite the dissimilarity of the three signals, the multiple filtering technique finds the same dispersion curves for all three of them. The dispersion curves are determined in the period range 5.5 – 40.8 s using 53 filters.

The separated Love wave fundamental modes are compared in the second panel of Fig. 1.28. The three colors (blue, red and black) are retained for the same signal types as in the first panel. Last three panels in Fig. 1.28 present a comparison of particular records with their corresponding separated fundamental modes. The original record of ground velocity is closest to the separated surface wavegroup when comparing the frequency content. A similarity of the displacement record with the separated fundamental mode can be also seen, however, the Love waves are almost not recognizable in the record of ground acceleration due to the prevailing high frequencies.

As our multiple filtering method is not relaying on amplitudes, and, instead, it looks for the dispersion curve according to the criterion of continuity of the dispersion ridge, it is no problem for the method to find the proper fundamental wavegroup even in the case of such a high-frequency contaminated record.

1.7 Tests of the multiple filtering method

For the test of any technique, the particular implementation of the method has to be used. For the frequency time analysis, we use the SVAL program. During the SVAL program development, many tests of its function and of the multiple filtering technique were performeds. We present three of them here. The first and the second test verifies the ability of the SVAL program (Chapter 6) to determine the proper group velocity dispersion curve, the third test also benchmarks the ability of the PhaseCorr program (Chapter 7) to determine the phase velocity dispersion curve using the two-station method. Modifications of the second and third test are further developed in the papers by Kolínský and Brokešová (2007) (Chapter 3) and Kolínský et al. (2010) (Chapter 5), respectively.

The idea of the first and the second test is based on using a signal with analytically known dispersion. The first test was introduced by Kolínský (2003). We process a synthetic signal by the multiple filtering technique and then we compare the result with the synthetic analytically derived dispersion.

For the testing signal, a time dependence of the angular frequency $\omega(t)$ is set to be

$$\omega(t) = \frac{2}{C}t + \frac{1}{D} \qquad \text{or} \qquad T(t) = \frac{2\pi}{\frac{2}{C}t + \frac{1}{D}} \,, \tag{1.33}$$

since period $T = 2\pi/\omega$. For the beginning of the signal, $t_0 = 0$, we choose the maximal period $T_{t=0}^{max}$ of the signal, which is related to constant D as

$$D = \frac{T_{t=0}^{max}}{2\pi} \,. \tag{1.34}$$

Constant C is related to the shortest period $T_{t=N}^{min}$ of the end of the signal $t_N = N$. N is the number of samples used. After choosing the longest period $T_{t=0}^{max}$, computing the constant D and choosing also the

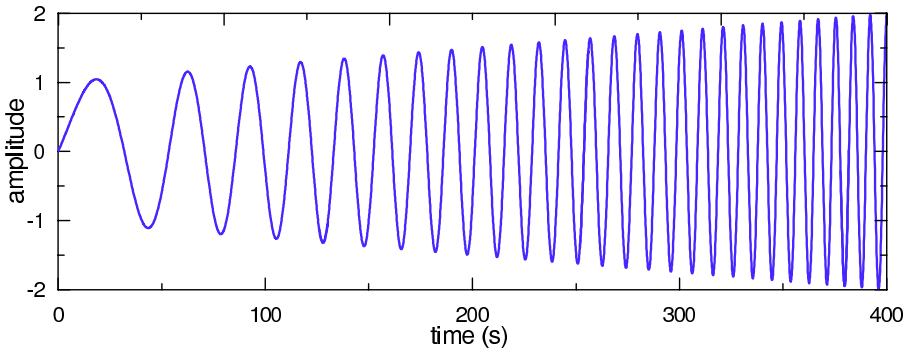


Figure 1.31: (*Fig. 4.7 in Kolínský, 2003; modified*) Synthetic seismogram with analytically known (synthetic) dispersion computed using the expression (1.37).

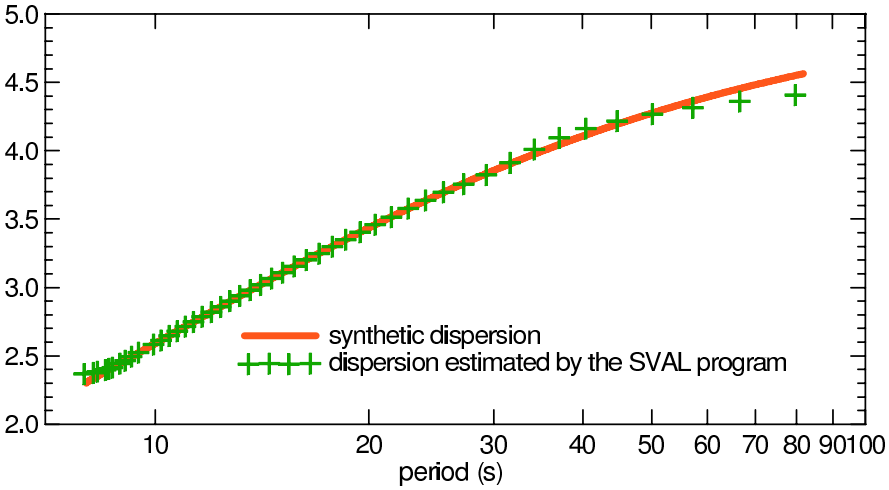


Figure 1.32: (*Fig. 4.8 in Kolínský, 2003; modified*) Comparison of synthetic dispersion curve with the curve determined by the SVAL program.

shortest period $T^{min}_{t=N}$, the constant C may be expressed as

$$C = \frac{2t_N T^{min} D}{2\pi D - T^{min}} \ . \tag{1.35}$$

The phase ϕ of the signal is given by an integration of the dispersion relation 1.33 with respect to time t as

$$\phi(t) = \frac{t^2}{C} + \frac{t}{D} \ . \tag{1.36}$$

Desired discrete signal $s_{synth}(t_n)$ with linearly increasing amplitude Amp, where n is the sample index, is then

$$s_{synth}(t_n) = \underbrace{\left(1 + \frac{A}{N} t_n\right)}_{Amp} cos\left(\frac{t_n^2}{C} + \frac{t_n}{D}\right) \ , \tag{1.37}$$

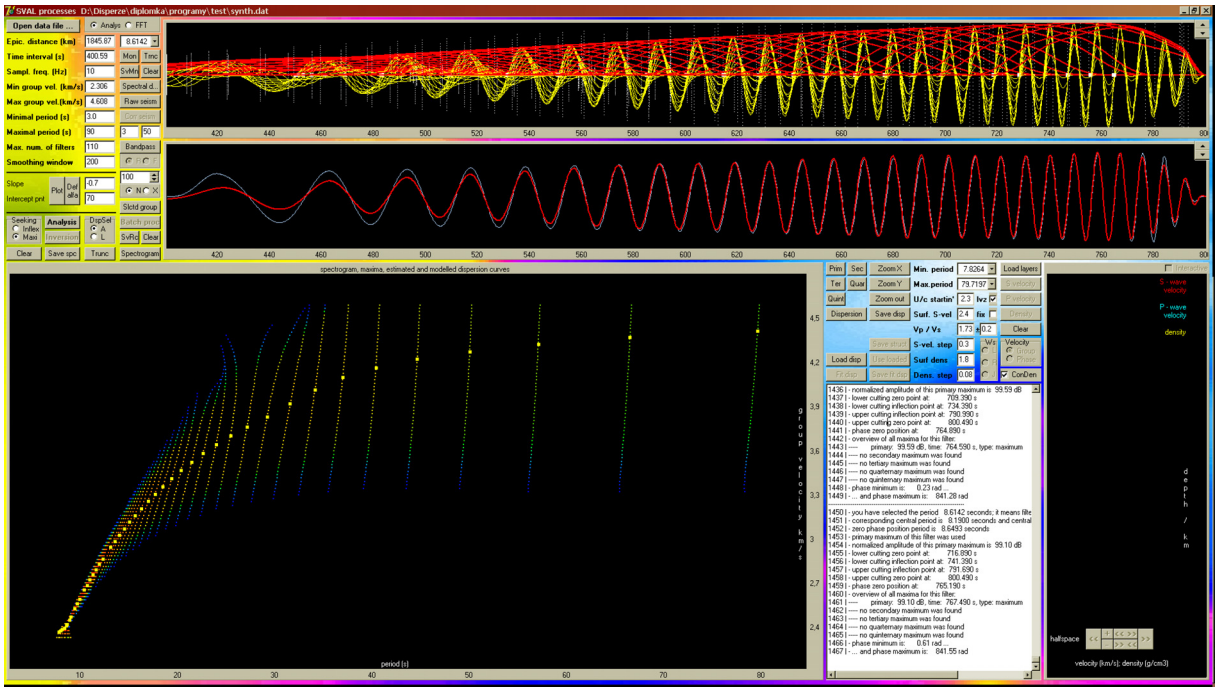


Figure 1.33: Screenshot of the SVAL program processing the testing synthetic seismogram from Fig. 1.31 (according to expression (1.37)). Light blue is the original seismogram with smoothed beginning and end, red is the selected separated wavegroup, yellow are the truncated harmonic components with red envelopes and rainbow-colored is the truncated spectrogram containing only the ridge belonging to the yellow dispersion curve. The dispersion curve is exactly the same as presented by green crosses in Fig. 1.32.

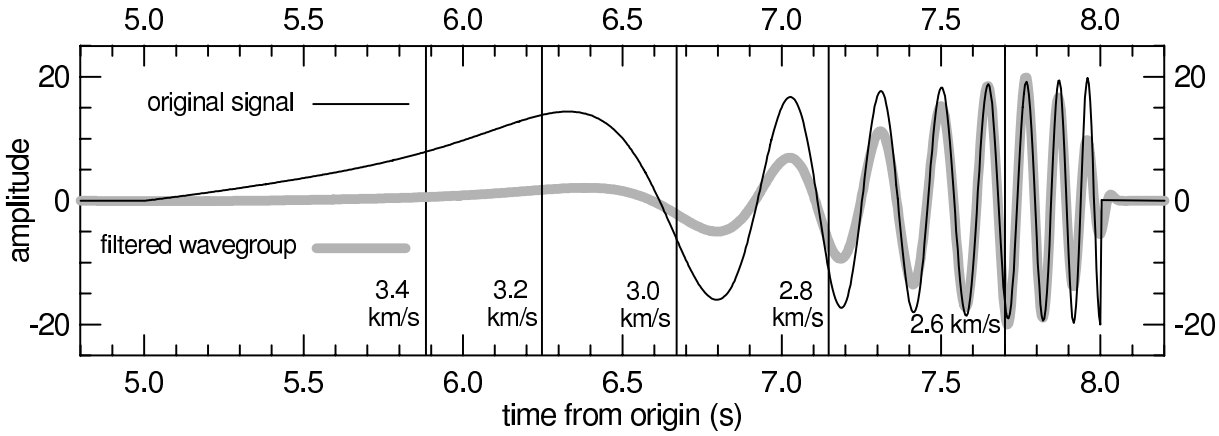


Figure 1.34: Synthetic signal computed according to the relation 1.37 but with parameters resembling the record of quarry blast. Original signal as well as separated surface wavegroup are shown.

where A is the constant setting the difference of the final amplitude with respect to the beginning amplitude $Amp = 1$ for $t = 0$. The n-th sample has an amplitude of At_n/N higher then the first sample. The synthetic signal is given in Fig. 1.31.

This signal is processed by the SVAL program and as a result, we obtain a dispersion curve. For the comparison, the analytical synthetic dispersion curve $U(T)$ is used. The period T of this analytical dispersion is computed according to the equation (1.33) and the group velocity U as

$$U = \frac{\Delta}{t}\,, \tag{1.38}$$

where Δ is the epicentral distance. This synthetic dispersion is given by the red line in Fig. 1.32. The constants and other parameters of the test are set to resemble the record of earthquake from Turkey, see caption of Fig. 1.3 for details, as it would be measured at station Praha (PRA), Czech Republic. The shortest period was set $T^{min} = 8\,\mathrm{s}$ and the longest one $T^{max} = 90\,\mathrm{s}$. The epicentral distance $\Delta = 1846\,\mathrm{km}$ and sampling frequency is 10 Hz.

The resultant determined dispersion curve is presented in Fig. 1.32 by green crosses. We see good agreement of this determined dispersion curve with the synthetic dispersion. The discrepancy is to be seen for longer periods, however, it is not given by the absolute value of the periods but by the fact that these periods are at the end of the spectra and their resolution is not so good. Similar effect of worse fit at the end of the period range is observed for arbitrary period range. If we set the signal to contain only shorter periods, again, we would observe not so good match for the periods at the edge of the range. A screenshot of the SVAL program main window is given in Fig. 1.33. The testing signal as well as the dispersion curve are visible. Harmonic components with their envelopes for the whole period range from 8 to 80 s are also drawn.

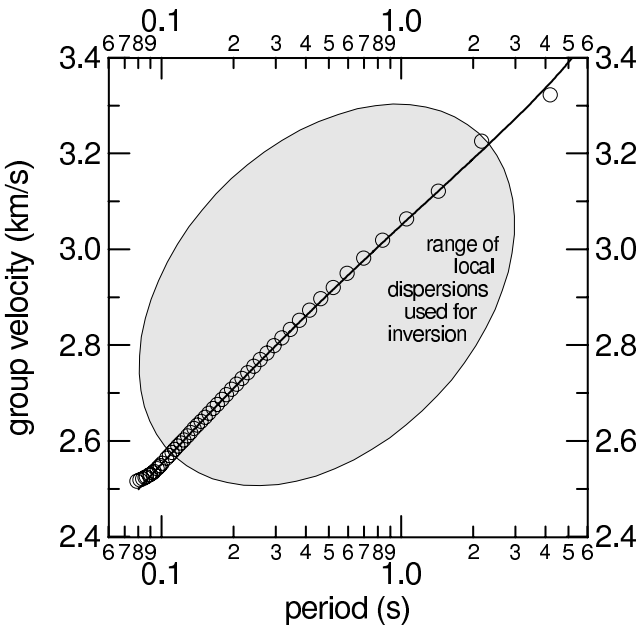


Figure 1.35: Comparison of synthetic and determined dispersion curves from the second test. Synthetic curve is drawn according to the dispersion relation 1.33.

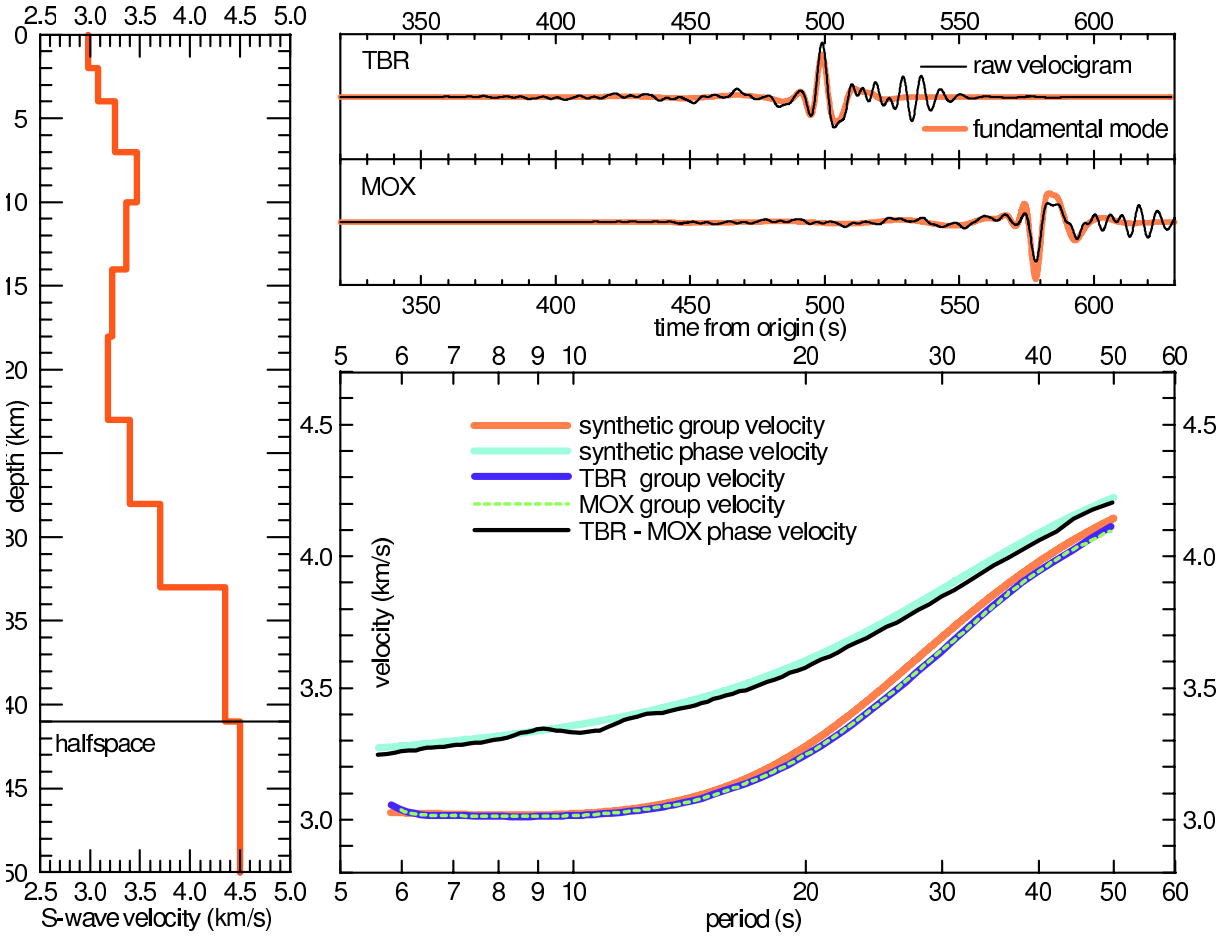


Figure 1.36: For given structure, synthetic seismograms are computed by the DWN technique. Synthetic and determined phase and group velocity curves are compared.

The second test is similar to the first one, however, different geographical parameters and properties of the synthetic record are used. The second test is set to resemble the record of a measurement of the quarry blast – the period range is 0.08 – 10.0 s, epicentral distance is $\Delta = 20$ km. Synthetic record with separated fundamental surface wavegroup is shown in Fig. 1.34. Fig. 1.35 presents the comparison of the synthetic dispersion curve with the one measured by the SVAL program. By the ellipsis, a range of velocities and periods of dispersion curves commonly measured at the records of quarry blasts is marked.

A modified version of this second test have been included in the paper by Kolínský and Brokešová (2007), refer to Chapter 3, where additional random noise has been added to the synthetic record. Comparing the results of both versions of the test we see no difference concerning the match of the synthetic and determined dispersion curves and so we conclude that the additional noise have not affected the dispersion curve estimation at all.

The third test is aimed at testing the ability of determination of both the group and phase velocity dispersion curves. Both the multiple filtering technique provided by the SVAL program (Chapter 6) and the time-domain correlation technique for estimation the phase velocities provided by the PhaseCorr program (Chapter 7) are used in this test. The analysis procedure is tested using the given shear wave velocity model, for which synthetic seismograms are computed for two stations. For this model, synthetic group velocity dispersion curves as well as synthetic phase velocity dispersion curve are also computed. The synthetic seismograms are processed by the multiple filtering technique. Besides the determined group velocity dispersion curves at both stations, the records are also correlated to estimate the relative phase velocity dispersion curve. The resultant dispersion curves are compared with the synthetic ones. Modification of this third test is also given in the paper by Kolínský et al. (2010), see Chapter 5 for details.

For the third test, we use following geographical setting: the source is in the Aegean Sea, Greece, and synthetic seismograms are computed for stations Tábor (TBR) and Moxa (MOX) in the Bohemian Massif (Czech Republic and Germany) by the Discrete Wavenumber method (Bouchon, 1981). The structure including low velocity zone (LVZ) (bold red line in Fig. 1.36) does not correspond to the real average structure between the Aegean Sea and the Bohemian Massif and so the seismograms are not resembling the real measurements. However, we use the LVZ structure for the test to emphasize the ability of the



method to determine the group and phase velocity dispersion curves for the complicated medium. Orange lines in the upper right plots of Fig. 1.36 represent estimated separated fundamental mode wavegroups.

Synthetic phase and group velocity dispersion curves are computed using the modified Thomson-Haskell matrix method (Proskuryakova et al., 1981) – see solid light green and solid orange curves in the right bottom plot of Fig. 1.36.

Two group velocity dispersion curves estimated separately using the synthetic seismograms corresponding to TBR and MOX stations (solid dark blue and dashed light green lines in Fig. 1.36) are determined by the frequency-time analysis using the SVAL program as in the previous two tests. Comparing them with the synthetic group velocity dispersion curve (orange) we see a good agreement provided by the multiple filtering method.

This third test provides also an additional assessment of the phase velocity measurement reliability using the two-station method. Harmonic components of the records from two stations are correlated in the time domain to determine precisely the time shifts between the two records for each period. Details are given in Chapter 5. In Fig. 1.36 we show also the determined relative phase velocity dispersion (solid black line). In comparison with synthetic phase velocity dispersion (solid green line), it proves the reliability of the two-station phase velocity measurement implemented in the PhaseCorr program.



Chapter 2

Surface wave inversion methods

2.1 Overview of the inversion methods

In the first half of the 20th century, surface waves were observed and at the same time, attempts to use the group and phase velocities for structural studies were performed. However, no inversion methods were used. In Section 1.1, paragraph *early surface wave observations*, we describe, how the synthetic dispersion curves were computed for simple media consisting of one or two layers over the halfspace and compared with the curves estimated from records. Such error-and-trial methods led to qualitative results only and could not provide exact velocity distributions.

An important step forward was the Haskel's (1953) matrix method for computation of arbitrary number of layers above the halfspace for both Love and Rayleigh waves. However, these computations, presented analytically, were still demanding practically and hence only three – four layers were used. For next few years, only the comparison with the observation was provided in the same manner as earlier. In the 60's, true inversion techniques were elaborated. However, Gupta et al. (1977) still used the simple comparison of given theoretical models with observed phase velocities to make conclusion for the crustal and upper mantle structure of Southeast Asia. In the following paragraphs, we will mention the basic methods of the inversion techniques to obtain structural parameters from surface wave dispersion data.

dispersion curve inversion (1962 – 2009)

As a first study which proposed an objective approach to estimate the structural parameters from the measured dispersion data may be considered the one made by Dorman and Ewing (1962). They were the first who introduced the numerical inversion method to obtain layered model from phase velocities. They used the *least-squares curve-fitting* program based on matrix computation given by Haskell (1953). Derivatives of phase velocity with respect to structural parameters were iteratively computed and different sets of parameters were used to produce the new dispersion curve. They also mentioned that any dispersion curve can correspond to an infinity of possible distributions of structural parameters. Their method was tested using the simplified data from Oliver et al. (1961), who studied the New York-Pennsylvania area. In the paper by Oliver et al. (1961), the classical trial-and-error method was used for interpretation and in that of Dorman and Ewing (1962), the new inversion technique produced more precise structure estimation.

Brune and Dorman (1963) used the same inversion technique to obtain the crust and upper mantle velocities. They tried to estimate optimum number of layers for the crustal structure. They also observed a nonuniqueness given by the trade-off between the change of the discontinuity depth and shear wave velocities in the layer above and below the discontinuity. They found that too great number of layers produced unreasonably high and low velocities in neighboring layers. However, the method still needed trial-and-error approach to get reasonable results when combining the phase velocity dispersion data with body waves arrival times. Their advanced paper is mentioned also in the review given by Widmer-Schnidrig and Laske (2007). The same least squares method was used also for example by McEvilly (1964).

Knopoff et al. (1966) studied only Rayleigh waves. They introduce constrains on P-wave velocity and density with respect to S-wave velocity to keep the inversion unique. Trial computations were made to fit approximately the main characteristics of the dispersion curves. Similar approach is also used in the SVAL program presented in this thesis – one may play with the forward modeling to try to fit the

dispersion and to use these trials as a starting model for the real inversion.

Along with the new techniques of inversion, the forward computation methods were further developed. Schwab (1970) described a novel method of dispersion curve computation, called the Knopoff's method. It was compared with the older Haskell's matrix method and the Knopoff's methods turn out to be more effective for the Rayleigh wave dispersion curve computation, however, the speed of computation of the dispersion of Love waves was nearly the same as in the case of the Haskell's matrix method.

Concerning the forward modeling needed for the inversion, the partial derivatives of dispersion curves are often necessary. Novotný (1970) proposed a method of computing the partial derivatives using the Haskell's matrix method. Only the phase velocities were computed numerically. The group velocity and all the derivatives were determined analyticaly, what overcame the former problems with numerical determination. Modification of the classical dispersion relation for surface waves using the quadratic slowness was proposed by Novotný et al. (1995). They simplified analytical expressions for the derivatives and for the group velocity computation. Holub and Novotný (1997) inverted dispersion curves from quarry blasts using the least squares technique for a series of a single-parameter changes. Another simplification of the partial derivatives solutions was achieved by Novotný (1999) and Novotný et al. (2005) who introduced the squared wavenumber instead of the phase velocity in the analytical equations for computing the group velocity and group and phase velocity partial derivatives. Novotný et al. (2005) also demonstrated the proposed method during inversion of observed dispersion curves from the Moravo-Silesian region and Western Carpathians by implementing the forward modeling into the gradient method.

Wielandt et al. (1987) used also a least squares approach to invert phase velocity dispersion curves of both Love and Rayleigh waves crossing the Bohemian Massif.

For inversion of Love wave group velocity dispersion curves, a modified method of the single-parameter variation was used by Novotný et al. (2001) for estimating 1D models of Earth crust between the Turkey and western Greece. For forward computation, the matrix method of Proskuryakova et al. (1981) was used, as is it used also in all computation in the presented thesis.

Herrmann (1992, 2002) assembled several programs for inversion and forward modeling of waveforms concerning all phenomena of seismology including surface waves. His procedures for inversion of phase velocity dispersion curves to shear wave velocities of upper mantle were used, for example, by Mitra et al. (2006) and by Raykova and Nikolova (2000 and 2003). In the presented thesis, Herrmann's software is also used for synthetic surface wavegroup computation using the modal summation technique, see Chapter 3. Another inversion computed by the Herrmann's programs was published by López-Pineda et al. (2007) who inverted fundamental mode dispersion curves to reveal the shear wave velocity structure and crustal thickness of Baja California and Mexico.

Luo et al. (2007) presented an inversion of both fundamental and higher mode dispersion curves to estimate the shear wave velocity. Sensitivity of different modes for different depths was discussed with respect of specific frequency ranges. For the joint multimodal inversion, the damped least-square method was used. Chen et al. (2007) used the *generalized linear inversion* for inverting the phase velocities measured at the array for the Slave craton in the Canadian shield to obtain shear wave velocity down to the depth of 400 km.

Sebe et al. (2009) used the *neighborhood algorithm* to invert the phase velocities of Love waves into the shear wave structure down to the depth of 2 km underneath Bucharest. Liang and Langston (2009) used the simulated annealing for the dispersion curve inversion in their ambient seismic noise tomography.

inversion used for advanced measurement techniques (1982 – 2009)

Besides the dispersion curves, inversion techniques were used for inverting the whole surface waveforms to obtain 1D path averaged shear wave velocities. Phase velocities from array measurements were inverted to reveal the structure beneath the array. 2D tomographic images were mapped using many path-averaged dispersion measurements. Joint inversions, for example, of surface wave data and receiver function were developed. Here we mention only a few of the hundreds of works dealing with different types of inversion techniques.

The least square inversion was used not for the structure determination but for the expression of observed global group velocities in terms of spherical harmonics by Nakanishi and Anderson (1982).

Snieder (1988a) proposed the inversion for lateral heterogeneity using the linearized scattering theory. He used the least squares method to invert the waveform in terms of fitting both the phases and amplitudes of the records. Numerical examples were given and the possibility of inversion for the local scatterers was discussed. Snieder (1988b) then used the proposed inversion method to the real records revealing the structure beneath Europe and Mediterranean. Low velocity zones were revealed under the western Mediterranean and higher velocities under the Scandinavian shield were found. He also found the effect of Massif Central and sharp transition along the Teiseeyre-Tornquist zone dividing Central Europe and the Eastern European platform. Resolution analysis of the method is given.

Stange and Friederich (1993) inverted phases, amplitudes and backazimuths of propagation of surface

waves from teleseismic event using nine stations forming an array in Southern Germany by the non-linear least squares scheme. It was also used for similar purposes by Friederich and Wielandt (1995). The downhill simplex method of simulated annealing was used for inverting the wavefield parameters and backazimuths of propagation in the two plane wave approximation by Forsyth and Li (2005) in the first stage of their surface wave array processing. In the second stage, structural parameters were found using the non-linear least squares method.

Ritzwoller and Levshin (2002) proposed the *multiwave inversion method* to obtain shear wave velocities using the fundamental and higher modes of surface waves as well as P and S wave traveltimes and guided waves for oil and gas prospection. They provided 1D structural model estimation, but the method was potentially suitable also for 2D and 3D inversion, when sufficient amount of data was available. Monte-Carlo method was used for the inversion computation, however, the authors stated that any other technique may by used as well.

Forbriger (2003a and 2003b) proposed a method for inverting the whole spectrograms stacked along the receiver line during the shallow seismic prospection experiment. He showed that since it is not possible to distinguish between the many higher modes, it is convenient to invert the whole spectrograms without the separation of the particular dispersion curves. In the first part of his work, Forbriger (2003a) developed a method of representing the spectrograms by parameterizing them using the Fourier coefficients given as an integrals of Bessel's functions. The study is extremely mathematically, theoretically and computationally difficult and besides the fact he mentioned some of the higher-mode problems and properties, the inversion method itself does not seem to be useful for practical use in prospection seismology.

Shapiro et al. (2004) constructed an inversion problem when surface waves together with thermodynamical constrains were jointly inverted to obtain a structure of the Canadian Shield. The Monte-Carlo technique was used for the computation of the task. Yoshida and Suetsugu (2004) used the hybrid method combining the grid search and non-linear inversion methods to reveal the lithospheric thickness beneath the Pitcairn hot spot from phase velocity dispersion curve measurement.

Julia et al. (2009) presented joint inversion of P wave receiver functions and Rayleigh wave group velocities to obtain a structure of the Indian shield. Group velocities were used to constrain the absolute values of shear wave velocities and receiver functions constrained relative velocity contrasts. The background velocity of the inversion was thus given by the dispersion measurement while detailed variations were recovered using the receiver functions measurement. Local 1D models were proposed beneath several station in the region.

Almost all the inversion procedures may be used for different computation, since their use for the surface wave observables inversion is a matter of the application of the particular method for the given problem and not a matter of the inversion method itself. In the next sections, we introduce the isometric method and its application for dispersion curve inversion.

2.2 Isometric method description

Isometric method is an inversion algorithm developed by Jiří Málek at the Department of Seismology, Institute of Rock Structure and Mechanics, Academy of Sciences of the Czech Republic, see Málek et al. (2005 and 2007).

The isometric method (IM) is a fast algorithm for solving weakly non-linear inverse problems with many parameters. It combines several advantages of standard methods such as simulated annealing, Newton's least-squares method and the simplex method (see Tarantola, 1987), and others. It employs linearization of the forward problem similar to Newton's least-squares method. A model closest to the measured data is found; the population of $m+1$ best models, where m is the number of model parameters, is stored in the memory. The new model is generated as the optimal linear combination of these models.

The distance is estimated in data space D using L_2 metric, what is the difference from the classical simplex method. The basic idea of IM is to define the distance ν_M between two models p_1 and p_2 in model space M as the distance ν_D of their functional values in data space D. Since the data vector $\vec{d}$ is obtained as $\vec{d} = F(\vec{p})$, where F is the operator describing the forward problem using model parameter vector $\vec{p}$, the distance is defined as

$$\nu_M\left(\vec{p_1};\vec{p_2}\right) = \nu_D\left(F(\vec{p_1});F(\vec{p_2})\right) \ . \tag{2.1}$$

This definition means that the model space and the data space are isometric, i.e. the distances in both spaces have the same measure. Distance ν_M is invariant with respect to the change of parameterization, which has many advantages as opposed to the situation of classical inverse methods when the distance of model parameters is measured in model space.

The main advantage of the IM is that it can solve inverse problems using a smaller number of forward problem computations than commonly used methods, because all model-data vector pairs are used many

times in successive iterations. The searching for the new model is more complicated and more costly, but it is overbalanced by the lower number of forward computations. It is not necessary to deal with derivatives. Typical problems, which are effectively solved by IM, are weakly non-linear problems with tens of parameters and complicated forward modeling. Therefore it fits quite well the inversion of dispersion curves using the matrix method. If the inverse problem is linear, IM finds the optimal solution in the first iteration. For non-linear inverse problems, many iterations are necessary.

The IM is described in the papers by Málek et al. (2005 and 2007). It was used for inversion and briefly introduced for example in Kolínský and Brokešová (2007) (Chapter 3), Kolínský et al. (2010) (Chapter 5) and Gaždová et al. (2008).

During the inversion the dispersion curve is computed for a given model and the distance (misfit function) between measured dispersion points and the modeled dispersion curve is determined, see Fig. 2.1.

The model is changed in order to minimize the misfit function. The first changes of the starting model (velocity with a constant step between all layers) are generated randomly in the vicinity of the starting model and then the new models are created considering the previously estimated best models. Sometimes, the new model is generated in a random way to prevent the algorithm from reaching a local minimum.

2.3 Application of the isometric method for dispersion curve inversion

When inverting the dispersion curves by the isometric method, we have several options. We can invert Love wave dispersion only, Rayleigh wave dispersion only or both Love and Rayleigh wave dispersion curves together. For each of these three options, we can invert also the densities or we can keep them constant. We can also keep the shear wave velocity in the first layer constant or we can let it to be found as well as the velocities for other layers. All these options are applicable for inversion of both group and phase dispersion curves and for all these options we can choose if the low velocity zone (LVZ) should be found or if we force the inversion to look only for monotonously increasing velocity with depth.

During the inversion, the modeled dispersion curve is compared with the measured one. For the velocity (density) distribution found in each iteration, the dispersion curve is computed and the misfit with respect to the measured dispersion is estimated, see Fig. 2.1. The forward modeled dispersion curve is computed for a periods step (red points in Fig. 2.1) corresponding to a bit smaller value than is the smallest difference in periods of the measured curve (blue dots in Fig. 2.1). The smallest period step for the measured curve is usually found somewhere in the short-period part of the period range, since, thanks to the multiple filtering setting, the discretization of the measured dispersion curve has a geometrical step in period with larger differences toward longer periods. We need more dispersion points for the modeled curve to be able to assign some of them to the dispersion points in the measured curve. The variable step of forward modeling is set to save the computational time. When long dispersion curve (wide period range) has to be computed by the matrix method, and when the discretization is finer (period step is small), the computation becomes more time consuming. When inverting the short-period dispersion curve (for example 0.5 – 5.0 s), the step would be probably set smaller (for example 0.04 s), since the sampling of the measured curve is also expected to be small, but, the length of the curve would probably not be as great. When inverting long period surface wave dispersion, as seen in the example in Fig. 2.1, the dispersion curve is long (20 – 200 s), but the discretization step is about 0.3 s and hence the number of points to be computed is not so high.

In next paragraphs we summarize the setting for several options of the inversion. All parameters controlling the inversion can be changed by the user. The mutual relations between the parameters, constrains of the inversion giving the range of possible velocity values in each layer and options for keeping the set velocity in the first layer constant were developed after years of experience with the isometric method and dispersion curve inversion. Some of the settings is rather subjective and to provide reliable results, several values of parameters should be tried. However, the reliable inversion result is confirmed right by the fact that it does not depend on the given set of parameters strongly. In other words – by constraining the inversion by unrealistic parameters, we obtain false results. By setting proper values, the reliable results are stable with respect to small change of these parameters.

- **Love group/phase dispersion with constant density, with LVZ and all layers inversion**: The number of parameters inverted is equal to the number of layers including halfspace, because only the v_s is to be found for each layer. The inversion does not look for the absolute values of the velocities in each layer, instead, it founds the differences of the velocity in the next (deeper) layer with respect to the previous layer. In case of the uppermost first layer, it finds the difference to the v_s set by the user as a surface shear velocity. We use the differences to the previous layers to control the oscillation of the found model. By constraining the possible values of the differences, we damp the inversion to produce smooth models. The user is asked to set the value of the difference before

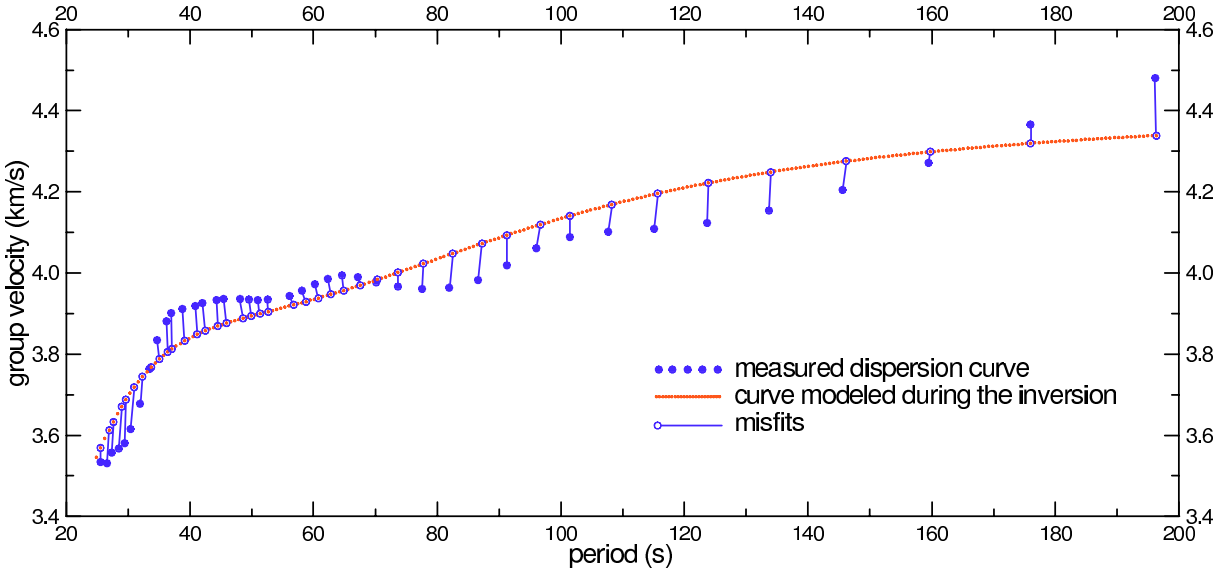


Figure 2.1: Example showing how the assignment of the actually measured points to some of the forward modeled dispersion points works. Blue dots are the measured dispersion curve, red points are the discretized forward modeled synthetic dispersion and blue lines with circles represent misfits between the two curves with assigned points marked.

the inversion starts. One value is set by the user and then it is used for setting both the positive and negative difference, however, each of them is set differently. Since we assume that the increase of the velocity with depth is more probable than the decrease, the possible range of velocities in the next layer is asymmetrical with respect to the velocity in the previous layer. The value set by the user is multiplied by six to set the maximal positive allowed difference and it is kept at the given value for the maximal negative difference. It means that the velocity in the next layer may be in the range from minus the set value up to plus six times the value set by the user with respect to the previous layer. Example: The user set the surface v_s to be 2.4 km/s and the difference to be 0.2 km/s. It means that in the first layer, the inversion will look for the velocity in the range from $(2.4-0.2)$ to $(2.4+1.2)$ km/s.

- **Rayleigh group/phase dispersion with constant density, with LVZ and all layers inversion**: The number of parameters inverted is twice as high as the number of layers including halfspace, because both v_s and v_p are found. In case of v_s, the inversion works in the same manner as in the previous case. The v_p are found using the v_p/v_s ratio. Similarly as in the case of v_s, the inversion does not look for the absolute value of the ratio, but it finds the differences of it. As opposed to the v_s, the ratio difference is found with respect to the v_p/v_s ratio set by the user for all layers. Thus no dependence on the previous layer is used. Similarly to the case of v_s, also the range of possible values of the v_s/v_s ratio is set by the user.

- **Love/Rayleigh group/phase dispersion with inverted density, with LVZ and all layers inversion**: The velocities are treated in the same manner, as in the previous two cases. For Love wave, only v_s are found, for Rayleigh waves, both v_p and v_s are found. In this case, also the densities are inverted and so, in case of Love waves, the number of parameters is twice as high as the number of layers and in case of Rayleigh wave, the number of parameters is even three times as high as the number of layers including halfspace. The densities are treated in the same manner as the v_s. We are looking for differences of the density in the next layer with respect to the previous layer. So, the user is again expected to set the surface density and the density step. The density is set to only increase with depth and the possible range is six times the step given by the user. However, as opposed to the velocities, we do not have any measured densities, in other words, we have no data to be compared with the modeled densities produced by the inversion. We decided to generate additional "data" by producing artificial set of densities for each layer. Our density "data" are given directly as the differences of the densities between two neighboring layers and for all layers, these "data" are set constantly as the density step given by the user. This feature is implemented to allow the inversion treat the densities in the same manner, as the velocities. The only difference is that for the velocities, the measured data number is generally different from the number of layers. In case of densities, the number of "data" exactly match the number of layers.



- **Love and Rayleigh group/phase dispersion curves with constant/inverted density, with LVZ and all layers inversion**: In this case, both Love and Rayleigh dispersion curves are inverted together. It differs from the previous cases only by the fact that two dispersion curves are modeled by the forward matrix method computation in each iteration and compared with appropriate measured dispersion curve. The v_s is estimated using both Love and Rayleigh dispersion and v_p using the v_p/v_s ratio from the Rayleigh wave dispersion. All other features are treated in the same manner as before. Both the measured dispersion curves have to have the same number of dispersion points.

- **No LVZ (applicable for all previous options)**: When we do not want to look for the low velocity zone, the inversion is not allowed to find smaller velocity in the next layer than was the one in the previous layer. It is ensured by setting the range of possible velocity differences from zero up to the six times the given velocity step – no negative difference is allowed. This option constrains the inversion strongly and is intended to be used when weaker inversion constraints produce unrealistic velocities.

- **Fixed first layer (applicable for all previous options)**: Sometimes it is useful to fix the uppermost layer's v_s (and constrain also the v_p), because we may know them from other a priori measurements or we simply want to constrain the inversion more, not to oscillate even in the first layer. In that case, the range of possible velocities in the first layer is set to be zero for both negative and positive differences. In other words, the searched parameter (difference to the set velocity) is always zero and hence the same velocity set by the user is used by the inversion for all iterations and cannot be changed by the procedure.

The surface wave v_s and its range of possible values in the next layer is used not only for damping the inversion, but also for setting the starting model. The starting model has the values of the given surface shear wave velocity in the first layer and then, in each next layer, it is increased by the value set by the user as a velocity step. For examples of how such starting models may look, see Fig. 6.44 in Section 6.13. The same applies for the density. The starting density model is set using the surface density and in each next layer, the density is of the given step higher then the density in the previous layer. Since we need the density step for the starting model to be different from the possible range of the densities in the next layer found by inversion, we set the possible range of densities as a multiple of the step and for the starting model, we use the step directly. So, by setting one value – v_s, two variables of the inversion are influenced – the starting model as well as the possible range of parameters in the next layer. In case of density step, even three "variables" are influenced, the starting model, the possible range of parameters in the next layer and also the additional "data" of densities, which were not measured, but artificially generated.

The velocity and density steps constrain the inversion. By setting the larger steps, we allow the inversion to look for the velocities/densities in broader range. It may help to fit the data better, but, on the other hand, the velocities may oscillate layer by layer and hence the result would be unreliable. When we set the steps to be small, we force the inversion to keep the results in narrower range. The resultant velocity distribution will be smooth, but the data would not be fitted so precisely.

The number of layers and their thickness is also set by the user. This is done according to the desired resolution and smoothness of the resulted velocity distribution. There is a trade-off between the resolution and smoothness. Higher number of layers would not necessarily produce better resolution – unreliably thin layers will led to unrealistically oscillating velocity distributions. Examples how to set the number and thickness of the layers are given in Sections 6.13 and 6.14.

Inversion of dispersion curves by any means suffers from the nonuniqueness by the process. The same dispersion may be found in different models, as commented for example in Dorman and Ewing (1962) and many authors later. This disadvantage may be partly eliminated by the constrains on the velocity distribution smoothness (given by the searching for the differences and not directly for the absolute velocities). The other option is that we found several models for one dispersion curve and one inversion procedure setting and as a conclusion, we present the mean velocity distribution with standard deviations given by the different models. This approach is used in Chapter 3 (Kolínský and Brokešová, 2007) where six models were estimated and their simple average is used with the total range of the six models marked. In Chapter 5 (Kolínský at al., 2010), we used twenty models, and their mean value with the standard deviation was given as a result. The examples how to deal with the actual performance of the isometric method inversion implemented in the SVAL program is given in Chapter 6, Sections 6.13 and 6.14.

2.4 Inversion tests

In this section, we present a test of the inversion process. We use the implementation of the isometric method in the SVAL program for inversion of group velocity dispersion curves, as described above.



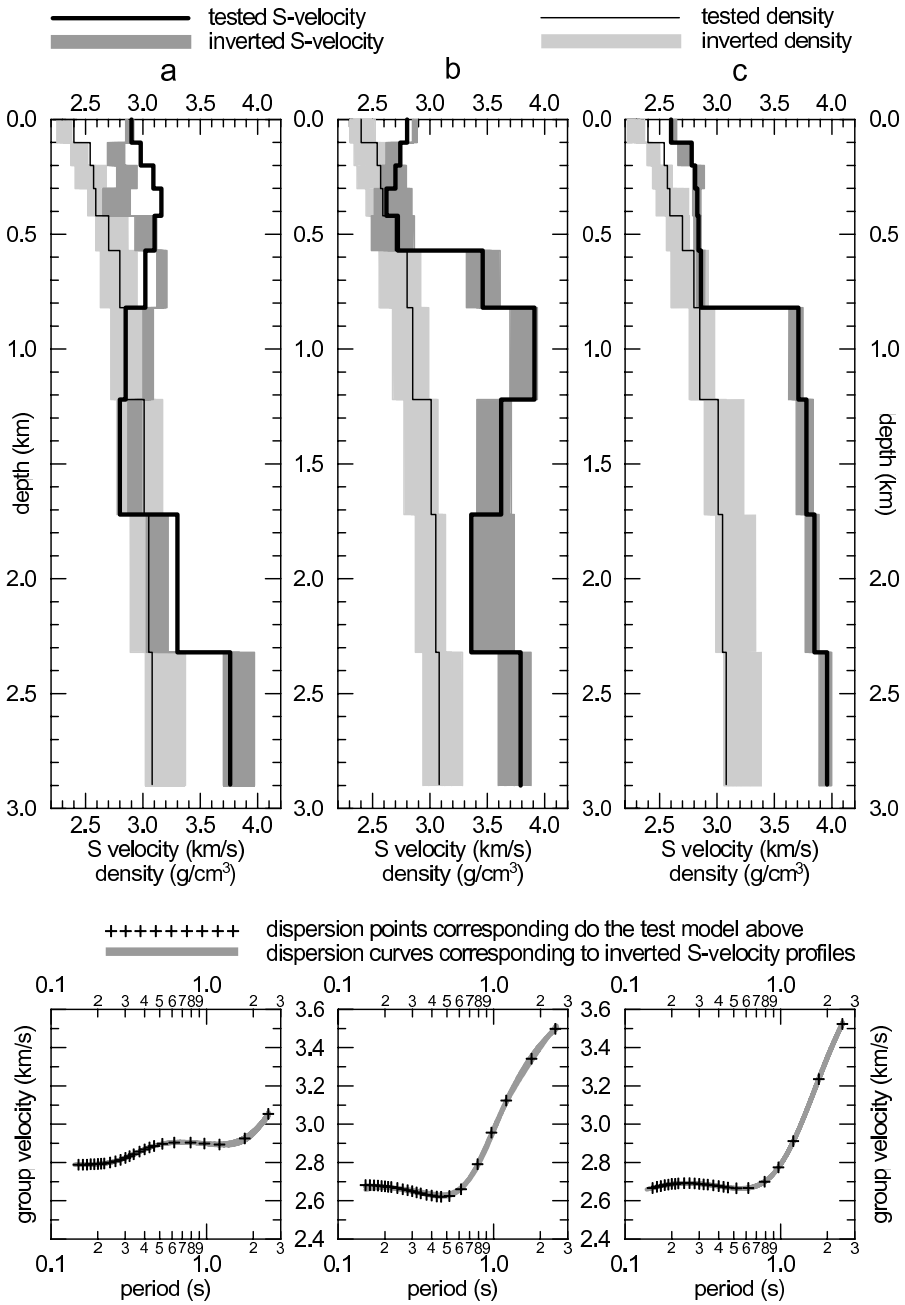


Figure 2.2: Tested (bold black line) and inverted (dark gray stripes) structures as well as tested density (thin black line) and inverted density (light gray stripes) are shown. In this test, layer thicknesses for the inversion are manually set to be the same as in the tested structures.

Modification of this test is also given in the paper by Kolínský and Brokešová (2007), see Chapter 3. A test of the phase velocity inversion is given in Chapter 5.

For the test, three shear wave velocity models are set (solid bold black lines in Fig. 2.2**a**, **b** and **c**) and synthetic group velocity dispersion curves are computed for each of them. Then, only some of the points from each of the dispersion curves are selected to resemble the real measurement, see crosses in the lover panels of Fig. 2.2. Such dispersion curves are inverted (gray lines in the lower panels of Fig. 2.2) and the resultant structures are compared with the original tested ones (gray stripes in the upper panels of Fig. 2.2).

Layer thicknesses for the inversion are set exactly as the layer thicknesses for the original testing structures. Such test is not resembling the real measurement, however, it may allow us to reveal, how the inversion works if we "help" it by setting the proper layer distribution. In the reality, we do not know the layer thicknesses. For a modification of the test with arbitrarily set layer thicknesses, see Chapter 3.

We implement also the inversion of the densities here. These are much more constrained than the velocities and they are usually not inverted during the real dispersion curve inversion.

The fits of the dispersion curves in Fig. 2.2 are excellent, however, the comparison of the structures failed in the case of structure **a**. We see good results for the profiles **b** and **c** since the sharp discontinuities are well pronounced in the estimated velocity distributions. We conclude that if we set the layer thicknesses for the inversion exactly as they were set in reality (original models), it allows the inversion to find proper velocities including the contrasts. These contrast are not so well pronounced when we

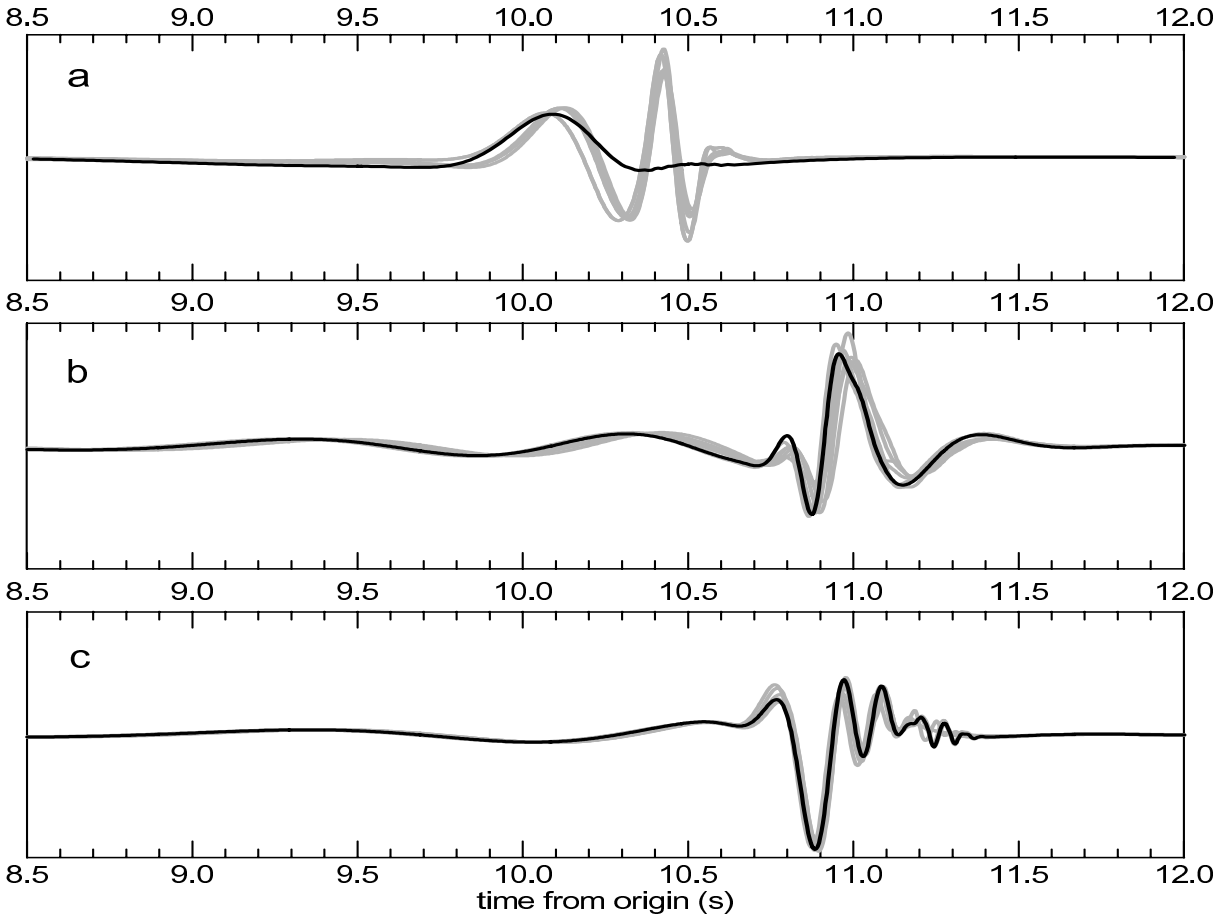


Figure 2.3: Synthetic velocigrams for tested and inverted velocity distributions from Fig. 2.2. Solid black lines represent synthetic velocigrams computed for the tested structures (solid black lines in Fig. 2.2) and gray lines show synthetic velocigrams computed for the inverted structures (gray stripes in Fig. 2.2). There are six of them for each of the three structures from Fig. 2.2**a**, **b** and **c**.

set the thicknesses of the layers arbitrarily, as in Chapter 3. Sharp discontinuities are blurred between several layers around the original velocity contrast.

However, profile **a** in Fig. 2.2 reveals the "mirror" effect. When the testing distribution is composed of sets of layers with decreasing and increasing velocities, the inversion finds mirrored distributions no matter that we have helped it by proper layer distribution in the test presented in Fig. 2.2**a**.

For both the tested structures and also for the estimated ones, synthetic seismograms are computed by the modal summation method (Herrmann, 2002). These seismograms are mutually compared for all three testing examples, see Fig. 2.3. The synthetics do not play any role in the inversion and are shown here only for comparison to determine the reliability of the inversion with respect to the real measurements – in case of the inversion of real records, the synthetics are also used for comparison after the inversion of the dispersion curves.

We see that for both structures with sharp discontinuities (panels **b** and **c** of Fig. 2.2), the synthetic seismograms for the inverted structures fit the original ones well. However, for the mirrored velocity distribution, the synthetics for inverted profiles in Fig. 2.3**a**, failed in comparison with the original one, as may have been expected from the bad test results seen in Fig. 2.2**a**. In the real case, we can only look at the fits of dispersion curves. This test shows that we would not be able to reveal the false inversion result (case **a**) since the dispersion curve fit is as good for this false example as it is for the two good ones (panels **b** and **c**). Synthetic modeling of seismograms can provide us with additional information on how successful the inversion was.



Part II: Applications





author of the figure is unknown

Chapter 3

Application A: Uppermost crust shear wave velocities

3.1 Dealing with the topic

We started to analyze the records of quarry blasts in 2005. Not only the analysis itself was the main reason – we also tuned many details of our procedures, programs and methods while looking for the short-period surface waves in the Western Bohemia region. This project was the one which moved the developing of the SVAL program into a universal tool for analysis of the surface waves of all wavelengths, different sampling frequency and arbitrary record lengths. Until this moment, the SVAL program was mainly used for the analysis of teleseismic event records with surface waves of period >10 s. During the project, many tests of the surface wave analysis were made with the aim to use the multiple filtering method in the best way possible. We created synthetic records with analytically known dispersion and we compared this dispersion to the dispersion determined by the SVAL program to check the reliability of the method and the program. Similar tests were made during my Master studies a few years ago and both sets of tests were successful and proved that the SVAL program may be used for any kind of surface wave measurement.

When we were satisfied with the short-period surface wave measurement, we tried to develop also the inversion procedures to obtain the velocity distribution of uppermost crust of the target region. We implemented the isometric method, developed by Jiří Málek (Málek et al., 2005 and 2007), into the SVAL program and we inverted results of the analysis for the 1-D shear wave velocity distributions. We also computed synthetic dispersion curves for known structural models and then we inverted the dispersion curves to see if we got the same models in order to check the reliability of the isometric method and its implementation for the dispersion curve inversion in the SVAL program.

This chapter consists of the paper Kolínský and Brokešová (2007) which has been published in the Journal of Seismology. Not all the tests and examples have been introduced in the paper. We cite the complete paper here and we add some additional remarks at the end of the chapter. Some of the sections of the paper complement the methodology sections from Part I – *Theory* of the thesis, because the paper is aimed at both methodological description of the procedures and also at the data processing and structural results.

---

here the original text of the paper starts

3.2 The Western Bohemia uppermost crust shear wave velocities from Love wave dispersion

Petr Kolínský and Johana Brokešová, 2007, Journal of Seismology, Vol. 11, p. 101–120

3.2.1 Abstract

We present a detailed study of Western Bohemia Love waves generated by blasts with an intention to estimate the uppermost crust structure for a more detailed layer distribution than the previous studies have used. The use of short-period (4 s and shorter) Love waves represents a new approach in the studied

region. Properties of multiple filtering as a tool of frequency-time analysis are discussed. A new method of selecting the dispersion ridges is introduced. Tests of filtering are provided by analyzing signals with analytically known dispersion. The isometric algorithm for the inversion problem is applied, the problem of non-uniqueness is discussed and tests of reliability of the inversion are presented. During the inversion, the forward problem is solved by use of the matrix method. Six records of blasts from the Western Bohemia region are analyzed to separate the fundamental modes of Love wavegroups, and shear wave velocity distributions down to a depth of 3.0 km are inferred. Modal summation is used to compute synthetic velocigrams, which are compared to measured ones. The lateral heterogeneity of the region is discussed and the presented models are compared to those of previous studies and to the geological setting of the region.

key words frequency-time analysis, group velocity, Love wave dispersion, isometric method

3.2.2 Introduction

In this paper we present a contribution to the long-term survey conducted in the Western Bohemia (WB) region. We deal with Love waves and we estimate the seismic velocity structure down to a depth of 3 km. In contrast to previous studies, we use a more detailed layer distribution and deal with six different propagation paths, which disclose the lateral diversity of the studied area.

The Western Bohemia region, part of the Bohemian Massif, attracts the interest of geoscientists mostly because of its complicated geological features and the occurrence of seismic swarms. For an overview of seismic swarm occurrence, see Horálek et al. (2000) and Fischer and Horálek (2003). In the following, a brief summary of previous structural studies using body waves is provided according to depth.

Earlier works have focused on the whole crust structure. Plomerová et al. (1987) presents apparent velocities of Sg and Pg body waves generated by the 1985-86 earthquake swarm in WB and measured at epicentral distances of hundreds of kilometers. Plomerová et al. show the crust to be laterally heterogeneous. The report by Antonini (1987) concerns the local scale of epicentral distances of about 40 km around the swarm area in WB. One of the results is that the v_p/v_s ratio is azimuthally dependent. Problems of the v_p/v_s ratio are also discussed by Kolář and Boušková (2003). Horálek et al. (1987) use quarry blasts for measuring the average v_p and v_s of the homogeneous crust in the region. The same data are used for a more detailed analysis by Janský and Novotný (1997) and simple 1D velocity distribution models are also estimated there. Comparison of Pg and Sg crust wave velocities concerning Europe and the Bohemian Massif can be found in the report by Lokajíček et al. (1987). Janský et al. (2000) estimates 20-km-deep homogeneous models for four seismic swarm subregions in WB; for the method, refer to Janský (2000). As a continuation of this work, Málek et al. (2000) studied three-layered models of the upper 15 km of the crust for the same four regions. Values of both v_p and v_s are in a good agreement with the results of Janský et al. (2000). The distribution of v_p down to the depth of 5 km for part of the WB region is estimated by Novotný et al. (2004) using the Wiechert-Herglotz method. A simple 3-D type block v_p model down to a depth of 4.5 km for another WB subregion is presented by Nehybka and Skácelová (1997). A review of deep seismic sounding in Bohemian Massif is presented by Málek et al. (2001); maximum values of the v_p of two layers (upper 1.6 km) above a halfspace are estimated in that work. More detailed studies of the uppermost 5 and 15 km of the crustal v_p of several geological units can be found in Málek et al. (2004 and 2005, respectively).

The velocities presented in the studies described above are estimated from the first arrivals of body P and S waves or from their inversion used for source localization. In the following, we cite studies that also deal with surface waves.

Novotný (1996) compared several 1-D models of the Bohemian Massif and also its western sector (the target region of our study). His average WB95 model consists of nine layers for the 32-km-thick crust and also concerns the upper mantle. The depths, which are within the scope of this study – down to 3 km, are represented only by three layers in the WB95 model. Studies of Bohemian Massif crust structure by measuring the dispersion of surface waves can be found in Novotný et al. (1995) (concerning Rayleigh waves), and in Novotný et al. (1997) and Wielandt et al. (1987) (concerning both Rayleigh and Love waves). Malinowski (2005) gives the crust structure of upper 2 km estimated from the dispersion of short-period Rayleigh waves. His study uses wavelengths similar to ours, but it mostly concerns the different parts of the Bohemian Massif; however, some paths used in this study also cross the WB region.

The aim of this paper is to present an example of short-path structures in Western Bohemia – epicentral distances vary from 5 to 50 km. We analyze the dispersion curves of short-period Love waves and invert them for a 1D layered shear wave velocity model for each path. We decided to deal with Love waves because we found them in our records. We do not address the question how shear waves are generated by explosions. For a discussion about the Love waves generated by explosions, see, for example, Bukchin et al. (2001) or Levshin and Ritzwoller (1995). The advantage of using Love waves is that they depend only on shear wave velocities and hence the number of model parameters is lower than if we would try to

invert Rayleigh waves. The period range of observed Love waves is from 0.15 s to 4.0 s. The uppermost crust structure is divided into homogeneous layers overlaying the halfspace. The number of layers varies from 8 to 14. To estimate dispersion curves, we use multiple filtering; for inverting the dispersion curves for 1-D models, we use the isometric method. During the inversion, the forward problem is solved by the matrix method many times. We compute synthetic velocigrams for the resulting structures by modal summation and compare them with the original records. These methods are discussed and tested in the following sections. We have studied several tens of paths across the WB region, and examples of the velocity distribution along six paths are presented. The paths for this study were selected in order to show different path lengths crossing different part of the WB region. Dispersion curves with broader period range and with clear fundamental mode dispersion at these paths were used.

3.2.3 Group velocity analysis

To estimate the dispersion curves, the method of Fourier transform-based multiple filtering (Dziewonski et al., 1969) is applied. It is a classical technique and we have made some modifications for processing signals where the amplitudes of surface waves do not exceed the amplitudes of body waves. An overview of frequency-time analysis techniques can be found in Kocaoglu and Long (1993). For the original record $g(t)$ we use the complex frequency-time representation $S(t, f_{cent})$ in the general form of the inverse Fourier transform

$$S(t, f_{cent}) = \int_{-\infty}^{+\infty} G^{f_{cent}}(f) e^{i2\pi ft} df = \int_{-\infty}^{+\infty} G(f) e^{-\alpha(f)\frac{(f-f_{cent})^2}{f_{cent}^2}} e^{i2\pi ft} df \quad , \tag{3.1}$$

where the record spectrum $G(f)$, as a function of frequency f, is multiplied by weighting function $e^{-\alpha(f)[(f-f_{cent})/f_{cent}]^2}$. The weighting function represents a Gaussian transfer function of the filter with central frequency f_{cent}. As we apply this weighting for many central frequencies f_{cent}^j, we obtain a set of filtered spectra $G^{f_{cent}^j}(f)$ and we understand $S(t, f_{cent})$ to be a function of two variables. For each j the real part of equation (3.1) yields the quasi-monochromatic signal

$$g^{f_{cent}^j}(t) = Re\left\{S(t, f_{cent}^j)\right\} = Re\left\{\int_{-\infty}^{+\infty} G^{f_{cent}^j}(f) e^{i2\pi ft} df\right\} \quad , \tag{3.2}$$

which represents the original record $g(t)$ Gaussian-filtered at central frequency f_{cent}^j.

The width of the Gaussian filters depends not only on difference $(f - f_{cent})$, but also on ratio $(f - f_{cent})/f_{cent}$ – this is the so-called constant relative resolution filtering (for details see Dziewonski et al., 1969). Coefficient $\alpha(f)$ depends on the frequency – it provides another opportunity for controlling the width of the filter. Examples of estimating the optimal coefficient $\alpha(f)$ can be found in Levshin et al. (1972, 1992); for details concerning the width of filters, see also Cara (1973) and Canitez (1977). In this study, we use linear dependence $\alpha(T) = a + bT$, where period $T = 1/f$ is used instead of frequency f. For details on estimating the linear $\alpha(T)$ dependence, see Kolínský (2004).

Because symmetric Gaussian filters of finite width are applied to generally asymmetric spectrum $G(f)$, the frequencies, which prevail in the filtered spectra, do not match the central frequencies of the filters (Dziewonski et al., 1972). We have solved the problem of errors caused by the shift in the actual frequencies of filtered quasi-monochromatic signals by estimating the instantaneous frequency (Levshin et al., 1989). In general, we can determine the instantaneous frequency for the whole filtered signal to see how it changes along this signal. Nevertheless, in seeking the group velocity we need to estimate the instantaneous frequency only at the moment when the energy maximum arrives (see also Shapiro and Singh, 1999).

The instantaneous frequency of each real quasi-monochromatic filtered signal $g^{f_{cent}^j}(t)$ is estimated using the analytical signal corresponding to $g^{f_{cent}^j}(t)$:

$$S_a^{f_{cent}^j}(t) = 2\int_0^{\infty} G^{f_{cent}^j}(f) e^{i2\pi ft} df \quad . \tag{3.3}$$

The real part of the analytical signal equals the real filtered signal $Re\left\{S_a^{f_{cent}^j}(t)\right\} = g^{f_{cent}^j}(t)$ and the imaginary part corresponds to the Hilbert transform of the real filtered signal. The modulus of the analytical signal $\left|S_a^{f_{cent}^j}(t)\right|$ represents an envelope of the filtered signal $g^{f_{cent}^j}(t)$.

The instantaneous frequency $f_{inst}^{f_{cent}^j}(t)$ at each moment t of each filtered signal $g^{f_{cent}^j}(t)$ is computed according to the expression (see Boashash and Jones, 1992)

$$f_{inst}^{f_{cent}^j}(t) \cong \frac{1}{2\pi}\frac{d\Phi^{f_{cent}^j}(t)}{dt} \quad , \tag{3.4}$$

where $\Phi^{f^j_{cent}}(t)$ is the phase of analytical signal $S_a^{f^j_{cent}}(t)$ given as

$$\Phi^{f^j_{cent}}(t) = -arctan\left(Im\left\{S_a^{f^j_{cent}}(t)\right\}/Re\left\{S_a^{f^j_{cent}}(t)\right\}\right) \quad . \tag{3.5}$$

In the following, we use instantaneous period $T_{inst}^{f^j_{cent}} = 1/f_{inst}^{f^j_{cent}}(t)$. Since the filtered signals are not exactly monochromatic, they form curved lines in the time-period plane. The frequency-time representation (3.1) becomes $S(t, f_{cent}) \rightarrow S(t, f_{inst}(t))$ and the spectrogram $\left|S_a^{f^j_{cent}}\left(t, T_{inst}^{f^j_{cent}}(t)\right)\right|$ of the original record $g(t)$ is given as a set of moduli for all central frequencies f^j_{cent} with the instantaneous period dependence added to each of these moduli.

The surface wave group velocity $U\left(T_{inst}^{f^j_{cent}}(t_k)\right)$ for the energy maximum arrival time t_k of the given envelope $\left|S_a^{f^j_{cent}}(t)\right|$ (with central frequency f^j_{cent} and with estimated instantaneous period $T_{inst}^{f^j_{cent}}(t_k)$) is computed as

$$U = \frac{\Delta}{t_k} \quad , \tag{3.6}$$

where Δ is the epicentral distance.

By the term dispersion point, we understand the point to be in the group velocity-period plane, where the group velocity corresponds to the arrival time at the maximum of the filtered signal envelope, and the period value is the instantaneous period of the signal at this maximum. In general, each of the filtered signals contains several such maxima. There is an assumption in classical analysis that the surface waves form the most significant part of a whole record and the fundamental dispersion ridge is to be found using the highest amplitudes of spectrogram. As our records contain significant higher modes and body waves, we had to use another approach. During our frequency-time analysis, the arrival times of all local energy maxima of each filter were found and the dispersion points were set to the group velocity-period plane according to their respective instantaneous periods. Thus we obtain several dispersion ridges formed by those dispersion points. The instantaneous periods of dispersion points were independent both of the central periods and of other dispersion point periods. Next, we applied a procedure that picks out the fundamental mode dispersion ridge. This procedure is not based on the absolute values of amplitudes but it selects the dispersion points according to the fact that they belong to the same continuous ridge regardless of their amplitude. The fundamental mode can be formed by arrival times t_k of primary $t_{k=1}$, secondary $t_{k=2}$ and other ($k > 2$) maxima of filtered signal envelopes. An example of a spectrogram is shown in Fig. 3.1.

After selecting the proper dispersion point for each of the filtered signals, we truncated and smoothed these signals in the time domain to eliminate other wavegroups. We visually inspected all the filters one by one to ensure the continuity of the dispersion ridge and to confirm that the truncated signals contain only the desired wavegroup. We created a filtered seismogram containing only the surface wavegroup by summing these truncated filtered signals. This seismogram was used for comparison with the original record to highlight the surface wavegroup.

As we were dealing with real records, we had to apply a time shift corresponding to the phase characteristic of the instrumental transfer function. The group velocity of each raw dispersion point was changed as if it would be estimated from the instrument independent velocigram. However, it made no difference if we estimated the dispersion curves by using displacement, velocity or acceleration records.

All details concerning the above-mentioned process are described in the paper by Kolínský (2004), including other parameters involving the filtering, selecting among different dispersion ridges, computing the instantaneous periods and constructing filtered seismograms. The dispersion curves (points) used in this study are the result of the multiple filtering described above, instantaneous period estimation and selecting between local maxima only – no artificial smoothing is applied.

3.2.4 Inversion for shear wave velocities

The isometric method (IM), which was recently developed by Málek et al. (2005), is a fast algorithm. It combines features of several standard methods, particularly the simplex method, Newton's least-squares method and simulated annealing (see Tarantola, 1987). The population of $m + 1$ best models (m is the number of model parameters) is stored in the memory. The new model is generated as the optimal linear combination of these models. The metrics of data space is consistently used during this process (what is the difference from the classical simplex method). Sometimes, a new model is generated in a random way to prevent the algorithm from reaching a local minimum. For details, see Málek et al. (2005). If the inverse problem is linear, IM finds the optimal solution in the first iteration. For nonlinear inverse problems, many iterations are necessary. In comparison with other methods, IM usually needs smaller

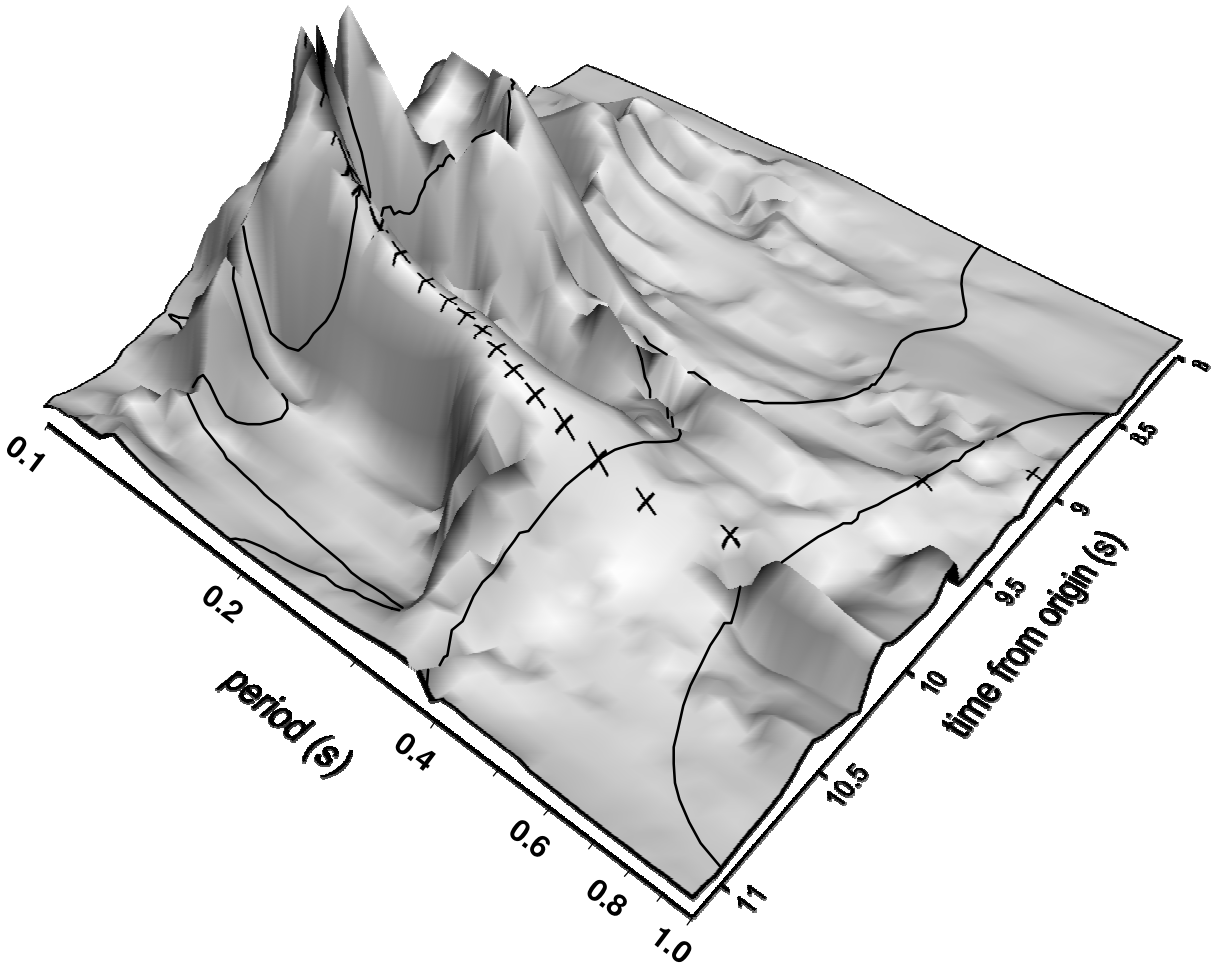


Figure 3.1: (*Fig. 1 in Kolínský and Brokešová, 2007*) KYNZ station record of the HROZ quarry blast is used for creating the spectrogram using an instantaneous period estimation along the whole quasi-monochromatic signal. The 3D representation shows the time-period-amplitude distribution. The envelopes are curved in 3D space; both instantaneous period and amplitude vary with time. The whole surface is created by 21 envelopes curved in 3D space, but for simplicity only three of them are drawn. Crosses represent dispersion points of the fundamental mode. Note that the six dispersion points in the period range from 0.2 s to 0.3 s are estimated to be at the secondary energy maxima arrival times. The primary maxima arrival times in this range correspond to the first higher mode.

number of forward problem computations; however, the finding of the new model is more complicated and more costly. Typical problems, which are effectively solved by IM, are weakly non-linear problems with tens of parameters and complicated forward modeling. Therefore it fits quite well the inversion of dispersion curves using the matrix method.

During the inversion the dispersion curve is computed many times (for details, see Section 3.2.5) and the distance between theoretical and measured dispersion points (misfit function) is minimized. The starting models (velocity with a constant step between all layers, see thin dashed lines in Figs. 3.4, 3.7 and 3.8) are randomly generated in the vicinity of the initial starting model.

The distribution of layers is set manually according to the properties of the measured dispersion. The most significant part of the dispersion curve is the Airy phase; the maximum of the surface wavegroup amplitude and the minimum of the group velocity display a sharp velocity contrast in the medium. Murphy and Shah (1988) give the relation

$$T_0 = \frac{2.3H}{\bar{\beta}} \quad , \tag{3.7}$$

where T_0 is the period of the minimum of the group velocity of the fundamental mode (s), H is the depth to the significant discontinuity (km), and $\bar{\beta}$ is the average shear wave velocity above this discontinuity (km/s). Since the shear wave velocities of the uppermost hundreds of meters in the WB region have the expected average value around 2.6 km/s (Novotný, 1996), a simple relation between the period of the

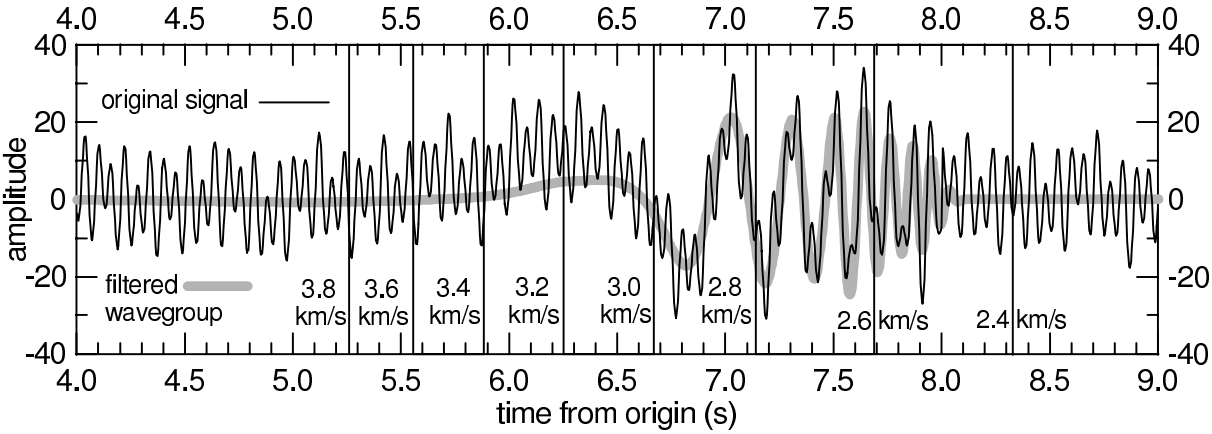


Figure 3.2: (*Fig. 2 in Kolínský and Brokešová, 2007*) Artificial signal $s(t)$ (black line) created according to relation 3.8 with random noise added. The gray line represents the filtered wavegroup composed of quasi-monochromatic filtered signals obtained by multiple filtering and corresponding to dispersion points shown in Fig. 3.3. Group velocity marks are also shown to compare the seismogram with the dispersion curve in Fig. 3.3. The filtered wavegroup can display the surface waves compared to the original records also in case of complicated seismograms where the surface wavegroup is not clearly visible, as described in Section 3.2.3.

wave and the depth of penetration is used – the period of the wave in seconds corresponds approximately to the depth in kilometers. For example, if there is an Airy phase between periods 0.4 and 0.5 s, we set the number of layers to be higher and the layers to be thinner (0.1 km) at depths from 0.3 down to 0.6 km, because a sharp velocity increase is expected within this depth range. This approach enables us to unveil the velocity discontinuities at certain depths. In case of thick layers, the discontinuity would be forced to emerge at an incorrect depth. Thinner layers are set also for the near-surface part of the crust, since the highest velocity gradient is expected here (for a discussion of estimation reliability for upper several hundreds meters, see Section 3.2.10). For a flat portion of the measured dispersion curve, the layers can be thicker.

As the thicknesses of layers d_i are set prior to the computation of the inverse problem, we seek for two parameters for each layer i: shear wave velocity β_i and density ρ_i in case of Love waves. Theoretically, the inverse problem is well resolved if we have more independent data measured than the number of independent parameters we seek, e.g., if we have more dispersion points than twice the number of layers including the halfspace. However, the dispersion points contained in one ridge are not independent data and the sought velocities are likewise not independent parameters of the model. We constrain the velocities to keep them in reasonable range and to avoid their oscillation in such a manner that the velocity in lower layer is influenced by the velocity in an upper layer (see Section 3.2.7). Because we also introduce strong additional constrains for the densities (see Section 3.2.7), we are in fact seeking for only one parameter β_i in each layer. In our case, the number of useful dispersion points is in the range 25 – 60 and by tests we have confirmed that we can estimate the 1-D model for 8 up to 14 layers.

3.2.5 Forward computations

Two different methods are used to ensure the independence of the dispersion curve computation and of comparing the synthetic and measured velocigrams.

For solving the forward problem during the inversion, we apply a modified Thomson-Haskell matrix method. Dispersion curves for selected Love modes are found in a 1-D layered model above a halfspace. Constant values of shear wave velocities β_i, densities ρ_i and layer thicknesses d_i have to be set for each layer i and for the halfspace. For details, refer to Proskuryakova et al. (1981). Theoretical dispersion curves are computed with a period step corresponding to the smallest measured period difference of two neighboring filters (usually in the short-period part of the measured curve). In the case of a larger measured period difference, only the values of the group velocity for periods corresponding to measured dispersion points are used to estimate the misfit function.

Herrmann's (2002) computer codes are used to compute the synthetic surface wavegroups by modal summation technique. Only fundamental modes of Love waves are computed to compare the synthetics with filtered records.

For comparing the raw record and dispersed wavegroup, the filtered velocigram without any instrument phase characteristic correction is used. For further processing, however, the effect of the instrument has to be corrected. The period-dependent arrival time shift is estimated according to the phase characteristic of the instrument and each filtered signal is shifted according to the time shift of the instantaneous

period of the selected local energy maximum of the signal. These shifted elements are summed and we obtain the filtered velocigram, which is instrument independent; a signal of the same kind is computed by modal summation.

3.2.6 Test of the multiple filtering

To prove the reliability and to validate the use of the multiple filtering described in Section 3.2.3, we perform several numerical tests. For this purpose, we use a signal

$$s(t) = (10 + At)sin(\phi) \tag{3.8}$$

with analytically known dispersion, where A is the coefficient of the amplitude magnification over signal duration t_s, and the phase ϕ is defined as

$$\phi(t) = C\frac{t^5}{5} + Dt \ , \tag{3.9}$$

which is an integration of the dispersion relation

$$\omega(t) = Ct^4 + D \quad or \quad T(t) = \frac{1}{Ct^4 + D} \tag{3.10}$$

with respect to time t. By setting constants C and D we adjust the shortest period T_{min} and the longest period T_{max} corresponding to $t = t_s$ and $t = 0$, respectively. To simulate realistic properties, we choose the parameters so that period 3.10 changes from $T_{mas} = 10$ s to $T_{min} = 0.08$ s at distance $\Delta = 20.0$ km from a fictitious blast. Additional random noise with five frequencies is added to the signal: 10 and 15 Hz to simulate body waves, 2 and 3 Hz to simulate a civilization noise and 0.2 Hz as a microseismic noise, see Fig. 3.2. The respective amplitudes of this noise are set according to the properties of real records of quarry blast in WB region.

Figure 3.3 shows a dispersion curve (solid line), where group velocity U and periods T are calculated according to expressions (3.6) and (3.10), respectively. Comparison of the dispersion points (circles) obtained by multiple filtering with the analytically computed curve shows very good agreement in the range of interest. Thus this analysis method gives satisfactory results for the purposes of our study concerning noisy signals with period and velocity ranges of 0.15 – 4.0 s and 2.0 – 4.0 km/s, respectively. Many further tests for different period ranges (for different parameters C and D) have been made with similar results.

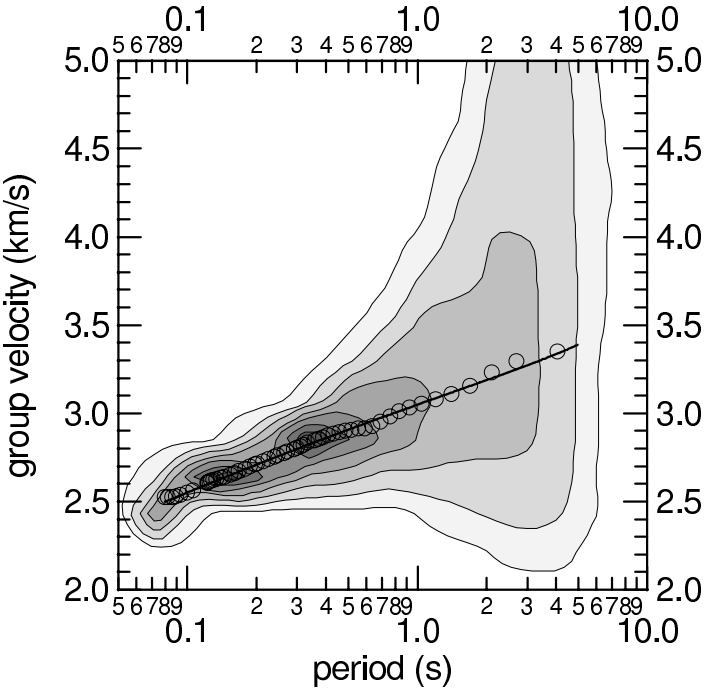


Figure 3.3: (*Fig. 3 in Kolínský and Brokešová, 2007*) The solid line represents the known dispersion according to relation 3.10 and circles represent the dispersion points estimated by multiple filtering. Contours of truncated spectrogram amplitudes are also depicted.

3.2.7 Test of the inversion

To test the inversion scheme and to find out what is the effect of the random generation of starting models in the IM, we tested the inversion problem on synthetic examples. Two parameters, shear wave velocity

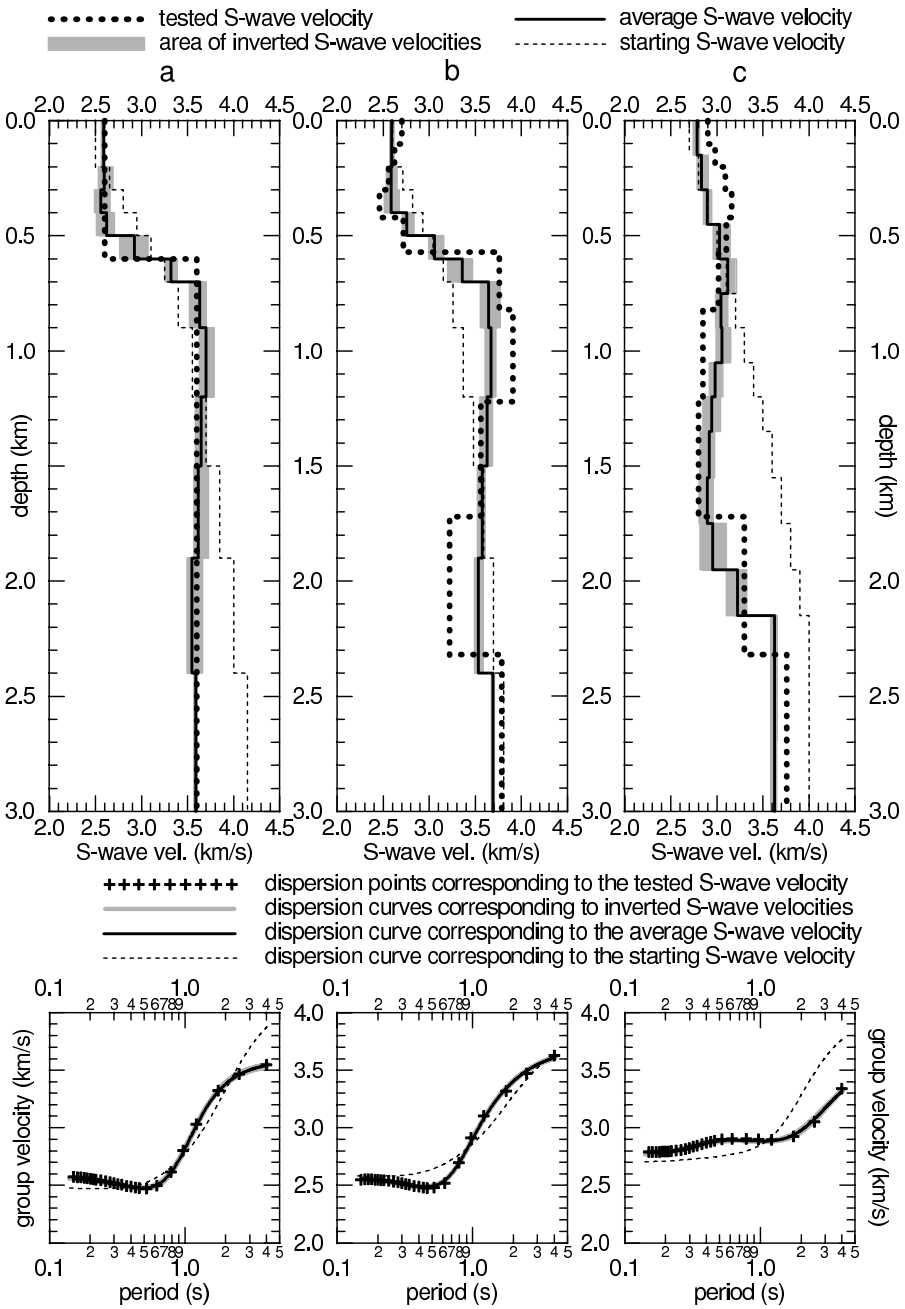


Figure 3.4: (*Fig. 4 in Kolínský and Brokešová, 2007*) Three testing velocity (bold dotted line) distributions are shown in panels (a), (b) and (c). Corresponding dispersion points (crosses) at the bottom panels are compared with six inverted dispersion curves (gray lines) for each of the testing structures (for each structure the distance between the curves is smaller than their thickness). These curves correspond to the six velocity (gray areas) structures estimated by the inversion. The resultant average structure and corresponding dispersion curve is indicated by a thin solid black line for each of the three tests. The starting model and corresponding dispersion curve is shown by dashed line.

β_i and density ρ_i, are found for each layer using the inversion. The propagation of surface waves depends predominantly on the velocity, much less on the density, and the density is thus not well constrained by the dispersion curve. Consequently, a small difference in velocities can be compensated by a big difference in density for us to obtain the same dispersion curve. Accordingly, we constrain density within a range of 1.5–3.5 g/cm^3 and we force them to increase with depth with a difference 0.08±0.02 g/cm^3 between two neighboring layers. In such a way we reduce the scattering of velocities. Hence, this inversion can only be used to correctly estimate the velocities; the densities operate as a fine tuning of the inversion. The velocities are also constrained: we keep the velocities within the range of 1.5–5.0 km/s.

The non-uniqueness of the problem has to be noted: nearly the same dispersion curve can be obtained by propagation through different 1-D velocity structures. Since the generation of models in the IM is random, the non-uniqueness causes slightly different results of inversion even for the same input data.

Results for three structures (a, b and c) used for testing the inversion procedure are shown in Fig. 3.4. The dispersion curves are computed for the known structure (bold dotted line in top panels) by the modified Thomson-Haskell matrix method mentioned in Section 3.2.5. We have computed these curves with a fine constant period step of 0.01 s and then 26 discrete points were selected on each dispersion curve (crosses in group velocity–period diagrams at the bottom of Fig. 3.4) to resemble the measured dispersion points. These points serve as the input data for the inversion test. The starting models are set by two parameters: (a) shear wave velocity at the surface (affecting the absolute values of velocities and hence the absolute position of corresponding dispersion curve in the group velocity–period plane)

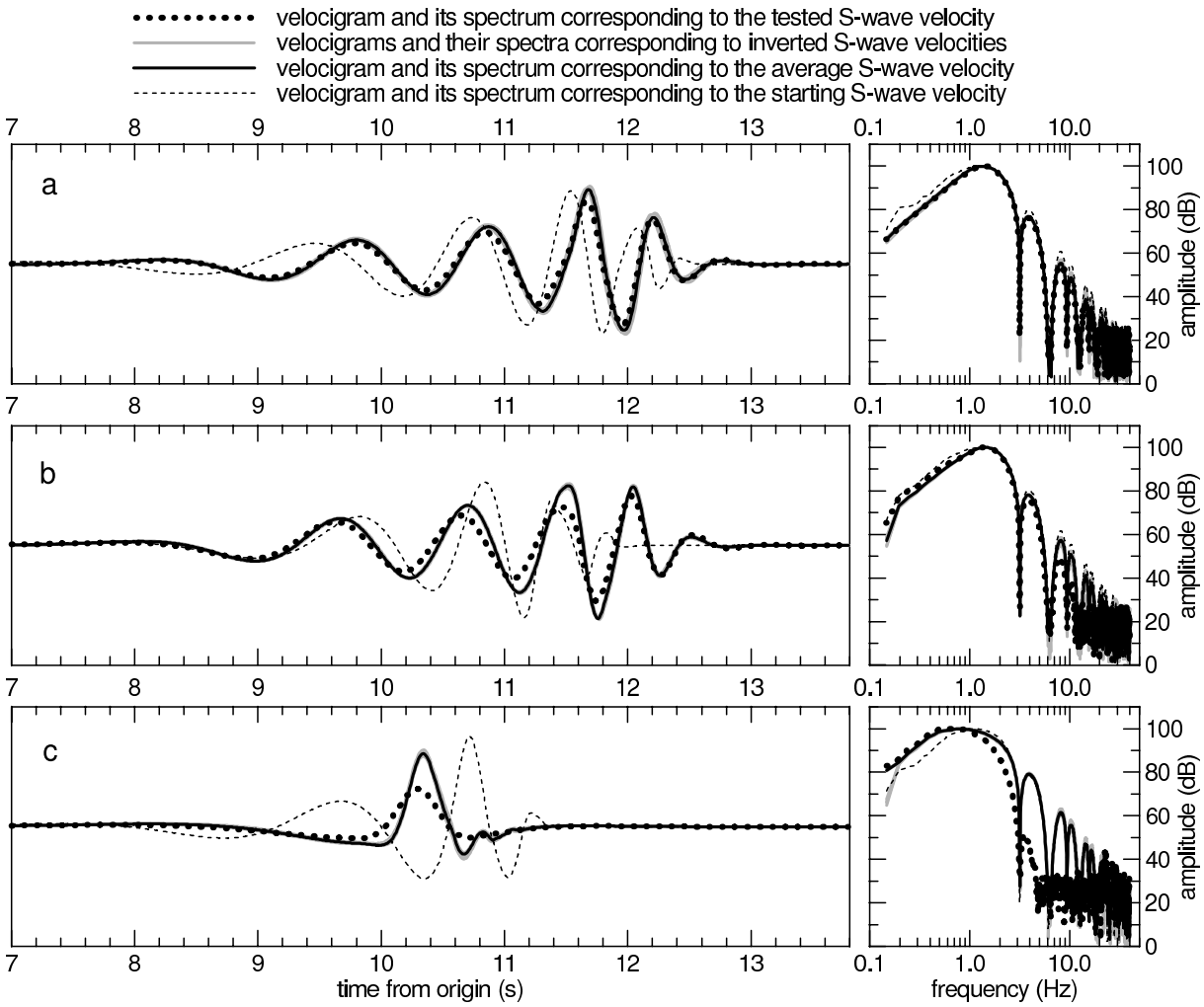


Figure 3.5: (*Fig. 5 in Kolínský and Brokešová, 2007*) Bold dotted lines represent three (a, b and c) synthetic velocigrams computed by modal summation for three testing structures (Fig. 3.4a, b and c, also depicted by bold dotted lines). Gray lines represent six synthetic velocigrams for six structures estimated by inversion for each of the three tests (Fig. 3.4a, b and c, gray areas). The resultant average structure estimated for each test is used for computing the resultant velocigram – it is shown by the same bold solid line as the resultant average structure in Fig. 3.4. Velocigram for starting structure is drawn by thin dashed line. Corresponding amplitude spectra are depicted in right-hand panels.

and (b) the constant velocity step between the layers (affecting the slope of the dispersion curve). For each starting model, we compute the corresponding dispersion to compare it visually with the measured (tested) one (also shown in Fig. 3.4). Results of inversion do not depend significantly on the starting model; however, by using a suitable starting model we save the computation time.

The inversions for each testing structure are computed six times for unchanged input data to see the non-uniqueness of the process. The dark gray areas in the top panels of Fig. 3.4 represent the range of obtained velocities. The dispersion curves for all six results for each structure are shown as gray lines in the group velocity–period graphs (bottom panels). Although the velocity values vary, all the dispersion curves fit the data very well; the misfit function values, which measure the distance of the input dispersion points and the resultant dispersion curve, are approximately the same for all six computations for each of the three tests. Resultant structures obtained by averaging of the six inverted structures are presented by solid black line in top panels. The corresponding dispersion curves are drawn by the same line in bottom panels for each of the three testing structures. The inversions are carried out for the layer thickness distributions which are set according to the properties of the dispersion curves, as described in Section 3.2.4. It simulates the same conditions used for processing the real records.

Figure 3.5 shows synthetic velocigrams and their amplitude spectra computed for the epicentral distance of 29 km for the testing structure, for six inverted structures corresponding to each of the three testing structures, for the resultant average structure, and for the starting structure.

Figure 3.4a presents the test for a simple model of one layer overlaying the halfspace. In general, the inverted velocities are in a good agreement with the tested model both above and below the sharp step at

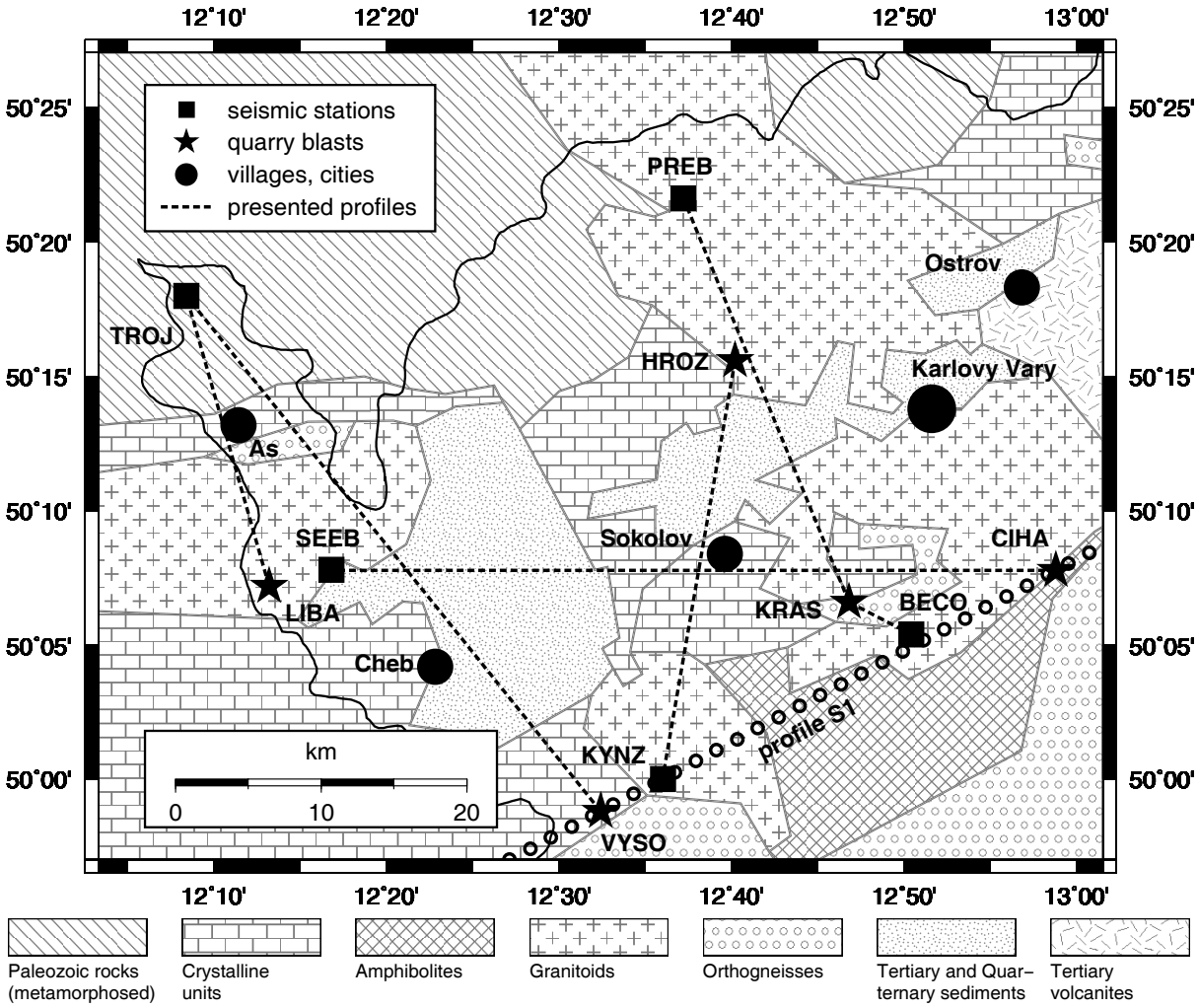


Figure 3.6: (*Fig. 6 in Kolínský and Brokešová, 2007*) Six paths across the Western Bohemia region are shown. For details, see Table 3.1. The solid line represents the border between the Czech Republic and Germany. Main geological units are sketched according to Mlčoch et. al (1997); the map is simplified by using straight geological boundaries in order to provide future tomography studies of the region.

the depth of 0.6 km, but the discontinuity is blurred into 3 layers. Figure 3.5a shows the corresponding synthetics for the structures in Fig. 3.4a. All the obtained synthetic wavegroups fit the tested one well.

Figure 3.4b display a similar structure with a two low-velocity zones present both in the part above as well as below the strong discontinuity. The two layers below the discontinuity present a high-velocity zone. The inversion partially smoothes these zones. In Fig. 3.5b, the agreement between the testing and obtained synthetic velocigrams is also relatively good, although worse than in the previous case.

Figure 3.4c shows the most peculiar problem: no strong Airy phase is present in this dispersion curve because no sharp velocity contrast is implemented in the testing structure. Values of the velocities increase in the upper four layers and subsequently decrease in the next four layers. All six inversions yield incorrect solutions. The minimal misfit function is estimated for a mirrored velocity distribution: the velocity values increase and decrease in an opposite manner than in the testing velocity structure. The absence of velocity contrast causes the short duration of the testing surface wavegroup (compare Fig. 3.5c with Fig. 3.5a and b). As the testing velocity values in the upper five layers are higher than the resultant values obtained by inversion, the amplitudes of the short-period part of the corresponding synthetic are lower. For details about the influence of the velocity contrasts between layers on the wavegroup length as well as about the influence of the absolute velocity values on the amplitudes, see, for example, Murphy and Shan (1988) and Yamanaka et al. (1989). By comparing the testing structure of Fig. 3.4c with that of Fig. 3.4a and b, we see that the presence of Airy phase can significantly help the inversion to find a correct solution.

Most of the dispersion curves measured in the WB region is similar to those presented in the bottom panels of Fig. 3.4a and b.

3.2.8 Data

Records used in the present study were acquired during the seismic refraction experiment SUDETES 2003 (see Grad et al. 2003) which was a part of the Seismic Lithospheric Investigation of Central Europe (SLICE) international experiment; for an overview of recent refraction experiments in Central Europe, see Guterch et al. (2003). The SUDETES 2003 profile S1 (small white circles in Fig. 3.6) crossed the Vysoká (VYSO) shot point and Číhaná (CIHA) quarry, where in-line shots were fired. Four off-line shots were made in the vicinity of profile S1 in the WB region, three of them, Krásno (KRAS), Horní Rozmyšl (HROZ) and Libá (LIBA), are also used in this study. Sixteen temporary off-line stations were deployed in the WB region during the SLICE experiment. Data from five 3-component stations Trojmezí (TROJ), Kynžvart (KYNZ), Přebuz (PREB), Bečov (BECO) and Seeberg (SEEB) are used in this study. Sampling frequency of all the stations was 250 Hz. The main purpose of this measurement was to acquire data for 3-D body wave tomography of the WB region. As a by-product, we have obtained several tens of three-component surface wave records covering an area of 50 x 60 km.

shot point	E ° WGS84	N ° WGS84	alttd (m)	charge (kg)	date (y/m/d)	origin time (UTC)	station	E ° WGS84	N ° WGS84	alttd (m)	seismo meter	epc.dist. (km)
LIBA	12.223	50.120	590	400	2003/06/04	17:09:59.525	TROJ	12.144	50.303	570	STS-2	21.115
VYSO	12.543	49.978	700	400	2003/06/04	19:09:59.526	TROJ	12.144	50.303	570	STS-2	46.034
HROZ	12.668	50.261	560	400	2003/06/05	17:49:59.546	KYNZ	12.604	50.004	580	LE-3D	28.954
KRAS	12.776	50.114	740	270	2003/06/04	17:20:00.476	PREB	12.622	50.364	870	LE-3D	29.895
KRAS	12.776	50.114	740	270	2003/06/04	17:20:00.476	BECO	12.838	50.086	590	LE-3D	5.396
CIHA	12.983	50.133	730	400	2003/06/04	17:40:06.311	SEEB	12.283	50.132	550	LE-3D	50.056

Table 3.1: Coordinates, origin times, epicentral distances and other parameters of the six selected blast-station paths.

The origin times of the shots have been accurately measured by a technique specially developed for this purpose. Several BR3 receivers (see Brož, 2000) were installed at a distance of tens of meters from the shot to extrapolate the origin time with an accuracy of about 5 ms. For a description of the measurement method, see Málek and Žanda (2004); typical features of quarry blast records are also described there. In this paper, we have studied Love waves measured on the transverse component of six selected records despite the fact that the sources were explosions. See Table 3.1 for details (after Málek and Žanda, 2004). The respective paths are depicted by dashed lines in Fig. 3.6. Compared to natural earthquakes, we know the epicenter coordinates and origin times with negligible errors.

3.2.9 Results

Results are presented in Table 3.2. For each blast–station path, the thicknesses of layers, the corresponding depths of the upper boundary of each layer and the shear wave velocities are given there. Twenty inversions have been performed for each path and six velocity distributions having the smallest misfit function values (drawn as the gray areas in top panels of Figs. 3.7 and 3.8) were used for a final shear wave velocity estimation. For each layer, a simple average of v_s is determined (shown in Table 3.2 and plotted by a solid black line in Figs. 3.7 and 3.8). The scattering is quite small in the case of inverted dispersion curves, but larger in the case of velocity distribution. Because of the strong density constraint

LIBA – TROJ			VYSO – TROJ			HROZ – KYNZ			KRAS – PREB			KRAS – BECO			CIHA – SEEB		
d	h	v_S	d	h	v_S	d	h	v_S	d	h	v_S	d	h	v_S	d	h	v_S
0.05	0.00	2.56	0.05	0.00	2.91	0.10	0.00	2.94	0.10	0.00	3.03	0.10	0.00	2.27	0.10	0.00	2.06
0.05	0.05	2.63	0.05	0.05	3.05	0.10	0.10	2.93	0.10	0.10	3.20	0.10	0.10	2.29	0.10	0.10	2.13
0.10	0.10	2.67	0.10	0.10	3.14	0.10	0.20	2.82	0.10	0.20	3.05	0.10	0.20	2.20	0.10	0.20	2.16
0.10	0.20	2.60	0.10	0.20	3.20	0.12	0.30	3.07	0.10	0.30	3.00	0.10	0.30	2.76	0.10	0.30	2.15
0.10	0.30	2.62	0.10	0.30	3.24	0.15	0.42	3.30	0.10	0.40	3.01	0.10	0.40	3.28	0.20	0.40	2.15
0.10	0.40	2.87	0.10	0.40	3.27	0.25	0.57	3.88	0.10	0.50	3.27	0.20	0.50	3.41	0.20	0.60	2.24
0.10	0.50	3.20	0.10	0.50	3.33	0.40	0.82	4.13	0.20	0.60	3.73	0.30	0.70	3.63	0.20	0.80	2.33
0.20	0.60	3.43	0.20	0.60	3.42	0.50	1.22	4.03	0.20	0.80	4.16	0.40	1.00	3.64	0.20	1.00	2.38
0.20	0.80	3.37	0.20	0.80	3.69	0.60	1.72	4.01	0.20	1.00	4.14	hsp.	1.40	3.49	0.20	1.20	2.41
0.20	1.00	3.29	0.20	1.00	3.89	hsp.	2.32	4.39	0.20	1.20	3.99				0.20	1.40	2.42
0.20	1.20	3.31	0.20	1.20	4.08				0.30	1.40	3.81				0.20	1.60	2.43
0.30	1.40	3.44	0.30	1.40	4.21				0.30	1.70	3.69				0.20	1.80	2.43
0.30	1.70	3.52	0.30	1.70	4.27				hsp.	2.00	3.78				0.20	2.00	2.44
hsp.	2.00	3.53	hsp.	2.00	4.27										0.20	2.20	2.40
															hsp.	2.40	2.43

Table 3.2: Resultant shear wave velocities for six selected paths in the WB region; d = thickness of layer (km), h = depth of the upper layer boundary (km), v_s = shear wave velocity (km/s), hsp. = halfspace.

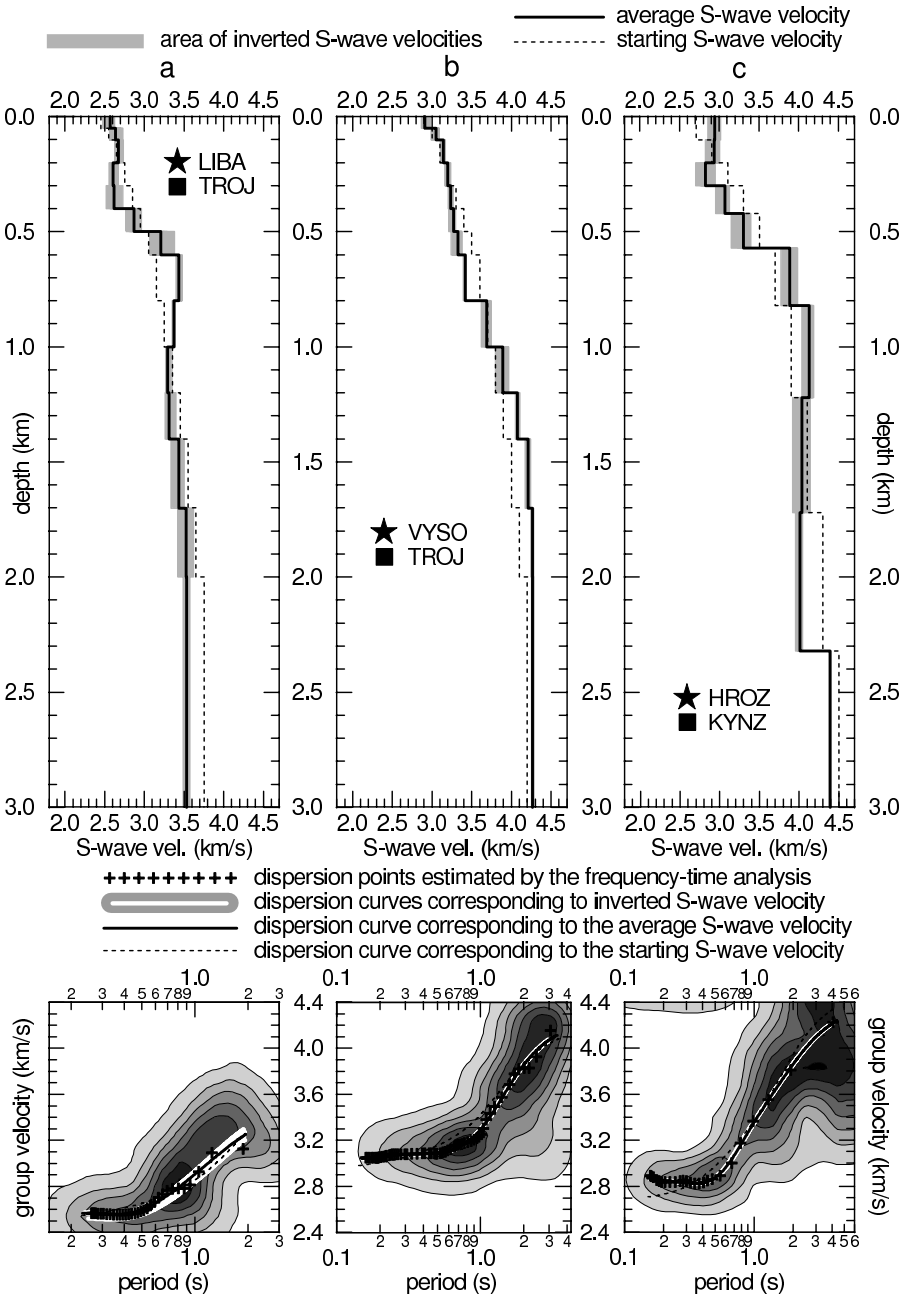


Figure 3.7: (*Fig. 7 in Kolínský and Brokešová, 2007*) Results for LIBA – TROJ, VYSO – TROJ and HROZ – KYNZ paths. Top panels (for each path): six inverted velocity distributions (gray areas), average velocity distribution (bold solid line) and starting models (thin dashed lines) are shown. Bottom panels (for each path): measured dispersion points (crosses), six dispersion curves corresponding to the six inverted S-wave velocity distribution (white lines), dispersion curve corresponding to the resultant average S-wave velocity distribution (black solid line) and starting dispersion curve (thin dashed line) are depicted. Truncated spectrogram amplitude contours are also drawn.

(as noted in Section 3.2.7), we do not present density results. Comparisons of original, filtered and synthetic velocigrams of Love wavegroups are given in Figs. 3.9 and 3.10. We do not present this comparison as a result of our inversion. Reliability of the inversion has been proved by the agreement in dispersion curves. Comparison of the measured and synthetic velocigrams and its disagreement can show that the real path structures are more complicated than the 1-D inversion can reveal. The comparison is influenced by several factors. Explosions have been used as sources of the active seismic experiment and Love waves have been measured. As it is not possible to compute shear waves generated by explosions in 1-D isotropic structure, point force Green's functions are used and time series for the tangential component of the horizontal ground velocity are obtained by modal summation. Since we have measured the origin times (described in Section 3.2.8), we have obtained an estimation of the source time function length (0.2–0.3 s), while the shape of the source time functions of explosions has been not determined. Hence, the default parabolic pulse, 0.256 s in duration, is used in the modal summation. We are not interested in amplitudes of synthetics or radiation patterns – we compare only the velocities (and hence the shape of the wavegroup) of Love waves. Differences in synthetics caused by different source time function are negligible in our comparison. Another problem is the truncating of the filtered quasi-monochromatic signal (mentioned in Group velocity analysis). Although it is designed to keep the proper wavegroup, its length can sometimes be inaccurate and the remaining wavegroup can contain several wavelengths in addition. This can cause more oscillating measured velocigrams in comparison with the synthetics. In viewing

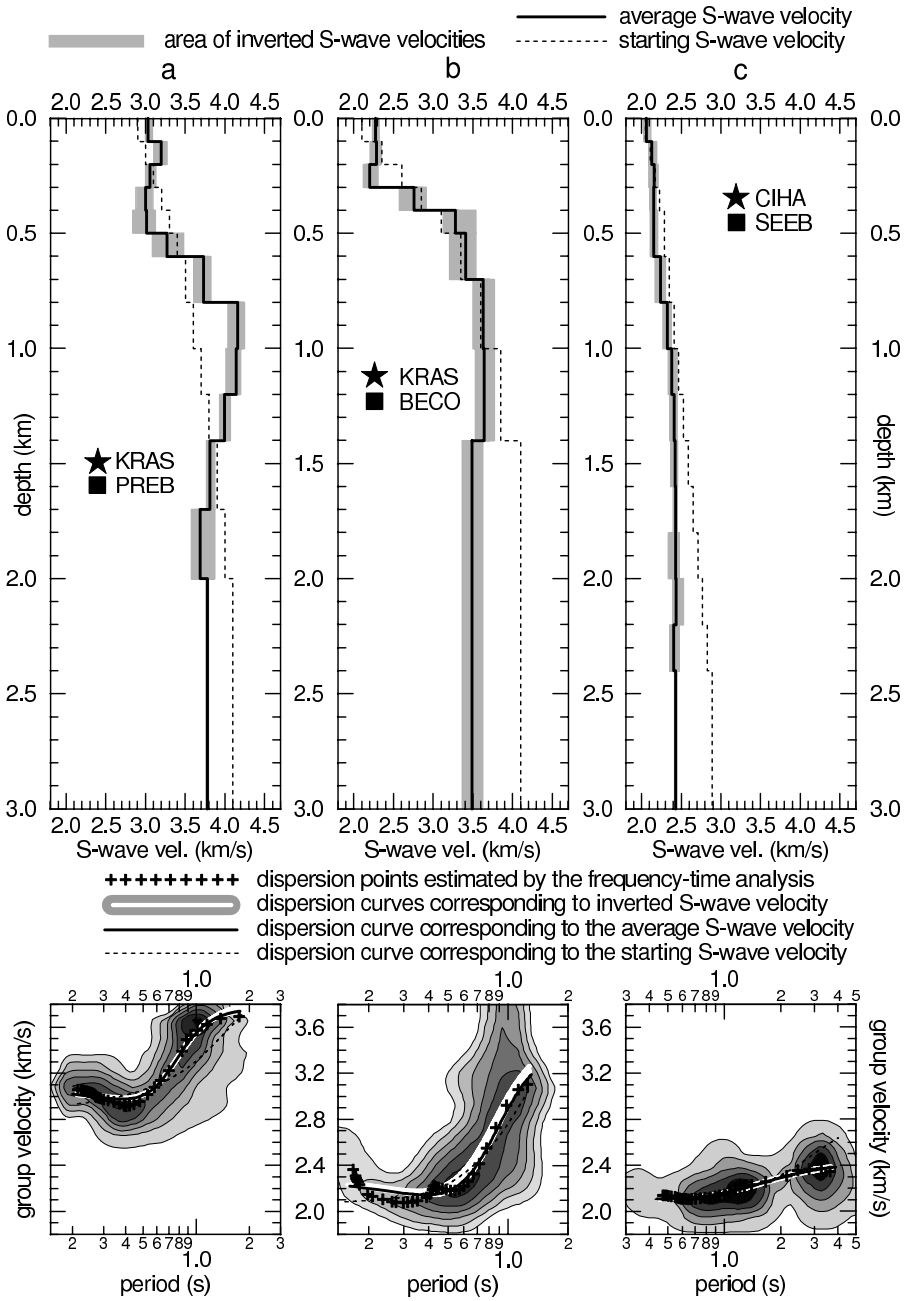


Figure 3.8: (*Fig. 8 in Kolínský and Brokešová, 2007*) Same as in Fig. 3.7 for KRAS–PREB, KRAS–BECO and CIHA–SEEB paths.

the comparison, one should bear in mind that different source mechanisms, source time function shapes, period ranges and truncating can cause the disagreement. Despite these facts, the velocity agreement of the most significant parts of all six records and synthetics is good.

The depths in Table 3.2 (and presented in Figs. 3.7 and 3.8) are measured from the average surface altitude between shot point and station; no topographic corrections are used in our study. Differences in altitude of the respective shot points and stations are in the range 20 – 180 m (see Table 3.1), hence in the most problematic case the average path altitude differs from the actual altitudes of the shot point CIHA and station SEEB by 90 m. As noted below, the depths down to 100 m are not well resolved by this method and so the altitude differences are neglected.

The results for LIBA–TROJ path are shown in Figs. 3.7a and 3.9a. The measured dispersion points indicate an Airy phase between 0.4 and 0.5 s, which is caused by the velocity contrast between the depths from 0.4 to 0.6 km. Another small Airy phase is found at 0.9 s, but it is not revealed by the inversion. The number of measured dispersion points is 33 and the structure consists of 13 layers and the halfspace. A low velocity zone is seen around the depth of 1.2 km. The synthetic velocigrams in Fig. 3.9a fit the observed data well.

Figs. 3.7b and 3.9b display the structure and comparison of the VYSO–TROJ path. No strong Airy phase is found there. The velocity gradually increases with depth to become nearly constant below the depth of 1.4 km. Sixty dispersion points have been measured and 13 layers over the halfspace are set for

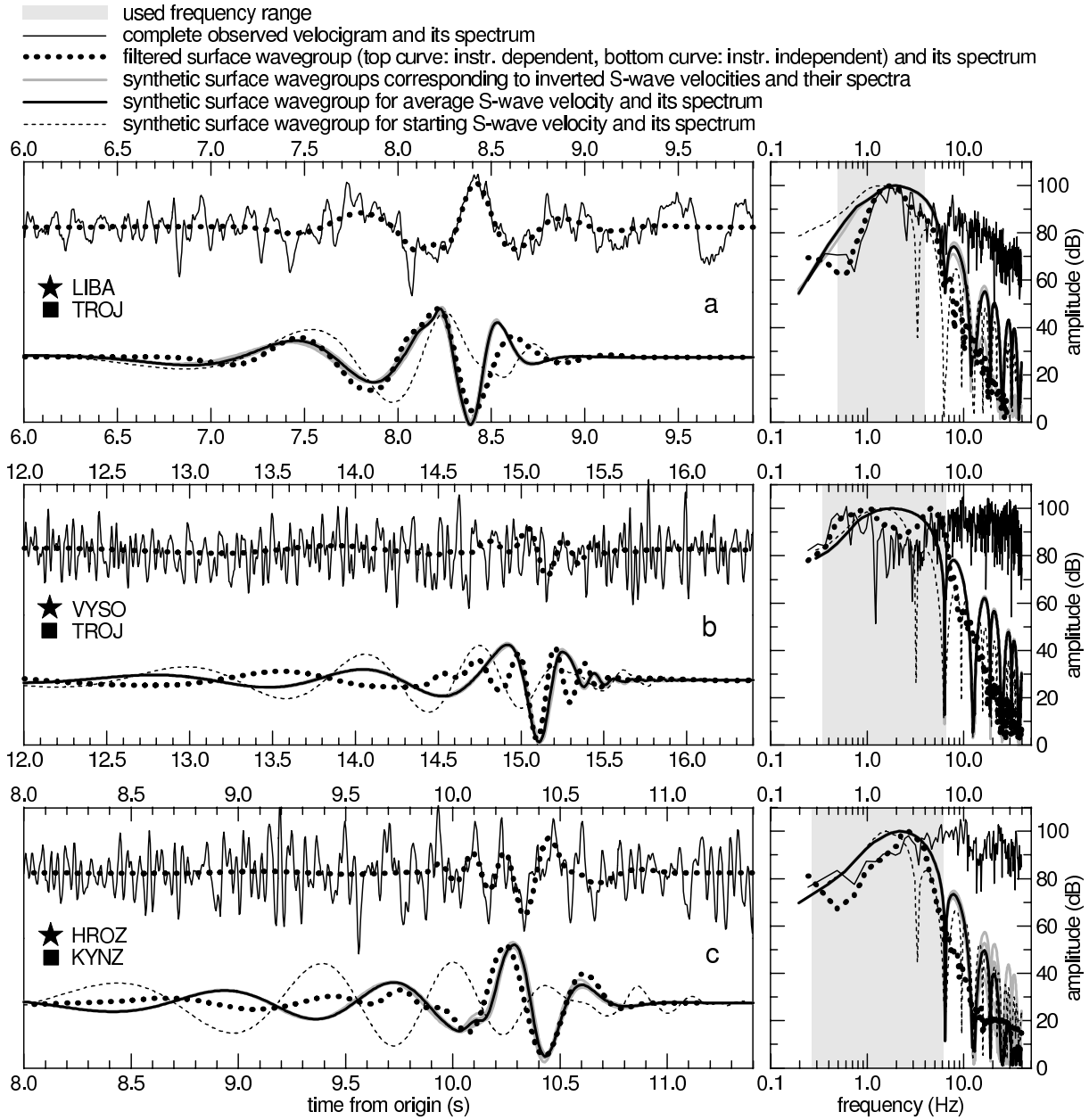


Figure 3.9: (*Fig. 9 in Kolínský and Brokešová, 2007*) Comparison of original records and instrument-dependent filtered surface wavegroups (top panels of a, b, and c) as well as comparison of instrument-independent surface wavegroups and synthetic signals (bottom panels) for the LIBA–TROJ, VYSO–TROJ and HROZ–KYNZ paths are drawn. Corresponding amplitude spectra normalized to 100 dB scale (with the 100 dB maximum in the frequency range of interest) are also shown (amplitude spectra for instrument-dependent and instrument-independent wavegroups are the same). Line types are used according to Figs. 3.7 and 3.8. Amplitudes both for the original and filtered record comparison and for instrument-independent and synthetic wavegroup comparison are normalized, but the eight synthetics for each path have their respective amplitudes.

the inversion. As opposed to the synthetic ones, the filtered wavegroup displays short-period oscillations between the arrival times of 14.5 and 15.0 s. The fit for the long-period part of the surface wavegroup is not good either.

The HROZ – KYNZ path structure is shown in Fig. 3.7c. The number of measured dispersion points is 25 and velocities for nine layers over the halfspace are found. A sharp velocity increase causes a strong Airy phase at 0.5 s. The agreement of the measured and synthetic velocigram in Fig. 3.9c is rather good for short-period part and worse for the long-period part of velocigrams.

Figure 3.8a shows the velocity distribution for the KRAS–PREB path. Even though the fit for the Airy phase between 0.4 and 0.5 s is not as good as in the above-mentioned cases, the velocity contrasts found at the depths of 0.6 and 0.8 km are sharp. The measured Airy phase is deeper than that of the computed dispersion curves and this is the reason why the main amplitude peak of the synthetic

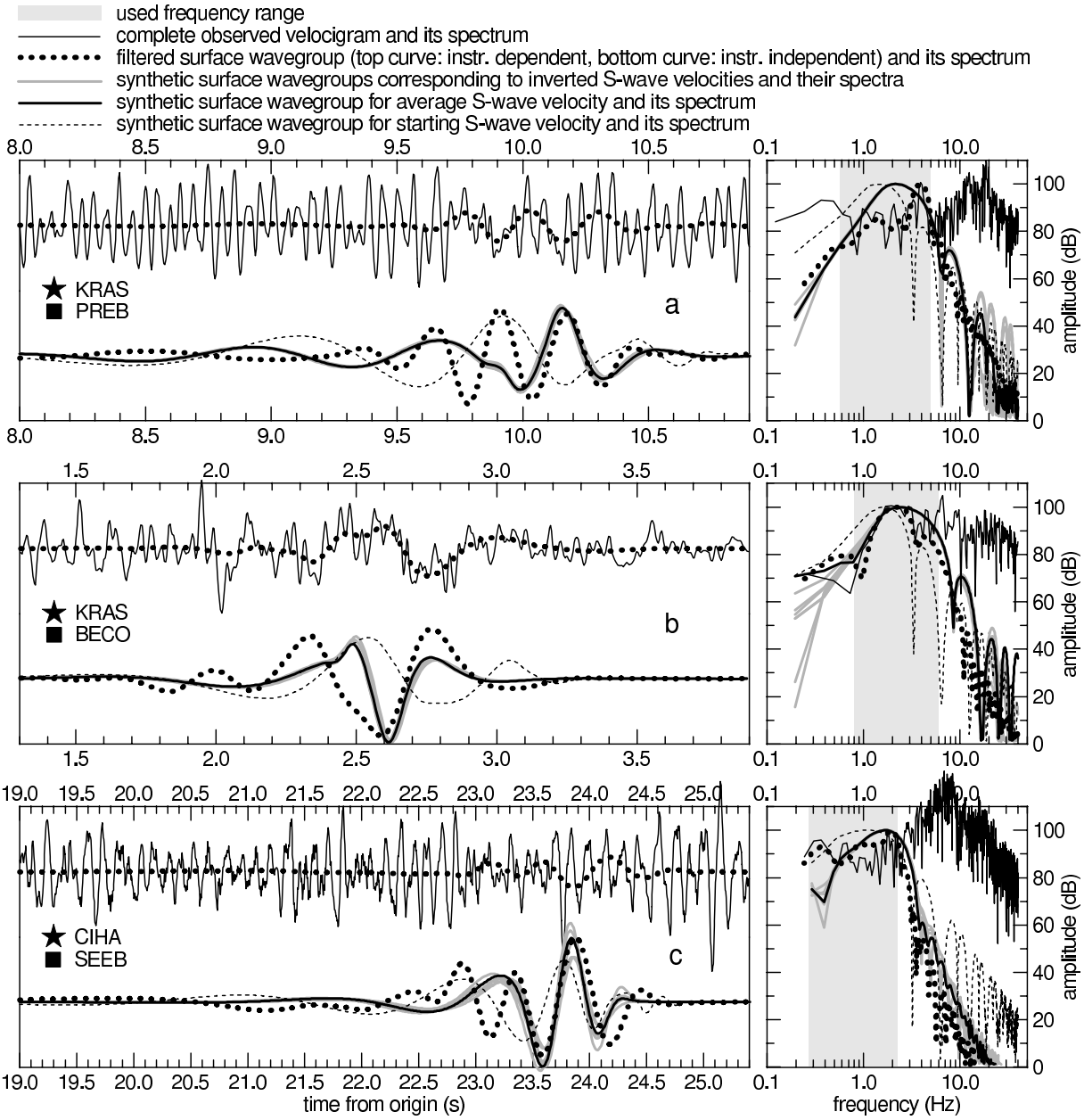


Figure 3.10: (*Fig. 10 in Kolínský and Brokešová, 2007*) The same as in Fig. 3.9 for KRAS–PREB, KRAS–BECO and CIHA–SEEB paths.

velocigrams in Fig. 3.10a comes earlier than the peak of the measured velocigram. The real velocity distribution is probably even more complicated. Small scatter of velocity can be seen in the layers below and above the depth of 0.5 km, however, the scatter of the six synthetics is rather small. The measured velocigram again shows a more complicated group than the synthetic ones. The number of measured dispersion points is 40 and 12 layers over the halfspace were set for inversion.

The KRAS–BECO path in Figs. 3.8b and 3.10b is the shortest one in our study. The measured dispersion points contain a small local maximum at 0.55 s, which the inversion did not reveal. The surface shear wave velocity is lower compared with the previously mentioned distributions. Since 36 dispersion points have been measured, we have found the distribution for 8 layers and the halfspace. The shapes of both measured and synthetic velocigrams in Fig. 3.10b are similar, but the main amplitude peak of the synthetic velocigrams is more compressed.

The longest path, CIHA–SEEB, presented in Figs. 3.8c and 3.10c, has been inverted by using 31 dispersion points and 14 layers above the halfspace. Although the distribution of layers is dense, the velocity is nearly constant from the surface to the halfspace at the depth of 2.4 km, and the values are very low compared to other velocity distributions. The agreement of the velocigrams is rather good for the main surface wavegroup part. The measured velocigram oscillates more than the synthetic one between arrival times of 22.5 and 23.5 s.

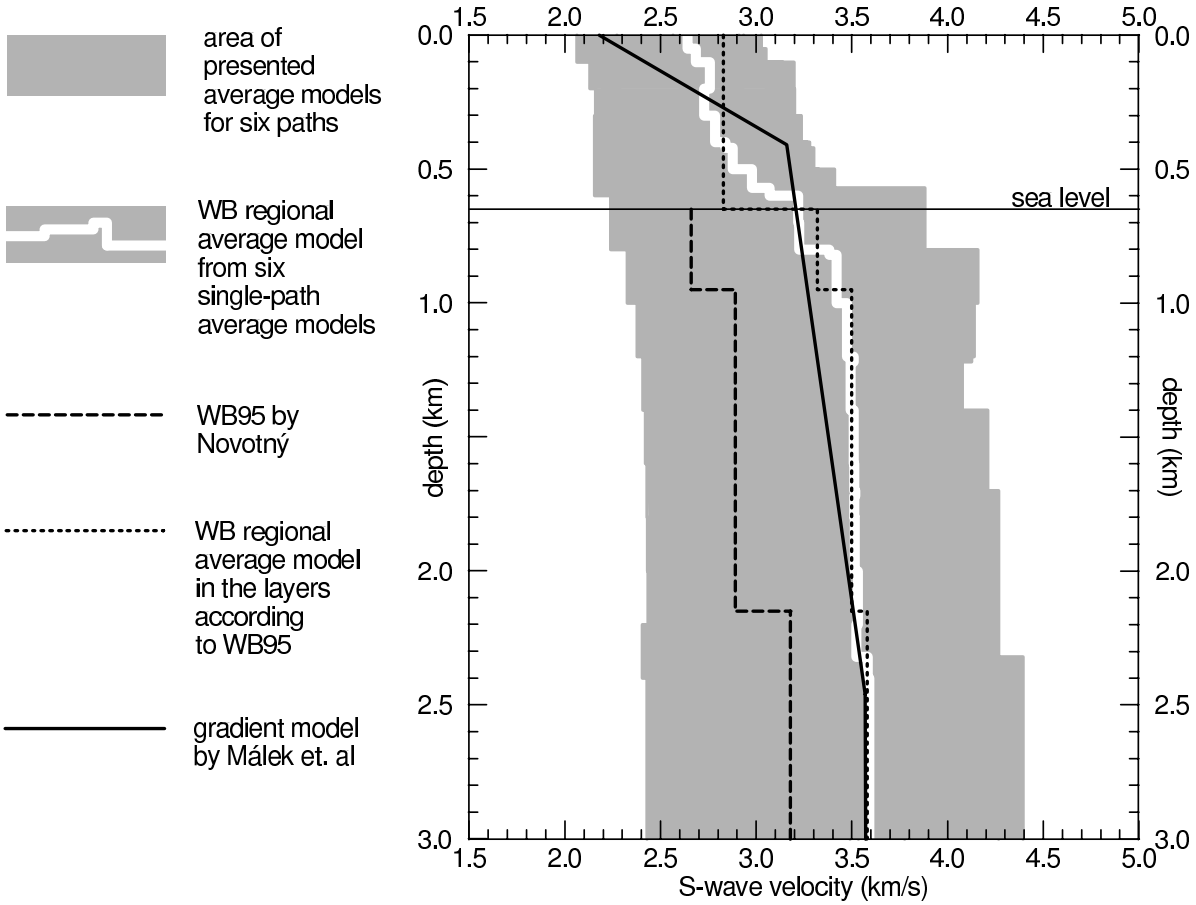


Figure 3.11: (*Fig. 11 in Kolínský and Brokešová, 2007*) Comparison of six single-path models (gray area), the WB regional average model (bold white line), the WB95 model (long-dashed black line), the WB regional average model distributed in the same layers as the WB95 model (short-dashed black line, we added also an average velocity for upper 0.65 km above the seal level) and the model by Málek at al. (solid black line).

3.2.10 Discussion and conclusion

The six presented structures show the outstanding lateral heterogeneity of the WB region down to the depth of 3 km. The path differences are stronger than predicted in previously published studies. In four cases (LIBA–TROJ, HROZ–KYNZ, KRAS–PREB and KRAS–BECO), there are sharp velocity discontinuities at depths from 0.3 to 0.8 km. The shear wave velocities along the VYSO–TROJ path gradually increase with depth and the CIHA–SEEB velocity distribution is nearly constant. Not only are velocity contrasts different, but the absolute values also range from 2.1 to 3.0 km/s at the surface and from 2.4 to 4.4 km/s at a depth of 3.0 km. The gray area in Fig. 3.11 shows the interval of single-path average models (bold black lines in Figs. 3.7 and 3.8) for all six paths.

The shortest period used for inversion is 0.15 s. This means a wavelength of about 300 m near the surface. The upper layer thicknesses are set to 50 – 100 m, which seems to be too small to be well resolved by such a wave. But if we tried to set the layers to be thicker, we would not been able to fit the measured dispersion points. Some of our models can be simplified using a smaller number of layers. The reason why we use so many layers is to show the ability of the inversion to reveal the velocity contrast at a certain depth, or to prove that there is no such sharp contrast and that the velocity changes gradually. Using, for example, only two layers over the halfspace, we would not be able to prove this.

For the comparison of our results, we have chosen the two models mentioned in Section 3.2.2 – Introduction: WB95 model by Novotný (1996) and gradient model by Málek at al. (2005). The other models mentioned in Introduction deal with simpler structures (homogeneous halfspace) or concern only a limited part of the WB region.

For comparison with the model by Málek et al. (consisting of three layers over the halfspace with constant velocity gradients, solid black line in Fig. 3.11) we have taken all the depths of the layer boundaries of all six estimated velocity structures, we have split the previously estimated layers into these new 32 layers, and we have made a WB regional average v_s model from single-path averages (bold white line in Fig. 3.11). The v_s are weighted both by layer thicknesses and by the lengths of the corresponding paths. We have made this average model despite the fact that the particular paths are so

different, in order to obtain a model to be compared with that of Málek et al. This average model is not to be considered as a result of our study, because it is not representative for the target region due to the enormous diversity of single paths structures. Although some paths (VYSO–TROJ and HROZ–KYNZ) show significantly higher velocities than usually obtained at a depth of 3 km, our average model shows a good agreement with the results of Málek et al.

For the comparison with the WB95 model (long-dashed black line in Fig. 3.11), we have apply the same three layers used by Novotný (1996) and we have weighted the estimated velocity values again by the thicknesses of the original layers and by the lengths of the blast station paths (short-dashed black line). The model by Novotný starts at the altitude of the sea level. Our model shows higher velocities compared to all three WB95 layers.

The highest velocity gradient near the surface concerns only a few tens of meters and it is not possible to determine it by using the fundamental modes, because the dispersion points of periods shorter than 0.15 are scattered.

A schematic geological sketch in Fig. 3.6 shows that each of the presented six surface wave paths crosses several geological units. We expect different propagation velocities in as different units as volcanic plutons, metamorphosed rocks and sediments. The depth range of these geological formations is not yet clear and, for example, sedimentary basins are probably less then 500 m deep; their influence on surface waves longer than 0.4 s would be small. For example the CIHA–SEEB path crosses a sedimentary basin, which may account for its slow velocities; however, VYSO–TROJ path crosses it as well and the velocities are higher even near the surface. Most of the KRAS–PREB path goes through granitoids (plutons), but the velocity distribution is rather complicated. The HROZ–KYNZ path crosses sedimentary, volcanic and metamorphosed rocks and its dispersion shows sharp velocity contrast around the depth of 0.6 km. All this implies that the distribution of geological formations changes significantly with depth.

To obtain a more reliable model of the whole region, surface wave tomography methods seem to be most suitable for continuing this work. We have shown that quarry blast records can be used for studying the local scale uppermost crust although the upper 100 – 200 m have to be studied using other methods.

3.2.11 Acknowledgements

This research was supported by grant No. A300460602 of the Grant Agency of the Academy of Sciences of the Czech Republic, by grant No. 205/06/1780/A of the Czech Science Foundation and by Institute research plan No. A VOZ30460519. Acknowledge the SPICE project (http://www.spice-rtn.org) funded by the 'European Commisions's Human Resources and Mobility Programme'. We are grateful to Jiří Málek for providing programs for the isometric method and for consultations on inversion problems. We also thank Oldřich Novotný for programs and consultations concerning matrix method computations. We thank Robert B. Herrmann for providing his Computer Programs in Seismology and for useful advice on how to use them. One of the figures was illustrated using Generic Mapping Tools (Wessel and Smith, 1991).

3.2.12 References

Antonini, M., 1987: Statistics and source parameters of the swarm from digital recordings, in: Procházková, D. (ed): *Earthquake swarm 1985/86 in Western Bohemia – proceedings of workshop in Mariánské Lázně*, Czechoslovak Academy of Sciences, Geophysical Institute, Prague 1987, 205–217.

Boashash, B. and Jones, G., 1992: Instantaneous frequency and time-frequency distributions, in: Boashash, B. (ed): *Time-frequency signal analysis: methods and applications*, Longman Cheshire, Melbourne, 43–73.

Brož, M., 2000: Detection of the origin time and seismic ground motion of quarry blasts, *Acta Montana*, 16 (118), 17–24.

Bukchin, B. G., Mostinsky, A. Z., Egorkin, A. A., Levshin, A. L. and Ritzwoller, M. H., 2001: Isotropic and nonisotropic components of earthquakes and nuclear explosions on the Lop Nor test site, China, *Pure Appl. Geophys.*, 158, 1497–1515.

Canitez, N., 1977:, Optimum filter for surface-wave group-velocity determination, *Bull. Seism. Soc. Am.*, 67, 79–85.

Cara, M., 1973: Filtering of dispersed wavetrains, *Geophys. J. R. Astr. Soc.*, 33, 65–80.

Dziewonski, A., Bloch, S. and Landisman, M., 1969: A Technique for the analysis of transient seismic signals, *Bull. Seism. Soc. Am.*, 59, 427–444.

Dziewonski, A., Mills, J. and Bloch, S., 1972: Residual dispersion measurement – a new method of surface-wave analysis, *Bull. Seism. Soc. Am.*, 62, 129–139.

Fischer, T. and Horálek, J., 2003: Space-time distribution of earthquake swarms in the principal focal zone of the NW Bohemia/Vogtland seismoactive region: period 1985 – 2001, *J. Geodyn.*, 32 (1–2), 125–144.

Grad, M., Špičák, A., Keller, G. R., Guterch, A., Brož, M., Hegedüs, E. and working group, 2003: SUDETES 2003 seismic experiment, *Stud. Geophys. Geod.*, 47, 681–689.

Guterch, A., Grad, M., Špičák, A., Brückl, E., Hegedüs, E., Keller, G. R., Thybo, H. and CELEBRATION 2000,

ALP 2002, SUDETES 2003 working groups, 2003: An overview of recent seismic refraction experiments in Central Europe, *Stud. Geophys. Geod.*, 47, 651–657.

Herrmann, R. B. (ed), 2002: Computer programs in seismology – An overview of synthetic seismogram computation, version 3.30, Saint Louis University, http://www.eas.slu.edu/People/RBHerrmann/CPS330.html.

Horálek, J., Vavryčuk, V., Plešinger, A., Pšenčík, I., Jedlička, P. and Soukup, J., 1987: Refined localization of selected Jan. 5 – Feb. 6, 1986 events of the West-Bohemian earthquake swarm, in: Procházková, D., (ed) 1987: *Earthquake swarm 1985/86 in Western Bohemia – proceedings of workshop in Mariánské Lázně*, Czechoslovak Academy of Sciences, Geophysical Institute, Prague, 226–235.

Horálek, J., Fischer, T., Boušková, A. and Jedlička, P., 2000: The Western Bohemia/Vogtland region in the light of the WEBNET network, *Stud. Geophys. Geod.*, 44, 107-125.

Janský, J., 2000: Grid search hypocentral location method in simple 1-D media, *Acta Montana*, 16 (118), 71–84.

Janský, J., Novotný, O., 1997: Reinterpretation of the travel times of P waves generated by quarry blasts in Western Bohemia, *Acta Montana*, 11 (104), 35–48.

Janský, J., Horálek, J., Málek, J. and Boušková, A., 2000: Homogeneous velocity models of the West Bohemian swarm region obtained by grid search, *Stud. Geophys. Geod.*, 44, 158–174.

Kocaoglu, A. H., Long, L. T., 1993: A review of time-frequency analysis techniques for estimation of group vVelocities, *Seism. Res. Lett.*, 64, 157–167.

Kolář, P. and Boušková, A., 2003: On some anomalies of v_P/v_S ratio of West Bohemian swarm 2000 – preliminary results, *Acta Montana*, 22 (129), 51–57.

Kolínský, P., 2004: Surface wave dispersion curves of Eurasian earthquakes: the SVAL program, *Acta Geodyn. Geomater.*, 1 (134), 165–185.

Levshin, A. L. and Ritzwoller, M. H., 1995: Characteristic of surface waves generated by events on and near the Chinese nuclear test site, *Geophys. J. Int.*, 123, 131–148.

Levshin, A. L., Pisarenko, V.F. and Pogrebinsky, G.A., 1972: On a frequency-time analysis of oscillations, *Ann. Geophys.*, 28, 211–218.

Levshin, A. L., Yanovskaya, T. B., Lander, A. V., Bukchin, B. G., Barmin, M. P., Ratnikova, L. I. and Its, E. N., 1989: Interpretation of Surface Wave Observations – Frequency-time Analysis, in: Keilis-Borok, V. I. (ed.): *Seismic Surface Waves in a Laterally Inhomogeneous Earth*, Kluwer Academic Publishers, Dordrecht/Boston/London, 153–163.

Levshin, A. L., Ratnikova, L. and Berger, J., 1992: Peculiarities of surface-wave propagation across Central Eurasia, *Bull. Seism. Soc. Am.*, 82, 2464–2493.

Lokajíček, T., Janatková, Z., Plomerová, J., 1987: Travel times of seismic waves of the 1985-86 swarm in Western Bohemia, in: Procházková, D. (ed): *Earthquake swarm 1985/86 in Western Bohemia – proceedings of Workshop in Mariánské Lázně*, Czechoslovak Academy of Sciences, Geophysical Institute, Prague, 236–246.

Málek, J. and Žanda, L., 2004: Seismic effects of the quarry blasts on the territory of Bohemia, *Acta Geodyn. Geomater.*, 1 (134), 291–302.

Málek, J., Janský, J. and Horálek, J., 2000: Layered velocity models of the Western Bohemia region, *Stud. Geophys. Geod.*, 44, 475–490.

Málek, J., Brož, M., Fischer, T., Horálek, J., Hrubcová, P., Janský, J., Novotný, O., Růžek, B. and the CELEBRATION working group, 2001: Seismic measurements along short profiles in Western Bohemia during the CELEBRATION 2000 experiment, *Acta Montana*, 18 (121), 15–28.

Málek, J., Janský, J., Novotný, O. and Rössler, D., 2004: Vertically inhomogeneous models of the upper crustal structure in the West-Bohemian seismoactive region inferred from the CELEBRATION 2000 refraction data, *Stud. Geophys. Geod.*, 48, 709–730.

Málek, J., Horálek, J. and Janský, J., 2005: One-dimensional qP-wave velocity model of the upper crust for the West Bohemia/Vogtland earthquake swarm region, *Stud. Geophys. Geod.*, 49, 501–524.

Malinowski, M., 2005: Analysis of short-period Rayleigh waves recorded in the Bohemian Massif area during CELEBRATION 2000 experiment, *Stud. Geophys. Geod.*, 49, 485–500.

Mlčoch, B., Schulmann, K., Šrámek, J., Manová, M., Pokorný, L., Fiala, J. and Vejnar, Z., 1997: Geological interpretation of major regional units – the Saxothuringian zone, in: Vrána, S. and Štědrá, V. (eds): *Geological model of Western Bohemia related to the KTB borehole in Germany*, Czech Geological Survey, Prague, 51–61.

Murphy, J. R. and Shan, H. K., 1988: An analysis of the effects of site geology on the characteristics of near-field Rayleigh waves, *Bull. Seism. Soc. Am*, 78, 64–82.

Nehybka, V. and Skácelová, Z., 1997: Seismological Study of the Kraslice/Vogtland-Oberpfalz Region, in: Vrána, S. and Štědrá, V. (eds.): *Geological model of Western Bohemia related to the KTB borehole in Germany*, Czech Geological Survey, Prague, 186–190.

Novotný, O., 1996: A preliminary seismic model for the region of the West-Bohemian earthquake swarms, *Stud. Geophys. Geod.*, 40, 353–366.

Novotný, O., Proskuryakova, T. A., Shilov, A. V., 1995: Dispersion of Rayleigh waves along the Prague-Warsaw profile, *Stud. Geophys. Geod.*, 39, 138–147.

Novotný, O., Grad, M., Lund, C. E. and Urban, L., 1997: Verification of the lithospheric structure along profile Uppsala-Prague using surface wave dispersion, *Stud. Geophys. Geod.*, 41, 15–28.

Novotný, O., Janský, J. and Málek, J., 2004: Some aspects of the application of the Wiechert-Herglotz method to refraction data from Western Bohemia, *Acta Geodyn. Geomater.*, 1 (134), 157–164.

Plomerová, J., Babuška, V., Janatková, Z. and Lokajíček, T., 1987: Directional dependence of seismic waves propagation of the 1985-86 earthquake swarm in Western Bohemia, in: Procházková, D. (ed.): *Earthquake swarm 1985/86 in Western Bohemia – proceedings of workshop in Mariánské Lázně*, Czechoslovak Academy of Sciences, Geophysical Institute, Prague, 197–204.

Proskuryakova, T.A., Novotný, O. and Voronina, E. V., 1981: Studies of the Earth's structure by the surface-wave method (Central Europe) (Izuchenie stroeniya Zemli metodom poverkhnostnykh voln (Tsentral'naya Evropa)), Nauka, Moscow, in Russian, 92 pp.

Shapiro, N. M. and Singh, S. K., 1999: A systematic error in estimating surface-wave group-velocity dispersion curves and a procedure for its corrections, *Bull. Seism. Soc. Am.*, 89, 1138–1142.

Tarantola, A., 1987: Inverse problem theory: methods for data fitting and model parameter estimation, *Elsevier Science B.V.*, Amsterdam, Netherlands.

Wessel, P., and Smith, W. H. F., 1991: Free software helps map and display data, *Eos Trans. AGU*, 72, 441.

Wielandt, E., Sigg, A., Plešinger, A. and Horálek, J., 1987: Deep structure of the Bohemian Massif from phase velocities of Rayleigh and Love waves, *Stud. Geophys. Geod.*, 31, 1–7.

Yamanaka, H., Kazuoh, S. and Samano, T., 1989: Effects of sedimentary layers on surface wave propagation, *Bull. Seism. Soc. Am.*, 79, 631–644.

here the original text of the paper ends

3.3 Additional remarks to the paper

During the paper elaboration, a flow chart depicted in Fig. 3.12 was created. It was not used in the published version of the paper, however, we think it may complement Sections 3.2.3, 3.2.4 and 3.2.5.

All the processes, computations and methods are shown in white boxes and all the input data, measurements, parameters and products of computations are in gray boxes.

As an input for the frequency-time analysis we need an epicentral distance and origin time of the event as well as the (generally instrument dependent) record of the event. Then we provide the frequency-time analysis and we obtain a set of quasimonochromatic signals with their envelopes. When we plot them together side by side, we get a spectrogram. From the set of quasimonochromatic signals, we compute the set of dispersion points given by the arrival time of some of the local maxima of an envelope of each of the signal. According to these dispersion points, we truncate the quasimonochromatic signals as well as we truncate their envelopes in the time domain. By summing the truncated signals, we obtain a separated dispersed surface wavegroup, which is still instrument dependent and we can compare it with the original record to check if the filtration and surface wave identification went well.

Using the truncated envelopes we can plot a truncated spectrogram which is just to show a comparison with the original spectrogram to see if the dispersion ridge is really continuous. Then we apply an instrumental time shift to the dispersion points – it means, we shift the points in time to get the real arrival time of the maxima of the signal envelope. The time shift is computed using the phase characteristic of the instrument. According to the phase and period of the wave, for each dispersion point, a specific time shift is computed. So we have a dispersion curve as if it was computed from the instrument independent record. We also apply the instrumental time shift to each of the truncated quasimonochromatic signal in the same manner as we do it for the dispersion points. Summing these shifted truncated signals, we obtain an instrument independent separated surface wavegroup.

Then we invert the instrument independent dispersion curve by the isometric method which uses the matrix method for forward computations. As a result of the inversion, we have a 1D model of shear wave velocity distribution down to the given depth – 3 km in our case. This structural model is used as an input for the modal summation forward computation. In addition to this, we need to set also the epicentral distance and the source time function to compute the synthetic waveform. Epicentral distance should be the same as in the case of the real measured record, the problems with unknown source time function are discussed in Section 3.2.9. We compute a synthetic (instrument independent) record corresponding to the propagation of fundamental mode in the shear wave velocity model obtained by the dispersion curve inversion and we can compare this synthetic waveform with the instrument independent separated surface wavegroup from the measurement.

In the paper, as it is shown in the flow chart, instrumental corrections were computed by a simple method when the phase transfer function of the seismometer is used directly for the dispersion points. For each period of the wave, the phase characteristic gives us a phase shift. The phase shift gives us a time we need to shift the dispersion point or the whole signal at this period to avoid the influence of the seismometer. For short period instruments and for measurement in the period range near the natural period of the instrument, this approach is justified. However, this approach is not exactly correct even it is used in literature sometimes. After the paper Kolínský and Brokešová (2007) was prepared, we implemented a new method of applying the instrumental transfer function which is theoretically exact.

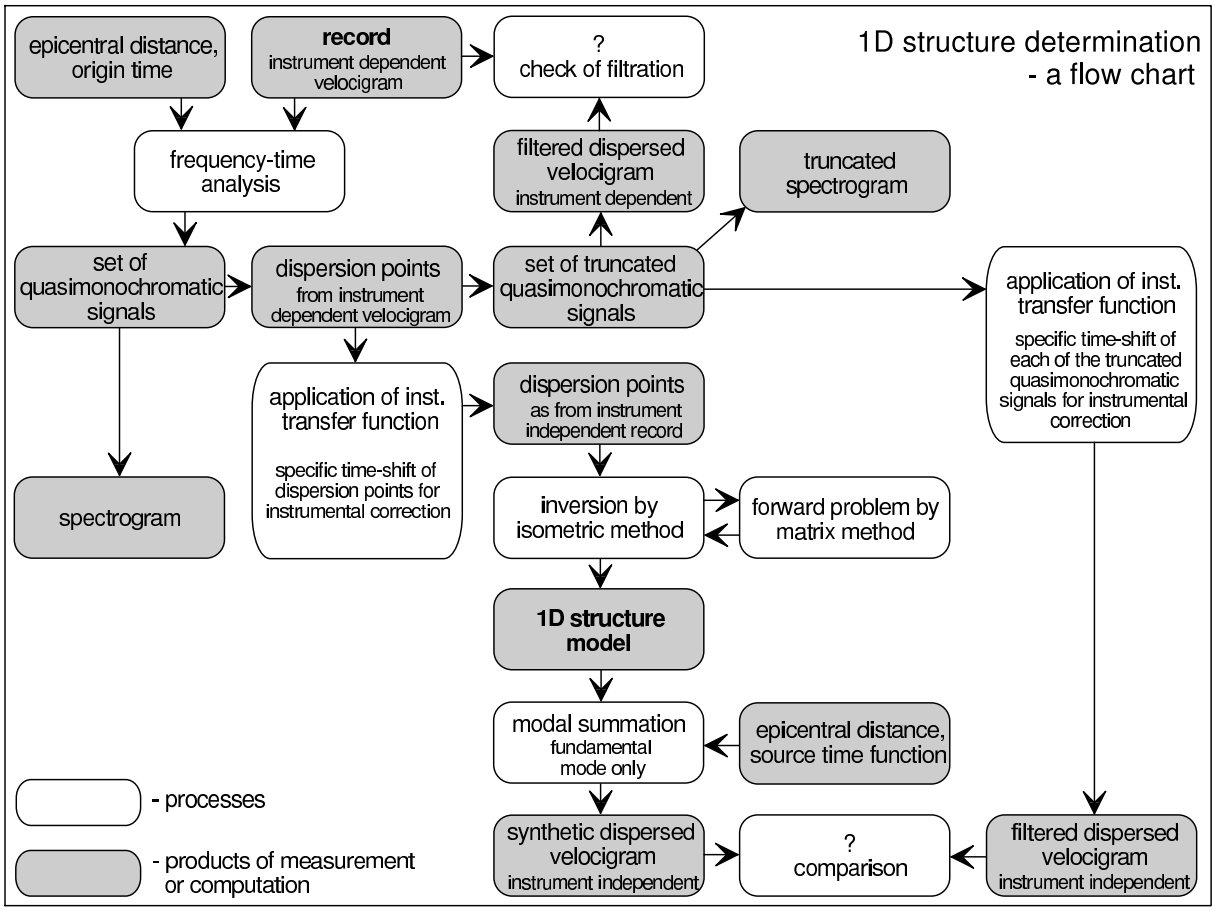


Figure 3.12: A flow chart of the processing used in the paper Kolínský and Brokešová (2007). This figure was not used in the original paper, however, we show it here to demonstrate the steps of computation and estimation of velocity distribution.

We compute the spectrum of the whole record, we apply the complete instrument transfer function in the frequency domain by dividing the record spectrum by complex spectrum of the instrument characteristic and hence we obtain an instrument independent spectrum. After that, we use this instrument independent spectrum as an input for our multiple filtering method. All quasimonochromatic signals and their envelopes are then instrument independent.

The issue is that phase characteristic of the instrument concerns only the phase shifts of the quasimonochromatic signals and not the shifts of their envelopes. The envelopes do not shift in the same manner as their underlying waves and as the dispersion points are computed as maxima of the envelopes, we should not used the phase shifts for them in the manner described in the scheme.

Detailed description of the instrument characteristic application is given in Chapter 1, Section 1.5 and Chapter 6, Section 6.11.

Chapter 4

Application B: Rayleigh wave tomography

4.1 Dealing with the topic

As we have prepared the paper concerning 1-D structural models of the Western Bohemia region (Chapter 3), the idea of surface wave tomography seemed to be a natural continuation of our work. We started with Love waves and even during the preliminary analysis of surface wave data, we used a simple tomography approach dealing with boxes with constant values of Love wave group velocities. We used geometrical surface ray paths crossing the boxes and we estimated the velocity distribution using simple linear one-step approach given by (see, for example, Tarantola, 1987)

$$p = \left(G^T L G\right)^{-1} \cdot \left(G^T L r\right), \tag{4.1}$$

where p is the slowness vector containing the resultant velocities for each box, matrix G represents lengths of each ray in each box, matrix L represents inverse values of measurement errors and vector r are the travel times for selected wavelength for each ray. As we have the matrix G, the only complicated operation is to make an inverse matrix $(G^T L G)^{-1}$. The linear inverse problem is thus solved in one step.

The preliminary result for period of 0.8 s is shown in Fig. 4.1. We use 25 boxes and we oriented them without any a priori information along the geographical coordinate system. The resolution is poor but the velocity distribution is not random and areas with higher and lower velocities are to be distinguished in the figure. However, the velocity contrasts are rather unrealistic high ranging from 1.0 to 4.0 km/s.

After the final analysis of Love waves and after the inversion of the six 1D structures, we looked for a method to provide the surface wave tomography with better resolution. As we would like to invert as few parameters as possible, we thought about the idea to invert the velocities for each geological block in the region with an assumption that in each block the velocity for given period would be constant. In other words, to use the same approach as computing the tomography in rectangular boxes, but to use the boundaries of the geological blocks instead of boxes. Fig. 4.2 shows the distribution of such blocks (description of the geological units is given in caption to Fig. 4.4).

As the boundaries are very complicated and the computation of ray distances in each block would be complicated too, we continued to look for other method, which would not force the results to fit in artificial boxes, as in Fig. 4.1, and which would not be so complicated as the real geological structure in Fig. 4.2. In addition to this, the depths of geological formations are not so well known and their boundaries are clearly given only on surface. The shortest wavelengths of used surface waves are sensitive to the structure of the first hundreds of meters from the surface what would approximately correspond to the depth of the sedimentary basins – longer waves would not be affected by them at all. As it is shown in the paper, the geological structure is probably not the most important phenomenon influencing the distribution of surface wave group velocities. From this point of view, the use of the geological units for constant velocity values estimation would not be justified.

For surface wave tomography, we use a program developed by prof. Tatiana B. Yanovskaya with her permission. The program computes 2D group velocity maps in a plane and it has all the advantages we looked for – it is easy to use, it is designed for areas with linear distance smaller than 100 km, it can deal with uneven distribution of rays, it has variable number of grid nodes where the velocity values are

estimated and it gives not only the velocity distribution, but it also allows to see the averaging area for each grid node. This averaging area corresponds to the resolution of the method in given node and we can easily compare the results and their reliability for different smoothing parameters and different grid node distributions.

Instead of Love waves, we finally decided to use the Rayleigh waves for the paper dealing with surface wave tomography in the Western Bohemia region. The paper Kolínský and Brokešová (2008) is cited in the following paragraphs. After it, some comments on defining the smoothing parameter and discussion of the resolution is added as well as two more figures of tomography maps computed using different smoothing parameters are presented.

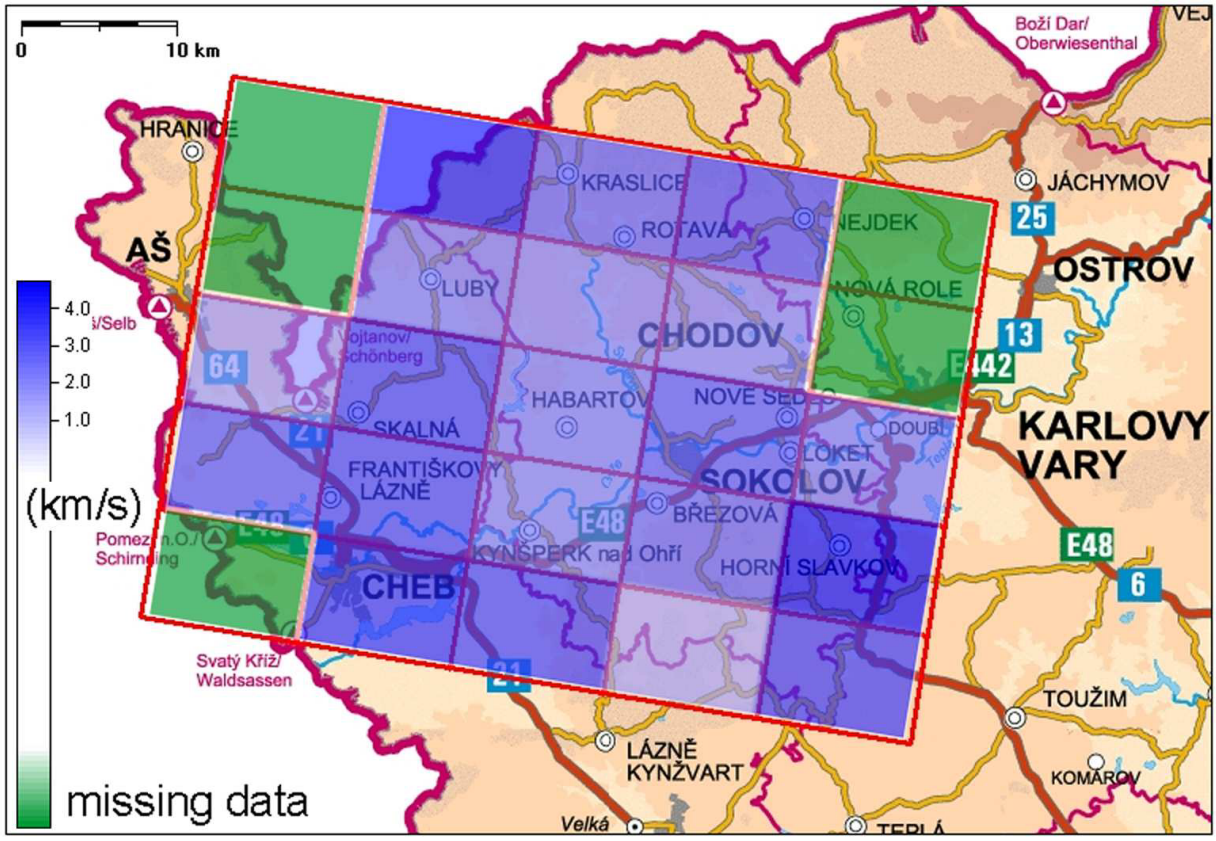


Figure 4.1: Map of the Western Bohemia region with preliminary tomography map of Love wave group velocities. 25 rectangular boxes were used to estimate constant values of velocities in each of them using linear inverse problem solution.

---

here the original text of the paper starts

4.2 The Western Bohemia uppermost crust Rayleigh wave tomography

Petr Kolínský and Johana Brokešová, 2008, Acta Geodyn. Geomater., Vol. 5, No. 1(149), p. 5–17

4.2.1 Abstract

We apply a traditional method of surface wave tomography as a new approach to investigate the uppermost crust velocities in the Western Bohemia region (Czech Republic). It enables us to look for velocity distribution in a small scale of tens of kilometers. We measure Rayleigh wave group velocity dispersion curves in a period range 0.25 – 2.0 s along paths crossing the region of interest. We use modified multiple filtering method for frequency-time analysis. We compute 2-D tomography maps of group velocity distribution in the region for eight selected periods using the standard methods and programs described in literature. We discuss the velocity distribution with respect to results of former study by Nehybka and Skácelová (1997). We present a set of local dispersion curves which may be further inverted to obtain a 3-D shear wave velocity image of the area.

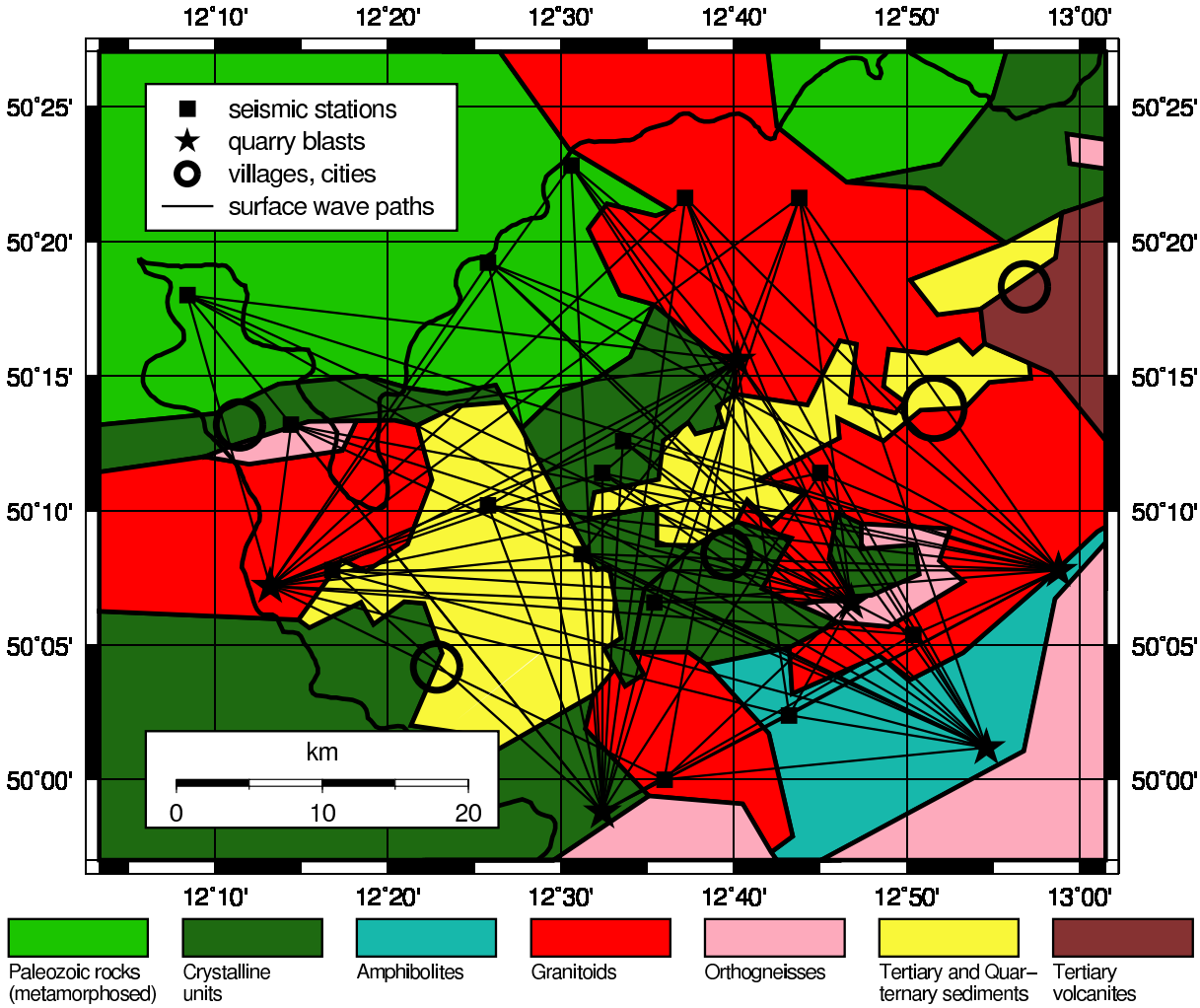


Figure 4.2: The Western Bohemia region with geological blocks in different colors. Analyzed ray paths are also shown.

key words group velocity, frequency-time analysis, multiple filtering, Rayleigh wave tomography, Western Bohemia

4.2.2 Introduction

Let us present a short summary of former surveys in the region of our interest. While looking for the published papers concerning the Bohemian Massif (BM) and the Western Bohemia region (WB) especially, we may categorize them as follows:

1. *Seismicity and geology*

We mention the work by Fischer and Horálek (2003) with an overview of the seismic swarm occurrence. The idea of magma injection to the crust has been formulated by Špičák et al. (1999) for the WB region. These works summarize the main motivations for studying the WB region – an active area of seismic swarms is situated beneath our target region and complicated crust models were presented for the WB. Our study does not reach the depths of latter papers; however, the knowledge of uppermost parts is essential for studying the deeper crust structure.

2. *Refraction and reflection experiments*

In the 1960s, international deep seismic sounding profiles were performed across the BM. Data were interpreted by Beránek et al. (1973) and reinterpreted later by Novotný (1997). In 2000, the CELEBRATION (Central European Lithospheric Experiment Based on Refraction) took place (Guterch et al., 2003). Resultant 2-D models can be found in Hrubcová et al. (2005) and Růžek et al. (2007). Deep seismic sounding gave 1-D sets of block models with poor lateral resolution. Refraction experiments studied the uppermost parts of the crust. They resolved anomalies in the scale of tens of kilometers and with poor depth accuracy near the surface. We would like to present a study with refinement of the velocity structure accuracy both laterally and vertically.

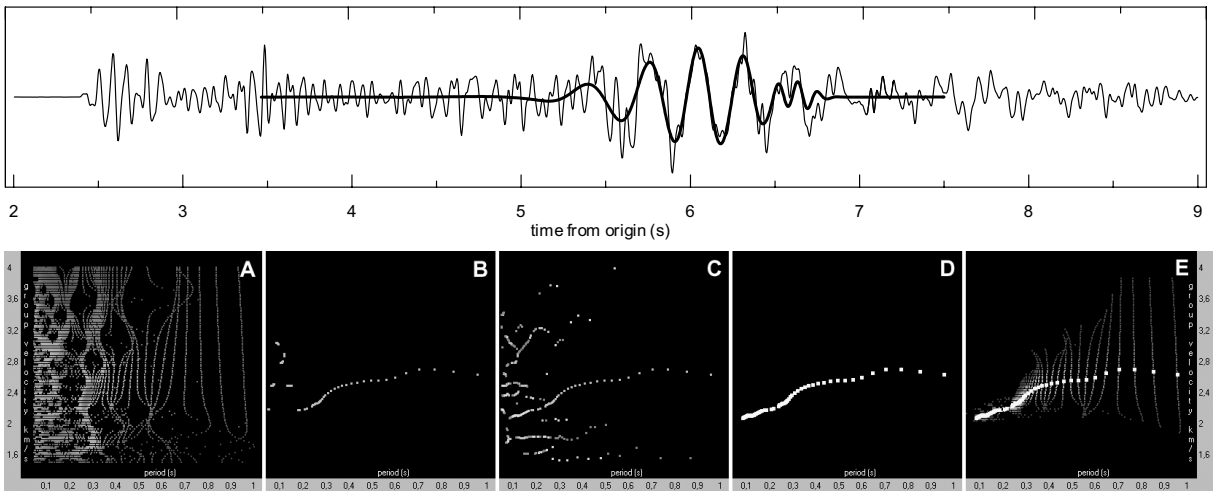


Figure 4.3: (*Fig. 1 in Kolínský and Brokešová, 2008*) Surface wave analysis example. Thin line in the upper plot represents the record from the quarry blast OTRO at the station PRAM (see Fig. 4.4), epicentral distance is 13.855 km and sampling frequency is 250 Hz. Bottom panels show five steps of frequency-time analysis. A: spectrogram of the record is computed. B: For each filter its absolute envelope maximum is found and plotted – we may see that only a part of the dispersion curve is formed by the arrival times of these maxima. C: All other local envelope maxima are found and plotted. D: According to the criterion of continuity the fundamental dispersion curve is compiled using all available maxima regardless of their amplitudes. E: Fundamental dispersion ridge is cut from the spectrogram along the found dispersion curve. These truncated parts of selected signals are summed to obtain the surface wavegroup as shown in upper plot by thick black line.

3. *1-D body wave propagation*

The study by Plomerová et al. (1987) presented apparent velocities of Sg and Pg waves generated by WB swarms. 1-D velocity models were given by Janský and Novotný (1997). A simple 3-D block model of the uppermost crust was published by Nehybka and Skácelová (1997). Janský et al. (2000) estimated crustal homogeneous models for four swarm subregions in WB. Málek et al. (2000) studied layered models of the upper crust of the same subregions. Novotný et al. (2004) used refraction data for uppermost crust velocity estimation. These studies provide reference models for our results. They deal with the same region of interest and concern also the uppermost crust depths of several kilometers. We choose for comparison the work by Nehybka and Skácelová (1997). The authors were the first who attempted to show the 3-D distribution of P wave velocities in the WB region. Other detailed studies of several WB geological units may be found in Málek et al. (2004 and 2005).

4. *1-D surface wave propagation*

Wielandt et al. (1987) presented surface wave profile crossing the BM in southwest-northeast direction. Plešinger et al. (1991) gave the crustal velocity estimation for profile in southwest BM. These studies are important for the surface wave analysis methodology and as a first attempts to use surface waves for studying the BM. However, their wavelengths concern the whole crust and resolution ability is limited. Novotný (1996) compiled an average 1-D model of the WB region using surface wave studies. In this work, he concentrates on our WB area of interest, but his uppermost crust model consists of two layers only. We propose a more detailed model. Studies concerning the BM surface wave propagation and crust structure estimation were presented by Novotný et al. (1995 and 1997). These studies gave more detailed velocity distributions than Wielandt et al. (1987) and Plešinger et al. (1991), but they concern different parts of BM. Malinowski (2005) gave a structure of the uppermost crust in southwestern BM using the short-period Rayleigh waves – these waves are used in our present study. Part of his 2-D profile crosses WB. Kolínský et al. (2010) estimated 1-D models of the crust and uppermost mantle in the southwestern BM crossing three major geological units of this area using relative phase velocity measurements of Aegean Sea earthquakes. This study was aimed for the whole crust velocity structure estimation and one of the profiles reaches WB region. This study uses waves longer than 9 s and near surface structure is not resolved well.

Kolínský and Brokešová (2007) estimated several 1-D models of WB uppermost crust v_s using short-period Love wave group velocities from quarry blasts. Our present study is a continuation of the latter paper, but as opposed to the latter work, we use Rayleigh waves for our tomography. The methodology of surface wave analysis is the same as in latter paper. We extended the amount of data and we concentrate on the same area of interest.

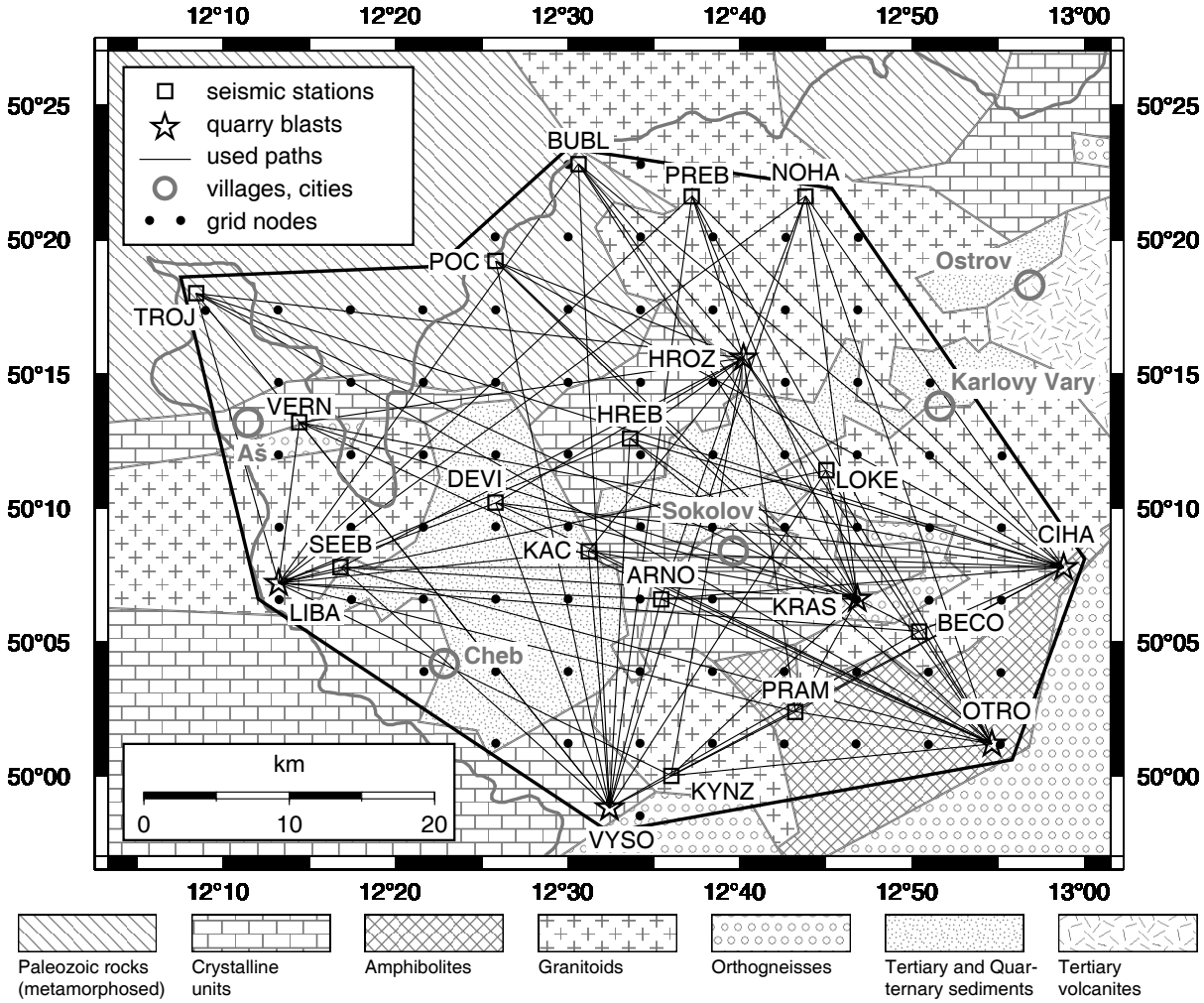


Figure 4.4: (*Fig. 2 in Kolínský and Brokešová, 2008*) Map of the Western Bohemia region. There are 15 stations (squares), 6 shot locations (stars) and 87 surface wave paths (thin solid lines) as well as several cities (gray circles) shown in the figure. Main geological units are sketched according to Mlčoch et al. (1997). Used grid nodes (dots), studied area border (bold black line) and the border between the Czech Republic and Germany (bold gray line) are shown.

5. *Receiver functions*

Wilde-Piórko et al. (2005) published detailed v_s models under several stations in the BM obtained by the receiver function technique. Heuer et al. (2007) presented the differences between Saxothuringian and Moldanubian units in the western BM using also the receiver function technique. Geissler (2005) presented a large study of WB region using the receiver function technique as well as other geophysical exploration methods. Receiver function method gives whole crust and upper mantle structure. The uppermost crust is smoothed and not well resolved.

Our WB region surface wave tomography aims to get higher resolution of seismic velocity estimation of the region. Despite the fact that our study concerns only limited uppermost layer of the crust the results are important both for WB event localization and for understanding the seismic swarm generation since the upper crustal layers are supposed to be the most heterogeneous.

4.2.3 Group velocity analysis

For the surface wave tomography, we first need to measure the group velocity dispersion. We use the method of Fourier transform-based multiple filtering frequency-time analysis (Dziewonski et al. 1969). This is a classical technique and we have made modifications for processing signals in which the amplitudes of surface waves do not exceed the amplitudes of body waves. All the standard procedures as well as the new enhancements of the modified technique are described in details in the paper by Kolínský and Brokešová (2007). We use constant relative resolution filtering with the opportunity of controlling the width of the filters during the dispersion curve estimation. Some notes on this problem may be found in Levshin et al. (1972) and Cara (1973). The actual implementation of the parameters controlling the filtration is described in Kolínský (2004).

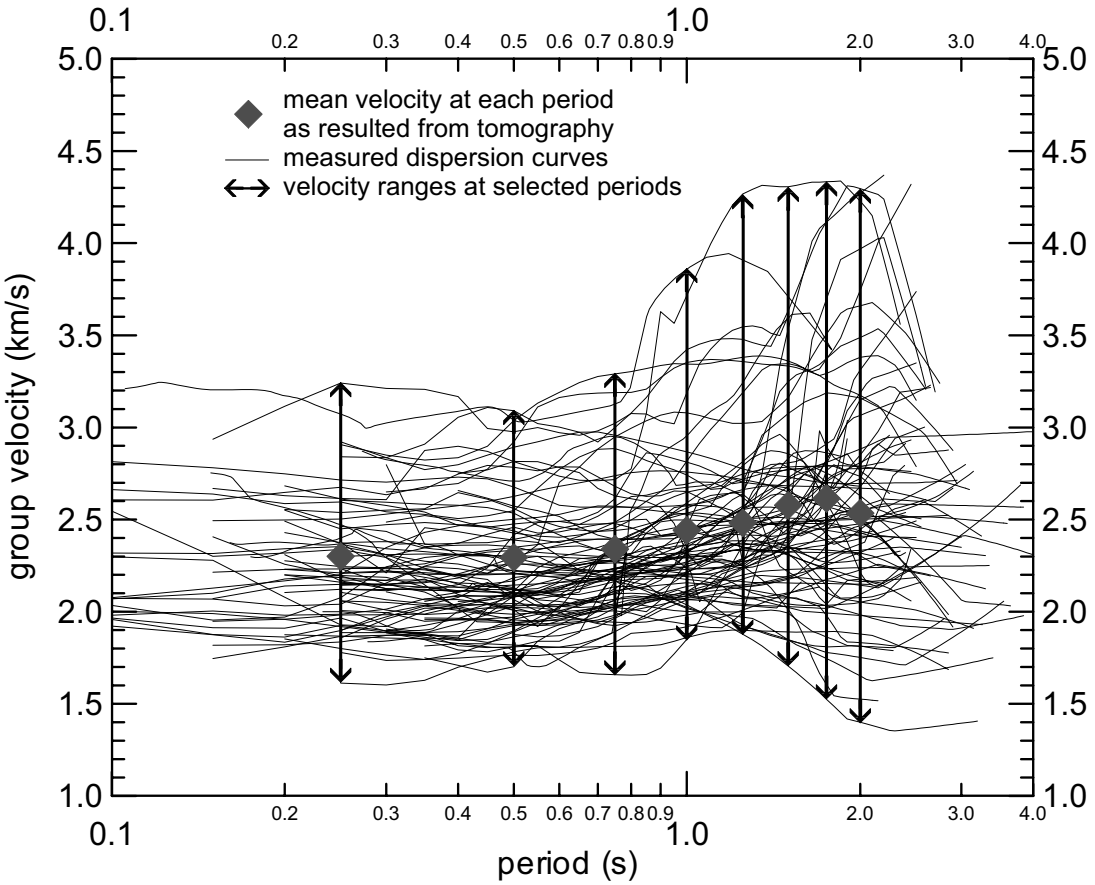


Figure 4.5: (*Fig. 3 in Kolínský and Brokešová, 2008*) Dispersion curves of Rayleigh wave group velocities measured along 87 paths (Fig. 4.4). Velocity ranges at eight selected periods are shown to depict the increasing velocity differences for longer waves. Values of mean velocities vm in the studied region obtained by 2-D tomography at each period are shown by gray diamonds.

We use the instantaneous period computation for our filtered quasimonochromatic signals to ensure appropriate estimation of slightly varying periods along these signals. We use this procedure according to the study of Levshin et al. (1989).

We show the record envelope distribution in frequency-time plot (Fig. 4.3, panel A). We look for dispersion ridge representing the group velocity-period dependence (Fig. 4.3, panel B). Here we apply a modification of the classical technique – we do not use only the absolute amplitude values to determine the fundamental dispersion ridge, but instead, we look for all local dispersion ridges in the whole frequency-time domain (Fig. 4.3, panel C) and we provide a procedure for compiling the resultant dispersion curve using the combination of the local ridges (Fig. 4.3, panel D). The criterion of ridge continuity is used instead of criterion of highest amplitude values. Hence, we look for a ridge passing through our group velocity-period plots in the areas where we assume the fundamental mode should be present. After selecting the dispersion points, we truncate the spectrogram in the time domain to keep only the fundamental mode dispersion ridge (Fig. 4.3, panel E), which is used to create filtered surface wavegroup (Fig. 4.3, bold line in upper plot).

In case that the automatic procedure is not successful, we have the opportunity to select the dispersion ridge manually – the step from panel C to D is done by hand. Sometimes the analyst can see the dispersion ridge on a first glance in the frequency-time plots where the computer-based procedures would hardly give any reliable result.

We use the data from the same experiment as in Kolínský and Brokešová (2007) and so the formal description of the procedures, examples and tests given in the latter work hold for this study as well. During the group velocity measurement, sets of filtered quasimonochromatic signals and filtered surface wavegroups are inspected in comparison with the raw data for each path to ensure the reliability of measurement (Fig. 4.3, upper plot). Different widths of filters are used for each record according to the actual properties, signal-to-noise ratio and body wave presence. Trial-and-error attitude is used for filtration parameter settings in case of complicated records to have the opportunity to choose the best resolution in both time and frequency domains in order to obtain as broad dispersion curve as possible.

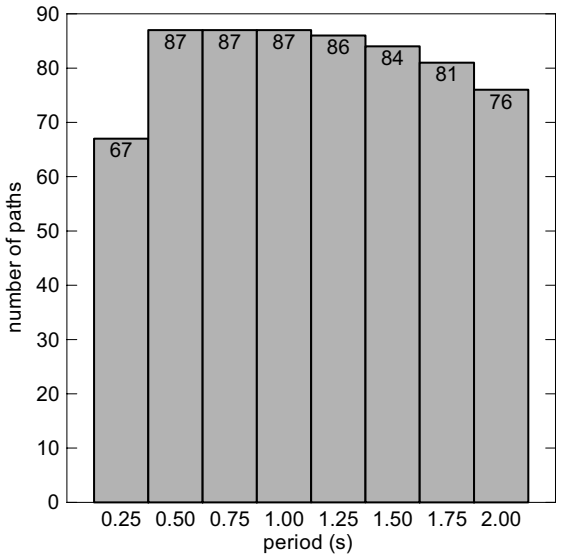


Figure 4.6: (*Fig. 4 in Kolínský and Brokešová, 2008*) Number of paths used for the tomography maps computation with respect to eight periods.

4.2.4 Group velocity tomography

Surface wave tomography became a standard procedure for imaging the large scale heterogeneities of the Earth crust and upper mantle. We focus on local surface wave tomography study.

In the present paper we use the method described in Ditmar and Yanovskaya (1987) and Yanovskaya and Ditmar (1990). The advantage of the method is that it works also in cases when we do not have uniformly covered area with surface wave paths. The method does not use any boxes or other a priori division of the studied area. Measured velocities are entered along the ray paths and the actual velocity is given in required grid nodes. The velocity value for each grid is computed as an average of surrounding values given along the rays. In case we have only sparse ray coverage, this averaging area is larger. As it is possible to show the velocity distribution as well as the size of the averaging area, one may easily see the results with their resolving power together.

The use and further elaboration of the method is given in Yanovskaya et al. (1998), Yanovskaya et al. (2000) and Yanovskaya and Kozhevnikov (2003). This approach was successfully employed by studies dealing with regional surface wave tomography in scales smaller than continental, see for example papers by Bourova et al. (2005) (Aegean Sea) and Raykova and Nikolova (2007) (Balkan Peninsula). We use the same approach as in latter papers even for much more local problem.

Our area of interest is only 50 x 60 km and so we use the computational code, kindly provided by prof. Yanovskaya, where the area is regarded as a plane. We transform the geographical coordinates of station and blast locations to the new Cartesian coordinate system. The XY crossing zero point is located at 12.5° E and 50.2° N. The system is orientated so that at this point the Y axis is parallel to the actual meridian. Distance in the XY plane is measured in kilometers.

The tomographic procedure requires positions of each source-station pair and the velocity of propagation of the selected period of the corresponding dispersion curve. We may set the variance of each measured velocity and we define the positions of grid nodes where we want the resultant velocity to be estimated. As a most important tool for controlling the tomography is the regularization parameter. The higher is the value of the regularization parameter, the larger is the smoothness of the resulting velocity distribution and the larger is the averaging area for each grid node. We tested several values of the regularization parameter. Smaller value of this parameter gives very perturbed 2-D group velocity distributions. It gives smaller averaging areas and smaller residuals and hence theoretically better resolution. But it is not possible to "improve" the resolution only by using a smaller regularization parameter without considering the consequences for physical sense of the results. We choose the smoothness of the maps and hence the resolution to be comparable with wavelengths regardless of the residual improvement. This is the reason why this residual improvement is so different for different periods, as shown in Section 4.2.6.

In the above mentioned papers we found recommended values of the regularization parameter, however, since our period ranges differs significantly, we used trial-and-error process to look for optimal parameter for each period.

An initial mean square travel time residual is estimated for the constant mean velocity distribution. After the tomographic procedure the remaining mean square residual is estimated. The ratio between these two residuals gives us an "improvement" of the tomography map in comparison with initial homogeneous mean velocity model.

As an output we obtain the values of velocity in required grid nodes and the size of the circular

averaging area for each grid node in km. This averaging area represents the uncertainty of the tomography; as the area is smaller, the resolution of the map is better. In case of non-isotropic ray coverage, instead of circular averaging areas, areas elongated in the direction of rays with predominant azimuth could be considered, see Yanovskaya et al. (1998). The rms of each grid point is given. At the end, we transform the results back to the geographical coordinates.

4.2.5 Data

Records used in the present study have been acquired during the seismic refraction experiment SUDETES 2003 (see Grad et al., 2003) which was a part of the SLICE (Seismic Lithospheric Investigation of Central Europe) international experiment. Small amount of the data have been used in the study by Kolínský and Brokešová (2007). Six shots were fired in the WB region during the experiment: Vysoká (VYSO), Číhaná (CIHA), Krásno (KRAS), Horní Rozmyšl (HROZ), Otročín (OTRO) and Libá (LIBA) and we use them in this study, see Table 4.1 and Fig. 4.4. Sixteen temporary stations were deployed in the WB region during the experiment. Data from 15 of them are used in this study; one of the stations was disturbed by some agricultural equipment. Lennartz LE-3D and Streckeisen STS-2 seismometers were used. Sampling frequency of all the stations was 250 Hz. The main purpose of this measurement was to acquire data for 3-D body wave tomography of the WB region. As a by-product of 6 blast recorded at 15 stations we have obtained 90 records containing surface waves covering an area of approximately 50 x 60 km, see Fig. 4.4. We use 87 of these surface wave paths in present tomography study; two of the records could not be analyzed for their low quality of signal-to-noise ratio and one of the record was discarded because it produce large arrival time residual in the whole period range.

We analyze the surface wave dispersion in a period range from 0.15 to 4.0 s, however, only few of the records produce such broad period range dispersion. This is the reason why we limit the period range from 0.25 up to 2.0 s for the tomography study.

The raw records are corrected for the instrumental response using the appropriate transfer function in the spectral domain. The velocity changes caused by the application of the transfer function are comparable with errors given by the frequency-time analysis in the given period range. However, they cause a systematic shift and so we use the corrected records for estimating the velocities to avoid this error.

The origin times of the shots have been accurately measured by a technique especially developed for this purpose. Several BR3 receivers (Brož, 2000) were installed at a distance of tens of meters from the shot to extrapolate the origin time with an accuracy of about 5 ms. For a description of the measurement method, see Málek and Žanda (2004); typical features of quarry blast records are also described there. Compared to natural earthquakes, we know the epicenter coordinates and origin times with negligible errors.

shot point	East longitude ° WGS84	North latitude ° WGS84	altitude (m)	charge (kg)	date (y/m/d)	origin time (UTC)
LIBA	12.223	50.120	590	400	2003/06/04	17:09:59.525
VYSO	12.543	49.978	700	400	2003/06/04	19:09:59.526
HROZ	12.668	50.261	560	400	2003/06/05	17:49:59.546
KRAS	12.776	50.114	740	270	2003/06/04	17:20:00.476
OTRO	12.909	50.021	605	200	2003/06/05	02:59:59.569
CIHA	12.983	50.133	730	400	2003/06/04	17:40:06.311

Table 4.1: Coordinates, origin times and charges of the blasts.

4.2.6 Tomographic images

We set grid nodes every 5 km in both directions in our Cartesian coordinate system. We clip the area of interest by an octagon corresponding to our path coverage. We present only the results for grid nodes inside of this octagon. Fig. 4.4 shows 79 nodes projected into geographical coordinates.

Fig. 4.5 presents 87 group velocity dispersion curves estimated using the dataset described in the previous section. The period values of the dispersion points are obtained using the instantaneous period estimation which is generally different for each of the curves and so we linearly interpolate the estimated group velocity values for the period values with the step of 0.05 s to have the opportunity to use the velocities of all the 87 curves at the same periods. We have decided to use the eight periods in the range from 0.25 to 2.0 s for the tomography study. Some of the curves do not cover the whole range of periods

and Fig. 4.6 shows the number of paths for each period.

Since we do not know the group velocity variance, we set all the variances for all paths to 1.0 to give the same weight to all the data.

The averaging area, which gives us information about the resolution of the tomography maps, depends on ray coverage and on the regularization parameter controlling the smoothness of the results. We have to introduce different resolution for different wavelengths by using different regularization parameters for different periods. We set the regularization parameter in such a way that for the longest period we get the smallest averaging area twice larger than corresponding wavelength. This criterion was set after many tests with different regularizations and different results. We checked the resulted maps and we choose the regularization to obtain the group velocity perturbation in reasonable range (smaller averaging area gives larger perturbations) and to obtain acceptable residual improvement (greater averaging area gives worse residual improvement). For approximate mean velocity 2.5 km/s for the period of 2.0 s the wavelength is 5.0 km. So the resolution of our longest wave is 10.0 km (radius of the averaging area is 5.0 km) and worse. In case of the shortest period we may use the same criterion, however, it has no sense to set the averaging area to be smaller than the distance of two neighboring grid nodes. If we introduced so small area, we would lose some information along parts of the paths. We set the regularization parameter so that we obtain the smallest radius of the averaging area to be 2.5 km in the best resolved grid node since our grid points are in a distance of 5.0 km. For our shortest wave of period 0.25 s and approximate mean group velocity 2.3 km/s the resolution is 4.3 times the wavelength and worse. So we obtain relatively worse resolution for shorter waves than for the longer ones in comparison to the wavelength, but absolutely the resolution of the shortest waves is twice as good as the resolution of the longest ones.

Table 4.2 summarizes the number of paths (see also Fig. 4.6) initial and remaining travel time residuals and the resultant improvement and mean group velocities (see also Fig. 4.5). We see decreasing residual improvement toward longer periods. The reason is that while the initial residuals are comparable for all eight periods, due to the different regularization, which is larger for longer periods, the resulted smoother tomography maps for longer periods are able to explain smaller part of travel time residuals.

period (s)	0.25	0.50	0.75	1.00	1.25	1.50	1.75	2.00
number of paths	67	87	87	87	86	84	81	76
initial residual (s)	1.84	1.99	1.75	1.73	1.82	1.97	2.17	2.27
remaining residual (s)	0.48	0.61	0.63	0.79	0.99	1.23	1.48	1.80
improvement (%)	74	69	64	54	46	38	32	21
mean velocity (km/s)	2.301	2.295	2.339	2.442	2.482	2.578	2.615	2.534

Table 4.2: Number of used paths, initial and remaining residuals, improvement and mean velocities for eight selected periods.

As a result, we present 2-D Rayleigh wave group velocity perturbation distributions for eight periods in the Western Bohemia region in Fig. 4.7. Each map is related to the mean group velocity v_m for the given period (as in Table 4.2 and Fig. 4.5) and shows the perturbation of actual group velocities to this mean value in percent. The velocity perturbations given in Fig. 4.7 reach up to $\pm$ 25 % in some places in case of the shorter periods.

Our ray path coverage does not prefer any azimuth considerably and so the resolution of the data is isotropic. We use the size of the averaging area for each grid node in Fig. 4.7 to depict this resolution. We may imagine these values as radii of circles in km of the area where the distribution of velocities using the values along the ray paths is used to estimate the resultant velocity for each grid node. These values are depicted in Fig. 4.7 using contours delineating the regions with the same averaging area. As the averaging area is smaller, the resolution of the tomography is better.

For comparison with Fig. 4.7 showing the maps for different periods, we compile the results to show the distribution of local dispersion curves around the region. Fig. 4.8 presents dispersion curve plots inserted into the Cartesian coordinate map. Corresponding grid nodes are to be placed in the center of each square plot. Each of the curves is compiled using eight values of group velocity of Rayleigh waves for selected eight periods in the range from 0.25 to 2.0 s. The number in each plot gives the size of the averaging area in km for period 0.5 s. Bold gray line shows the clipped region of interest as in Figs. 4.4 and 4.7. Station and blast locations with annotations are shown.

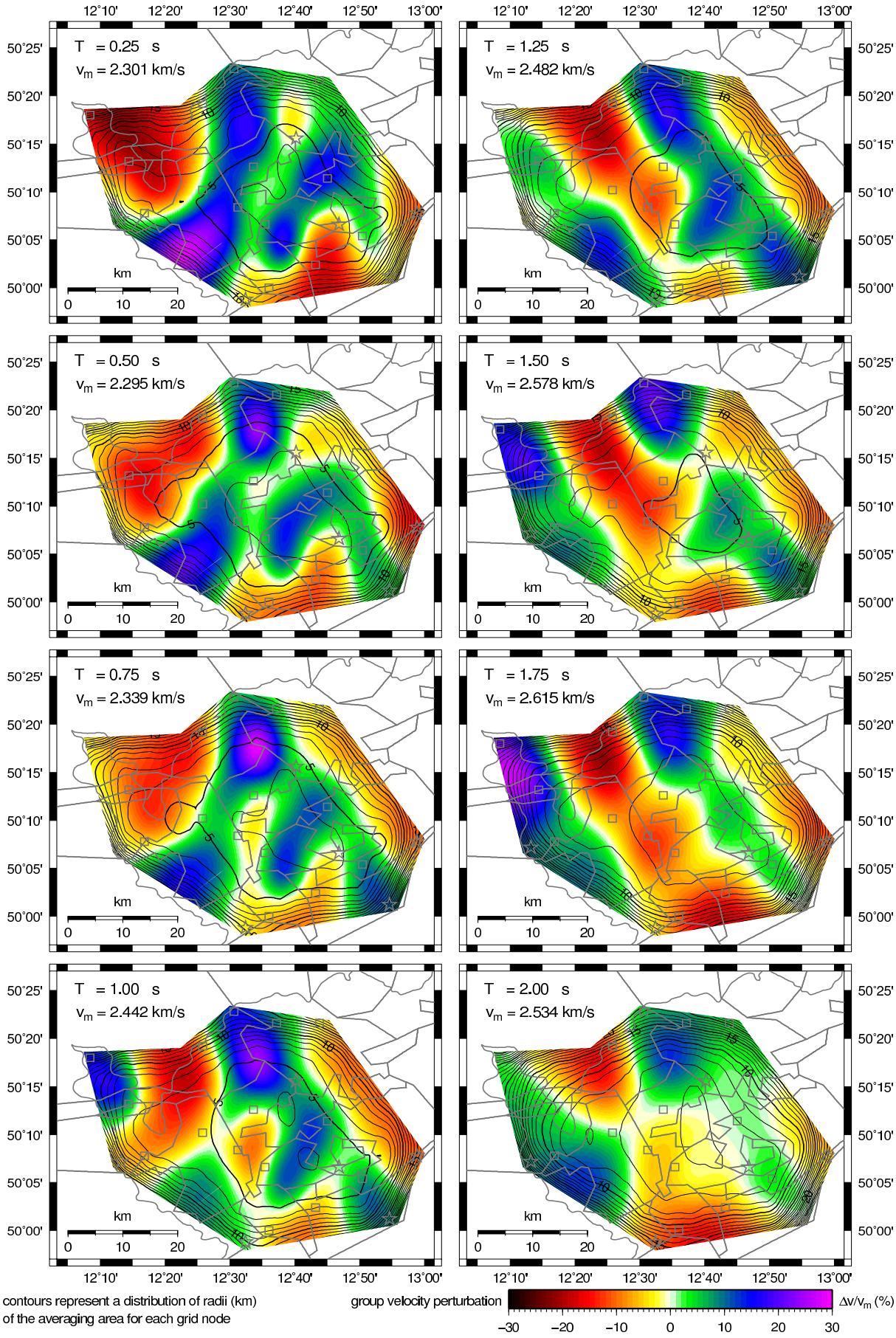


Figure 4.7: (*Fig. 5 in Kolínský and Brokešová, 2008*) 2-D Rayleigh wave group velocity tomography maps of the Western Bohemia region. Each of the eight panels corresponds to the value of period T of the presented group velocity distribution and to the mean velocity value v_m (see Fig. 4.5). The color scale represents a group velocity perturbation in percent with respect to this mean velocity. Isolines represent the distributions of radii of the averaging areas in km.

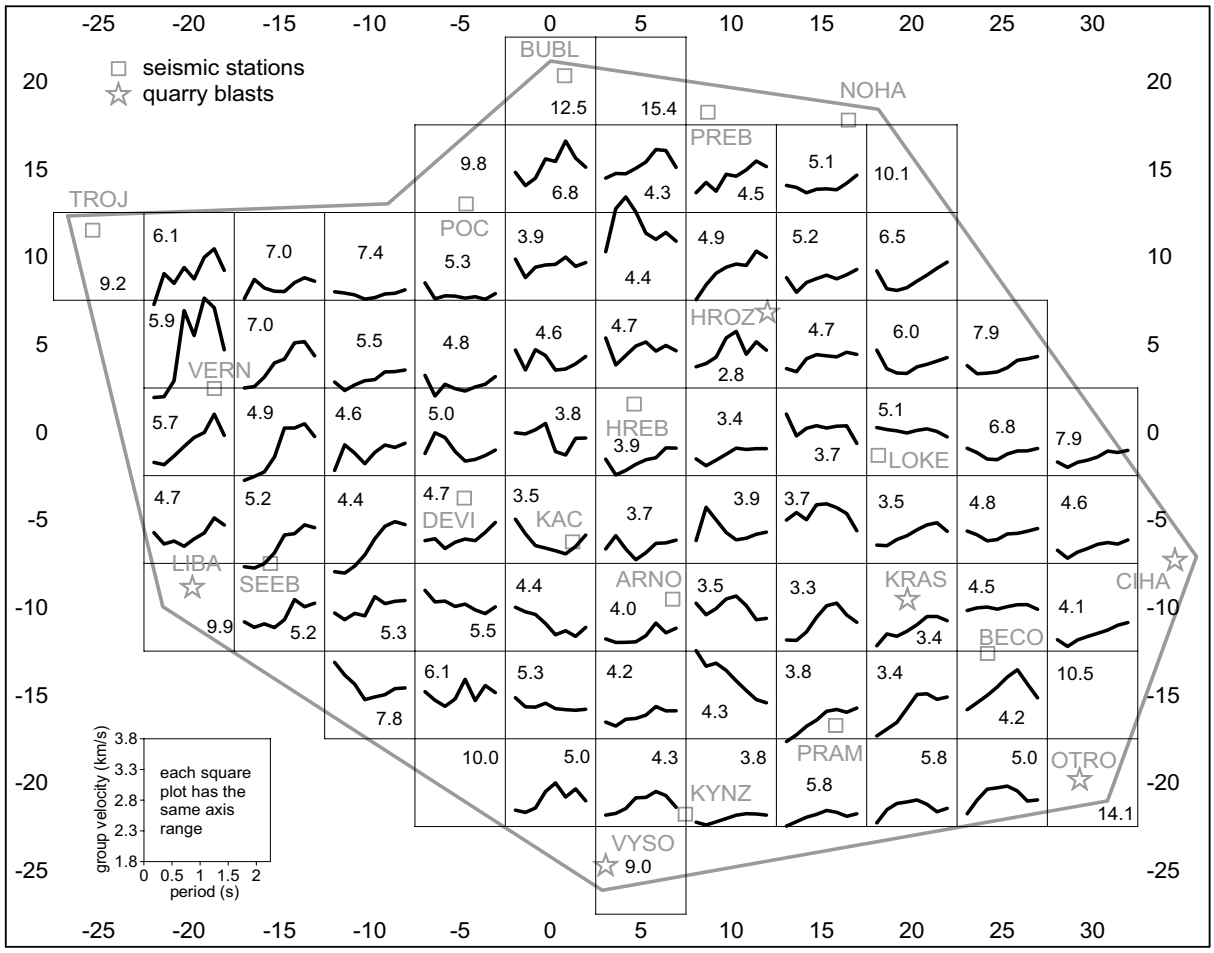


Figure 4.8: (*Fig. 6 in Kolínský and Brokešová, 2008*) Local dispersion curves corresponding to individual grid nodes (Fig. 4.4) presented in the Cartesian coordinate system. The nodes are to be imagined in the centre of each square plot. Each of the 79 plots has the same ranges of both axes. Studied area border is shown as well as the location of the stations (squares) and blasts (stars). The number in each plot gives the size of the averaging area in km for corresponding grid node and for period T = 0.5 s. Curves for nodes with averaging area size grater than 9.0 km are discarded.

4.2.7 Discussion and conclusion

We provide the Rayleigh wave tomography for a small region of tens of kilometers in size. It is unusual to deal with such a local problem and methodologically we may compare our results only with the works concerning larger regions. One of the parameters which help us to evaluate the results is the improvement between initial and remaining residuals. The work of Bourova et al. (2005) presents the improvement around 50 % in the Aegean Sea tomography. She uses only limited number of paths and the main criterion of her results is the smoothness of the resultant velocity distribution. The surface wave tomography of the Black Sea by Yanovskaya et al. (1998) reaches the improvement of even two thirds of the initial residual. Our results give improvement from 74 % in case of short periods down to 21 % in case of longer ones.

As we see the diversity of the dispersion curves in Fig. 4.5 we may assume a great heterogeneity of the studied region for the first glance, what was already shown in Kolínský and Brokešová (2007) for six of the paths. The group velocity ranges grow with the period as shown by arrows in Fig. 4.5 and so we may expect more pronounced 2-D velocity distribution for longer periods. The results would correspond to this assumption if we set the same regularization parameter for all eight periods, as we have tried during the tests. This approach gives the same averaging areas and hence the same resolution for all maps. In such a case the longer periods really do produce larger perturbations than the shorter ones. This is of course an approach which does not take into account the finite wavelength effect of different periods and hence a more limited resolution of longer periods.

We cannot make any conclusions whether the heterogeneity is higher near the surface or if it is more pronounced in the depth. The dispersion curve set in Fig. 4.5 imply for more pronounced heterogeneity

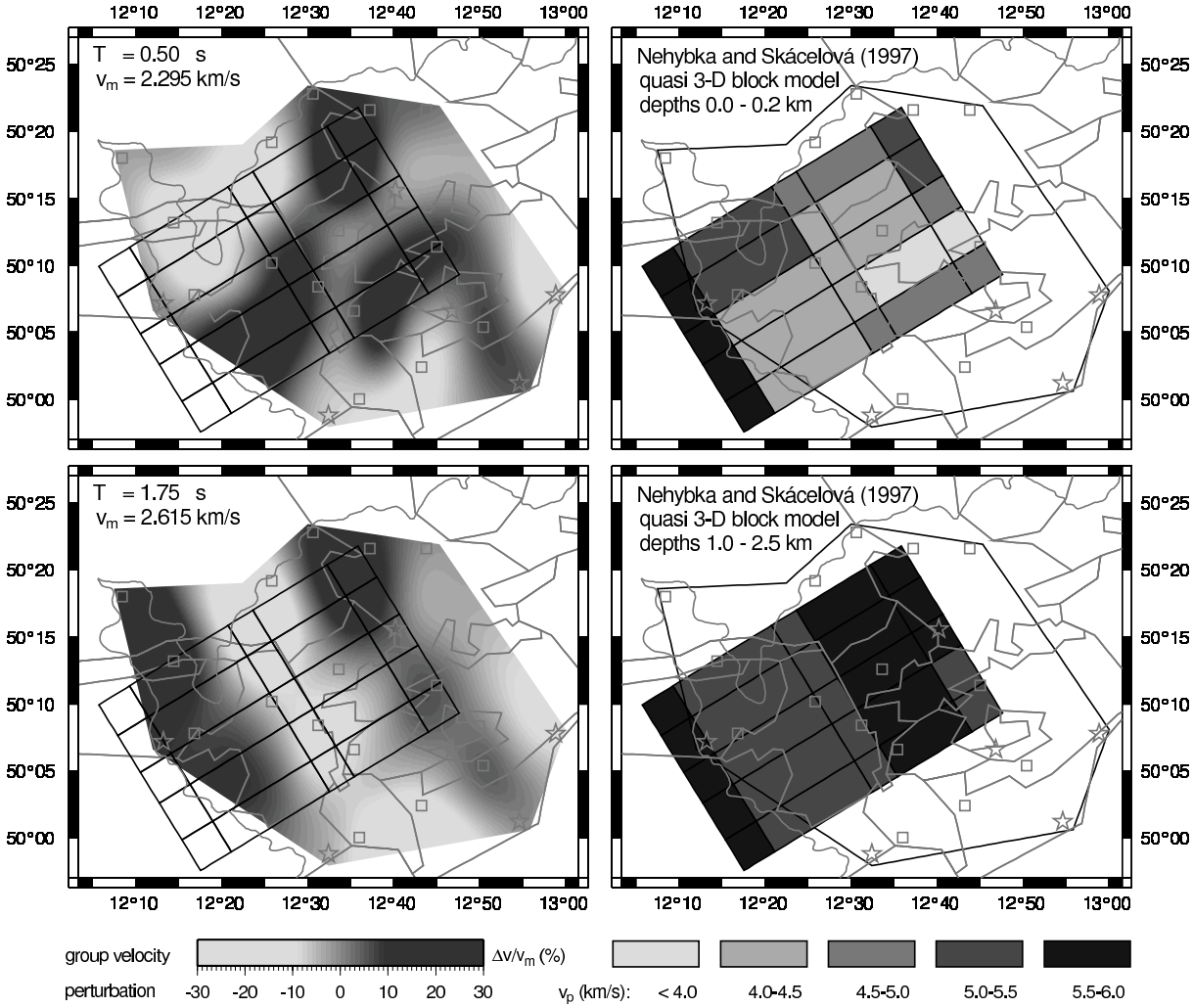


Figure 4.9: (*Fig. 7 in Kolínský and Brokešová, 2008*) Comparison of 2-D tomography maps for periods 0.5 and 1.75 s (the same as in Fig. 4.7) with the quasi 3-D block models of Nehybka and Skácelová (1997) for the depths of 0.0 – 0.2 km and 1.0 – 2.5 km respectively. Block edges are imagined in the left maps and tomography map borders in the right ones for better comparison.

in the depth but the limitation of our tomography gives us less smooth maps for shorter periods and thus higher heterogeneity for smaller depths. Generally, taking into consideration the whole Earth crust, the highest geological diversity is supposed to be at the surface. But our depth range is so limited that we may encounter higher velocity variations in the greater depths of our model in comparison with the surface covered by more uniform sediments and disintegrated metamorphosed rocks. So, as a conclusion, we have to state that less perturbed results for longer periods are given by limitations of the method and worse resolution ability of these wavelengths and that it does not necessarily mean that the surface structures are more heterogeneous than the deeper ones.

In all the map figures we depict a sketch of main geological features; they are described in the legend in Fig. 4.4. The most important features are two sedimentary basins, but our tomography does reveal only slight evidence of the smaller Sokolov basin (Fig. 4.4) as implies from lower velocity anomaly which is seen in the maps for periods of 0.25 to 1.0 s almost in the middle of the region of interest. Both basins are too shallow to be seen clearly even by the shortest periods and the Cheb basin (Fig. 4.4) produce even higher velocity anomaly for short periods. The basins are encircled by metamorphosed rocks and the velocity variations in them are rather random. The geological composition would probably not be the main phenomenon influencing the seismic velocities; the complicated fault system of the region and consequential surface wave multipathing and reflection may play a more important role in the scattered dispersion measurement.

The feature which we would like to emphasize is the direction of velocity anomalies. In case of shorter period maps (0.25 – 0.75 s) we see both high and low group velocity anomalies elongated in the southwest-northeast direction. On the other hand, in case of longer periods (1.25 – 2.0 s) we see a perpendicular direction – the anomalies are placed predominantly in the northwest-southeast direction. These are

two main directions of complicated fault system in the Western Bohemia region. Southwest-northeast direction belongs to the Eger rift fault system and the perpendicular northwest-southeast direction follows the Mariánské Lázně fault. In the WB region, both fault systems meet each other.

We compare our velocity distribution with the results of Nehybka and Skácelová (1997). Their work is one of the few studies which deal with comparable depths and comparable geographical area, however, with body waves only. They used several 2-D refraction profiles to construct quasi 3-D block model of 125 blocks (5x5x5) of constant velocity. Their model covers only limited part the region of our interest and it reaches from surface to the depth of 4.5 km. Nehybka and Skácelová (1997) present only P wave velocity and we choose two layers from their results. Murphy and Shah (1988) give the relation

$$T = \frac{2.3H}{\bar{\beta}}, \tag{4.2}$$

where T is the period of the group velocity in seconds, H is the depth to the significant discontinuity in kilometers, and $\bar{\beta}$ is the average shear wave velocity above this discontinuity in km/s. Since the shear wave velocities of the uppermost hundreds of meters in the WB region have the average value around 2.3 km/s (it is given by the limit of the group velocity for the shortest periods), a simple relation between the period of the wave and the depth of penetration is used: the period of the wave in seconds corresponds approximately to the depth in kilometers. We used this approach to compare our group velocity maps with the v_p distribution with depth. The 0.25 s group velocity tomography map is compared with 25-block map for the depth range 0.0 – 0.2 km of the model of Nehybka and Skácelová (1997) and our 1.75 s group velocity map is compared with their block velocity distribution in depths 1.0 – 2.5 km, see Fig. 4.9.

On the left panels of Fig. 4.9 we present the same group velocity perturbation maps as in colored Fig. 4.7. We sketch the block edges in our map for better comparison. On the right panels we show the results of Nehybka and Skácelová (1997) with the border of our tomography maps added. Nehybka and Skácelová (1997) set their block edges in the direction of predominant faults of the WB region. Even we are conscious of the comparison limitations of distributions of v_p and group velocity, we can make some qualitative conclusions. Both compared pairs show the same general directions of velocity anomalies. The 0.5 s and 0.0 – 0.2 km models show anomalies elongated in the southwest-northeast direction. Anomalies in both models tent to be more north-south directed than it is delineated by block edges. Low velocity anomaly in the center of our map is located more to the east than it is shown in the model of Nehybka and Skácelová. Similarly, the 1.75 s and 1.0 – 2.5 km models present anomalies in the predominant northwest-southeast direction. In this case they are elongated exactly along the block edges of v_p model. There are two low and two high velocity anomalies in the model of Nehybka and Skácelová and we have also found two pairs of anomalies in the same configuration. And again, our anomalies are shifted to the northeast in comparison with the v_p anomalies. The range of v_p in the 0.0 – 0.2 km model is from 4.0 to 6.0 km/s, what presents distribution with perturbations 5.0 km/s ± 20 %. Our models concern group velocities, which are sensitive more to the shear wave velocities, but the range of perturbation is in similar order of ± 25 %, as clearly seen in colored Fig. 4.7. The 1.0 – 2.5 km model show smaller amount of perturbation of v_p from 5.0 to 6.0 km/s and our 1.75 s model is also smoother – the main anomalies in the center of the image range in order ± 15 %. As we have already stated, this smoothness does not have necessarily structural consequences – it is influenced predominantly by worse resolution of the methods in greater depths. We may conclude that the main features and general properties of both models are the same. The direction of fault system is clearly visible in both studies and the correlation with geological composition is not found in either of them.

The high heterogeneity of the WB region may imply for more complicated surface wave propagation paths then assumed in our ray tomography. Anisotropy plays an important role as well but for its determination Love wave tomography would be needed. A surface topography of the region has an ability to influence the scattering of the dispersion measurement.

Better insight of the region's diversity may be seen in Fig. 4.8. If we look at the western part of our area of interest, around the node <–15,0>, we see dispersion curves with steep slope and wide range of velocities. As we go to the east, the slope of the curves becomes smaller. In the middle of the studied area around the node <+5,–5> there is almost no dispersion pronounced in the given period range. The same feature can be seen also in the northwest part around the node <–10,+5>. In the area of <+15,–5> the dispersion curves show even slower velocities for longer periods as well as it result in the southeastern and northern parts. Some of the dispersion curves around the border of our area are a bit scattered. Since the averaging areas are larger and hence the resolution is worse near the edges of the map, the information contained in these dispersion curves is less credible. Curves for nodes with averaging area size grater than 9.0 km are discarded.

These changes in dispersion curve slopes provide us with information about the vertical heterogeneity of different parts of the WB region. Detailed inversion of each of the local dispersion for S-wave velocity distribution with depth is needed in future studies.

4.2.8 Acknowledgements

This research was supported by grants No. A300460602 and No. A300460705 of the Grant Agency of the Academy of Sciences of the Czech Republic, by grant No. 205/06/1780 of the Czech Science Foundation and by Institute research plans No. A VOZ30460519 and No. MSM0021620860. We are grateful to prof. Tatiana B. Yanovskaya for providing her programs for surface wave tomography and for useful advice how to use them. Two of the figures are illustrated using Generic Mapping Tools by Wessel and Smith (1998).

4.2.9 References

Beránek, B., Mayerová, M., Zounková, M., Guterch, A., Materzok, R. and Pajchel, J., 1973: Results of deep seismic sounding along international profile VII in Czechoslovakia and Poland, *Stud. Geophys. Geod.*, 17, 205–217.

Bourova, E., Kassaras, I., Pedersen, H. A., Yanovskaya, T., Hatzfeld, D. and Kiratzi, A., 2005: Constraints on absolute S velocities beneath the Aegean Sea from surface wave analysis, *Geophys. J. Int.*, 160, 1006–1019.

Brož, M., 2000: Detection of the origin time and seismic ground motion of quarry blasts, *Acta Montana*, 16 (118), 17–24.

Cara, M., 1973: Filtering of dispersed wavetrains, *Geophys. J. R. Astr. Soc.*, 33, 65–80.

Ditmar, P. G. and Yanovskaya, T. B., 1987: An extension of the Backus-Gilbert technique for estimating lateral variations of surface wave velocities, *Izvestia AN SSSR, Fizika Zemli*, 6, 30–40 (in Russian).

Dziewonski, A., Bloch, S. and Landisman, M., 1969: A technique for the analysis of transient seismic signals. *Bull. Seism. Soc. Am.*, 59, 427–444.

Fischer, T. and Horálek, J., 2003: Space-time distribution of earthquake swarms in the principal focal zone of the NW Bohemia/Vogtland seismoactive region: period 1985 – 2001, *J. Geodyn.*, 32 (1–2), 125–144.

Geissler, W. H., 2005: Seismic and petrological investigations of the lithosphere in the swarm-earthquake and CO_2 degassing region Vogtland/NW-Bohemia, *PhD thesis, scientific technical report STR05/06*, GeoForschungsZentrum Potsdam, Potsdam, 150 pp.

Grad, M., Špičák, A., Keller, G. R., Guterch, A., Brož, M., Hegedüs, E. and Working Group, 2003: SUDETES 2003 seismic experiment, *Stud. Geophys. Geod.*, 47, 681–689.

Guterch, A., Grad, M., Keller, G. R., Posgay, K., Vozár, J., Špičák, A., Brückl, E., Hajnal, Z., Thybo, H., Selvi, O. and CELEBRATION 2000 experiment team, 2003: CELEBRATION 2000 seismic experiment, *Stud. Geophys. Geod.*, 47, 659–669.

Heuer, B., Kämpf, H., Kind, R. and Geissler, W. H., 2007: Seismic evidence for whole lithosphere separation between Saxothuringian and Moldanubian tectonic units in central Europe, *Geophys. Res. Lett.*, 34, L09304, doi: 10.1029/2006GL029188.

Hrubcová P., Środa P., Špičák A., Guterch A., Grad M., Keller G. R., Brueckl E., and Thybo H., 2005: Crustal and uppermost mantle structure of the Bohemian Massif based on CELEBRATION 2000 data, *J. Geophys. Res.*, 110, B11305.

Janský, J. and Novotný, O., 1997: Reinterpretation of the travel times of P waves generated by quarry blasts in Western Bohemia, *Acta Montana*, 11 (104), 35–48.

Janský, J., Horálek, J., Málek, J. and Boušková, A., 2000: Homogeneous velocity models of the West Bohemian swarm region obtained by grid search, *Stud. Geophys. Geod.*, 44, 158–174.

Kolínský, P., 2004: Surface wave dispersion curves of Eurasian earthquakes: the SVAL program, *Acta Geodyn. Geomater.*, 1 (134), 165–185.

Kolínský, P. and Brokešová, J., 2007: The Western Bohemia Uppermost Crust Shear Wave Velocities from Love Wave Dispersion, *Journal of Seismology*, 11, 101–120.

Kolínský, P., Málek, J. and Brokešová, J., 2010: Shear wave crustal velocity model of the western Bohemian Massif from Love wave phase velocity dispersion, *Journal of Seismology*, in press.

Levshin, A. L., Pisarenko, V.F. and Pogrebinsky, G.A., 1972: On a frequency-time analysis of oscillations, *Ann. Geophys.*, 28, 211–218.

Levshin, A. L., Yanovskaya, T. B., Lander, A. V., Bukchin, B. G., Barmin, M. P., Ratnikova, L. I. and Its, E. N., 1989: Interpretation of Surface Wave Observations – Frequency-time Analysis, in: Keilis-Borok, V. I. (ed.): *Seismic Surface Waves in a Laterally Inhomogeneous Earth*, Kluwer Academic Publishers, Dordrecht/Boston/London, 153–163.

Málek, J., Janský, J. and Horálek, J., 2000: Layered Velocity Models of the Western Bohemia Region, *Stud. Geophys. Geod.*, 44, 475–490.

Málek, J., Janský, J., Novotný, O. and Rössler, D., 2004: Vertically inhomogeneous models of the upper crustal structure in the West-Bohemian seismoactive region inferred from the CELEBRATION 2000 refraction data, *Stud. Geophys. Geod.*, 48, 709–730.

Málek, J. and Žanda, L., 2004: Seismic effects of the quarry blasts on the territory of Bohemia, *Acta Geodyn. Geomater.*, 1 (134), 291–302.

Málek, J., Horálek, J. and Janský, J., 2005: One-dimensional qP-wave velocity model of the upper crust for the West Bohemia/Vogtland earthquake swarm region, *Stud. Geophys. Geod.*, 49, 501–524.

Malinowski, M., 2005: Analysis of short-period Rayleigh waves recorded in the Bohemian Massif area during CELEBRATION 2000 experiment, *Stud. Geophys. Geod.*, 49, 485–500.

Mlčoch, B., Schulmann, K., Šrámek, J., Manová, M., Pokorný, L., Fiala, J. and Vejnar, Z., 1997: Geological interpretation of major regional units – the Saxothuringian zone, in: Vrána, S. and Štědrá, V. (eds): *Geological model of Western Bohemia related to the KTB borehole in Germany*, Czech Geological Survey, Prague, 51–61.

Murphy, J. R. and Shan, H. K., 1988: An analysis of the effects of site geology on the characteristics of near-field Rayleigh waves, *Bull. Seism. Soc. Am*, 78, 64–82.

Nehybka, V. and Skácelová, Z., 1997: Seismological study of the Kraslice/Vogtland-Oberpfalz region, in: Vrána, S. and Štědrá, V. (eds.): *Geological model of Western Bohemia related to the KTB borehole in Germany*, Czech Geological Survey, Prague, 186–190.

Novotný, M., 1997: The ray interpretation of DSS data from the VI/70 seismic transect across the Bohemian Massif, in: Vrána, S. and Štědrá, V. (eds): *Geological model of Western Bohemia related to the KTB borehole in Germany*, Czech Geological Survey, Prague, 131–139.

Novotný, O., Proskuryakova, T. A., Shilov, A. V., 1995: Dispersion of Rayleigh waves along the Prague-Warsaw profile, *Stud. Geophys. Geod.*, 39, 138–147.

Novotný, O., 1996: A preliminary seismic model for the region of the West-Bohemian earthquake swarms, *Stud. Geophys. Geod.*, 40, 353–366.

Novotný, O., Grad, M., Lund, C. E. and Urban, L., 1997: Verification of the lithospheric structure along profile Uppsala-Prague using surface wave disperison, *Stud. Geophys. Geod.*, 41, 15–28.

Novotný, O., Janský, J. and Málek, J., 2004: Some aspects of the application of the Wiechert-Herglotz method to refraction data from Western Bohemia, *Acta Geodyn. Geomater.*, 1 (134), 157–164.

Plešinger, A., Neunhöfer, H. and Wielandt, E., 1991: Crust and upper mantle structure of the Bohemian Massif from the dispersion of seismic surface waves, *Stud. Geophys. Geod.*, 35, 184–195.

Plomerová, J., Babuška, V., Janatková, Z. and Lokajíček, T., 1987: Directional dependence of seismic waves propagation of the 1985-86 earthquake swarm in Western Bohemia, in: Procházková, D. (ed.): *Earthquake swarm 1985/86 in Western Bohemia – proceedings of workshop in Mariánské Lázně*, Czechoslovak Academy of Sciences, Geophysical Institute, Prague, 197–204.

Raykova, R. and Nikolova, S., 2007: Tomography and velocity structure of the crust and uppermost mantle in Southeastern Europe obtained from surface wave analysis, *Stud. Geophys. Geod.*, 51, 165–184.

Růžek B., Hrubcová P., Novotný M., Špičák A., Karousová O., 2007: Inversion of travel times obtained during active seismic refraction experiments CELEBRATION 2000, ALP 2002 AND SUDETES 2003, *Stud. Geophys. Geod.*, 51, 141–164.

Špičák, A., Horálek, J., Boušková, A., Tomek, Č. and Vaněk, J., 1999: Magma intrusions and earthquake swarm occurrence in the western part of the Bohemian Massif, *Stud. Geophys. Geod.*, 43, 87–106.

Wessel, P., and Smith, W. H. F., 1998: New, improved version of generic mapping tools released, *Eos Trans. AGU*, 79 (47), 579.

Wielandt, E., Sigg, A., Plešinger, A. and Horálek, J., 1987: Deep structure of the Bohemian Massif from phase velocities of Rayleigh and Love waves, *Stud. Geophys. Geod.*, 31, 1–7.

Wilde-Piórko, M., Saul, J. and Grad, M., 2005: Differences in the crustal and uppermost mantle structure of the Bohemian Massif from teleseismic receiver functions, *Stud. Geophys. Geod.*, 49, 85–107.

Yanovskaya, T. B. and Ditmar, P. G., 1990: Smoothness criteria in surface wave tomography, *Geophys. J. Int.*, 102, 63–72.

Yanovskaya, T. B., Kizima, E. S. and Antonova, L. M., 1998: Structure of the Black Sea and adjoining regions from surface wave data, *Journal of Seismology*, 2, 303–316.

Yanovskaya, T. B., Antonova, L. M. and Kozhevnikov, V. M., 2000: Lateral variations of the upper mantle structure in Eurasia from group velocities of surface waves, *Phys. Earth Planet. Inter.*, 122, 19–32.

Yanovskaya, T. B. and Kozhevnikov, V. M., 2003: 3D S-wave velocity pattern in the upper mantle beneath the continent of Asia from Rayleigh wave data, *Phys. Earth Planet. Inter.*, 138, 263–278.

here the original text of the paper ends

4.3 Smoothing and resolution of the tomography

In paragraph 4.2.6 Tomographic images we explained how we set the regularization parameter. We used different parameters for eight different periods. The criterion was developed so that we would get reasonable resolution of the resultant tomographic map for each period corresponding to its wavelength. Before we concluded to use the regularization parameters in such a way, we had tested many possibilities. We started with computing the tomographic maps with constant parameters for all eight plots. To show the changes in the maps and the unreasonable resolution and perturbation of the results, we add two Figures – 4.10 and 4.11.

Fig. 4.10 shows the eight group velocity tomographic images for the same periods of Rayleigh waves as are presented in Fig. 4.7. For all eight plots, the same regularization parameter is used. Its value is the same as it was used for the plot of 2.0 s period map in Fig. 4.7. Hence, the right bottom plots in Figs. 4.7 and 4.10 are exactly the same. We see that the map for the period of 2.0 s in Fig. 4.10 has reasonable

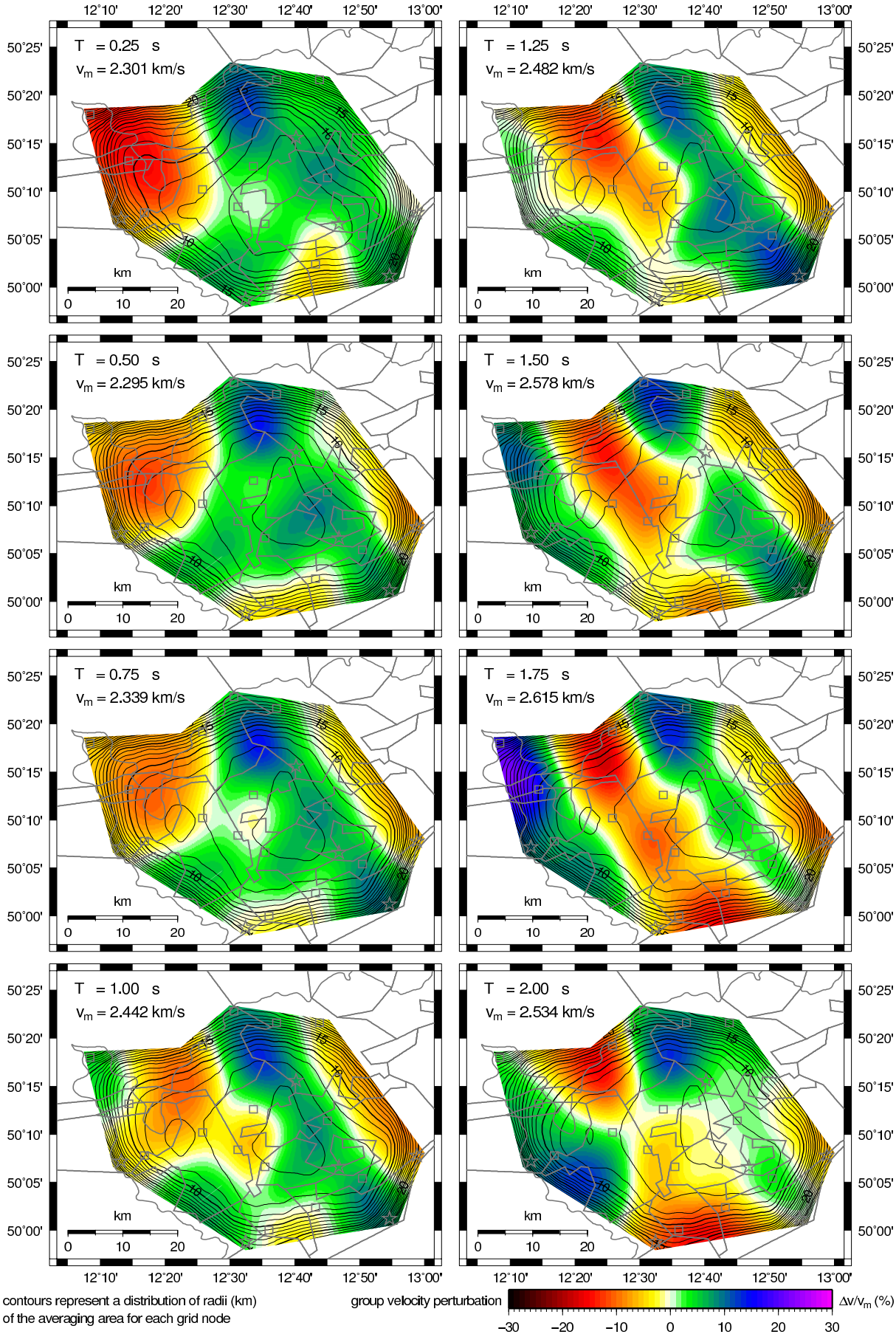


Figure 4.10: Group velocity maps for the same eight periods as in Fig. 4.7. Here the same smoothing parameter (better smoothing) was used for all eight plots. The value of the parameters is equal to the one used for 2.00 s plot in Fig. 4.7. Hence the right bottom plots in Figs. 4.7 and here are exactly the same.

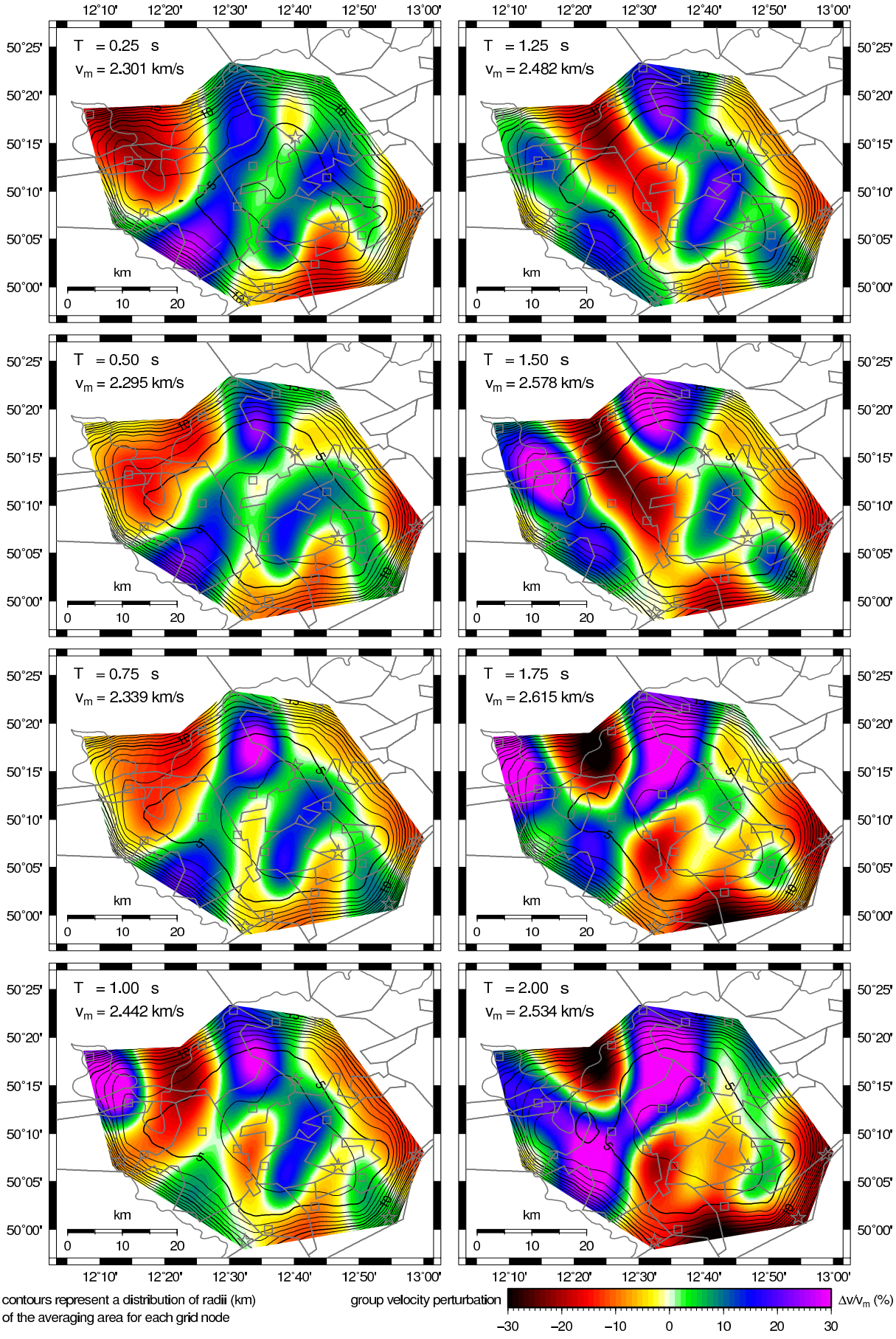


Figure 4.11: Group velocity maps for the same eight periods as in Fig. 4.7. Here the same smoothing parameter (worse smoothing) was used for all eight plots. The value of the parameters is equal to the one used for 0.25 s plot in Fig. 4.7. Hence the left top plots in Figs. 4.7 and here are exactly the same.

resolution as described in paragraph 4.2.7. But when we look at the plots of shorter wavelengths, we see the maps to be more and more blurred. We have to not only take into account that the maps are blurred "absolutely" comparing one to another, but it is much more important to see that even if they were blurred all in the same way, the shorter periods and hence shorter wavelengths would have "relatively" worse resolution, which is neither reliable nor expectable. We have shown in paragraph 4.2.6 that even if we used different regularization parameters for each wavelength, we would get relatively worse resolution for the shorter wavelength because we would be limited by the distance of grid nodes. It has no sense to shrink the averaging areas to be smaller than is the distance of grid nodes, because we would loose the information of the travel times in between the nodes, as the rays would cross the areas outside of any averaging areas of neighboring nodes.

In the paper, we used the regularization parameter to get the best resolution of the longest wave to be twice larger ($\approx 10\,km$) than their wavelength ($\approx 5\,km$). Limited by the distance of grid nodes, we got the resolution of the shortest waves to be four times larger ($\approx 2.5\,km$), than their wavelength ($\approx 0.6\,km$). If we forced the method to smooth the shorter wave maps in the same way as the longer waves, as it is shown in Fig. 4.10, it would make this relatively worse resolution of the shorter waves even lower.

Fig. 4.11 shows again eight maps for the same eight periods as the two previous figures. Here, the regularization parameter is used also constant for all eight plots, as it is used in Fig. 4.10, but its value is now equal to the value used for the shortest period of 0.25 s in Fig. 4.7. So, the left top plots in Figs. 4.7 and 4.11 are the same. We see that in case of using less smoothing parameter, we get unreasonable "good" resolution ($\approx 5\,km$) for the longer wavelengths. In the same time, we obtain unreasonable high perturbations of the group velocities for these waves. As the true resolution of the longer waves is lower, the method gives unrealistic perturbation when we allow it to produce worse smoothing.

These examples are shown to explain in detail how we set the regularization parameters in the paper to obtain realistic perturbations and reliable resolution of the Rayleigh wave group velocity tomographic maps. Fig. 4.10 represents smoothing suitable only for the largest period and as opposed to that, Fig. 4.11 represents smoothing suitable for the shortest periods of surface waves. The smoothing used to present the final result in Fig. 4.7 was set to vary between these two extrema to provide proper resolution for all used wavelengths.

Chapter 5

Application C: Phase velocity and crustal structure

5.1 Dealing with the topic

This chapter is based on the paper by Kolínský et al. (2010). The idea of the phase velocity measurement in the Bohemian Massif emerged in 2005. We started with four stations TBR (Tábor), HAJ (Háje), NEC (Nečtiny) and KHU (Komorní Hůrka). These stations were operated by the Institute of Rock Structure and Mechanics, Academy of Sciences of the Czech Republic. All these stations were equipped with 30 s Guralp CMG-40T sensors. We selected several earthquakes from Greece since their backazimuth coincides with the profile delineated by our stations. We tested several methods of phase velocity measurement and we add the stations NKC (Nový Kostel) instead of KHU because its location was more convenient to our purposes. NKC station is equipped with 120 s STS2 instrument and hence we have to deal with instrument transfer function to measure phase velocities between different types of sensors. The profile KHC (Kašperské hory) – NKC was used as a reference model for our measurement and finally we add also the German station MOX (Moxa).

The primary goal of the paper was to find out the differences between the short profiles and to compare the crust structure between the eastern and western part of the profile TBR-NKC. Then we concern ourselves not only to the structure estimation, but mainly to the surface wave propagation paths and true backazimuth correction.

As it is shown at the end of this chapter, we applied several methods of phase velocity measurements and we selected the time shift measurement as the most suitable one. We do not argue that there are not new methods of phase velocity measurement, however, the goal of this project was not to develop or test new methods, our aim was to contribute to the crust structure estimation efforts of the Bohemian Massif. The other goal was to develop a unique technique to estimate the true backazimuths of propagation of surface wave of different wavelengths.

The paper has been accepted for publication in the Journal of Seismology. Now the paper is in press and we present here the original text of the latest paper version which will be published soon.

---

here the original text of the paper starts

5.2 Shear wave crustal velocity model of the Western Bohemian Massif from Love wave phase velocity dispersion

Petr Kolínský, Johana Brokešová and Jiří Málek, 2010, Journal of Seismology, in press

5.2.1 Abstract

We propose a new quantitative determination of shear wave velocities for distinct geological units in the Bohemian Massif, Czech Republic (Central Europe). The phase velocities of fundamental Love wave modes are measured along two long profiles (≈ 200 km)) crossing three major geological units and one rift-like structure of the studied region. We have developed a modified version of the classical

multiple filtering technique for the frequency-time analysis and we apply it to two-station phase velocity estimation. Tests of both the analysis and inversion are provided. Seismograms of three Aegean Sea earthquakes are analyzed. One of the two profiles is further divided into four shorter sub-profiles. The long profiles yield smooth dispersion curves; while the curves of the sub-profiles have complicated shapes. Dispersion curve undulations are interpreted as period-dependent apparent velocity anomalies caused both by different backazimuths of surface wave propagation and by surface wave mode coupling. An appropriate backazimuth of propagation is found for each period, and the dispersion curves are corrected for this true propagation direction. Both the curves for the long and short profiles are inverted for a 1D shear wave velocity model of the crust. Subsurface shear wave velocities are found to be around 2.9 km/s for all four studied sub-profiles. Two of the profiles crossing the older Moldanubian and Teplá-Barrandian units are characterized by higher velocities of 3.8 km/s in the upper crust while for the Saxothuringian unit we find the velocity slightly lower, around 3.6 km/s at the same depths. We obtain an indication of a shear wave low velocity zone above Moho in the Moldanubian and Teplá-Barrandian units. The area of the Eger Rift (Teplá-Barrandian – Saxothuringian unit contact) is significantly different from all other three units. Low upper crust velocities suggest sedimentary and volcanic filling of the rift as well as fluid activity causing the earthquake swarms. Higher velocities in the lower crust together with weak or even missing Moho implies the upper mantle updoming.

key words Love waves, phase velocity dispersion, frequency-time analysis, structure inversion, Bohemian Massif

5.2.2 Introduction

Our present study is a new contribution to the effort of determining the shear wave model of the crust in the Western Bohemian Massif. This region is characterized by three major geological units. Details concerning geophysical surveys and geological settings of these units can be found in Vrána et al. (1997) for the Moldanubian unit, in Cháb et al. (1997) for the Teplá-Barrandian unit and in Mlčoch et al. (1997) for the Saxothuringian unit.

The Moldanubian unit is the oldest of the units consolidated during the Proterozoic to Paleozoic age. Its crystalline composition experienced high-pressure and high-temperature metamorphosis. Lithological composition proves crust-mantle interaction. Smaller bodies intruded the unit during the Variscan orogeny. The Teplá-Barrandian unit is slightly younger. Its Neoproterozoic parts are slightly metamorphosed while its older Paleozoic parts are not metamorphosed at all. It has a more heterogeneous density than the Moldanubian unit and displays a positive gravimetric anomaly. The boundary between the Teplá-Barrandian and Moldanubian units is of tectonic origin. The Saxothuringian unit is again formed by Proterozoic and Cambrian metamorphosed rocks with Variscan intrusions. It is characterized by a negative gravimetric anomaly. The boundary between the Saxothuringian and Teplá-Barrandian units is formed by the Eger rift, which is a linear tectonic structure filled with Tertiary sediments complemented by Neogenic volcanism.

The history of seismic survey of the Earth crust and uppermost mantle of the Bohemian Massif covers more than forty years. Refraction and reflection experiments as well as surface wave studies along several profiles crossing the Bohemian Massif have been performed.

In the 1960s, an international deep seismic sounding profile was shot across the southwestern Bohemian Massif. Data were interpreted by Beránek (1971) and Beránek et al. (1973). Beránek (1971) gave an indication of lower velocities in the upper and middle crust for the Teplá-Barrandian and Moldanubian units – he interpreted it as evidence of their sedimentary composition and pointed out the fact that we can find low velocities down to the depths of 20 km although these units are so old.

Beránek and Zounková (1977) complemented the results from the deep seismic sounding profile by measurements of P-wave velocities from quarry blasts round the whole Czech Republic. They constructed a map of the Moho discontinuity, which was the deepest beneath the Moldanubian unit – 39 km. The Moho then rises in all directions towards the edges of the Bohemian Massif.

In the 1990s, reflection profile 9HR was shot in the southwestern part of the Bohemian Massif. Tomek et al. (1997) presented the interpretation of many reflections along the 9HR profile and discussed their possible origin. Positions of seismic interfaces were estimated, however, no information about seismic velocities was provided. The conclusion was that the Moldanubian unit yielded significantly different patterns from both the Teplá-Barrandian and Saxothuringian units. A detailed review of older deep seismic sounding experiments in the Bohemian Massif was given by Málek et al. (2001).

In 2000, the CELEBRATION (Central European Lithospheric Experiment Based on Refraction) took place (Guterch et al., 2003). The profile C09 was nearly parallel to the deep seismic sounding profile and to our TBR-MOX profile. Data from C09 were processed by several methods and the results in the form of 1-D or 2-D models can be found in Hrubcová et al. (2005) and Růžek et al. (2007). Hrubcová et al.

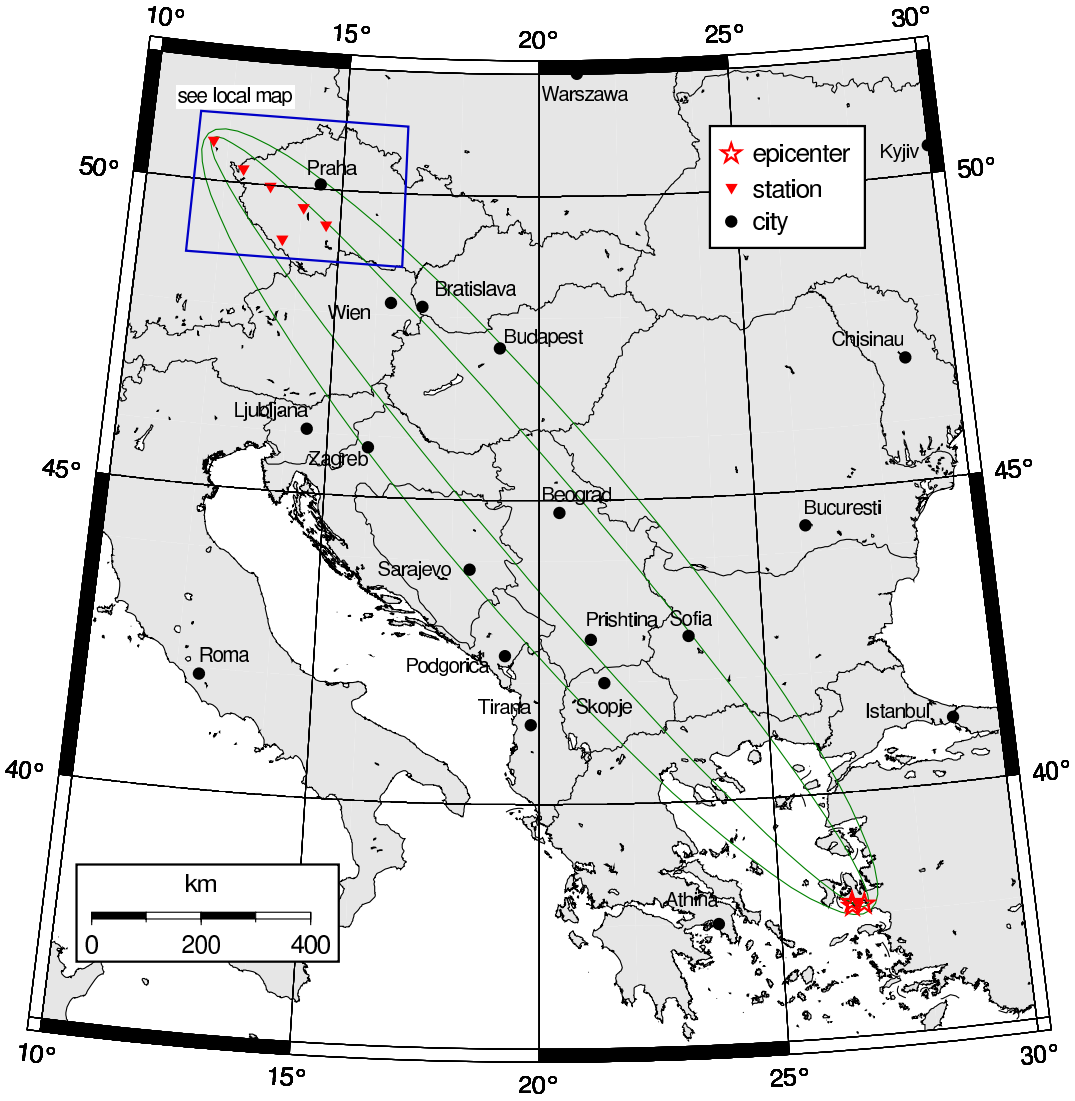


Figure 5.1: (*Fig. 1 in Kolínský et al., 2010*) Surface wave paths across Europe shown in terms of influence zones for 12 and 40 s period surface waves. The epicenters of three Aegean Sea earthquakes are situated close to one another.

(2005) suggested a clear Moho discontinuity for the Teplá-Barrandian and Moldanubian units, but they proposed a laminated lower crust structure for the Saxothuringian unit. Růžek et al. (2007) suggested a 2D v_p model for the whole C09 profile and as the most interesting feature they highlighted a very low-velocity anomaly reaching through the whole crust down to a depth of just a few kilometers above the Moho beneath the Moldanubian unit.

All these studies concerned only P-wave velocity distributions. There is a relative lack of information about S-wave velocities in the region of our interest. Only a few studies concerning S-waves have been performed. Malinowski (2005) used the CELEBRATION data for the analysis of short-period Rayleigh waves; he studied S-wave velocities, however, he estimated the crustal structure for only the upper 2 km along the C09 profile. Plešinger et al. (1991) gave the crustal shear wave velocity estimation from surface waves for the KHC-MOX profile (also used in our study, see below). In recent years, the receiver function method has also been used to study the Bohemian Massif. Wilde-Piórko et al. (2005) published detailed v_s models under several stations in the Bohemian Massif obtained by the receiver function technique. For the Saxothuringian unit, the depth of the Moho was estimated to be 28 – 31 km. In the Moldanubian unit, the Moho was estimated to be at a depth of 33 – 34 km. In the paper by Heuer et al. (2006) the depth of the Moho was again estimated to be deeper beneath the Moldanubian unit (35 – 40 km), shallower beneath the Teplá-Barrandian unit (30 – 33 km) and closest to the surface beneath the Saxothuringian unit (27 – 31 km). Another study dealing with receiver functions by Heuer et al. (2007) revealed a whole lithosphere separation between the Moldanubian unit on the one hand, and the Teplá-Barrandian and Saxothuringian units on the other. The thickness of the lithosphere of the Moldanubian unit was estimated as 130 km while the lithosphere of the other two units was found to be only 80 – 90 km thick.

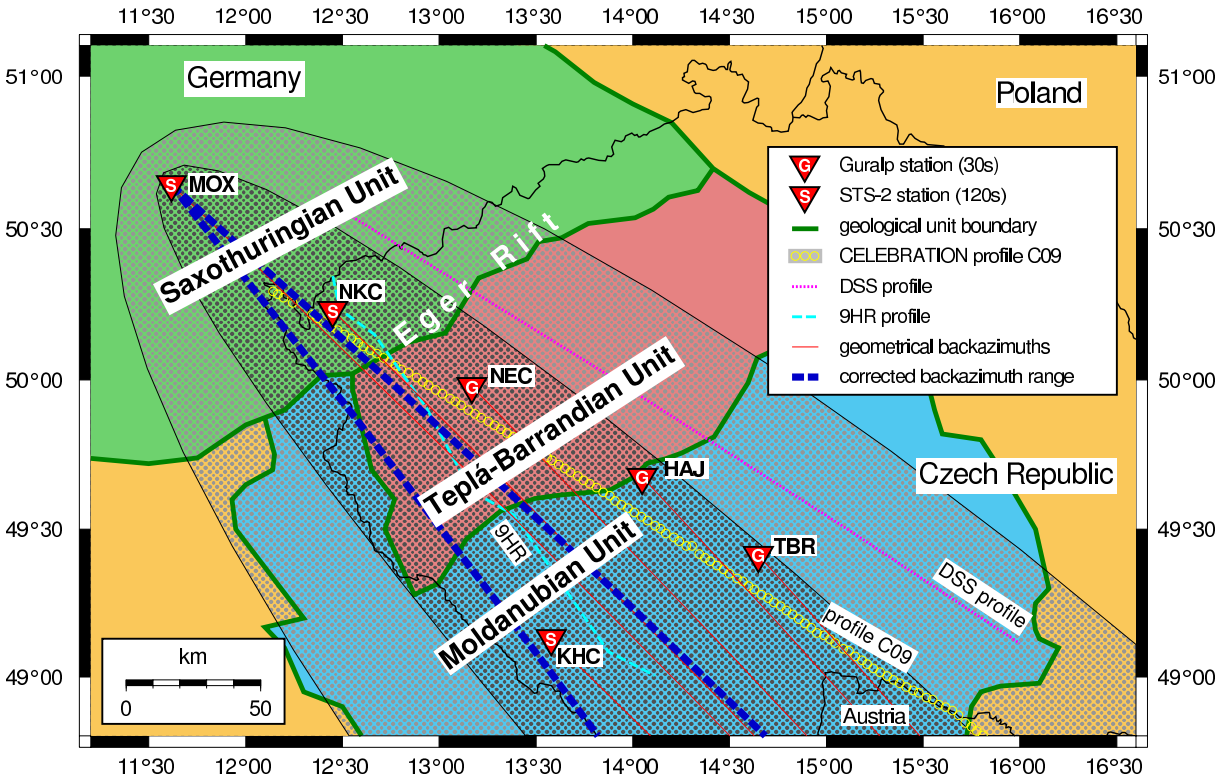


Figure 5.2: (*Fig. 2 in Kolínský et al., 2010*) Five stations TBR, HAJ, NEC, NKC and MOX forming the 260 km long profile and two stations KHC and MOX forming the 220 km long profile are shown in the context of the main geological units (Saxothuringian unit by green, Teplá-Barrandian unit by red and Moldanubian unit by blue, other units not used in this study are yellow) and former refraction and deep seismic sounding experiments. The influence zones for the most distant station MOX for 12 and 40 s period surface waves are drawn for one of the three Aegean Sea earthquakes used in this study (e20 – 2005/10/20). Bold blue dashed line shows the corrected backazimuth range for different periods (see Fig. 5.12).

These results were discussed by Heuer et al. (2007) with respect to the previous study revealing the depths of the Moho – both the depths of the Moho and of the lithosphere-asthenosphere boundary are deeper for the Moldanubian unit than for the western units.

Kolínský and Brokešová (2007, 2008) estimated Western Bohemia uppermost crust v_s and group velocities using short-period surface waves. 1D models of several Love wave profiles crossing the region proved the lateral heterogeneity of the given area, and Rayleigh wave tomography provided a detailed image of the Western Bohemia region's upper crust. For an overview of other studies concerning only the Western Bohemia region, part of the Saxothuringian unit, refer to the introduction of the paper by Kolínský and Brokešová (2007).

The above mentioned studies concerned only a limited depth range (Malinowski, 2005); they estimated the structure only locally, beneath a single station (Wilde-Piórko, 2005; Heuer et al., 2006, 2007) or they concerned only a limited area (Kolínský and Brokešová, 2007 and 2008). In contrast, our present study estimates S-wave velocities along whole profiles with better depth resolution than achieved by Plešinger et al. (1991). Moreover, in our study, we focus on the differences between the three particular geological units.

There were several stations available for the given region which were situated along profiles coinciding (in terms of influence zones) with the surface wave paths from three selected Aegean Sea earthquakes (close to the coast of Turkey), see Fig. 5.1. Fig. 5.2 shows a detailed map of the region of interest with station names indicated. The stations form two long profiles: Tábor (TBR) – Moxa (MOX) and Kašperské Hory (KHC) – MOX.

Although there are a number of papers on phase velocity determination using advanced techniques and considering also non-plane-wave character of the waves (McMechan and Yedlin (1981), Gabriels et al. (1987) – shallow seismic profiling using higher modes; Stange and Friederich (1993) – regional network phase velocity inversion; Forbriger (2003a, 2003b) – theory for shallow seismic wave-field inversion), we adopt the well known two-station approach assuming the plane-wave propagation to determine the phase velocities of surface waves. This is justified not only by long epicentral distance, but also by

the use of sufficiently long-period waves which are not influenced by local lateral heterogeneities. Such approach is reported in many papers (Nafe and Brune, 1960 – global phase velocity study from an Alaska earthquake; McEvilly, 1964 – phase velocities across Central US; Levshin et al,. 1992 – regional phase velocities across Asia; Mitra et al., 2006 – phase velocity in the south Indian shield). We do not attempt to develop a new method of phase velocity measurement; we rather use the classical and simple one to obtain new information about the structure of the Bohemian Massif. We present some modifications of the classical interstation phase-velocity measurement: we correct the dispersion curves for the true backazimuth propagation instead of using directly the geometrical great circle paths, and we also use the two-station method for stations which are much closer to one another with respect to the wavelengths than it is usually used in the literature.

5.2.3 Data

During 2005, three temporary stations TBR (Tábor), HAJ (Hája) and NEC (Nečtiny) (Fig. 5.2) were operated by the Institute of Rock Structure and Mechanics, Academy of Sciences of the Czech Republic, forming a southeast-northwest oriented profile across the Bohemian Massif. Guralp CMG-40T seismometers with a flat response characteristic up to 30 s were used at all stations. At the same time, two permanent Streckeisen STS-2 (120 s) stations KHC (Kašperské hory) and NKC (Nový Kostel) (Fig. 5.2) were operated by the Geophysical Institute, Academy of Sciences of the Czech Republic, as a part of the Czech Regional Seismic Network. We also add one permanent STS-2 MOX (Moxa) station from Germany. For the investigation of crustal velocities along the profiles, we selected three shallow Aegean Sea (Fig. 5.1, Table 5.1) earthquakes with clear Love wavegroups.

These three earthquakes have similar magnitudes and are located close to each other. They are processed independently and only the period ranges that yield the same results for all three earthquakes are taken into account. This procedure ensures highly reliable results. Three events close to one another may eliminate random errors; however, systematic errors caused, for example, by multipathing cannot be removed using this approach.

location	M_W	date	origin time	epic. longitude	epic. latitude	depth	label
Aegean Sea	5.7	2005/10/17	05:45:16.0	26.50° E	38.13° N	8 km	e17a
Aegean Sea	5.8	2005/10/17	09:46:53.9	26.50° E	38.20° N	10 km	e17b
Aegean Sea	5.9	2005/10/20	21:40:04.1	26.75° E	38.15° N	10 km	e20

Table 5.1: Basic information about the events used in this study; according to the USGS National Earthquake Information Center PDE Catalog (2006).

The events were selected to fit approximately the great circle delineated by the stations. This gives us a rare opportunity to study the structure directly within the selected profiles and not averaged over various azimuths.

Backazimuths of great circles and epicentral distances of each event-station pair computed by the method of Novotný and Málek (2002) are given in Table 5.2. However, considering the wavelengths of surface waves, we use the theory of influence zones given by Yoshizawa and Kennett (2002). These zones represent the region of surface wave coherence. Figs. 5.1 and 5.2 show simplified influence zones corresponding to the laterally homogeneous structure for the most distant station MOX. The simplified influence zones are presented as ellipses with major axes oriented along the epicenter-station (geometrical) paths.

We consider two long profiles KHC-MOX (219 km) and TBR-MOX (249 km). The latter is further divided into four sub-profiles: TBR-HAJ (50.7 km), HAJ-NEC (68.0 km), NEC-NKC (56.4 km) and NKC-MOX (74.3 km), see Fig. 5.2. The lengths of profiles are measured as differences between epicentral distances of the corresponding stations along great circles. In case of the three earthquakes, these lengths vary in the range of ± 0.1 km, as implied by Table 5.2.

In Fig. 5.2, we see that all stations are situated within the influence zone for the 12 s period for station MOX; hence, the theory supports the possibility of using these stations for relative phase velocity measurements with MOX station from 12 s to longer periods. The maximum difference in azimuths as seen from the epicenter (geometrical backazimuths) to stations is found for the pair TBR and MOX and its value is 2.1°, see Table 5.3. This meets well the condition proposed by Levshin et al. (1992) according to which the azimuths should differ by less than 6°.

Profile	TBR-MOX profile								KHC-MOX profile			
Station	TBR (Guralp)		HAJ (Guralp)		NEC (Guralp)		NKC (STS-2)		KHC (STS-2)		MOX (STS-2)	
°E/°N	14.6484	49.4129	14.0490	49.6747	13.1686	49.9774	12.4480	50.2331	13.5782	49.1309	11.6161	50.6461
event	dist.	backaz.	dist.	backaz.	dist.	backaz.	dist.	backaz.	dist.	backaz.	dist.	backaz.
e17a	1571.5	138.5	1622.1	137.6	1690.0	136.1	1746.4	135.0	1602.1	134.9	1820.8	134.1
e17b	1565.0	138.3	1615.7	137.4	1683.6	135.9	1740.1	134.8	1595.8	134.7	1814.4	133.9
e20	1581.7	137.7	1632.5	136.9	1700.7	135.4	1757.3	134.4	1613.3	134.2	1831.7	133.5

Table 5.2: Locations of stations, epicentral distances (km) and backazimuths (degrees) for event-station pairs

	azimuths of propagation from epicenter (°)						differences of azimuths (°)					
event	TBR	HAJ	NEC	NKC	KHC	MOX	TBR-MOX	TBR-HAJ	HAJ-NEC	NEC-NKC	NKC-MOX	KHC-MOX
e17a	326.7	326.3	325.4	324.9	323.9	324.6	2.13	0.46	0.81	0.57	0.28	0.73
e17b	326.6	326.1	325.3	324.7	323.7	324.4	2.11	0.46	0.81	0.57	0.28	0.75
e20	326.2	325.7	325.0	324.4	323.4	324.2	2.02	0.44	0.78	0.55	0.26	0.81

Table 5.3: Azimuths of propagation from epicenters and mutual differences of these azimuths for all three events and all six station pairs.

The largest difference between interstation backazimuths and geometrical backazimuths was found for the NEC station on the HAJ-NEC profile (18°). It is significantly larger than is usually accepted. For instance, Mitra et al. (2006) used only station pairs, whose mutual paths differed from the geometrical backazimuths by less than 7°. In these studies, interstation and epicentral distances could be compared; in our study, however, there is a significant difference between interstation distances (50 km) and the epicentral distances (1700 km). Therefore, despite the 18° difference, our stations are still well aligned.

The above-mentioned findings as well as quality of data available imply that it is reasonable to use the dispersion curves in the period range of 12 s to 40 s in case of the TBR-MOX profile and of 12 s to 73 s in case of the KHC-MOX profile. Dispersion measurement was performed also for shorter periods down to 8 s, however, shorter wavelengths suffered by higher scattering and were not used for the final inversion.

We present an analysis of phase velocities of Love waves measured at a broad period range. The reason why we did not used also the Rayleigh waves is that they suffer by much higher scattering and incoherence and clear phase velocities can be found only in the period range of 15 – 25 s. Moreover, Love wave propagation depends only on vs. Thus the inverse problem is qualitatively simpler when inverting for only one quantity distribution (vs).

5.2.4 Love wave analysis

As it is usual in studies dealing with phase velocity, first we need to analyze the records to isolate the fundamental mode (Dziewonski et al., 1972; Yoshida and Suetsugu, 2004). We follow the procedure described by Kolínský and Brokešová (2007). The classical method of Fourier transform-based multiple filtering was applied to analyze the dispersive records. We use non-constant relative resolution filtering; see Dziewonski et al. (1969). Examples of estimating the optimum coefficient for controlling the width of the filters can be found in Levshin et al. (1972 and 1992). In the present paper, we use the linear dependence of the filter coefficient on period, see Kolínský (2004). As symmetric Gaussian filters are applied to a generally asymmetric spectrum, the frequencies which prevail in the filtered spectra do not match the central frequencies of the filters (Dziewonski et al., 1972). We solve this by estimating the instantaneous frequency (Levshin et al., 1989) which is computed using the analytical signal corresponding to each filtered quasi-monochromatic signal. The modulus of the analytical signal represents an envelope of the filtered signal, and we use the amplitudes of these envelopes to pick up the fundamental mode. Selecting the dispersion ridge of the fundamental mode is described in Kolínský and Brokešová (2007). We use the criterion of continuity – among all ridges found in the spectrogram, the desired fundamental mode is selected to present a smooth curve regardless of the amplitudes. We obtain group velocity dispersion curves, which are visually compared to decide whether the records are suitable for further relative phase velocity measurements.

After we select the wavegroup corresponding to the fundamental mode in each harmonic component, we truncate each of these harmonic components by a window centered at the envelope maximum with cosine taper on both window sides. Parameters are set so that the taper smoothes two periods around one period which is kept unchanged. Because we need to compare the records from different stations, we use the same width of filters in the frequency domain and the same width of truncating windows in the time

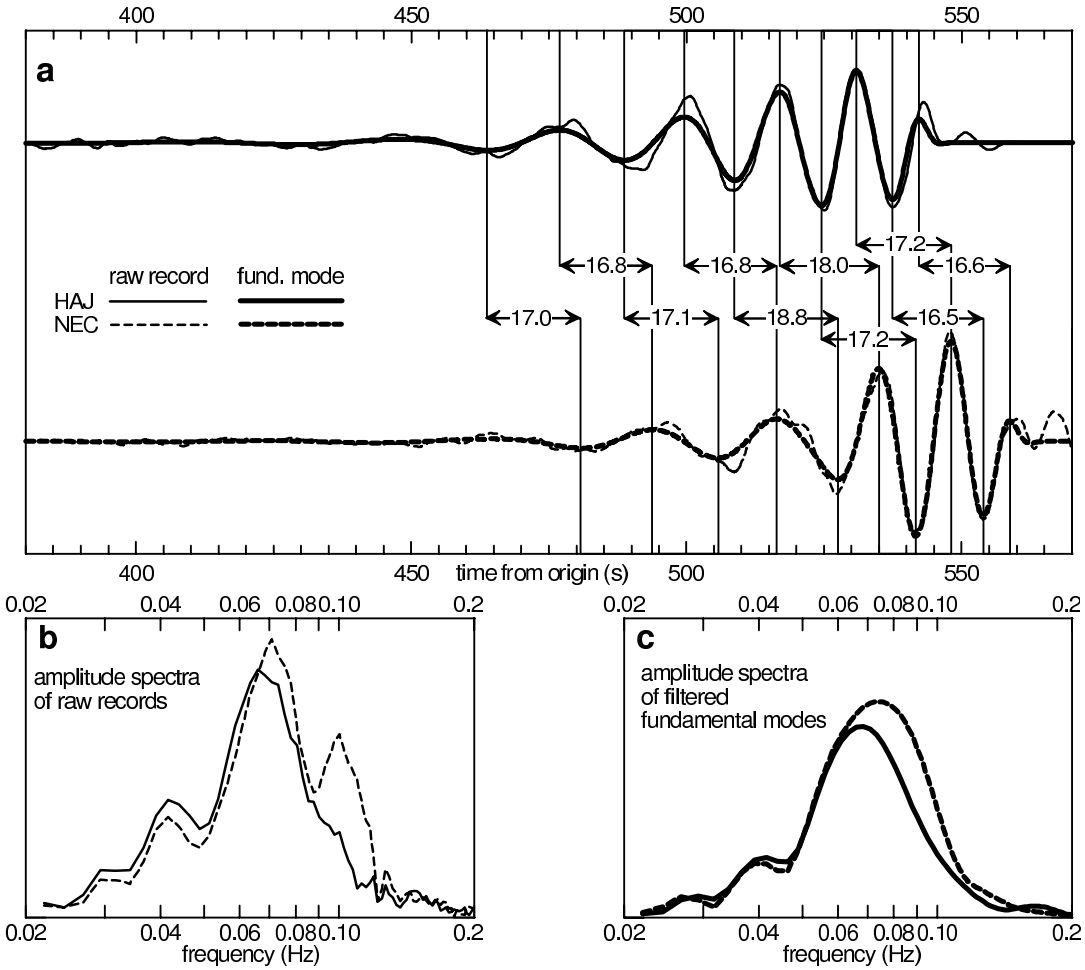


Figure 5.3: (*Fig. 3 in Kolínský et al., 2010*) Raw records at two stations are shown in comparison with the filtered fundamental modes (**a**). Fundamental modes are drawn for the period range 12 – 40 s. The peak and trough technique sketch shows a mutual time shift of the corresponding filtered records. Amplitude spectra for both stations and both raw records (**b**) and fundamental modes (**c**) are shown. The instrumental transfer function is applied both in the time and frequency domain.

domain for all stations to ensure the coherency of the records. We create a filtered seismogram containing only the Love wavegroup by summing these truncated filtered signals. This filtered seismogram is shown together with the original record in Fig. 5.3a. The traditional peak and trough technique of manual estimation of phase velocity is demonstrated in this figure. The difference between the spectra of raw records and filtered fundamental modes is shown in Figs. 5.3b and 5.3c. The filtered fundamental modes display similar waveforms in the time domain and similar shapes of spectra in the frequency domain. The amplitudes of signals differ by about 10 percent.

5.2.5 Phase velocity measurement

Methods of cross-correlation and other time domain methods were discussed, for example, by Nafe and Brune (1960), McEvilly (1964), Wielandt et al. (1987). We use the correlation of filtered and truncated quasi-monochromatic components measured at two stations. Fig. 5.4 shows the coincidence of the harmonic components of stations HAJ and NEC shifted in time by 17 s. This rough time shift was introduced according to Fig. 5.3a. In Fig. 5.4, we see that the time shift is set correctly in the period range around 19 – 20 s in this example, but for other periods, the waveforms are not so well correlated. We used the L1-norm to estimate the similarity of two signals while mutually shifting the signals sample by sample. We thus directly find the time difference for each filtered component and we compute the phase velocity. The central period of multiple filtering is used for matching the respective components at two stations. However, since the instantaneous period of the filtered signals differs from the central, we use the average of these instantaneous periods from both stations to plot the phase velocity dispersion curve. These instantaneous periods are estimated for the quasi-monochromatic signal at the time corresponding to the envelope maximum of the signal, as mentioned in the Love wave analysis.

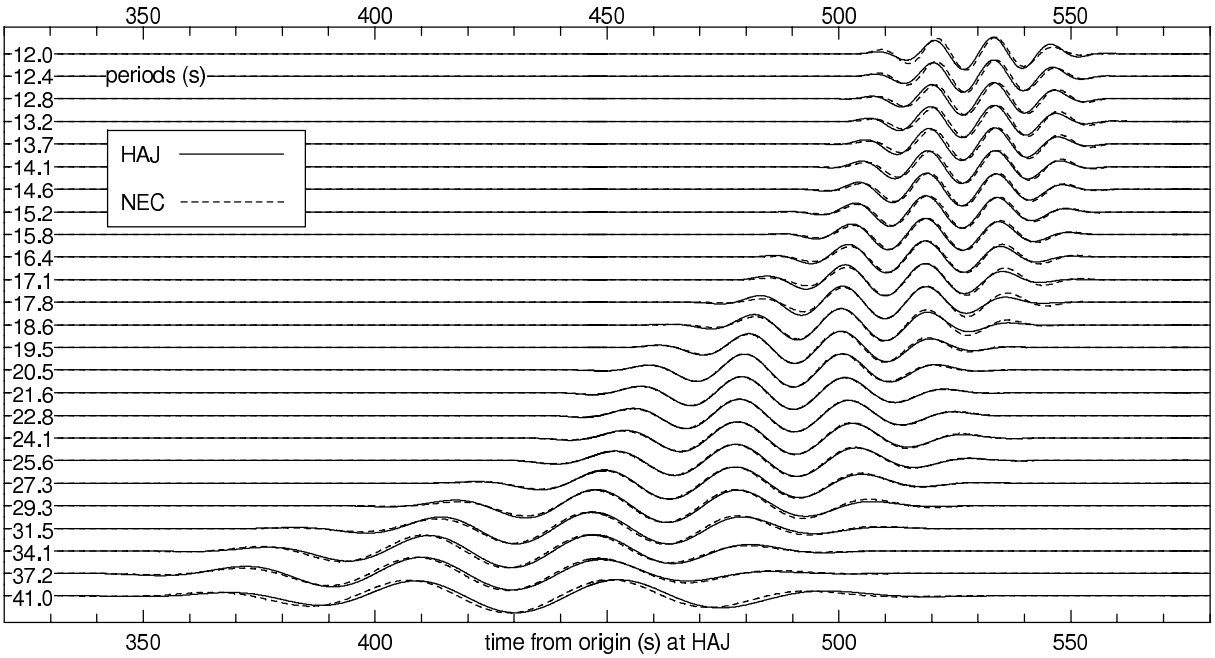


Figure 5.4: (*Fig. 4 in Kolínský et al., 2010*) Fundamental mode harmonic components of the same two station as in Fig. 5.3. Record from the NEC station is shifted by 17 s in time to correspond roughly to the HAJ station record. We see well-correlated signals with slight mutual shifts, which are used to estimate the phase velocities. The amplitudes are normalized.

The number of wavelengths between the stations is checked to obtain the correct value of the time shift. We consider three possible dispersion curves – one for the global minimum of L1-norm and two for the neighboring local minima. These three dispersion curves correspond to the different cycles of waves which were correlated. We select the proper curve according to the fact that the phase velocity is expected to be around 4.0 km/s for periods around 20 s.

5.2.6 Backazimuth correction

As the Earth is not laterally homogeneous, surface waves do not propagate precisely along great circles. Therefore, the real backazimuth differs from the geometrical one.

The dispersion curves for long profiles KHC-MOX and TBR-MOX are expected to be similar as both profiles are situated inside the same influence zone, and the geological structure of the Bohemian Massif is not expected to be very different for both profiles. We want to test, whether mutual differences of the measured dispersion curves can be explained by considering the true backazimuths. We assume that the difference between the two dispersion curves measured along the two long profiles KHC-MOX and TBR-MOX is caused only by errors in the backazimuth. Under this assumption, the true backazimuth $\beta(\omega)$ and phase velocity $c(\omega)$ for the given frequency ω can be obtained by solving the system of equations:

$$t_i(\omega) = \frac{R_i cos\left(\alpha_i - \beta(\omega)\right)}{c(\omega)}, \qquad i = 1 \;..\; (n-1), \tag{5.1}$$

where t_i is the time difference, R_i is the geographical distance between the stations, α_i is the interstation backazimuth and n is the number of stations. All three quantities refer to the i-th and the last station. In our case $n = 3$, so we have two equations and two unknown parameters $\beta(\omega)$ and $c(\omega)$.

5.2.7 Inversion

During the inversion process, we followed the procedure described by Kolínský and Brokešová (2007). The isometric method is used, which is a fast inverse algorithm developed by Málek et al. (2005) and tested by Málek et al. (2007). Typical problems, which are effectively solved by the isometric method, are weakly non-linear problems with tens of parameters and complicated forward modeling. The basic underlying idea of the isometric method is to postulate the distance in the model space in such a way that the model and data spaces are isometric, i.e. the distances in both spaces have the same measure. As all model-data vector pairs are used many times in successive iterations, the number of the forward

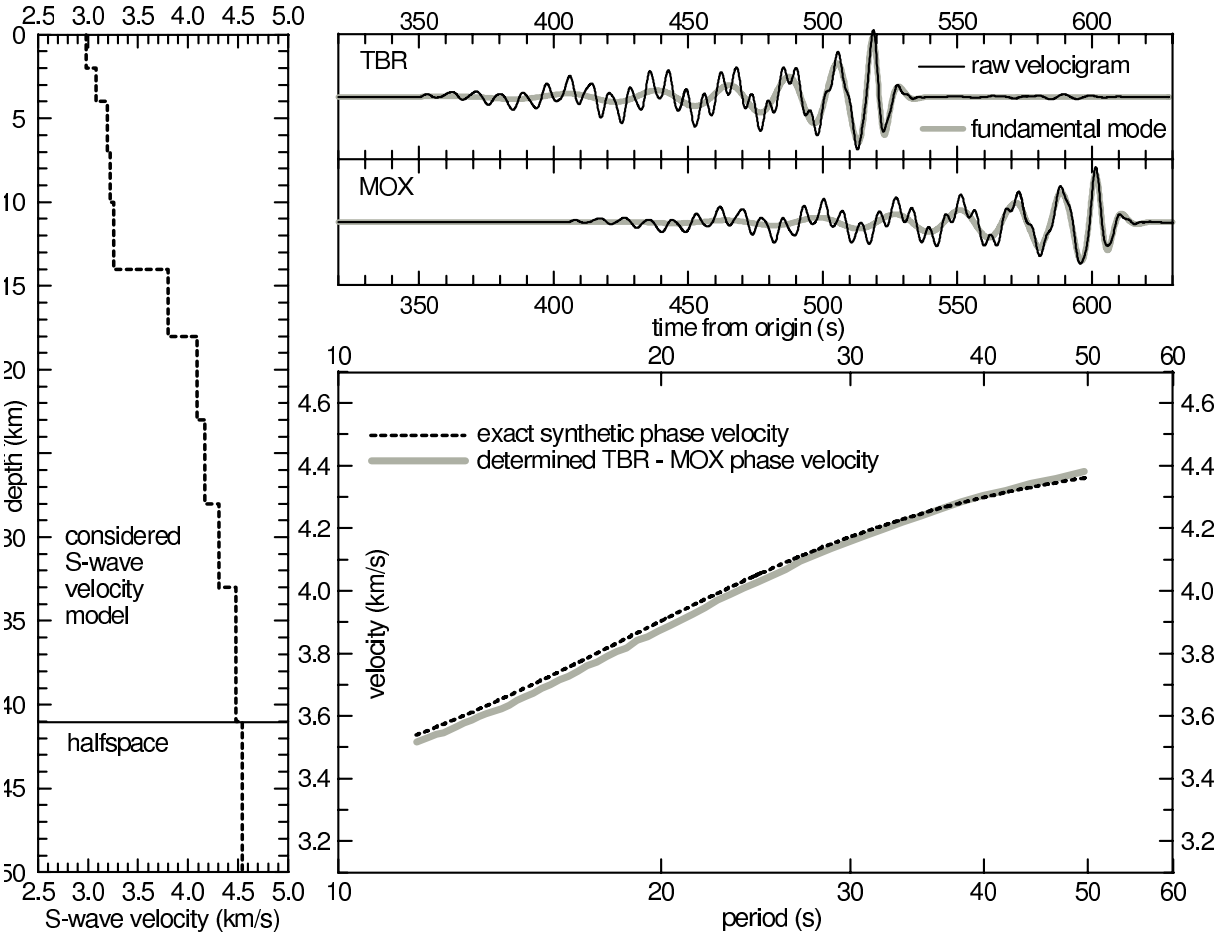


Figure 5.5: (*Fig. 5 in Kolínský et al., 2010*) Surface wave analysis test. Left panel represents the considered shear wave velocity model. Upper right panel shows synthetic seismograms with fundamental modes estimated by the frequency-time analysis. Lower right panel shows a comparison of synthetic (exact) and determined phase velocity dispersion curves.

problem computations is minimized. It is not necessary to deal with derivatives. Therefore, this method is suitable for the inversion of dispersion curves.

The forward problem is solved by the modified Thomson-Haskell matrix method; see Proskuryakova et al. (1981). Dispersion curves are found in a 1-D layered model above a halfspace with constant values of v_s and density in the individual layers and the halfspace.

During the inversion, the phase velocity dispersion curve is computed many times and the distance between theoretical and measured dispersion points (misfit function) is minimized. The thicknesses of layers are set manually. In the present study, we consider layers 2 or 4 km thick, which ensures a good resolution for finding the properties of the velocity distribution and keeps the number of parameters reasonable.

We seek one parameter in each layer: the shear wave velocity. Density is kept unchanged during the inversion as well as the thicknesses of layers. Density values are introduced according to the gravity measurements along the 9HR profile, see Švancara and Chlupáčová (1997). Surface wave propagation does not depend on density significantly; the density effect is of an order of magnitude lower than the effect of the shear wave velocities. Any unrealistic oscillation of the velocities is avoided by constrains of the velocity difference between neighboring layers. The number of parameters with respect to the number of measured dispersion points and starting models were discussed in Kolínský and Brokešová (2007). The results of inversion do not depend on the starting model; however, we may save computational time by setting the starting model appropriately. Since the inversion of the dispersion curves is highly non-unique, even for the same starting parameters, different results are obtained. We compute the inversion problem twenty times, and as a result we obtain the mean value of twenty velocities in each layer with its standard deviation. For details refer to Kolínský and Brokešová (2007), where tests of the inversion reliability and a discussion on the resolution of the procedure can be found.

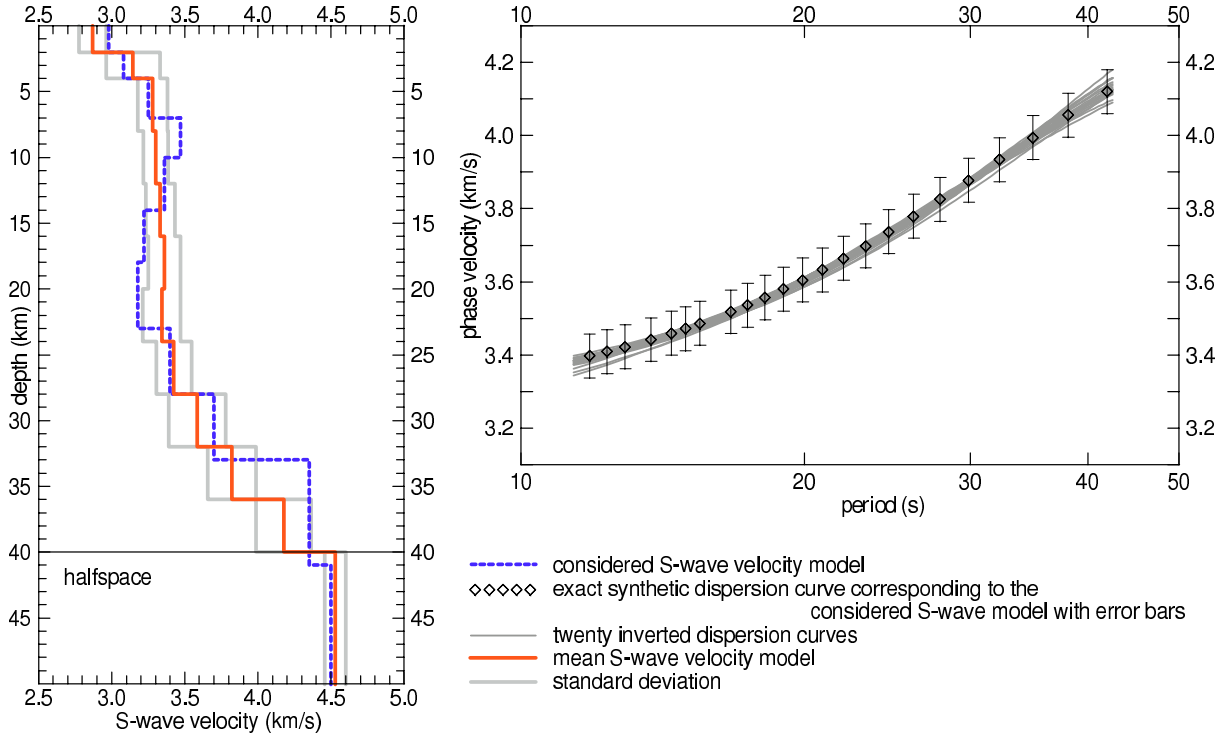


Figure 5.6: (*Fig. 6 in Kolínský et al., 2010*) Dispersion curve inversion test. Dashed blue line in the left panel represents the considered S-wave velocity model. The corresponding exact synthetic dispersion curve is shown in the right panel as diamonds. Error bars are derived from real measurements to make the synthetic test as similar to the real situation as possible. Twenty inverted dispersion curves are drawn as dark gray lines in the right panel and the resultant mean S-wave velocity distribution is plotted as the solid red line in the left panel. Light gray lines represent its standard deviation.

5.2.8 Synthetic tests of the analysis and inversion

We propose three synthetic tests to verify our methodology. The first of them benchmarks the surface wave analysis procedure itself, the second one tests the dispersion curve inversion method, and the third one tests both surface wave analysis and dispersion curve inversion together.

The goal of the first test is to convince ourselves that our methodology is able to determine the correct phase velocity dispersion curve. For this test we consider a theoretical velocity model and compute the corresponding synthetic seismograms and exact synthetic dispersion curve. We then determine the dispersion curve from the synthetic seismograms and compare the determined dispersion curve with the theoretical one. We assume a 1D shear wave velocity model (Fig. 5.5, left panel) consisting of 10 layers over a halfspace. This model is chosen to resemble the model obtained by inverting the group velocity dispersion curve estimated from the Aegean Sea earthquake measured at station TBR, and hence it may be considered as a realistic model for the real surface wave path. We compute two synthetic seismograms by the discrete wavenumber method, Bouchon (1981), corresponding to stations TBR and MOX, see Fig. 5.5, upper right panels. These synthetics are processed as if they were real records (i.e. as described in the previous section) to determine the phase velocity dispersion curve. In Fig. 5.5 (upper right panels), the filtered fundamental modes are shown as gray lines. We compute an exact synthetic phase velocity dispersion curve between TBR and MOX, see Fig. 5.5 (lower right panel), using the modified matrix method for computing the dispersion curve, Proskuryakova et al. (1981). The lower right panel of the figure shows the comparison of the synthetic dispersion curve and that determined by our methodology. We see that both curves match each other with an average difference of $\pm$ 0.02 km/s. Thus, this test verifies our analysis procedure on a synthetic example.

To prove the reliability of our phase velocity inversion method, we propose another test. We compute an exact synthetic dispersion curve for a considered theoretical structure using the modified matrix method by Proskuryakova et al. (1981), invert it, and compare the determined structure with the considered one. Note that no synthetic seismograms are involved in this test. We again assume a 1D shear wave velocity model; see Fig. 5.6, left panel. The layer distribution (number and thicknesses) is the same as in the previous test of the surface wave analysis method, compare it to Fig. 5.5, left panel. However, the velocity values are different. Here we consider a low velocity zone (LVZ) to test whether the inversion is capable of retrieving it. Note that this velocity distribution with LVZ is similar to the real velocity model found for the HAJ-NEC profile. We compute the synthetic phase velocity dispersion curve

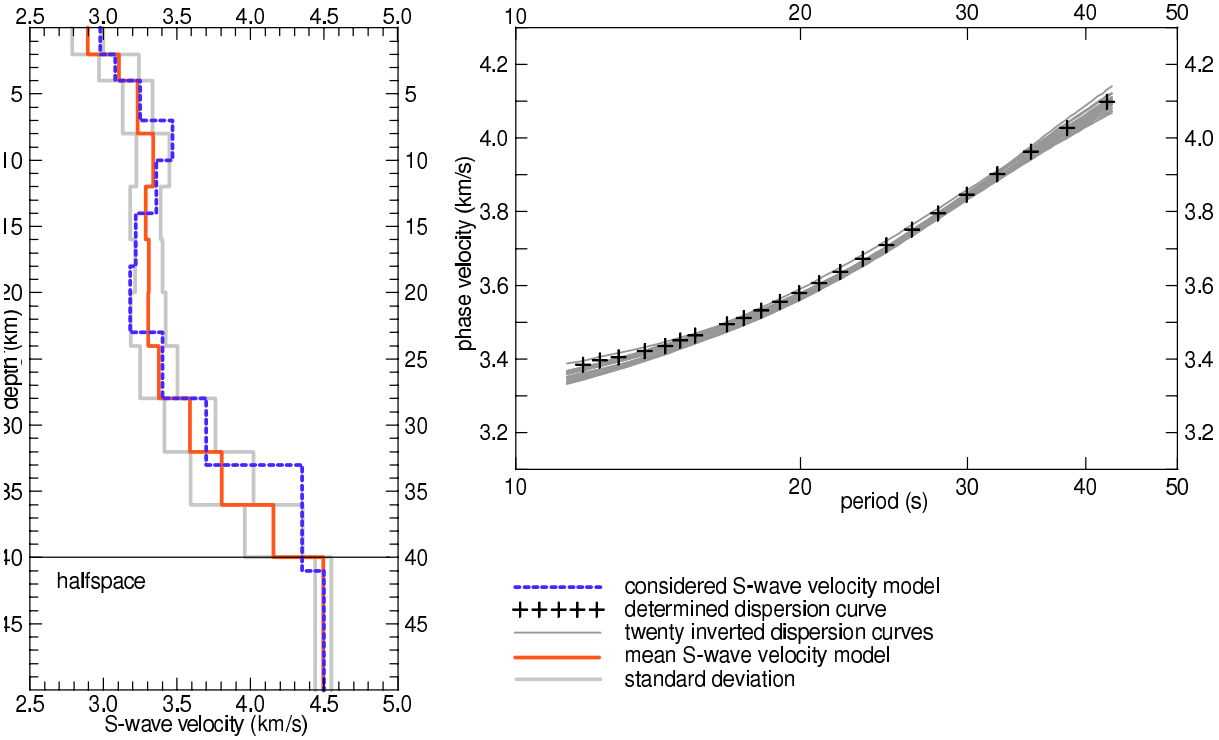


Figure 5.7: (*Fig. 7 in Kolínský et al., 2010*) Combined test of the analysis and inversion. Dashed blue line in the left plot represents the considered model. Crosses in the right plot represent the dispersion curve determined by the surface wave analysis using synthetic seismograms. Dark gray lines represent twenty dispersion curves found by the inversion. Bold red line in the left plot is the mean shear wave velocity model with its standard deviation given by light gray lines.

for this model and select only a limited number of dispersion points to resemble the real measurement; see Fig. 5.6, right panel, diamonds. We estimate the error of each dispersion point to be ± 0.06 km/s (see error bars in Fig. 5.6, right panel) based on the quality of the real measured data at our disposal (see next sections). We propose a suitable number and thicknesses of layers for the inversion – this system is the same in the test as it is in the real data processing. Generally, layer thicknesses differ from those used in the considered theoretical model, because we do not know them in the real case.

We perform twenty inversions so that for each inversion, each of the dispersion points has a random error in the range of ± 0.06 km/s. These randomly disturbed dispersion curves (indicated only implicitly by the error bars in Fig. 5.6) enter the inversion procedure. The twenty dispersion curves, shown as gray lines in Fig. 5.6, right panel, correspond to the structures found by the inversion according to the lowest misfit function criterion. We see that, despite relatively large error bars, all the found curves fit the original (exact) synthetic curve well. This is due to the inversion procedure being sufficiently robust and insensitive to the local disturbance of the dispersion curve. We see that for longer periods, the curves exhibit larger scattering. We treat the twenty resultant shear wave velocity models exactly in the same way as the real data-based models: we compute the mean value for each layer, and we show this mean shear wave velocity distribution with its standard deviation in the left panel of Fig. 5.6 in comparison with the considered theoretical model. We see that, except for the sharp discontinuities at depths of 7 and 33 km, the considered model is within the range of the standard deviation of the mean determined velocity distribution. LVZ is a bit smoothed in our test. It is a general feature of the procedure that it smooths sharp discontinuities and LVZs, as proved by many tests. It never produces a false discontinuity or LVZ.

The third test combines both previous tests, i. e. we consider a 1D theoretical structure, compute synthetic seismograms and determine the dispersion curve in the same way as if the seismograms were measured. We treat this dispersion curve in exactly the same way as explained in the previous test. We invert the curve and compare the determined structure with the considered theoretical one. More specifically, we use the same velocity distribution including the LVZ as in the previous test, see the blue dashed line in Fig. 5.7, left plot. For stations TBR and MOX, the synthetic seismograms are computed by the discrete wavenumber method. The phase velocity dispersion curve between both stations is determined, see the crosses in Fig. 5.7, right plot. The dispersion curve is disturbed randomly to obtain twenty curves processed by the inversion. These curves are inverted to obtain shear wave velocity models (gray lines represent their standard deviations) and their mean, see solid red line in Fig. 5.7, left plot. As

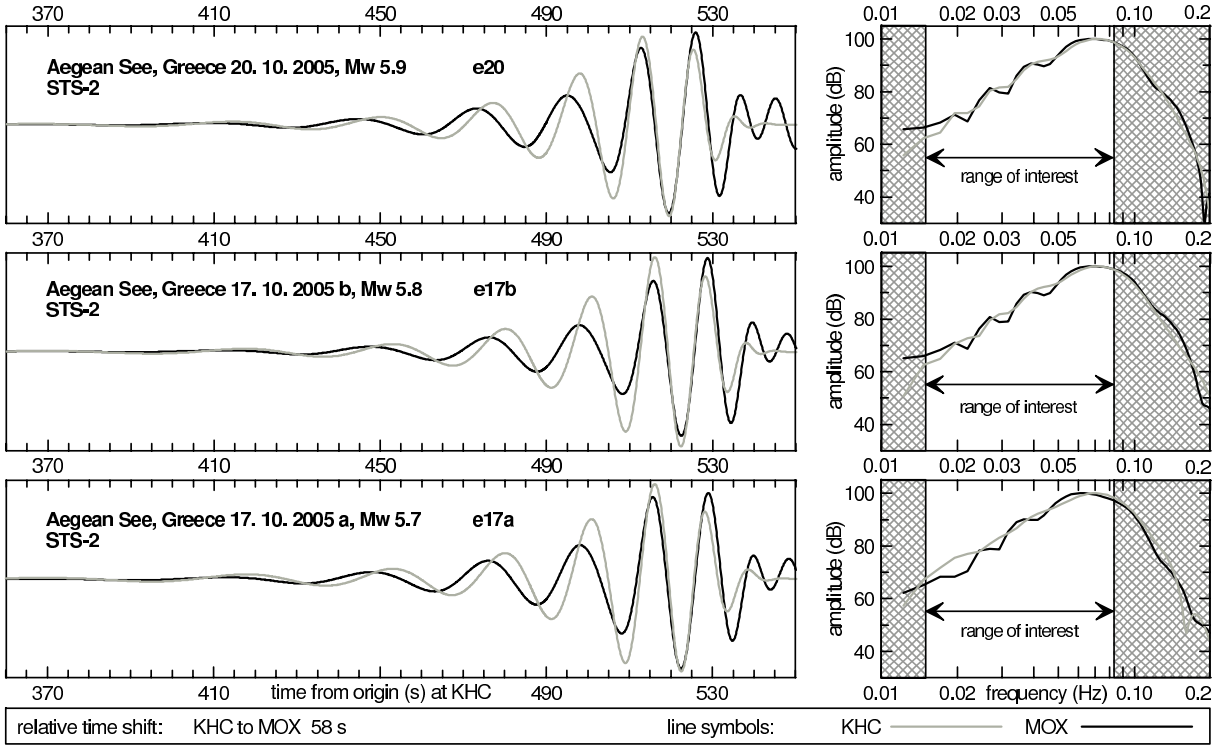


Figure 5.8: (*Fig. 8 in Kolínský et al., 2010*) KHC-MOX profile: Filtered fundamental modes and amplitude spectra of Love waves from three Aegean Sea earthquakes at two STS-2 stations KHC and MOX, mutually shifted by 38 s in time, what corresponds to the phase velocity around 4.0 km/s. Instrumental correction is applied both in the time and frequency domain.

expected, since the structures considered in the second and in the third tests are the same, we obtained similar results, i. e. the original structure is retrieved within the range of the standard deviation. However, only the third test works exactly in the way we also treat the real data.

5.2.9 Results

Figures 5.8 and 5.9 show the fundamental modes and their spectra of three earthquakes for the KHC-MOX and TBR-MOX profiles, respectively. The records are mutually shifted in time to fit the most significant amplitudes approximately – the Airy phases. Both signals and spectra are corrected using the instrumental transfer function. We see that the records are well coherent and suitable for phase velocity measurements.

Fig. 5.10 shows reduced travel-time curves for the TBR-MOX profile for a set of periods and for the reduction velocity of 4.0 km/s. This means that the travel-time curve with this velocity would be represented by a horizontal line. The travel times correspond to the amplitude maximum of the signal envelope for each period so that the figure shows the group velocity dispersion. The reduced travel time is considered relatively to the arrival of the 40 s wave at station TBR. Generally, short periods are slower and longer periods are faster than the reduction velocity. This figure enables us to check the quality of the analysis intuitively. The travel-time curves form a smooth system of lines, which do not intersect each other. We see also differences of the curves for the individual sub-profiles. For example, longer periods for the NEC-NKC sub-profile display faster wave propagation than for the other sub-profiles. The phase velocity measurement for each sub-profile is capable of revealing these differences precisely.

Two panels displaying phase velocity dispersion curves are shown in Fig. 5.11. The curves measured for each earthquake for the two long profiles KHC-MOX and TBR-MOX are shown in Fig. 5.11a as light-colored lines and their averages as dark-colored lines. Fig. 5.11b concerns the TBR-MOX profile; we see four sets of dispersion curves measured for each of the four sub-profiles using the records of all three events.

We also compute the average curve for the whole TBR-MOX profile obtained as the average of four sub-profile curves (Fig. 5.11a, orange line) and we compare this average curve with the original curve measured for the whole TBR-MOX profile (Fig. 5.11a, dashed dark green line). They are almost identical, which confirms that the surface wave paths for the long profile and its sub-profiles are similar.

Let us discuss in more detail the behavior of the dispersion curves in Fig. 5.11b. The curves display significant differences; for periods longer than 25 s their scatter is lower than that for shorter periods. In

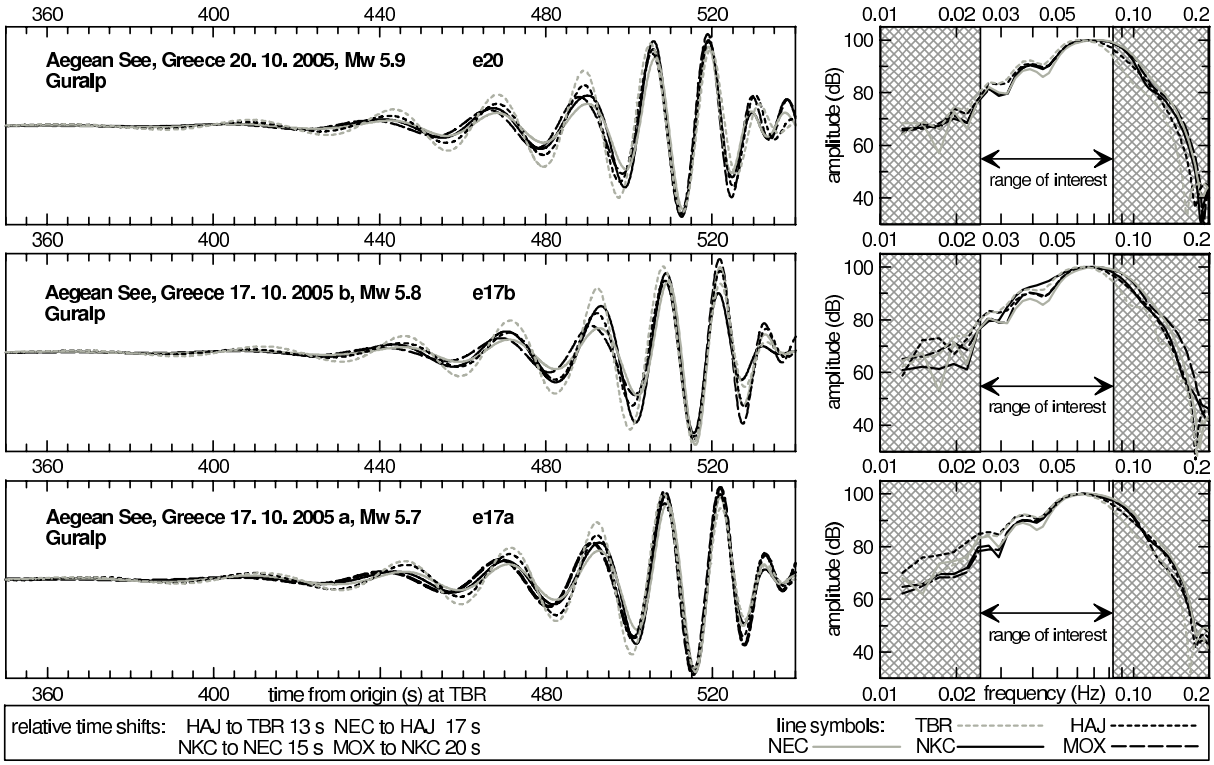


Figure 5.9: (*Fig. 9 in Kolínský et al., 2010*) TBR-MOX profile: Filtered fundamental modes and amplitude spectra of Love waves from three Aegean Sea earthquakes at three Guralp stations TBR, HAJ, NEC and two STS-2 stations NKC and MOX. The mutual time shifts are marked in the figure and correspond to the phase velocity around 4.0 km/s. Instrumental correction is applied both in the time and frequency domain.

general, Love wave phase velocity curves should monotonically increase with period for 1D structures. However, the dispersion curves for the four sub-profiles in Fig. 5.11b have complicated shapes with decreasing velocity in some period intervals. This behavior cannot be explained by velocity measurement errors: the dispersion curves are smooth, they are determined independently for three earthquakes, and the undulations of the curves have amplitudes which exceed the measurement error. One possible explanation of these undulations is that they are due to the deviations of surface wave propagation paths from the great circle (geometrical backazimuth). As waves of different periods reflect from heterogeneities of different scales, different backazimuths for arrivals of different periods are expected.

The paper by Wilde-Piórko et al. (2005) suggests that the structure (derived from the receiver functions) in the direction perpendicular to our profiles does not change considerably. Moreover, the geological unit boundaries in the region of interest are also nearly perpendicular to our profiles. This allows us to hypothesize that the geological structure of the Bohemian Massif does not vary much from the KHC-MOX profile to the TBR-MOX profile so that both profiles should display a similar dispersion curve. We further assume that the differences between the dispersion curves are due to the off-great circle propagation. Let us find the backazimuths for which the curves become the same (we use the TBR/KHC-MOX label for it below).

Fig. 5.12 shows corrected backazimuths computed according to equation (5.1). In Fig. 5.2 we depict the range of true backazimuths for station MOX as two bold dashed blue lines; these lines represent the highest and the lowest corrected backazimuth values from Fig. 5.12.

In Fig. 5.12, we see a smooth, generally monotonic dependence of the corrected backazimuth of the limited range of 10° (from 131° to 141°) with respect to period, however, small variations appear. For shorter periods, surface waves arrive at the Bohemian Massif under greater backazimuths (more from the south) than for the longer periods. Fig. 5.12 shows also both the inter-station backazimuths and geometrical backazimuths (ranging from 134° to 138°, see Table 5.2) of the great circle paths between the Aegean Sea and the respective stations (these are averages of the three events). We see that, for all profiles, the corrected backazimuth for shorter periods is larger while for the longer periods it is smaller than the geometrical backazimuth. Consequently, the corrected backazimuth can be either more or less distant from the inter-station backazimuth than the geometrical. If it is less distant, the apparent inter-station distance (with respect to the wave propagation direction) increases and approaches the true inter-station distance and, therefore, the corrected phase velocity increases, and vice versa.

As Fig. 5.11a implies (comparison of the sub-profile averaged curve and the long-profile TBR-MOX

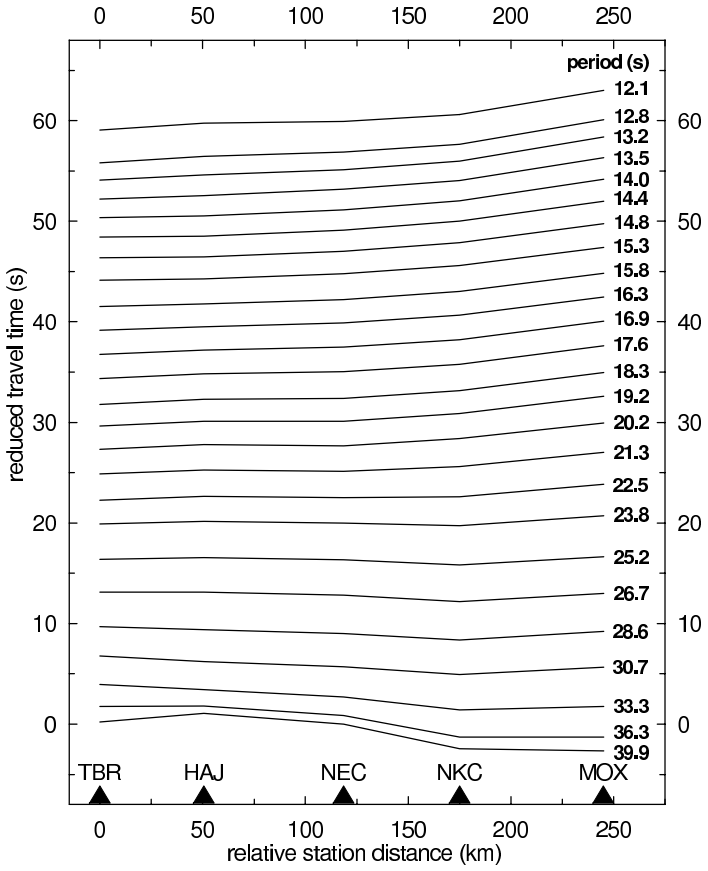


Figure 5.10: (*Fig. 10 in Kolínský et al., 2010*) TBR-MOX profile: Reduced group travel-time curves for periods used along the TBR-MOX profile. The reduction velocity is 4.0 km/s.

curve) that the averaged propagation direction in the four sub-profiles is similar to the propagation direction in the long profile, and hence we are justified in applying the true backazimuth corrections found for the long profile to the sub-profiles.

Fig. 5.13a provides the corrected TBR/KHC-MOX dispersion curve. The reason, why the corrected TBR/KHC-MOX curve is so similar to the measured KHC-MOX curve, is that, by chance, the corrected backazimuth range is centered almost at the KHC-MOX inter-station backazimuth. Looking at the corrected backazimuth range in Fig. 5.22, we see that station KHC is situated nearly in the middle of this range with respect to station MOX.

Fig. 5.13b shows the corrected curves for the four sub-profiles from Fig. 5.11b. The corrected dispersion curves in Fig. 5.13b are steeper as the phase velocity becomes lower for shorter periods and higher for longer periods. This is due to the fact that all the inter-station backazimuths for the TBR-MOX profile and all its sub-profiles are smaller than the geometrical backazimuths. Contrary to this, for the KHC-MOX profile (Fig. 5.13a), the inter-station backazimuth is larger than the geometrical, and hence the corrected TBR/KHC-MOX dispersion curve rises less with period than the uncorrected curve for the KHC-MOX profile.

Fig. 5.13 shows that the dispersion curve undulations are slightly smoothed (except for the TBR-HAJ sub-profile) in comparison with the measured ones. The variations of the corrected backazimuth-period dependence (Fig. 5.12) affect especially the HAJ-NEC sub-profile curve in such a way that the most pronounced undulation is diminished.

Since the dispersion curve undulations still remain after the backazimuth correction, another explanation is needed. One of the possible reasons is that we observe a coupling of Love wave modes, probably due to reflection and diffraction at heterogeneities, where the fundamental mode is converted into higher modes. A detailed theory may be found in the paper by Maupin (2007). Waves of the same period can then propagate with different velocities, interfere with one another, and may cause the undulations we observe. Since, in general, inversion produces smooth dispersion curves, we expect the misfit between measured and inverted curves to be greater for profiles where undulations are more pronounced.

We inverted the corrected dispersion curves for all five profiles: TBR/KHC-MOX, TBR-HAJ, HAJ-NEC, NEC-NKC and NKC-MOX using the methodology described above. Since the period range 8 – 40 s was measured, we provided inversions for four different period ranges starting with 8, 10, 12 and 15 s. We than compared the resultant shear wave velocity distributions. Since the models differed for the inversions taking account short periods (8 and 10 s) and since there was no change in the models for the inversion starting from 12 and 15 s, we decided to use the period range 12 – 40 s for the final inversion. The results

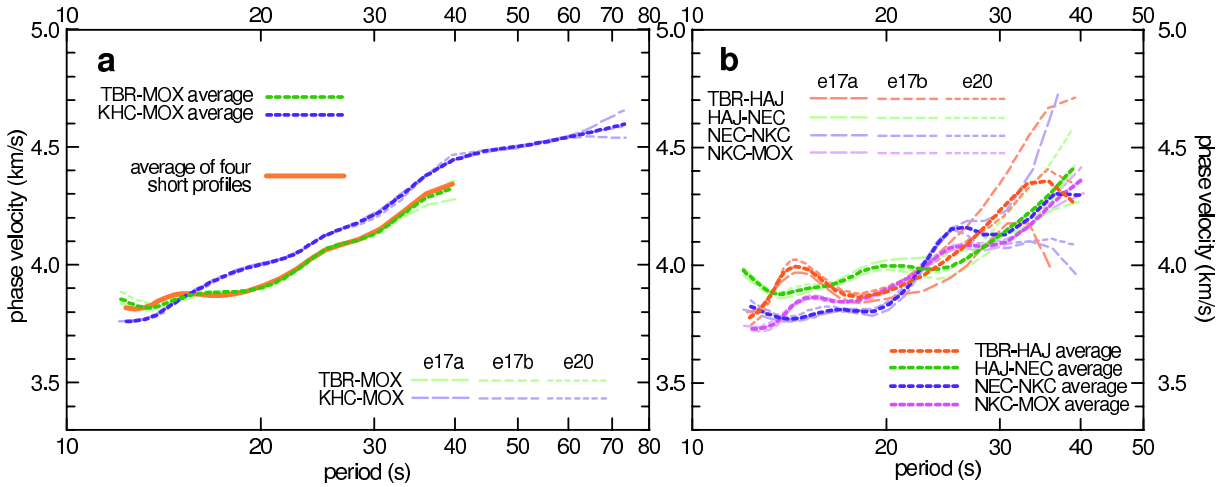


Figure 5.11: (*Fig. 11 in Kolínský et al., 2010*) Measured phase velocity dispersion curves. Panel **a**: Dispersions for the TBR-MOX and KHC-MOX profiles from three earthquakes are shown as light green and light blue lines, their averages as dark green and dark blue lines, respectively. The dispersion curve taken as the average of four sub-profiles from Panel **b** is shown as the solid orange line. Panel **b**: Dispersions for four sub-profiles dividing the TBR-MOX profile from three earthquakes are shown as light-colored lines and their averages as dark-colored lines.

are summarized in Table 5.4 and Figs. 5.14a – e. Crosses (lower panels) represent the backazimuth-corrected dispersion curves. Only the average corrected curve is shown for each profile, however, for inversion, twenty different curves with random errors ranging ± 0.06 km/s around this corrected curve are used exactly in the same way as in the tests described previously. Twenty dispersion curves obtained by the inversion are shown as gray lines. We see that all twenty curves are almost identical although the corresponding twenty velocity models differ. This is due to the non-uniqueness of the dispersion curve inversion – the same dispersion curve can be obtained from different velocity models. The resultant mean structure is shown as the red line and its standard deviations as gray lines in each upper panel of Fig. 5.14.

We obtain five velocity structures for the five profiles which, in general, differ from each other. The standard deviations of the estimated structures are nearly the same for all the profiles, see Table 5.5 (upper line), although the scattering of the twenty inverted dispersion curves varies considerably from profile to profile, Table 5.5 (lower line). The lowest dispersion curve error of 0.019 km/s (the best misfit) is obtained for the TBR/KHC-MOX profile. Its dispersion curve is of a smooth monotonic shape, and the inversion thus matches it almost perfectly for the whole period range. Contrary to this, the worst misfit is obtained for the most undulated dispersion curve corresponding to the TBR-HAJ profile (0.058 km/s). Note that, as expected, the test examples are characterized by significantly smaller misfits.

Fig. 5.14 allows us to compare the structures along the individual profiles. It shows certain common features (high-gradient subsurface layers, no sharp Moho discontinuity) as well as distinct qualitative differences (LVZ).

The two eastern TBR-HAJ and HAJ-NEC sub-profiles, crossing the Moldanubian and Teplá-Barrandian units (Fig. 5.2), display LVZ in the middle crust (Fig. 5.14c and d). The high gradient in the depth range of 32 – 40 km can be interpreted as a manifestation of the Moho discontinuity. This blurring of the discontinuity over several layers can also be seen in the test example in Figs. 5.6 and 5.7, and we cannot thus distinguish whether it is a real structural feature or only an artifact of the method. The third NEC-NKC sub-profile crossing the Eger Rift (boundary between the Teplá-Barrandian and Saxothuringian units, Fig. 5.2) displays a nearly constant increase of velocity across the whole crust (Fig. 5.14b). No gradient increase is seen there. The last sub-profile, the most western NKC-MOX, crossing the Saxothuringian unit (Fig. 5.2), is characterized by nearly constant v_s in the middle crust (Fig. 5.14a). Contrary to the two eastern TBR-HAJ and HAJ-NEC sub-profiles, the NKC-MOX sub-profile displays a much weaker gradient increase spread over a larger depth interval (20 km to 40 km). This range is too wide to be interpreted as an inversion artifact. Hence, the two western sub-profiles show no indication of the Moho.

The long TBR/KHC-MOX profile shows nearly constant v_s in the middle crust below the high-gradient in the upper 4 km (Fig. 5.14e). Its structure is qualitatively similar to that obtained for the NKC-MOX sub-profile, however, in this case, the high gradient in the narrower depth range of 32 – 40 km can be interpreted as an indication of the Moho discontinuity.

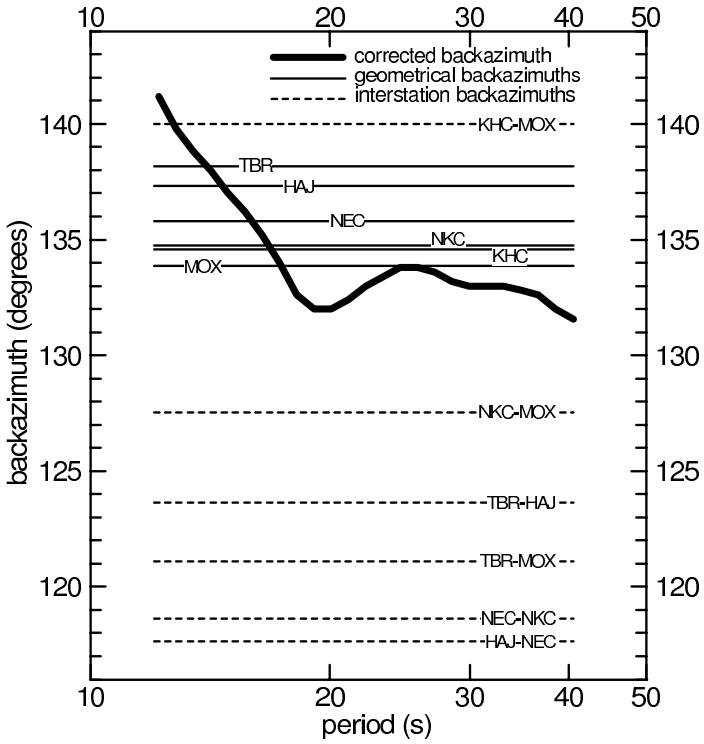


Figure 5.12: (*Fig. 12 in Kolínský et al., 2010*) The bold black line represents the corrected backazimuths of propagation for different periods of Love waves. Thin solid lines show geometrical backazimuths for all six stations (averages for the three events). Dashed lines represent inter-station backazimuths.

5.2.10 Discussion

We have found a v_s distribution for both long profiles and the short sub-profiles. The agreement of the averaged sub-profile dispersion curve with the TBR-MOX long-profile one (Fig. 5.11) suggests that local lateral inhomogeneities do not influence the propagation azimuths of the waves in the given period range.

We would like to verify the results by comparison with the results published by other authors, if available. Note that we can only compare our results with studies yielding structures representing whole profiles and not with those representing local structures beneath individual stations (e.g., obtained by the receiver function method).

Concerning the long profiles, the only comparison possible is for the KHC-MOX profile. There are no suitable studies for comparison with our TBR-MOX profile. In Fig. 5.15 we present a comparison with the v_s structure by Plešinger et al. (1991). Plešinger's KHC-MOX v_s structure (dashed blue) is estimated for the crust and upper mantle using the surface wave period range from 10 to 100 s. We show the result for the backazimuth-corrected TBR/KHC-MOX dispersion curve (Fig. 5.13a) as the bold red line, and as the bold green line we also show the result obtained using the same methodology for the original KHC-MOX profile (with no backazimuth correction, Fig. 5.11a). This original KHC-MOX profile corresponds geographically exactly to the Plešinger's KHC-MOX profile. We see that the differences between our KHC-MOX and the TBR/KHC-MOX profiles are very small and both match Plešinger's model well. The most striking difference between our and his study concerns the upper 7 kilometers. In our study, the subsurface structure is characterized by a considerably lower velocity which is compensated by higher velocities in other layers. The explanation is that Plešinger's model has a small number of layers for the whole crust and, therefore, it cannot be as detailed. The total depth of our first three layers corresponds to the thickness of the first layer in Plešinger's model. The velocity averaged over our first three layers roughly corresponds to the velocity in his first layer. In the middle crust, both our and his measurements yield very similar velocities. Another feature is Plešinger's distinct discontinuity (Moho) at a depth of 32 km, which is replaced by a gradient zone in our study, since our approach is not capable of revealing sharp discontinuities, see also the synthetic test section. On the other hand, it is questionable whether Plešinger's distinct Moho is a real structural feature and not only an artifact of his method (model parameterization).

As regards the four sub-profiles, only a few v_s models are available for comparison, e. g., Malinowski (2005). He found a quasi-2D structure from surface waves along the C09 profile, see Fig. 5.2, roughly coinciding with our segmented TBR-MOX profile. Due to the short periods considered in his study, his results cover only depths down to 2 km. Malinowski refers to the lower sub-surface velocities in the Saxothuringian unit (western part of the C09 profile) than in the Moldanubian unit (eastern part of the C09 profile). Our result give nearly the same velocities around 2.90 – 2.95 km/s in the 2 km uppermost layer for all four sub-profiles what is in agreement with the velocity range of 2.5 – 3.4 km/s given by Malinowski for the same depth.

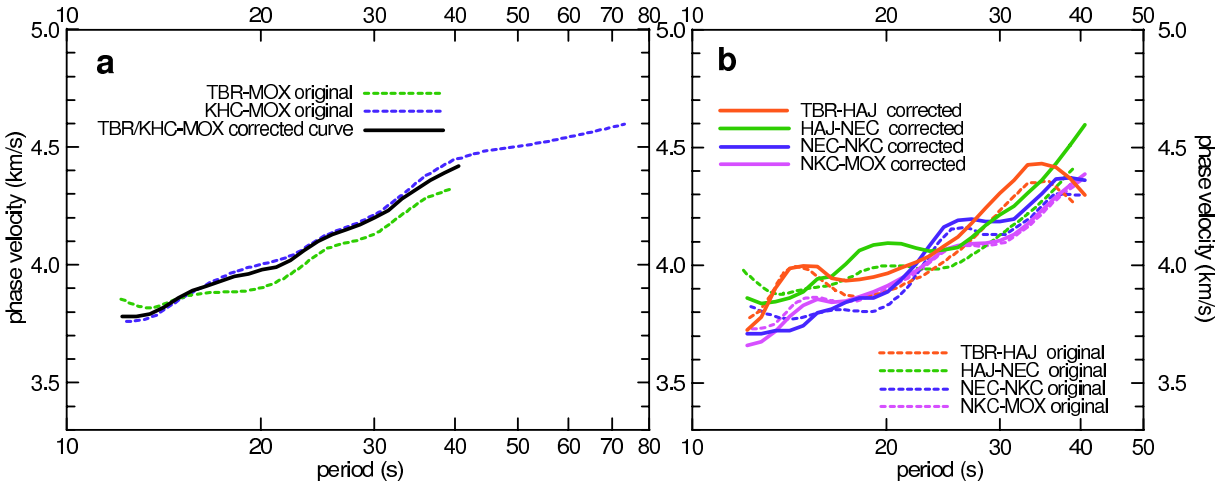


Figure 5.13: (*Fig. 13 in Kolínský et al., 2010*) Corrected dispersion curves (bold) in comparison with measured ones (dashed). Two long profiles (panel **a**) were used for estimating the corrected curve, which is shown as solid black line. Corrected dispersions are shown (panel **b**) using the same correction applied to the four sub-profiles. Dashed dark-colored lines are the same as in Fig. 5.11 in both panels **a** and **b**.

		TBR/KHC-MOX		TBR-HAJ		HAJ-NEC		NEC-NKC		NKC-MOX	
d	h	v_s	rms	v_s	rms	v_s	rms	v_s	rms	v_s	rms
2	0	2.94	0.133	2.91	0.109	2.95	0.138	2.88	0.152	2.88	0.105
2	2	3.41	0.215	3.45	0.154	3.48	0.208	3.27	0.169	3.24	0.168
4	4	3.68	0.135	3.69	0.152	3.79	0.103	3.44	0.137	3.52	0.133
4	8	3.69	0.084	3.80	0.118	3.86	0.095	3.55	0.081	3.67	0.125
4	12	3.69	0.100	3.77	0.092	3.80	0.082	3.58	0.124	3.71	0.112
4	16	3.69	0.120	3.77	0.094	3.74	0.078	3.68	0.157	3.74	0.083
4	20	3.73	0.121	3.76	0.116	3.72	0.087	3.79	0.199	3.75	0.106
4	24	3.81	0.162	3.77	0.120	3.67	0.122	3.97	0.172	3.78	0.112
4	28	3.87	0.169	3.82	0.136	3.70	0.163	4.22	0.152	3.84	0.182
4	32	4.15	0.187	4.06	0.265	3.91	0.200	4.40	0.185	3.98	0.220
4	36	4.34	0.149	4.44	0.179	4.29	0.226	4.58	0.137	4.29	0.223
hsp.	40	4.73	0.072	4.74	0.070	4.87	0.055	4.66	0.042	4.64	0.060

Table 5.4: Mean shear wave velocities for all five profiles TBR/KHC-MOX, TBR-HAJ, HAJ-NEC, NEC-NKC and NKC-MOX, see also Fig. 5.14. Explanations: d = thickness of layer (km), h = depth of the layer's upper boundary (km), v_s = mean shear wave velocity (km/s), rms = standard deviation (km/s).

Other studies dealing with profile measurements in the region of our sub-profiles concern P-waves only and, therefore, any comparison with these results is very questionable, since v_s structural features may not even qualitatively be manifested in the v_p structure. For example, the presence of the LVZ in the v_s model does not imply that the LVZ must be present also in the v_p distribution. On the other hand, the LVZ in v_p model indicates that similar behavior can be seen also in the v_s structure. This is due to the physical processes which can cause the decrease of both v_p and v_s at the same time, or the decrease of v_s only. For example partial melting would affect v_s more seriously than the v_p. Beránek (1971) found the LVZ in the v_p distribution using reflection for Moldanubian and Teplá-Barrandian units. Since we have found the LVZ for the same two units for v_s as well, we think that our results may be realistic in this respect. Růžek at al. (2007) also found very low values down to the lower crust only for the Moldanubian unit, but report increasing v_p for the other two units. However, the fact that they did not find the LVZ in the v_p distribution in the Teplá-Barrandian unit does not imply that the LVZ cannot be found in the v_s distribution.

Another feature qualitatively comparable both in v_p and v_s structures is the presence of the Moho discontinuity. Hrubcová et al. (2005) found evidence of a distinct Moho at the depth of 39 km for the Moldanubian unit and 35 km for the Teplá-Barrandian unit. As discussed above, our methodology is unable to determine a sharp Moho. Both their Moho depths fall within the range of the high-gradient zone found in our study for these two units. For the Saxothuringian unit, they suggest a laminated lower crust structure without any clear Moho discontinuity, which is in agreement with our results for this unit.

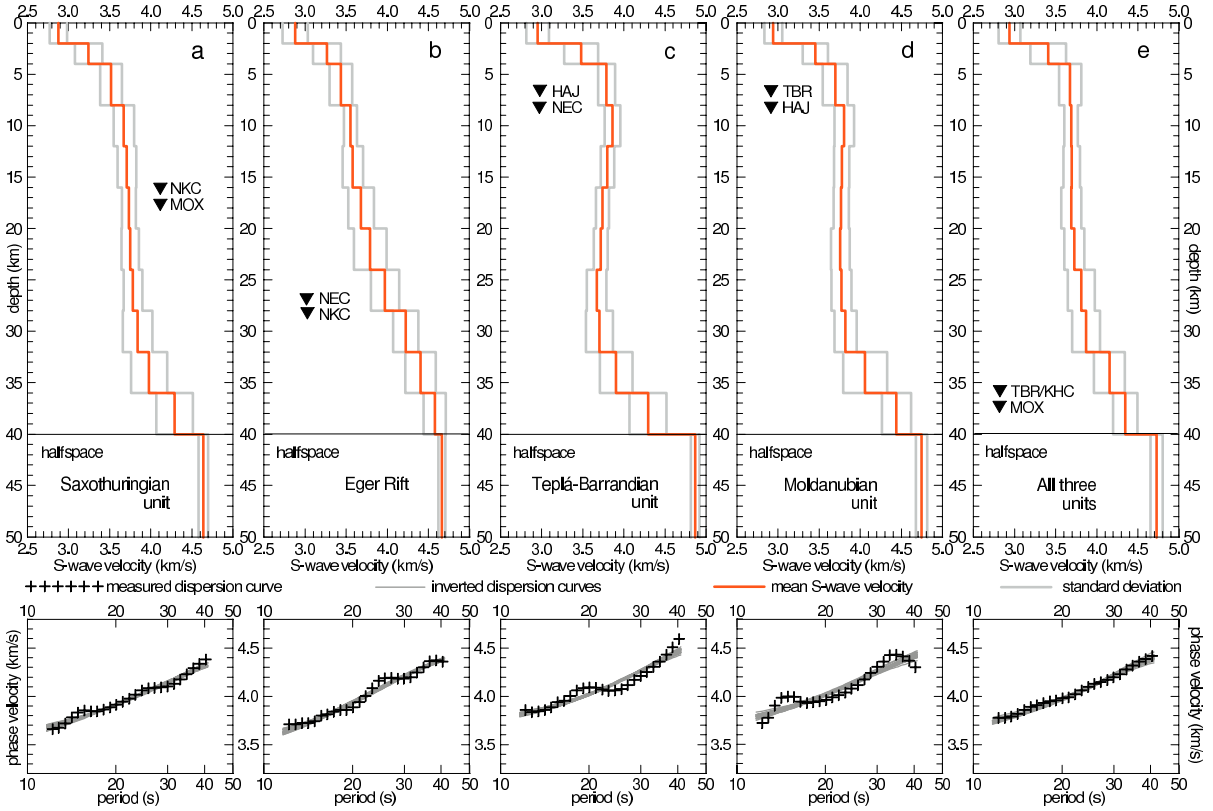


Figure 5.14: (*Fig. 14 in Kolínský et al., 2010*) Determined v_s structures: (**a**–**d**) four short sub-profiles and (**e**) TBR/KHC-MOX long profile. Standard deviations (gray lines) of mean S-wave velocities (bold red line) from the twenty found models are presented. Crosses in the lower panels represent the backazimuth-corrected dispersion curves entering the inversion. Twenty dispersion curves found by the inversion are shown as dark gray lines.

Comparing the shear wave velocity distributions of the four sub-profiles (Fig. 5.14), we see that three of them, which are fully included in one of the units, present similar features. TBR-HAJ profile (Moldanubian unit) reveals nearly constant shear wave velocities in a broad range of depths from 8 to 32 km with slight LVZ. The non-increasing shear wave velocity is probably a consequence of the old sedimentary composition of the whole unit. Even the Moldanubian unit was highly metamorphosed, it still keeps its nearly homogeneous composition from the Proterozoic age. HAJ-NEC profile (Teplá-Barrandian unit) is characterized by significant LVZ in the middle crust, what would correspond to its only slightly (if at all) metamorphosed sedimentary composition. Its LVZ is more pronounced than it is in the Moldanubian unit, but both units follow nearly the same general shear wave velocity distribution what confirms their similar age. The depths 4 – 12 km are characterized by slightly lower velocities in the Moldanubian than in the Teplá-Barrandian unit, what may be caused by the intrusions which penetrated the Moldanubian unit during the Variscan age (Central Bohemian Pluton). NKC-MOX profile (Saxothuringian unit) has the same shear wave velocities as both latter units from the depths of 16 km down to the upper mantle, however, its upper crust velocities in the depth range of 2 – 16 km are even lower than those of the Moldanubian, what may be again caused by the Variscan intrusions.

NEC-NKC profile, which crosses the Teplá-Barrandian and Saxothuringian unit border, is distinctively

	TBR/KHC-MOX	TBR-HAJ	HAJ-NEC	NEC-NKC	NKC-MOX	inversion TEST	combined TEST
Mean rms (km/s) (shear wave vel.)	0.137	0.134	0.130	0.142	0.136	0.129	0.128
Mean fit error (km/s) (phase vel.)	0.019	0.058	0.049	0.031	0.028	0.010	0.013

Table 5.5: Upper line presents deviations computed as an average of the rms deviations for all layers in each profile; see Table 5.4. Bottom line presents the error computed as the average distance between the measured dispersion curve and the twenty inverted dispersion curves; see Fig. 5.14, lower panels. The five measured profiles are complemented by the same information for the test structures from Figs. 5.6 and 5.7.

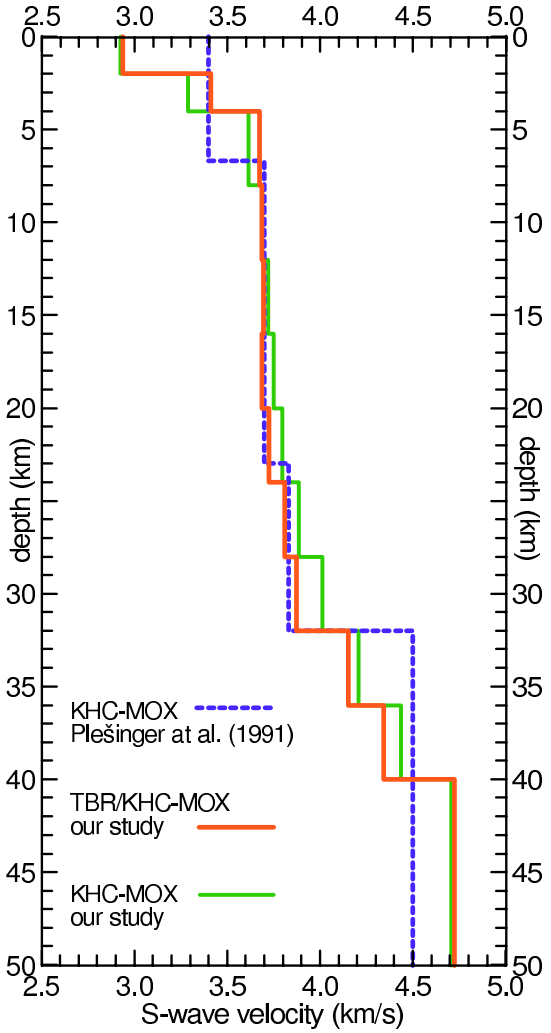


Figure 5.15: (*Fig. 15 in Kolínský et al., 2010*) A comparison of our TBR/KHC-MOX profile (backazimuth-corrected), KHC-MOX profile (uncorrected) with the surface wave profile KHC-MOX measured by Plešinger et al. (1991).

different. Shear wave velocities along the whole depth range differs significantly from those for the other three profiles. They are lower in the upper crust (4 – 16 km) and higher in the lower crust and upper mantle (16 – 40 km). The contact between Teplá-Barrandian and Saxothuringian unit is formed by the Eger Rift, which is filled by Tertiary sediments and by products of Neogenic volcanism. The profile also crosses the area of seismic swarm activity around the village of Nový Kostel (near the station NKC). The hypocenter depths of the swarm activity are around 8 – 12 km and the origin of the swarms are believed to be caused by fluid redistribution. The region is also known for higher heat flow. Both the presence of fluids and higher temperature would correspond to lower shear wave velocities observed in that depth range. Higher velocities in the lower crust are a consequence of nearly missing Moho, what is possibly caused by updoming of the upper mantle, as described by Heuer et al. (2006).

Although none of the above mentioned studies made by other authors contradicts our findings, we are aware that the found 1D structures represent only averaged velocity distributions along profiles. Moreover, several important phenomena have been omitted both by us and by the other authors as well. For example, attenuation or anisotropy has not been taken into account. The reason is that there is a lack of information. Anisotropy of the region of interest is discussed in the paper by Plomerová et al. (2007) who reveal different patterns of teleseismic P-wave anisotropy beneath the Moldanubian, Teplá-Barrandian and Saxothuringian units. However, these results concern only the upper mantle and no conclusions are made for the crustal structure we are interested in.

5.2.11 Conclusion

The phase velocity dispersion curves of Love waves, generated by moderate regional earthquakes, are analyzed to estimate v_s in the crust of the western part of the Bohemian Massif. The reliability of both measurement and inversion is benchmarked by tests. Two profiles crossing three main geological units of the Bohemian Massif are investigated. A comparison of our v_s models with those previously published for the same region shows a generally good agreement.

We propose detailed 1D models of v_s for both the long TBR/KHC-MOX profile as well as for the sub-

profiles of the TBR-MOX profile, where only v_p were measured in the past. We found that the dispersion curves of the sub-profiles are non-monotonic. Such curves cannot be interpreted in detail using forward modeling as their shape is complicated and hence cannot be described fully by the inversion. We suggest that the undulations of phase velocity curves are caused by different backazimuths of propagation with respect to period and we find the corrected backazimuths using the two long profiles KHC-MOX and TBR-MOX as the reference profiles. The dispersion curves corrected for the true backazimuths have slightly smaller undulations for some sub-profiles and become steeper. However, the undulations cannot be explained by the corrected backazimuth fully. The inversion of undulated dispersion curves yields larger misfit errors in comparison with the smooth TBR/KHC-MOX long profile curve, but standard deviations of sub-profile v_s are of the same order as for the inversion of the long profile. The two eastern parts of the TBR-MOX profile (TBR-HAJ and HAJ-NEC sub-profiles) display LVZ at depths of 12 to 28 km what is connected with their old sedimentary origins. The Moho discontinuity is manifested along the two eastern sub-profiles and is missing along the two western sub-profiles, what may be caused by the upper mantle updoming. NEC-NKC profile shear wave velocities of the Eger Rift are significantly different than those of the other three profiles crossing consolidated units of the Bohemian Massif. Subsurface (first layer) shear wave velocity is nearly the same for all four sub-profiles (around 2.9 km/s) suggesting that the uppermost crust is not influenced much by old Variscan tectonic processes.

5.2.12 Acknowledgements

This research was supported by Grants No. A300460602 and No. A300460705 of the Grant Agency of the Academy of Sciences of the Czech Republic, by Grant No. 205/06/1780/A of the Czech Science Foundation and by the Institute's Research Plan No. A VOZ30460519. This work was also supported in part by the Ministry of Education, Youth and Sports of the Czech Republic, Project No. MSM0021620860. Data from two of the stations used in this study were kindly provided by Jan Zedník of the Czech Regional Seismic Network, Geophysical Institute, Academy of Sciences of the Czech Republic, v.v.i. We thank Oldřich Novotný for programs and consultations concerning matrix method computations. We are grateful to Monika Wilde-Piórko for providing her results. Two of the figures were made using Generic Mapping Tools by Wessel and Smith (1998). We are grateful to RWE Transgas, s.r.o., for providing the data from station HAJ. We also thank two anonymous reviewers for their suggestive comments.

5.2.13 References

Beránek, B., 1971: Study of the velocity conditions in the Earth's crust in the regions of the Bohemian Massif and the Carpathian system along international profiles VI and VII, *Stud. Geophys. Geod.*, 15, 316–330.

Beránek, B., Mayerová, M., Zounková, M., Guterch, A., Materzok, R. and Pajchel, J., 1973: Results of deep seismic sounding along international profile VII in Czechoslovakia and Poland, *Stud. Geophys. Geod.*, 17, 205–217.

Beránek, B. and Zounková, M., 1977: Investigations of the Earth's crust in Czechoslovakia using industrial blasting, *Stud. Geophys. Geod.*, 21, 273–280.

Bouchon, M., 1981: A simple method to calculate Green's functions for elastic layered media, *Bull. Seism. Soc. Am.*, 71, 959–971.

Cháb, J., Šrámek, J., Pokorný, L., Chlupáčová, M., Manová, M., Vejnar, Z., Waldhausrová, J. and Žáček, V., 1997: Geological interpretation of major regional units – the Teplá-Barrandian Unit, in: Vrána, S. and Štědrá, V. (eds): *Geological model of Western Bohemia related to the KTB borehole in Germany*, Czech Geological Survey, Prague, 80–104.

Dziewonski, A., Bloch, S. and Landisman, M., 1969: A technique for the analysis of transient seismic signals. *Bull. Seism. Soc. Am.*, 59, 427–444.

Dziewonski, A., Mills, J. and Bloch, S., 1972: Residual dispersion measurement – a new method of surface-wave analysis, *Bull. Seism. Soc. Am.*, 62, 129–139.

Forbriger, T., 2003a: Inversion of shallow-seismic wavefields. Part I: Wavefield transformation, *Geophys. J. Int.*, 153, 719–734.

Forbriger, T., 2003b: Inversion of shallow-seismic wavefields. Part II: Infering subsurface properties from wavefield transforms, *Geophys. J. Int.*, 153, 735–752.

Gabriels, P., Snieder, R. and Nolet, G., 1987: In situ measurements of shear wave velocity in sediments with higher-mode Rayleigh waves, *Geophys. Prospect.*, 35, 187–196.

Guterch, A., Grad, M., Keller, G. R., Posgay, K., Vozár, J., Špičák, A., Brückl, E., Hajnal, Z., Thybo, H., Selvi, O. and CELEBRATION 2000 experiment team, 2003: CELEBRATION 2000 seismic experiment, *Stud. Geophys. Geod.*, 47, 659–669.

Heuer, B., Geissler, W. H., Kind, R. and Kämpf, H., 2006: Seismic evidence for asthenospheric updoming beneath the western Bohemian Massif, central Europe, *Geophys. Res. Lett.*, 33, L05311, doi: 10.1029/2005GL025158.

Heuer, B., Kämpf, H., Kind, R. and Geissler, W. H., 2007: Seismic evidence for whole lithosphere separation between Saxothuringian and Moldanubian tectonic units in central Europe, *Geophys. Res. Lett.*, 34, L09304, doi: 10.1029/2006GL029188.

Hrubcová P., Środa P., Špičák A., Guterch A., Grad M., Keller G. R., Brueckl E., and Thybo H., 2005: Crustal and uppermost mantle structure of the Bohemian Massif based on CELEBRATION 2000 data, *J. Geophys. Res.*, 110, B11305.

Kolínský, P., 2004: Surface wave dispersion curves of Eurasian earthquakes: the SVAL program, *Acta Geodyn. Geomater.*, 1 (134), 165–185.

Kolínský, P. and Brokešová, J., 2007: The Western Bohemia uppermost crust shear wave velocities from Love wave dispersion, *Journal of Seismology*, 11, 101–120.

Kolínský, P. and Brokešová, J., 2008: The Western Bohemia uppermost crust Rayleigh wave tomography, *Acta Geodyn. Geomater.*, 5 (149), 5–17.

Levshin, A. L., Pisarenko, V.F. and Pogrebinsky, G.A., 1972: On a frequency-time analysis of oscillations, *Ann. Geophys.*, 28, 211–218.

Levshin, A. L., Yanovskaya, T. B., Lander, A. V., Bukchin, B. G., Barmin, M. P., Ratnikova, L. I. and Its, E. N., 1989: Interpretation of surface wave observations – frequency-time analysis, in: Keilis-Borok, V. I. (ed.): *Seismic surface waves in a laterally inhomogeneous Earth*, Kluwer Academic Publishers, Dordrecht/Boston/London, 153–163.

Levshin, A. L., Ratnikova, L. and Berger, J., 1992: Peculiarities of surface-wave propagation across Central Eurasia, *Bull. Seism. Soc. Am.*, 82, 2464–2493.

Málek, J., Brož, M., Fischer, T., Horálek, J., Hrubcová, P., Janský, J., Novotný, O., Růžek, B. and the CELEBRATION working group, 2001: Seismic measurements along short profiles in Western Bohemia during the CELEBRATION 2000 experiment, *Acta Montana*, 18 (121), 15–28.

Málek, J., Horálek, J. and Janský, J., 2005: One-dimensional qP-wave velocity model of the upper crust for the West Bohemia/Vogtland earthquake swarm region, *Stud. Geophys. Geod.*, 49, 501–524.

Málek, J., Růžek, B., Kolář, P., 2007: Isometric method: efficient tool for solving non-linear inverse problems, *Stud. Geophys. Geod.*, 51, 469–491.

Malinowski, M., 2005: Analysis of Short-Period Rayleigh Waves Recorded in the Bohemian Massif Area During CELEBRATION 2000 Experiment, *Stud. Geophys. Geod.*, 49, 485–500.

Maupin, V., 2001: A multiple-scattering scheme for modelling surface wave propagation in isotropic and anisotropic three-dimensional structures, *Geophys. J. Int.*, 146, 332–348.

Maupin, V., 2002: The amplitude of the Love-Rayleigh discrepancy created by small-scale heterogeneities, *Geophys. J. Int.*, 150, 58–64.

Maupin, V., 2007: Introduction to mode coupling methods for surface waves, in: Wu, R.-S. and Maupin, V. (eds.): *Advances in wave propagation in heterogeneous Earth, Advances in geophysics*, vol. 48, chapter 2, Elsevier, 127–155.

McEvilly, T. V., 1964: Central U.S. crust-upper mantle structure from Love and Rayleigh wave phase velocity inversion, *Bull. Seism. Soc. Am.*, 54, 1997–2015.

McMechan, G. A. and Yedlin, M. J., 1981: Analysis of dispersive waves by wave field transformation, *Geophysics*, 46, 869–874.

Mitra, S., Priestley, K., Gaur, V. K. and Rai, S. S., 2006: Shear-wave structure of the South Indian lithosphere from Rayleigh wave phase-velocity measurements, *Bull. Seism. Soc. Am.*, 96, 1551–1559.

Mlčoch, B., Schulmann, K., Šrámek, J., Manová, M., Pokorný, L., Fiala, J. and Vejnar, Z., 1997: Geological interpretation of major regional units – the Saxothuringian zone, in: Vrána, S. and Štědrá, V. (eds): *Geological model of Western Bohemia related to the KTB borehole in Germany*, Czech Geological Survey, Prague, 51–61.

Nafe, J. E. and Brune, J. N., 1960: Observations of phase velocity for Rayleigh waves in the period range 100 to 400 seconds, *Bull. Seism. Soc. Am.*, 50, 427–439.

NEIC (National Earthquake Information Center), 2006: PDE Catalog, Washington, US, neic.usgs.gov.

Novotný, O., Málek, J., 2002: Note of the direct computation of geodetic distances and azimuths on an ellipsoid of revolution, *Acta Montana*, 22 (129), 75–78.

Plešinger, A., Neunhöfer, H. and Wielandt, E., 1991: Crust and upper mantle structure of the Bohemian Massif from the dispersion of seismic surface waves, *Stud. Geophys. Geod.*, 35, 184–195.

Plomerová, J., Achauer, U., Babuška, Vl., Vecsey, L. and BOHEMA working group, 2007: Upper mantle beneath the Eger Rift (Central Europe): plume or asthenosphere upwelling?, *Geophys. J. Int.*, 169, 675–682.

Proskuryakova, T.A., Novotný, O. and Voronina, E. V., 1981: Studies of the Earth's structure by the surface-wave method (Central Europe) (Izuchenie stroeniya Zemli metodom poverkhnostnykh voln (Tsentral'naya Evropa)), Nauka, Moscow, in Russian, 92 pp.

Růžek B., Hrubcová P., Novotný M., Špičák A., Karousová O., 2007: Inversion of travel times obtained during active seismic refraction experiments CELEBRATION 2000, ALP 2002 AND SUDETES 2003, *Stud. Geophys. Geod.*, 51, 141–164.

Stange, S. and Friederich, W., 1993: Surface wave dispersion and upper mantle structure beneath southern Germany from joint inversion of network recorded teleseismic events, *Geophys. Res. Lett.*, 20 (21), 2375–2378.

Švancara, J. and Chlupáčová, M, 1997: Gravimetry – Density model of geological structure along the profile 9HR, in: Vrána, S. and Štědrá, V. (eds): *Geological model of Western Bohemia related to the KTB borehole in Germany*, Czech Geological Survey, Prague, 32–35.

Tomek, Č., Dvořáková, V. and Vrána, S., 1997: Geological interpretation of the 9HR and 503M seismic profiles in Western Bohemia, in: Vrána, S. and Štědrá, V. (eds): *Geological model of Western Bohemia related to the KTB borehole in Germany*, Czech Geological Survey, Prague, 43–50.

Vrána, S., Šrámek, J., Pokorný, L., Manová, M., Chlupáčová, M., 1997: Geological interpretation of major regional units – the Moldanubian Zone, in: Vrána, S. and Štědrá, V. (eds): *Geological model of Western Bohemia related to the KTB borehole in Germany*, Czech Geological Survey, Prague, 104–123.

Wessel, P., and Smith, W. H. F., 1998: New, improved version of generic mapping tools released, *Eos Trans. AGU*, 79 (47), 579.

Wielandt, E., Sigg, A., Plešinger, A. and Horálek, J., 1987: Deep structure of the Bohemian Massif from phase velocities of Rayleigh and Love waves, *Stud. Geophys. Geod.*, 31, 1–7.

Wilde-Piórko, M., Saul, J. and Grad, M., 2005: Differences in the crustal and uppermost mantle structure of the Bohemian Massif from teleseismic receiver functions, *Stud. Geophys. Geod.*, 49, 85–107.

Yoshida, Y. and Suetsugu, D., 2004: Lithospheric thickness beneath the Pitcairn hot spot trail as inferred from Rayleigh wave dispersion, *Phys. Earth Planet. Inter.*, 146, 75–85.

Yoshizawa, K. and Kennett, B. L. N., 2002: Determination of the influence zone for surface wave paths, *Geophys. J. Int.*, 149, 440–453.

here the original text of the paper ends

5.3 What is not included in the paper

comparison with v_p studies

While preparing the manuscript, we proposed another comparison with studies dealing with P-wave velocities. By the same method as described in the paper, we determined also the shear wave velocity distribution between stations TBR and NKC, see Fig. 5.16, since several v_p studies were made along nearly the same profile. We included this comparison in the thesis to show alternative approach to the study of the crust. However, the comparison was finally excluded from the manuscript.

We used the digitized v_p models of Earth crust blocks along DSS profile VI (see Fig. 5.16 and also 5.2). Tables with the respective values were published by Novotný, O. and Urban (1988). We used only blocks A to D (Fig. 5.16), which correspond to our localization of profile TBR-NKC in the Bohemian Massif. We do not discuss the differences among these four blocks as the present idea of distribution of geological units in this region is different from that in 1960s, when the DSS measurement was made.

For another comparison, we made a 1D v_p structure by weighted averaging of the 2D model presented by Hrubcová et al. (2005) for profile C09 of the CELEBRATION project (see Figs. 5.2 and 5.16). We averaged the appropriate part of this profile. The latter structure is very similar to the DSS results with slower velocities in the middle crust and higher velocities in the lower crust.

Comparable results were obtained by averaging the 2D v_p model by Růžek et al. (2007) which was also derived from C09 data. This model presents higher velocities in the middle crust with an indication of a LVZ in the lower crust. While comparing the results obtained from body waves with those obtained from surface waves, we remind that surface waves at the same profile sample broader region due to their longer periods than do the body waves.

Despite the fact that latter three publications present somewhat different results for nearly the same profile, we herein show a v_p/v_s ratio computed using our v_s for profile TBR-NKC and v_p for profiles DSS and C09, see Fig. 5.17. We see a general agreement between the particular v_p models.

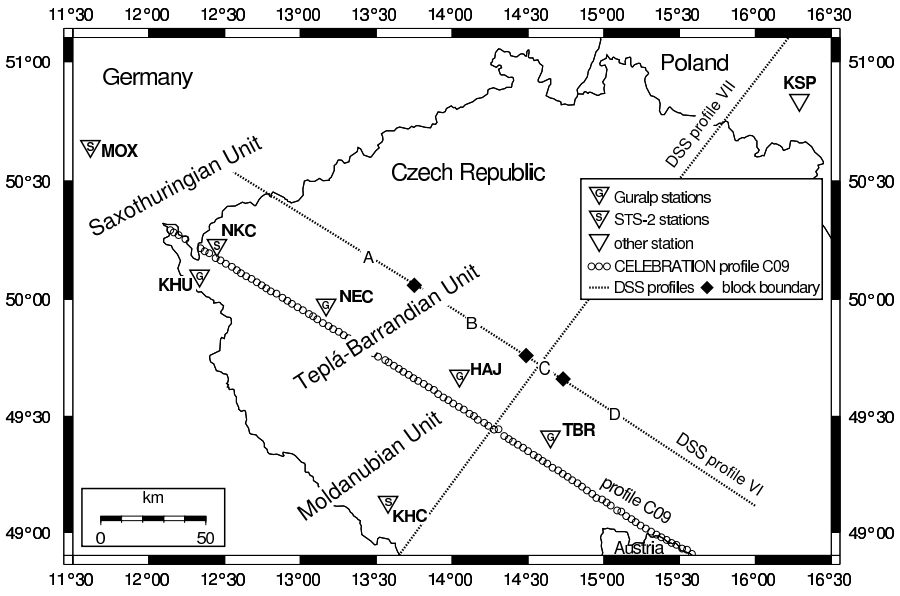


Figure 5.16: Map of the Czech Republic with stations and profiles marked. As opposed to the map in Fig. 5.2, additional stations and profiles are shown here.

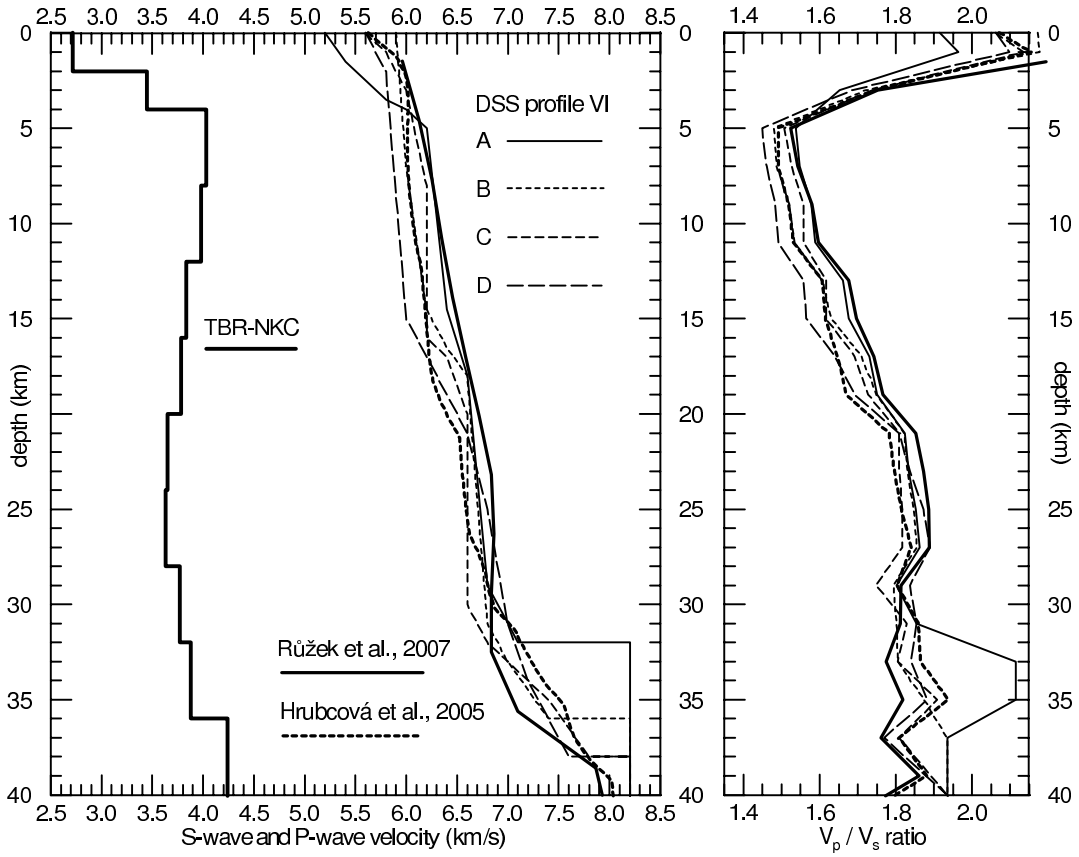


Figure 5.17: A comparison of profile TBR-NKC with DSS profile VI (Novotný, O. and Urban, 1988) and CELEBRATION C09 (Hrubcová et al., 2005 and Růžek et al., 2007) v_p structures. For the block division along the DSS profile VI, see Fig. 5.16. The v_p/v_s ratio for all compared structures is shown.

The strongest features are the relatively high v_p/v_s ratio values in the uppermost layers and extremely low v_p/v_s ratio between the depths of 5 and 10 km. The models differ substantially below the 30 km and we do not make any conclusion for these depths. Some notes to the v_p/v_s ratio problem concerning the Wester Bohemia region can be found in Kolář and Boušková (2003).

Another interesting feature of the presented models is the high v_p/v_s ratio in the middle crust with its maximum between 21 – 27 km, reaching the value of 1.80 – 1.88. The reason for such unusually high ratio values in the middle crust is that, unlike S-waves, P-waves do not indicate a LVZ. In the papers of Beránek (1971) and Beránek et al. (1973), the authors mentioned the presence of v_p LVZ in the structure from DSS, but they did not resolve it well and rather proposed a monotonously increasing v_p for the whole crust. Plešinger at al. (1991) also argued that there is an indication of v_p LVZ in the DSS profile VI data. Hrubcová et al. (2005) mentioned the possibility of LVZ in the C09 profile data but they did not implement this fact into the inversion. They also proposed the idea that the v_p/v_s ratio does not change considerably in the crust. The 2D model of Růžek et al. (2007) revealed the LVZ in some parts of the profile. We therefore consider their v_p model as the most appropriate. While averaging their 2D model into a 1D for comparison with our results, a small LVZ can be seen around the depth of 30 km. However, this does not make any difference concerning the unusual v_p/v_s ratio. In Table 5.6 the results for comparison with the model by Růžek et al. (2007) are given.

Unusual v_p/v_s ratio could be disputed only if the v_p or v_s models were not correct. This may apply for the uppermost layer, where, probably, v_p are too high. However, concerning the middle crust, the v_p models from all previous studies (which were obtained independently) are consistent and reach the value of 6.50 – 6.75 km/s at the depth of 21 km. The LVZ in our resulting v_s model for TBR-NKC is also well pronounced and reliable, as the test of analysis and inversion proved. So, any major errors are improbable in either v_p or v_s models. We therefore consider the high value of the v_p/v_s ratio in the middle crust to be realistic.

One of the possible geological interpretations of v_p/v_s anomaly (due to low v_s) is the presence of partly melted rocks. The idea of magma injection to the crust was formulated by Špičák et al. (1999) for the Western Bohemia region (in the NW edge of our profile), which is characterized by post-volcanic activity. Our result, however, is the average model for the whole profile TBR-KHU about 170 km long, crossing three geological units. In case of 1D model, the volume of (partly) melted rock would be enormous. The

TBR-NKC			C09 by Růžek et al. (2007)		
d	h	v_s	z	v_p	v_p/v_s
2	0	2.72	1.5	5.96	2.20
2	2	3.45	3	6.04	1.75
4	4	4.03	5	6.15	1.52
			7	6.22	1.54
4	8	3.98	9	6.29	1.58
			11	6.36	1.60
4	12	3.83	13	6.43	1.68
			15	6.51	1.70
4	16	3.78	17	6.59	1.74
			19	6.68	1.77
4	20	3.65	21	6.76	1.85
			23	6.83	1.87
4	24	3.63	25	6.85	1.89
			27	6.86	1.89
4	28	3.77	29	6.84	1.81
			31	6.84	1.81
4	32	3.88	33	6.88	1.77
			35	7.05	1.82
4	36	4.24	37	7.46	1.76
			39	7.89	1.86
halfspace	40	4.47	40	7.93	1.77

Table 5.6: Resulting shear wave velocities for profile TBR-NKC in the Bohemian Massif and v_p/v_s ratio using v_p from Růžek et al. (2007) and v_s of TBR-NKC. Explanations: d = thickness of layer (km), h = depth of the layer's upper boundary, v_s = shear velocity (km/s) and z = depth.

other possibility is the existence of smaller magma chambers with very low v_s, which decreases the average value for the whole profile. In this case the v_s model would be strongly laterally inhomogeneous. This is confirmed by the complicated dispersion curves obtained from short profiles (Fig. 5.11b). However, the exact location of the magma chambers cannot be done only by interpretation of surface waves.

phase velocity measurement in the time domain

One more figure is presented here to explain the phase velocity measurement in the time domain by an example of broad period range of harmonic signals. Fig. 5.18 shows two records from two stations, shifted in time by 17 s, similarly as in Fig. 5.4. The red record is from the station closer to the epicenter, the blue one from the more distant station. Short period part of the spectrum starting from 3 s represents complicated signals with unclear surface wavegroups. In each record, we see several envelope peaks with no correlation to the other record. Starting by the period of 5.3 s, we see that the shape of the envelopes begins to be similar, however, around the period 7.2 s two peaks at the blue record appear and only one peak at the red record is present at the same time. For periods longer than 8.0 s the records are coherent and the phase velocity measurement by their cross-correlation is straightforward. Between the periods of 17 and 24 s the time shift of 17 s between the records, corresponding to the phase velocity of 4.0 km/s, gives us very precise estimate of the true phase velocity. For the shorter range, the red record (closer) comes earlier – the time shift (exactly given by cross-correlation) between the phases is more than 17 s and hence the phase velocity is lower. For the periods longer than 24 s, the blue record is apparently before the red one – the time shift between them should be smaller and it means, the phase velocity is higher.

phase velocity measurement by spectral method

As we mentioned in paragraph 5.2.5, we started our phase velocity measurement by computing the differences of record phases in the spectral domain. Here we would like to give some details about this method and examples, how it works.

At first, we tried to compute the phases using spectra of the raw records, what gave us very unstable results. Raw record contains noise, body waves and higher surface wave modes, their shape is complicated and the phase estimation is hence not well constrained. We propose another approach – to provide the spectral phase measurement using only the separated fundamental modes of the desired surface wavegroup.

Let us remind, how this separated fundamental mode is calculated (detailed description is in Chapter 1, Sections 1.3 and 1.4 and in Chapter 3, Section 3.2.3). We decompose the raw record in spectral domain by multiple filtering and we obtain a set of quasimonochromatic signals corresponding to chosen harmonic components of the record. Then we find the appropriate maximum of the envelope of each of the compo-

nents and we truncate the signal before and after this maximum to keep only the desired wavegroup. These truncated harmonic components are again summed in the time domain to create corresponding seismogram of the fundamental mode containing again the whole period range that we had used for decomposition at the beginning. The spectrum of this separated surface wavegroup is computed and its phase are saved. The same is done with the second record at the other station and then the time shift $t(\omega)$ with help of the phase difference $\varphi_2(\omega) - \varphi_1(\omega)$ between the two spectra using the well-known formula (McEvilly, 1964; Proskuryakova et al., 1981; Levshin et al., 1992; Yoshida and Suetsugu, 2004) is determined as

$$t(\omega) = \frac{\varphi_2(\omega) - \varphi_1(\omega) + n2\pi}{\omega}. \tag{5.2}$$

The phase velocity is then computed according to

$$c(\omega) = \frac{r}{t(\omega)}, \tag{5.3}$$

where r is the interstation distance. To avoid the uncertainty of the unknown whole wave cycles n which may occur between the stations, for this spectral measurement we use records shifted in time by a priori estimated general time shift, usually corresponding to the velocity of 4 km/s. The lengths of both records are the same, but their beginnings differ by this time shift. Hence we ensure that the phase shift from equation (5.2) is around zero. After computing the propagation time corresponding to the phase shift, we again add the previously introduced time shift to obtain the real propagation time between the two stations for given period.

Fig. 5.19 shows eight plots (**A**–**H**) to explain the fundamental mode approach. Power spectra of two records are shown by red and yellow lines. Four top panels (**A**–**D**) correspond to the raw records (rugged power spectra) and four bottom panels (**E**–**H**) correspond to the spectra of separated fundamental modes (smooth power spectra). Blue and green lines represent real and imaginary parts of the spectra of the first and the second record, respectively. Dark blue and dark green are real parts and light blue and light green are imaginary parts. Panel **A** and **B** for raw spectra as well as panels **E** and **F** for spectra of separated fundamental modes show the spectra of the first and second record with corresponding real and imaginary parts. Panels **C** and **G** show the comparison of both spectra with the real and imaginary parts and panels **D** and **H** show the comparison of both power spectra only. Panel **D** of raw power spectra compared with panel **H** of spectra of fundamental modes give us an estimate how the coherency of both signals is made better using the fundamental modes spectra instead of the raw ones, see also Fig. 5.3. Equivalent of this spectral domain plots are Figs. 5.8 and 5.9 with the fundamental surface wavegroups in the time domain.

This approach, however it is used often in literature, gave us reliable results only in limited period range. We demonstrate it in Fig. 5.20, where estimated phase velocity from three earthquake records (different symbols) are plotted for three short profiles (different colors). Notice the difference in the last station location – we use the station Komorní hůrka (KHU) (Fig. 5.16) instead of NKC during this research since KHU is equipped with the same Guralp instrument as the other stations TBR, HAJ and NEC and hence no instrumental corrections were needed for the relative phase velocity measurement. In the period range from 12 to 19 s we see general agreement of the phase velocity dispersion curves computed for each profile using the records of all three earthquakes (the curves of the same color are similar). Out of this range, the curves from

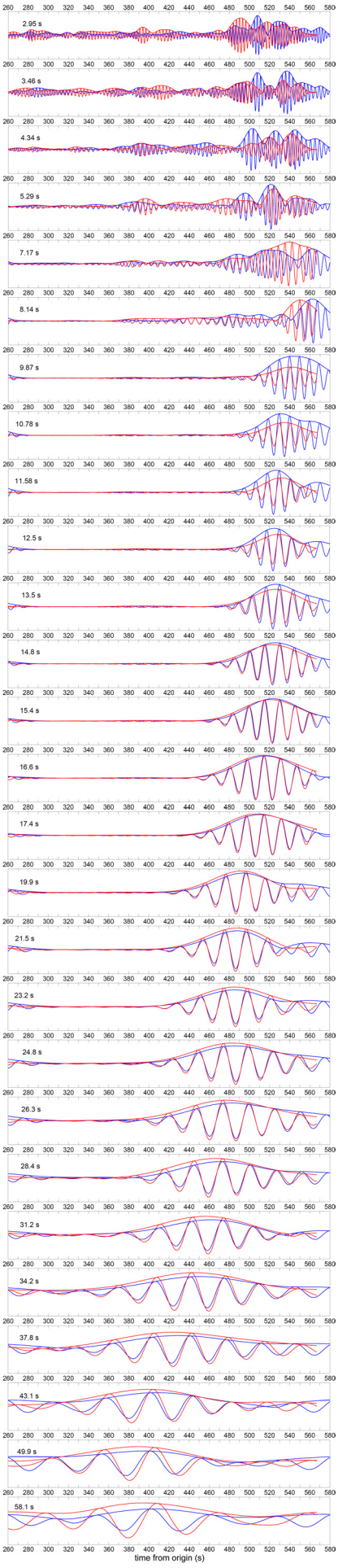


Figure 5.18: Shifted components.

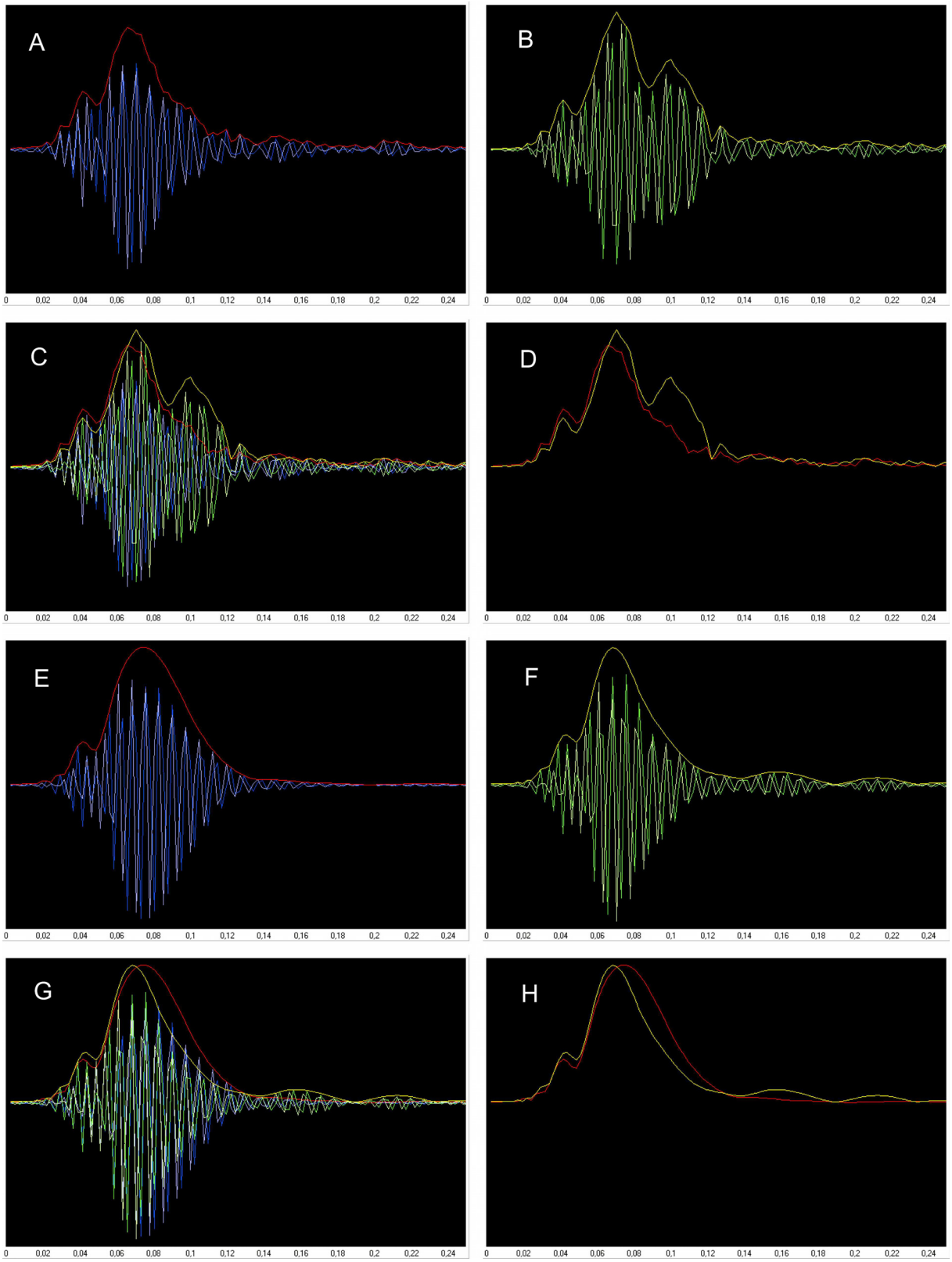


Figure 5.19: Spectra of two records of the Aegean Sea earthquake recorded at stations HAJ and NEC (red and yellow). Four top panels show raw record spectra and four bottom panels show spectra of separated fundamental modes. Blue and green lines represent real and imaginary parts of the spectra. Dark blue and dark green are real parts and light blue and light green are imaginary parts.

each record differ more than curves for each profile and hence we do not consider this result as reliable.

The most probable reason for introducing such a big error in this measurement is the complicated processing we have to deal with. We use Fast Fourier Transform (FFT) to make spectrum of the raw

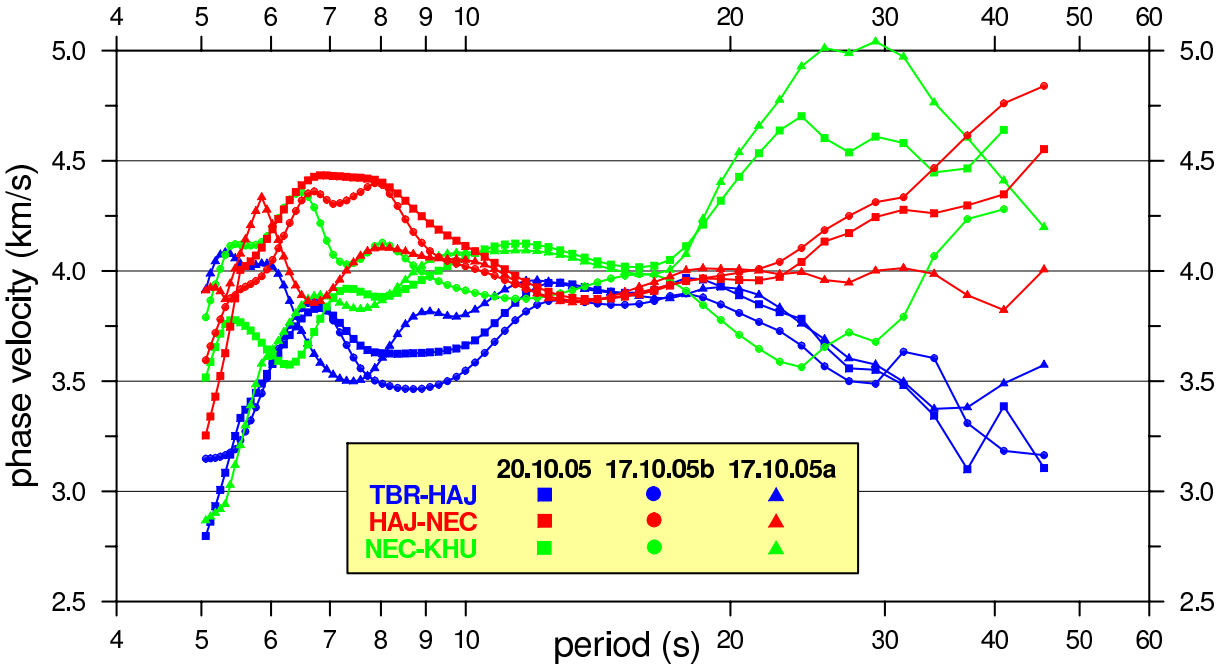


Figure 5.20: Comparison of phase velocity measurement at three short profiles (different colors) from three earthquakes (different symbols).

records, we decompose it by multiple filtering technique, we use inverse FFT to get the quasimonochromatic signals in time domain, we truncate the signals, we sum them and we again use forward FFT to compute the spectrum of the separated fundamental surface wavegroup. The truncating in the time domain has crucial influence on the shape and frequency content of the separated fundamental mode and is not defined so well to keep exactly the desired wavegroups in each harmonic component since this wavegroup has no clear beginning as well as no clear end. To avoid this uncertainty, we decided to measure the phase velocity in the time domain. We use directly the truncated wavegroups to measure the time shift between the same harmonic components at two stations. We again use the components, but in this case, the shape of the truncated wavegroup is not so important – as it is nearly monochromatic signal and as we measure the shift between two similar wavegroups, we are not limited by the fact that one or both of them are of little bit distorted shape. We use cross-correlation to fit the wavegroup one to each other and small changes of their shape at the beginnings and at the ends of them are unimportant.

Other possibility we have tried with similarly bad results as the spectral phase measurement is to estimate the instantaneous phase of each of the harmonic component in the time domain and to make differences between these phases. As the harmonic quasimonochromatic signals resulted as an inverse FFT of filtered spectra, it has both real and imaginary parts. Since we use only the positive frequencies for the inverse FFT, as described in Section 3.2.3, these real and imaginary parts are connected by the Hilbert Transform and hence, each of the quasimonochromatic signals is also an analytic signal. Using the ratio between the real and imaginary part, we may estimate the instantaneous phase. In fact, we do exactly this procedure to get also the instantaneous period for estimating the slight changes of this period along the signal in time. As we can obtain also the instantaneous phase, we may again compute the differences between these phases for two harmonic components from two stations.

Both latter approaches (time shift in the time domain and phase estimation in the time domain) have the advantage of dealing with lower number of FFTs than the phase measurement in spectral domain using the fundamental modes. However, only the measurement of time shifts in the time domain gave us reliable results in a broad range of periods. Thus we finally decided to propose this measurement in the given paper as the one to be used for our purposes.

inversion of twenty curves

The methodology of the tests made by Kolínský et al. (2010) is nearly the same as in the case of the test from Kolínský and Brokešová (2007). For the testing structure, synthetic dispersion curve is computed by the modified Thomson-Haskel matrix method, only some of the points from this synthetic dispersion curve are selected to resemble the real measurement and inverted. The main difference of the tests made by Kolínský et al. (2010) is that we introduce a measurement error to leak into the inversion process. The synthetic curve is artificially disturbed by random errors in the range of ± 0.06 km/s. The inversion is provided 20 times for 20 different disturbed curves. This is described in detail in the text of the

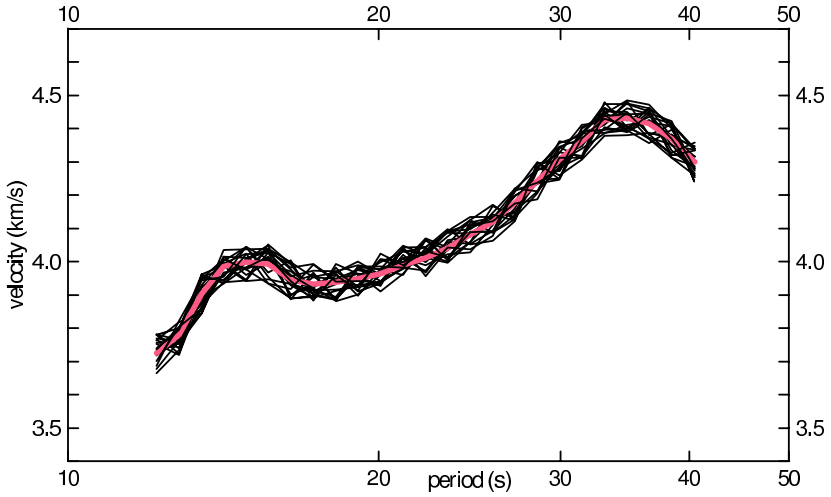


Figure 5.21: By the red line, original phase velocity dispersion curve is drawn. Twenty black lines represent dispersion curves disturbed by random error of ± 0.06 km/s with respect to the original dispersion. These twenty disturbed curves enter the inversion process. This example shows a dispersion curve measured by the two-station method for the profile TBR-HAJ, see Section 5.2.9, Figs. 5.11 and 5.13.

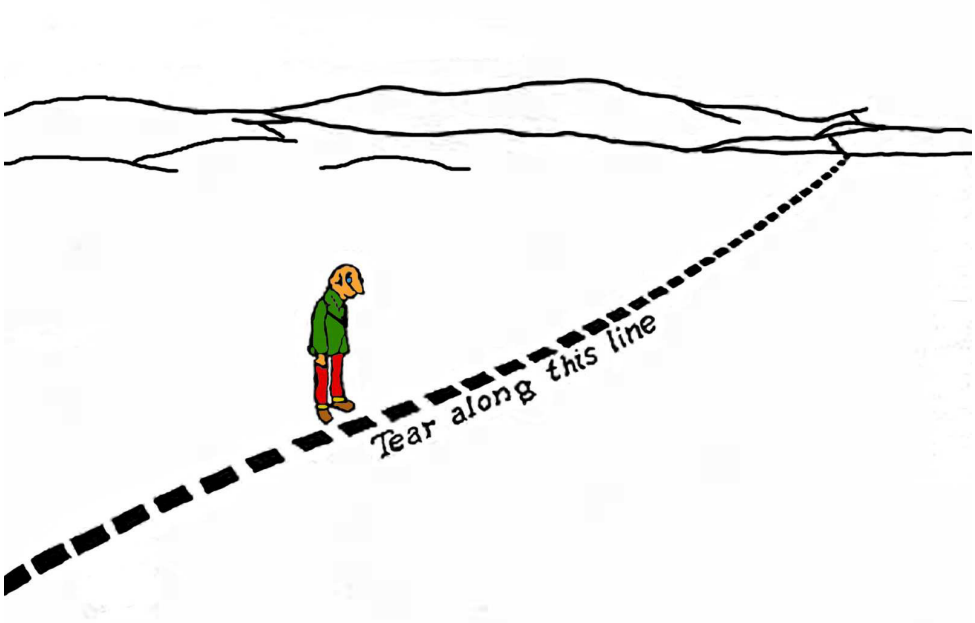
paper. In Fig. 5.21, we present an example of such set of disturbed curves. By such a method also the real measured dispersion curves are treated and the example in Fig. 5.21 represents one of the actually measured curves from Kolínský et al. (2010).

The other difference of the inversion process used in Chapter 3 (Kolínský and Brokešová, 2007) and Chapter 5 (Kolínský et al., 2010) is that in Chapter 3, the whole range of six inverted velocity distributions is shown in the figures. As opposed to that, in Chapter 5, we provide twenty inversions for each curve and by the gray stripes we present the standard deviation of these twenty results. This applies both for the inversion tests and for the inversion of actual measurements. We prefer the latter methodology using more inversion runs and their standard deviations since it better describes the range of possible resultant values.



Part III: Software





author of the figure is unknown

Chapter 6

The SVAL program

In this chapter, we present a detailed description of the SVAL program. The SVAL program is an interactive software for frequency-time analysis of dispersed signals of any dynamic and frequency range. It also enables to make an inversion of measured dispersion curves for 1-D velocity structure.

This chapter also contains practical examples of surface wave analysis and inversion. The SVAL program is based on methods mentioned in the previous chapters assembled in a software which is easy to understand and friendly to use.

6.1 History of the program

I have been developing the SVAL program for seven years. The first version was made during my diploma thesis elaboration in 2003 and hence for the basic procedures refer also to my work Kolínský (2003). The source code has been under permanent development, however, several major upgrades may be noted:

- After defending my diploma thesis, the instantaneous frequency estimation of filtered quasimonochromatic signals was implemented in the program, what improved the dispersion curve estimation significantly. This was done during my work at the Department of Seismology, Institute of Rock Structure and Mechanics, Academy of Sciences of the Czech Republic, as we need a practical tool for dispersion estimation.

- In 2004, the source code was translated into Borland Pascal Delphi. This major modification was needed because as some additional features and detailed controlling of many parameters has been added, some kind of interactivity was asked. This would be hardly done for Fortran-type program, where all the controlling parameters have to be set in text files. The second reason was to enable fast and comfortable browsing of both partial and final results of analysis, what was enabled by using graphical components for Delphi. Compiling these requests together, we have now a software, which can be interactively handled. Each detailed step of the computation can be checked both in numerical and graphical form and the controlling parameters may be changed during the program run in order to process the records in fast and reliable manner. It also enables to use trial and error attitude to some problems – as it is comfortable to change the parameters of filtration, it is often convenient to try several possibilities to find out the behavior of the filtration in the specific case of the given record.

- In 2005 the inversion procedures were implemented. The inversion for 1-D structure is available. Using this feature, after the record analysis and dispersion curve estimation, we may invert the dispersion curve for the velocity distribution and complete the whole process starting with the data of ground motion measurement and resulting into longitudinal and shear wave velocity distribution. For the inversion, the original program for dispersion curve computation by matrix method, developed by Oldřich Novotný in Fortran (Proskuryakova et al., 1981), was translated into Delphi. The program for isometric method written by Jiří Málek in Delphi (Málek et al., 2005 and 2007) was implemented into SVAL as one of its units.

- In 2006, joint inversion of Love and Rayleigh wave dispersion curves was implemented as well as the possibility of using both group and phase velocity dispersion curves for inversion.

- In 2007, interactive graphical interface for manual setting of the velocity models was added for forward modeling of dispersion curves.
- Interactive mouse-clicking option was added to the spectrogram/dispersion plot for easier selecting of the dispersion ridges in case we are not satisfied with the results of the automatic procedure.
- In 2008, an option for reading the records using the KUK file format was added. The KUK program is a software developed by Jiří Málek at the Department of Seismology, Institute of Rock Structure and Mechanics, Academy of Sciences of the Czech Republic, for viewing and preprocessing of seismic records. This option enables us to use the KUK and the SVAL programs together and to pass the data from KUK to SVAL without any additional modification of the files.
- In 2009, a new feature enabling the batch processing was added to the SVAL program. As we needed to process hundreds of records at once, SVAL got an option to do it itself. It reads file by file, provides the computation, saves the results and continues with other data file. Of course, when no seismologist is communicating with the program, the proper dispersion curve compilation cannot be ensured. However, we needed only the basic analysis and the envelope maxima arrival times for each quasimonochromatic signal as a result of our analysis. In this case, the automatic data handling and processing is justifiable. By this feature, the SVAL program reached the advantages of both types of data processing software commonly used by the seismologist – when detailed dispersion curve is to be estimated, manual handling and checking is available. When many records are to be processed and only the basic properties of the signals are to be estimated, automatic batch processing is implemented.

As mentioned above, in 2003, the SVAL program was written in Fortran open file format. The basic procedures and algorithms were assembled according to the classical multiple filtering program SVAM, which is described in the works of Veselý (1997), Čermák (1990) and Sekereš (1983). Their contribution went further in the development of older version of a frequency-time analysis program developed at the Institute of the Physics of the Earth in Moscow. For an overview of their contribution, see Kolínský (2003).

The Moscow version of the program was called SVAN, what is an abbreviation for Russian term ***S**pektralno-**V**remenniy **A**nalyz **N**abludeniy*, what means *frequency-time analysis of observations*. As the Czech version of the program had the name SVAM with M added instead of N to imply the continuation of the work and to note that some changes were made, I persisted in this attitude and I changed the last letter to L, as it is the next letter of alphabet using the direction delineated by the previous two terminal letters: N – M – L. Hence, we have now SVAL, what means, as a unintentional consequence, a *muscle* in Czech.

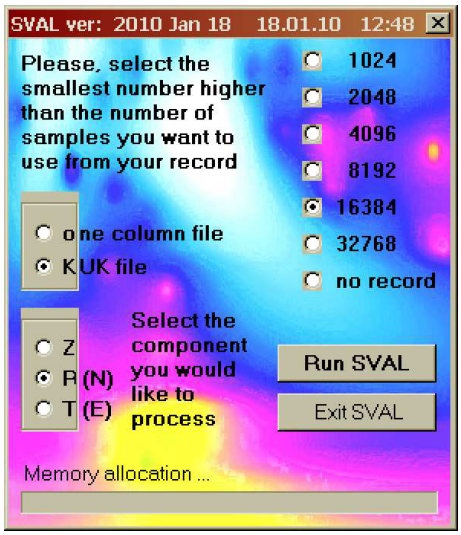


Figure 6.1: Auxiliary window of the SVAL program enables to select an appropriate number of samples we want to use as well as the type of the data file format and component of the record.

6.2 Basic characteristic

The SVAL program is to be used for frequency-time analysis of seismic records. It is possible to estimate the dispersion curve of selected mode and to make an inversion for 1D layered velocity and density model. In theory, no limitation is made for analysis of fundamental modes as well as higher modes of surface

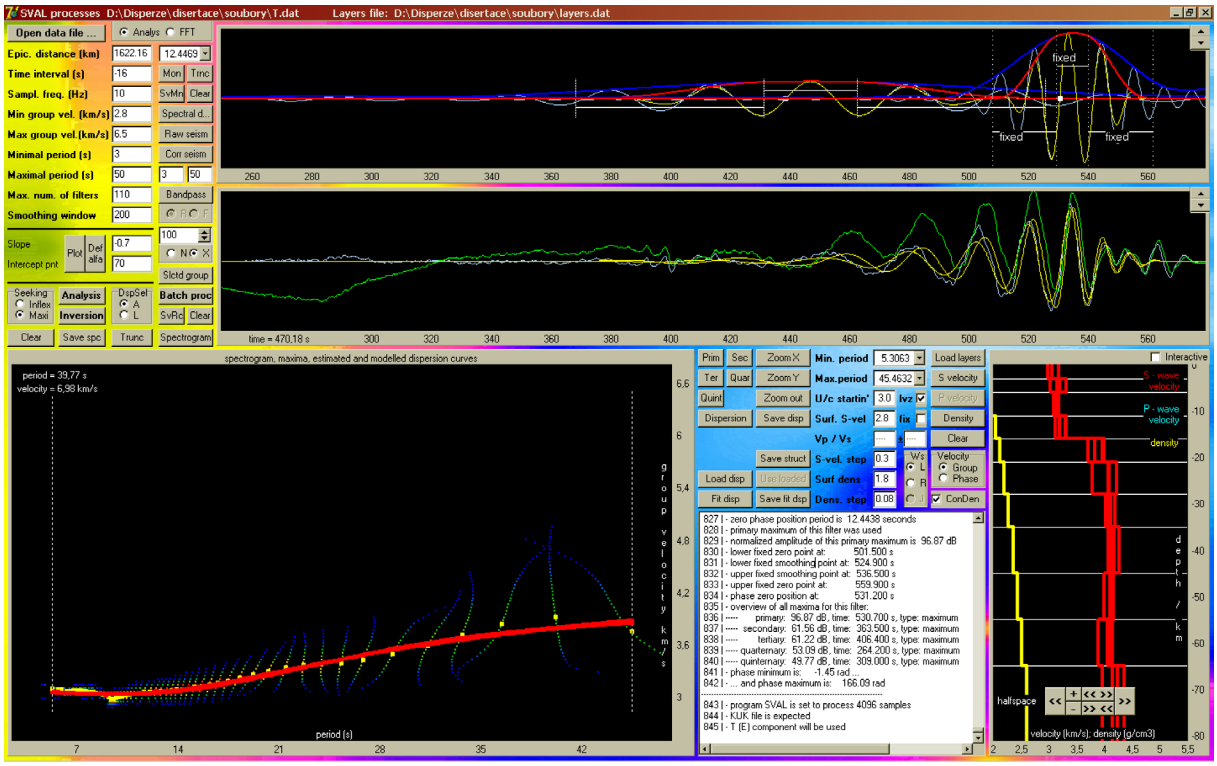


Figure 6.2: The main SVAL window. Time domain signals, frequency-time representations and inversion results are located here as well as most of the controlling buttons.

waves. Records of lengths up to 32768 samples may be processed and two types of input data files are supported. Any surface wave modes and also body waves can be extracted, properties of the signal in time and frequency domains can be determined, automatic procedure for compiling the dispersion curve as well as manual selection of the dispersion points is available. Manual mode for processing of one record with detailed investigation of all its properties as well as batch processing mode for extracting the group travel times from hundreds of records automatically is enabled.

At current time we provide the program version which can invert Love wave dispersion for 1D shear wave velocity and density model, Rayleigh wave dispersion for 1D longitudinal and shear wave velocity and density model and both Love and Rayleigh wave dispersion curves for longitudinal and shear wave velocity and density model. The density values may be optionally kept constant during the inversion and only velocities are found. The velocity value in the first layer may be optionally kept constant during the inversion.

As only one record at the same time may be analyzed and hence only one dispersion curve is kept in the computer memory from the analysis process, for inversion of two dispersion curves there is a need to prepare them separately, save them and load them using a separate file. All three types of inversions (Love, Rayleigh, joint) may be done both for group and phase velocities. The group velocity inversion may be done directly after SVAL analyzes the record but the inversion of phase velocity dispersion has to be done using loaded dispersion curve saved in a file because phase dispersion curves need to be estimated by some other means, using the PhaseCorr program, for example.

For estimating the group velocity dispersion curve, only one record is needed – this is exactly what the SVAL program does. For estimating phase velocity between the two stations, we need to analyze the two records separately by the SVAL program, save the information about the harmonic components at each station, and then load the two files into the PhaseCorr program to estimate the phase shifts between the harmonic components. After the phase velocity dispersion curve is estimated and saved by the PhaseCorr program, we may load it into the SVAL program to provide the inversion.

As the SVAL program uses graphical interface it is possible to check all the computational steps both in time and frequency domains. It is possible to change the parameters of analysis and inversion to obtain the results by requested and reliable way. It is designed to repeat selected portions of the analysis with different parameters to ensure the proper filtration and dispersion curve compilation.

We use the multiple filtering technique for the frequency-time analysis (programmed by Petr Kolínský), the isometric method for inversion (developed and programmed by Jiří Málek) and the matrix method for forward modeling (developed and programmed by Oldřich Novotný). As the SVAL program computation

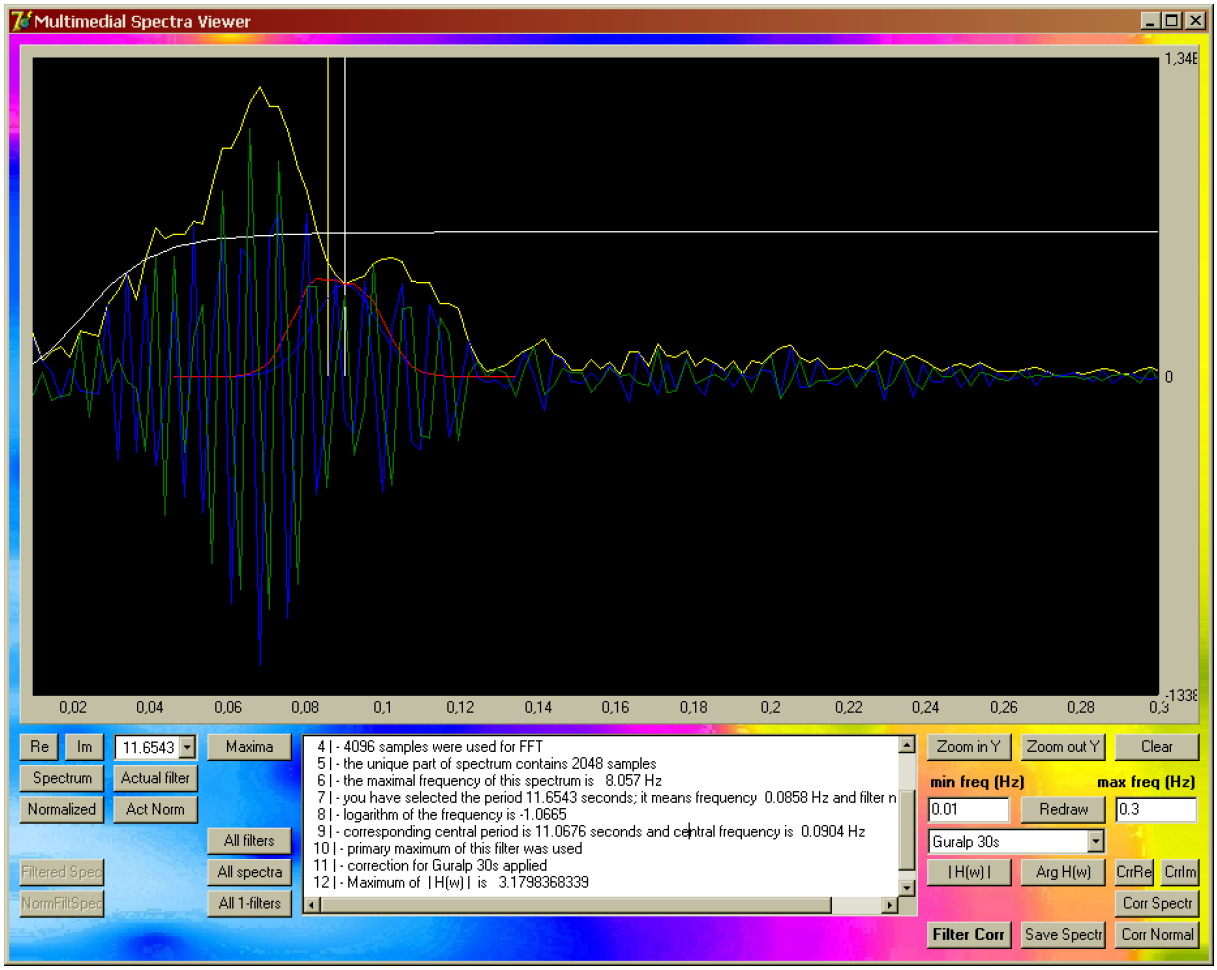


Figure 6.3: The frequency domain window. Results of multiple filtering are displayed as well as instrument transfer function is set using this window.

is divided into separated procedures, it is possible to go through only a part of the task. It is possible, for example, to make only the analysis of the record or to make only the inversion of the previously estimated dispersion curves.

6.3 How it looks

The source code is written in PASCAL using Delphi environment (Borland, version 7.0). It uses standard components implemented in the environment and one freeware component – the PlotPanel created by Marien van Westen and distributed under the terms of the GPL license. The SVAL's source code consists of six units which contain tens of procedures with approximately 9500 command lines all together. The code emerges as a result of translation of some codes from FORTRAN language (previous versions of the SVAL program, matrix method). Then it was compiled together with other codes written in Delphi (isometric method). One FORTRAN subroutine for FFT computation from FORTRAN's Numerical Recipes translated to PASCAL is also used.

It is possible to distribute and execute the SVAL program using one *.exe file (3.2 MB). It is not needed to have any other file installed in the computer to execute the SVAL program. The SVAL program is a freeware and users are supposed to cite the respective papers. All the source files and other working materials needed to compile the executable file are attached to this thesis on the CD ROM as well as is also the executable SVAL file itself. The executable file is also provided at the web page: http://www.irsm.cas.cz/~kolinsky/. The SVAL program is compiled to run using Windows OS.

There are two basic, one auxiliary and one inversion windows to be displayed at the monitor while the program is running. Many dialog and message boxes appears during the data processing.

At first, we meet the auxiliary window, see Fig. 6.1. It asks the user for selecting the number of samples he want to process. It allocates the memory what takes a few seconds. But it is worth of it because if we select proper number it may save much time and memory during further processing. It also asks for the type of the input file. The length of the input file does not play any role. The number of

samples we choose corresponds to the length of the record which will be processed – no matter how long is the record in the file. The SVAL program reads only the desired part of the file corresponding to the time window given by the velocity range and epicentral distance.

The time domain basic window, Fig. 6.2, is used for setting all the parameters and for checking the results in the time domain and in the group velocity-period plane. The result of inversion is also displayed in this window. The frequency domain basic window, Fig. 6.3, allows to see the raw spectra, Gaussian filters and filtered spectra and it enables to apply the instrumental transfer function for correcting the spectra. The inversion window, Fig. 6.4, displays information about the inversion task progression. It also allows to enter additional parameters for the inversion procedure execution.

Some of the examples in later sections of this chapter present the SVAL program screenshots using the older versions of the program where not all the buttons and functions have already been implemented. The new versions of the program keep all previous functions and buttons and add some new, so, all older screenshots are still valid.

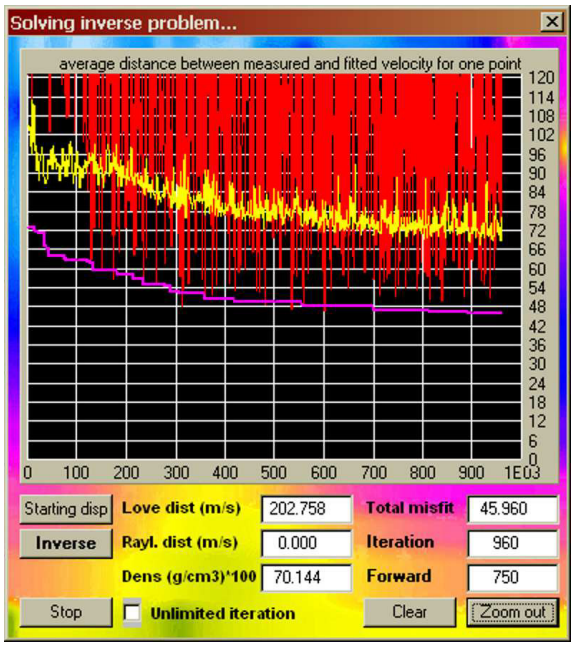


Figure 6.4: Inversion windows informs about the inverse procedure progression and gives values of misfit functions. It is also possible to switch between automatic termination of the inversion process and unlimited iteration mode, when process is to be stopped by the user.

Program buttons in all windows are enabled and disabled according to the current state of the computation. So it is only possible to use buttons which do have a good purpose in the given situation. It ensures that the program does not make any unexpected and undesired operation and hence it prevents the program from error-terminating. However, for example, if inappropriate file format is to be read, the program will send an `Invalid numeric input` error message to the screen. It may also happen that the program gives a `Range check error` or `Invalid floating point operation` message when the computation fails. An attention was paid to treat all the bugs which occurred during the years of the SVAL program utilization, but in case of some special occurrences, error message may still pop-up.

In following pages, we use screenshots of program buttons and windows without numbering for simplicity and because we do not reference them elsewhere.



`Invalid floating point operation` error message.

The program is set to be able to process the record of length up to $2^{15} = 32768$ samples (no matter how long is the input file). The minimal monitor resolution is 1024 x 768 pixels, optimal is 1280 x 960 pixels. Under the Windows XP OS, both the size of the main SVAL window as well as the frequency domain window may be arbitrarily changed. As we enlarge the window size, the size of buttons and edit boxes remains the same and only the size of plotting panels is enlarged. Using older versions of Windows OS, some problems with the SVAL window size enlargement occurs.

We intentionally did not use any command drop-down menus since we prefer all the command buttons to be directly available at the desktop. One may see all settings during the work with the program directly. Also all the checkbox options are placed directly in the main window. The only drop-downs enable to

choose from a long list of periods both in the time and frequency domain windows – it is reasonable since the list of tens of numbers cannot be displayed by any other means. Other advantage is that it is possible to "save" the actual setting by simply printing the screen. The screenshot will contain everything (including the data file name and path) needed to repeat the same analysis in the future with exactly the same parameters. No hidden setting is used.

The output text information about the SVAL computational steps may be copied and pasted in separate text file for further checking. Edit boxes are to be changed using the standard numerical keys or also by clicking on the arrows in case of amplitude scaling measure. The layout of the windows is designed to be easily controlled by mouse clicking, however, buttons, edit boxes and check boxes may be reached also using the Tab (Shift+Tab) key to browse the controlling elements in a preset order. This is handy especially while changing the basic setting for analysis because there are a lot of edit windows to be filled and mouse clicking would waste our time and patience. The check boxes may be altered using arrow keys.

In the following text, we describe all the functions and handling options of the SVAL program. Since there are lot of them, we emphasize those few, which are necessary for the basic analysis. We may distinguish three categories of parameters and settings:

- **basic**: parametres and functions necessary for the SVAL program run or highly recommended to be set
- **default**: parameters needed for the program run, however, SVAL may run with the default setting
- **advanced**: optionally parameters and functions not needed for the basic analysis and not needed for the program run

In the following pages, we denote each controlling feature of the SVAL program by one of the **basic / default / advanced** label. Some of the features are labeled by a combination of two of the categories. For example (default / basic) means that we do not have to change this setting, however, it is higly recommended to do so. Combination (default / advanced) means that the setting is usually used in the default value, but in some special cases, we may want to change it. In other words:

- (**basic**) means, we HAVE TO set it
- (**default / basic**) means, we DO NOT HAVE TO set it, but it is recommended to do so; the program NEEDS this parameter at least in its default value
- (**default**) means, we DO NOT HAVE TO to change it, but the program NEEDS the parameter
- (**default / advanced**) means, we DO NOT HAVE TO set it and this setting is usualy NOT changed by the user, but the program NEEDS this parameter to run
- (**advanced**) means we DO NOT have to set it and the program DOESN'T need it to run

Before we explain all of them in details, see the list of the processing steps needed for the most simple run of the analysis right now:

- prepare the ASCII file with one column of amplitudes of one component of the record
- start the SVAL program
- select `one column file` input file option in the auxiliary window
- select the number of samples higher than the number of samples you would like to process
- pres the `Run SVAL` button
- in the main SVAL window, open the prepared file with data clicking on `Open data file ...` button
- set the epicentral distance from the source to the station in km
- set the time interval between the origin time and the beginning of the record in seconds
- set the sampling frequency of the record in Hz
- minimal and maximal group velocity and minimal and maximal period to be analyzed are the parameters highly recommended to set, however, you may use the default settings for the first run
- pres the `Analysis` button and check the text output box to see, what happened

- pres the `Raw seism` button to see the portion of the data you have analyzed
- pres the `Dispersion` button to see the estimated dispersion curve
- select the minimal and maximal period of the estimated dispersion in the `Min. period` and `Max. period` drop-downs to tell the program which portion of the dispersion you want to save
- pres the `Slctd group` button to see the surface wavegroup compiled using the selected period range and compare it with the original record
- save the estimated dispersion curve by the `Save disp` button

6.4 File inputs

There are three open dialog buttons implemented in the SVAL program. Files are expected to be ASCII text files, there is no limitation concerning the file names or their extensions when in the manual mode. Batch processing mode requires *.dat extension for input data files. It is expected that there are not any headers or any other information in the one-column input files. In contrary to that, the header is required while reading data from the KUK files. It is up to the user to select, if simple one-column file or KUK file is read by the program.

The auxiliary window enables to set one of the two options of input files we would like to use. The most simple is the `one colum file` option (basic), which is designed for reading a file with only one component in a single column of ASCII text. No header is required for this input file. If we open a file with more than one column, only the first column is used by the SVAL program. The other option enables to read a `KUK file` (advanced). The KUK program is used for wieving seismograms and for basic record handling and was developed at the Department of Seismology, Institute of Rock Structure and Mechanics, Academy of Sciences of the Czech Republic, by Jiří Málek. KUK files contains all three components and eight-rows header. Two types of the KUK file format are supported – the older version with limited information in the KUK header and the new version where the epicentral distance and time difference is also given in the KUK header. The program distinguishes between the two KUK file formats itself and no interaction with the user is needed.

When the older version of the KUK file format is used, the sampling frequency is read by the program from the KUK header, however, the epicentral distance and time interval between the origin time and beginning of the record have to be set manually. When the new KUK file format is used, all three quantities are read by the program and thus it makes the parameter setting faster.

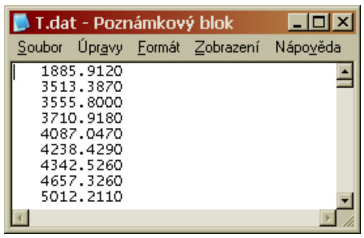
For the batch processing, the data must be of the KUK file format with additional information about the epicentral distance and time interval given in the KUK header (the new KUK file format). The file name may be arbitrary, but the name extension must be *.dat. Since the program automatically saves output files with group times, it needs to create also the output file names. For this, it uses the name of the station taken from the KUK file header.

Further, in the auxiliary window, we can select the component we would like to use from the KUK file (advanced). It does not matter if we use the original `Z-N-E` file or the file with rotated horizontal components `Z-R-T`. The advantage of this selection (besides the fact that we can use directly the output files from the KUK program) is that we can easily switch between the components of the same record while processing it without reading any new file. So, it is easy to process for example radial and vertical components for the analysis of Rayleigh waves with the same settings of the SVAL filtration parameters and compare the results of dispersion curves obtained from both components.

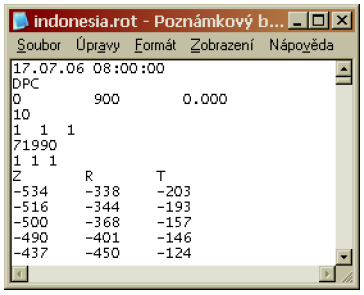
In the next paragraphs, we introduce the file opening buttons and their functions.



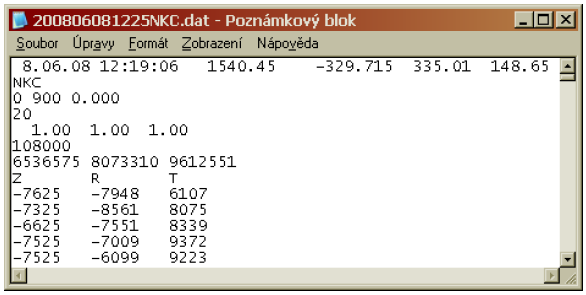
(basic) Reads seismogram or velocigram record. It is supposed that the data are in a file containing one column (basic) or in the KUK format with three columns (advanced) with the amplitude values; integer and real format available (KUK files contains integers only). If we open a `one colum file` containing more than one column, only the first column is used. If we open the `KUK file`, we should select the component (column) we would like to analyze. It is not possible to make an analysis of more than one record component at the same time, because the memory requirements would be too high. The file name is displayed in the SVAL's main window upper bar. The number of samples in the file is counted and displayed in the text output box. The KUK file header also includes the information about the samples number, but the information given by the SVAL program is independent of that header.



(basic) Example of the record input data file containing one component with the amplitudes at given sampling frequency. If any file with more than one column is open, only the first column is used by the SVAL program. No header should be present in this input file. Before opening this kind of file, select the `one column file` (basic) option in the auxiliary window, see Fig. 6.1.



(advanced) Example of the SVAL input file produced as an output by the KUK program. This is the older KUK file format version. The header is read and displayed by the SVAL program, however, only the information about the sampling frequency (4th row) is used from the header. Before opening this file, select the `KUK file` option (advanced) in the SVAL auxiliary window, see Fig. 6.1. This KUK file cannot be used for the batch processing since it does not contain the information about the epicentral distance and time difference. The program will recognize this older KUK file version itself.



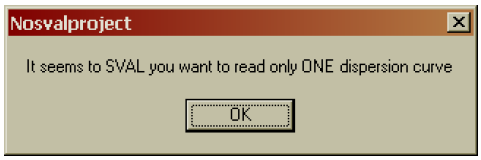
(advanced) Example of the SVAL input file produced as an output by the KUK program. This is the new KUK file format version. The header is read and displayed by the SVAL program and the information about the epicentral distance and time interval between the origin time and the beginning of the record (both in the 1st row) and the sampling frequency (4th row) are used from the header. In case of the batch processing, also the name of the station from the 2nd row is used to create an automatic name for the *.rdg output file. In addition, the last two values in the 1st row represent azimuth and backazimuth between the epicenter and the station. These values are not used by the SVAL program. Before opening this file, select the `KUK file` option (advanced) in the SVAL auxiliary window, see Fig. 6.1. The program will recognize this newer KUK file version itself.



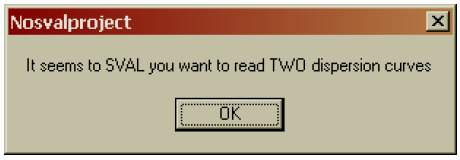
(advanced) Reads the previously estimated dispersion curve. There are two possibilities of the dispersion curve file format.

- one dispersion curve only: The file should contain two columns; the first one with the values of period (s) and the second one with the respective velocity values (km/s). Either group or phase velocity may be used.
- two dispersion curves at the same time: File should contain four columns with the values of periods (s) in the first column and with the values of Love wave velocities (km/s) in the second column. Third and fourth columns contain the periods and velocities of Rayleigh waves, respectively. This is the only allowed settings that the first two columns contains the dispersion of Love waves and the other two contain the dispersion of Rayleigh waves. Either group or phase velocity may be used, but both dispersion curves must be of the same kind.

While opening the file, the SVAL program informs about the number of dispersion curves (one or two) it can read.



SVAL informs that it recognized that the loaded file contains only one dispersion.



SVAL informs that it recognized that the loaded file contains two dispersion curves.

If this information does not fit our expectation, the input file has probably a wrong format. When file with two dispersion curves is open, the checkbox with a possibility of joint Love and Rayleigh wave curve is active. While inverting the dispersion curve directly estimated by the SVAL analysis, only one curve at the moment may be inverted. So, when there is a need to invert both Love and Rayleigh curves together, the only possibility is to load a file with both of them. Starting with the record, we may make an analysis of transverse component and save a file with the group velocity dispersion of Love waves, then make an analysis of vertical component and save the group velocity dispersion of Rayleigh waves. Than it is necessary to compile the two saved files into one appropriate input file and load it for the inversion.

The number of dispersion points in the opened file is estimated and the dispersion is plotted in the group velocity-period diagram. In that moment no other changes of actually processed record or dispersion curve are made. Thus this button only reads and displays the previously saved dispersion.

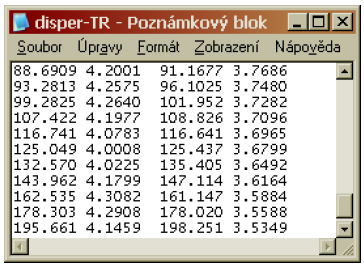
If we want to use it for further processing, we have to press the `Use loaded` (advanced) button. This two-step loading has the reason that sometimes we just want to look at some previously estimated dispersion to be compared with the currently processed one but we do not want to make anything with the saved one – we simply display it. SVAL also displays the name of the loaded dispersion file in the main window upper bar.

It is possible to work with such loaded dispersion in the same manner as with the computed one but it is not possible to apply an instrument correction on it since this is done only in spectral domain for the whole record. The dispersion is estimated regardless of the fact that we process raw or corrected record. While saving the dispersion curves for later processing after the analysis, we have to be sure we save the corrected one, or, preferably, both raw and corrected ones.

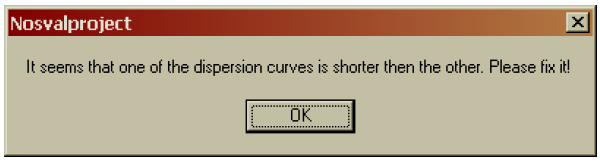
Using the SVAL analysis one may obtain only group velocity curve. If there is a need to invert the phase velocity dispersion curve estimated by some other means (by the PhaseCorr program, for example), it may be loaded as well. It is also possible to load two phase velocity dispersion curves in one file for joint inversion. Be sure to check the appropriate checkbox with `Group / Phase` velocity option (advanced).



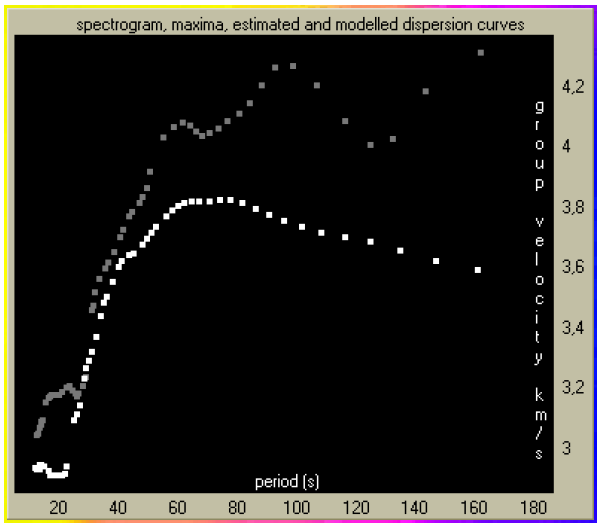
(advanced) Example of the dispersion input data file with one dispersion curve. The first column gives values of period (s) and the second one contains corresponding velocities (km/s).



(advanced) Example of the dispersion input data file with two dispersion curves. The first column gives values of period (s) and the second one contains corresponding velocities (km/s) for Love waves. The other two columns gives respective values for Rayleigh waves. The values of periods of each of the dispersion curves may differ, but it is supposed that both dispersion curves have the same number of points. If they do not, an error message is given and the input file has to be edited.



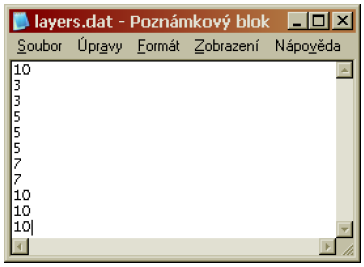
Error message when one of the two dispersion curves in the file has lower number of points then the other one.



(advanced) Two dispersion curves were loaded. Love wave dispersion curve is drawn by gray and Rayleigh wave dispersion curve by white dots.



(advanced) Reads a file containing the depths of layers which are to be used for structure estimation. The file contains one column; in the first row there is a number of layers without halfspace (an integer) and in the next rows there are thicknesses of the layers in km, both reals and integers available. SVAL displays the name of the layers file in the main window upper bar.



(advanced) Example of the layers input data file; the first value gives the number of layers, the other are layer thicknesses (km).



When a file with inappropriate format is selected for opening, this error message pops-up. This applies for any of the above mentioned buttons for file opening.

6.5 Keyboard inputs

Event parameter



(basic) Epicentral distance (km). When the new KUK file format is used, the epicentral distance is set automatically. It is displayed in the edit box, but the edit box is disabled and no changes can be made in it.



When no epicentral distance is available, this message pops-up.

Record parameters



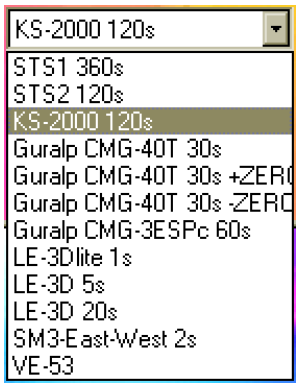
(basic) Time interval between the origin time and the beginning of the record (s); positive value if the record starts after the origin time, negative value if it starts before the origin time. When the new KUK file format is used, the time difference is set automatically. It is displayed in the edit box, but the edit box is disabled and no changes can be made in it.



(basic) Record sampling frequency (Hz). When any of the two KUK file formats is used (old or new version), the sampling frequency is set automatically. It is displayed in the edit box, but the edit box is disabled and no changes can be made in it.



If the sampling frequency is zero, this message is displayed.



(advanced) Instrument transfer function selection (STS-1 360 s, STS-2 120 s, KS-2000 120 s, Guralp CMG-40T 30 s [also derived and integrated], Guralp CMG-3ESPc 60 s, Lennartz 3D lite 1 s, Lennartz 3D 5 s, Lennartz 3D 20 s, SM3-EW component 2 s, VE-53). The transfer function is computed according to the given poles and zeros. Poles and zeros setting of a new instrument is only possible by changing the source code of the SVAL program.

```
instrumentbox.Add('Guralp 30s');
instrumentbox.Add('STS2 120s' );
instrumentbox.Add('LE-3D / 5s');
```

(super advanced) To add a new instrument to the list of transfer function selecting option, one should create a command line as those on the left.

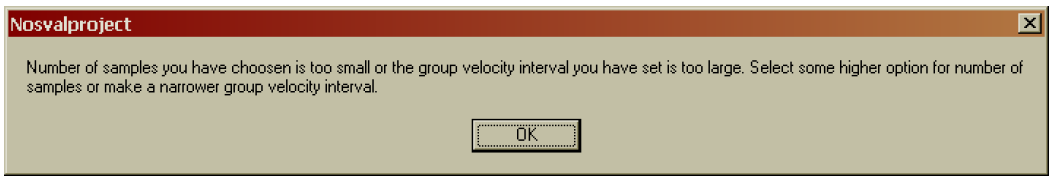
```
if instrument = 'Guralp 30s' then begin
  pol[1] := VarComplexCreate( -0.02356,  +0.02356);
  pol[2] := VarComplexCreate( -0.02356,  -0.02356);
  pol[3] := VarComplexCreate(-50.0    ,   0.0    );
  nul[1] := VarComplexCreate(  0.0    ,   0.0    );
  nul[2] := VarComplexCreate(  0.0    ,   0.0    );
  nul[3] := VarComplexCreate(159.0    ,   0.0    );
  numofnules := 3;
  numofpoles := 3;
  Teigen := 30; {instrument eigenperiod in seconds}
  Charakteristika;
end;
```

(super advanced) Part of the SVAL source code with poles and zeros for Guralp 30 s settings. In case we need to add a new instrumental transfer function, we simply copy this `if` loop and set the corresponding poles and zeros (Hz). Remember to set also the number of poles end zeros and instrument eigenperiod (s). The string in the `instrument` variable should match the name of the instrument given in the `instrumentbox.Add` command.

Filtration parameters



(default / basic) Minimal and maximal group velocity (km/s). This setting gives the range of the time interval used for analysis. The record file may be arbitrarily long, but the velocity range has to fit into the preferred number of samples set in the SVAL auxiliary window. If it does not fit the given number of samples, SVAL gives a message and we can either set some higher number of samples or make the group velocity interval narrower.



If we already set the highest number of samples available (32768), we could try to make the velocity range narrower. But this would cause a lost of same of the parts of the record. We probably have to cut out the higher modes at the beginning of the time window or the coda and surface wave reflections at the end of the time window. This problem occurs when the epicentral distance is large, because then the given velocity range produces too long time window. Since we cannot change the epicentral distance, and when we do not want to narrow the velocity range, the only option is to resample the record. When analyzing surface waves at a distant station, it is needless to have the records sampled by more than 20 Hz. For stations of epicentral distances more than 1000 km, the sampling rate of 5 – 10 Hz is sufficient and hence a time window of satisfactory length may be analyzed. For example, using the sampling rate of 10 Hz and the number of samples to be 32768, we may analyze a time window of a length of 54 minutes (3276 s). For the distance of 2000 km it means the velocity range could be for example 0.6 – 7.0 km/s what is more than enough. When analyzing records at more distant stations, short period surface waves are attenuated anyway and hence the use of lower sampling rate is justifiable.

If we enter maximal velocity to be too large or the minimal one to be too small, so that the arrival times corresponding to these velocity values are out of the range of our data file, SVAL corrects them for the nearest possible value and gives a massage of it.



Information that the maximal group velocity set by the user is too big and that the suggestion for the new one – the maximal available in the file – is set into the `Max group vel.` edit box. SVAL looks for the first sample in the file, computes the velocity corresponding to this sample and set it in the edit box. It may still be changed (lowered) by the user.



Information that the minimal group velocity set by the user is too small and that the suggestion for the new one – the minimal available in the file – is set into the `Min group vel.` edit box. SVAL looks for the last sample in the file, computes the velocity corresponding to this sample and set it in the edit box. It may still be changed (increased) by the user.

In the case the program suggested the velocity values, we do not have to change any settings and we may simply use the suggested velocity range – the data file will be used from/to the first/last sample. If still some problems occur, check the `Sampling frequency` (basic) setting.



(default / basic) Minimal and maximal period (s) for filtration. These values are checked by the SVAL program and corrected, if necessary. Information about the applied correction is given in the text output box. The minimal period for filtration is set to be equal to four times of the sampling interval. For example, for sampling rate 100 Hz (0.01 s) the maximal frequency can be 25 Hz (0.04 s). If the minimal period is set to be shorter by user, the program sets it to the default shortest possible value and gives message in the text box. Maximal period is set to be two times longer than is the time window we process. So, if we analyze the record in the window of 25 s, the maximal period for filtration can be 50 s.



(default / advanced) Maximal number of filters of the multiple filtering (number). Usually, this value of 110 is enough. For detailed explanation, see Section 6.11.



Maximal available number of filters is 300. If the user set this value to be higher, this notice is given and the number is set to 300.



(default / advanced) Length of a smoothing window for the record edges (number of samples).



If the length of a smoothing window is set to be higher then half of the samples used in the processed time window, this message is displayed and the analysis terminates.



(default / basic) Coefficient α (width of filters) (dimensionless), intercept point and slope of the linear dependence, default value button, button for plotting the $\alpha(T)$ – a dependence of the coefficient on the period. For details, see Section 6.11. This is the most powerful tool to control the filtration.



If the slope of the `alpha` coefficient is set to be positive, this notice is given and the analysis terminates and waits for the negative value.

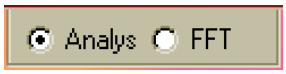
We have seven options to control the run of the analysis. There are five pairs of check boxes. It is possible to influence the analysis by mutually independent checking of them. Besides it, there are other two possibilities how to start the analysis.



1. (default / advanced) Option for setting the compilation method of the dispersion curve from the dispersion points: `A` from the **A**bsolute maximum of whole spectrogram and `L` from the **L**ast filter. For details, see the paragraphs concerning the analysis procedure and also Section 6.11. Anyway, if both options do not fulfill our requirements on how the dispersion curve should look, we may use the mouse and click the required dispersion points by hand.



2. (default / advanced) Option `Maxi` for finding only the local maxima or `Inflex` for finding also the inflection points. See Section 6.11.



3. (default / advanced) Option `Analys` for making standard analysis or `FFT` for computing only the Fourier transform without filtration. If we select the `FFT` option, some of the edit boxes and buttons of the SVAL main window go gray and we cannot fill them. It enables us to compute the spectra of given record without the need to set any other parameters.

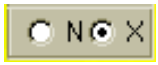


4. (default / advanced) Option `R` for using the measured **R**aw record or `F` for using the bandpass **F**iltered version. If we want to process the record, which should be both completely bandpass filtered and corrected for instrument characteristic, it must be bandpass filtered at first and than it is possible to make the instrument correction. Always only the original raw data from the data file enters the procedure for bandpass filtering and it is not possible to sent the instrumentally corrected seismogram into this procedure.

When using the `Filter corr` button for correcting the spectra of the bandpass filtered record, be sure, after selecting the `F` option, to press the `Analysis` button first and after that to use the `Filter corr` button. Because some of the quantities are computed only after the `Analysis` button is pressed, when pressing the `Filter corr` button directly after selecting the option `F`, the bandpass filtered record cannot be used.



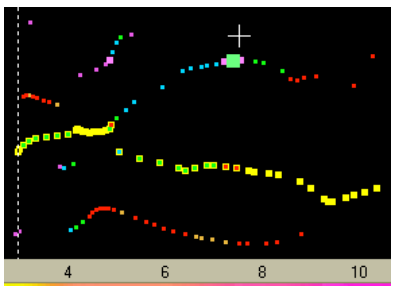
After selecting the `F` option, this alerts us, how to proceed in case we would like to make an analysis of the bandpass filtered record with instrumental correction applied.



5. (default / advanced) Option `N` for using the **N**atural truncating of the quasimonochromatic signal according to the derivative in inflection points of their envelopes or `X` for using the fi**X**ed width of the truncating. For details, see Section 6.11.



6. (basic) Another possibility how to influence the steps which are or which are not fulfilled during the analysis process, is to start the analysis by `Analysis` button from the time domain window – an analysis of the raw record is provided – or by the `Filter Corr` button from the frequency domain window – an analysis of the instrumentally corrected record is followed. The whole analysis is divided into two procedures. If we process the raw record by pressing the `Analysis` button, both of them are followed. If we start the analysis using the `Filter Corr` button in the frequency domain window, only the second part is used. For example, we do not need to compute the record spectrum again because we apply the transfer function in the frequency domain and we have already estimated the spectrum in previous steps.



7. (advanced) Manual dispersion points clicking. If we run the analysis for the first time, most of the computational steps are processed. After the first run, we have the possibility to manually select some of the dispersion points from the previous dispersion ridges estimation in the period-velocity diagram to ensure that they will be used for the dispersion curve compilation. We use this when we are not satisfied with the automatic procedure for selecting the dispersion points of different ridges into the main dispersion ridge compilation.

If we click some of the points, we substitute the formerly selected point in the respective filter by the clicked one. In the next analysis run, the substituted point is used and only part of the second analysis procedure is fulfilled, because most of the computations remains from the previous run. In fact, only the signals truncating according the new clicked point is provided. Hence, it is not possible to change the parameters of the filtration at the same time as we select some dispersion points by clicking on them. The analysis for the clicked point skips the filtration parameter reading and dispersion points estimation. The reason is that the manual selecting is aimed to improve the already done dispersion compilation while all other computations must remain the same.

If we do not click any of the points, the analysis will process normally all the steps and it will again select all the points by the automatic way as for the first time. Hence, if we click some point by accident and we want to undo it, we must press the `Analysis` button twice – for the first time it will process the unwanted accidentally clicked points and after that, it will return to the automatic processing.



(basic) Starts the main analysis procedures and computations. The details how to use the options are given above and in Section 6.11.

First part of the analysis

- it reads an epicentral distance (km)
- it reads a time interval between the origin time and the beginning of the record (s)
- it reads the sampling rate (Hz)
- it reads minimal and maximal group velocity used for filtration (km/s)
- if `Analys` checkbox is selected (whole analysis in process) (default option)
  - it reads minimal and maximal period to be used for filtration (s)
  - it reads the number of filters
  - it reads slope of the α coefficient
  - it reads the intercept point of the α coefficient
- it continues after the `Analys` checkbox loop
- it reads the number of samples to be smoothed by cosine window
- if the `R` is checked (record from a data file is used) (default option)
  - it reads the data from a file
  - it deducts a mean value from the data to keep the record oscillating around zero
  - it smooths edges of the record
- it continues after the `R` checkbox loop
- if the `F` is checked (advanced option)
  - it uses the bandpass filtered record
- in continues after the `F` loop
- it estimates an exponent of 2 for computing the number of samples to enter the FTT
- the power of 2 is calculated according to the number of samples

- it computes the time for each record sample according to the information given in the `Time interval` and `Sampl. freq.` edit boxes
- if `Analys` checkbox is selected (whole analysis in process) (default option)
  - the gamma coefficient as a geometric step between neighboring central periods is estimated according to the given number of filters in the given period range
  - if some of the filters are too close to each other, some of them are rejected and hence the final number of filters may be smaller than the one given in the edit box
  - central periods are estimated
- it continues after the `Analys` checkbox loop
- using the FFT a complex spectrum of the record is computed
- the spectrum is normalized into 100 dB scale
- if `FFT` checkbox is selected (FFT only without filtration) (advanced option)
  - the process terminates here
- it continues after the `FFT` loop
- α coefficients for each central period are estimated

End of the first part of analysis, the next procedure starts automatically and immediately.

Second part of the analysis

This procedure may be started by clicking the `Filter Corr` (advanced) button in the frequency domain window or it starts automatically after the first procedure terminates.



(advanced) Starts the analysis of instrumentally corrected record. As in the case of using `Analysis` button (basic), most of the quantities are deleted or overwritten. The drop-down lists of periods are filled with newly estimated values. However, contrary to the use of `Analysis` button, the frequency domain window keeps its settings and drawings from previous analysis to allow comparison of raw and corrected filtering. When using the `Filter corr` button for correcting the spectra of the bandpass filtered record, be sure, after selecting the `F` option (as **F**iltered), to press the `Analysis` button first and after that to use the `Filter corr` button. Because some of the quantities are computed only after the `Analysis` button is pressed, when pressing the `Filter corr` button directly after selecting the option `F`, the bandpass filtered record cannot be used.

Following steps are fulfilled in both cases after pressing the `Analysis` or `Filter corr` buttons.

- it filters the spectra for all central periods by weighting the original spectrum by Gaussian functions of appropriate width and centered to the appropriate periods
- it normalizes the filtered spectra
- each filtered spectrum is transformed back to the time domain using the inverse FFT; we obtain a complex time domain signals; by using only the positive frequencies for the inverse FFT we ensure that the real and imaginary part of this complex signals are connected by Hilbert transform – such signals are called "analytical signals"
- the analytical signals are used for computing envelopes and the spectrogram is created by a set of these envelopes

- the envelopes are normalized in respect to the absolute maximum of amplitude of all envelopes of all analytical signals
- five highest local maxima for each of the envelopes are found
- if `Inflex` is checked (advanced option)
  - also the inflection points with zero derivation are found; in some special cases, also these inflection points may be important for dispersion ridge estimation
- it continues after the `Inflex` loop
- if `L` is checked (advanced option)
  - the procedure for compiling the dispersion curve using all the local maxima of all filters starts from the highest maximum at the filter with the longest period; this option is used for example if we want to estimate the fundamental mode and we see some higher modes in the shorter-period part of the spectrogram; if we are sure that the maximum at the longest period belongs to the fundamental mode, we may choose this option to start the compilation of dispersion ridge at this maximum
- end of the `L` loop
- if `A` is checked (default option)
  - the procedure for compiling the dispersion curve using all the local maxima of all filters starts from the absolutely highest maximum of all the filter regardless of its position within the spectrogram; this option may be useful if the fundamental mode, which is wanted to be compiled, is clearly visible and its amplitudes are generally higher then the amplitudes of all other unwanted modes and body waves
- end of the `A` loop

  In both `L` and `A` cases the dispersion ridge is compiled by comparing all local maxima of each filter with respect to their position to the "starting" (`L` or `A`) maximum. The criteria are set to ensure that the resultant ridge will be as continuous as possible. In this compilation, only the position of the dispersion points in the period-velocity plane takes part, no respect is paid to their amplitudes.

For the automatically selected dispersion points, the next steps are also followed, but when some dispersion points were manually selected by clicking (advanced) in the period-velocity diagram, it starts the analysis procedure here and all the previous steps are skipped.

- the time moments for truncating each quasimonochromatic signals are found; four different times for each signal have to be found; between the inner two time moments the signal and its envelope remains the same and between the outer two and the inner moments the signal and its envelope is smoothed to zero by cosine window
- if `N` is checked (advanced option)
  - the four truncating points are found by natural way; using the envelope inflection points with the highest derivation closest to the selected maximum, the two inner points are found; the derivation of these points is then used for linear prolongation into the zero amplitude and so the outer two time moments are found; such truncating is generally asymmetric since the behavior of the envelope before and after its maximum may be different
- end of the `N` loop
- if `X` is checked (default option)

  - the truncating procedure is followed according to the fixed length both for the quasimonochromatic signal an for its envelope; as an optimal ratio we prefer that it keeps the signal of half of its central period before and after the maximum and the zero points of truncating are set to be at the distance of two and a half of central period to the both sides from the maximum; we use this fi**X**ed option when we want to process several records by the same way to ensure the same length of the truncated quasimonochromatic signals at the same central period from different records; it is useful especially for consecutive phase velocity estimation using the PhaseCorr program; this fixed length may be changed only in the source code of the SVAL program

- end of the `X` loop
- using the truncation time moments, the truncated and smoothed quasimonochromatic signals and their respective truncated and smoothed envelopes are estimated
- these truncated signals and envelopes are also normalized into the 100 dB scale using the absolute maximum of all signals as in the non-truncated case
- for each signal, the times when its phase crosses zero amplitude as close in time to the envelope maximum as possible are found; this time moments may be saved and used for rough estimation of phase velocity between two coherent records of the same event at two stations
- an instantaneous phase of all time samples of all signals is estimated
- an instantaneous frequency is computed as a derivation of the instantaneous phase with respect to time
- a group velocity of each time sample is estimated as a simple ratio of the epicentral distance and the respective time

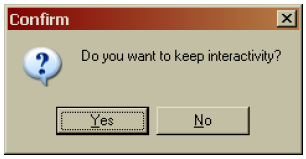
The analysis terminates by estimating the time which was needed for its processing. After the `Analysis` button was used, most of the formerly estimated quantities are overwritten or deleted. Also the frequency domain window is cleared. All the drop-down lists of periods are overwritten with the newly estimated values.

Batch processing

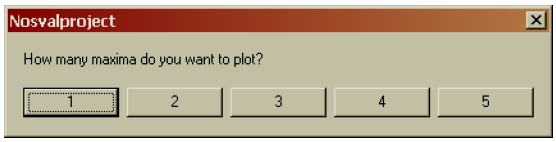
In next pages we describe the batch processing. We distinguish between the batch processing and the batch processing mode. By the term "batch processing" we mean the fact that the SVAL program automatically reads the files and analyzes them. By the term "batch processing mode" we mean that, even when the program is not currently processing any record, it keeps in memory some information about the batch processing. These are especially two facts: One is that it remembers the name of the last processed file and so it is able to process the next one when we again start the batch processing. The second fact is that the batch mode ensures that only the *.rdg file is saved by the `Save disp` button.



(advanced) Starts automatic batch processing and switch to the batch processing mode. Further dialogs appear after pressing this button to set the parameters of the batch processing and to select the directory which the data files are to be read from. Detailed description of the batch processing follows after the dialogs are introduced.



(advanced) Dialog box appears after pressing the `Batch proc` button. If `Yes` is selected, the SVAL program stops after the analysis of each data file and asks, if we are satisfied with the results or not. If `No` is selected, SVAL continues with the automatic batch processing file by file without stopping through the whole directory and analyzes all the data files in that directory.



(advanced) By pushing one of the five buttons, we may select the number of maxima which will be plotted during the batch processing. Selecting all five maxima gives us the most comprehensive information about the analysis results, but the plot becomes a bit busy and illegible. Recommended value is 2 or 3. See Section 6.11 for further details and Fig. 6.36 for plot examples.

After we choose the answers to the latter two dialogs, the batch processing starts. It simply provides operations as if they are initialized by pushing the following buttons:



Standard dialog for opening the file appears and asks for the directory from which the data files should be read. We have to select a file, not directory, however, it will remember only the directory, so it does not matter which file from the desired directory we select. Than it looks for the oldest file with the extension *.dat in the given directory. Only the new version of KUK file format data files are expected in the directory. There should not be any other *.dat files in the directory. The epicentral distance, time difference between the origin time and the time of the beginning of the record, sampling frequency and the name of the station are read from the header of the KUK file.



Provides all the computations exactly as if the `Analysis` button is pushed by clicking on it.



Clears the plot for drawing the seismograms. Each new raw record will be shown in a clear plot.



Draws the raw seismogram in the plot.



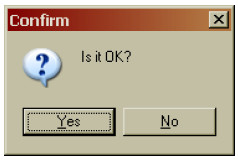
According to the number of maxima selected in the dialog, one to five maxima are plotted into the spectrogram plot window. This plot is not cleared during the batch processing and the new maxima are plotted over the old ones. See Fig. 6.36 for example.



The first and the last period from the drop-down lists are selected to save the propagation times for the broadest period range. The period values are displayed in the drop-down list edit boxes.



The propagation times are saved into the *.rdg file. When in the manual mode, the `Save disp` button saves three files, when in the batch mode, only the *.rdg file is saved. Only the *.rdg file is saved even in case the `Save disp` button is pressed manually while in the batch processing mode. See the details in the **file outputs** paragraph.



(advanced) When the `Do you want to keep interactivity?` dialog box was answered by `Yes`, after each analysis of each data file, this new box appears to ask us to continue. If `Yes` is selected, the SVAL program automatically reads next data file and continues with the batch processing. When `No` is selected, the program abort the batch processing and wait for next instructions.

Even in case the batch processing is aborted, the program keeps the batch processing mode. We may, for example, provide a manual correction for analysis of given data file and then again return to the batch processing. The `Save disp` button behaves as it is set for the batch processing even we press it manually when processing was aborted but batch mode is kept. We may save the file by pressing the `Save disp` button, but only the *.rdg file is saved, no other files with dispersion curves are created. The program keeps the name of the last file we processed and continues with the batch processing with the next file in the directory.

The number of processed files is written in the caption of the main SVAL window. After the processing terminates, the total number of processed files is also given in the text output box.

The whole automatic process treats one of the `Z-R-T` components selected in the auxiliary window. After the automatic procedure analyzes all the data files using that component, we can change the component in the auxiliary window and start the batch processing again to analyze all the files using the other component.

The batch processing may be arbitrarily aborted by answering `No` to the dialog box asking, if the analysis of the previous record went well. We may start it again, and the process will find the next file and continue with it.

Even in case we selected the non-interactive mode, when the program does not stop after each analysis, we may still abort the process and mode by pressing the `Open data file ...` button. It finishes the current analysis and then it asks, if we really want to cancel the process. If we answer `Yes`, not only the batch processing but also the batch processing mode is terminated and SVAL is ready to read and analyze any other files manually.

Most of the messages which may pop-up during the manual analysis are disabled when in the batch processing mode not to break the automatic analysis. However, some fatal ones may still be displayed on the screen and wait for confirmation. It concerns especially the situation, when the number of samples allocated in the memory is insufficient to cover the desired time window for the analysis. In this case, the user's interaction is expected, since the program itself cannot solve this problem. Thus it is recommended to use the highest option of 32768 samples for the batch processing. However, problems may still occur. In case even this highest option is not enough, after the message box is confirmed, the batch processing is aborted and we can narrow the group velocity range to fit the time window into the number of samples available. Then we have to provide the analysis manually, as well as we have to save the file manually. After that, we can again broaden the velocity range and start the batch processing again. Since it keeps the batch mode, it proceeds with the next file in the directory.

The same apply for the massage which pops-up when the time window given by the velocity interval set for the processing is out of the data in the input file. In this case, the message displays and after confirming it, the processing is aborted and we can proceed exactly as in the previous case. We may set the velocity interval to be narrower, provide the analysis manually, save the *.rdg file manually by pressing the `Save disp` button, and start the batch processing again.

Please notice the difference – when in the manual mode, in case the velocity is out of the file range, a new velocity is set in the `Min group vel.` or `Max group vel.` edit boxes and the analysis continues. However, in case of the batch processing, when the new velocity is set, the analysis terminates. It is implemented to allow the user to decide, how to deal with the short data file in the case of batch processing, because it is supposed that the seismologist wants to process all the records for the same velocity range. Thus, by terminating the analysis, we may skip the record or process it for narrower velocity range and then go back with the broader range. If the batch analysis proceeded itself, we would not have the possibility to set the original broad velocity range for the rest of the records.

In these cases, this manually analyzed record is not counted in the total number of files analyzed by the batch processing. We may even completely skip the problematic record. After confirming the message that it was out of the sample range or out of the input file, simply start the batch processing again and it will continue with the next file without the processing of the problematic record. In case the velocity range was out of the input file, remember that the new velocity is set into the edit box to tell us, what is the limiting possible velocity for the first/last sample in the file. If we want to skip the problematic

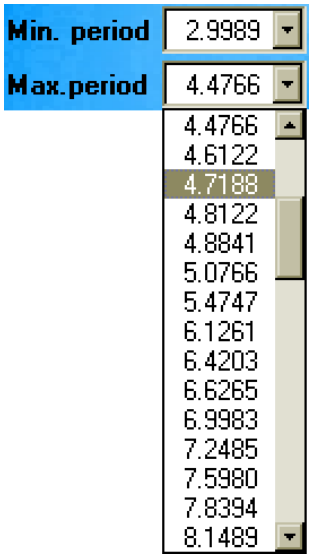
record and to continue with the rest of the files, we must not forget to set the changed velocity again to the desired value in the edit box.

Batch processing is intended to analyze many records at once. Since the seismologist is not checking all the computational steps in detail, no dispersion curve is compiled. This is the reason why the files *.dat and *.itp are not saved by the `Save disp` button while in the batch mode. This automatic procedure is there to help us to extract the basic properties of the records and to save the propagation times of the dispersed surface wavegroups. Five propagation times corresponding to the five highest maxima are saved for each harmonic component (each period) with no specification which time corresponds to which mode.

For further processing, we have developed sequential program called Widle, which is able to read the *.rdg files for many stations and with the help of the seismologist it extracts the times corresponding, for example, to the fundamental mode or to some surface wave reflected modes.

Inversion parameters

As in case of analysis, the processing of the inversion problem is also controlled by several options and by setting of starting values of velocities and densities. All this setting is considered to be advanced, because the inversion is not a part of the basic SVAL analysis.



Minimal and maximal period (drop-down option list) to be inverted (advanced) or to be used for creating the filtered (separated) velocigram (seismogram) containing only the surface wavegroup (advanced) and needed for selecting of a part of the dispersion curve for saving (basic). Hence, selecting the period range by this option we may influence both inversion and separated surface waveform compilation. This period range influences also the period-velocity plot zooming. While loading the dispersion saved in a file, we set the periods of this dispersion curve in this drop-down lists by pressing the `Use loaded` button (advanced). In case that two-dispersion file is loaded, only the periods of the first column (Love waves) are displayed in the list. But selecting any of the period affects not only the selected value of Love wave dispersion point, but also the period of the Rayleigh wave dispersion point given in the same file row. Hence, there is a good reason to manage the two-dispersion file in such a manner that it contains an approximately similar periods in each row to enable an easy period range selection for both dispersion curves together.



If the selection of the minimal period fails after clicking on the drop-down list, this notice is given.



If the selection of the maximal period fails after clicking on the drop-down list, this notice is given.



If the number of parameters to be estimated by the inversion is greater than the number of dispersion points, this message is given. But we may still proceed, no limitation is given to the number of parameters – number of data ratio. This is only to notice that the number of dispersion points we have selected is a bit small or the number of layers is a bit high.



(default / advanced) This option allows the program to look for low velocity zones (LVZ) durign the inversion. Default options is checked. If unchecked, the inversion procedures seeks only a velocity distribution which is increasing with the depth all the time.



(default / advanced) Group / phase velocity starting value for the forward problem computing (km/s). It is possible to change this value but it is not necessary, the value of group / phase velocity of the minimal period selected for inversion is automatically set into this edit box.



(default / advanced) Approximate shear wave velocity in the surface layer.



(default / advanced) When this check box is selected, the shear wave velocity in the first layer remains unchanged during the inversion. Default value is unchecked and hence the velocity in the first layer is also looked for.



(default / advanced) Chosen value of the v_p/v_s ratio and range of its variability; applicable only when inversion for Rayleigh waves is to be applied.



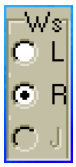
(default / advanced) Maximal decrease of S-wave velocity in the next layer when LVZ is enabled. The maximal increase of S-wave velocity in next layer is six time this value. It is also a constant step of velocity increase of the default starting model. See Section 6.13 for details.



(default / advanced) Approximate density value in the surface layer (g/cm^3).



(default / advanced) Approximate step of density in next layer (g/cm^3). It is also a constant step of density increase of the starting model. This starting model is used as additional "measured" data and the density can vary within the interval of (–1*`Dens.step`; +6*`Dens.step`); the density handling differs from the velocity one and so the density could not be presented as a unaffected result of inversion because it is strongly constrained. When the option for keeping a constant density values during the inversion is checked (default option), the starting density model given by `Surf dens` and `Dens. step` is kept for all inversion iteration.



(default / advanced) Love `L`, Rayleigh `R` or joint `J` inversion option. The `J` option is available only when a file with two dispersion curves is loaded and set for inversion. After it is possible to select one of these options, we are asked to select the period range for inversion again even in case we have already selected it before.



This message asks to select the period range again. This is a bit bothering bug. It is not possible to select the type of the wave before the period range is selected and it is not possible to send the proper previously selected period range to next procedures after the wave type is selected. So this inconvenience ensures the proper function. During the `L-R-J` option selection, many parameters have to be set in the SVAL arrays again and the number of inversion parameters has to be computed. Hence this re-selecting is asked. Simply click again in the roll-down menus with the lists of periods to do this. The `Inversion` button will be disabled until the minimal and maximal period is selected again.



(default / advanced) Group or phase velocity inversion option.



(default / advanced) Option for keeping the density constant during the inversion. The density keeps the value for each layer given by the starting model. Hence, it does not mean that the values are the same in all the layers, but it means that the individual value of density for each layer is not changed by the inversion process.



(default / advanced) Starts the inversion. This button is placed in the inversion window showing the inversion progression. Do not confuse it with the `Inversion` button placed in the SVAL's main window. The inversion procedure is ended by fulfilling of the given misfit function condition (provided in the source code) or may be canceled by the user. When `Unlimited iteration` is checked, it runs forever.



(default / advanced) Inversion problem progression canceling. This button may be pressed anytime, but the action takes place only every twenty iteration. For example, if we pres this button during the iteration number 1243, we have to wait until 1260 when the run will be canceled. This is because of saving the computational time – SVAL does not check the pressed button all the time while processing some other task. This button cancels the inversion process before the misfit function conditions for terminating are fulfilled but in this case its using is optional and it does not have much sense. When `Unlimited iteration` is selected, this button is the only possibility to terminate the inversion since the terminating conditions are disabled.



When the inversion is stopped by the above described `Stop` button, this message is displayed after the inversion really terminates.

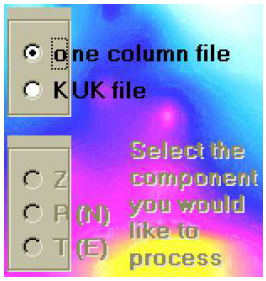


(default / advanced) During standard inversion process, this box is unchecked and after the terminating condition of the inversion is fulfilled (the misfit is low enough, for example), the inversion process ends. When this box is checked, the parameters controlling the finishing of the inversion are out of order and the process runs forever. This is suitable for testing if many iterations make the results better (what is usually not the case). The inversion process can be interrupt by pushing the `Stop` button.

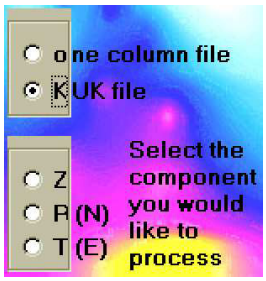
Window and mode switching



(basic) Options for maximal number of samples selection. The `no record` option (advanced) is used when we deal with a loaded dispersion curve and hence we do not need any memory to be allocated for processing the records. In fact, even in this case some small amount of memory is allocated not to have a zero-sized arrays.



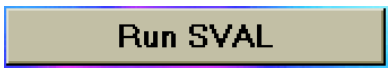
Option for selecting the input file. As a default, the option for `one column file` is selected (basic). In case we want to use the three-component file from the KUK program, we can select the `KUK file` option (advanced). We do not have to care about the old/new version of the KUK format, the program recognizes it itself.



(advanced) Option for selecting the component from the KUK file. No component is selected by default and we have to select one of them to proceed when the `KUK file` selection is provided.



When no component is selected after the KUK file option was enabled, this message is displayed on the screen.



(basic) Opens the main SVAL window.



(advanced, but useful) Closes all windows and terminates the SVAL program.



(advanced) Opens the window for frequency domain viewing.



(advanced) Opens the window for inversion progression checking. Several parameters and inversion settings are controlled when pressing this button. Do not confuse this button with the `Inverse` button placed in the inversion window.



In case the type of the waves is not selected, this message pops-up and the inversion window does not open.



In case the starting velocity for inversion given in the `U/c startin'` edit box is negative, this message pops-up.



In case the surface velocity given in the `Surf. S-vel` edit box is negative, this message pops-up.



In case the v_p/v_s ratio given in the `Vp / Vs` edit box is negative, this message pops-up.



In case the v_p/v_s ratio deviation given in the $\pm$ edit box is negative, this message pops-up.



In case the shear wave velocity step given in the `S-vel step` edit box is negative, this message pops-up.



In case the surface density given in the `Surf dens` edit box is negative, this message pops-up.



In case the density step given in the `Dens. step` edit box is negative, this message pops-up.



(advanced) Opens and closes the auxiliary window for memory allocation settings and for selection of a component (if `KUK file` option is given). These settings may be altered during the run of the SVAL program and the SVAL main window settings remain unaffected.



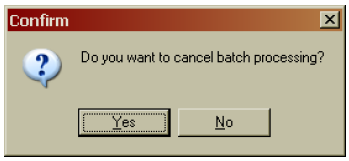
(advanced) By checking this option we switch into the interactive mode for manual structural model setting. By clicking into the detached velocity distribution in the depth-velocity plot we may create a new velocity distribution, which may be used for forward computation of corresponding dispersion curve by clicking the `Starting disp` button in the Inversion window. It can be used also as a new starting model. If we manually set some new velocity distribution and then we start the inversion, it uses the manually set model as a starting one. Before the inversion starts, it is useful to check the reliability of the set starting model by clicking the `Starting disp` button and visually compare the starting dispersion curve with the measured one.



(advanced) Starts automatic batch processing and switch to the batch processing mode. The other functions of the `Batch proc` button are described in detail in the **keyboard inputs** paragraph.



(advanced) While in the batch processing mode, this button terminates this mode. It asks if we really want to do it. When the batch processing is running in the mode without asking for continuation with the next file, this button can abort this processing and then terminate the batch mode.



(advanced) When the SVAL program is in the automatic batch processing mode and the `Open data file...` button is pushed, the program asks if we really want to cancel the batch processing. By selecting `No` the dialog box disappears and the program continues with the batch processing. By selecting `Yes` the program terminates the batch processing mode and shows a dialog box to open the data file intended for the manual analysis. If we do not want to open a new file, we simply cancel this opening dialog box (the batch processing mode remains canceled even in this case). The other functions of the `Open data file...` button are described in the **file inputs** paragraph.

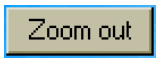
Display controls



(advanced) Zooms the view of desired part of the dispersion curve in the direction of the X (period) axis according to the selected minimal (`Min. period`) and maximal period (`Max. period`).



(advanced) Zooms the view of selected part of the dispersion curve in the direction of the Y (velocity) axis according to the fastest and slowest dispersion point of the selected part of the dispersion. When no minimal and maximal period is selected (and hence the Zoom X button is disabled) it zooms to the fastest and slowest dispersion point found in the whole spectrogram.



(advanced) In the main window: zooms to the default view of the period-group velocity plane.



(advanced) In the inversion window: zooms to the whole iteration-misfit plot view.



(advanced) Increases and decreases the amplitude of seismograms and quasimonochromatic signals.



(advanced) Enlarges, narrows and shifts (left / right) the window for the structure depiction. The "+" symbol also zooms into the upper part of the layers near the Earth surface and the "–" symbol returns to the previous greater depth view.



(advanced) Zooms in the Y (amplitude) axis of the frequency domain plot, the range of the Y axis is set to the half of the previous value. It means that amplitude of the spectrum is doubled.



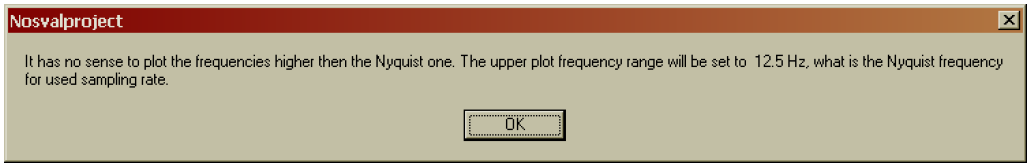
(advanced) Zooms out the Y (amplitude) axis of the frequency domain plot, the range of the Y axis is doubled, it means that the amplitude of the spectrum is half of the previous value.



(advanced) Edit box for entering the minimal frequency (Hz) which should be displayed in the frequency domain plot.



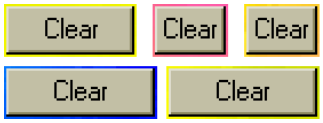
(advanced) Edit box for entering the maximal frequency (Hz) which should be displayed in the frequency domain plot. Both latter edit boxes are operated in the frequency (Hz) mode also in the case of log-log spectrum depiction.



When the user tries to redraw the plot up to the frequency higher then the Nyquist one, this message is displayed. The same message is displayed when any other button drawing spectra or filters in the plot is pushed while too high frequency is set in the `max freq (Hz)` edit box. This does not apply for drawing the instrumental transfer functions, when higher frequencies then the Nyquist one may be shown.



(advanced) Zooms in the frequency range selected by the two latter edit boxes.



(advanced) Clear the nearest plot.

6.6 File outputs

All output files contain headers with information about the quantities in corresponding columns. These headers are written in one or two lines to be easily erased. While using the output files for imaging by Grapher or Surfer, the headers may be used for identification of the columns with quantities since both graphical programs enables to skip the first line and display its text in the dialogs for selecting the columns. In case of two-lines header it is comfortable to delete on of the lines while loading the files for Grapher depiction. The only exception is the large output file with all the quasimonochromatic signals,

where one/two lines are not sufficient as a header and so its header is made of four lines. While working with Grapher, it is useful to delete three of them.

The output files generally enables to save the raw signals or the signals with instrument correction applied. It concerns as well the original record, as well the filtered (separated) wavegroups, dispersion curves, spectrogram, single quasimonochromatic signals and the file with all the filtered signals together. Generally, type of the saved files depends on the fact, if we have selected the instrument correction using the dialog box in the spectral domain window and if we have pressed the `Filter corr` button, which starts the analysis of the corrected record. After that, all the quantities are operated in the "corrected" manner. For example, after using the `Analysis` button in the time domain window, all the consequently created files will be saved in raw modification. While saving output files, the SVAL program gives an announcement, if the raw or instrumentally corrected data are saved. The headers of files contain the information about what type of data is written in the corresponding column. While saving the data with instrument correction applied, the column label start with `Corr`, as "Corrected". For easy recognition, it is useful to give the names of files in such a manner that one can directly see, if it is the file with raw or corrected data.

This duality of saving the raw/corrected data has nothing to do with the fact that some of the `Save` buttons create two or three files at the same moment with different quantities in them. This multiple-saving feature was implemented because the structure of some data does not allow to save it in columns of the same number of lines, or the number of columns would be too high to keep the output files well arranged. So, regardless of the fact that one or more files are saved by one button at the same moment, generally, saved file / files may be created in one of two raw/corr modifications.

Generally, all file names should be set without any extension. The extensions are made by the SVAL program. Regardless of the extension, all the files are saved as a simple ASCII text files.

The `Save` buttons are located as near as possible to the plots which display the quantities saved by the corresponding buttons. All `Save` buttons are to be considered as advanced, because it is an optional feature to save the results. We do not label the buttons in further text by the (advance) sign.

Save records



One file is saved by this button. `SvRc` means "**S**a**v**e **Rc**ords". It's SVAL extension is *.dat. There are four possibilities of the file structure clearly displayed in their headers: we may save the raw or corrected record and we may or may not create and save the filtered (separated) wavegroup. This separated wavegroup is again operated in raw or corrected manner. Before the separated wavegroup may be saved, we have to select the period range of the wavegroup and we have to press the `Slctd group` button to create the wavegroup.



In case no filtered (separated) surface wavegroup was created, this message pops-up. After it, the next message is displayed. When we want to create the separated wavegroup, we have to confirm also the next message and then cancel the dialog for saving the file.



In case no instrumental correction was applied, this message informs that only raw records will be saved. Appropriate headers are set to the saved files.



In case both previous messages were confirmed and the file was named and saved, this messages informs, what was saved in the file.



In case the period range had been selected and filtered (separated) surface wavegroup had been created and saved, this messages informs, what was saved in the file. It does not matter if we had created the separated wavegroup before we attempted to save the file, or if we canceled the saving when the notice of no separated wavegroup popped-up and we created the separated wavegroup additionally.



In case no filtered (separated) surface wavegroup was created, but instrumental correction was applied, this message pops-up. After it, the next message is displayed. When we want to create the instrumental corrected separated wavegroup, we have to confirm also the next message and then cancel the dialog for saving the file.



In case the instrumental correction was applied, this message informs that corrected records will be saved. Appropriate headers are set to the saved files.



In case both previous messages were confirmed and the file was named and saved, this messages informs, what was saved in the file.

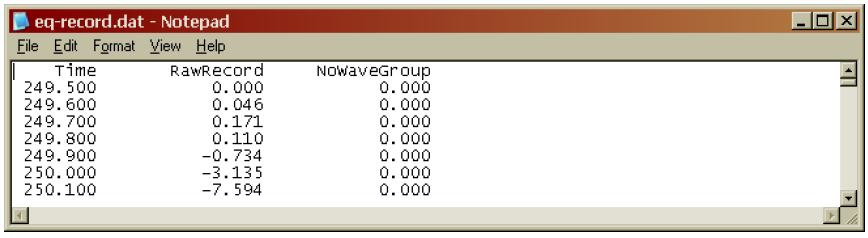


In case the period range was selected and corrected filtered (separated) surface wavegroup was created and saved, this messages informs, what was saved in the file. It does not matter if we had created the corrected separated wavegroup before we attempted to save the file, or if we cancel the saving when the notice of no corrected separated wavegroup popped-up and we created the corrected separated wavegroup additionally.

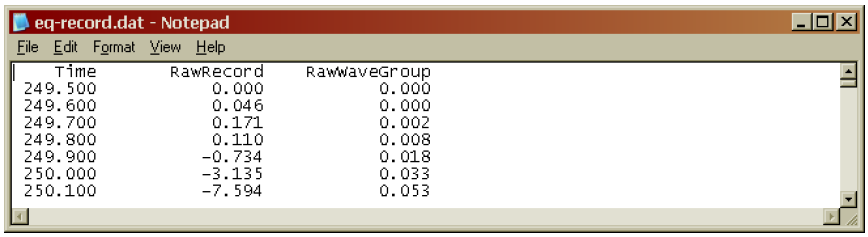
File columns containing following values are saved:

- time measured from origin time (s)
- record (amplitude)
- filtered (separated) seismogram for the selected period range (amplitude), optionally

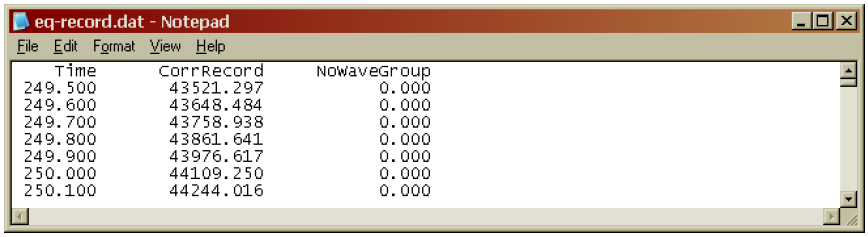
The four header possibilities are:



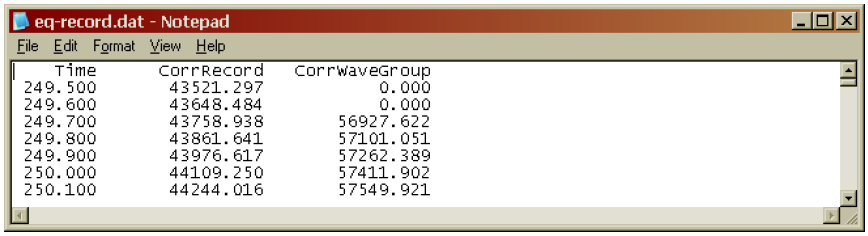
Header for time, raw record and no filtered (separated) wavegroup.



Header for time, raw record and raw filtered (separated) wavegroup.



Header for time, instrument-corrected record and no filtered (separated) wavegroup.



Header for time, instrument-corrected record and instrument-corrected filtered (separated) wavegroup.

Save dispersion



Three files are saved by this button. Before this file may be saved, we have to select the period range for the dispersion we want to save.



If no period range is selected, this message pops-up and the saving terminates.

The file's #1 SVAL extension is *.dat and this file is saved only when in the manual mode. Batch mode processing does not save this file. File columns containing following values are saved:

- instantaneous period of given filter (s)
- instantaneous frequency of given filter (Hz)
- propagation time of the dispersion point (s)
- group velocity of the dispersion point (km/s)
- normalized amplitude (100 dB scale) of the dispersion point (the same as in spectrogram)
- central period of given filter (s)
- instantaneous period of the phase zero point which is the nearest one to the group maximum (s)
- propagation time of this phase zero point (s)

Two latter columns contain information about the phase arrival. The arrival time of the zero amplitude of the quasimonochromatic signal is saved as well as its instantaneous period. This information may be used for rough estimation of the phase velocity between two stations for the record of the same event. Thus these two columns presents something as phase velocity dispersion curve, but single station estimation of these quantities has no direct use and sense. The two header possibilities for file #1 are:

dispersion.dat - Poznámkový blok

Soubor Úpravy Formát Zobrazení Nápověda

InstPeriod	InstFrequency	PropagTime	GroupVeloc	Amplitude	CentralPeriod	PhasePeriod	PhasePosition
3.0370	0.3293	518.520	3.1485	220.7922	3.0912	3.0164	517.4900
3.1149	0.3210	518.920	3.1460	194.5039	3.1813	3.0903	517.4600
3.2376	0.3089	518.920	3.1460	168.9286	3.2767	3.2210	517.4000
3.4509	0.2898	518.770	3.1469	153.8391	3.3780	3.4563	517.2900
3.6406	0.2747	518.690	3.1474	155.1649	3.4492	3.6599	517.2100
3.9198	0.2551	518.760	3.1470	180.1344	3.5616	3.9273	517.1000
4.1160	0.2430	519.390	3.1432	235.6737	3.6817	4.1685	521.1100

Header for raw dispersion.

dispersion.dat - Poznámkový blok

Soubor Úpravy Formát Zobrazení Nápověda

InstPeriod	CorrInstFrqnc	CorrPropgTime	CorrGrupVeloc	Amplitude	CentralPeriod	PhasePeriod	PhasePosition
3.0369	0.3293	518.440	3.1489	220.8714	3.0912	3.0199	517.5500
3.1146	0.3211	518.830	3.1466	194.5109	3.1813	3.0952	517.5300
3.2376	0.3089	518.820	3.1466	168.8981	3.2767	3.2260	517.4700
3.4513	0.2897	518.670	3.1475	153.8300	3.3780	3.4570	517.3800
3.6411	0.2746	518.590	3.1480	155.1998	3.4492	3.6559	517.3100
3.9203	0.2551	518.660	3.1476	180.2570	3.5616	3.9231	517.2200
4.1152	0.2430	519.260	3.1440	235.8158	3.6817	4.1760	521.2400

Header for corrected dispersion.

The file's #2 SVAL extension is *.itp; extension abbreviation stands for "**i**n**t**er**p**olated" and this file is saved only when in the manual mode. Batch mode processing does not save this file. This file contains interpolated dispersion curve. There are fixed values of period with the step of 0.05 s (for saved period range grater than 1 s) or 0.005 s (for saved period range smaller than 1 s) for which the dispersion is linearly interpolated according to the neighboring estimated dispersion points. The first and the last point of this file are extrapolated out of the range of periods selected for saving. The interpolated dispersion file is useful for comparing dispersion curves estimated for different records by using generally different central periods. This file is also saved for raw or corrected dispersion. File columns containing following values are saved:

- period (s) with the 0.05 (or 0.005) s step
- interpolated (to the period values) propagation time (s)
- interpolated group velocity (km/s)

The two header possibilities for file #2 are:

dispersion.itp - Notepad

File Edit Format View Help

Period	InterpolTime	InterpolGroupVel
3.100	519.300	3.124
3.150	518.687	3.127
3.200	518.074	3.131
3.250	517.461	3.135
3.300	516.883	3.138
3.350	516.679	3.140
3.400	516.476	3.141

Header for raw interpolated dispersion.

dispersion.itp - Notepad

File Edit Format View Help

Period	CorrIntrplTime	CorrIntrplGrpVel
3.100	519.323	3.124
3.150	518.729	3.127
3.200	518.135	3.131
3.250	517.542	3.134
3.300	516.982	3.138
3.350	516.779	3.139
3.400	516.576	3.140

Header for corrected interpolated dispersion.

The file's #3 SVAL extension is *.rdg; extension abbreviation stands for "**ridg**e". This file is saved in both manual and batch processing mode. But when in the batch processing mode, only this file is saved and files #1 and #2 are not saved by the `Save disp` button. If in the batch processing mode, it does not matter, if the file is saved by the automatic procedure or manually by clicking the `Save disp` button. In both cases, only this *.rdg file is saved. When in the batch processing mode, the name of the *.rdg file is created automatically. It is given by the name of the station with 3 to 5 characters. If the station name has less then 5 characters, it is complemented by zeros up to the number of 5 characters. The sixth character is the underscore '_' and the seventh is one of the letters `Z`, `R` or `T` to mark the record component. When the `Save disp` button is pushed and the program is in the batch processing mode, this action does not pop-up the save file dialog. It simply creates the name of the file and saves it into the active directory. It is used when the batch processing is aborted to correct some of the record analysis which did not result properly. The SVAL program remains in the batch processing mode, however, we may change the parameters of analysis, provide the analysis again, select the period range, push the `Save disp` button and the *.rdg file will be created, named and saved as it would be done by the automatic batch processing procedure itself.



Example of the automatic name of the *.rdg file. This is for the station `TREC` and transverse component `T`.

When in the manual mode, the name of the *.rdg file is arbitrarily set by the user and is the same as for the #1 *.dat and #2 *.itp files. This file contains travel times (group times) of all five maxima for each filter. The width of the envelope maxima is also given as an estimation of the error. The width is measured as a distance between the two closest inflection points before and after the time of the envelope maxima. These widths are given in seconds, however, the absolute values of the widths have no specific meaning, they are given to relatively compare the quality of estimation with respect to period. One may decide that the "'true"' error of time determination would be, for example, 10 % of these widths. The first line of the file contains the epicentral distance in km. Because only travel times are saved in this file, the epicentral distance may be required to compute the group velocities in further processing. This file is also saved for raw or corrected dispersion curve. File columns containing following values are saved:

- instantaneous period (s) of the 1^{st} (highest) maximum
- travel time from origin (s) of the 1^{st} (highest) maximum
- width of the 1^{st} (highest) maximum (s)
- instantaneous period (s) of the 2^{nd} maximum
- travel time from origin (s) of the 2^{nd} maximum
- width of the 2^{nd} maximum (s)
- instantaneous period (s) of the 3^{rd} maximum
- travel time from origin (s) of the 3^{rd} maximum
- width of the 3^{rd} maximum (s)
- instantaneous period (s) of the 4^{th} maximum
- travel time from origin (s) of the 4^{th} maximum
- width of the 4^{th} maximum (s)

- instantaneous period (s) of the 5th maximum
- travel time from origin (s) of the 5th maximum
- width of the 5th maximum (s)

The two header possibilities for file #3 are:

dispersion.rdg - Poznámkový blok

Soubor Úpravy Formát Zobrazení Nápověda

1622.000

InsPer1	Time1	Err1	InsPer2	Time2	Err2	InsPer3	Time3	Err3	InsPer4	Time4	Err4	InsPer5	Time5	Err5
13.190	531.300	23.900	12.463	612.400	22.350	13.708	388.500	38.850	11.419	441.600	3.150	14.846	310.100	8.550
13.548	530.400	24.500	12.829	613.200	18.600	13.831	389.100	74.650	12.543	441.400	6.450	0.000	0.000	0.000
13.915	529.300	25.450	13.216	615.700	17.100	14.120	391.100	23.600	0.000	0.000	0.000	0.000	0.000	0.000
14.295	528.100	26.800	13.755	619.500	18.350	14.574	394.100	21.650	14.367	341.600	27.750	0.000	0.000	0.000
14.700	526.500	28.000	14.437	621.900	22.350	15.158	397.800	21.300	15.366	323.000	26.200	0.000	0.000	0.000
15.140	524.600	28.450	15.230	621.500	19.750	15.742	401.300	23.700	15.659	315.500	33.750	0.000	0.000	0.000
15.627	522.300	28.600	16.124	614.800	18.050	16.247	402.500	24.950	15.901	312.600	35.900	0.000	0.000	0.000
16.172	519.700	29.700	16.817	400.300	30.900	16.203	309.100	31.200	0.000	0.000	0.000	0.000	0.000	0.000
16.787	516.600	31.600	16.723	609.900	24.950	17.459	396.200	25.000	17.133	296.200	12.750	0.000	0.000	0.000
17.468	513.200	33.650	17.514	612.800	26.900	18.075	392.400	28.100	0.000	0.000	0.000	0.000	0.000	0.000
18.225	508.700	33.050	18.742	605.800	21.850	18.774	390.400	33.450	0.000	0.000	0.000	0.000	0.000	0.000
19.113	502.600	30.750	19.765	392.500	28.050	19.637	291.400	18.100	0.000	0.000	0.000	0.000	0.000	0.000

Header for raw travel time file.

corrdispersion.rdg - Poznámkový blok

Soubor Úpravy Formát Zobrazení Nápověda

1622.000

InsPer1	CrrTime1	Err1	InsPer2	CrrTime2	Err2	InsPer3	CrrTime3	Err3	InsPer4	CrrTime4	Err4	InsPer5	CrrTime5	Err5
13.196	529.800	23.900	12.470	611.200	22.250	13.715	386.300	38.300	11.483	438.800	3.800	14.881	308.700	8.450
13.556	528.800	24.500	12.841	611.900	18.550	13.844	387.500	73.950	12.797	439.900	6.150	0.000	0.000	0.000
13.922	527.700	25.500	13.228	614.200	17.250	14.137	389.500	23.650	0.000	0.000	0.000	0.000	0.000	0.000
14.303	526.400	26.900	13.762	617.800	18.400	14.592	392.400	21.450	14.455	338.600	28.150	0.000	0.000	0.000
14.710	524.700	28.000	14.443	620.200	22.350	15.171	395.900	21.250	15.388	320.600	26.400	0.000	0.000	0.000
15.152	522.600	28.400	15.241	619.600	19.650	15.749	399.200	23.750	15.668	313.400	34.350	0.000	0.000	0.000
15.641	520.200	28.700	16.159	612.500	18.000	16.258	400.200	25.450	15.901	310.500	36.150	0.000	0.000	0.000
16.191	517.300	29.700	16.839	397.800	31.550	16.199	306.600	21.950	0.000	0.000	0.000	0.000	0.000	0.000
16.808	514.100	31.750	16.735	607.300	25.150	17.488	393.500	24.150	17.190	293.100	12.400	0.000	0.000	0.000
17.492	510.400	33.950	17.526	610.200	26.800	18.116	389.400	28.500	0.000	0.000	0.000	0.000	0.000	0.000
18.255	505.600	33.200	18.773	602.800	21.700	18.832	387.500	33.800	0.000	0.000	0.000	0.000	0.000	0.000
19.161	499.100	30.500	19.852	390.300	27.550	19.706	288.200	17.350	0.000	0.000	0.000	0.000	0.000	0.000

Header for corrected travel time file.



In case all files with no instrumental correction are to be saved by the `Save disp` button, this message is displayed.



In case all files with the instrumental correction are to be saved by the `Save disp` button, this message is displayed.

Save spectrogram



Three files are saved by this button, all of them in one of two raw/corrected options. The file's #1 SVAL extension is *.dat. A standard frequency-time spectrogram is saved into this file. Selected period range does not influence the data saved in this file, however, the period range has to be selected, because the file #3 needs it. Columns containing following values are saved:

- time (s)
- frequency (Hz)
- amplitude
- normalized amplitude (dB)

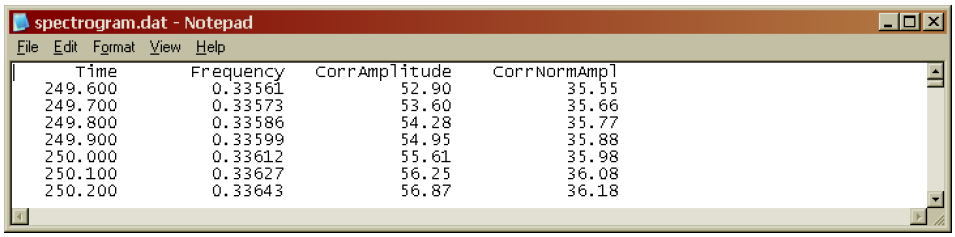
The two header possibilities for file #1 are:

spectrogram.dat - Notepad

File Edit Format View Help

Time	Frequency	Amplitude	NormAmpl
249.600	0.33563	53.39	37.80
249.700	0.33574	54.08	37.91
249.800	0.33587	54.75	38.01
249.900	0.33601	55.41	38.12
250.000	-4.66384	56.05	38.22
250.100	0.33632	56.68	38.31
250.200	0.33649	57.30	38.41

Header for raw frequency-time distribution.

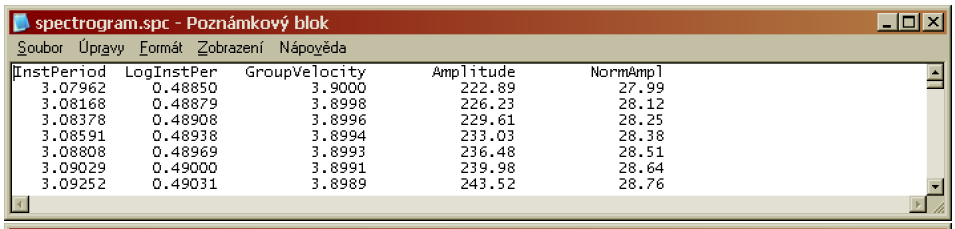


Header for corrected frequency-time distribution.

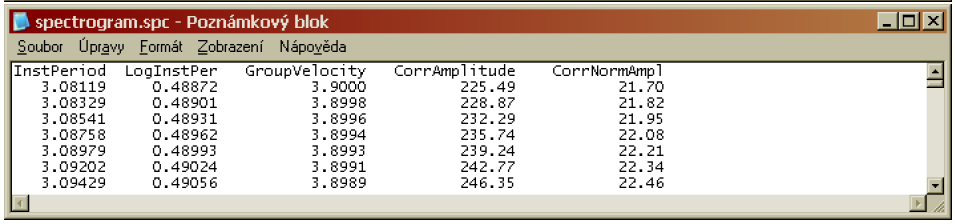
The file's #2 SVAL extension is *.spc; extension abbreviation stands for "**spec**trogram". A spectrogram for a complete period / velocity plot is saved. Selected period range does not influence the data saved in this file, however, the period range has to be selected, because the file #3 needs it. Columns containing following values are saved:

- instantaneous period (s)
- log of instantaneous period
- group velocity (km/s)
- amplitude
- amplitude normalized into 100 dB scale

The two header possibilities for file #2 are:



Header for complete raw period-group velocity distribution.



Header for complete corrected period-group velocity distribution.

The file's #3 SVAL extension is *.trc. Extension abbreviation stands for "**trunca**ted" spectrogram. Before this file is saved, we have to select the period range for the truncated spectrogram we want to save.

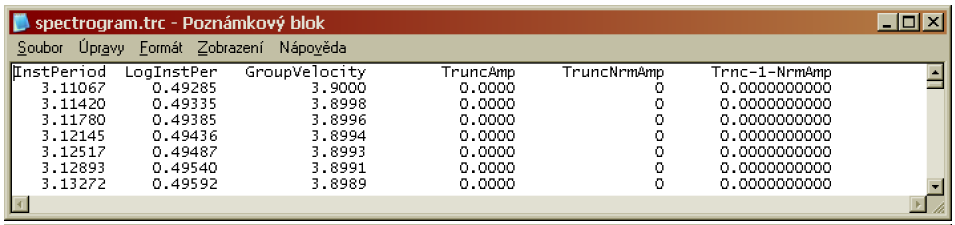


When no period range is selected, this message is displayed and after its confirmation, the saving terminates.

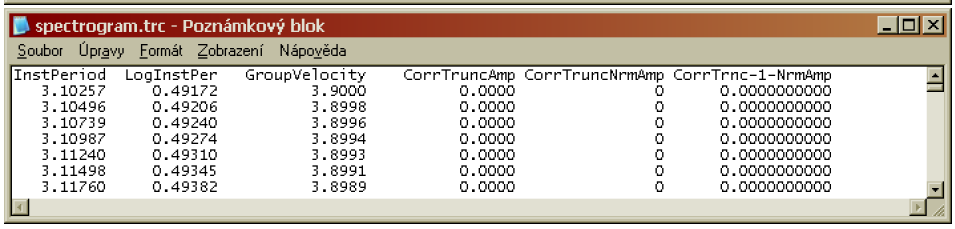
Columns containing following values are saved:

- instantaneous period (s)
- log of instantaneous period
- group velocity (km/s)
- truncated amplitude
- truncated amplitude normalized into 100 dB scale
- truncated amplitude normalized in such a way that selected maximum of each filter has the value of 1.0

The two header possibilities for file #3 are:



Header for truncated raw period-group velocity distribution.



Header for truncated corrected period-group velocity distribution.

All these "spectrogram" files are used for imaging the spectrogram as a 3D plane, for example in Surfer (Golden Software).



This message informs that spectrograms with no instrumental correction will be saved.



This message informs that spectrograms with the instrumental correction will be saved.

Save monochromatic signals



Three files are saved by this button, all of them in one of two raw/corrected options. The file's #1 SVAL extension is *.dat. Only the channel selected from the period drop-down list is saved into this file. Columns containing following values are saved:

- time measured from origin time (s)
- instantaneous period of nearly monochromatic signal (s)
- amplitude of nearly monochromatic signal
- envelope of nearly monochromatic signal
- amplitude of truncated nearly monochromatic signal
- envelope of truncated nearly monochromatic signal
- instantaneous phase of the analytical signal corresponding to the quasimonochromatic signal; the real part of the analytical signal equals the monochromatic signal and the imaginary part is a Hilbert transform of it; the instantaneous phase is arctan of the Im/Re ratio

The two header possibilities for file #1 are:

monochrom.dat - Notepad

File Edit Format View Help

Time	InstPeriod	WholeMonochrom	WholeEnvelope	TruncMonochrom	TruncEnvelope	AnPhase
249.600	3.1719	-43.346	49.699	0.000	0.000	2.6304
249.700	3.1732	-47.748	50.188	0.000	0.000	2.8285
249.800	3.1746	-50.322	50.658	0.000	0.000	3.0264
249.900	3.1759	-50.931	51.106	0.000	0.000	3.2243
250.000	3.1772	-49.517	51.532	0.000	0.000	3.4221
250.100	3.1787	-46.107	51.933	0.000	0.000	3.6198
250.200	3.1801	-40.811	52.310	0.000	0.000	3.8174

Header for raw single channel file.

monochrom.dat - Notepad

File Edit Format View Help

Time	InstPeriod	CorrWholeMonochrm	CorrWholeEnvelope	CorrTruncMonochrm	CorrTruncEnvelope	CorrAnPhase
249.600	2.9796	39.901	52.904	0.000	0.000	-0.7163
249.700	2.9786	46.896	53.598	0.000	0.000	-0.5054
249.800	2.9775	51.944	54.280	0.000	0.000	-0.2945
249.900	2.9763	54.758	54.949	0.000	0.000	-0.0834
250.000	2.9751	55.152	55.605	0.000	0.000	0.1278
250.100	2.9738	53.046	56.247	0.000	0.000	0.3390
250.200	2.9724	48.477	56.874	0.000	0.000	0.5503

Header for corrected single channel file.

It is possible to save this file for each separate channel.

The file's #2 SVAL extension is *.all; what means that "**all**" monochromatic signals in the selected period range are saved. Before this file may be saved, it is necessary to select the period range we want to save from the two drop-down lists `Min. period` and `Max. period`.



If no period range is selected, this message is displayed and only the file #1 with the *.dat extension is saved.

Columns containing following values are saved:

- first column: time (s)
- all other columns: amplitude of the nearly monochromatic signals as in the third column of the file #1 above

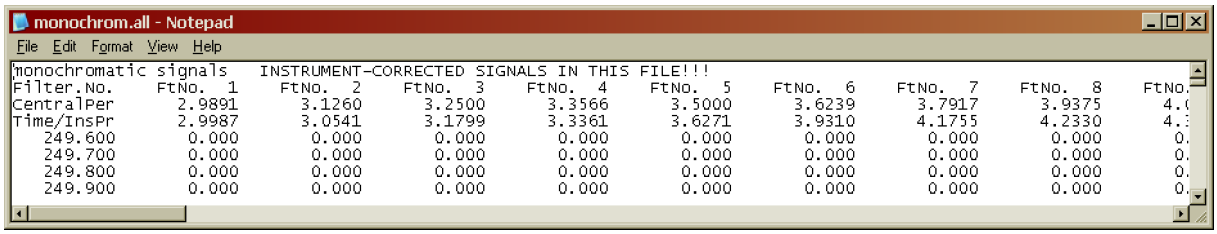
A header section of this multi-channel files corresponds to the complexity of the saved data. First line informs about what quantities are saved and if they are operated in raw or corrected manner. Second line informs about the filter numbers. Third line contains central periods of corresponding filters and fourth line contains corresponding instantaneous periods of each monochromatic signals at the time of its envelope maximum arrival. The two header possibilities for file #2 are:

monochrom.all - Notepad

File Edit Format View Help

monochromatic signals	RAW SIGNALS IN THIS FILE!!!								
Filter No.	FtNo. 1	FtNo. 2	FtNo. 3	FtNo. 4	FtNo. 5	FtNo. 6	FtNo. 7	FtNo. 8	FtNo.
CentralPer	2.9891	3.1260	3.2500	3.3566	3.5000	3.6239	3.7917	3.9375	4.
Time/InsPr	2.9989	3.0528	3.1801	3.3361	3.6269	3.9308	4.1770	4.2327	4.
249.600	0.000	0.000	0.000	0.000	0.000	0.000	0.000	0.000	0.
249.700	0.000	0.000	0.000	0.000	0.000	0.000	0.000	0.000	0.
249.800	0.000	0.000	0.000	0.000	0.000	0.000	0.000	0.000	0.
249.900	0.000	0.000	0.000	0.000	0.000	0.000	0.000	0.000	0.

Header for raw multi-channel file.



Header for corrected multi-channel file.

The file's #3 SVAL extension is *.phs; what means that "**ph**ases" of the monochromatic signals in the selected period range are saved. Before this file may be saved, it is necessary to select the period range we want to save from the two drop-down lists `Min. period` and `Max. period`.

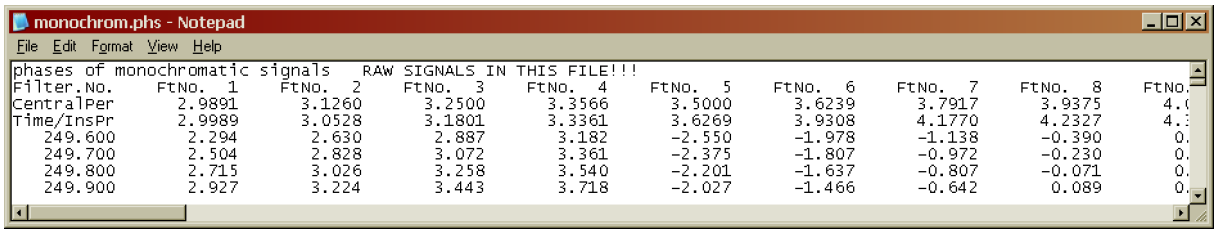


If no period range is selected, this message is displayed and only the file #1 with the *.dat extension is saved.

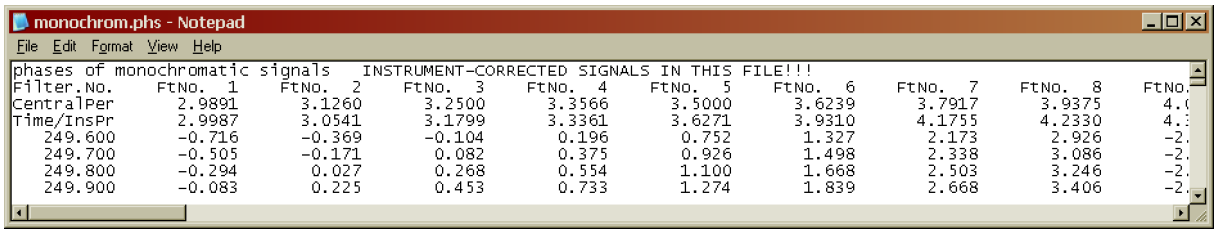
Columns containing following values are saved:

- first column: time (s)
- all other columns: instantaneous phase of the nearly monochromatic signals as in the last column of the file #1 above

The header of this *.phs file contains the same information as the header of the *.all file; only the first line informs about the fact that phases instead of amplitudes are saved. The two header possibilities for file #3 are:



Header for raw multi-channel phase information file.



Header for corrected multi-channel phase information file.

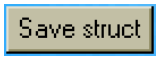


When files with no instrumental correction are to be saved, this message is displayed.



When files with the instrumental correction are to be saved, this message is displayed.

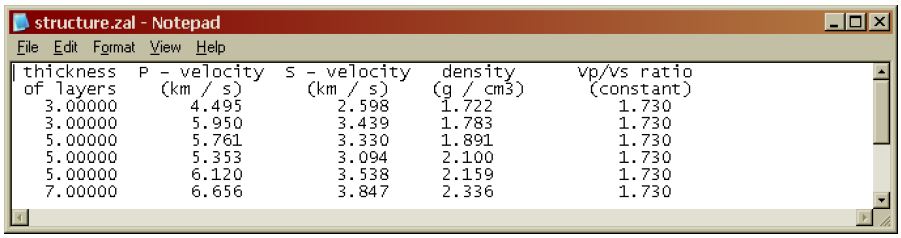
Save structure



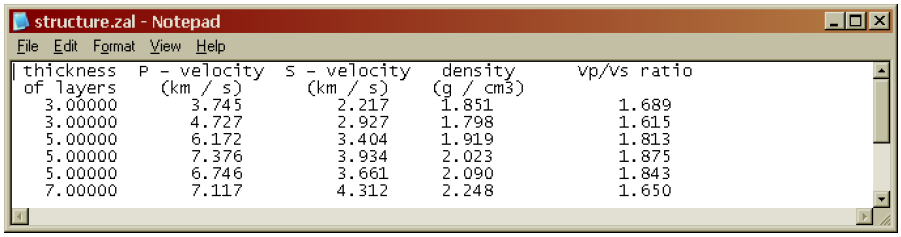
Three files are saved by this button, two of them have Love/Rayleigh version. The file's #1 SVAL extension is *.zal; extension abbreviation stands for "**zal**oha", what means a "back-up" in Czech. Structural quantities in a user-readable format are saved in this file. Columns containing following values are saved:

- thickness of layer (km)
- P-wave velocity (km/s); in case of the Rayleigh wave inversion this is the velocity computed according to the real found v_p/v_s ratio and in case of Love wave inversion this velocity is saved as 1.73*S-wave velocity
- S-wave velocity (km/s)
- density (g/cm^3)
- v_p/v_s ratio; it is real inverted ratio for the Rayleigh wave inversion and it is a constant (1.73) ratio for Love wave inversion

Two header possibilities for file #1 are:



Header for *.zal file saved for Love wave inversion.

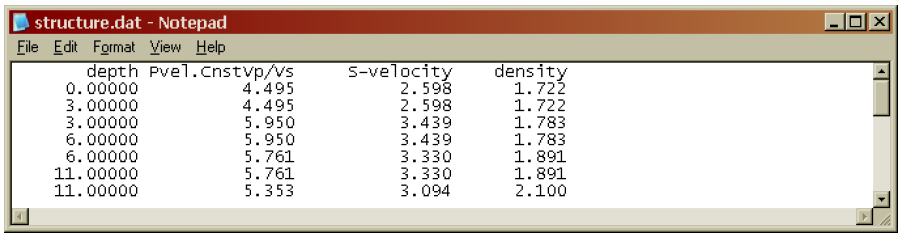


Header for *.zal file saved for Rayleigh wave inversion.

The file's #2 SVAL extension is *.dat. This file contains the same values as the file #1, but the format is designed for Grapher to draw a line representing the velocity distribution. All quantities are repeated twice in such a manner that the resulted depth-dependent line for velocity and density corresponds to the constant values in a homogeneous layers with steps at the layer boundaries. Columns containing following values are saved:

- depth of top and bottom of the layer (km) (two lines)
- P-wave velocity at the layer boundaries; in case of Rayleigh wave inversion this is the velocity computed according to the real found v_p/v_s ratio and in case of Love wave inversion this velocity is saved as 1.73*S-wave velocity
- S-wave velocity at the layer boundaries
- density at the layer boundaries

Two header possibilities for file #2 are:

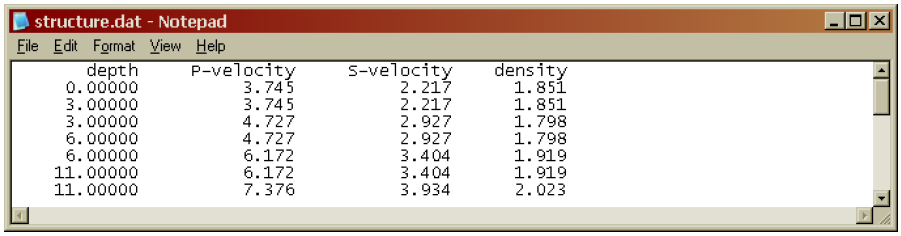


structure.dat - Notepad

File Edit Format View Help

depth	Pvel.Cnst Vp/Vs	S-velocity	density
0.00000	4.495	2.598	1.722
3.00000	4.495	2.598	1.722
3.00000	5.950	3.439	1.783
6.00000	5.950	3.439	1.783
6.00000	5.761	3.330	1.891
11.00000	5.761	3.330	1.891
11.00000	5.353	3.094	2.100

Header for *.dat file saved for Love wave inversion.



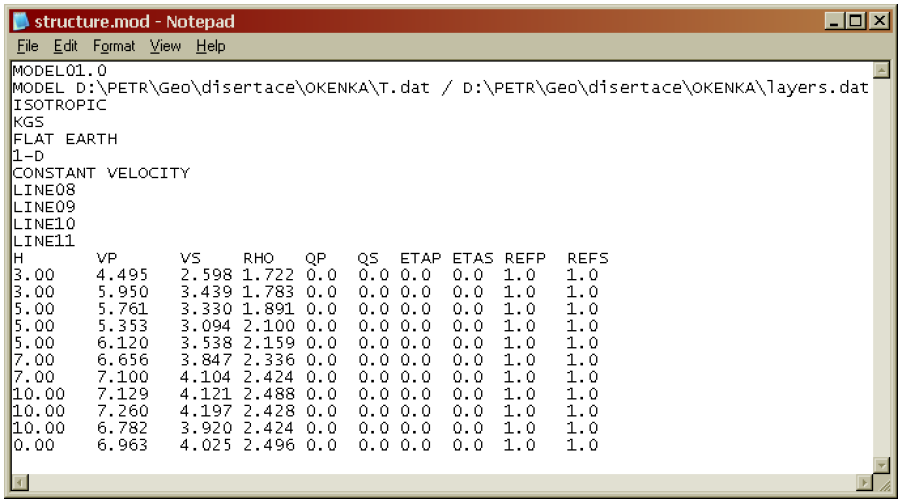
structure.dat - Notepad

File Edit Format View Help

depth	P-velocity	S-velocity	density
0.00000	3.745	2.217	1.851
3.00000	3.745	2.217	1.851
3.00000	4.727	2.927	1.798
6.00000	4.727	2.927	1.798
6.00000	6.172	3.404	1.919
11.00000	6.172	3.404	1.919
11.00000	7.376	3.934	2.023

Header for *.dat file saved for Rayleigh wave inversion.

The file's #3 SVAL extension is *.mod, as a "**mod**al" summation. This file contains again generally the same quantities as the previous two files and it is designed as an input file for a modal summation program, Herrmann (2002). Hence, by saving the inverted structure using SVAL, we may directly use this file to compute synthetics using the modal summation program. The format of this file is described in Herrmann (2002) and all the quantities are clearly marked directly in the file. The P-wave velocities are estimated for a constant v_p/v_s ratio in case of Love waves and by real inverted v_p/v_s ratio in case of Rayleigh waves as in the previous two file types.



structure.mod - Notepad

File Edit Format View Help

```
MODEL01.0
MODEL D:\PETR\Geo\disertace\OKENKA\T.dat / D:\PETR\Geo\disertace\OKENKA\layers.dat
ISOTROPIC
KGS
FLAT EARTH
1-D
CONSTANT VELOCITY
LINE08
LINE09
LINE10
LINE11
H       VP      VS     RHO    QP    QS  ETAP ETAS REFP  REFS
3.00    4.495   2.598 1.722 0.0   0.0 0.0   0.0  1.0   1.0
3.00    5.950   3.439 1.783 0.0   0.0 0.0   0.0  1.0   1.0
5.00    5.761   3.330 1.891 0.0   0.0 0.0   0.0  1.0   1.0
5.00    5.353   3.094 2.100 0.0   0.0 0.0   0.0  1.0   1.0
5.00    6.120   3.538 2.159 0.0   0.0 0.0   0.0  1.0   1.0
7.00    6.656   3.847 2.336 0.0   0.0 0.0   0.0  1.0   1.0
7.00    7.100   4.104 2.424 0.0   0.0 0.0   0.0  1.0   1.0
10.00   7.129   4.121 2.488 0.0   0.0 0.0   0.0  1.0   1.0
10.00   7.260   4.197 2.428 0.0   0.0 0.0   0.0  1.0   1.0
10.00   6.782   3.920 2.424 0.0   0.0 0.0   0.0  1.0   1.0
0.00    6.963   4.025 2.496 0.0   0.0 0.0   0.0  1.0   1.0
```

Complete *.mod file; the information about Love/Rayleigh inversion is not saved in this file.

Save fitted dispersion

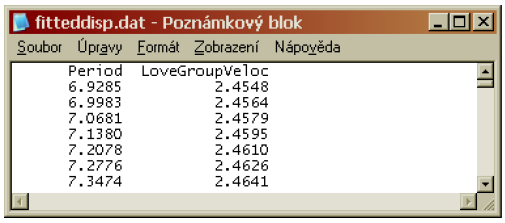


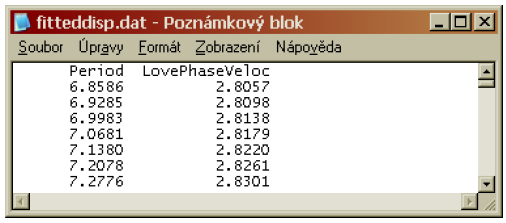
One file is saved by this button and six possibilities of its headers may occur because we may save the phase or group velocity for Love, Rayleigh or joint inversions. File contains the dispersion curve which resulted as the best fit from the inversion. In case of using the `Starting disp` button to create dispersion corresponding to the starting model, this dispersion is handled in the same manner as a result of the inversion. This is due to the fact that the starting dispersion results as a first forward computation using the starting model as an input parameters. Hence, this starting dispersion may be saved by this `Save fit dsp` button as any other result of inversion. SVAL extension is *.dat Columns containing following values are saved:

- period (s) with the step according to the forward modeling computation; this step is set according to the smallest distance between two nearest dispersion points in the measured dispersion curve

- group or phase velocity (km/s) of Love or Rayleigh waves

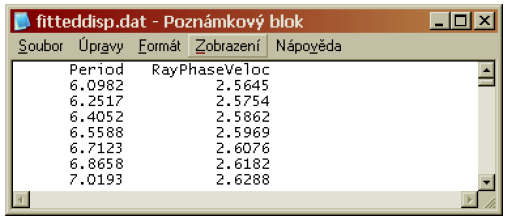
In case of the joint inversion there are three columns in the file with Love wave velocities in the second column and with Rayleigh wave velocities in the third column.





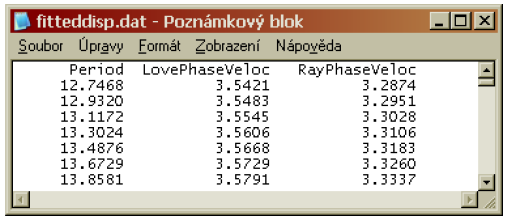
Header for fitted dispersion file, options: group or phase velocity of Love waves.





Header for fitted dispersion file, options: group or phase velocity of Rayleigh waves.





Header for fitted dispersion file, options: group or phase velocity of both Love and Rayleigh waves.

Save spectrum



Two files may be saved by this button. One of them is saved always and it has two options. The second one is saved only if the instrument correction was applied and has only one option. The file's #1 SVAL extension is *.dat. When the `Bandpass` button was pressed, the spectrum of the bandpass filtered record is also saved. When this button was not used, only the spectrum of raw record is saved in the *.dat file.



In case no bandpass filtered spectrum is available, this message is displayed.



In case bandpass filtered spectrum is available, it is saved too and this message is displayed.

The analysis of raw record deletes the bandpass filtered record and spectra. The bandpass filtered spectra is available for saving only directly after it was created by the `Bandpass` button.

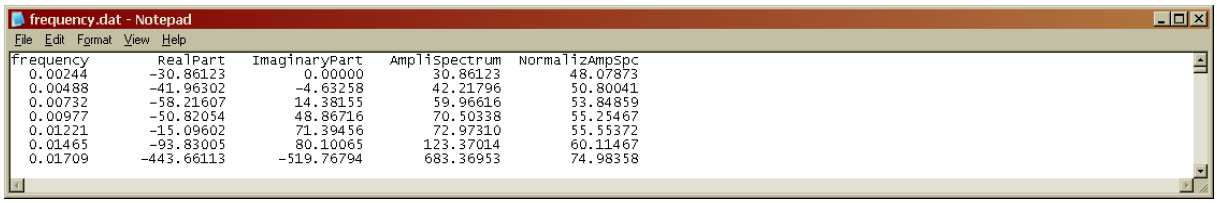
The `Spectrum` button in the frequency domain window draws the spectrum of the used data, so in fact, when the analysis of bandpass filtered record is made, the `Spectrum` button draws the bandpass filtered spectra. This may be checked by pressing again the `Bandpass` button after the analysis of bandpass filtered record and by drawing both `Spectrum` and `Filtered spec`, what should give the same result. However, since the `Bandpass` button computes the bandpass filtered spectra using always the raw data (it computes the raw spectrum and then it smooths its edges according to the given period range), and since the `Analysis` button computes the spectrum using the entering record, in case the entering record is bandpass filtered, the two spectra shown using the `Spectrum` and `Filtered spec` button may differ a bit because of numerical reasons.

Because the saving of the bandpass filtered spectra is enabled only right after the `Bandpass` button was used, the saved bandpass filtered spectrum is the one shown by `Filter spec` button. When saving the spectra after the bandpass filtered record was used and after the `Bandpass` button was used again, what is the case when the `Spectrum` and `Filtered spec` buttons give (nearly) the same result, the "raw" spectrum saved is the one produced by the `Analysis` button during the analysis and hence it is also bandpass filtered. In other words, the `Save spectr` button saves exactly the spectra shown by the `Spectrum` and `Filtered spec` buttons.

Columns containing following values are saved for the file with raw spectrum only:

- frequency (Hz)
- real part of the spectrum
- imaginary part of the spectrum
- amplitude spectrum
- amplitude spectrum normalized into the 100 dB scale

The header of the file looks like:



Header for *.dat file with raw spectrum only.

Columns containing following values are saved for the file with both raw and bandpass filtered spectra. The first five columns are the same as in the case of the previous file:

- frequency (Hz)
- real part of the spectrum
- imaginary part of the spectrum
- amplitude spectrum
- amplitude spectrum normalized into the 100 dB scale
- real part of the bandpass filtered spectrum
- imaginary part of the bandpass filtered spectrum
- bandpass filtered amplitude spectrum
- bandpass filtered amplitude spectrum normalized into the 100 dB scale

The header of the file looks like:

frequency.dat - Notepad

File Edit Format View Help

frequency	RealPart	ImaginaryPart	AmpliSpectrum	NormalizAmpSpc	BandPassRe	BandPassIm	BndPssAmplSpec	NrmBndPssAmpSpc
0.00244	54.56931	0.00000	30.86123	48.07873	0.00000	0.00000	0.00000	0.00000
0.00488	1108.70410	496.20541	42.21796	50.80041	0.00000	0.00000	0.00000	0.00000
0.00732	1089.75244	121.23718	59.96616	53.84859	0.00126	0.00014	0.00127	0.00000
0.00977	-892.99915	1714.93250	70.50338	55.25467	-0.14151	0.27175	0.30639	8.02066
0.01221	162.25296	624.12646	72.97310	55.55372	1.18209	4.54705	4.69819	31.73387
0.01465	-991.84351	236.76224	123.37014	60.11467	-111.28176	26.56399	114.40837	59.46441
0.01709	-810.94897	-943.87988	683.36953	74.98358	-469.34126	-546.27577	720.20721	75.44441

Header for *.dat file with both raw and bandpass filtered spectra.

The file's #2 SVAL extension is *.crr. This file is saved when the instrument "**corr**ection" has been applied. It has only one option – the corrected spectrum which was used for analysis. If we analyze complete record, it saves complete corrected spectrum, if we analyze bandpass filtered record, it saves bandpass filtered corrected spectrum. However, this information is not to be seen in the text of the file. In other words, it is not possible to save corrected complete and corrected bandpass filtered spectra at the same time.



If corrected spectra is available, the *.crr file is saved and this message is displayed to confirm it.

Columns containing following values are saved for the file *.crr:

- frequency (Hz)
- corrected real part of the spectrum
- corrected imaginary part of the spectrum
- corrected amplitude spectrum
- corrected amplitude spectrum normalized into the 100 dB scale

The header of the file looks like:

frequency.crr - Notepad

File Edit Format View Help

frequency	CorrRealPart	CorrImaginarPart	CorrAmpliSpectrm	CorrNormalizAmpSpc
0.00244	0.00000	0.00000	0.00000	0.00000
0.00488	-1867.07899	-616.23270	1966.14514	83.92478
0.00732	-1238.98660	-91.52470	1242.36249	79.93744
0.00977	-776.58701	274.55559	823.69178	76.36776
0.01221	-373.06837	402.08802	548.50231	72.83604
0.01465	-649.25576	32.23576	650.05552	74.31148
0.01709	191.57434	-2678.93595	2685.77709	86.63387

Header for *.crr file with instrumentally corrected spectrum.

6.7 Outputs displayed in the auxiliary window



Information about the version of the SVAL program we are currently using. First, there is a manually set date as yyyy mmm dd. This manually set date is given in the SVAL source code by the author. In addition to this manual date information, it has also the automatic date/time format of dd.mm.yy hh:mm. As we start the SVAL program, it looks for an *.exe file in the given directory and writes the date/time of the last change of this *.exe file. It will probably go wrong if we have more than one *.exe file it the current directory. The manual and automatic dates may generally differ, as it is to be seen in the example.



Memory allocation progression bar. Indicates, how much memory has been already allocated for the program arrays dealing with the record's time and frequency series.

6.8 Outputs displayed in the main window



When in the manual mode, it informs about the processed file name with the full path of the record file.



When in the batch processing mode, the SVAL program gives the actually processed file name without its path. It differs from the manual mode, where the whole paths and file name is given. So, it can be easily distinguished, in which mode the program operates. The file name may be arbitrary, but the file extension for the batch processing must be *.dat.



When in the batch processing mode, this informs about the directory from where the data files are read. During one batch process, this directory does not change.



When in the batch mode, it gives the number of the file currently processed. When the batch processing is aborted, but the SVAL program still remains in the batch processing mode, after the batch processing is again activated, the program continues with the next file and the number of files given in the caption increases accordingly. When the batch processing mode is terminated confirming the dialog box which appears after clicking the `Open data file...` button, the next activation of the batch processing mode will number the files form 1 again since it starst with the analysis form the first file in the directory again.



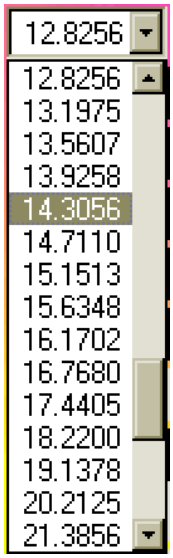
File name and path of the previously estimated and loaded dispersion curve.



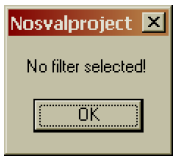
File name and path of the file containing layer thicknesses.



When the KUK file format is used (both in the manual and batch processing modes), this informs you, which component was selected in the auxiliary window and is processed during the analysis.



(advanced) Option for selecting an instantaneous period of filter for its depiction in the period-group velocity plot and for drawing of corresponding nearly monochromatic signals, their envelopes, truncated nearly monochromatic signals and their truncated envelopes in the upper time-amplitude plot.



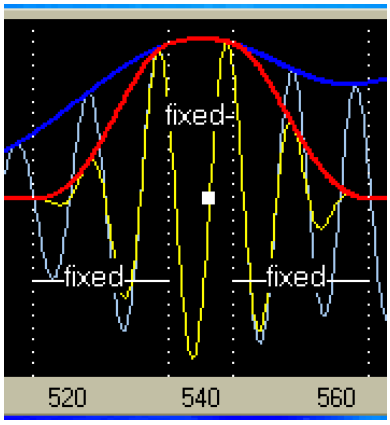
If no filter is selected after clicking on the latter drop-down menu, this message pops-up.

Mon

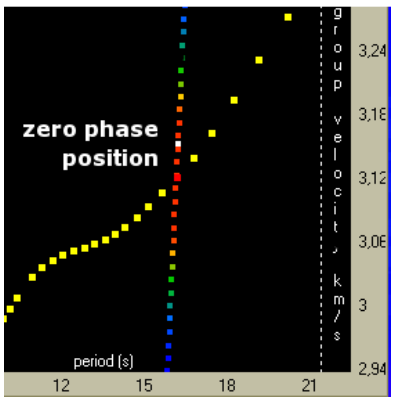
(advanced) Selected nearly monochromatic signals and their envelopes are displayed. The envelope of selected nearly monochromatic signal is also drawn in the period-group velocity plot; the variation of instantaneous period with time (velocity) can be seen; the envelope amplitude (to be clearly seen in the time plot) is depicted by rainbow-changing colors in the group velocity-period plot.

Trnc

(advanced) Selected truncated nearly monochromatic signal and its envelope is displayed. The times where the truncated envelope remains to be the same as the original one are depicted by white dotted lines. The times from which the truncated envelope is zero to both sides are also depicted. The truncated envelope is smoothed by a cosine window between the two pairs of lines on both sides. If an `X` option is checked, fi**X**ed positions of truncating are marked by label. The truncated envelope amplitude is depicted by rainbow-changing color in the group velocity-period plot in the same manner as the complete envelope amplitude drawn by the previous button.



At the same time when we press the `Trnc` button, the zero phase is depicted by a white dot. The arrival time and instantaneous period of this zero phase is saved by the `Save disp` button.



The zero phase position is marked by white dot also in the period-velocity plot.

100

(advanced) Scale factor of filtered (separated) seismogram amplitude (percents, options); selected scale is used also for saving the separated seismogram. The increment of this spin edit box is 10 % but arbitrary value between 0 % and 500 % may be entered.

3 50

(advanced) Edit boxes for entering the minimal and maximal period (s) for bandpass filtering of the record.



(advanced) Creates and draws the bandpass filtered record according to the selected period range. Always, only the raw record enters the bandpass filtering. It does not matter, how many time we press the `Bandpass` button. It always uses the same input and produces bandpass filtered spectra and record based on this raw input.

The `Spectrum` button in the frequency domain window draws the spectrum of the used data, so in fact, when the analysis of bandpass filtered record is made, the `Spectrum` button draws the bandpass filtered spectra. This may be checked by pressing again the `Bandpass` button after the analysis of bandpass filtered record and by drawing both `Spectrum` and `Filtered spec`, what should give the same result. However, since the `Bandpass` button computes the bandpass filtered spectra using always the raw data (it computes the raw spectrum and then it smooths its edges according to the given period range), and since the `Analysis` button computes the spectrum using the entering record, in case the entering record is bandpass filtered, the two spectra shown using the `Spectrum` and `Filtered spec` button may differ a bit because of numerical reasons.



(advanced) Filtered (separated) velocigram (seismogram) for selected period range (by two drop-down dialogs `Min. period` and `Max. period`) is computed and displayed.



(basic, but not needed for run) Raw velocigram (seismogram) is displayed. This button displays the record used (or prepared to be used) for analysis. In case of checking the `F` option – it means that the bandpass filtered record is to be used for analysis – this button draws this bandpass filtered record. To return to the original raw seismogram, simply check the `R` (Raw) option. If the `R` option check box is not available, press the `Bandpass` button again. This `Raw seism` button is available only after the analysis has been processed. In case of using the `R` option, the applied edge-smoothing is shown. In case of `F` option, no smoothing is applied at all.



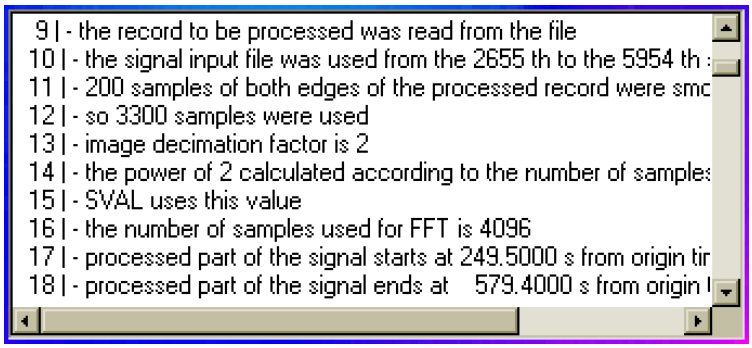
(advanced) Instrumentally corrected velocigram (seismogram) is displayed. Available only after the analysis using the corrected spectrum was made by pressing the `Filter corr` button.



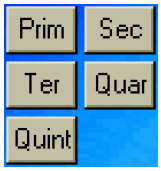
(advanced) Spectrogram is displayed in the period-group velocity plot. No smoothing is applied. SVAL simply draws a set of envelopes of all quasimonochromatic signals. We may check a mutual distribution of filters along the period axis and velocity-period curvature of each of the filters separately. Using the `Mon` button retraces the selected filter envelope by bolder line.



(advanced) Truncated spectrogram is displayed for selected period range. Using the `Trnc` button (near the upper time-amplitude plot) retraces the selected filter truncated envelope by bolder line in the spectrogram plot.



Text box containing information about all important computational steps: input parameters for checking, estimated parameters of filtration, corrected values of minimal and maximal period, number of used filters, information about FFT, list of estimated dispersion points and types of their maxima, information about the inversion parameters, about the period step of forward modeling and about the results of inversion. While pressing some of the buttons which compute, draw or select something, this text box gives information about what happens.



(advanced) Arrival times of 1^{st} to 5^{th} maxima of each filter are marked in the upper time plot and these 1^{st} to 5^{th} maxima are also displayed in the period-group velocity plane as different dispersion ridges. The first maximum is always available, but the other ones are not necessarily estimated for some of the filters.



When there is no secondary maximum for all the filters and hence there is nothing to be plotted after clicking the `Sec` button, this message is displayed.



When there is no tertiary maximum for all the filters and hence there is nothing to be plotted after clicking the `Ter` button, this message is displayed.



When there is no quarternary maximum for all the filters and hence there is nothing to be plotted after clicking the `Quar` button, this message is displayed.



When there is no quinternary maximum for all the filters and hence there is nothing to be plotted after clicking the `Quint` button, this message is displayed.



(basic, but not needed for run) Estimated dispersion curve is displayed. In case of using loaded dispersion by the `Use loaded` button this loaded dispersion is drawn.



(advanced) Prepares the loaded dispersion curve for the program arrays in the same manner as if it was computed. This is useful for further inversion of the loaded dispersion. The period values are also set into the drop-down lists to enable the range selection. This works for the two drop-down lists (`Min. period` and `Max. period`) only – the third drop-down list for drawing the signals has no meaning in case of loaded dispersion because we do not have any signals at all. In case that two-dispersion file is loaded, only the period values of the first column (Love waves) are shown in the drop-down lists.



(advanced) Dispersion curve for final structure is displayed (for comparing with the measured dispersion curve). This computed dispersion is also displayed automatically after the inversion terminates.



(advanced) Draws the theoretical dispersion curve for the starting model and also this starting model (the button is in the inversion window). Standard shear wave starting model is made using constant-step-velocity distribution specified by entered values of `Surf. S-vel` and `S-vel. step`. By manual setting, we may create our own starting model which may be as complicated as desired. In that case, the `Starting disp` button draws the curve corresponding to this new model. Inversion procedure uses this new model as a starting one. If we want to return to the default starting model, we have to uncheck the `Interactive` check box. It automatically returns to the default settings after the inversion procedure is over, after the depth-velocity plot is cleared and after a new analysis is processed. If we made a change of parameters creating the automatic starting model, we have to press the `Inversion` button first. It is needed not only to switch into the inversion window, but mainly for the parameters to be read by the SVAL program. Only after this action, the `Starting disp` button is able to draw the new starting model and dispersion and also the `Inverse` button will use this model as a new starting one. In case of manual setting of the starting model, it is not necessary to use `Inversion` button and we may directly use the `Starting disp` button to see the corresponding dispersion curve.



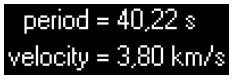
(advanced) Displays S-wave velocity distribution in the given set of layers (result of the inversion).



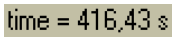
(advanced) Displays P-wave velocity distribution in the given set of layers (result of the inversion).



(advanced) Displays density distribution in the given set of layers (result of the inversion, strongly constrained or unchanged).



Current mouse position in the group velocity-period plane diagram.



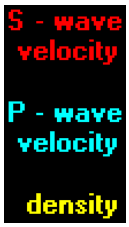
Current mouse position in the time plots. The time axis of both of them is kept to be always of the same range.



Current mouse position in the depth-velocity plot; shows the velocity.



Current mouse position in the depth-velocity plot; shows the depth.



P and S wave velocities as well as density are depicted by different colors.

6.9 Outputs displayed in the frequency domain window



(advanced) Draws real part of the spectrum.



(advanced) Draws imaginary part of the spectrum.



(advanced) Draws amplitude spectrum of the processed record. If raw record is processed, it is the raw spectrum. If bandpass filtered record is processed, it is the spectrum of this bandpass filtered record.



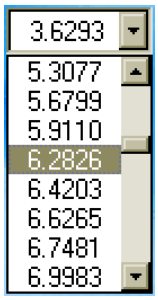
(advanced) Log-log normalized amplitude spectrum is displayed. The same for raw / bandpass filtered record applies as in the previous button.



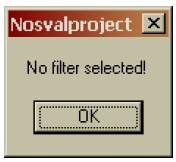
(advanced) Bandpass filtered spectrum is drawn. This button is enabled right after the `Bandpass` button was used and when the `Analysis` button was not used. If, after the analysis, the `Bandpass` button is pressed again, it is again possible to draw the bandpass filtered spectra. In case the `F` option was selected and an analysis of the bandpass filtered record was made, the `Spectrum` button draws the spectrum of the bandpass filtered record computed during the analysis and the `Filtered spec` button draws the bandpass filtered spectrum made by cropping and smoothing the original raw spectrum. Theoretically, both these spectra should be the same, however, small numerical discrepancies may occur.



(advanced) Log-log normalized bandpass filtered spectrum is drawn. The same as in the previous button applies also for raw / bandpass filtered record.



(advanced) Options for selecting the periods of filters in the frequency domain. Despite the fact, it controls the depiction in the frequency domain window, we keep the values of periods (s) for this drop-down list instead of frequencies. It is easier to compare it with the same values contained in the three drop-down lists in the main time domain window. The text output of the frequency domain window gives corresponding values of instantaneous frequency and central period and central frequency as well as a logarithm of the instantaneous frequency for the selected filter's instantaneous period.



If no period is selected after clicking on the drop-down menu, this message is displayed.



(advanced) Draws each separate Gaussian filter and corresponding filtered spectrum in amplitude spectrum representation according to the selected period. Instantaneous period is marked by the yellow line and the central period (center of the Gaussian filter) by the white line.



(advanced) Draws each separate Gaussian filter and corresponding filtered spectrum in log-log normalized amplitude representation.



(advanced) All used Gaussian filters are displayed together. Two possibilities of representation may occur: filters are shown in a frequency-amplitude plot or in a log-log normalized amplitude representation. What happens is dependent on the last depiction of the spectrum – if it is drawn using the `Spectrum` button, the filters have the same representation and if it is drawn using the `Normalized` button, the filters are also normalized; the filters have their actual heights in both cases.



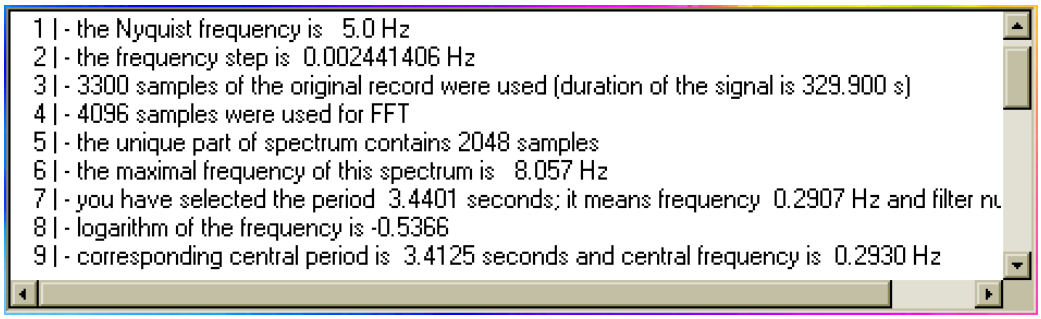
(advanced) All filtered spectra are displayed together; two representation may be used, see the explanation to the `All filters` button.



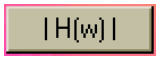
(advanced) All used Gaussian filters are displayed together and the filters have the same height. Two representations may be used, see the explanation to the `All filters` button.



(advanced) Instantaneous frequencies of 1^{st} to 5^{th} maxima of the selected filter are marked by the same colors as used also on the velocity-period plot in the main SVAL window.



Information about the processes in the frequency domain.



(advanced) Draws the amplitude transfer function for selected instrument. The transfer function is computed according to the poles and zeros given in the source code for each instrument. Hence, for inserting a new instrument characteristic one needs to work with the SVAL source code. Also the eigenfrequency of the instrument is depicted by this button. For source code explanation see Section 6.5 – record parameters. Two representations may be used, see the explanation to the `All filters` button.



(advanced) Draws the phase transfer function for selected instrument, see also explanation for `H(w)` button. Both amplitude and phase characteristic have relative amplitude to visualize their influence on the record spectrum. Also the eigenfrequency of the instrument is depicted by this button. Two representations may be used, see the explanation to the `All filters` button.



In case of the latter two buttons for drawing the instrumental transfer function, we may plot it for higher requencies than is the Nyquist one. It is only for the information, how does the transfer function look. But when too high frequency is set in the `max freq (Hz)` edit box, this message is displayed and the frequency is lowered according to the highest sample available.



(advanced) Draws real part of the instrumentally corrected spectrum.



(advanced) Draws imaginary part of the instrumentally corrected spectrum.



(advanced) Draws the instrumentally corrected spectrum.



(advanced) Draws the log-log normalized instrumentally corrected spectrum. The latter four buttons have similar function as the corresponding four buttons for raw data.

6.10 Outputs displayed in the inversion window



Current distance between the measured Love wave dispersion points and the theoretical Love wave dispersion curve computed by the inversion procedure; graphical depiction in red; dimension: m/s. In this example, the average distance between each of the measured dispersion points used for inversion and the fitted dispersion is 0.05496 km/s what may represent a quite good result.



Current distance between the measured Rayleigh wave dispersion points and the theoretical Rayleigh wave dispersion curve computed by the inversion procedure; graphical depiction in light blue; dimension: m/s. In this example no Rayleigh wave dispersion curve was used for inversion.



Current distance between the measured density points (in fact set by `Surf. dens.` and `Dens. step` edit boxes) and the theoretical density computed by the inversion procedure; graphical depiction in yellow; dimension: g/cm^3*100. In this example the average distance between each of the "measured" density values used for inversion and the fitted density is 0.48 g/cm^3. In case the `ConDen` option is checked (default / advanced), the value of `Dens (g/cm3)*100` is constant because the density values are not changed by the inversion and hence the misfit remains the same.



Misfit function; dimensionless; graphical depiction in violet. This number is a weighted sum of single misfit functions for each quantity described above, the inversion procedure process the task in such a manner that this misfit function is minimized and hence during the progress it must decrease. As opposed to it, the single misfit functions of Love and Rayleigh waves and density may oscillate, but their sum (normalized) is always decreasing.



Number of inversion procedure iteration.



Number of forward modeling procedures. This number may be lower than the number of inversion iteration because not all the iteration request forward task; in case of inapplicably wrong parameter estimation, the forward computation is skipped.

6.11 Working with the SVAL program – analysis

In this section we will introduce some of the features which the SVAL program uses for surface wave analysis. We assume that we have previewed the record using some other graphical interface before we use the SVAL program for surface wave analysis. This condition is not compulsory, of course, but a priori knowledge of the record visual characteristics would help us much during the first run of surface wave analysis. We have to save the desired component as an ASCII file containing only one column with the component amplitudes. It does not matter if the values are reals or integers and it does also not matter what is the absolute value of amplitudes. The other option is to use directly the output files from the KUK program. There are all three components in the KUK file and eight-rows header. Values of amplitudes in the KUK file are integers.

After executing the SVAL *.exe file we see small auxiliary window as depicted in Fig. 6.1 in Section 6.3. Using the checkbox options we set the number of samples we expect to use for the Fast Fourier Transform. We have to set the power of two higher than the number of samples of the longest time window which we want to analyze from our record. This feature is implemented for saving the memory and computational time in case of short records. In case we process records with sampling rate 10 Hz and we analyze the regional events, it is often enough to use `4096` or `8192` option. The memory allocation take few second and this is worth of saving much time during the analysis process. In case of a distant earthquakes where we have to deal with a long period of time to found the whole dispersed wavegroup, we choose the `16384` option; in case of 10 Hz rate it represents 27 minutes. The greatest option of `32768` samples may even overflow the PC memory, it depends on the hardware available. But we work with the `32768` option using 512 MB RAM without any problems.

One may consider to lower the sampling rate in case of distant events, because short periods are often scattered and attenuated and if looking for surface waves longer than 20 s it is enough to have a low sampling rate of 1 Hz or so. It enables us to process very long parts of record and save the computational time as well. The option `no record` enables to skip the memory allocation in case we are interested in saved dispersion file loading only. This option enables to process all the inverse procedures concerning the loaded dispersion without any memory to be allocated for records and their spectra.

After the memory setting, we choose the input file type to be open and start the main SVAL program by the `Run SVAL` button. If we prepared one of the possible input files, we simply open it using the `Open`

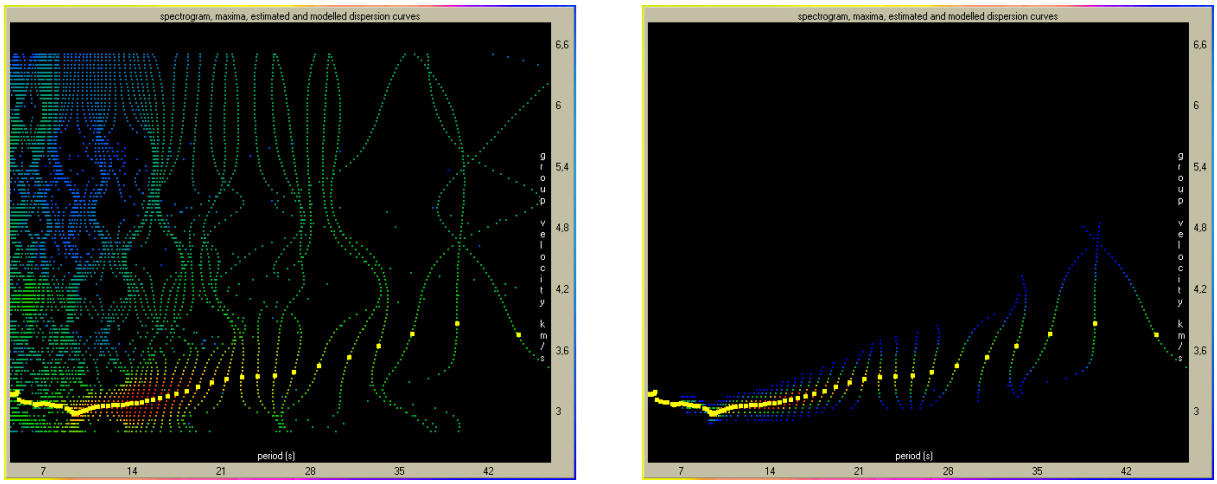


Figure 6.5: Spectrograms. Left: complete spectrogram, right: spectrogram truncated along the fundamental mode estimated by multiple filtering in the frequency domain and by truncating in the time domain. Amplitudes are normalized into the 100 dB scale; they increase from dark blue to the red.

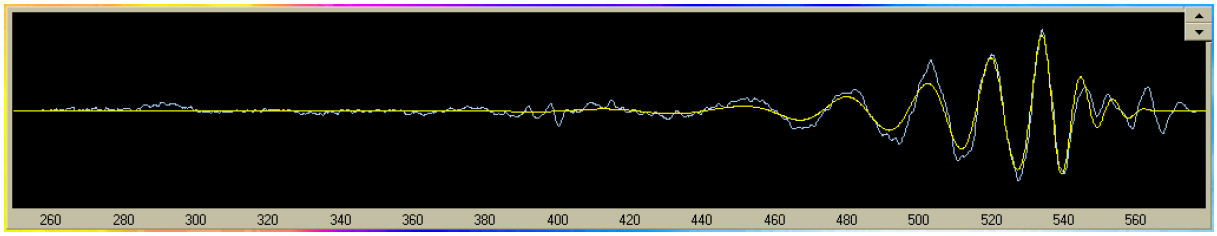


Figure 6.6: Raw record (blue) and fundamental mode surface wavegroup (yellow) estimated for the period range of 7 – 44 s.

`data file ...` button. In that moment the path and file name appear in the upper SVAL window bar starting with the expression `SVAL processes` and continuing with the complete path and file name.

As we want to make a complete analysis, we leave the `Analys` checkbox to be checked. We fill the `Epic. distance` edit box with the appropriate value in kilometers.

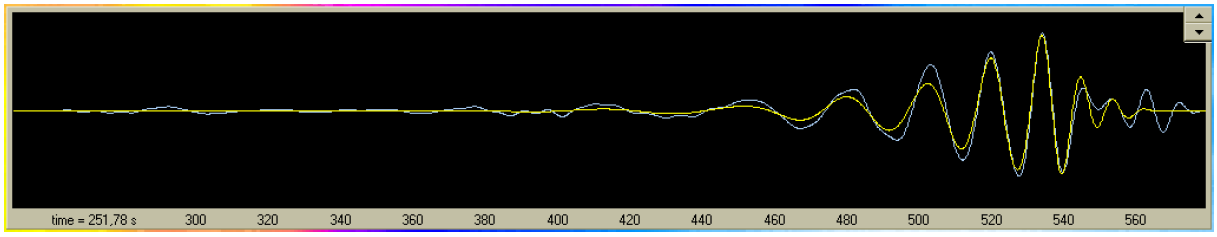


Figure 6.7: Bandpass filtered record (blue) and estimated fundamental mode (yellow, as in Fig. 6.6) – both for the same period range 7 – 44 s.

After that, we set the time difference between the origin time and the time of the first record sample in the `Time interval` edit box. If the record starts after the origin time, what is a usual situation, we enter a positive value in seconds. However, if our record starts before the origin time, what may easily happen in the case of near events, we have to enter a negative value. Both options are returned in the SVAL text output and the recognized possibility is clearly stated there, so we may check it after the analysis.

To fill the `Sampl. freq.` edit box should not be a problem, please, enter the value in Hz. If a new version of the KUK file format is used, these latter three quantities are filled in the edit boxes automatically as they are read from the header of the KUK file. It is not possible to change them, they are directly used for computation and displayed only for the information. If an old version of the KUK file format is used, only the `Sampl. freq.` edit box is filled automatically and the epicentral distance and the time interval must be set by the user.

Next four edit boxes govern the dimensions of the spectrogram – two of them are minimal and maximal values in the time domain and two of them represent the minimal and maximal values in the frequency domain. For easier use and according to the traditional surface wave analysis we prefer the velocity to

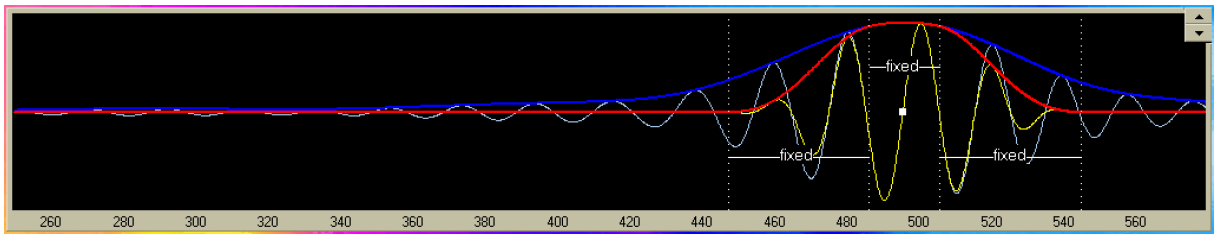


Figure 6.8: Signal filtered at the period of 20 s (light blue) and its envelope (dark blue) as well as truncated fundamental wavegroup of this signal (yellow) and its envelope (red). Truncating ranges are also shown.

be set instead of time and periods instead of frequency. The use of default velocity range enables us a reasonable first trial. In case we do not know anything about our record, it is easy to start with the standard velocity range – for example to set the `Min group vel.` to be 2.5 km/s and `Max group vel.` to be 6.0 km/s in case of regional or teleseismic events would be a good starting point. The appropriate velocity range depend on when the surface waves arrives, so we are sometimes forced to change this values according to our first unsuccessful analysis results. In other words, we have to look for the useful velocity range.

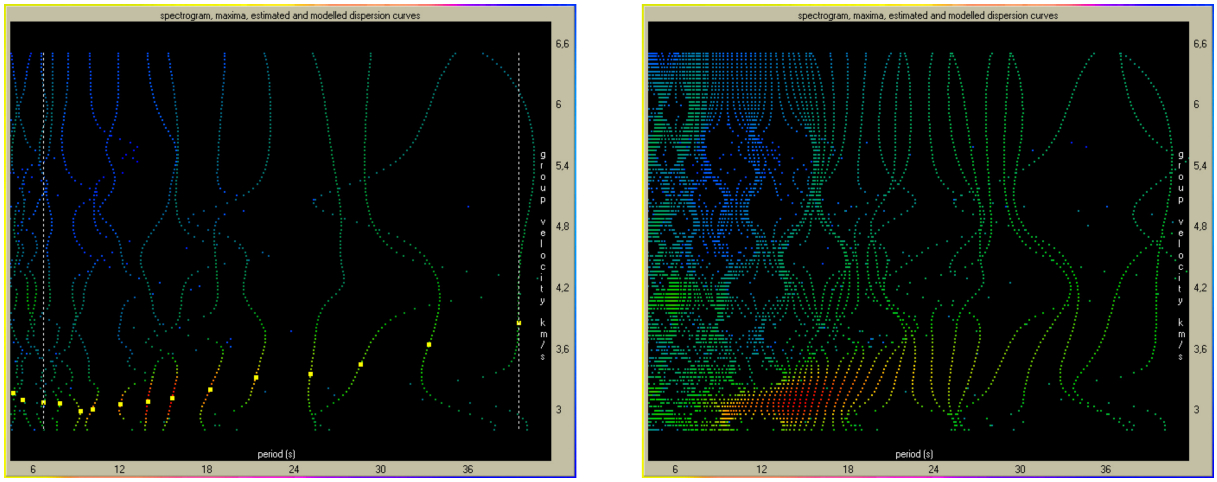


Figure 6.9: Left: spectrogram for limited number of filters used during the analysis, as in Fig. 6.27. Right: Spectrogram estimated by high filter density as in Fig. 6.26.

On the other hand, the period range depends only on our desire. We put the `Minimal period` and `Maximal period` according to our wish. Of course, we are constrained by the used sampling frequency, by the frequency content of the signal and things like that, but, in general, we may prefer any period range. The SVAL program checks these values and in the case we set the `Minimal period` to be shorter than four times the sampling time rate, the minimal period is set to equal this length. Thus, analyzing for example the record with 10 Hz sampling rate we may encounter the minimal period to be 0.4 s. SVAL informs us about the fact it was needed to change the minimal period we entered and writes out also this new estimated minimal period. Similarly, the constraint for long periods is set to be so that the length of the processed part of the signal may not be shorter than half of the maximal period. Again, if we enter longer period, the SVAL program corrects it and gives us a notice about this change.

For most standard cases, the default value for `Max. num. of filters` given as 110 will be enough. In fact, in most cases we use smaller number of filters. SVAL is designed to use as much filters as possible in the given period range. It informs us about the actually used number. For other details see also Section 6.5 with the description of all the computational steps called by the `Analysis` button. If we encounter on the output that all the 110 filter were used, we may try to use higher value to cover the period range with more dense Gaussian filters. If we want to use less number of filters, we may lower this value. For example in case we do not want to have such a large overlapping of filters, we may use a smaller number. We obtain a less number of dispersion points and hence our measurement of the velocities will be not so accurate. In Fig. 6.9 we see how it looks in the period-group velocity plot.

The overlapping of the filters has no influence on the filtering procedures, since each filter is applied separately and each corresponding quasimonochromatic time signal is also computed separately using only the filtered spectrum. The only reason for a wish not to have such great number of filters is the physical meaning of the spectrogram amplitude. If we cover the frequency range with the filters which amplitude sum would be constant and equal to one, we get the energy distribution clearly represented by

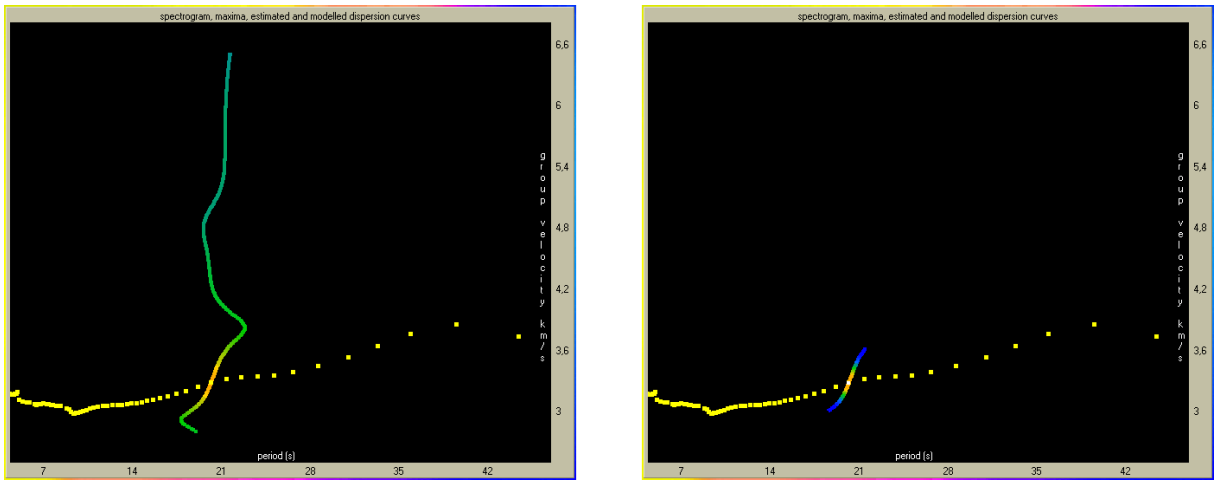


Figure 6.10: Left: envelope of signal filtered at the period of 20 s drawn with respect to period. Right: truncated fundamental mode in the same depiction. This plot enables to check a variation of the instantaneous period along the envelope.

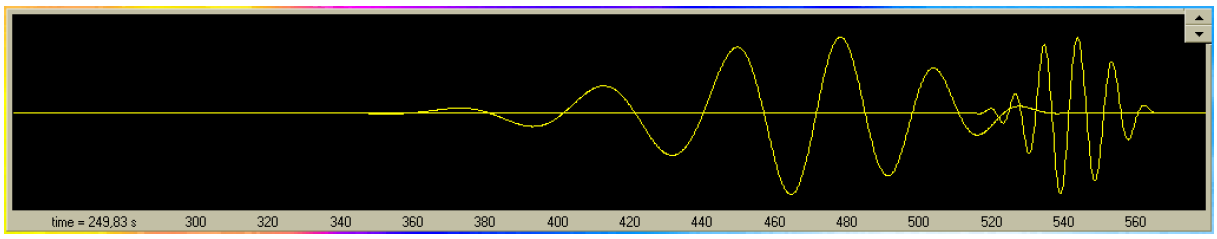


Figure 6.11: Fundamental modes of one record for two period ranges. Long period part: 25 – 44 s, short period part: 7 – 10 s.

spectrogram amplitude. In case of using higher number of filters we get envelopes of overlapped filters in the frequency domain and hence a lot of energy is included many times.

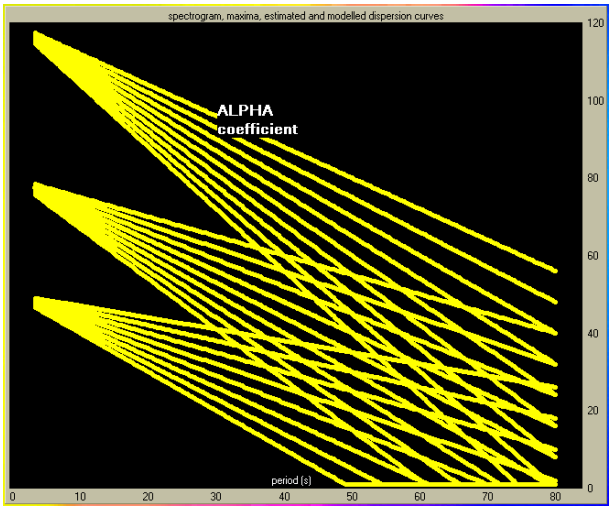


Figure 6.12: Examples of coefficient $\alpha(T)$ dependence. Three sets of linear coefficients are shown for intercepts points 50, 80 and 120 with slopes varying from –0.5 to –1.5.

In the last edit box of this basic settings we enter the number of samples to be smoothed at the record edges – `Smoothing window`. It is advised to enter a non-zero value, however, it is possible to enter the zero too. This number of samples will be smoothed by cosine window both at the beginning and at the end of the processed record time interval. If we change the group velocity range, the appropriate time window of processed record also changes and again the record edges will be smoothed. The record drawn by the `Raw seism` button already contains this smoothing, so we may check what happened and make a correction for the next analysis.

Next two edit boxes, `Slope` and `Intercept pnt`, are for Gaussian filters width settings. The α coefficient controls the width of the filter – as the coefficient increases, the filter becomes narrower. Since we use a linear dependence of the α coefficient on the period, we have to set both its slope and intercept point. By pressing the `Plot` button we draw the set dependence. Starting with the new record of a new

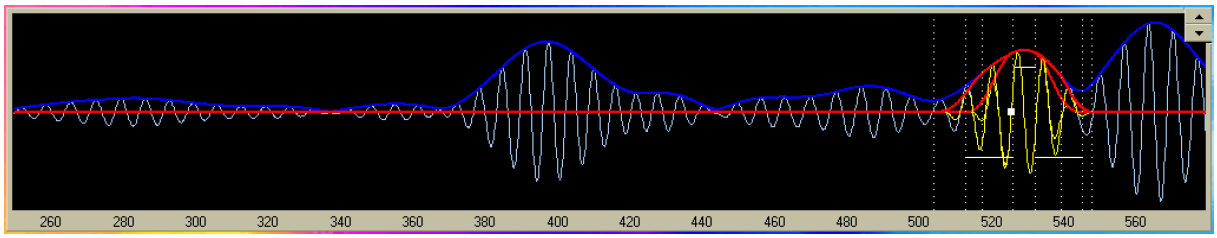


Figure 6.13: Quasimonochromatic signal at the period of 7 s. One of the truncated signals is estimated using the natural `N` option and the other using the fixed `X` option. The main difference is not the signal duration, but the fact that the naturally truncated envelope is not symmetric. For the effect which this small difference may have, see Fig. 6.15.

event, it is the most problematic and most difficult question how to set this dependence. The appropriate values depend on many things. After a few analysis one may get an experimental sense of what would be the proper setting. For example, analyzing a record of the earthquake with epicentral distance around 1500 km and with sampling rate of 10 Hz, we use the values –0.7 ± 0.2 for the `Slope` and 70 ± 20 for the `Intercept pnt`. For analysis of the record of 8000 km distant earthquake with the same sampling rate, we use something around –0.4 and 40. For near quarry blast with epicentral distances around 50 km and sampling rate 100 Hz we use the `Slope` around –1.5 and the `Intercept point` around 20.

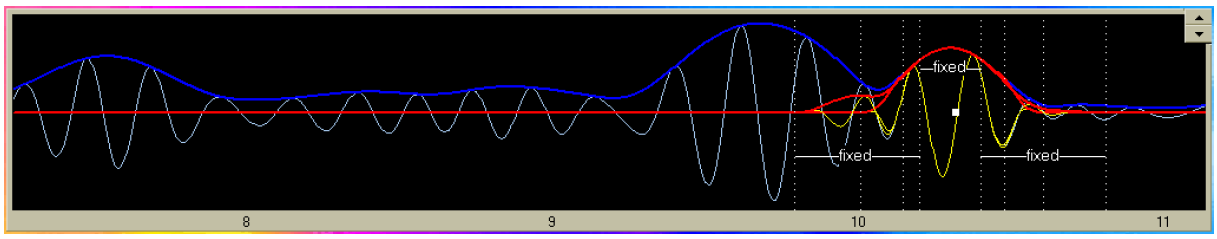


Figure 6.14: The same as in Fig. 6.13 but for different period range; this quasimonochromatic signal is filtered at period of 0.2 s. Note that in this case, as opposed to the previous figure, the natural option gives more symmetric result than the fixed one.

Generally, the `Slope` must be negative, since the α coefficient must decrease with period. It ensures that the filters will broaden a little for longer periods. In case we set the dependence in such a manner that for longer periods the coefficient will become negative, SVAL ensures it has some small positive value. For examples of difference $\alpha(T)$ dependence see Fig. 6.12. In the figure one may also see the constant near-zero values for longer periods, where the linear dependence tried to cross X axis and where SVAL changed the coefficient to be a positive constant.

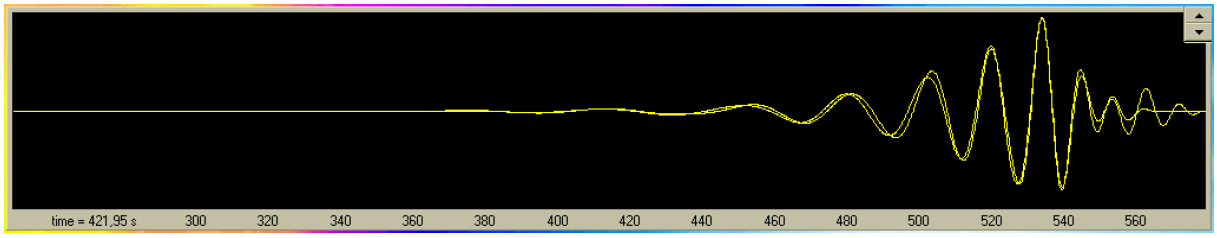


Figure 6.15: Comparison of two fundamental modes. One of them is created using the natural `N` option, the other using the fixed `X` option. Both modes are estimated for the same period range 7 – 44 s. To see the behavior of the shortest period of this mode at 7 s look at Fig. 6.13.

Do not be confused by narrower filters shown in all the figures in the frequency domain: the basic SVAL procedure uses so called *constant relative resolution*, what means that the width of the filters is controlled by central period in such a manner that the filters are narrower for longer periods. By changing the α coefficient settings we lower the influence of this *constant relative resolution* and hence we call it *optimal relative resolution*. One may make several trial and errors to get these settings. It is often useful to check the filter width influence also in the frequency domain. This is the most important setting during the analysis. In fact, making analysis of surface waves using the SVAL program means to set the proper α coefficient values. So these will be the most frequently changed edit boxes during the work with the SVAL program.

For the first analysis run, we have three more options to choose from. First we have to decide if we

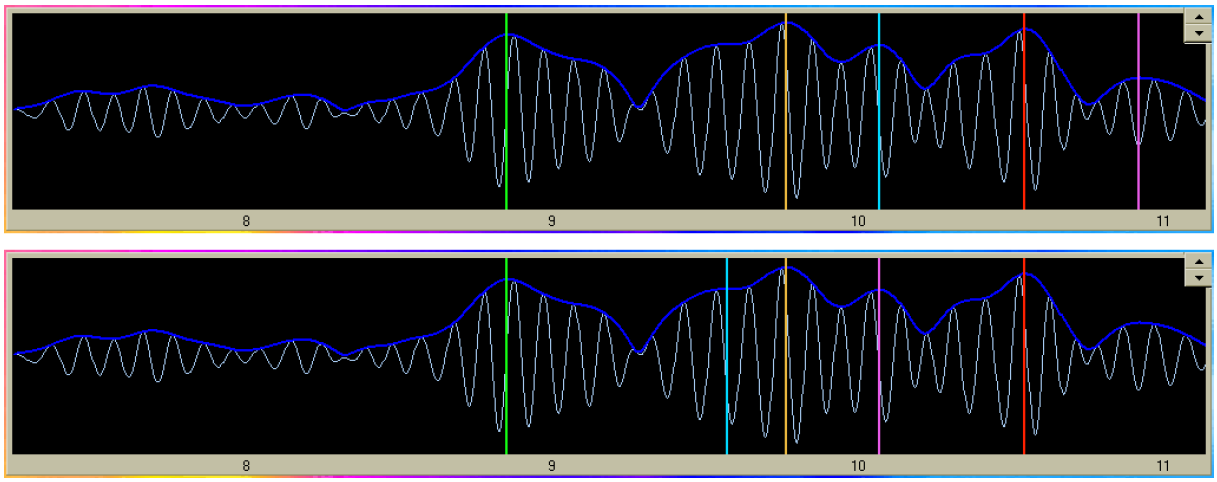


Figure 6.16: Signal at the period of 0.1 s. Five maxima (1st – orange, 2nd – red, 3rd – green, 4th – blue and 5th – violet) are found using the `Maxi` option (upper plot) and the `Inflex` option (lower plot). The lower plot has an additional 4th (blue) "maximum" near the time of 9.5 s and hence the 5th (violet) maximum replaced the 4th (blue) one from the upper plot at the time of 10.1 s. See text for explanation.

want to use natural `N` or fixed `X` quasimonochromatic signal truncating. This option has no influence on the dispersion points estimation since these points are found at the local maxima of the filtered quasimonochromatic signals and so the truncating does not affect them. But this option is crucial for the design of filtered (separated) mode wavegroup. Natural option is suitable for single station (group velocity) fundamental mode estimation. It uses envelope's inflection points with highest derivation at both sides of the used maximum, it computes the derivation at these inflection points, it prolongs the corresponding tangential direction and found the point when this tangent reach the zero amplitude. Between the two inflection points, the signal and its envelope are kept. Between the inflection point and the zero amplitude the quasimonochromatic signal and its envelope are smoothed by cosine window. Outside of the zero points the truncated signal is zero.

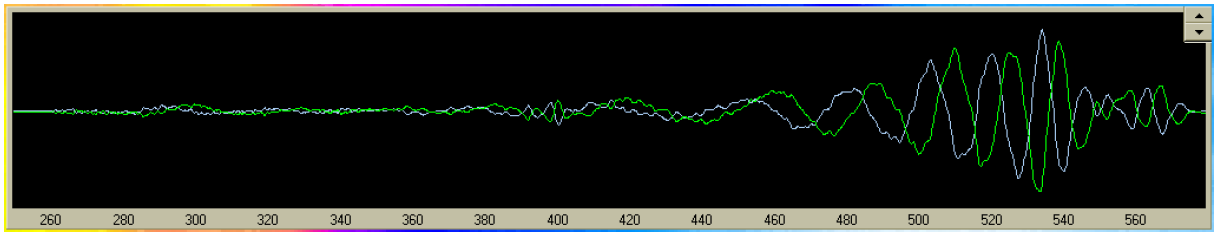


Figure 6.17: Comparison of raw seismogram (blue) and seismogram with instrumental transfer function applied (green). Both are bandpass filtered in the period range 7 – 44 s.

Thus such naturally truncated signal may look differently before and after the maximum and at each period this truncated signals for different records will be, in general, of different duration. As opposed to that, if we want to process two records from two stations and if we want to keep the same filtration and truncating for both of them, we use the fixed `X` option. This option ensures that for any quasimonochromatic signals, the point where the cosine window will take effect are set in a distance of 1/2 of the given central period before and after the used maximum. The zero points of truncating are at the distance of 2+1/2 period from the used maximum. So the whole truncated signal last exactly for a time equal to 5 periods.

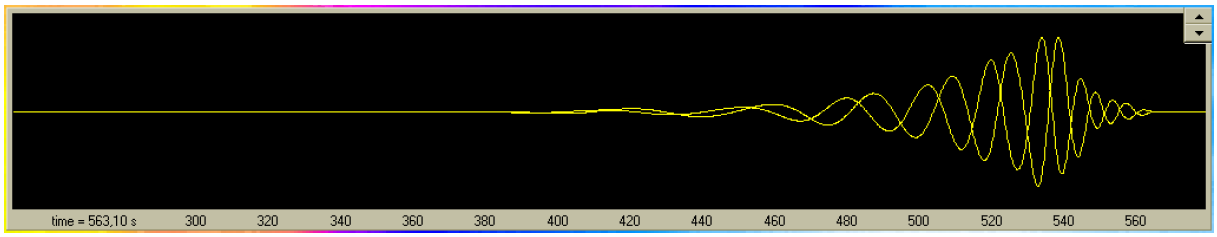


Figure 6.18: Comparison of the two fundamental modes estimated for the period range 7 – 44 s using the raw (as in Fig. 6.6) and corrected seismogram.

We use central periods for estimating this duration because the central periods may be set to the same values for any other record, but the instantaneous periods vary according to the properties of given signal. Thus we ensure exactly the same processing of any number of arbitrarily selected records. Separated fundamental (or higher) modes estimated by such attitude may be mutually compared and we are sure their properties has the same meaning. For the different truncating methods behavior see Fig. 6.13, Fig. 6.14 and Fig. 6.15. The big wavegroup which precedes our selected one in Fig. 6.14 have a strong influence on the shape of the truncated group while using the fixed `X` option. On the contrary, the natural `N` option gives more convenient result. The naturally truncated wavegroup is shorter, but nearly symmetric and does not contain any traces of the preceding group. This is, of course, an exceptional example, where the natural option gives more symmetric result than the fixed one.

The truncated signals are also saved in the complete table of signals by the `SvMn` button. The format of this file is designed for direct comparison with the same file saved for another record using the software called PhaseCorr, see Chapter 7. Thus we may easily estimate the relative phase velocity.

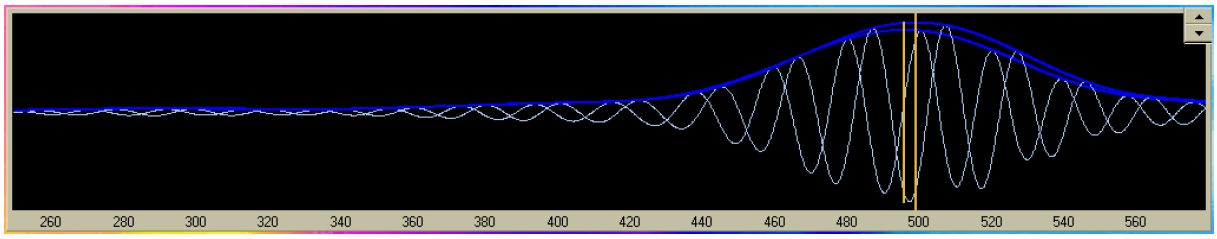


Figure 6.19: Comparison of the two 20 s quasimonochromatic signals estimated using the raw (as in Fig. 6.6) and corrected (as in Fig. 6.18) seismogram. The first orange line represents the arrival time of the raw maximum and the second one the arrival time of the maximum estimated using corrected record. We see that the time difference between those two maxima is generally different (smaller in this case) than the time difference between the two wave phases. After the correction, the envelope maximum shifts with different time than its harmonic component.

Next option influences the way how the final dispersion curve is automatically compiled using available dispersion points at maxima of five orders. The basic method is the continuity rule. It means that SVAL starts at some maximum in the spectrogram and it looks for the closest maximum at the neighboring filter. The *closest* means that it has the smallest time difference from the previous one in the neighboring filter. It processes filter by filter to compile the curve along the whole analyzed period range. The `A` / `L` option says SVAL where to start with this compilation. `L` means **L**ongest and it tells the program to start at the longest (period) filter. This option is useful in case of fundamental mode estimation where we have an assumption that the highest amplitude at longer periods belongs to the fundamental mode. The `A` means **A**bsolute and this option tells the program to start at the point of the absolute amplitude of the whole spectrogram. This option may be used in case of records containing high body waves and several higher modes of surface waves along the whole period range. We assume that the highest amplitude at all will belong to the desired mode and the program starts its compilation here using the continuity rule filter by filter to the both sides from this absolute maximum.

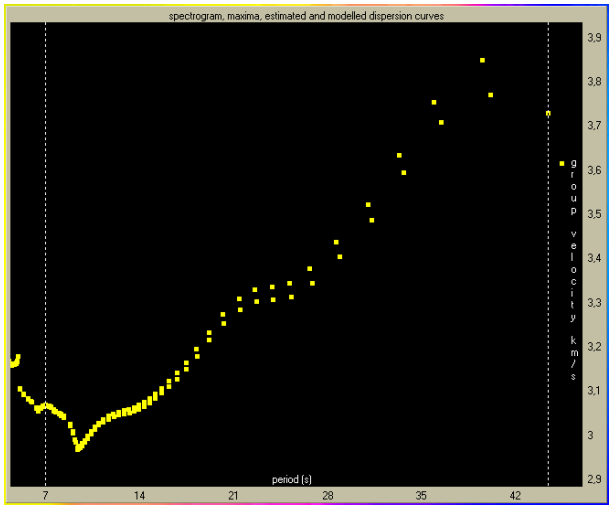


Figure 6.20: Dispersion curves estimated for raw (as in Fig. 6.6) and corrected (as in Fig. 6.18) seismogram. One should be careful considering the fact that the phase shift caused by instrumental transfer function application does not match the group velocity shift and that they may even take effect in the opposite manner. For comparison of the two filtered signals at 20 s period see Fig. 6.19.

The last option enables to choose from two types of points which will be found along each quasimonochromatic filter. The `Maxi` option means *maxima* and it forces SVAL to look for standard local

maxima as we are talking about them through the text. The `Inflex` option means *inflection points* and by checking this option we allow also the estimation of hidden maxima, which may be described as local inflection points with zero derivation. The `Inflex` option is used rarely only in cases of complicated records where several modes and body waves may overlap the wanted fundamental mode or when we are looking for the surface waves among many body wavegroups. See Fig. 6.16 for visual experience: the `Maxi` option used in the upper plot of Fig. 6.16 means that only real maxima are considered. The fifth maximum (violet) at the end of this signal was not recognized in the lower plot, where the `Inflex` option was used. `Inflex` procedures have already spent the fourth maximum (blue) for an inflection point and the fifth one has to replace the fourth. The fourth maximum (blue) of lower plot is located in the inflection point and the fifth (violet) is located in the same place as the fourth maximum (blue) of the upper plot.

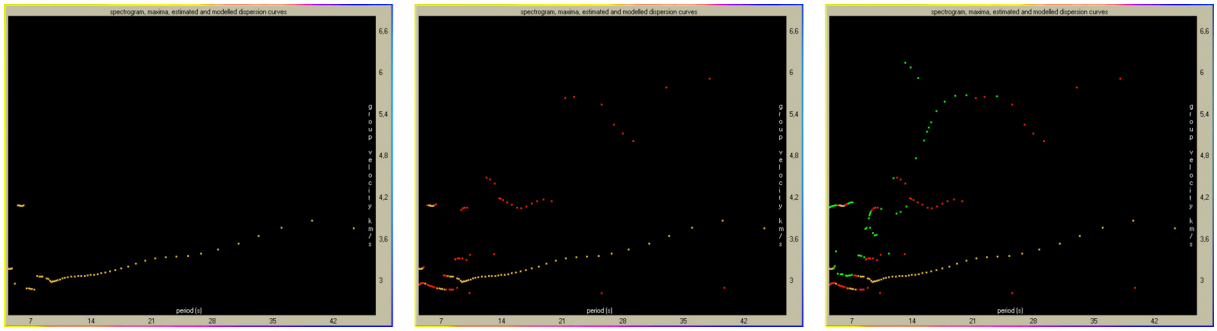


Figure 6.21: Spectrograms with primary (left), primary and secondary (middle) and primary, secondary and tertiary (right) local maxima.

After we set all these settings, we may press the `Analysis` button. What happens is described in Section 6.5. Now we will see some possibilities how to check the results of analysis, what may help us with new and better parameter settings.

It is usually advisory to go through the SVAL's text output and check if there is some anomalous or unexpected message. If yes, we should first try to improve the error by changing the appropriate edit box value or trying to run the analysis with some other option checked.

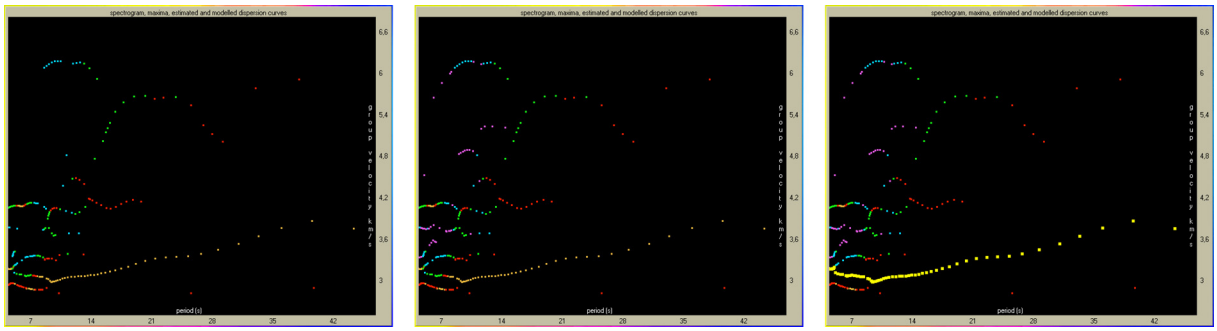


Figure 6.22: Spectrograms with primary to quaternary (left), primary to quinternary (middle) and all maxima with dispersion curve compiled (yellow) (right).

We may draw the whole spectrogram by `Spectrogram` button, see Fig. 6.5. It gives us the basic overview of what we may do in next steps. SVAL has already estimated the dispersion by one of the two automatic compiling methods. We draw the truncated spectrogram and corresponding dispersion curve, see also Fig. 6.5. To see if we really get the right mode, we may draw both raw seismogram and dispersed wavegroup corresponding to the selected dispersion curve, see Fig. 6.6. Before the button `Slctd group` is enabled, we have to select the period range by choosing from the drop-down options of minimal and maximal periods. By `Slctd group` we create the appropriate wavegroup and it is drawn into the same plot as the raw seismogram. It is possible to increase or decrease the relative amplitude of the separated wavegroup with respect to the original seismogram by changing the value of a spin edit box. To check, if there is also other wavegroup containing the same periods, we may use the `Bandpass` button to draw the separated seismogram without any truncating in the time domain, see Fig. 6.7. Before using the `Bandpass` button we have to enter the period range for this bandpass filtering. For checking the desired period range we advise to enter the same period range as we have selected for truncated wavegroup computation.

We may be interested in some of the filtered quasimonochromatic signals to see why SVAL has estimated maxima at the points where it has done it. We may go through some of the filters using the

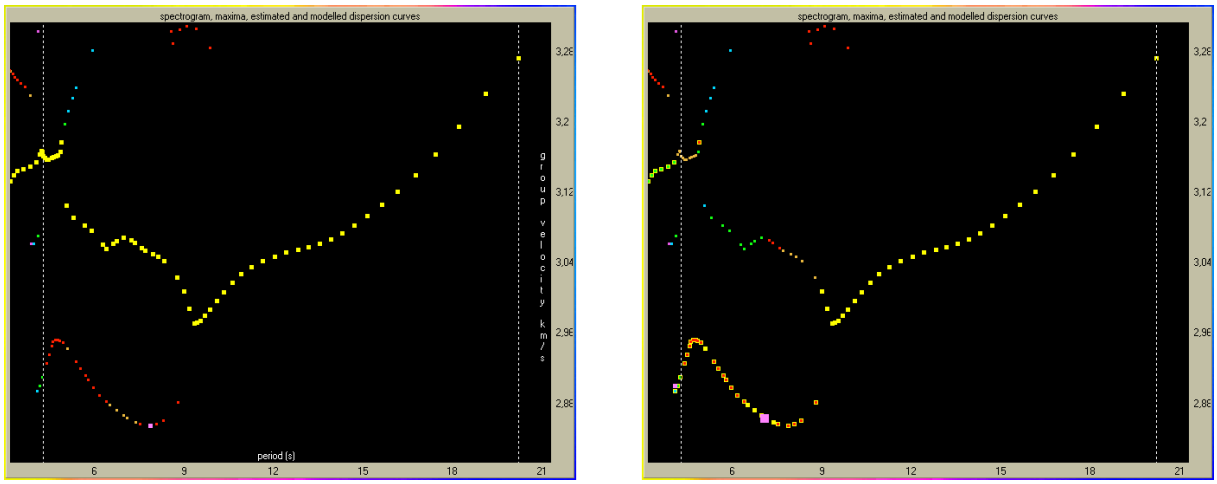


Figure 6.23: Details of spectrogram. Left: automatically compiled dispersion curve (yellow), right: in the range of 4 – 9 s the dispersion points were changed by manually selecting the desired points of different local maxima by mouse-clicking into the spectrogram (yellow with small points with color appropriate to the maximum quality).

upper time plot and its period drop-down menu selection. It is usually suitable to see both whole filtered signal and its truncated version, see Fig. 6.8. At the same time we also see the envelopes to be drawn in the period-group velocity plot. As opposed to the upper plot, we see here the envelopes to be drawn with respect to period. In fact, the envelopes are curves of three variables: time, amplitude and instantaneous period, see Fig. 6.10. If we are interested in what happens for different period ranges, we may draw it by selection of the ranges and by repeated pressing the `Slctd group` button after each range selection, see Fig. 6.11.

If we select the minimal and maximal period for the period range to be equal, by pressing the `Slctd group` we obtain the single wavegroup which is equal to the truncated quasimonochromatic signal drawn by `Trnc` button for selected period in the upper time plot.

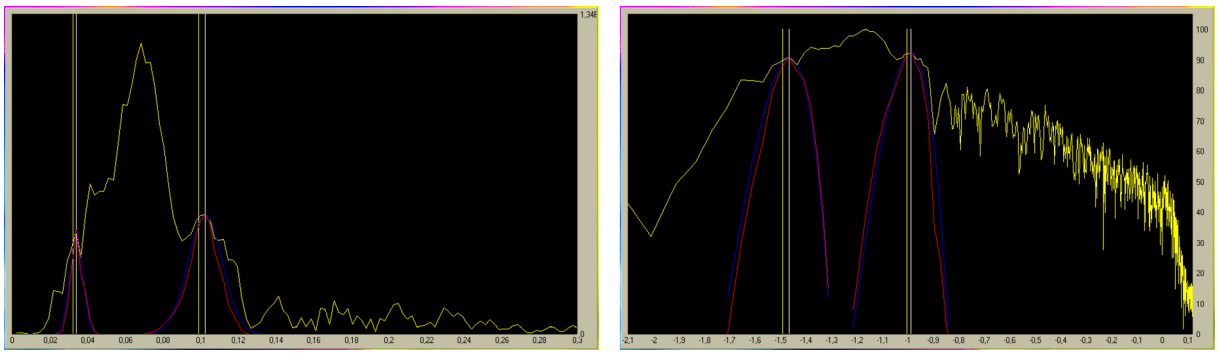


Figure 6.24: Spectrum of the raw record (yellow) with weighting Gaussian filters (blue) and with filtered spectra (red) at periods of 10 and 30 s. White lines represent the central period and yellow lines show the instantaneous frequency of corresponding filter used in the dispersion compilation. Left: normal view, right: log-log representation. All other following spectra figures are depicted by the same two representations.

If we are interested in the absolute group velocity estimation, we have to apply the instrument transfer function. It is done in the frequency domain, so we have to switch into the frequency domain window by the `Spectral d...` button. We apply the correction and as we start the analysis of the corrected record by the `Filter corr` button, it also draws the whole seismogram with the instrumental correction applied. We may compare the raw and corrected seismogram as in Fig. 6.17.

If we let the desired mode to be drawn from the previous analysis of the raw record, we may now draw by the same `Slctd Group` button the same mode for the same period range, if selected, but with instrumental correction applied. We may compare these two, as it is seen in Fig. 6.18. For the presented example the instrumental transfer function has completely changed the wavegroup design. But the dispersion curve does not change dramatically, see Fig. 6.20. Reason for that is the epicentral distance of 1600 km. So, the several-seconds shift in time does not affect the group velocity greatly because the whole propagation time is in order of hundreds of seconds, as we may see at the time plots, where the time on the X axis is measured from the origin time.

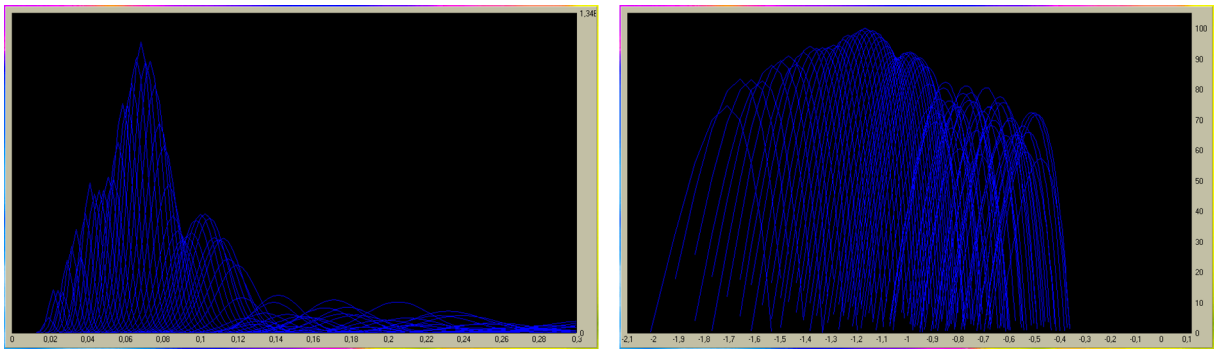


Figure 6.25: All Gaussian filters used in the analysis for selected period (frequency) range. The filters have their actual height. Left: normal view, right: log-log representation.

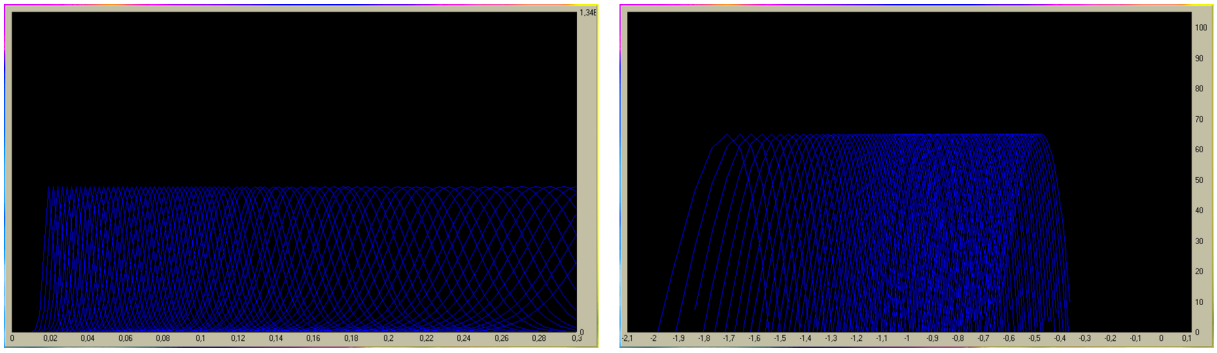


Figure 6.26: All Gaussian filters used in the analysis for selected period (frequency) range. The filters have normalized height. Left: normal view, right: log-log representation.

In similar way we may also compare the single quasimonochromatic signals estimated from raw and corrected record, see Fig. 6.19. A disadvantage is that for each pair of filtered signals to be drawn together we have to run again both raw `Analysis` and/or `Filter corr` analysis procedures.

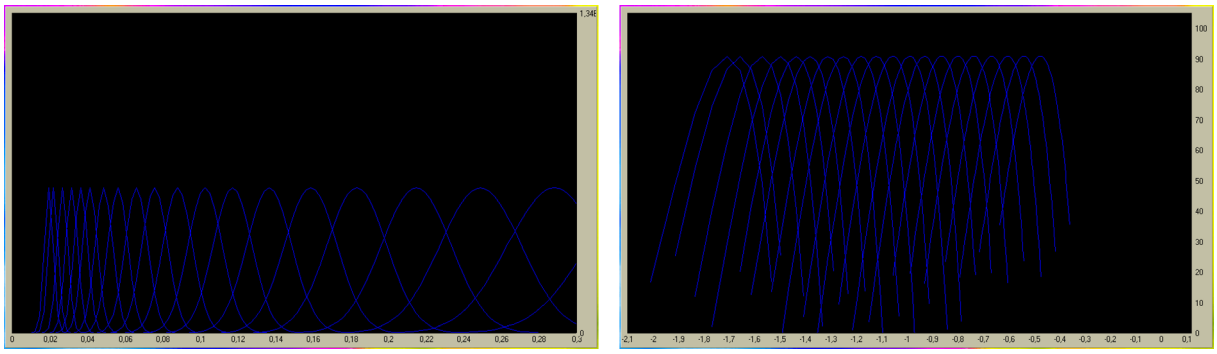


Figure 6.27: Gaussian filters used in the analysis for selected period (frequency) range. The number of the filters were set to be only twenty although the analyzed period range is the same as in Fig. 6.26. Left: normal view, right: log-log representation.

If we are not satisfied with the automatic procedures of dispersion curve compilation, we have to check also the other local dispersion points maxima. First to third of them are depicted in Fig. 6.21 and first to fifth in Fig. 6.22. The last plot of Fig. 6.22 shows an automatically compiled dispersion. We may manually select the dispersion points by choosing and clicking any of the not-automatically-used maxima, see Fig. 6.23. While clicking on some of the points, SVAL gives a feedback in the text output box to tell us, what point we clicked and which of the filters it affects. The automatically estimated maximum at given filter is replaced by the clicked one. Of course, we may also click the already selected dispersion points – however, this action has no effect. After we finish our manual dispersion points selection, we have to run the whole analysis again with the exactly same parameters, as before. This is the reason why due to clicking almost all of the setting edit boxes are disabled – we have to keep the present values in them.

If some single quasimonochromatic signal period is selected, the appropriate button for drawing the five maxima types draws also the maxima position in time into the upper time plot. The colors are the

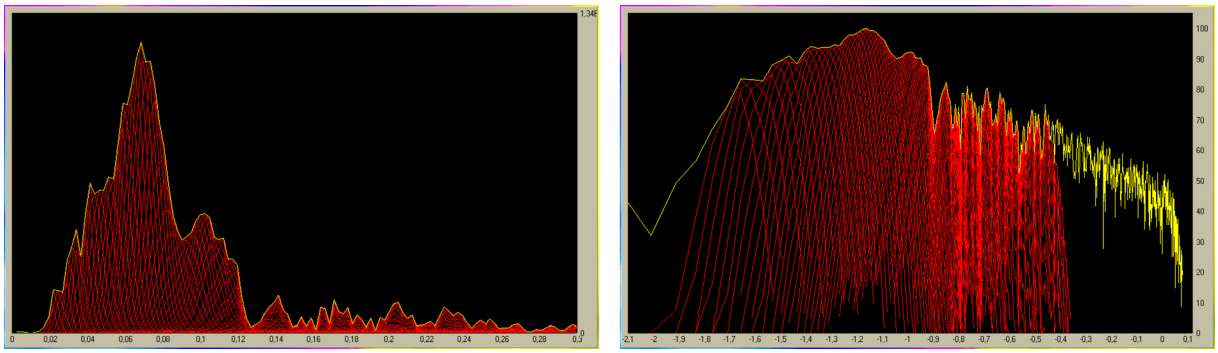


Figure 6.28: All filtered spectra. Left: normal view, right: log-log representation.

same to recognize maximum type, see Fig. 6.16. In the frequency domain we may check the position of the five maxima instantaneous frequencies as shown in Fig. 6.29.

In the spectral domain, we may see all the features as in the time domain. In Fig. 6.24 we see whole spectrum of the record and two filters forcing as a weighting function on this spectrum and creating two filtered spectra. In all figures of frequency domain plots we will use both standard and log-log representation, which may be easily switched in the SVAL program.

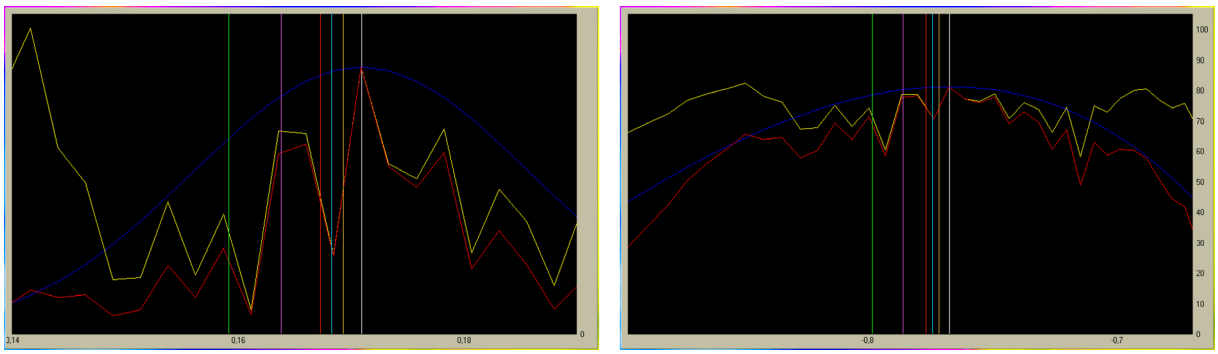


Figure 6.29: Instantaneous frequencies of five maxima depicted along spectrum filtered at period of 6 s. The color of each maximum corresponds to the color used in the spectrogram plot and in the frequency domain depiction. Left: normal view, right: log-log representation.

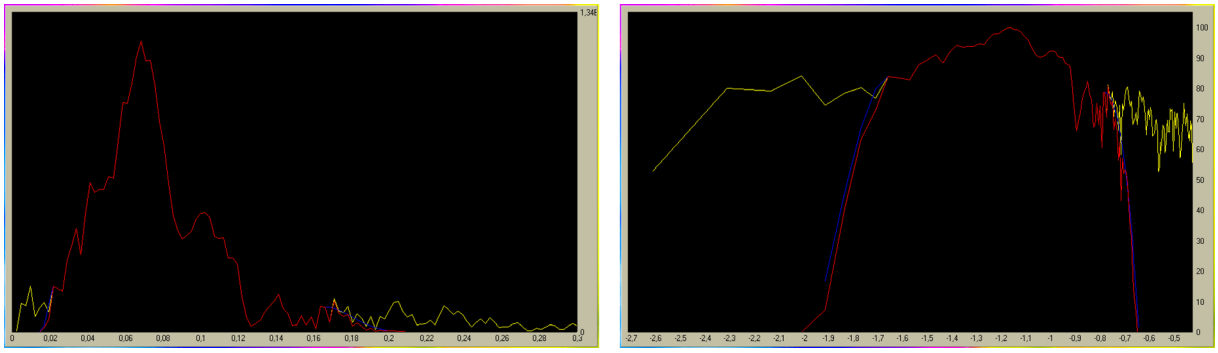


Figure 6.30: Comparison of raw spectrum (yellow) and spectrum bandpass filtered in the period range of 7 – 44 s (red). Smoothing edges of Gaussian weighting function are shown (blue). Left: normal view, right: log-log representation.

To get the idea of how the filters weight the spectrum we may plot all the used filters with their actual heights, as in Fig. 6.25 or with normalized heights, as in Fig. 6.26. We have already discussed Fig. 6.27, and Fig. 6.9, where only smaller number of filters is used.

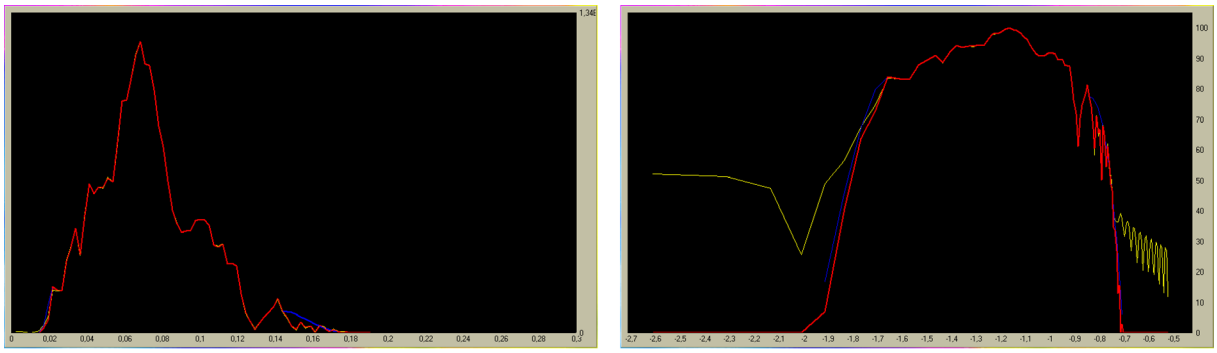


Figure 6.31: The spectrum drawn by the `Spectrum` button is the "raw" one (yellow), but after the bandpass filtered record for analysis was used. Hence, it is a bandpass filtered spectra estimated from bandpass filtered record. The other one (red) is drawn by the `Filter spec` button. It is a bandpass filtered spectra made by cropping and smoothing from the original raw one. Theoretically, both these spectra are the same, however, thanks to the repeated Fourier transform, some numerical differences occurs, what is visible especially in the log-log representation.

As a result of filtering we get a set of filtered spectra, which is shown in Fig. 6.28.

In principle, the bandpass filtering method is the same as the multiple filtering one. In case of bandpass filtering, we weight the spectrum in such a manner that desired part of the selected period/frequency range remains the same and the edges are smoothed by half-Gaussian functions, see Fig. 6.30.

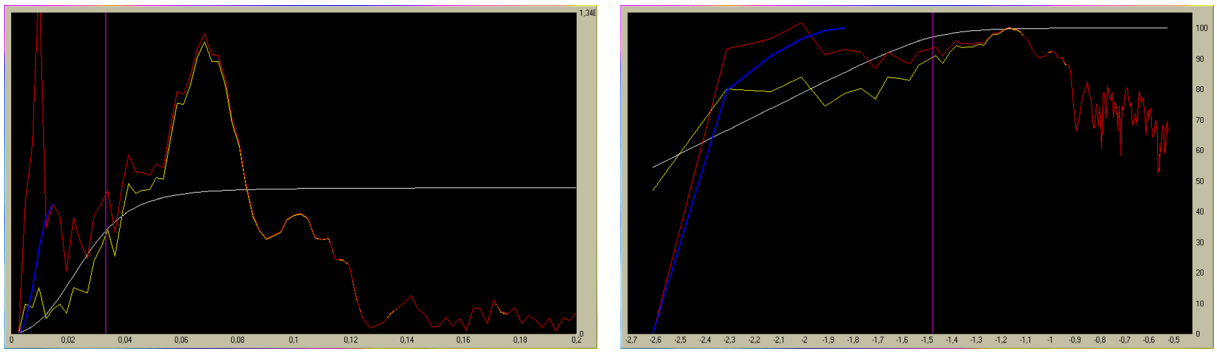


Figure 6.32: Comparison of raw spectrum (yellow) and spectrum with instrumental transfer function applied (red). The amplitude transfer function with relative amplitude is depicted (white function). Eigenfrequency of the instrument is drawn (violet straight line). By the blue color, smoothing cosine window is presented.

The "raw" spectrum drawn by the `Spectrum` button is always the spectrum computed from the record used for the analysis. So, when using the bandpass filtered spectra for analysis by selecting the `F` option after pressing the `Bandpass` button, the spectrum drawn by the `Spectrum` button is a spectrum of this bandpass filtered record. When we press the `Bandpass` button again after providing the analysis, we may plot both "raw" and bandpass filtered spectra together using the `Spectrum` and `Filtered spec` buttons. In this case, both buttons should give the same result. However, some numerical discrepancies occur since each of the spectra are computed by different way. Theoretically, they are the same, but the "raw" spectrum drawn by the `Spectrum` button is computed by the Fourier transform from the already bandpass filtered record and the spectrum drawn by the `Filtered spec` button is created by cropping and smoothing using the original raw spectrum computed by the Fourier transform using the original raw record directly from the data file. Both spectra are shown in Fig. 6.31. The spectrum drawn by the `Filtered spec` (red) is zero outside the limits of the bandpass filter by definition, however, the spectrum drawn by the `Spectrum` button (yellow) has a non-zero values outside the limits since both long and short periods leak into the spectra from the bandpass filtered record. This effect is well visible especially at the right panel of Fig. 6.31 where the log-log representation is shown.

One of the most important features applied in the frequency domain window is the instrumental transfer function. Again, we may consider the amplitude transfer function as it forces as an weighting function. In our case, Fig. 6.32, the amplitude transfer function will increase the longer periods and keep at the same level periods shorter than 30 s. In general, applying the transfer function on the spectrum means a division of two complex numbers for each frequency.

Because the lowest frequencies (longest periods) are usually increased to an unrealistic level since the amplitude transfer function approaches zero, we use a cosine window to smooth the longest periods to eliminate such long periods from both the spectra and the time domain signal. This cosine window is

applied from the period two times longer than is the natural one of the given instrument up to the longest period in the spectra. In frequencies, it means from the half eigenfrequency down to the zero frequency. This smoothing window is presented by blue color in Fig. 6.32. The other option how to get rid of these long periods is to bandpass the record at first and to apply the instrumental transfer function after that.

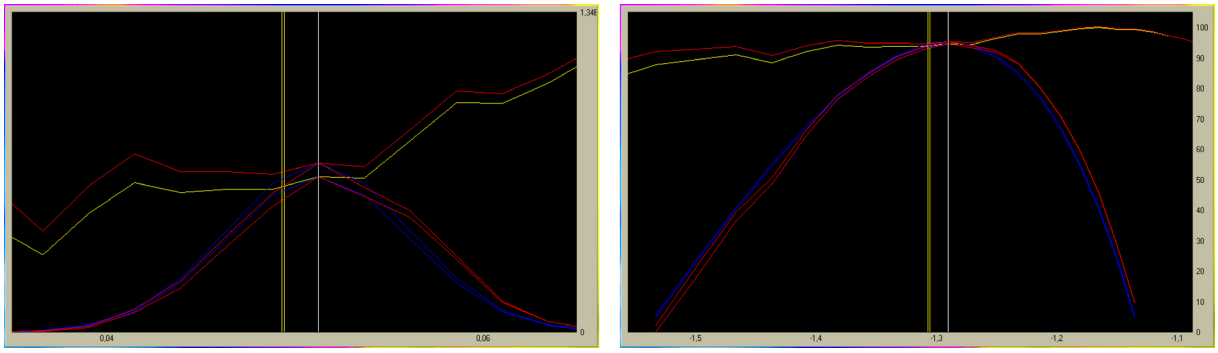


Figure 6.33: Weighting by Gaussian filters (blue) at central period of 19.5 s. Raw spectrum (yellow) and corrected (red) is depicted. Resulted filtered spectra are shown (red). The same central period of the filter (white straight line) and different instantaneous periods of the selected maxima (yellow straight lines) are drawn.

In Fig. 6.33 we see a comparison of weighting by Gaussian filter at one central period. The filter forces on the raw and also on the corrected spectrum. Although the central period of the filter is the same in both cases, the instantaneous period of the selected maximum differs a bit due to different frequency-time characteristic of raw and corrected records. The amplitudes of the raw and corrected filtered spectra, of course, differ to.

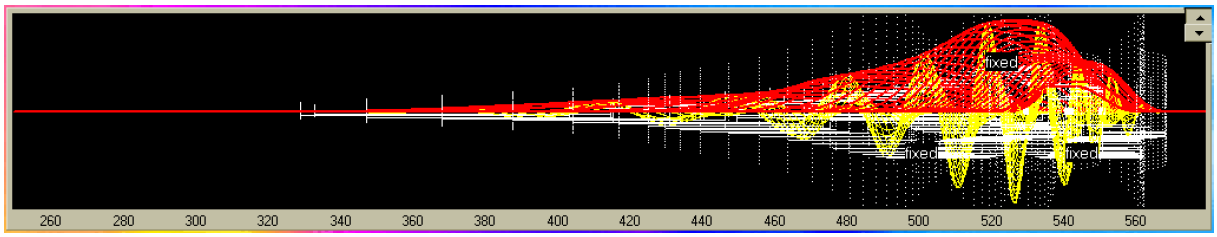


Figure 6.34: An example of truncated signal set in the period range of 9 – 44 s.

It may also happen that the instrumentally corrected spectrum normalized into the dB scale reaches more than 100 dB. It is due to the fact that SVAL uses the same scaling constant for both raw and instrumentally corrected spectrum. This is implemented for an easy relative comparison of both spectra in the frequency domain window plot. As the scaling 100 dB maximum is taken from the absolute amplitude maximum of raw spectrum, it may, in general, differ from the absolute maximum of the corrected spectrum. And hence, since the amplitude characteristic applied on the raw spectrum increases the longer periods, this increased part of the corrected spectrum may exceed the 100 dB range.

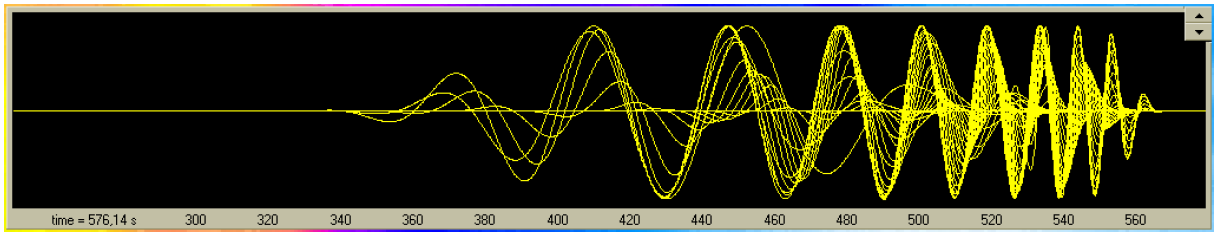


Figure 6.35: An example of truncated signal set in the period range of 9 – 44 s – the same as in Fig. 6.34, but drawn by `Slctd group` button with relatively normalized amplitudes to the same height for each filter.

By repeated checking of the above mentioned graphical plots, we may set more suitable filtration parameters and try to analyze the record again and again. While processing a similar earthquake records, one gets an idea of what parameters are suitable and the work proceed faster. But we may spend an hour of analyzing some new complicated record of event from Central Asia, where many complicated wavegroups come and it is hard to be sure what is the fundamental mode.

An example what may we see if we select period by period and if we draw each truncated quasi-monochromatic signal is shown in Fig. 6.34. In this figure the truncated signals have their actual relative

amplitudes. The same is shown in Fig. 6.35. This figure was obtained by repeated drawing of `Slctd group` with the minimal and maximal values of periods set to the same value. This plot shows the signals normalized to the same amplitude.

As we mentioned above, the most used parameters during the work with the SVAL program are those affecting the α coefficient. Of nearly the same importance are the frequency-time ranges of spectrogram set by minimal and maximal group velocity and by minimal and maximal period. Generally, after setting the appropriate width of filters, we change the frequency-time ranges to put aside the unwanted modes and coda and to aim our spectrogram estimation directly to the frequency-time area of our desired mode.

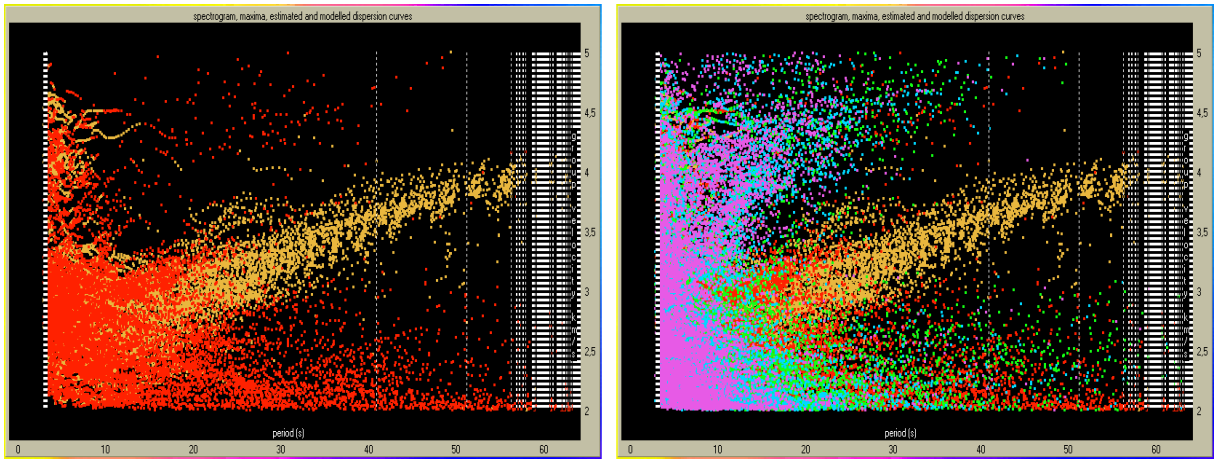


Figure 6.36: Left panel shows how does the plot look when 164 files have been processed by the automatic batch processing procedure and only two maxima of each harmonic component are plotted. Right panel shows the same situation with all five maxima plotted.

The batch processing was developed when there was a need to analyze many records from hundreds of stations across the whole Europe. Our aim was to measure propagation times from Greek earthquakes. The main task, where the interaction with the user is necessary while working with the SVAL program, is the dispersion curve compilation. When we decided not to look for the dispersion ridges of a specific mode, the idea of making the analysis completely automatic emerges. For seeking the dispersion ridges with no need to estimate the fundamental (or generally any) mode, we do not need the interaction with the seismologist. We decided to scan a long time window and try to find also surface wave reflections and converted modes. Thus, besides the broad period and velocity ranges, the only parameter to set is the width of filters. This is not a problem when we have records of the same sampling rate and from the same event.

The idea of the research supported by the batch processing is that we need only the propagation times of the five highest envelope maxima from each period at each station. The intention is to process the data further and to classify the modes later by means of other software. Such a program, which reads the *.rdg files produced by the SVAL's batch processing and analyzes the mutual relation between the five propagations times of the most significant wavegroups at different station for all periods with the dependence on azimuth and epicentral distance, is under development now. Preliminary versions are tested and used for preparatory data analysis.

The detailed technique is described in Sections 6.5 and 6.6. The core of the batch processing is that it calls the procedures which are normally called by the user. The only modification concerns the opening of the files, when the program has to recognize and open file by file from the given directory. Thus some limitation for the file format and names emerges – the files for the batch processing have to be of the new KUK format with all the necessary information given in the file header and their extension has to be *.dat. No other files with such an extension should be present in the working directory. There are several option to customize the batch processing, described also in Section 6.5.

The advantage of using the batch processing is not only the fact it saves time and effort of the seismologist. While visualizing the result of may records together, one may observe the features which are not to be noticed when only few stations are used. These are especially the surface wave reflections, higher modes and other phenomena, which are hard to find and easy to misinterpret. While looking at Fig. 6.36, we may see the fundamental mode using just visual "statistical" approach. The cumulation of orange dots is not random, as the fundamental mode in this case reveals the highest amplitudes for waves longer then 15 s and the group velocity dispersion curve is similar for many stations. Surface wave reflection propagating from other directions than the fundamental mode propagating directly from the source can be determined when we change the epicentral distances from the source to distances measured from some virtual "epicenter". This work is under development now and the batch processing

implemented into the SVAL program helps with this job significantly.

The batch processing is intended for specific tasks only. It cannot substitute the detailed and careful work of the seismologist when dispersion curves of specific modes and particular properties of individual records are to be discovered.

6.12 Examples of analysis

This section provides five examples of group velocity estimation of events of different epicentral distances and of different sources.

We propose:

- shallow seismic measurement

  epicentral distance: tens of meters
  period range: 0.02 – 0.2 s (5 – 50 Hz)

- local quarry blast

  epicentral distance: tens of kilometers
  period range: 0.15 – 4.0 s

- near regional earthquake

  epicentral distance: thousand of kilometers
  period range: 3.0 – 60 s

- far regional earthquake

  epicentral distance: thousands of kilometers
  period range: 12.0 – 40 s

- teleseismic earthquake

  epicentral distance: nearly nine thousand of kilometers
  period range: 13.0 – 220 s

Each example is made in such a way to be easily reproduced by any SVAL-beginner user. We start with some basic event's information and we present the SVAL main window with the filled parameters and option. For the first analysis run, the user is supposed to fill the edit boxes and to check the options in exactly the same manner as depicted. This should give the same results as shown, especially the same dispersion curve and the same separated wavegroup. Further we proposed some modifications of the parameters to see SVAL behavior. The users are encouraged to save some of the found dispersion curves for further use for inversion as described in examples in Section 6.14.

The only files needed for experience this examples are the data files with appropriate components of selected record. We provide them on a CD-ROM attached to this thesis. The file names of this data files contains information about the event location and component.

Do not forget to set all the parameters and all the options and checkboxes to the same values as shown in examples.

Each example description starts on its own page to simplify the example's reading.

Analysis Example #1: South Iran

event and record info:

date:	2005 November 17
magnitude:	6.0
event location:	55.847°E 26.784°N (South Iran)
depth:	10 km
origin time:	10:22:19 UTC
source:	natural tectonic earthquake
epicentral distance:	4441.38 km
station:	Nečtiny NEC (Western Bohemia, Czech Republic)
station location:	13.16864°E 49.97740°N
seismometer:	Guralp 30 s
samples for FFT:	32768

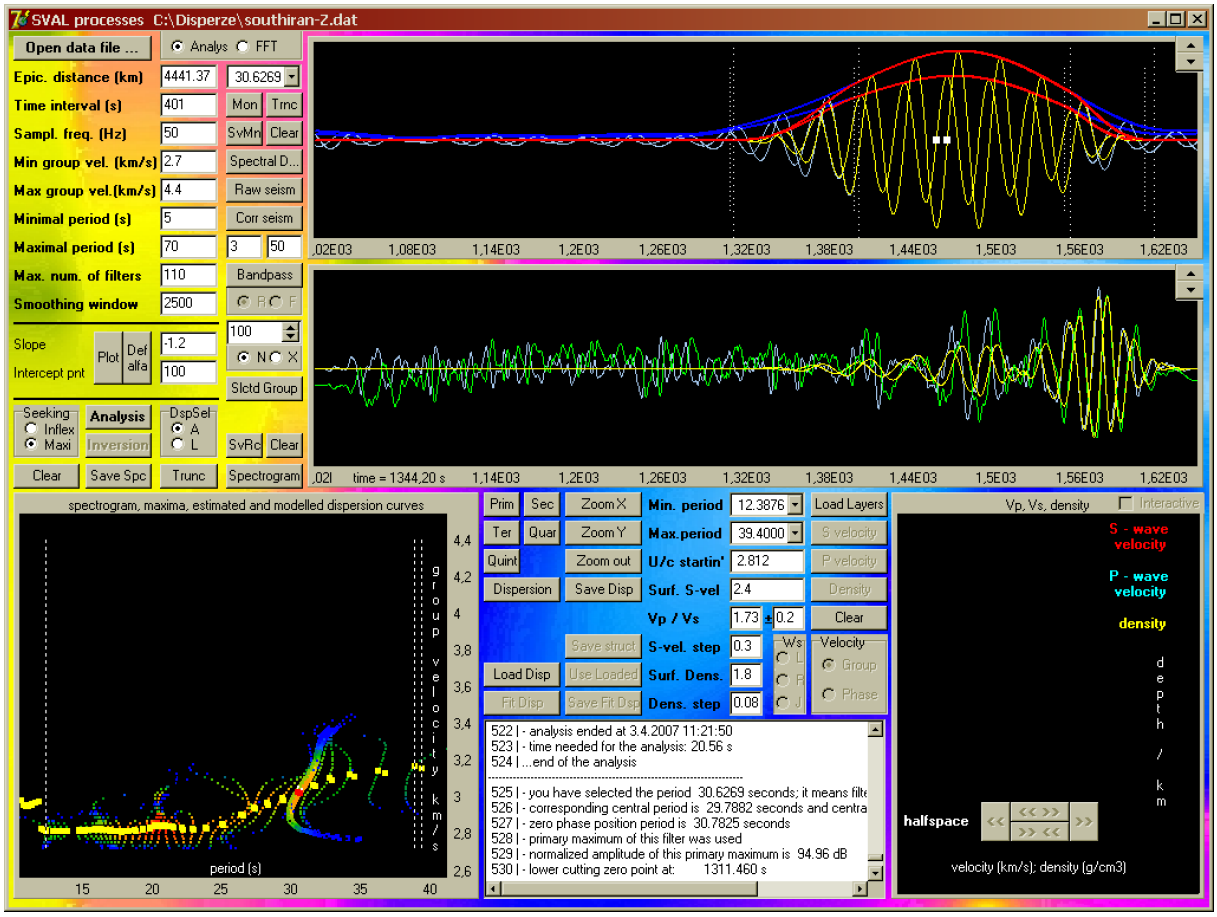


Figure 6.37: Analysis example #1 – South Iran.

Fig. 6.37 shows both raw and instrumentally corrected seismograms, both dispersion curves, both fundamental wavegroups and also raw and corrected 30.6 s quasimonochromatic signals. We use natural truncating of the quasimonochromatic signals.

Try to select a different period ranges for creating the fundamental mode wavegroup. It is also useful to look at the other quasimonochromatic signals. There are several more complicated wavegroups at shorter periods. The 30 s period signal is not so complicated. Records of earthquakes from Central Asia present complicated behavior with scattered and multipathed surface waves. This example is a typical problematic record where several groups are to be distinguished and it is a little bit tricky to analyze the broad period range. We present only the smooth dispersion for the range of periods of 12.4 – 38.4 s. Longer periods are also present in the record, but we are not sure what is the fundamental mode. The analysis is provided up to 70 s, so, look at the longer periods and guess what may be the Rayleigh wave dispersion.

If you are interested in processing the inversion tasks of this dispersion, look in Section 6.14 for further work with this example.

Analysis Example #2: Aegean Sea

event and record info:

date:	2005 October 20
magnitude:	5.9
event location:	26.75°E 38.15°N (Aegean Sea, Greece)
depth:	10 km
origin time:	21:40:04.09 UTC
source:	natural tectonic earthquake
epicentral distance:	1632.54 km
station:	Háje HAJ (Bohemian Massif, Czech Republic)
station location:	14.04897°E 49.67474°N
seismometer:	Guralp 30 s
samples for FFT:	32768

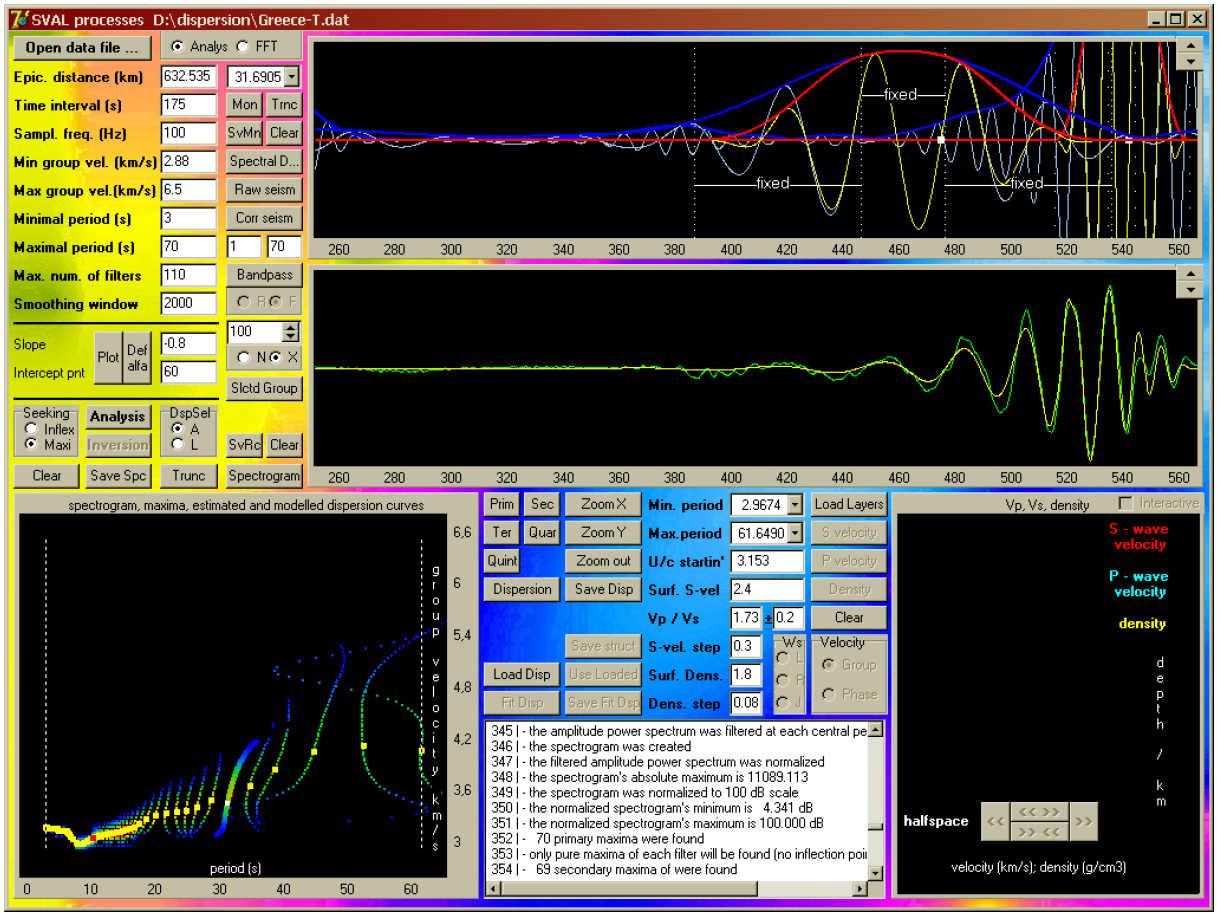


Figure 6.38: Analysis example #2 – Aegean Sea.

The example shown in Fig. 6.38 analyzes the regional event from Greek Aegean Sea. We bandpass filtered this event for the period range 1 – 70 s because some very long periods seems to occur along the seismogram. Do not forget to change the `R` to `F` option to set the bandpass filtered record for further analysis. After the analysis of the bandpass filtered record, we applied the instrumental transfer function and made the analysis of the corrected record. The figure shows only the resultant dispersion curve, instrumentally corrected seismogram and corresponding fundamental wavegroup. We used fixed truncating for this record. One may complain, why we present the dispersion curve up to nearly 62 s. The reason is simple – we found the periods to be well recorded and so we used them. The Guralp 30 s seismometer has a constant amplitude characteristic up to 30 s, but this does not mean that we cannot observe longer periods at its records. In the upper time plot the filtered quasimonochromatic signals at 10 and 30 s period are shown both in whole and truncated versions.

After we make an analysis of this event, we save the estimated instrumentally corrected dispersion by the `Save Disp` button. We will use it for an inversion in Section 6.14.

Analysis Example #3: Horní Rozmyšl

event and record info:

date:	2003 June 05	magnitude:	not estimated
event location:	12.668°E 50.261°N (Horní Rozmyšl, Western Bohemia, Czech Republic)		
depth:	surface	origin time:	17:49:59.546 UTC
source:	quarry blast	epicentral distance:	28.954 km
station:	Kynžvart KYNZ (Western Bohemia, Czech Republic)		
station location:	12.604°E 50.004°N	seismometer:	Lennartz 3-D 5 s
samples for FFT:	2048		

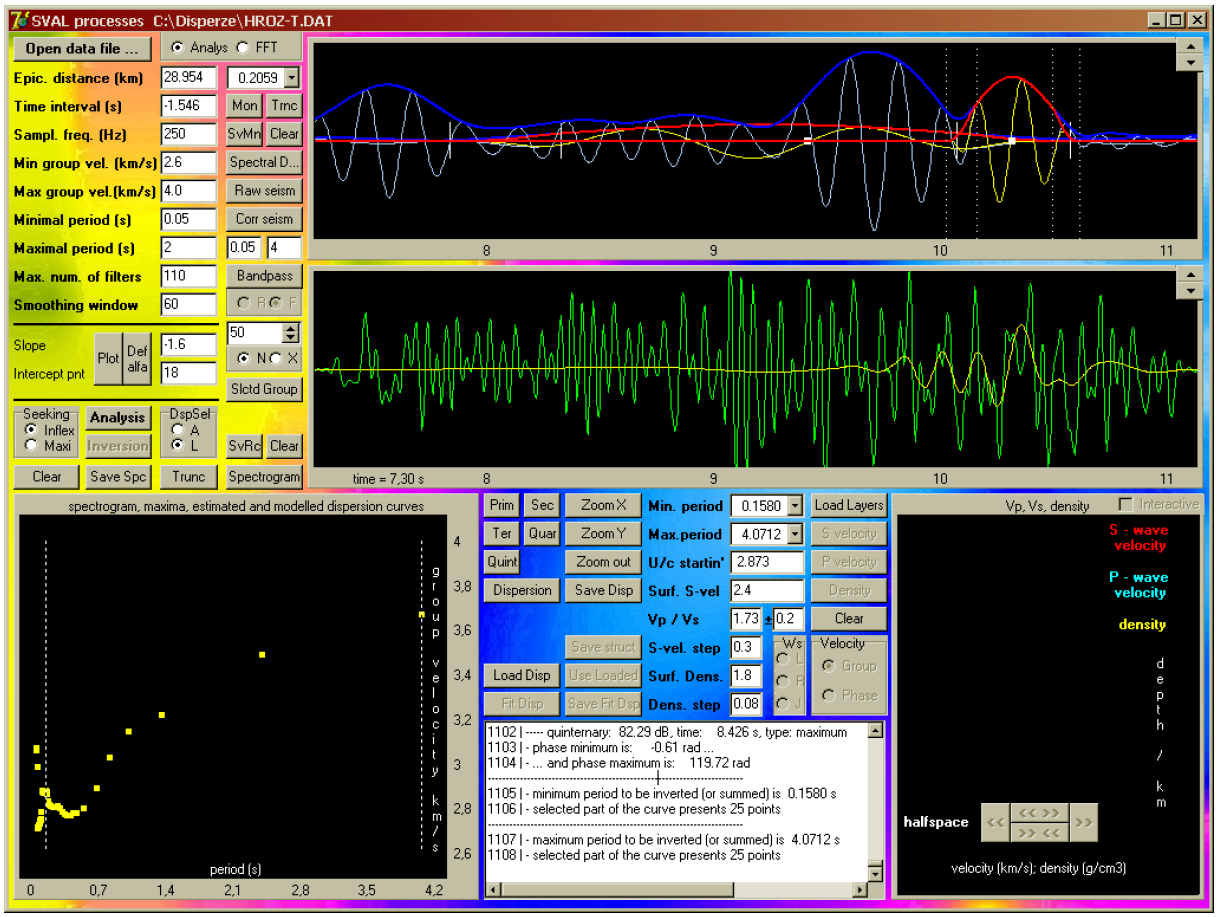


Figure 6.39: Analysis example #3 – Horní Rozmyšl.

We propose a quarry blast record measured during the SLICE 2003 project in Western Bohemia. Short period recorders were used, but since the epicentral distance is small, also only short period surface waves were generated. We advise to bandpass filter this record as shown in Fig. 6.39. It has no influence on the surface wave dispersion, but it makes the record more readable. If we look at the quasimonochromatic signal at the period of 4.0712 s, we may see it is a little bit blurred. This filter period is too long, the signal is too weak and its use may be disputable. In Fig. 6.39 we show also signals for 1.0 and 0.2 s. This 0.2 s signal is also used as an example of `N / X` truncating option in Fig. 6.14 in Section 6.11. We used the natural `N` truncating option in the example here. We can check what happens, if we change the `Inflex / Maxi` checkbox option. We used the `Inflex` here, but the use of `Maxi` influences only the short period part and hence does not affect our dispersion curve. However, we may check the change of the maxima positions for short period filters. A good chance to see this feature working is to select the filter at period 0.1026 s after the `Inflex` analysis, draw the whole quasimonochromatic signal and then press the first to fifth maxima. The fourth maximum, presented by light blue line, is at the inflection point. If we use the `Maxi` analysis, the same central period is now present in the drop-down list as a 0.1041 s, since using other maxima the instantaneous period changes slightly. If we draw the five maxima for this `Maxi` option, we see the difference. For detailed description see Fig. 6.16 in Section 6.11.

The information about the maxima type is given in the text output after we select one of the periods in the drop-down list. There we may also check the central periods of the filter – this is the way how to recognize that the 0.1026 s instantaneous period from the drop-down list generated by the `Inflex` option corresponds to the 0.1041 s instantaneous period generated by the `Maxi` option.

Analysis Example #4: Shallow seismic measurement

event and record info:

date:	2004 June 13
magnitude:	very small :-)
event location:	14.15°E 49.91°N (Karlštejn, Central Bohemia, Czech Republic)
depth:	surface
origin time:	13:15:12 UTC
source:	hammer beating a metal plate
epicentral distance:	50 m
station:	Karlštejn (Central Bohemia, Czech Republic)
station location:	14.15°E 49.91°N
seismometer:	SM 6 (4 Hz)
samples for FFT:	1024

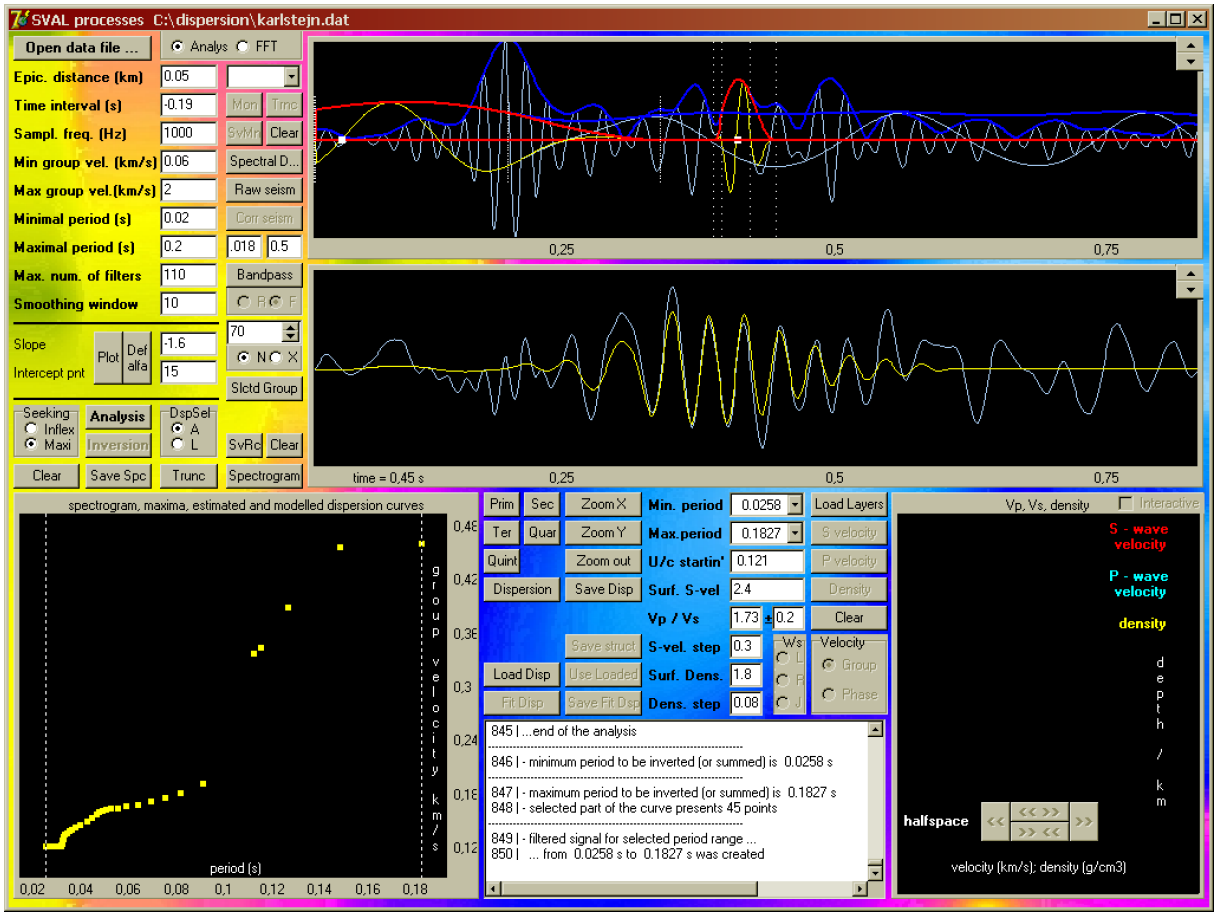


Figure 6.40: Analysis example #4 – Shallow seismic measurement at Karlštejn.

The analysis of this event was made to show how short-period may be the surface waves. This shallow seismic experiment was organized to obtain an anisotropy estimation of upper limestone layers in the area near Karlštejn Castle. We beat a metal plate by a hammer and we recorded the high frequency waves along several profiles with mutual station distances of 5 m. We present an analysis of raw data without any instrument correction. This is a transverse component. In the upper plot of Fig. 6.40 we see the signal at the shortest period of 0.022 s. Before the maximum used in the dispersion curve compilation, there is a much higher maximum around the time 0.2 which is probably the S-wave arrival. The record is bandpass filtered to clear out the high frequencies.

Analysis Example #5: Kuril Islands

event and record info:

date:	2007 January 13
magnitude:	8.2
event location:	154.80°E 46.18°N (Kuril Islands, Russian Federation)
depth:	12 km
origin time:	04:23:20.2 UTC
source:	natural tectonic earthquake
epicentral distance:	8607.75 km
station:	Panská Ves PVCC (Czech Republic)
station location:	14.5689°E 50.5282°N
seismometer:	STS-2 120 s
samples for FFT:	16384

For this extraordinary event we present an example of analysis of two components – radial and transverse. In Section 6.14 we advise how to invert both R and T component dispersion curves together.

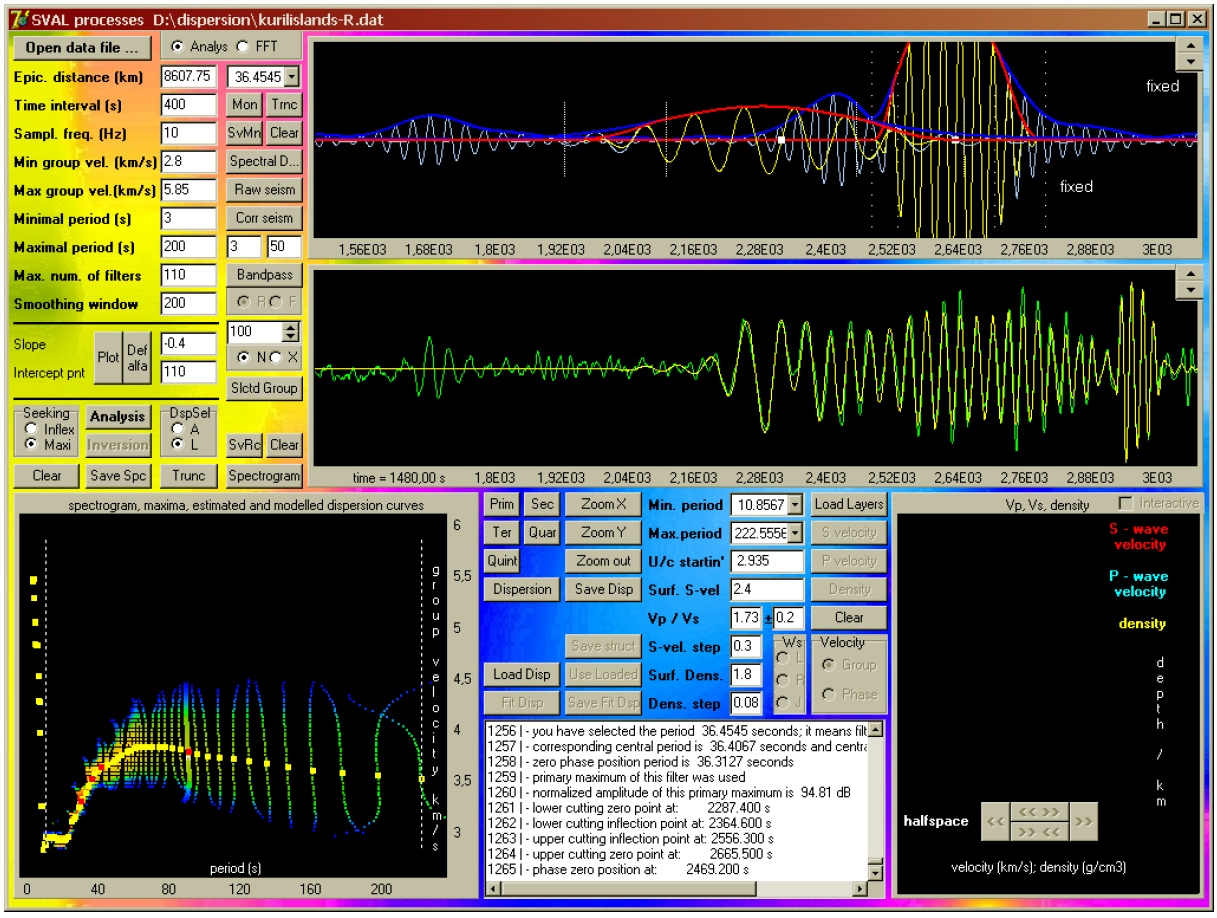


Figure 6.41: Analysis example #5 – Kuril Islands – radial component.

First we insert the advised parameters for analysis. We do not have to apply a bandpass filter because we would like to use all the recorded period range. STS-2 has a flat transfer function up to 120 s, but we may dare to make the analysis up to 200 s. After the raw analysis, we prefer to apply the instrument characteristic. After that we may try to improve the fundamental mode ridge selection in the short period range between 10 and 20 s. The automatic procedure has selected a different ridges here and by mouse-clicking we can select the proper one. Or those points, we think they are the proper ones. For the manual selection, it is better to zoom into the appropriate section of the period-group velocity plot. After the picking, we have to run the analysis again to create the fundamental mode using this new dispersion ridge selection. Remember to run the analysis using the `Filter corr` button from the frequency domain window! We may also try to change the α coefficient parameters – we will probably be able to get the right fundamental dispersion without the manual points picking. Save the estimated dispersion by `Save Disp` button. Check that the instrumentally independent dispersion was really saved.

In case of this record, there is a striking dissimilarity between fundamental wavegroups created by natural `N` or fixed `X` truncating. Try both options. Due to a great epicentral distance and partly oceanic

path, long wavetrains are present at each period. It is not enough to truncate them for five wavelengths only. The natural truncating seems to be much better option here.

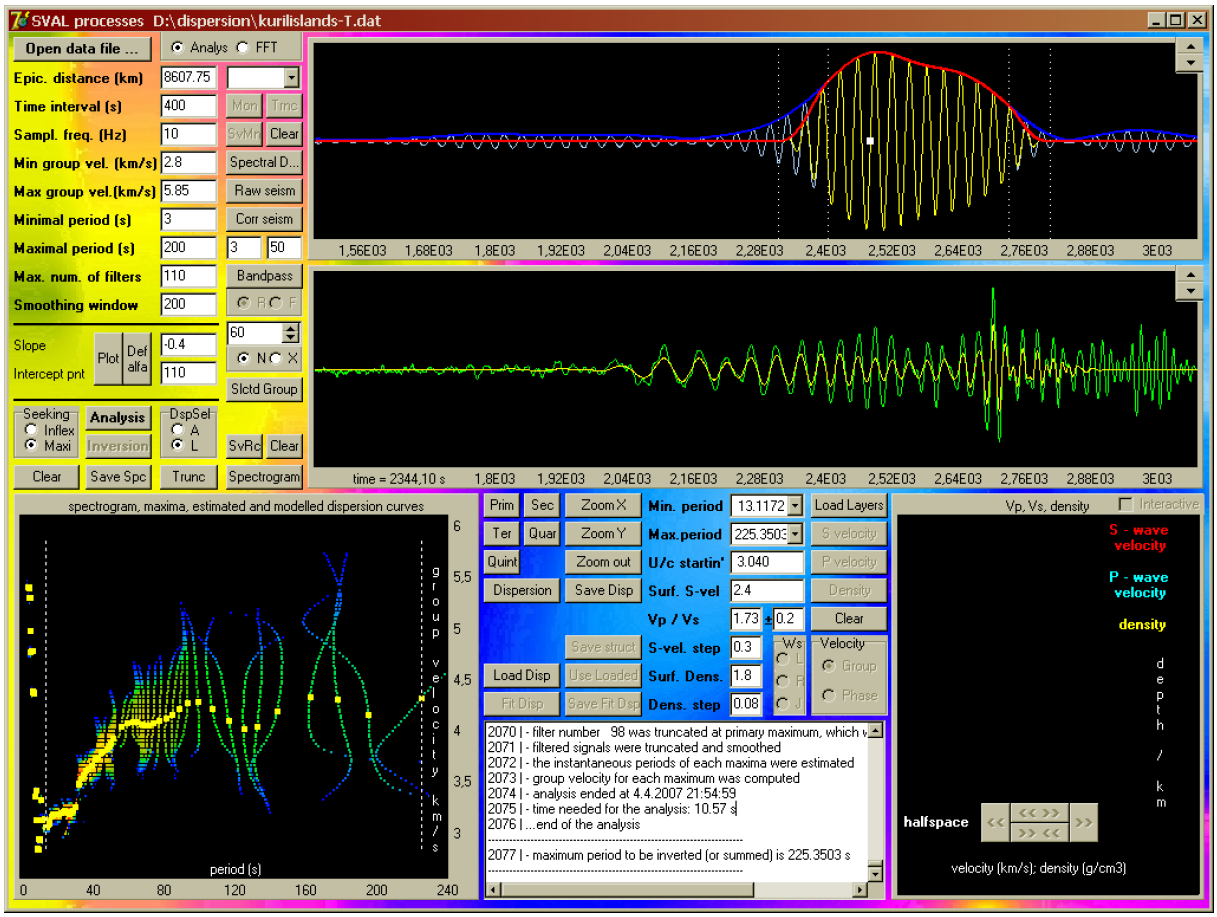


Figure 6.42: Analysis example #5 – Kuril Islands – transverse component.

Nearly the same filtering parameters we use also for analyzing the transverse component of the same event at the same station. Manual mouse-clicking is again applied for shorter period part of the dispersion. Again, we pick the dispersion points after we create the instrumentally corrected dispersion using the `Filter corr` button. And again we have to press this button one time more to apply the manual selection for the fundamental mode estimation. We see that the Love wave dispersion presents much more complicated features then the Rayleigh one.

As in the case of R component, please, save the estimated Love wave dispersion for instrumentally independent analysis.

All these five examples are made of analysis of real records of real events. I hope that the reader may be able to reach better results by analyzing these records than I did. My intention was not to make a perfect analysis, but to propose the examples.

6.13 Working with the SVAL program – inversion

Let us introduce how the inversion of dispersion curves may be provided. First of all we have to set layer thicknesses. It is done using the layers file with the number of layers in the first line and with thicknesses of layers in all other lines, see Section 6.4. Below the last layer an infinite halfspace is supposed to continue. After the file is loaded, SVAL automatically draws the layers distribution and also gives the text output with number of layers recognized. In Fig. 6.43 we present screenshots of five input files with appropriate graphical depiction in the depth-velocity plot. The graphical depiction of the halfspace boundary is set to be in the same position with respect to the plot for any layer distributions. Four of these five layer distributions are used in the examples of inversion in Section 6.14.



Figure 6.43: Five examples of layer distributions with corresponding input files.

The layer number, distribution and thicknesses are set manually and by this setting we may involve the inversion. Generally we may start with constant layers thicknesses. In case of using long periods or broad period range, we use larger thicknesses for greater depths since the resolution of inversion decreases with depth as well. Characteristic feature of the dispersion curve are broader intervals between dispersion points for longer periods – another reason for setting the deeper layers to be thicker. In case of monotonously shaped dispersion curve we may use also monotonously increasing layer thicknesses. In case of strong Airy phase in some period range, we may try to find out in which depth is the velocity contrast producing this Airy phase. In that case we set the number of layers to be higher an their thicknesses to be smaller around the assumed depth of velocity contrast. In case of the crust we may assume the easy relation that the period of the wave in seconds approximately corresponds to the depth of its propagation in kilometers. Details concerning the setting of the layer distribution may be found in Chapters 4 and 5. We present several examples in Section 6.14.

Next step is to set the starting model for inversion. The SVAL program gives two possibilities – automatic and manual. The starting model is not a crucial feature for this kind of inversion problem computation, however, by setting an appropriate starting model we may save o lot of computational resources.

For the automatic starting model generation we have to set the surface shear wave velocity `Surf. S-vel.` and its step between two neighboring layers `S-vel. step`. The model is created using the given constant step for all layer boundaries. Hence, the starting velocity in the halfspace is influenced both by the surface velocity and by the number of layers. In case of constant layers thicknesses, the starting model seems to present linearly growing velocity with depth, in case of increasing layer thicknesses it creates a model with decreasing gradient and in case of varying layer thicknesses we see a more complicated behavior of the starting model.

These three possibilities are shown in Fig. 6.44. In this figure, there are 15 layers with different thicknesses set so that the halfspace boundary is in the same depth for all three examples. In each

panel three starting models are set for the same density setting as `Surf. dens.` = 1.8 g/cm^3 and `Dens. step` = 0.04 g/cm^3 and with three different velocity settings given by `Surf. S-vel.` = 2.4 km/s and `S-vel. step` = 0.10, 0.15 and 0.20 km/s respectively. Hence, as the number of layers is the same for all three plots, the velocity in the halfspace is also the same for all of them. The $v_p/v_s = 1.73$ is the same for all three examples and all three possibilities in each plot.

We also have an option to fix the velocity in the first layer. When we check the `fix` checkbox, the inversion will not change the set velocity for the first layer and hence the range of possible velocities in the second layer will be always the same during the computation. This is useful when we do have some a-priori information about the surface shear or longitudinal velocities or in cases when the resulting model presents too scattered velocities. By fixing the surface layer, we may get more smooth velocity distribution since the uppermost layers influence all the wavelengths of surface waves. For example, too high estimate of the surface velocity will be "improved" by unrealistic lowering of the velocity in next layers, what will be again "corrected" by other unrealistic increase of velocities and hence we get an undesirably oscillating model.

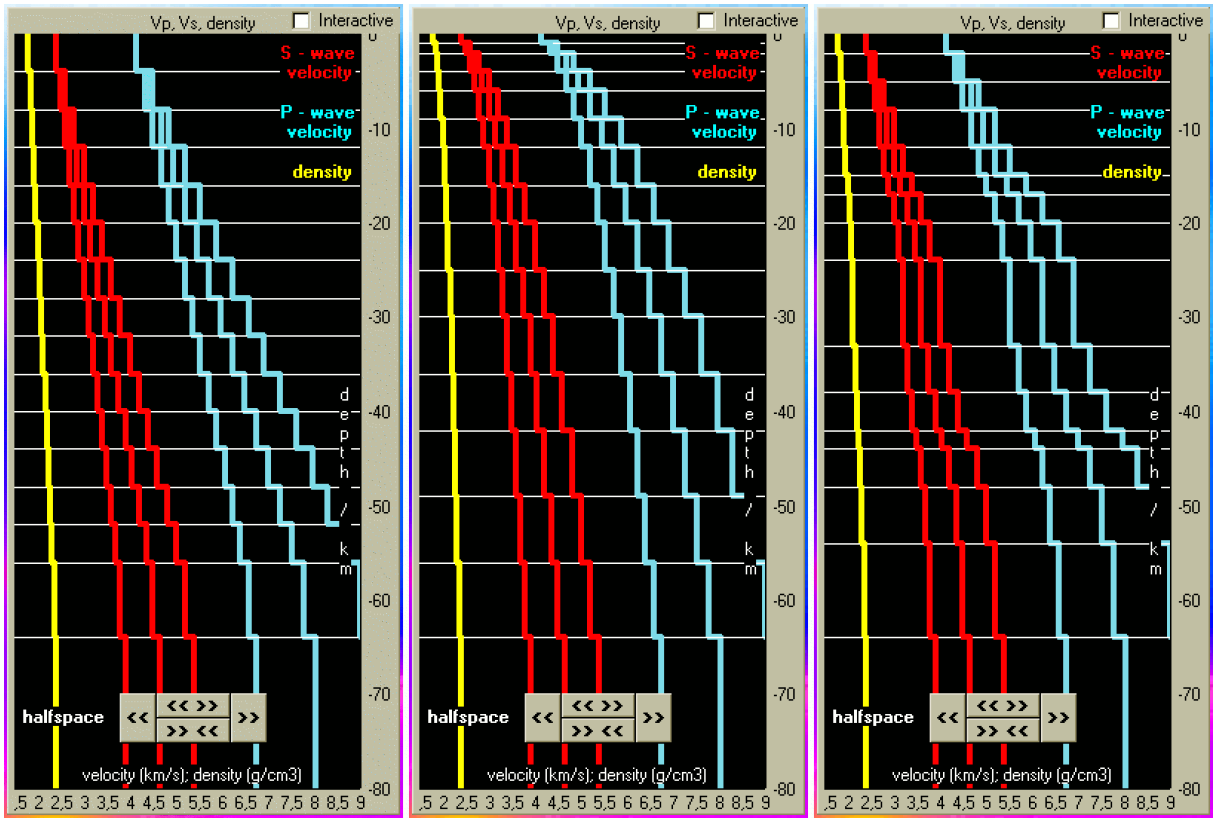


Figure 6.44: Examples of constant, increasing and mixed layer thickness distribution set for 15 layers with the same depth of halfspace boundary.

For the starting model we have to set also surface density and its step. Intuitively, it has the same meaning as in the case of the starting S-wave velocity. The difference is that the density is not measured and this setting is used not only as a starting model for inversion, but also as an artificially "measured" data. Hence, the starting density setting serves in the same manner as the measured dispersion curve. We create additional data – we have velocities of different periods and we have densities in different depths. For further discussion of this setting, see Section 2.3.

Because the density influences the velocities of surface waves only slightly, we have an option to set the density and keep it unchanged during the inversion. It is done using the `ConDen` checkbox. By default it is checked and thus the density is not inverted. Much lower number of parameters is looked for and we still do not constrain the task so much since the density values are not critical for the dispersion curves. Usually, we try to uncheck the `ConDen` box to provide the inversion including the density at first, and in case we get unrealistic density values or peculiar density changes with the depth, we may constrain the problem by keeping the density values constant in each layer.

Both density and velocity starting models are depicted using the `Starting disp` button in the inversion window. After we change any of the parameters creating the starting model, it is required to press the `Inversion` button in the SVAL main window first to let the new parameters to be read by to program and to open the inversion window. After that it is possible to draw the dispersion curve corresponding to the starting model as well as the starting model itself using the `Starting disp` button.

In case of Rayleigh wave inversion, we have an extra bonus – to set the velocity of P-waves. It is done using the v_p/v_s ratio. SVAL uses a constant value of this ratio for all layers in the starting model.

The inversion procedure is set to look not for the absolute values of S-wave velocities and densities in the layers, but to find the differences between two neighboring layers. This feature was implemented to lower the scattering of velocities due to the independent values in each layer. The value of velocity and density in next layer is influenced by the velocity and density in the upper layer. By this we may control the constraints of the inversion.

In the most complicated case – during the Rayleigh wave dispersion inversion – SVAL looks for three different quantities: for the density differences, for the S-wave velocity differences and for the v_p/v_s ratio in each layer.

The other important function of the velocity and density steps which are set for the starting model is that these quantities influence the range of possible values found by inversion. The step of S-wave velocity and density enables the inversion to look for the velocity and density in the next layers in such a manner that the difference of the values may be one time the step lower or six times the step higher than the velocity or density in the upper layer. So, if we set the `Surf. S-vel` to be 2.5 km/s and if we set the `S-vel. step` to be 0.2 km/s, in the first iteration, the velocity in the second layer from the top is found in the interval between 2.3 – 3.7 km/s. In the next iteration, as the velocity in each layer changes, the absolute value of the velocity range constrained for the next layer also changes, but the width of the interval remains the same. The asymmetric constraint reflects the fact, the the velocity is rather expected to increase with depth. The density behavior is the same.

As an additional feature, we may disabled the `lvz` checkbox. By default, this checkbox is selected and it means the inversion will work exactly as described in the previous paragraph. We allow the procedure to look for low velocity zones by keeping the possibility that the velocity in the next layer may be smaller than the velocity in the layer above. By disabling the `lvz` checkbox, we set the possible velocity in the next layer to be only higher than the velocity in the previous layer and so no low velocity zone can be found. This option is useful when complicated velocity distributions are obtained and we need stronger constrains for the inversion problem.

One of the way how to set this starting model "step" is to try to fit the measured dispersion by the `Starting Disp` button. In other words, we may try to help the inversion by setting the starting model to be as near to the measured one as possible. The disadvantage of this attitude may be that by setting too small "step" we may constrain the inversion so strongly that it would not be able to find any reasonable model. On the other hand, if we let the "steps" to be large enough, it means that the inversion has a broad range of values to use for the model estimation. But even by large "step" setting we may not be able to fit the measured dispersion accurately because the inversion problem would be too little constrained. One have to try to deal with the trade off between strong constrains (good starting model but little chance for improvement) and low constraints (unrealistic starting model but free inversion).

The interval $\pm$ in the v_p/v_s ratio setting has the same meaning as the `S-vel. step` and the `Dens. step`. It has no influence on the starting model, but it allows the inversion to look for the v_p/v_s ratio in the set interval. The only difference is that the interval for v_p/v_s ratio variation is symmetric – so by setting the ratio in the form 1.74 ± 0.08 the inversion will estimate the P-wave velocity in the range given by the S-wave velocity multiplied by the number in the interval 1.66 – 1.82.

The other option of creating the starting model is using the manual setting. But this graphical interface may be used not only for a starting model creation. There are at least three possibilities of its use:

- starting model
- modification of the inversion results
- forward modeling tool

The interface is activated by the `Interactive` check box. It is possible to activate it only when some model is already drawn in the depth-velocity plot. Thus, to work with the manually set model, we have to create whatever default automatic starting model first to obtain something to draw in the plot. Then we may click the `Interactive` check box and the drawn model is separated into single layer values, see Fig. 6.45. After that we may click using the mouse into any place of the plot to set the new velocity for the clicked layer. This is done for S-wave velocity only. The P-wave velocity is again controlled by the edit box `Vp/Vs` $\pm$. The density is also set only by the default automatic linear-step method. After pressing the `Starting Disp` button we get the dispersion curve corresponding to the set velocity model. If Rayleigh wave option is checked, we get also the appropriate P-wave velocity model. It is important to fill some reasonable value in the `S-vel. step` edit box also in the case of using the manual setting of the starting model because this value controls the range of possible values found by inversion as mentioned above.

Another option is to use the manual model for modification of the given inversion result. This is presented in the Example #3, see Section 6.14. We obtain an inverted dispersion curve with appropriate velocity model using the default linear-step starting model but we are not satisfied with the result. We try to change the velocity model in order to improve the dispersion curve misfit. We may try to modify the model again and again until we are satisfied with the dispersion.

In fact, we would probably not succeed with the new manually estimated model – the inversion finds the model with the lowest misfit and our trials would probably not make the misfit better. But there is a possibility how to lower the misfit manually – when we make the model in a manner when the velocities in the neighboring layers are out of the constrains given by the "steps". But such a model would probably be a bit "wild".

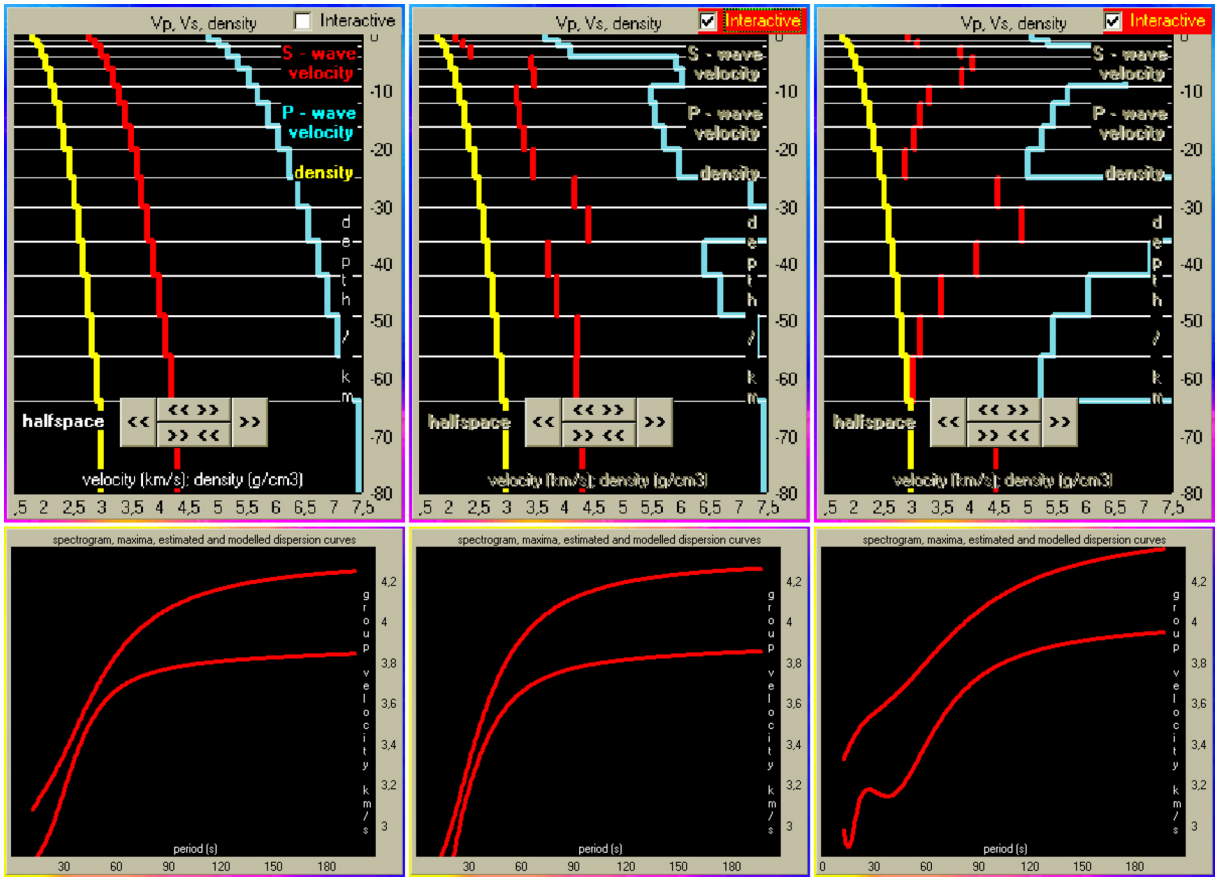


Figure 6.45: Examples of forward modeling; velocity models (top) and corresponding group velocity dispersion curves (bottom). We begin with linear-step starting model (left), we make light changes (middle) and we make a radical distortion of the model (right).

The last possibility is to use the manual model for direct forward modeling. This is the case of examples #4 and #5. We tried to invert the curves with little success and so we decided to try to estimate the model by trial and error method. One may improve his skills of such work while dealing with many records and dispersion curves. For the beginner it is not an easy problem to guess a velocity model. We advise to begin with linear-step starting model to get an approximate idea of the velocities by changing the step between layers and the surface velocity. As we obtain some dispersion which will at least intersect the measured one somewhere, we may start to modify the model manually. It is always useful to try to do this in case of new dispersion measurement especially if we are not familiar with given period and depth ranges. By simple playing with the model we may learn a lot about the dispersion behavior and especially we will see which of the layers influence which of the periods of dispersion.

The inversion is started by the `Inverse` button. When clicking the `Stop` button, we may cancel the procedure. The button action is checked every twenty iteration, so as we press the `Stop` button anytime, the inversion will be canceled after 20, 40, 60 and so on... iterations.

As the `Interactive` mode may be used for modification of the inversion result, we may take advantage of it even without any modification. There is an easy way how to stop and again start the inversion procedure from the stop point. We stop it using the `Stop` button. After confirming the canceling we switch into the interactive mode using the `Interactive` checkbox. This implies that what we see in the depth-velocity plot will serve as an starting model for the inversion. We may make some changes in this model and we can start the inversion again. However, we may also let the resultant model to be

as it is and start the inversion exactly from the point where it was canceled. This enables us to make the inversion in steps of 20 iterations. After each start we simply press the `Stop` button, we check what happens and we again start the next 20 iterations.

If we do have a suspicion that the conditions terminating the inversion works insufficiently and the inversion procedure is aborted too soon, we may select the option `Unlimited iteration` in the inversion window. By this we disable all conditions for the inversion procedure termination and the inversion will run forever. The only possibility how to stop it is to press the `Stop` button. Our experience says that in most cases, the conditions work well and no significant improvement of the misfit is reached by running more iterations.

6.14 Examples of inversion

In this section we will discuss five examples of inversion. We will use the results of examples of analysis from Section 6.12. For some records we will directly proceed with the computation of the analyzed dispersion curves, in some cases we will use the loaded dispersion curve saved in the file after the analysis in the previous examples. For the inversion, we will also need files with layer distribution setting. See the examples of layer files in Section 6.6 or, preferably, get the layer files provided on the attached CD ROM.

These examples do not deal with the options for fixed density, fixed first layer's velocity, disabled/enabled low velocity zone and unlimited iteration. These option were not developed in the SVAL program when the examples were prepared and we keep the examples as they were since their simplicity is more educative than if we use these four new features.

Inversion Example #1: South Iran

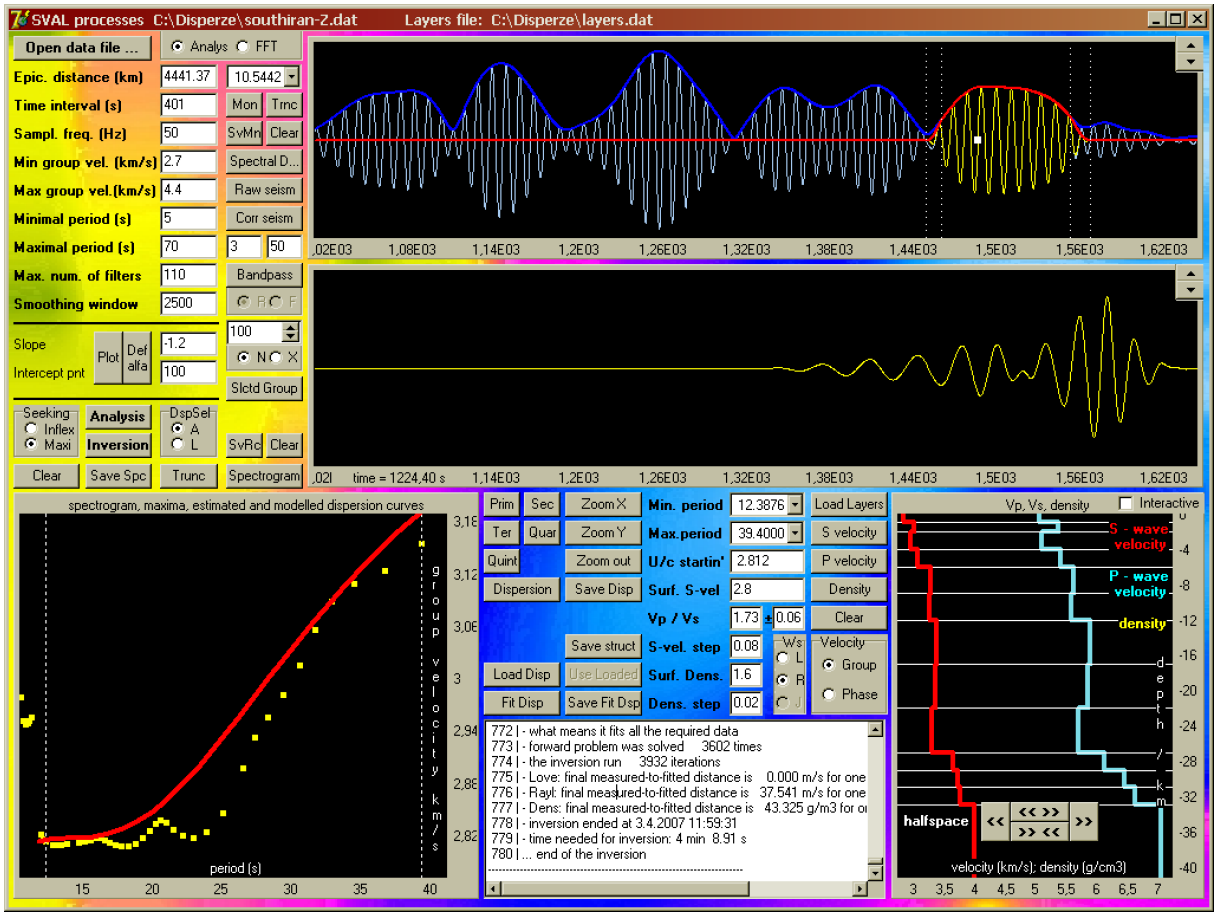


Figure 6.46: Inversion example #1 – South Iran.

This inversion example is based on the analysis made in Section 6.12 and presented in Fig. 6.37. As we analyzed the vertical component and hence we get the Rayleigh wave dispersion, we propose the inversion for both P and S waves velocity in given layers. We add the inversion settings according to Fig. 6.46 and we switch into the inversion window using the `Inversion` button. We may draw the starting dispersion or we may directly start the inversion. The results may be a little different from those presented in Fig. 6.46 because of a nonuniqueness of the inversion process. In addition, we show a 10 s quasimonochromatic signal with truncated wavegroup to see the complexity of the record around this period range as we have discussed it in the Analysis Example #1 in Section 6.12.

Inversion Example #2: Aegean Sea

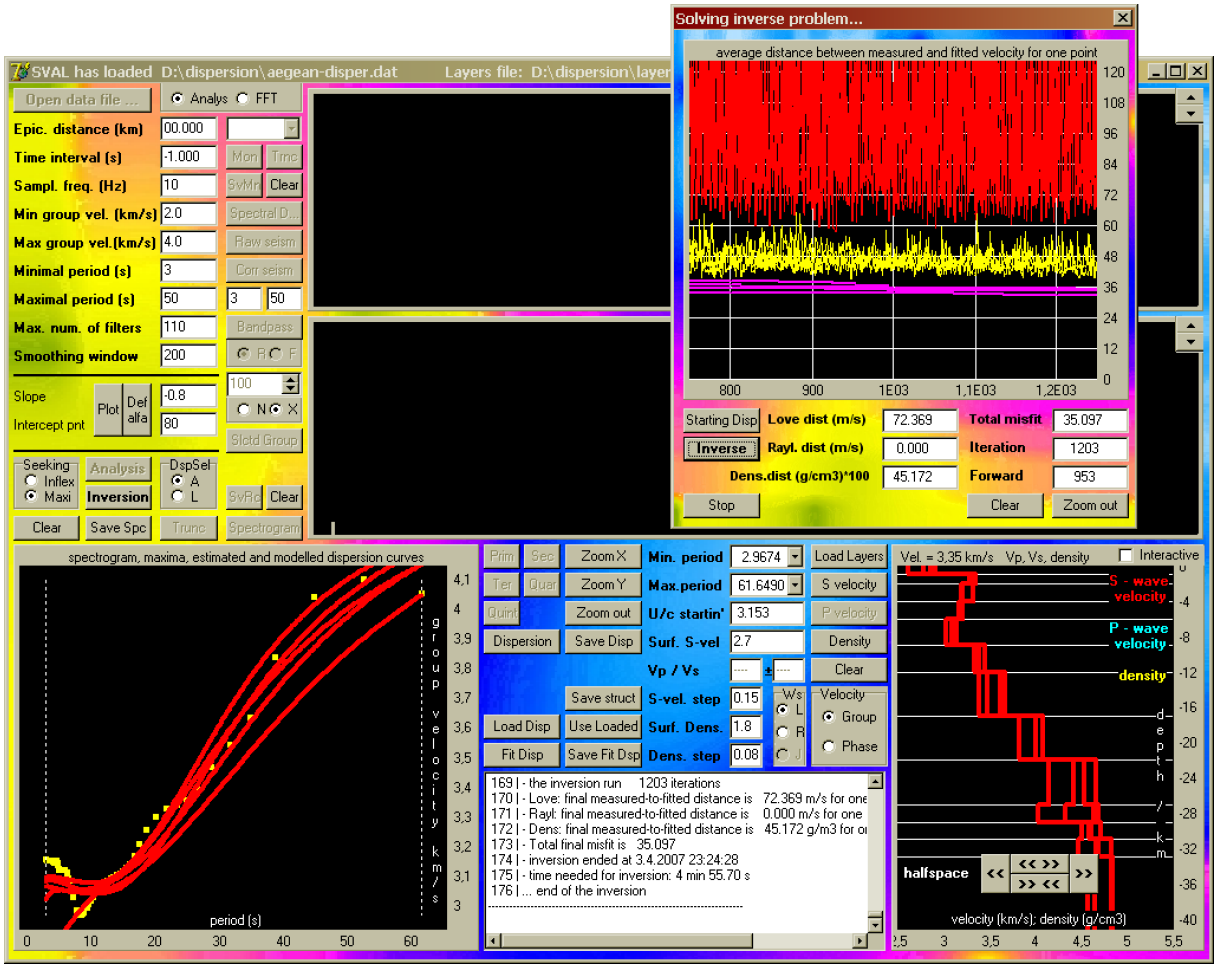


Figure 6.47: Inversion example #2 – Aegean Sea.

For this example we use the saved dispersion curve estimated using the instrumentally corrected record as we processed it in the Analysis Example # 2 in Section 6.12. It is a Love wave dispersion obtained by analysis of transverse component of the record. As we start the SVAL program, we may select the `no record` option, because we will need no memory to be allocated for records and spectra. We have to delete the unwanted columns from the file *.dat saved by `Save disp` button – we keep only the columns with headers `InstPeriod` and `CorrGroupVeloc`. However, these headers must be deleted too. We simply load the dispersion using the `Load disp` button. SVAL will recognize it as a `ONE` dispersion file, what we accept as a correct assumption. The loaded dispersion will appear in the period-group velocity plot. Then we press the `Use Loaded` button, since we decided to process this dispersion. We also load the layer file. After that we may select the period range and other parameters of inversion as shown in Fig. 6.47. After switching into the inversion window using the `Inversion` button, it is advised to draw also the starting dispersion. One may try to change the parameters settings for this default starting model to create another starting dispersion curves.

In the example, we show results of four inversions. We process them for the same starting model. The differences are due to strong nonlinearity of the inversion problem. The minimum of the misfit function is so poorly constrained that we may always expect a scatter of the results. Another reason is also the random generation of some model parameters during the inversion problem computation. The greater scatter occur just above the Moho boundary, which is not clearly visible in our models. On the contrary, the upper layers show similar velocities for all four models. The same situation is seen also in the period-group velocity plot – the fitted dispersion are of the same values around the short periods and differ towards the longer period part.

Inversion Example #3: Horní Rozmyšl

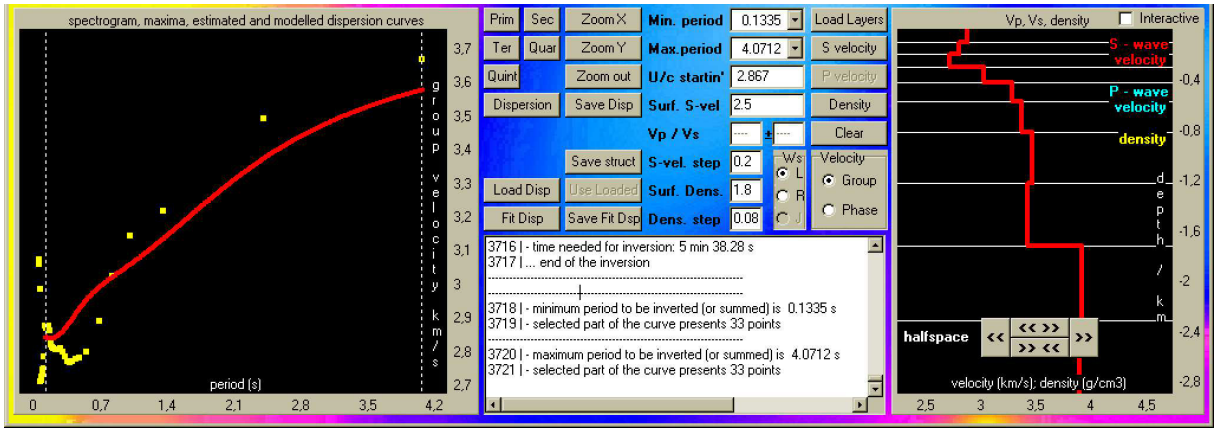


Figure 6.48: Inversion example #3 – Horní Rozmyšl.

We follow the analysis presented in Fig. 6.39. We load a layer file and set the parameters for inversion as shown in Fig. 6.48. However, the inverted dispersion does not fit the measured one accurately. We propose a result modification/forward modeling to improve this result. We use the structure result of inversion and modify it by using the `Interactive` option. If we set the model velocities to resemble those presented graphically in Fig. 6.49 and numerically in the attached file screenshot, we are able to fit the measured dispersion better then the inversion procedure did. The reason is that the inversion was too constrained to reach the desired model. Since the velocity of the mouse cursor position is displayed while moving with the mouse across the depth-velocity plot, it is easy to set the model exactly according to the file screenshot in Fig. 6.49. After the model setting, we press the `Inversion` button in the SVAL main window to switch into the inversion window or we may directly press the `Starting disp` button to compute and draw the dispersion corresponding to the manually set model. We should obtain the result as shown in the period-group velocity plot in Fig. 6.49.

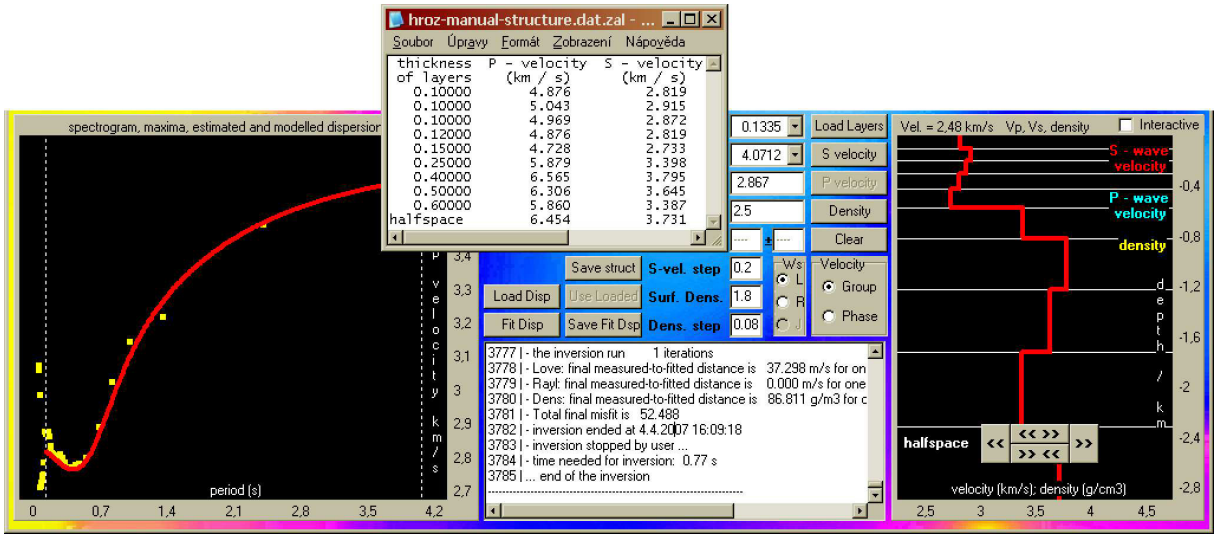


Figure 6.49: Manually set structure by trial and error method for Inversion Example #3. Resultant dispersion fit the measured one well.

Inversion Example #4: Shallow seismic measurement

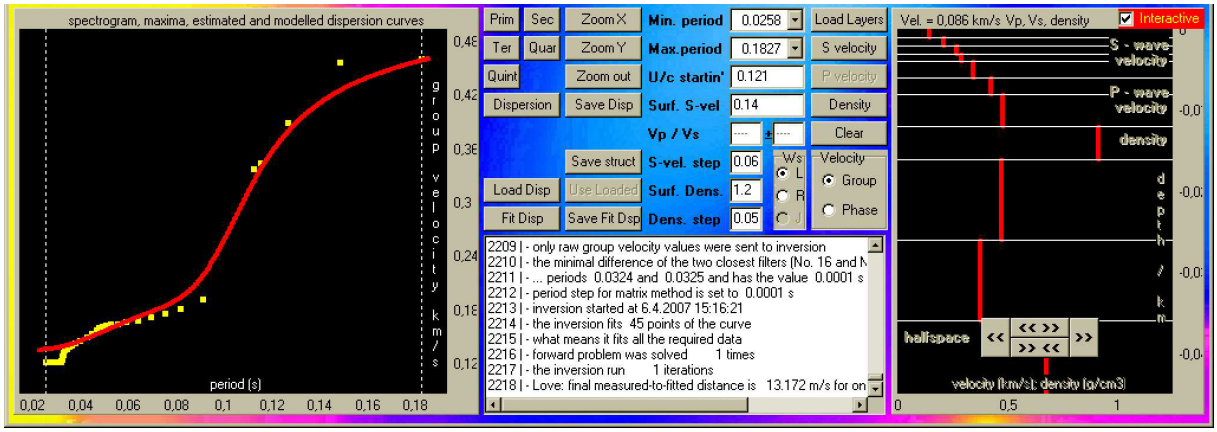


Figure 6.50: Analysis example #4 – Shallow seismic measurement at Karlštejn.

karlstejn-struc.zal - Poznámkový blok

Soubor Úpravy Formát Zobrazení Nápověda

thickness of layers	P - velocity (km / s)	S - velocity (km / s)	density (g / cm3)	Vp/Vs ratio (constant)
0.00100	0.251	0.145	1.200	1.730
0.00100	0.362	0.209	1.250	1.730
0.00100	0.464	0.268	1.300	1.730
0.00100	0.501	0.290	1.350	1.730
0.00200	0.594	0.343	1.400	1.730
0.00200	0.733	0.424	1.450	1.730
0.00400	0.826	0.477	1.500	1.730
0.00400	1.578	0.912	1.550	1.730
0.01000	0.817	0.472	1.600	1.730
0.01000	0.650	0.376	1.650	1.730
halfspace	1.169	0.676	1.700	1.730

Figure 6.51: Structure estimated for example #4.

We may try to make an automatic inversion using the parameter settings as shown in Fig. 6.50. However, also in case of this event, we propose the S-wave velocities set by trial and error in Fig. 6.51. As we enter these velocities using the mouse-clicking method we will obtain presented dispersion curve using the `Starting disp` button. We may also try to improve this fit by repeated starting of the inversion procedure. Surface wave measurement in the shallow seismic methods is not usual, but some references may be found. It is worth of further studying because dispersion estimation may add a new constraints for shallow structure estimation. These methods are mainly used in engineering and by development and constructing companies.

Inversion Example #5: Kuril Islands

For this example we have to prepare the input dispersion file with two curves saved during the analysis according to Fig. 6.41 and Fig. 6.42. We simply copy the appropriate columns into a new file. Use the `InstPeriod` and `CorrGroupVeloc` columns from the Love wave dispersion file and then the same two columns from the Rayleigh wave dispersion file. Since both curves starts at different periods, it is worth to erase the shorter periods from the Rayleigh wave dispersion. We also have to delete the header line from the new file. After that we may load this file using the `Load disp` button. SVAL asks if it understands it well that we want to load two dispersion curves. We will confirm it. By default the `J` option for joint inversion of both curves is automatically checked. However, we may check other options.

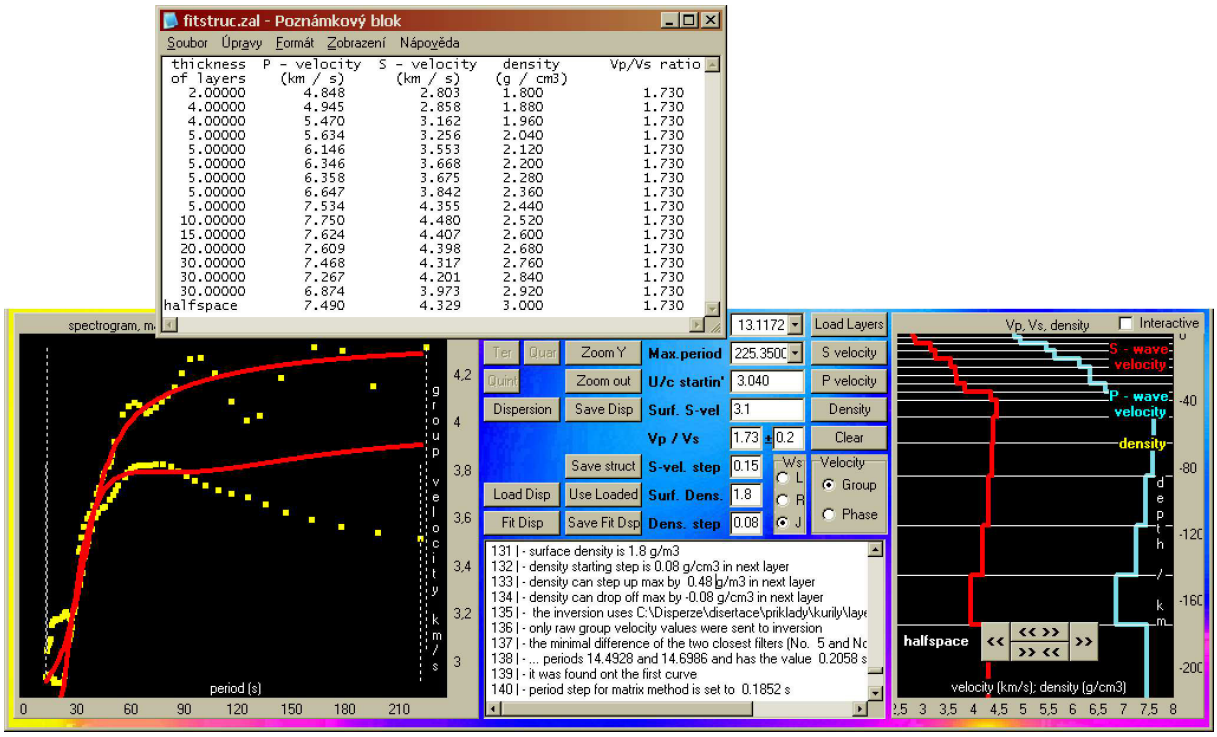


Figure 6.52: Manually set structure by trial and error method for Inversion Example #5. Resultant dispersion cannot fit both the measured ones due to the complex character of the structure.

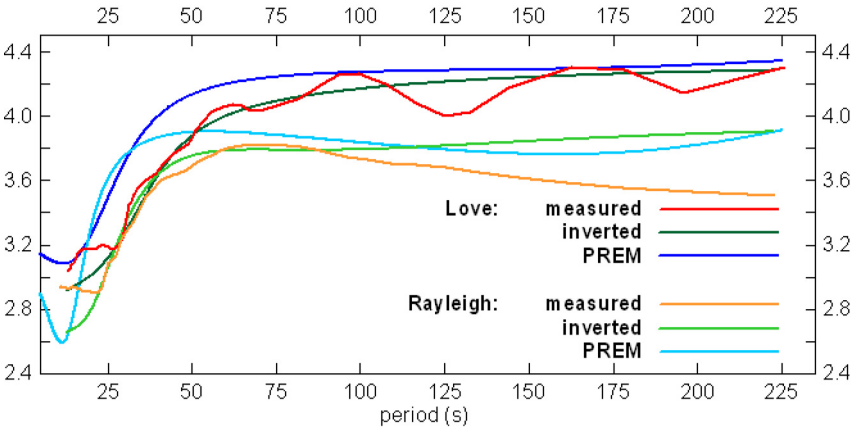


Figure 6.53: Comparison of measured, inverted and theoretical dispersions.

But let us assume we will use the J one. We may try to select different period ranges and different settings for the inversion task. What we prefer, is to manually set the starting model as shown in Fig. 6.52. Use the velocity values displayed in the depth-velocity plot for easier mouse-clicking. What we present is not a true inversion. We make the model by trial and error. The reader may try to do the same. We may also use this manually set model as a starting one and try to let the inversion find some better model. The problem is that we cannot fit these two dispersion curves in the whole period range by arbitrarily complicated model in case of an isotropic velocity distribution. And that is exactly what SVAL does. The SVAL program is not able, at this moment, to introduce anisotropy. And anisotropy is needed to explain such a complex behavior of Love and Rayleigh waves above 100 s period. This Love-Rayleigh discrepancy is described in the literature and anisotropy of some parts of an upper mantle may explain it. Again – as the reader may complain, what kind of curious example we present – it is just an example where are the possibilities and limits of the SVAL program use. Look at Fig. 6.53 to compare our results with the PREM.

Chapter 7

The PhaseCorr program

7.1 About the program

Unlike SVAL, the PhaseCorr program is a small program with only one purpose – to estimate the phase velocity dispersion curve between two seismic stations. The PhaseCorr program is an extension of the SVAL program. It uses the file outputs of SVAL and without the analysis of the records by the SVAL program, one would not be able to estimate the phase velocities by the PhaseCorr program itself.

The reason, why the functions of the PhaseCorr program are not included directly in the SVAL program is, that in the SVAL program, only one record is analyzed at one moment. In contrast to that, PhaseCorr needs two records from two different stations in the same time to read and to compare. It seemed to us easier to prepare independent program instead of adding next procedures into SVAL.

Estimating the phase velocities, we may use both programs simultaneously. Sometimes it is required, after estimating the phase velocities by the PhaseCorr, to prepare new versions of input files for PhaseCorr by the SVAL program. We may save new files by SVAL and open them by PhaseCorr to see what happens if the width of filters is changed in the frequency domain or if more filters are included, if an instrument transfer function is used and so on.

In the following paragraphs, we introduce the features of the PhaseCorr program. All phase velocity dispersion curves in Chapter 5 were estimated by this program. Besides that, many other profiles of two and more stations were analyzed by PhaseCorr for other projects and measurements. Some of these examples follows.

7.2 How it looks

The PhaseCorr program has only one window, see Fig. 7.1. Almost all what is needed for successful phase velocity computation is contained in the two *.all files produced by the SVAL program. This is the reason, why PhaseCorr has almost no analyzing tools and only a few parameters to be controlled. The PhaseCorr program just takes these two files and correlate corresponding quasimonochromatic signals to obtain the time shift between them. The only information needed for the phase velocity estimation is the distance of the two stations. We use not the actual distance between the two stations in a geographical sense, instead of it we simply compute the difference of the two epicentral distances from the source to the respective stations. The meaning of such an approach is that we would like to measure the phase velocity of the plane wave propagating from the source across the first station and then to the second station. In other words, we create a projection of the first station location perpendicularly to the ray path of the wave propagating to the second station.

All buttons and edit boxes in the PhaseCorr program window are designed in such an order that the easiest way how to process the data using the program is to simply use all the buttons and boxes on the left hand side of the window from the top to the bottom.

7.3 File inputs

For the phase velocity estimation, two independent files have to be read. These are the files produced by the SVAL program. Both files have to contain the same number of harmonic components for the same

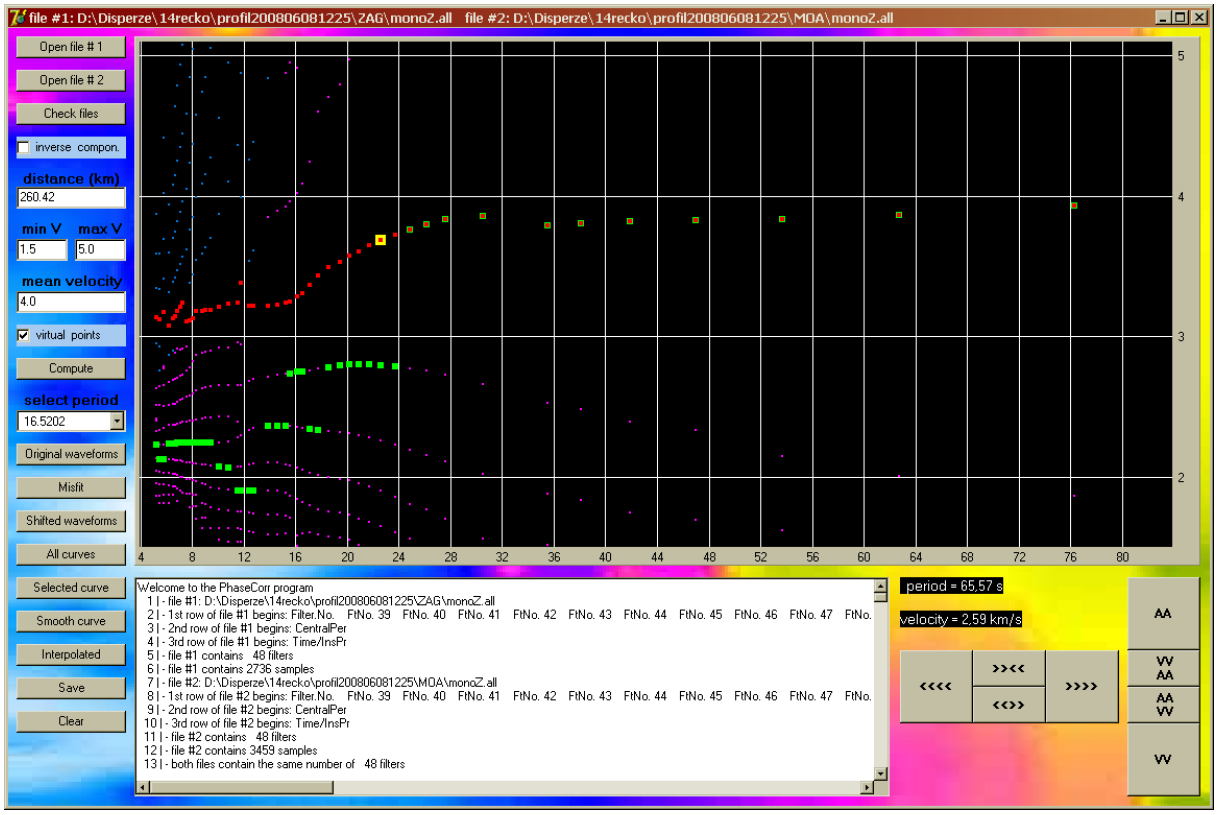


Figure 7.1: The PhaseCorr program window includes all setting edit boxes and all controlling buttons.

central periods. Hence it is useful to prepare the files by the SVAL program with respect to each other to ensure the consistency. It is sometimes necessary to modify the already saved file to get the same number of filters according to the other record analysis. For example – if we saved too many filters for one record and we are not able to find useful information for this number of filters in the other record, we would probably save less number of filters for the second record and than return to the first one to save the same number of filters also for this first record. Of course, it is also possible to save both files with the greater number of filters even in case we know that some of the filters are not reliable and useless in the second record – we will delete corresponding phase velocity dispersion points at the end of the analysis.

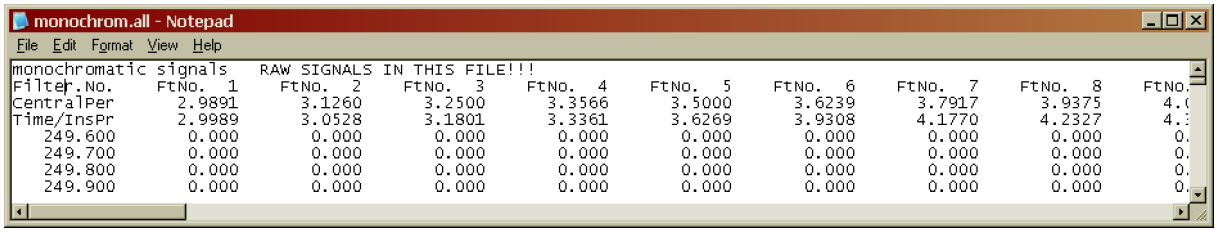


Reads the data file with truncated harmonic components of the record closer to the source. The file name is displayed both in the PhaseCorr window upper bar and in the text output box. The header of the file is also written in the text output box as well as the number of samples and filters in the file.

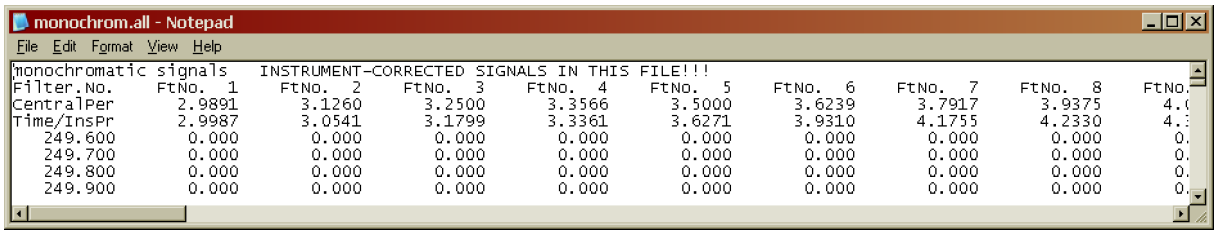


The same as the previous button but this one reads the file corresponding to the station more distant from the source.

As an input files, the files produced by the SVAL program when pressing the `SvMn` button are used. As described in Section 6.6, it is possible to save the quasimonochromatic components of each record in a file with following format:



Header for raw multi-channel file.


monochrom.all - Notepad

File Edit Format View Help

```
monochromatic signals   INSTRUMENT-CORRECTED SIGNALS IN THIS FILE!!!
Filter.No.    FtNo.  1    FtNo.  2    FtNo.  3    FtNo.  4    FtNo.  5    FtNo.  6    FtNo.  7    FtNo.  8    FtNo.
CentralPer      2.9891      3.1260      3.2500      3.3566      3.5000      3.6239      3.7917      3.9375      4.
Time/InsPr      2.9987      3.0541      3.1799      3.3361      3.6271      3.9310      4.1755      4.2330      4.
   249.600        0.000       0.000       0.000       0.000       0.000       0.000       0.000       0.000       0.
   249.700        0.000       0.000       0.000       0.000       0.000       0.000       0.000       0.000       0.
   249.800        0.000       0.000       0.000       0.000       0.000       0.000       0.000       0.000       0.
   249.900        0.000       0.000       0.000       0.000       0.000       0.000       0.000       0.000       0.
```

Header for corrected multi-channel file.

Three different files (*.all, *.dat and *.phs) are saved by the SVAL program at one moment, but only the file with the extension *.all may be used as an input for the PhaseCorr program. The first example shows the data saved for raw record and the latter for the instrument-corrected record. Both these examples were used also in Section 6.6 and both of them may be used as an input for the PhaseCorr program. The raw/corrected file contens has nothing to do with the *.all/*.dat/*.phs file format – all of these three files may have two raw/corrected options. The files contains the truncated quasimonochromatic signals with only the desired (fundamental mode) surface wavegroups. By the two buttons `Open file # 1` and `Open file # 2` two files for two records have to be opened before any computation is provided by the PhaseCorr program. From the input files, following items are read by the PhaseCorr program:

- the first row with any text is skipped
- second row with filter numbers is read (to compare the consistency of both input files)
- beginning of the third row (to check the file format)
- beginning of the fourth row (to check the file format)
- first column with time (s)
- all other columns with amplitudes of truncated nearly monochromatic signals

These *.all files may be generally a bit huge. Since they may contain thousands of rows and about a hundred of columns, it may reach several MB of volume.

7.4 Keyboard inputs

Following buttons start procedures for estimating the phase velocity dispersion curve. There is an option to tell the PhaseCorr program the range of velocities which the phase velocity dispersion curves are to be looked for in. Other edit box is used to set the value where the final dispersion curve compilation has to start. PhaseCorr has also a drop-down list of periods to view selected filter to see what happens for the particular quasimonochromatic truncated wavegroup. Other buttons shift and zoom the view of the plot.



The mutual consistency of both files is checked. The number of filters and the values of the first and last central periods in the two sets of filters are checked and if the two files are suitable for further computation, information is given in the output text box. The numbers of samples in the two files are also computed and the greater value is used for correlation shift index. An average of each pair of instantaneous periods for each filter is computed and prepared for selecting from the drop-down list.

```
13 | - both files contain the same number of   48 filters
14 | - both files start with the same central period
15 | - both files end with the same central period
16 | - the greater number of samples is   3459
17 | - the sampling time interval is   0.100 s
```

When the two files are consistent, such an output is displayed.



Makes an inverse value of all waveforms in the file No. 2. It is useful when looking for phase velocity dispersion using the stations with unknown polarity of horizontal components or to correct a wrong rotation of one of the records.



Edit box for entering the difference of epicentral distances of both stations. For comments on estimating this distance, see Section 7.2.



Correlation of the two harmonic components is provided for the time shift corresponding to the interval given by these two velocities. If we have some a priori information about the phase velocities we may expect, we can set this interval to be narrower to save the computation time. When no idea is present, we keep the interval broader to compute the correlations for longer time window. After preliminary phase velocity estimation we can shrink the interval to force the PhaceCorr program to select an appropriate final dispersion curve, see further paragraphs.



This value tells the PhaseCorr program where to start the compilation of the final dispersion curve. The procedure looks for all found values of local maxima of correlation coefficient at the period at filter near 3/4 of the whole filter range – if we analyze 80 filters, it taked the 60^{th} filter, for example. The procedure selects the value of possible phase velocity nearest to the velocity given in this edit box. Then it starts to compile a smooth dispersion curve by searching among all found possible values for both longer and shorter periods (filters). For each next filter, it selects the value nearest to the previous filter. By changing the value in the edit box, we force the procedure to start the compilation at some other branch of local correlation coefficients, hence, it will compile the dispersion curve shifted by one (or more) period to the lower or higher velocities. This procedure is equivalent to the similar procedure for compilation of the dispersion curve in the SVAL program. There we tell the program if we like to start the compilation form the last filter or from the absolute maximum. The rest of the process is the same.

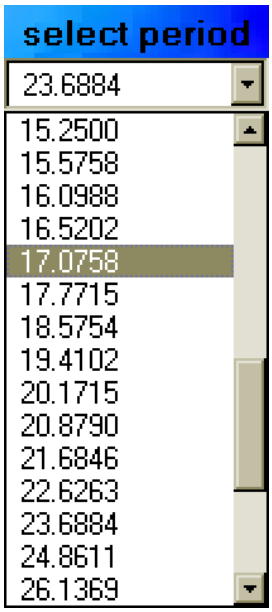


Enables the virtual dispersion points to be computed and used for final dispersion curve compilation. Details are given later.



Provides the main correlation computation. It reads the values in all previous edit boxes and it gives the information about these values in the output text box. It computes the time shift between the two input files using the first column in each file with information about the time of each sample. This time shift is added to the time shift given by the correlation. Then it computes the correlation and it keeps in memory the time shifts of all the local maxima of the correlation. For each of these time shifts the propagation (phase) velocity is computed using the mutual station distance. Then it looks for the velocity value at the period in the 3/4 of the whole range nearest to the value set in the edit box. It compiles the final dispersion curve as smooth as possible searching among all local correlation maxima in each filter. Then it also computes a dispersion curve smoothed by the running average with the window length of three samples. At the end, it produces also the interpolated dispersion curve.

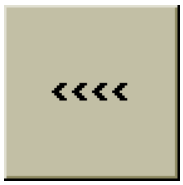
It also checks, where is the final correlation maximum with respect of all other maxima for given filter. If it is at the end of the time shift, it is possible that the true correlation maximum should be even out of the range of the time shift and hence we did not find the proper one since we did not have enough time shift to do so. In this case, the program extrapolates the correlation maxima position in time to obtain a new, presumed virtual correlation maximum. This presumed maximum is not measured, but it denotes the time of the phase shift, which would correspond to the measured correlation, if the two compared wavegroups were longer.



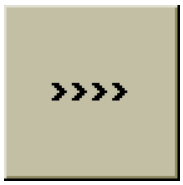
This drop down list of periods enables to select one of them to plot the original or shifted waveforms as well as the correlation coefficient dependence.



Clears the plot.



Shifts the view of the plot to the left by the step of 1/10 of the X axis range.



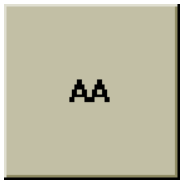
Shifts the view of the plot to the right by the step of 1/10 of the X axis range.



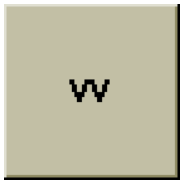
Broadens the view to both sides by the step of 1/10 of the original size and hence shrinks the objects in the plot.



Cut the view from both sides by the step of 1/10 of the original size and hence zooms in the objects in the plot.



Shifts the view of the plot up by the step of 1/10 of the Y axis range.



Shifts the view of the plot down by the step of 1/10 of the Y axis range.



Broadens the view up and down by the step of 1/10 of the original size and hence shrinks the objects in the plot.



Cut the view from top and bottom by the step of 1/10 of the original size and hence zooms in the objects in the plot.

7.5 File outputs

Save

Two files are saved by this button. Only the file name is required, extensions are set by the program itself. The file's #1 PhaseCorr extension is *.dat. Following quantities are saved in this file:

- period (s)
- phase velocity (km/s)
- smoothed phase velocity (km/s)

The *.dat file may look like this:

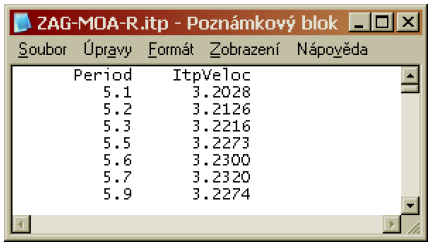


Header for *.dat file with estimated phase velocity dispersion curve.

The file's #2 PhaseCorr extension is *.itp. Following quantities are saved in this file:

- a-priori defined period (s)
- interpolated phase velocity (km/s)

The *.itp file may look like this:



Header for *.itp file with interpolated phase velocity dispersion curve.

7.6 Displayed outputs

Next four buttons draw phase velocity dispersion curves in various ways. They allow to check a distribution of all found correlation maxima, positions of the highest maxima, the starting point for the dispersion curve compilation, a compiled dispersion curve and smoothed and interpolated curves.

All curves

Draws all branches of local maxima of the correlation coefficient with respect to period, in other words, all dispersion curves corresponding to the waveforms shifted by the whole numbers of period forward and backward. Useful to get the idea of what shapes and what range of velocities we may expect. These curves are drawn by the violet color.

It also draws the virtual maxima extrapolated out of the range of the time shift given by the wavegroups, if available. It applies mostly for shorter periods, since the wavegroups of the shorter periods are also shorter and hence it is more probable that the possible correlation maximum is situated out of the measured time. These virtual maxima are shown in blue.

Then it also marks those of the correlation maxima which correspond to the highest correlation coefficient in each filter. This is given by bigger green dots. It helps us to distinguish, which of the dispersion curve may be the proper one. If one of the smooth curves contains much more of these highest coefficient's green dots, it is probably the proper one, especially, when it concerns the longer-period range.

It marks also the point where the compilation of the final dispersion is to be started. It is given by the velocity value set in the `mean velocity` edit box measured at the filter in the 3/4 of the whole filter range. This point is given by a big yellow dot.

It assumes that the period range is reasonable, and hence that in the 3/4 of the period range, the density of the dispersion branches is low enough to enable to select, which one is the proper one. The dispersion branches generally diverge toward longer periods. The procedure takes the velocity set in the `mean velocity` edit box and finds the dispersion branch nearest to this value at the filter nearest to the 3/4 of the filter range. The point in this selected dispersion branch is marked by the big yellow dot.

Selected curve

Draws the compiled final dispersion curve. If a wrong branch is select, we may shrink the velocity range using the two edit boxes `min V` and `max V` to eliminate unwanted branches or we can change the `mean velocity` edit box to start the final dispersion curve compilation at another branch.

Smooth curve

Draws the curve smoothed by a three-sample running average window.

Interpolated

Draws the interpolated dispersion curve. The values of velocities of the final compiled dispersion curve are used to compute the velocities for pre-defined set of periods. The interpolation is linear. It is used for comparing phase velocity dispersion curves from different measurements. Because generally the values of periods in each measurement differ, we can use the interpolated curve to compute an average of more measurements or for further processing where we need to compare the values of velocities for the same values of periods. The step between two neighboring periods for interpolation is geometrical. It starts with the period 0.05 s and each next period is given as 1.025 times the previous. Hence, the density of the dispersion points in the interpolated curve decreases toward longer periods.

Following three buttons are available only when some of the periods from the drop-down list is selected. The plots drawn by these buttons concern only the selected period.

Original waveforms

Plots the selected wavegroups in time as they were read from the input files. Closer station record is orange, more distant station record is violet. It enables us to see the original time shift of both wavegroups and also their similarity/dissimilarity. This may be drawn after one of the periods form the drop-down list is selected.

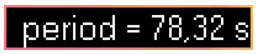
Misfit

Plots the value of the correlation coefficient with the indication of which extreme was selected during the final dispersion curve compilation. The selected extreme is given by red line, all other extremes are marked by yellow lines, see Fig. 7.10. If `virtual points` option is enabled, also the found virtual extremes are marked by blue lines, see Fig. 7.13. We use the misfit function between the two records for plotting. Hence, the minimum of the plot represents the biggest similarity of the two wavegroups. We use both the terms *correlation maximum* or *misfit minimum* through the text. The misfit function may be drawn after one of the periods form the drop-down list is selected.

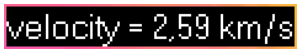


Plots the selected wavegroups after the shifting in time. Closer station record is orange, more distant station record is violet. The closer wavegroup remains at the same position as drawn by the `Original waveforms` button. Only the more distant wavegroup is shifted. It tells us how successful the measurement was. This may be drawn after one of the periods form the drop-down list is selected.

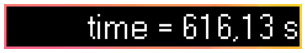
Following markers show the position of the mouse cursor in the plot. According to the quantities drawn by the previous buttons, the label of the position varies.



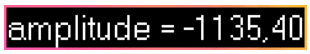
Gives the value of the period of the mouse cursor in the plot.



Gives the value of the velocity of the mouse cursor in the plot.



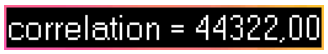
Gives the value of the time of the mouse cursor in the plot.



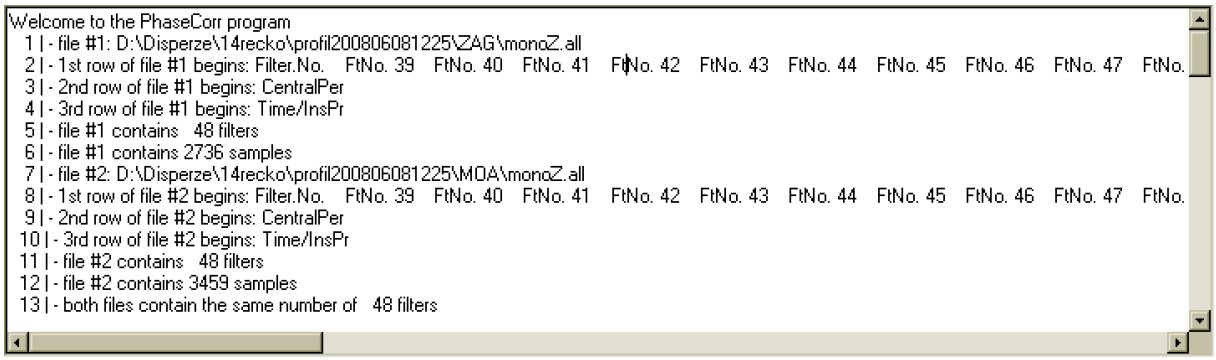
Gives the value of the amplitude of the mouse cursor in the plot.



Gives the value of the time shift of the mouse cursor in the plot.



Gives the value of the misfit function of the mouse cursor in the plot.



Text output informs about input files, their headers, all processing steps, number of correlation maxima found for particular filters and about values of periods selected for drawing the waveforms.

7.7 Working with the PhaseCorr program

Following figures give an idea how the screens look when we press selected buttons. Each figure has a short description which button was used to draw the depicted curve or plot. All the analyst's inputs are given in the four edit boxes and all the computation is provided by pressing the `Compute` button, so the other buttons are used for the results display only.

For figures showing the processing steps, we use the records of an earthquake which occurred in Greece, 2008 June 08, $M_w = 6.3$. We use the stations Molln (MOA) and Kašperské hory (KHC). The epicentral distance to MOA is 1246.8 km and to KHC it is 1395.4 km. Hence the mutual distance of these two stations measured along the geometrical raypath to the KHC station is 148.6 km. Vertical component of the records is used. After the basic functions are described using this event, also other records of different events are presented as examples.

As we mentioned before, the main job for successful phase velocity estimation is provided by the two files which are loaded to the PhaseCorr program and hence it is done using the SVAL program. Using the PhaseCorr, only limited number of procedures can be influenced by the analyst. The main goal of PhaseCorr is to depict all the possibilities of the dispersion curves – the different branches given by the correlation coefficient maxima, for an example, see Fig. 7.2. One may select among these option using the `mean velocity` edit box to tell the program where to start the compilation of the final curve.

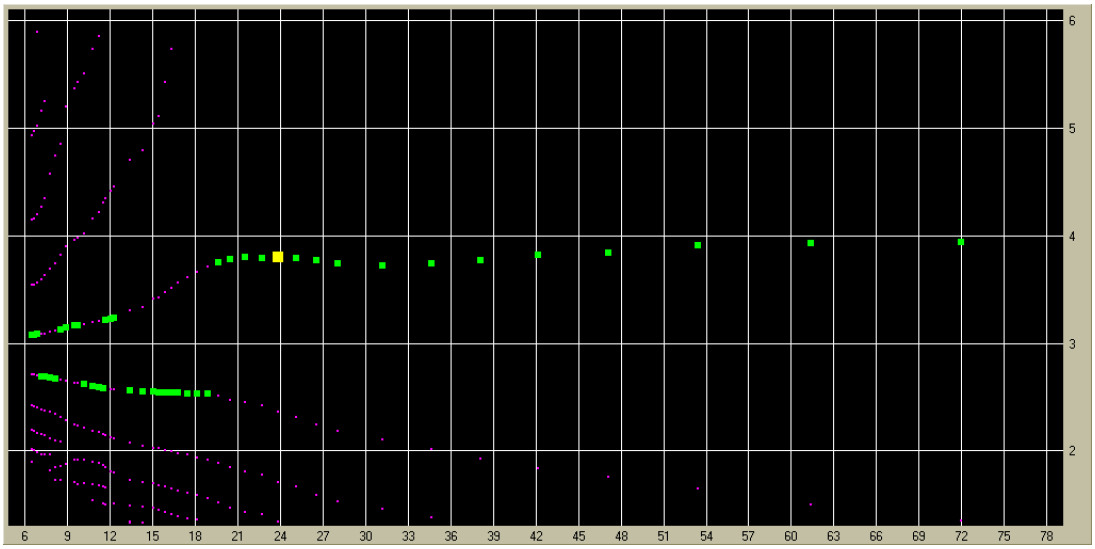


Figure 7.2: `All curves` button draws all the branches of local correlation maxima. The starting dispersion point is highlighted by the big yellow dot. Maximal correlation coefficients are emphasized by green.

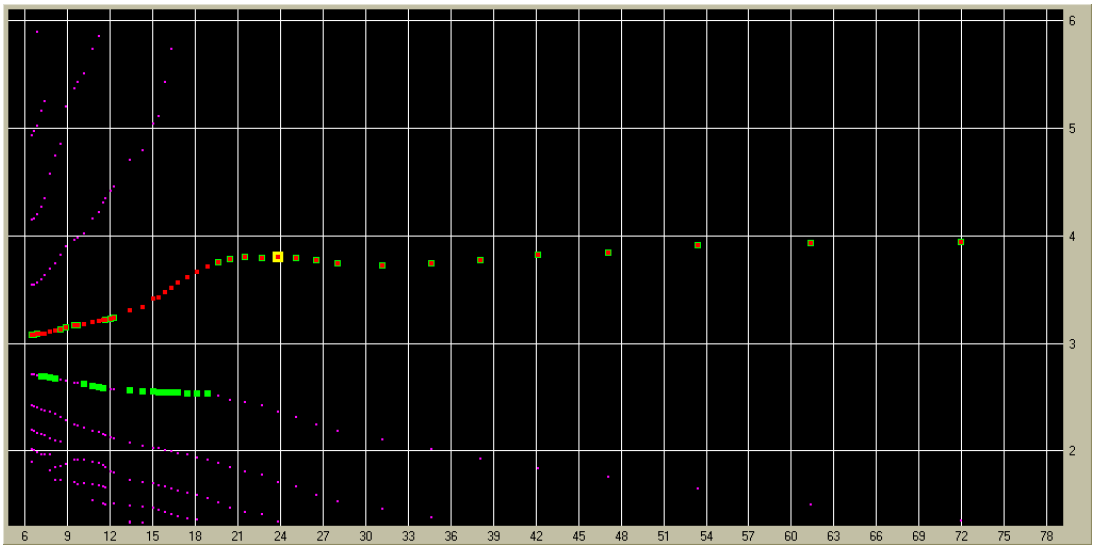


Figure 7.3: `Selected curve` button draws the final curve compiled from the point (big yellow dot) closest to the velocity set in the `mean velocity` edit box (4.0 km/s in this case).

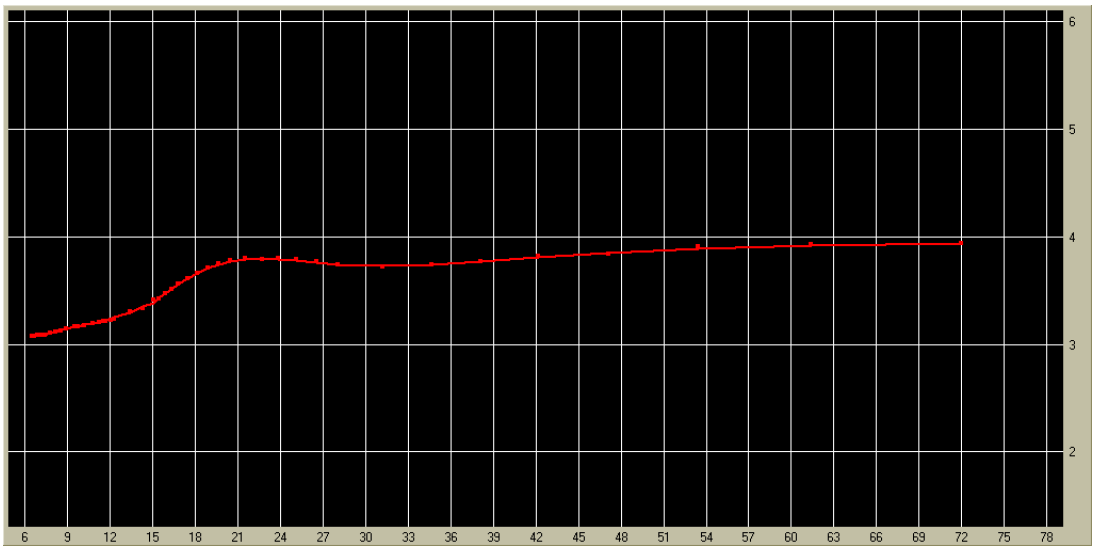


Figure 7.4: Smoothed dispersion curve is drawn along the computed one by the `Smooth curve` button.

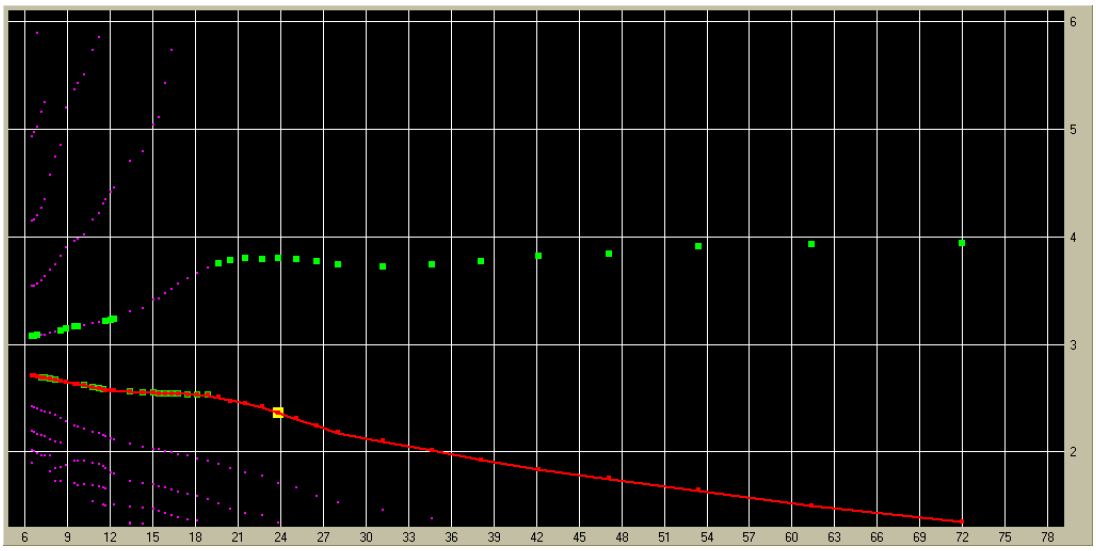


Figure 7.5: If "wrong" `mean velocity` is set (2.5 km/s in this case), the final curve may look like this. It started from the big yellow dot at a wrong dispersion branch.

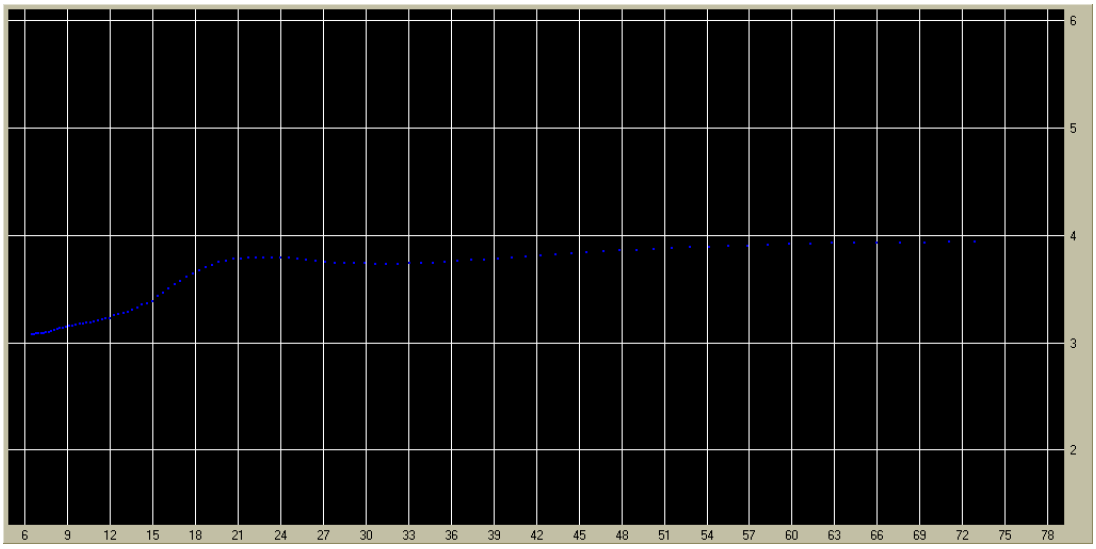


Figure 7.6: A curve interpolated for period values with a geometrical step is shown when `Interpolated` button is pressed.

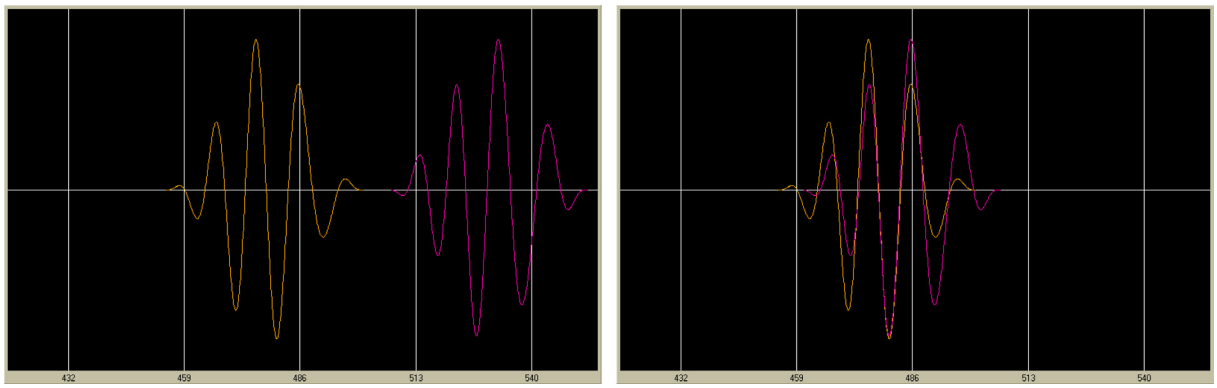


Figure 7.7: Wavegroups for period of 10 s in real position in time are drawn in the left panel by `Original waveforms` button. The same waveforms shifted to fit each other the best are depicted in the right panel by `Shifted waveforms` button.

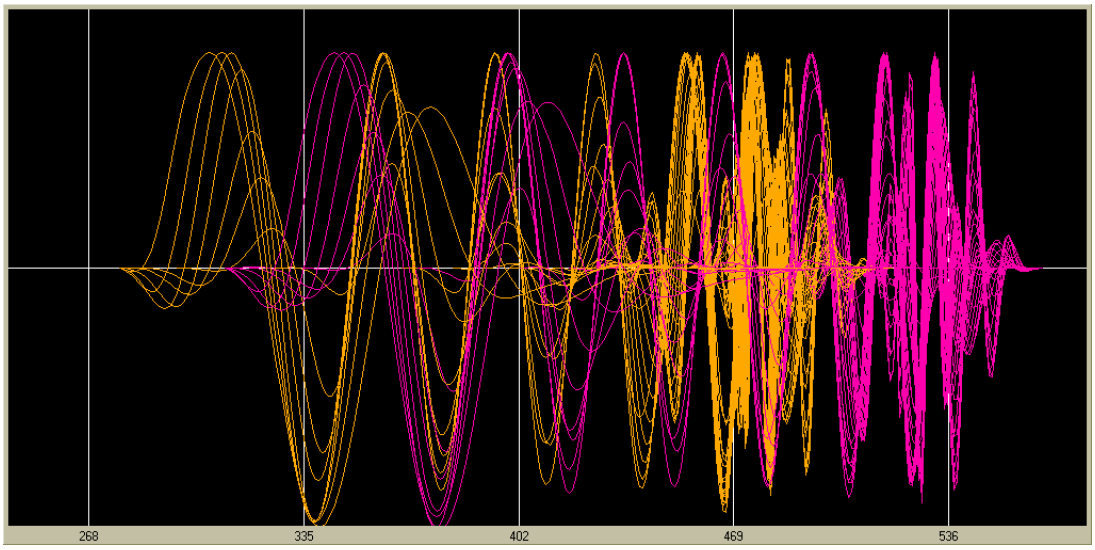


Figure 7.8: Original positions of all waveforms in the range from 6.5 s to 72 s (48 filters). Orange waveforms correspond to the station closer to the source and the violet ones to the more distant station.

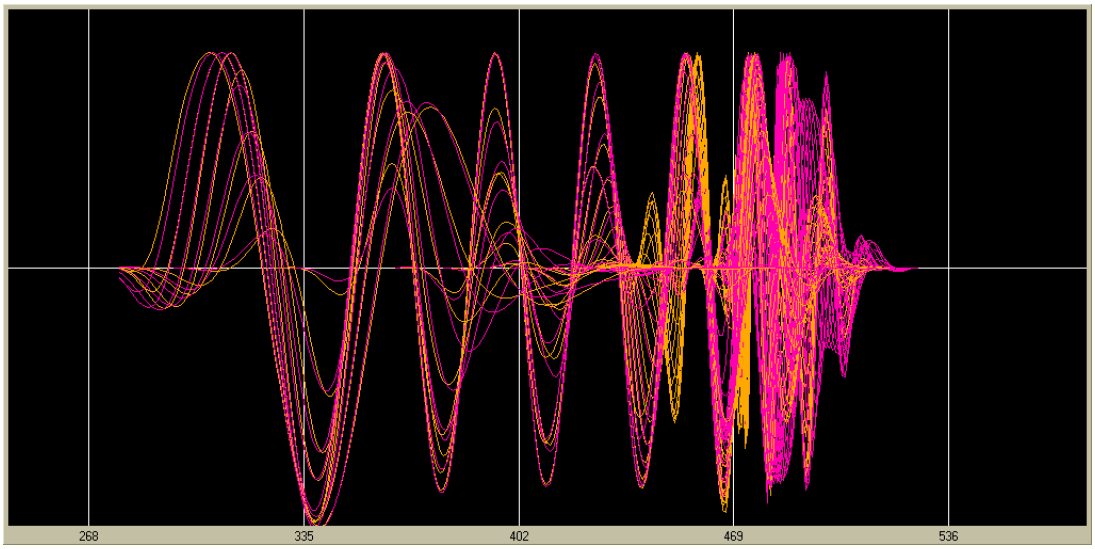


Figure 7.9: All shifted waveforms in the range from 6.5 s to 72 s (48 filters). Orange waveforms correspond to the station closer to the source and the violet ones to the more distant station.

Fig. 7.3 gives an example of the dispersion curve estimated by setting the `mean velocity` to the value of 4.0 km/s. It works in this way: The program looks at the period corresponding to the filter at 3/4 of the whole filter range. In this case, we use an amount of 44 filters and hence the filter No. 33 is used. The period corresponding to this filter is 23.9 s. In the used velocity range from 1.3 km/s to 6.0 km/s four extremes are found at this period. The one closest to the set velocity 4.0 km/s has a velocity of 3.8 km/s (big yellow dot in Figs. 7.2 and 7.3) and the dispersion curve compilation starts from this point. Fig. 7.4 shows how the compiled curve looks like when drawn with its smoothed form together.

The next Fig. 7.5 show, how the results are completely changed by setting the `mean velocity` to the value of 2.5 km/s. At the period of 23.9 km/s the dispersion point closest to the 2.5 km/s has the velocity 2.36 km/s and thus a different dispersion branch is selected.

To decide which of the branches is the correct one, we can use an a-priori knowledge of the presumed phase velocities – in this case, we can assume that the velocities for periods longer than 20 s should be around 4.0 km/s. In this example, when only two options are available for longer periods, it is clear which one is correct. The other possibility how to choose the right branch is to look at the green dots (Fig. 7.2, 7.3 and 7.5) which mark the absolutely highest correlation for each filter. We assume that for longer periods, these absolutely best correlations would correspond to the right dispersion branch, what is fulfilled for the longer periods too.

To reach the desired branch, we may change the `mean velocity` value. If still an inappropriate

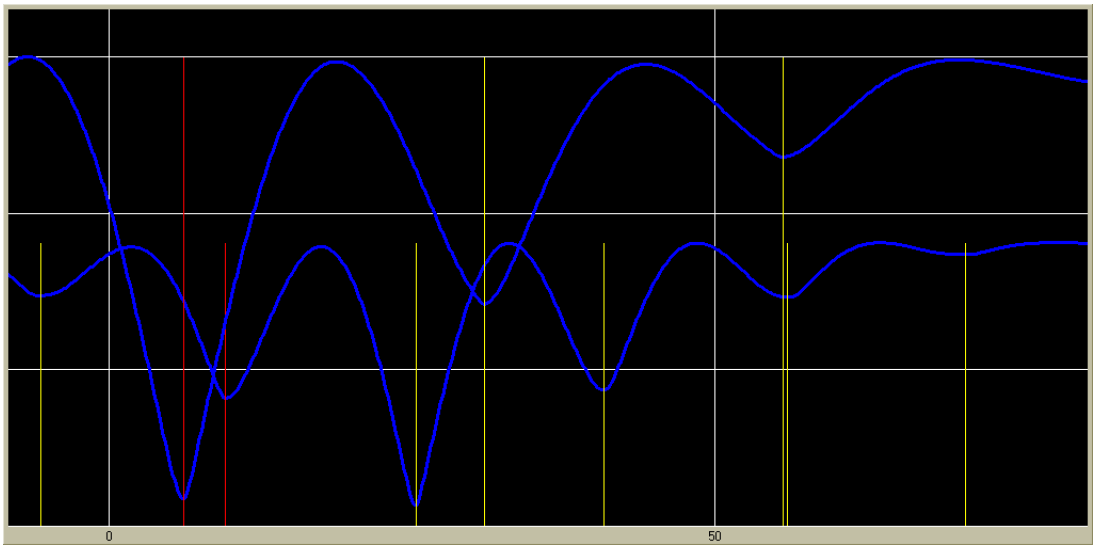


Figure 7.10: The correlation coefficient (misfit function) for 16 (lower) and 25 s (higher) period is drawn using the `Misfit` button with respect to the time shift between the two wavegroups. All misfit minima are depicted by yellow lines, the selected minimum used for the dispersion curve compilation is in red.

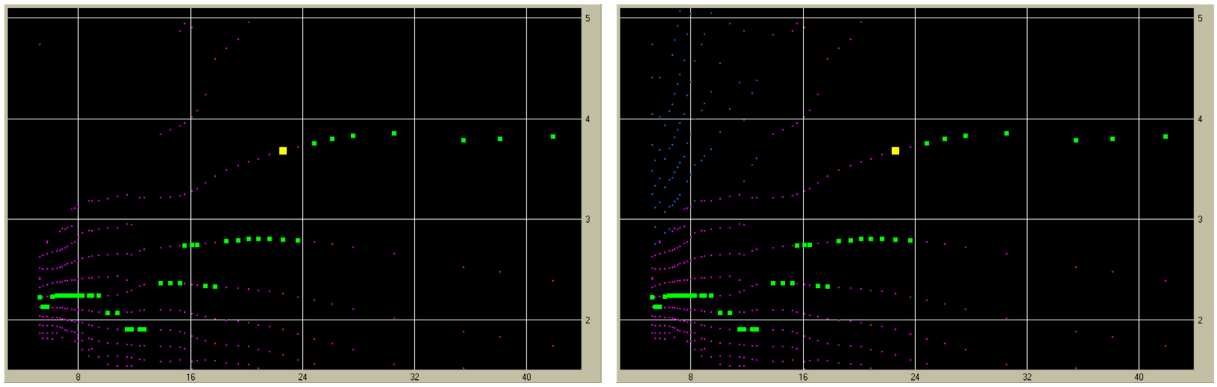


Figure 7.11: Vertical component phase velocities from stations Zagreb (ZAG) and Molln (MOA) using the records of the earthquake in Greece, 2008 June 08, $M_w = 6.3$. Distance between the two stations is 260 km. In the left panel, only the real branches are depicted (violet). In the right panel, the same real branches complemented by the virtual dispersion points (blue) are drawn.

dispersion branch is selected, we may also make the velocity inverval narrower using the two edit boxes `min V` and `max V`.

In special case when no value of `mean velocity` gives reasonable result for the whole period range, we may use a "hand made" phase velocity dispersion curve approach. Sometimes the program compiles the desired dispersion curve only for limited period range and then it jumps to some other, unwanted branch. We can save the dispersion curve for this case and then use another value of `mean velocity` to select the appropriate dispersion curve for the rest of the periods nevertheless it compiles a useless dispersion branch for the periods used in the first trial. Then, we can manually edit the saved text files to get the desired phase velocity dispersion curve – we use only the successfully compiled period ranges from the respective files.

The interpolated dispersion shown in Fig. 7.6 is designed to have to possibility to compare the results of different analysis of different records. These curves are saved always for the same periods and hence we may easily compare them, make an average of them and so on.

Fig. 7.7 shows the plots given by the `Original waveforms` and `Shifted waveforsm` buttons for period of 10 s selected using the drop-down list `select periods`. Left panel shows the position of the waveforms in real time measured from origin as they were recorded at the two respective stations MOA and KHC. The right panel depicts the waveform of the more distant station KHC shifted in time to fit exactly the waveform recorded at MOA. The mutual distance of the stations in km divided by the time shift in seconds is the phase velocity for this period of 10 s.

Figs. 7.8 and 7.9 present the same as in Fig. 7.7 but for all 44 filters used in the phase velocity

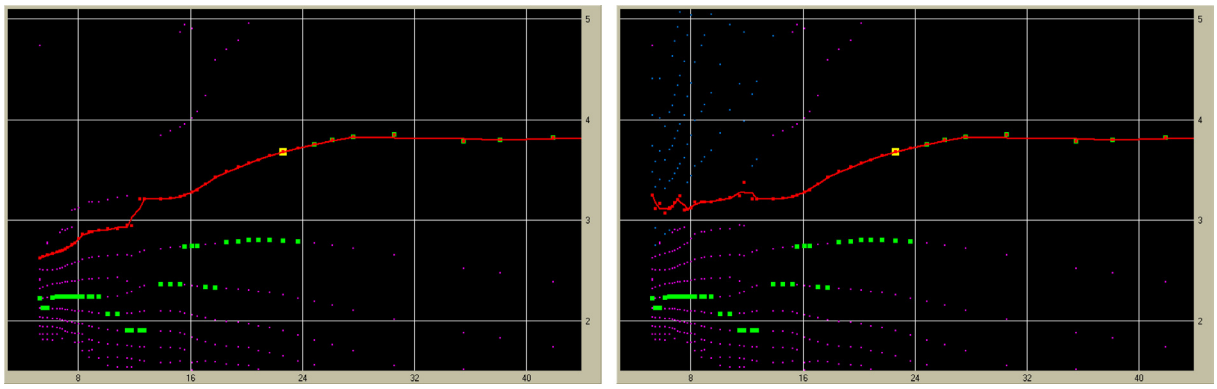


Figure 7.12: The same as in the previous figure with compiled phase velocity dispersion curves presented. We see mutual differences in the short-period range.

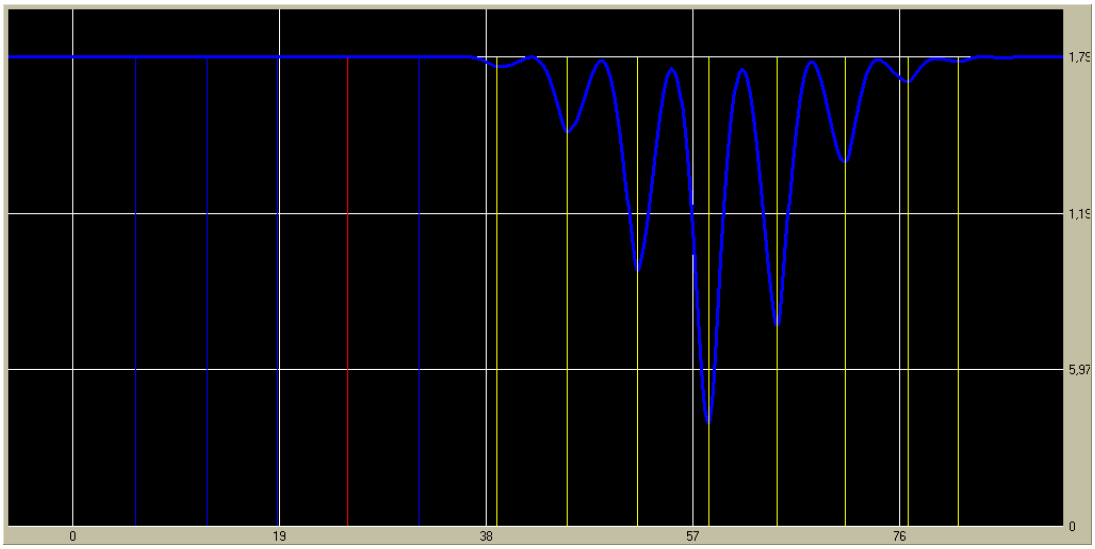


Figure 7.13: Misfit function with respect to the time shift between the two wavegroups of 6.5 s period from the previous two figures. Eight real minima were found (yellow lines) and five virtual minima (blue) complement the real ones for shorter time shifts (higher velocities). The second virtual minimum (red) was used for the final dispersion curve compilation, see the right panels of Figs. 7.11 and 7.12.

estimation. Fig. 7.8 shows the original positions of the waveforms and Fig. 7.9 the waveforms shifted in time.

The `Misfit` button draws the misfit function with respect to time for selected period. Fig. 7.10 shows two misfit functions for the periods of 16 s (lower blue line) and 25 s (higher blue line). For the 16 s period 6 misfit minima were found (shorter yellow lines) and the second one (shorter red line) was used for the final dispersion curve compilation. For the 25 s period, only 3 misfit minima wer found (longer yellow lines) and the first of them (longer red line) was used for the final curve.

When `virtual points` box is checked, also an additional virtual correlation maxima are found. The program computes and average position of all the real maxima in the time and then uses the average of the periods from both data files to estimate shifts from this average position. It starts with this estimating at the end of the real maxima toward lower time shifts (higher velocities). It simply deduct the average period from the average maxima position multiplied by the number of wavelengths higher than is the number corresponding to the slowest real maximum.

For introducing the virtual misfit minima we present screenshots made during an analysis of the same event from Greece, 2008 June 08, but with the use of other stations. Fig. 7.11 shows all dispersion branches between the stations Zagreb (ZAG) and Mollns (MOA). Their mutual distance is 260 km, what is much more than in the case of the stations MOA and KHC, where the distance was only 148 km. This is the reason why we see much more dispersion branches – the same wavelengths may fit several times more into the interstation distance than in the previous case. The left panel of Fig. 7.11 presents only the real branches (blue), the right panel shows these branches (blue) complemented by the virtual dispersion points (violet). Green dots suggest the right dispersion branch for longer periods. Fig. 7.12 depicts how

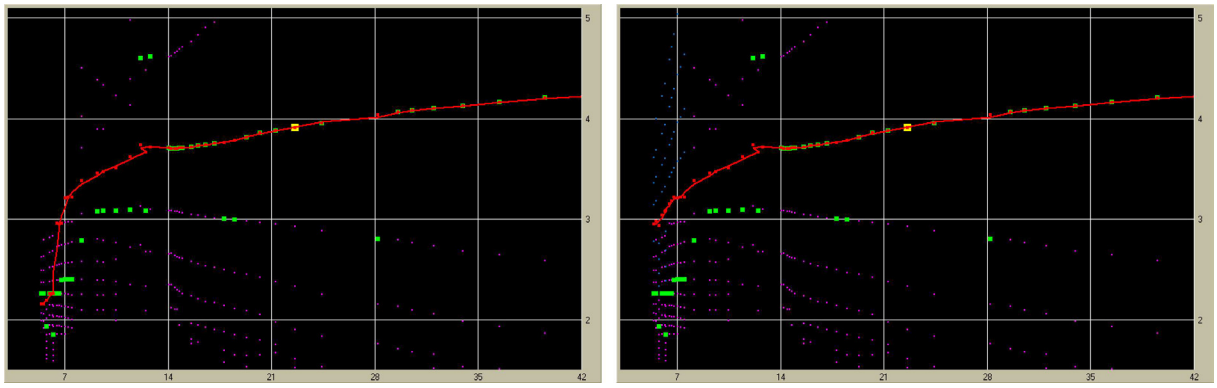


Figure 7.14: Another example for which the same event and the same stations ZAG and MOA were used as in the previous case. However, transverse component is now displayed. We again see that in the left panel where only the real points are used, the dispersion curve reveals unrealistic low velocities in the short-period part while the right panel shows a bit more reasonable estimate of the phase velocities.

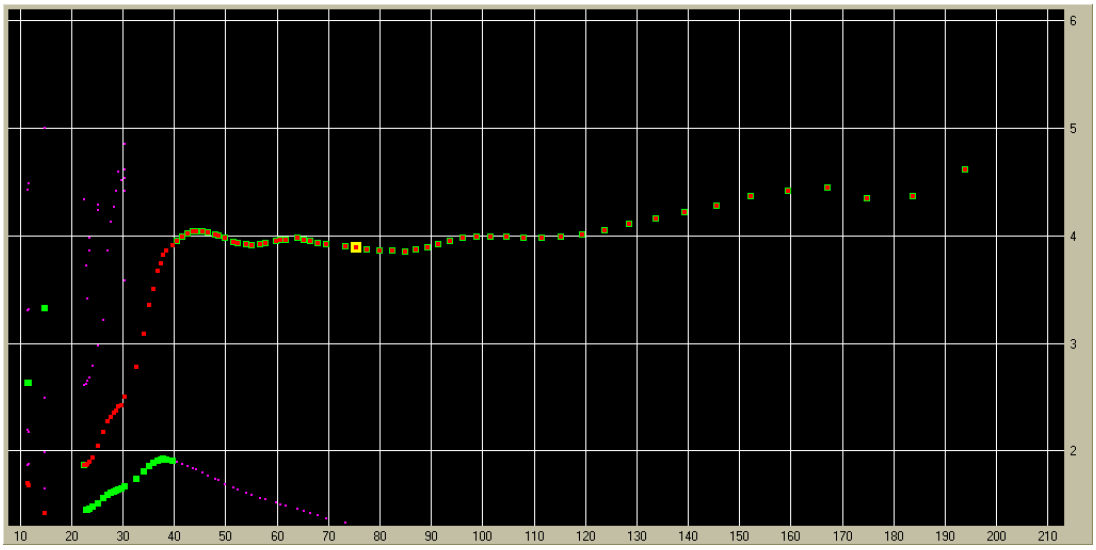


Figure 7.15: A broadband records allow to estimate phase velocity dispersion curves for long period ranges. This is a vertical component from the stations Bedřichov (BED) and Háje (HAJ) from the event which occurred near the Kuril Islands, 2006 November 15, M = 8.3. Mutual distance of the stations is 148 km. The period range from 22 s up to 194 s looks reasonable.

the dispersion compilation works for the same `mean velocity` of 4.0 km/s. The left panel shows the final curve compiled using the real points only (red dots and line) and the right panel presents the curve compiled using also some of the virtual points in the short-period range. In the left panel, we see an error when the dispersion "jumps" from the right branch down to the wrong one around the period of 12 s. The right panel avoid this error, however, the virtual dispersion points do not form a smooth lines as in the case of the real ones and hence the final dispersion is a bit scattered. For the periods shorter than 7 s the compiled dispersion is disputable in any case.

Using the `Misfit` button when the `virtual points` option is checked, changes also the plot of the misfit function. Fig. 7.13 shows the misfit function for the period of 6.5 s, the record is the same as in both previous figures. We see 8 real minima to be found (yellow lines) and 5 virtual ones (blue lines). The second virtual minimum was used for the final dispersion curve compilation (red line).

Fig. 7.14 uses the same event, and the same stations as in the previous case (Greek event, ZAG and MOA stations), but the transverse component is now analyzed. In this case, using only the real dispersion points, the final curve skip several dispersion branches in the short period part resulting in obviously wrong low velocities. As opposed to this, using the virtual points, see the right panel of Fig. 7.14, the same dispersion branch is kept from longer periods to the short ones and the final phase velocity dispersion curve look much more adequately.

To present another period range, the screenshot in Fig. 7.15 was made during the analysis of the big earthquake which occurred near Kuril Islands, 2006 November 15, M = 8.3. Since the stations Bedřichov

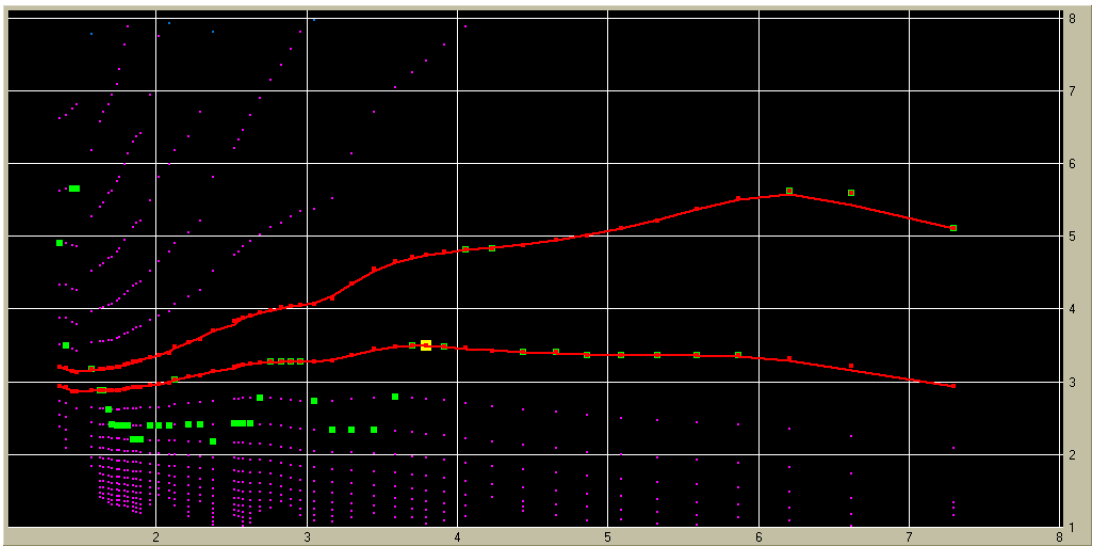


Figure 7.16: Using the stations Průhonice (PRU) and Jeruzalém (JER), the record of an induced event from Lubin, Poland, 2006 May 21, $M_b = 4.1$, was analyzed. Mutual distance of the two stations is 50 km. Several dispersion branches are to be seen close to each other, two of the possible compiled curves are emphasized by red.

(BED) and Háje (HAJ) are only 148 km distant, what is very close with respect to used wavelengths, we see only one dispersion branch in the longer-period part of the plot. The phase velocity dispersion is quite obvious and easily recognizable by the program using the real points only. The curve is smooth and reasonably estimated in the period range from 22 s up to 194 s.

As the last example, see Fig. 7.16, we present the phase velocity estimation from an event induced by the mining activity near the city of Lubin, Poland, 2006 May 21, $M_b = 4.1$. Since the mutual distance of the stations Průhonice (PRU) and Jeruzalém (JER) is only 50 km, what is several times the wavelength of the used period range, many dispersion branches are visible since several wavelengths fit into this distance. It is similar to the examples presented in Figs. 7.11 and 7.14. It is not easy to recognize which dispersion branch is the proper one. Green dots for the longest periods emphasize the branch near 5 km/s, but in the middle period range, much more green dots follows the branch between 3 and 4 km/s. We show both options. The compiled dispersion curves are both smooth and both of a reasonable velocity values. This is to show that even "nice" data with clear dispersion branches may produce disputable results.

Conclusion

In the next paragraphs, we present a conclusion of the thesis. *Resume* gives a brief recapitulation of what has been introduced in the previous chapters and *Outlooks* present projects and objectives which are to be utilized in the future. After all, *Epilogue* stating the final synthesis follows.

Resume

In the thesis, I have presented a complete set of tools for the analysis of dispersed records and for inversion of the dispersion curves for 1D layered velocity models. A comprehensive overview of papers and books concerning the surface wave phenomena has been given and ordered chronologically with pointing out the most important technique inventions both in terms of analysis and inversion. The multiple filtering technique has been introduced as a tool for surface wave analysis with no limitations for any period and velocity ranges and with sufficient resolution in time or frequency domains. Tests of both analysis and inversion have been presented; some of them have been included in the original papers written by the author and his supervisor and consultant, others solely prepared for the thesis. A new evidence of the dispersion curve determination independence of the record type (seismogram, velocigram and accelerogram) has been made and included.

An original SVAL program based on the multiple filtering method with interactive tools for controlling all the steps of the analysis and with parameter setting directly in the working environment by the user has been developed and described in detail. The program includes the isometric method (Málek et al., 2005 and 2007) for inversion of currently estimated or previously saved and uploaded dispersion curves and the matrix method for forward computation of dispersion curves (developed by Oldřich Novotný). The program is able to read input files containing the data in two formats – the first one is the single-column ASCII data format and the other is the ASCII format containing all three components of the record and additional information about the record and the event in its header. Using this advanced format, it is possible to use the information from the header and hence to proceed faster with the processing. However, when using the simple format, all necessary parameters can be given using the edit boxes of the program.

Additional tools for preprocessing of the records as a bandpass filtering and instrumental transfer function application are also available. Parameters of the multiple filering, as a velocity and period ranges, width of the filters, number of filters and many others can be adjusted directly during the processing. Options for dispersion curve compilation and separated mode waveform computation are included.

The main feature differing the SVAL program from other software for filtration is its extensive graphical interface. All steps of computation can be viewed. The user is able to check all the parameters and their influence on the record, spectrogram, harmonic components and dispersion curve. It is possible to use trial approach to the processing – when viewing the results, one can directly change the parameters to achieve desired resolution in time or frequency domain, to compile the dispersion curve by one of the two automatic procedures or to compile it manually selecting point by point by mouse-clicking. It is possible to check selected wavegroups at each harmonic components filter by filter and to adjust the truncating in the time domain. Using the spectral domain window, the user is able to check and adjust the width of the filters, to see the influence of the filters at the corresponding part of the spectrum and to observe the influence of the instrumental transfer function.

Inversion is to be adjusted in a similar manner – starting models including shear and longitudinal

wave velocity in each layer as well as density and possible ranges of their resulting values can be set. The SVAL program is able to invert Love or Rayleigh wave phase or group dispersion curves or even both Love and Rayleigh wave dispersion curves together. All features of the program has been mentioned and demonstrated on selected examples.

Another original software called PhaseCorr for phase velocity estimation has been introduced, tested and described with examples, too. It uses the results of the SVAL program – it reads the set of harmonic components from two stations analyzed and separated by the SVAL program and it provides a correlation between the two corresponding harmonic components to estimate the time difference and to compute the phase velocity for each period of the surface waves.

Applications of the method and the software for real structural parameters estimation have been given in three papers dealing both with Love and Rayleigh waves. The works concerning both short period dispersed wavegroups from local measurements as well as regional long period surface waves have been included. Upper crust as well as whole crust shear wave velocities have been estimated. Both group and phase velocity curves have been measured and inverted. Both 1D models and 2D tomographic velocity maps have been figured out.

The paper by Kolínský and Brokešová (2007) (application A) has described the heterogeneity of the Western Bohemia region using six profiles with 1D shear wave models estimated to the depth of 3 km. Despite the fact that the resultant averaged model has corresponded well to the previously published studies, the differences between the six different paths have been distinctively pronounced and the extraordinary complicated structure of the region has been proved.

The paper by Kolínský and Brokešová (2008) (application B) has provided the tomography of the same region. It has been the first attempt to reach the uppermost structure of Western Bohemia using surface wave tomography. Group velocity variations are compared with body wave distribution around the area with qualitatively comparable features. However, our results has again demonstrated the outstanding heterogeneity of the region with variations greater than those estimated form body waves by other authors. In addition to the original paper, detailed insight into smoothness and resolution of the tomographic method has been given in the thesis.

The paper by Kolínský et al. (2010) (application C) has concerned regional surface wave propagation and inversion of the phase velocity dispersion curves to the whole crust structure. The paper has given not only the comparison of the crustal shear wave velocity distribution of the three geological units among themselves. It has also provided a detailed analysis of the surface wave propagation across continental Europe from the Aegean Sea to the Bohemian Massif with discussion of the non-great-circle propagation and true backazimuths correction in the broad period range from 12 to 40 s.

These three papers have been complemented with comments, additional remarks and notes to the problems which emerged when dealing with the respective topics.

Outlooks

Several other projects concerning the surface wave analysis and inversion have been provided during the author's PhD studies. It has not been possible to include all of them in the thesis. The author would like to proceed in further studies with some of the topics to reveal velocity distributions of other parts of the Bohemian Massif.

One of the other projects has concerned especially the estimation of the average 1D anisotropic model of the Bohemian Massif using the phase velocities of earthquakes with good azimuthal distribution around Central Europe. This project is ongoing; the events have already been selected and difficulties with advanced phase velocity estimations are solved continuously. Using both Love (T component) and Rayleigh waves (both Z and R components), we would like to estimate the anisotropy of the crust and upper mantle. Preliminary results of the study have already been presented at conferences using the phase velocities of all three components from Kurile Islands earthquakes from November 2006 and January 2007.

Close cooperation between the Institute of Rock Structure and Mechanics, Academy of Sciences of the Czech Republic, and the Geophysical Institute, Bulgarian Academy of Sciences, started in 2008. Bulgarian broadband seismic station Provadia, near to the Black Sea, was equipped with Czech small aperture array and data between both Institutes are extensively exchanged. Phase velocity measurements between Bulgaria and the Bohemian Massif are provided using all three components of records from earthquakes from Turkey and Greece as well as from the North Atlantic Ridge and Iceland to confirm the dispersion curve determination using the surface waves propagating from both directions.

Other study has also turned our interest to the large amount of data processing. We have selected records of 8 earthquakes which had occurred in Greece from nearly 200 broadband stations from all around the Europe. For this project, the automatic batch processing has been implemented in the SVAL program. We have analyzed long time windows of the records to reveal not only the fundamental modes, but also surface wave reflection and converted modes which come after the fundamental mode. This study is at its final stage with developing a software to select among different surface wavegroups at 200 stations around the continent to found smooth propagation isochrones of fundamental, higher and reflected modes. Colleagues from the Department of Seismology, Institute of Rock Structure and Mechanics, Academy of Sciences of the Czech Republic, are working with the data using the SVAL and PhaseCorr programs developed and described in the presented thesis.

A tomographic study using the broadband data from the international PASSEQ experiment will cover the whole Central Europe and possibly reveal the distinct velocity distributions in front of as well as behind the Trans European Suture Zone (Teisseyre-Tornquist Zone) dividing the Phanerozoic and Proterozoic European platforms.

In terms of methodology, advanced techniques of estimating the true backazimuths of surface wave arrivals during the analysis as well as incorporating effects of finite wavelengths during the inversion are planned to be used. Since a broadband, seven-station array with an aperture of 5 km is operated in Příbram, Czech Republic, surface waves from even teleseismic events may be analyzed using the standard array techniques. A lot of data from the array has been collected, however, no systematic effort has been aimed to the surface wave analysis of it so far.

Several other small-aperture seismic arrays (with aperture of ≈ 100 m) have been deployed in the Bohemian Massif (Ostaš, Eastern Bohemia; Nový Kostel and Květná, Western Bohemia) and short-period surface waves from quarry blast and induced events may be analyzed using the array records.

Epilogue

I have shown that surface waves have various applications. Different sources, distances and wavelengths have been studied. Methods for analysis and inversion have been developed and used. New methodology advances are being implemented what will continue in the future work. Multipathing, reflection, refraction, mode conversion, finite wavelength effects and anisotropy have to be incorporated to increase the accuracy, lower the errors and reveal the structure with more details. Surface wave studies as a branch of seismology are continuously evolving and their applications are to be utilized henceforward.

This thesis, built up using the papers written by the author and his supervisor and consultant, offers not only a simple compilation of the published works. It introduces the papers in a comprehensive framework of theoretical background and software tools. Besides that, different topics of the papers enable different views at the single surface wave phenomenon. The papers are consistently joined in a standalone work which results in, as I hope, not only giving a sum of the results of the original papers. I have written the thesis to present the synergy of the particular topics, which enables close look at the surface wave theory, software, actual measurements and results.

Appendix

Explanatory dictionary

Some of the generally known expressions are explained to point out how they are used in the text.

BANDWIDTH, WIDTH OF A FILTER – in our case a subjective expression for the width of the Gaussian function, we use it only relatively (broader, narrower)

CENTRAL FREQUENCY / PERIOD – frequency / period of the maximum of the Gaussian function, the filter is "centered" to this frequency / period

COEFFICIENT α (alpha) – by using this coefficient we can intensify or weaken the effect of the constant relative resolution filtering, it gives the width of the Gaussian function

CONSTANT RELATIVE RESOLUTION FILTERING – the width of filters changes so as the ratio of the distance of the current and central frequency to the central one is constant, it means that the filter width grows for higher frequencies

DIFFRACTION TOMOGRAPHY – a tomography where finite wavelengths are taken into account and curved raypaths are used to estimate the tomographic maps

DISPERSION CURVE – in general: the group velocity-period dependence
– specially: a set of dispersion points which correspond to certain surface wave mode and to the certain dispersion ridge

DISPERSION POINT – a point in the group velocity-period plane; it corresponds to a local maximum of a filtered signal; certain amplitude value also corresponds to this point and we can image it in 3D

DISPERSION RIDGE – the part of the spectrogram corresponding to certain surface wave mode – this concerns not only the maxima, but also its vicinity (we use two options to set this vicinity in the SVAL program)

FILTERED / NEARLY MONOCHROMATIC SIGNAL – complex signal in the time domain, it comes as a result of the inverse FT of a filtered spectrum, it contains predominantly only one of the frequencies

FREQUENCY-TIME ANALYSIS (FTAN / SVAN) – general expression for methods which can display time and frequency domains together

FREQUENCY-TIME REPRESENTATION – the basic FTAN representation, we see both time and frequency domains together

FUNDAMENTAL MODE – the slowest surface wave mode, usually, it has the highest amplitudes for longer waves

GAUSSIAN FILTER – special case of weighting function, it has the shape of Gaussian function – good for an optimal resolution; when the spectrum is weighted by the Gaussian filter, it has the best resolution both in frequency and time domains

GROUP VELOCITY – the velocity of wavegroup energy propagation, computed as the velocity of propagation of the amplitude envelope maximum

GROUP VELOCITY-PERIOD DIAGRAM – similar to the spectrogram but it is used while imaging only the dispersion curve, it is only 2D representation, no amplitudes are depicted

HIGHER MODES / OVERTONES – faster modes; in the short period range their amplitudes can be higher then the amplitudes of the fundamental mode

HOMOGENEOUS FILTERING – the above mentioned ratio is left and no other changes of filter width are made, coefficient $\alpha = \text{const}$, it intensifies or weakens the effect of the constant relative resolution filtering, but it has the same effect for all the frequencies

INSTANTANEOUS FREQUENCY / PERIOD – each moment of the signal has an instantaneous frequency / period computed using the analytical signal corresponding to the original signal

MULTI-CHANNEL FILTERING, MULTIPLE FILTERING – one of the methods of FTAN, it works with Fourier Transform, the decomposition is done in frequency domain; we use the term "multiple filtering" to be not confused with the "multichannel" data acquisition

OPTIMAL FILTERING – using the coefficient α we can again change the filter width; the term "optimal" seems to be too poetic; in the SVAL program, the broadening of filters due to constant relative resolution filtering is weakened using α coefficient, $\alpha = \alpha(\text{period})$, and hence the effect of constant relative resolution filtering is weakened differently for different frequencies

PRIMARY, SECONDARY, TERTIARY ... LOCAL MAXIMUM – first, second, third etc. highest maxima of the filtered signal envelope for one (and each) of the nearly monochromatic signals; in the SVAL program, by the term "maxima" we mean also the inflection points with the lowest derivation (if the option is selected)

SEISMOGRAM, VELOCIGRAM, ACCELEROGRAM RECORDS – the meaning is clear, however, it does not make any difference if we estimate the dispersion using displacement, velocity or acceleration record – although the records look different, the envelopes maxima for all the nearly-monochromatic components arrive at the same time

SIGNAL ENVELOPE – the modulus of an analytical signal corresponding to the filtered signal

SPECTROGRAM – a 3D representation using frequency-time-amplitude or period-group velocity-amplitude; it is created by the above mentioned envelopes of the analytical signals

SURFACE WAVEGROUP – the dispersive part of a spectrogram containing one mode and type of waves (Rayleigh or Love); usually, different modes comes in the same time; we can also see both types of waves at the same component

SURFACE WAVE TOMOGRAPHY – generally: an approach to estimate 3D structure using the group or phase velocity dispersion curves of surface waves propagating in different directions; may be used as a 3-stage approach; as a 1D estimation, the dispersion curves are measured; as a 2D estimation, the tomographic maps are computed and as a 3D result, the depth-dependent distribution of shear wave velocities is estimated from local dispersion curves taken from these maps
– specially: a method, where 2D distribution of surface wave ray paths is used to estimate the 2D maps of group or phase velocity for given period; so it is only the second step in the 3-stage approach

TIME CORRECTION – we apply the time correction in the spectral domain using the phase and amplitude transfer function of the given instrument, we make a corrected spectrum of the whole record and after that, we provide the analysis using this "instrument independent" spectra

TOMOGRAPHY – a method where 2D or 3D distributed raypaths are used to estimate the structure of given medium

TRUNCATED FILTERED NEARLY MONOCHROMATIC SIGNAL – the same as above mentioned complex signal, but only the required (and smoothed) wavegroup remains

TRUNCATED SPECTROGRAM – the same as above mentioned spectrogram, but only the required dispersion ridge is present, so it is created using the envelopes of truncated nearly monochromatic signals

WEIGHTING FUNCTION – in general, these are all the functions which give a weight to other function

References

Aki, K. and Tsai, Y.-B., 1972: Mechanism of Love-wave excitation by explosive sources, *J. Geophys. Res.*, 77, 1452–1475.

Alsina, D., Snieder, R. and Maupin, V., 1993: A test of the great circle approximation in the analysis of surface waves, *Geophys. Res. Lett.*, 20, 915–918.

Alsop, L. E., 1964: Spheroidal free periods of the Earth observed at eight stations around the world, *Bull. Seism. Soc. Am.*, 54, 755–776.

Ammon, C. J., Velasco, A. A. and Lay, T., 2006: Rapid estimation of first-order rupture characteristic for large earthquakes using surface waves: 2004 Sumatra-Andaman earthquake, *Geophys. Res. Lett.*, 33, L14314, doi: 10.1029/2006GL026303.

An, M. and Assumpção, M. S., 2004: Multi-objective inversion of surface waves and receiver functions by competent genetic algorithm applied to the crustal structure of the Paraná Basin, SE Brazil, *Geophys. Res. Lett.*, 31, L05615, doi: 10.1029/2003GL019179.

Anderson, D. L. and Archambeau, C. B., 1964: Anelasticity of the Earth, *J. Geophys. Res.*, 69, 2071–2084.

Antonini, M., 1987: Statistics and source parameters of the swarm from digital recordings, in: Procházková, D. (ed): *Earthquake swarm 1985/86 in Western Bohemia – proceedings of workshop in Mariánské Lázně*, Czechoslovak Academy of Sciences, Geophysical Institute, Prague 1987, 205–217.

Arroucau, P., Rawlinson, N. and Sambridge M., 2010: New insight into Cainozoic sedimentary basins and Palaeozoic suture zones in southeast Australia from ambient noise surface wave tomography, *Geophys. Res. Lett.*, 37, L07303, doi: 10.1029/2009GL041974.

Backus, G. E., 1962: The propagation of short elastic surface waves on a slowly rotating Earth, *Bull. Seism. Soc. Am.*, 52, 823–846.

Baig, A. M.; Campillo, M.; Brenguier, F., 2009: Denoising seismic noise cross correlations, *J. Geophys. Res.*, 114, B08310, doi: 10.1029/2008JB006085.

Baker, G. E. and Stevens, J. L., 2004: Backzimuth estimation reliability using surface wave polarization, *Geophys. Res. Lett.*, 31, L09611, doi: 10.1029/2004GL019510.

Barmin, M. P., Ritzwoller, M. H. and Levshin, A. L., 2001: A fast and reliable method for surface wave tomography, *Pure Appl. Geophys.*, 158, 1351–1375.

Bedrosian, E, 1962: A product theorem for Hilbert transforms, memorandum RM-3439-PR, *United States Air Force project RAND*, the RAND corporation, Santa Monica, California, 15 pp.

Beghein, C., Resovsky, J. S. and Trampert, J., 2002: P and S tomography using normal-mode and surface waves data with a neighbourhood algorithm, *Geophys. J. Int.*, 149, 646–658.

Benioff, H., Press, F. and Smith, S., 1961: Excitation of the free oscillations of the Earth by earthquakes, *J. Geophys. Res.*, 66, 605–619.

Bensen, G. D., Ritzwoller, M. H., Barmin, M. P., Levshin, A. L., Lin, F., Moschetti, M. P., Shapiro, N. M. and Yang, Y., 2007: Processing seismic ambient noise data to obtain reliable broad-band surface wave dispersion measurement, *Geophys. J. Int.*, 169, 1239–1260.

Bensen, G. D., Ritzwoller, M. H. and Shapiro, N. M., 2008: Broadband ambient noise surface wave tomography across the United States, *J. Geophys. Res.*, 113, B05306, doi: 10.1029/2007JB005248.

Beránek, B., 1971: Study of the velocity conditions in the Earth's crust in the regions of the Bohemian Massif and the Carpathian system along international profiles VI and VII, *Stud. Geophys. Geod.*, 15, 316–330.

Beránek, B., Mayerová, M., Zounková, M., Guterch, A., Materzok, R. and Pajchel, J., 1973: Results of deep seismic sounding along international profile VII in Czechoslovakia and Poland, *Stud. Geophys. Geod.*, 17, 205–217.

Beránek, B. and Zounková, M., 1977: Investigations of the Earth's crust in Czechoslovakia using industrial blasting, *Stud. Geophys. Geod.*, 21, 273–280.

Beucler, E., Stutzmann, E. and Montagner, J.-P., 2003: Surface wave higher-mode phase velocity measurements using a Roller-Coaster-type algorithm, *Geophys. J. Int.*, 155, 289–307.

Boashash, B. and Jones, G., 1992: Instantaneous frequency and time-frequency distributions, in: Boashash, B. (ed): *Time-frequency signal analysis: methods and applications*, Longman Cheshire, Melbourne, 43–73.

Boschi, L., Ekström, G. and Kustowski, B., 2004: Multiple resolution surface wave tomography: The Mediterranean Basin, *Geophys. J. Int.*, 157, 293–304.

Bourova, E., Kassaras, I., Pedersen, H. A., Yanovskaya, T., Hatzfeld, D. and Kiratzi, A., 2005: Constraints on absolute S velocities beneath the Aegean Sea from surface wave analysis, *Geophys. J. Int.*, 160, 1006–1019.

Bouchon, M., 1981: A simple method to calculate Green's functions for elastic layered media, *Bull. Seism. Soc. Am.*, 71, 959–971.

Bourjot, L. and Romanowicz, B., 1992: Crust and upper mantle tomography in Tibet using surface waves, *Geophys. Res. Lett.*, 19, 881–884.

Berckhemer, H., 1956: Rayleigh-wave dispersion and crustal structure in the East Atlantic Ocean basin, *Bull. Seism. Soc. Am.*, 46, 83–86.

Brenguier, F., Shapiro, N. M., Campillo, M. Nercessian, A. and Ferrazzini, V., 2007: 3-D surface wave tomography of the Piton de la Fournaise volcano using seismic noise correlations, *Geophys. Res. Lett.*, 34, L02305, doi: 10.1029/2006GL028586.

Brooks, L. A., Townend, J., Gerstoft, P., Bannister, S. and Carter, L., 2009: Fundamental and higher-mode Rayleigh wave characteristics of ambient seismic noise in New Zealand, *Geophys. Res. Lett.*, 36, L23303, doi: 10.1029/2009GL040434.

Brož, M., 2000: Detection of the origin time and seismic ground motion of quarry blasts, *Acta Montana*, 16 (118), 17–24.

Brune, J. N., Nafe, J. E. and Oliver, J. E., 1960: A simplified method for the analysis and synthesis of dispersed wave trains, *J. Geophys. Res.*, 65, 287–304.

Brune, J. N., 1964: Travle times, body waves, and normal modes of the Earth, *Bull. Seism. Soc. Am.*, 54, 2099–2128.

Brune, J. N., Nafe, J. E. and Alsop, L. E., 1961: The polar phase shift of surface waves on a sphere, *Bull. Seism. Soc. Am.*, 51, 247–257.

Brune, J. N., Benioff, H. and Ewing, M., 1961: Long-period surface waves from the Chilean earthquake of May 22, 1960, recorded on linear strain seismographs, *J. Geophys. Res.*, 66, 2895–2910.

Brune, J. N. and Dorman, J., 1963: Seismic waves and Earth structure in the Canadian shield, *Bull. Seism. Soc. Am.*, 53, 167–210.

Brune, J. N., Espinosa, A. and Oliver, J., 1963: Relative excitation of surface waves by earthquakes and underground explosions in the California-Nevada region, *J. Geophys. Res.*, 68, 3501–3513.

Bukchin, B. G., 1995: Determination of stress glut moments of total degree 2 from teleseismic surface wave amplitude spectra, *Tectonophysics*, 248, 185–191.

Bukchin, B. G., Mostinsky, A. Z., Egorkin, A. A., Levshin, A. L. and Ritzwoller, M. H., 2001: Isotropic and nonisotropic components of earthquakes and nuclear explosions on the Lop Nor test site, China, *Pure Appl. Geophys.*, 158, 1497–1515.

Buskirk, R. E., Frohlich, C. and Latham, G. V., 1981: Unusual animal behavior before earthquakes: A review of possible sensory mechanisms, *Rev. Geophys. Space Phys.*, 19, 247–270.

Canitez, N., 1977:, Optimum filter for surface-wave group-velocity determination, *Bull. Seism. Soc. Am.*, 67, 79–85.

Capon, J., 1970: Analysis of Rayleigh-wave multipath propagation at LASA, *Bull. Seism. Soc. Am.*, 60, 1701–1731.

Cara, M., 1973: Filtering of dispersed wavetrains, *Geophys. J. R. Astr. Soc.*, 33, 65–80.

Carder, D. S., 1934: Seismic surface waves and the crustal structure of the Pacific region, *Bull. Seism. Soc. Am.*, 24, 231–302.

Cháb, J., Šrámek, J., Pokorný, L., Chlupáčová, M., Manová, M., Vejnar, Z., Waldhausrová, J. and Žáček, V., 1997: Geological interpretation of major regional units – the Teplá-Barrandian Unit, in: Vrána, S. and Štědrá, V. (eds): *Geological model of Western Bohemia related to the KTB borehole in Germany*, Czech Geological Survey, Prague, 80–104.

Chang, S.-J., Baag, C.-E. and Langston, C. A., 2004: Joint analysis of teleseismic receiver functions and surface wave dispersion using the genetic algorithm, *Bull. Seism. Soc. Am.*, 94, 691–704.

Chávez-García, F. J., Ramos-Martínez, J. and Romero-Jimenéz, E., 1995: Surface-wave dispersion analysis in Mexico City, *Bull. Seism. Soc. Am.*, 85, 1116–1126.

Chen, Ch. W., Rondenay, S., Weeraratne, D. S. and Snyder, D. B., 2007: New constraints on the upper mantle structure of the Slave craton from Rayleigh wave inversion, *Geophys. Res. Lett.*, 34, L10301, doi: 10.1029/2007GL029535.

Chimera, G., Aoudia, A., Saraó, A. and Panza, G. F., 2003: Active tectonics in Central Italy: constraints from surface wave tomography and source moment tensor inversion, *Phys. Earth Planet. Inter.*, 138, 241–262.

Čermák, F., 1990: Frequency and time-frequency methods of surface wave dispersion estimation, *Diploma thesis*, Department of Geophysics, Faculty of Mathematics and Physics, Charles University, Prague. (Spektrální a spektrálně časové metody výpočtu disperze povrchových vln. Diplomová práce, KG MFF UK, Praha, in Czech.)

Červený, V., 2001: Seismic ray theory, *Cambridge University Press*, Cambridge, UK.

Curtis, A., Trampert, J., Snieder, R. and Dost, B., 1998: Eurasian fundamental mode surface wave phase velocities and their relationship with tectonic structures, *J. Geophys. Res.*, 103, 26, 919–947.

Danesi, S and Morelli, A., 2001: Structure of the upper mantle under the Antarctic Plate from surface wave tomography, *Geophys. Res. Lett.*, 28, 4395–4398.

Das, T. and Nolet, G., 1995: Crustal thickness using high frequency Rayleigh waves, *Geophys. Res. Lett.*, 22, 539–542.

Davis, J. P. and Smalley, R. Jr., 2009: Love wave dispersion in central North America determined using absolute displacement seismograms from high-rate GPS, *J. Geophys. Res.*, 114, B11303, doi: 10.1029/2009JB006288.

Dean, E. A., 1986: The simultaneous smoothing of phase and group velocities from multi-event surface wave data, *Bull. Seism. Soc. Am.*, 76, 1367–1383.

De Lisle, J. F., 1941: On dispersion of Rayleigh waves from the North Pacific earthquake of November 10, 1938,

Bull. Seism. Soc. Am., 31, 303–307.

Delorey, A. A., Dunn, R. A. and Gaherty, J. B., 2007: Surface wave tomography of the upper mantle beneath the Reykjanes ridge with implications for ridge-hot spot interaction, *J. Geophys. Res.*, 112, B08313, doi: 10.1029/2006JB004785.

Deschamps, G. A., 1971: Gaussian beam as a bundle of complex rays, *Electr. Lett.*, 7, 684–685.

Ditmar, P. G. and Yanovskaya, T. B., 1987: An extension of the Backus-Gilbert technique for estimating lateral variations of surface wave velocities, *Izvestia AN SSSR, Fizika Zemli*, 6, 30–40 (in Russian).

Dobeš, K., 1981: Dynamic Spectral Analysis of Oscillatory Signals in Geophysics, *Geophysical Syntheses in Czechoslovakia*, Bratislava, 79–96.

Dorman, J. and Ewing, M., 1962: Numerical inversion of Seismic surface wave dispersion data and crust-mantle structure in the New York-Pennsylvania area, *J. Geophys. Res.*, 67, 5227–5241.

Durek, J. J., Ritzwoller, M. H. and Woodhouse, J. H., 1993: Constraining upper mantle anelasticity using surface wave amplitude anomalies, *Geophys. J. Int.*, 114, 249–272.

Drake, L. A. and Bolt, B. A., 1980: Love waves normally incident at a continental boundary, *Bull. Seism. Soc. Am.*, 70, 1103–1123.

Dziewonski, A., Bloch, S. and Landisman, M., 1969: A technique for the analysis of transient seismic signals, *Bull. Seism. Soc. Am.*, 59, 427–444.

Dziewonski, A., Mills, J. and Bloch, S., 1972: Residual dispersion measurement – a new method of surface-wave analysis, *Bull. Seism. Soc. Am.*, 62, 129–139.

Dziewonski, A. and Anderson, D.L., 1981: Preliminary reference Earth model, *Phys. Earth Planet. Inter.*, 25, 297–356.

Dziewonski, A. M. and Romanowicz, B. A., 2007: Overview; in Romanowicz, B. A. and Dziewonski, A. M (eds.): *Vol. 1 – Seismology and structure of the Earth*; in Schubert, G. (ed.): *Treatise on Geophysics*, Elsevier, Amsterdam, pp 1–29.

Ekström, G., Tromp, J. and Larson, E. W. F., 1997: Measurements and global models of surface wave propagation, *J. Geophys. Res.*, 102, 8137–8158.

Ekström, G., 2006: Global detection and location of seismic sources by using surface waves, *Bull. Seism. Soc. Am.*, 96, 1201–1212.

Ekström, G., Abers, G. A. and Webb, S. C., 2009: Determination of surface-wave phase velocities across USArray from noise and Aki's spectral formulation, *Geophys. Res. Lett.*, 36, L18301, doi: 10.1029/2009GL039131.

Essen, H.-H., Krüger, F., Dahm, T. and Grevemeyer, I., 2003: On the generation of secondary microseisms observed in northern and central Europe, *J. Geophys. Res.*, 108, B10. 2506, doi: 10.1029/2002JB002338.

Evernden, J. F., 1953: Direction of approach of Rayleigh waves and related problems (Part I), *Bull. Seism. Soc. Am.*, 43, 335–374.

Evernden, J. F., 1954: Direction of approach of Rayleigh waves and related problems (Part II), *Bull. Seism. Soc. Am.*, 44, 159–184.

Ewing, M. and Press, F., 1952: Crustal structure and surface-wave dispersion. Part II Solomon Islands earthquake of July 29, 1950, *Bull. Seism. Soc. Am.*, 42, 315–325.

Ewing, M. and Press, F., 1954: An investigation of mantle Rayleigh waves, *Bull. Seism. Soc. Am.*, 44, 127–147.

Feng, C. C. and Teng, T., 1983: An error analysis of frequency-time analysis, *Bull. Seism. Soc. Am.*, 73, 143–155.

Feng, M., Assumpção, M. and Lee, S. V. d., 2004: Group-velocity tomography and lithospheric S-velocity structure of the South American continent, *Phys. Earth Planet. Inter.*, 147, 315–331.

Feng, M., Lee, S. and Assumpção, M., 2007: Upper mantle structure of South America from joint inversion of waveforms and fundamental mode group velocities of Rayleigh waves, *J. Geophys. Res.*, 112, B04312, doi: 10.1029/2006JB004449.

Ferreira, A. M. G. and Woodhouse, J. H., 2007: Source, path and receiver effects on seismic surface waves,
Geophys. J. Int., 168, 109–132.

Fischer, T. and Horálek, J., 2003: Space-time distribution of earthquake swarms in the principal focal zone of the NW Bohemia/Vogtland seismoactive region: period 1985 – 2001, *J. Geodyn.*, 32 (1–2), 125–144.

Forbriger, T., 2003a: Inversion of shallow-seismic wavefields. Part I: Wavefield transformation, *Geophys. J. Int.*, 153, 719–734.

Forbriger, T., 2003b: Inversion of shallow-seismic wavefields. Part II: Infering subsurface properties from wavefield transforms, *Geophys. J. Int.*, 153, 735–752.

Forsyth, D. W. and Li, A., 2005: Array analysis of two-dimensional variations in surface wave phase velocity and azimuthal anisotropy in the presence of multipathing interference, in: Levander, A. and Nolet, G., (eds.) 2005: *Seismic Earth – Array analysis of broadband seismograms*, American Geophysical Union, Washington, DC, 81–97.

Foti, S., Lancellotta, R., Sambuelli, L. and Socco, L. V., 2000: Notes on fk analysis of surface waves, *Annali di Geofisica*, 43, 1199–1209.

Freybourger, M., Gaherty, J. B., Jordan, T. H. and the Kaapvaal seismic group, 2001: Structure of the Kaapvaal craton from surface waves, *Geophys. Res. Lett.*, 28, 2489–2492.

Friederich, W. and Wielandt, E., 1995: Interpretation of seismic surface waves in regional networks: joint estimation of wavefield geometry and local phase velocity. Method and numerical tests, *Geophys. J. Int.*, 120, 731–744.

Friederich, W., 1998: Wave-theoretical inversion of teleseismic surface waves in a regional network: phase-velocity maps and a three-dimensional upper-mantle shear-wave-velocity model for southern Germany, *Geophys. J. Int.*, 132, 203–225.

Fukao, Y., Nishida, K. and Kobayashi, N., 2010: Seafloor topography, ocean infragravity waves, and background Love and Rayleigh waves, *J. Geophys. Res.*, 115, B04302, doi: 10.1029/2009JB006678.

Gabriels, P., Snieder, R. and Nolet, G., 1987: In situ measurements of shear wave velocity in sediments with higher-mode Rayleigh waves, *Geophys. Prospect.*, 35, 187–196.

Gaždová, R., Kolínský, P., Málek, J. and Vilhelm, J., 2008: Shear wave velocities inferred from surface wave dispersion beneath the Příbram array in the Czech Republic, *Acta Geodyn. Geomater.*, 5 (151), 247–255.

Geissler, W. H., 2005: Seismic and petrological investigations of the lithosphere in the swarm-earthquake and CO_2 degassing region Vogtland/NW-Bohemia, *PhD thesis, scientific technical report STR05/06*, GeoForschungsZentrum Potsdam, Potsdam, 150 pp.

Gouédard, P., Cornou, C. and Roux, P., 2007: Phase-velocity dispersion curves and small-scale geophysics using noise correlation slantstack technique, *Geophys. J. Int.*, doi: 10.1111/j.1365-246X.2007.03654.x.

Grad, M., Špičák, A., Keller, G. R., Guterch, A., Brož, M., Hegedüs, E. and Working Group, 2003: SUDETES 2003 seismic experiment, *Stud. Geophys. Geod.*, 47, 681–689.

Gregersen, S. and Alsop, L. E., 1976: Mode conversion of Love waves at a continental margin, *Bull. Seism. Soc. Am.*, 66, 1855–1872.

Griot, D.-A., Montagner, J.-P. and Tapponnier, P., 1998: Phase velocity structure from Rayleigh and Love waves in Tibet and its neighboring regions, *J. Geophys. Res.*, 103, 21215–21232.

Gudmundsson, Ó., Khan, A. and Voss, P., 2007: Rayleigh-wave group-velocity of the Icelandic crust from correlation of ambient seismic noise, *Geophys. Res. Lett.*, 34, L14314, doi: 10.1029/2007GL030215.

Guidarelli, M. Saraó, A. and Panza, G. F., 2002: Surface wave tomography and seismic source studies at Campi Flegrei (Italy), *Physics of the Earth and Planetary Interiors*, 134, 157–173.

Gupta, H. K., Nyman D. C. and Landisman, M., 1977:, Shield-like upper mantle structure inferred from long-period Rayleigh- and Love-wave dispersion investigations in the Middle East and Southeast Asia, *Bull. Seism. Soc. Am.*, 67, 103–119.

Guterch, A., Grad, M., Špičák, A., Brückl, E., Hegedüs, E., Keller, G. R., Thybo, H. and CELEBRATION 2000, ALP 2002, SUDETES 2003 working groups, 2003: An overview of recent seismic refraction experiments in Central Europe, *Stud. Geophys. Geod.*, 47, 651–657.

Guterch, A., Grad, M., Keller, G. R., Posgay, K., Vozár, J., Špičák, A., Brückl, E., Hajnal, Z., Thybo, H., Selvi, O. and CELEBRATION 2000 experiment team, 2003: CELEBRATION 2000 seismic experiment, *Stud. Geophys. Geod.*, 47, 659–669.

Harkrider, D. G. and Anderson, D. L., 1962: Computation of surface wave dispersion for multilayered anisotropic media, *Bull. Seism. Soc. Am.*, 52, 321–332.

Harkrider, D. G. and Anderson, D. L., 1966: Surface wave energy from point sources in plane layered Earth models, *J. Geophys. Res.*, 71, 2967–2980.

Haskell, N. A., 1953: The dispersion of surface waves on multilayered media, *Bull. Seism. Soc. Am.*, 43, 17–34.

He, Z., Su, W. and Ye, T., 2004: Seismic tomography of Yunnan region using short-period surface wave phase velocity, *Acta Seismologica Sinica*, 17, 642–650.

Herrin, E. and Goforth, T., 1977: Phase-matched filters: Application to the study of Rayleigh waves, *Bull. Seism. Soc. Am.*, 67, 1259–1275.

Herrmann, R. B. (ed.), 1992, 2002: Computer Programs in Seismology (various versions), Department of Earth and Atmospheric Sciences, Saint Louis University, St. Louis, Missouri.
http://www.eas.slu.edu/People/RBHerrmann/CPS330.html.

Heuer, B., Geissler, W. H., Kind, R. and Kämpf, H., 2006: Seismic evidence for asthenospheric updoming beneath the western Bohemian Massif, central Europe, *Geophys. Res. Lett.*, 33, L05311, doi: 10.1029/2005GL025158.

Heuer, B., Kämpf, H., Kind, R. and Geissler, W. H., 2007: Seismic evidence for whole lithosphere separation between Saxothuringian and Moldanubian tectonic units in central Europe, *Geophys. Res. Lett.*, 34, L09304, doi: 10.1029/2006GL029188.

Hobiger, M., Bard, P.-Y., Cornou, C. and Bihan, N. L., 2009: Single station determination of Rayleigh wave ellipticity by using the random decrement technique (RayDec), *Geophys. Res. Lett.*, 36, L14303, doi: 10.1029/2009GL038863.

Holub, K., 1977: Short-period Rayleigh waves recorded in the Western Carpathians during DSS, *Stud. Geophys. Geod.*, 21, 281–284.

Holub, K. and Novotný, O., 1997: Interpretation of the dispersion curves of short-period Rayleigh waves observed in the West Carpathians, *Acta Montana*, 11, 49–58.

Horálek, J., Vavryčuk, V., Plešinger, A., Pšenčík, I., Jedlička, P. and Soukup, J., 1987: Refined localization of selected Jan. 5 – Feb. 6, 1986 events of the West-Bohemian earthquake swarm, in: Procházková, D., (ed) 1987: *Earthquake swarm 1985/86 in Western Bohemia – Proceedings of workshop in Mariánské Lázně*, Czechoslovak Academy of Sciences, Geophysical Institute, Prague, 226–235.

Horálek, J., Fischer, T., Bouškova, A. and Jedlička, P., 2000: The Western Bohemia/Vogtland region in the light of the WEBNET network, *Stud. Geophys. Geod.*, 44, 107–125.

Hrubcová P., Środa P., Špičák A., Guterch A., Grad M., Keller G. R., Brueckl E., and Thybo H., 2005: Crustal and uppermost mantle structure of the Bohemian Massif based on CELEBRATION 2000 data, *J. Geophys. Res.*, 110, B11305.

Hwang, R.-D. and Yu, G.-K., 2005: Shear-wave velocity structure of upper mantle under Taiwan from the array analysis of surface waves, *Geophys. Res. Lett.*, 32, L07310, doi: 10.1029/2004GL021868.

ISC, 2001: International Seismological Centre, *On-line Bulletin*, http://www.isc.ac.uk/Bull, Internatl., Seis. Cent., Thatcham, United Kingdom.

Isse, T. Suetsugu, D., Shiobara, H., Fukao, Y., Mochizuki, K., Kanazawa, T., Sugioka, H., Kodaira, S. and Hino, R., 2000: Rayleigh wave phase velocities beneath the northeastern Philippine Sea as determined by data from long term broadband ocean bottom seismographs, *Frontier research on Earth Evolution*, 1, 31–35.

Its, E. N. and Lee, J. S., 1993: Reflection and transmission of surface waves at a vertical interface in anisotropic elastic media, *Bull. Seism. Soc. Am.*, 83, 1355–1372.

Janský, J. and Novotný, O., 1997: Reinterpretation of the travel times of P waves generated by quarry blasts in Western Bohemia, *Acta Montana*, 11 (104), 35–48.

Janský, J., 2000: Grid search hypocentral location method in simple 1-D media, *Acta Montana*, 16 (118), 71–84.

Janský, J., Novotný, O., 1997: Reinterpretation of the travel times of P waves generated by quarry blasts in Western Bohemia, *Acta Montana*, 11 (104), 35–48.

Janský, J., Horálek, J., Málek, J. and Boušková, A., 2000: Homogeneous velocity models of the West Bohemian swarm region obtained by grid search, *Stud. Geophys. Geod.*, 44, 158–174.

Juliá, J., Assumpção, M. and Rocha, M. P., 2008: Deep crustal structure of the Paraná Basin from receiver functions and Rayleigh-wave dispersion: Evidence for a fragmented cratonic root, *J. Geophys. Res.*, 113, B08318, doi: 10.1029/2007JB005374.

Julia, J., Jagadeesh, S., Rai, S. S. and Owens, T. J., 2009: Deep crustal structure of the Indian shield from joint inversion of P wave receiver functions and Rayleigh wave group velocities: Implications for Precambrian crustal evolution, *J. Geophys. Res.*, 114, B10313, doi: 10.1029/2008JB006261.

Kang, T.-S. and Shin, J. S., 2006: Surface-wave tomography from ambient seismic noise of accelerograph networks in southern Korea, *Geophys. Res. Lett.*, 33, L17303, doi: 10.1029/2006GL027044.

Karagianni, E. E., Panagiotopoulos, D. G., Panza, G. F., Suhadolc, P., Papazachos, C. B., Papazachos, B. C., Kiratzi, A., Hatzfeld, D., Makropoulos, K., Priestley. K., Vuan, A., 2002: Rayleigh wave group velocity tomography in the Aegean area, *Tectonophysics*, 358, 187–209.

Keilis-Borok, ed., 1989: Seismic surface waves in a laterally inhomogeneous Earth, *Kluwer Academic Publishers*, Dordrecht/Boston/London 1989, 294 pp.

Keller, J. B. and Streifer, W., 1971: Complex rays with an application to Gaussian beams, *J. Opt. Soc. Am.*, 61, 40–43.

Kennett, B. L. N. and Yoshizawa, K., 2002: A reappraisal of regional surface wave tomography, *Geophys. J. Int.*, 150, 37–44.

Khan, A., Boschi, L. and Connolly, J. A. D., 2009: On mantle chemical and thermal heterogeneities and anisotropy as mapped by inversion of global surface wave data, *J. Geophys. Res.*, 114, B09305, doi: 10.1029/2009JB006399.

Knopoff, L., Mueller, S. and Pilant, W. L., 1966: Structure of the crust and upper mantle in the Alps from the phase velocity of Rayleigh waves, *Bull. Seism. Soc. Am.*, 56, 1009–1044.

Knopoff, L. and Mal, A. K., 1967: Phase velocity of surface waves in the transition zone of continental margins, *J. Geophys. Res.*, 72, 1769–1776.

Knopoff, L., Berry, M. J. and Schwab, F. A., 1967: Tripartite phase velocity observations in laterally heterogeneous regions, *J. Geophys. Res.*, 72, 2595–2601.

Kobayashi, R. and Nakanishi, I., 1998: Location of Love-to-Rayleigh conversion due to lateral heterogeneity or azimuthal anisotropy in the upper mantle, *Geophys. Res. Lett.*, 25, 1067–1070.

Kobayashi, R. and Zhao, D., 2004: Rayleigh-wave group velocity distribution in the Antarctic region, *Phys. Earth Planet. Inter.*, 141, 167–181.

Kocaoglu, A. H., Long, L. T., 1993: A review of time-frequency analysis techniques for estimation of group velocities, *Seism. Res. Lett.*, 64, 157–167.

Kolář, P. and Boušková, A., 2003: On some anomalies of v_p/v_s ratio of West Bohemian swarm 2000 – preliminary results, *Acta Montana*, 22 (129), 51–57.

Kolínský, P., 2003: Dispersion of seismic surface waves along selected Eurasian paths, *Diploma thesis*, Department of Geophysics, Faculty of Mathematics and Physics, Charles University, Prague (Disperze povrchových seismických vln podél vybraných euroasijských tras, *Diplomová práce*, KG MFF UK, Praha, in Czech).

Kolínský, P., 2004: Surface wave dispersion curves of Eurasian earthquakes: the SVAL program, *Acta Geodyn. Geomater.*, 1 (134), 165–185.

Kolínský, P., 2005: Seismic velocity model in the vicinity of Eger Rift from dispersion of surface waves, Final report about the Internal Start Project of the Grant Agency of the Academy of Sciences of the Czech Republic, *Acta Research Reports*, 14, 67–71.

Kolínský, P. and Brokešová, J., 2007: The Western Bohemia uppermost crust shear wave velocities from Love wave dispersion, *Journal of Seismology*, 11, 101–120.

Kolínský, P. and Brokešová, J., 2008: The Western Bohemia uppermost crust Rayleigh wave tomography, *Acta Geodyn. Geomater.*, 5, (149), 5–17.

Kolínsky, P., Eisner, L., Grechka, V., Jurick, D. and Duncan, P., 2009: Observation of shear-wave splitting from microseismicity induced by hydraulic fracturing – a non-VTI story, *71st EAGE Conference & Exhibition, Extended Abstracts*, X014.

Kolínský, P., Málek, J. and Brokešová, J., 2010: Shear wave crustal velocity model of the western Bohemian Massif from Love wave phase velocity dispersion, *Journal of Seismology*, in press.

Kristeková, M., 2006: Frequency time analysis of seismic signals, *PhD thesis*, Geophysical Institute, Slovak Academy of Sciences, Bratislava, (Časovo-frekvenčná analýza seizmických signálov, *dizertačná práca*, Geofyzikálny ústav, Slovenská aladémia vied, Bratislava), 182 pages (in Slovak).

Kugler, S., Bohlen, T., Forbriger, T., Bussat, S. and Klein. G., 2007: Scholte-wave tomography for shallow-water

marine sediments, *Geophys. J. Int.*, 168. 551–570.

Kuo, J., Brune, J. and Major, M., 1962: Rayleigh wave dispersion in the Pacific Ocean for the period range 20 to 140 seconds, *Bull. Seism. Soc. Am.*, 52, 333–357.

Kurrle, D., Igel, H., Ferreira, A. M. G. and Wassermann, J., 2010: Can we estimate local Love wave dispersion properties from collocated amplitude measurements of translations and rotations? *Geophys. Res. Lett.*, 37, L04307, doi: 10.1029/2009GL042215.

Landisman, M., Dziewonski, A. and Satô, Y., 1969: Recent improvements in the analysis of surface wave observations, *Geophys. J. Royal Astron. Soc.*, 17, 369–403.

Langston, Ch. A., 1989: Scattering of long-period Rayleigh waves in western North America and the interpretation of coda Q measurements, *Bull. Seism. Soc. Am.*, 79, 774–789.

Laske, G., 1995: Global observations of off-great-circle propagation of long-period surface waves, *Geophys. J. Int.*, 123, 245–259.

Laske, G. and Masters, G., 1996: Constraints on global phase velocity maps from long-period polarization data, *J. Geophys. Res.*, 101, 16059–16075.

Lawrence, J. F. and Wiens, D. A., 2004: Combined receiver-function and surface wave phase-velocity inversion using a niching genetic algorithm: Application to Patagonia, *Bull. Seism. Soc. Am.*, 94, 977–987.

Lay, T. and Kanamori, H., 1985: Geometric effects of global lateral heterogeneity on long-period surface wave propagation, *J. Geophys. Res.*, 90, 605–621.

Lay, T. and Wallace, T.C., 1995: Modern global seismology, *Academic Press, Inc.*, International Geophysics Series, San Diego.

Lee, van der, S. and Frederiksen, A., 2005: Surface wave tomography applied to the North American upper mantle, in: Levander, A. and Nolet, G., (eds.) 2005: *Seismic Earth – Array analysis of broadband seismograms*, American Geophysical Union, Washington, DC, 67–80.

Lebedev, S., Nolet, G. and Hilst, van der, R. D., 1997: The upper mantle beneath the Philippine Sea region from waveform inversions, *Geophys. Res. Lett.*, 24, 1851–1854.

Levshin, A. L., Pisarenko, V.F. and Pogrebinsky, G.A., 1972: On a frequency-time analysis of oscillations, *Ann. Geophys.*, 28, 211–218.

Levshin, A. L., Yanovskaya, T. B., Lander, A. V., Bukchin, B. G., Barmin, M. P., Ratnikova, L. I. and Its, E. N., 1989: Interpretation of surface wave observations – frequency-time analysis, in: Keilis-Borok, V. I. (ed.): *Seismic surface waves in a laterally inhomogeneous Earth*, Kluwer Academic Publishers, Dordrecht/Boston/London, 153–163.

Levshin, A. L., Ratnikova, L. and Berger, J., 1992: Peculiarities of surface-wave propagation across Central Eurasia, *Bull. Seism. Soc. Am.*, 82, 2464–2493.

Levshin, A. L., Ritzwoller, M. H., Ratnikova, 1994: The nature and cause of polarization anomalies of surface waves crossing northern and central Eurasia, *Geophys. J. Int.*, 117, 577–590.

Levshin, A. L. and Ritzwoller, M. H., 1995: Characteristic of surface waves generated by events on and near the Chinese nuclear test site, *Geophys. J. Int.*, 123, 131–148.

Levshin, A. L., Ritzwoller, M. H., Ratnikova, L. I. and Egorkin-Jr, A. A., 1997: Surface wave tomographic study of central Asia tectonic regimes, in Fuchs, K (ed.): *Upper mantle heterogeneities from active and passive seismology*, Proceedings of the NATO advanced research workshop, NATO ASI Series Volume, Kluwer Academic Publ., 257–268.

Levshin, A. L., Ritzwoller, M. H. and Resovsky, J. S., 1999: Source effects on surface wave group travel times and group velocity maps, *Phys. Earth Planet. Inter.*, 115, 293–312.

Levshin, A. L. and Ritzwoller. M. H., 2001: Automated detection, extraction and measurement of regional surface waves, *Pure Appl. Geophys.*, 158, 1531–1545.

Levshin, A. L., Ritzwoller, M. H., Barmin, M. P., Villaseñor, A., Padgett, C. A., 2001: New constraints on the Arctic crust and uppermost mantle: surface wave group velocities, P_n and S_n, *Phys. Earth Planet. Inter.*, 123, 185–204.

Levshin, A. L., 2002: Surface wave analysis and phenomenology, *6th Workshop on three-dimensional modeling of seismic waves generation and their propagation*, The Abdus Salam International Centre for Theoretical Physics.

Levshin, A. L., Ritzwoller. M. H. and Shapiro, N. M., 2004: The use of crustal higher modes to constrain crustal structure across Central Asia, *Geophys. J. Int.*, 160, 961–972, doi: 10.1111/j.1365-246x.2005.02535.x.

Levshin, A. L., Barmin, M. P., Ritzwoller, M. H. and Trampert, J., 2005: Minor-arc and major-arc global surface wave diffraction tomography, *Phys. Earth Planet. Inter.*, 149, 205–223.

Levshin, A. L., Schweitzer, J., Weidle, Ch., Shapiro, N. M. and Ritzwoller, M. H., 2007: Surface wave tomography of the Barents Sea and surrounding regions, *Geophys. J. Int.*, 170, 441–459.

Liang, Ch. and Langston, Ch. A., 2009: Three-dimensional crustal structure of eastern North America extracted from ambient noise, *J. Geophys. Res.*, 114, B03310, doi: 10.1029/2008JB005919.

Liebermann, R. C., King, C.-Y., Brune, J. N. and Pomeroy, P. W., 1966: Excitation of surface waves by the underground nuclear explosion Long Shot, *J. Geophys. Res.*, 71, 4333–4339.

Liebermann, R. C. and Pomeroy, P. W., 1969: Relative excitation of surface waves by earthquakes and underground explosions, *J. Geophys. Res.*, 74, 1575–1590.

Lin. F.-Ch., Ritzwoller, M. H., Shapiro, N. M., 2006: Is ambient noise tomography across ocean basins possible? *Geophys. Res. Lett.*, 33, L14304, doi: 10.1029/2006GL026610.

Lin, F.-Ch., Ritzwoller, M. H., Townend, J., Bannister, S. and Savage, M. K., 2007: Ambient noise Rayleigh wave tomography of New Zealand, *Geophys. J. Int.*, 170, 649–666.

Lin, F.-Ch., Moschetti, M. P. and Ritzwoller, M. H., 2008: Surface wave tomography of the western United States from ambient seismic noise: Rayleigh and Love wave phase velocity maps, *Geophys. J. Int.*, doi: 10.1111/j.1365-246X.2008.03720.x.

Lin, F.-Ch., Ritzwoller, M. H. and Snieder, R., 2009: Eikonal tomography: surface wave tomography by phase front tracking across a regional broad-band seismic array, *Geophys. J. Int.*, 177, doi: 10.1111/j.1365-246X.2009.04105.x.

Lokajíček, T., Janatková, Z., Plomerová, J., 1987: Travel times of seismic waves of the 1985-86 swarm in Western Bohemia, in: Procházková, D. (ed): *Earthquake swarm 1985/86 in Western Bohemia – Proceedings of Workshop in Mariánské Lázně*, Czechoslovak Academy of Sciences, Geophysical Institute, Prague, 236–246.

López-Pineda, L., Rebollar, C. J. and Quintanar, L., 2007: Crustal thickness estimates for Baja California, Sonora, and Sinaloa, Mexico, using disperse surface waves, *J. Geophys. Res.*, 112, B04308, doi: 10.1029/2005JB003899.

Love, A. E. H., 1911: Some problems of geodynamics, *Cambridge University Press*, Cambridge, 180 pp.

Luo, Y., Xia, J., Liu, J., Liu, Q. and Xu, S., 2007: Joint inversion of high-frequency surface waves with fundamental and higher modes, *Journal of Applied Geophysics*, doi: 10.1016/j.jappgeo.2007.02.004.

Maceira, M. and Ammon, C. J., 2009: Joint inversion of surface wave velocity and gravity observations and its application to central Asian basins shear wave velocity structure, *J. Geophys. Res.*, 114, B02314, doi: 10.1029/2007JB005157.

Málek, J., Janský, J. and Horálek, J., 2000: Layered velocity models of the Western Bohemia region, *Stud. Geophys. Geod.*, 44, 475–490.

Málek, J., Brož, M., Fischer, T., Horálek, J., Hrubcová, P., Janský, J., Novotný, O., Růžek, B. and the CELEBRATION working group, 2001: Seismic measurements along short profiles in Western Bohemia during the CELEBRATION 2000 experiment, *Acta Montana*, 18 (121), 15–28.

Málek, J., Janský, J., Novotný, O. and Rössler, D., 2004: Vertically inhomogeneous models of the upper crustal structure in the West-Bohemian seismoactive region inferred from the CELEBRATION 2000 refraction data, *Stud. Geophys. Geod.*, 48, 709–730.

Málek, J. and Žanda, L., 2004: Seismic effects of the quarry blasts on the territory of Bohemia, *Acta Geodyn. Geomater.*, 1 (134), 291–302.

Málek, J., Horálek, J. and Janský, J., 2005: One-dimensional qP-wave velocity model of the upper crust for the West Bohemia/Vogtland earthquake swarm region, *Stud. Geophys. Geod.*, 49, 501–524.

Málek, J., Růžek, B., Kolář, P., 2007: Isometric method: efficient tool for solving non-linear inverse problems, *Stud. Geophys. Geod.*, 51, 469–491.

Malinowski, M., 2005: Analysis of Short-Period Rayleigh Waves Recorded in the Bohemian Massif Area During CELEBRATION 2000 Experiment, *Stud. Geophys. Geod.*, 49, 485–500.

Marone, F. Lee, van der, S. and Giardini D., 2004: Shallow anisotropy in the Mediterranean mantle from surface waves, *Geophys. Res. Lett.*, 31, L06624, doi: 10.1029/2003GL018948.

Masterlark, T., Haney, M., Dickinson, H., Fournier, T. and Searcy, Ch., 2010: Rheologic and structural controls on the deformation of Okmok volcano, Alaska: FEMs, InSAR, and ambient noise tomography, *J. Geophys. Res.*, 115, B02409, doi: 10.1029/2009JB006324.

Maupin, V., 2001: A multiple-scattering scheme for modelling surface wave propagation in isotropic and anisotropic three-dimensional structures, *Geophys. J. Int.*, 146, 332–348.

Maupin, V., 2002: The amplitude of the Love-Rayleigh discrepancy created by small-scale heterogeneities, *Geophys. J. Int.*, 150, 58–64.

Maupin, V., 2007: Introduction to mode coupling methods for surface waves, in: Wu, R.-S. and Maupin, V. (eds.): *Advances in wave propagation in heterogeneous Earth, Advances in geophysics*, 48, chapter 2, Elsevier, 127–155.

McEvilly, T. V., 1964: Central U.S. crust-upper mantle structure from Love and Rayleigh wave phase velocity inversion, *Bull. Seism. Soc. Am.*, 54, 1997–2015.

McMechan, G. A. and Yedlin, M. J., 1981: Analysis of dispersive waves by wave field transformation, *Geophysics*, 46, 869–874.

Meier, T., Malischewsky, P. G. and Neunhöfer, H., 1997: Reflection and transmission of surface waves at a vertical discontinuity and imaging of lateral heterogeneity using reflected fundamental Rayleigh waves, *Bull. Seism. Soc. Am.*, 87, 1648–1661.

Meier, T., Lebedev, S., Nolet, G. and Dahlen, F. A., 1997: Diffraction tomography using multimode surface waves, *J. Geophys. Res.*, 102, 8255–8267.

Meier, U., Curtis, A. and Trampert, J., 2007: Fully nonlinear inversion of fundamental mode surface waves for a global crustal model, *Geophys. Res. Lett.*, 34, L16304, doi: 10.1029/2007GL030989.

Mellors, R. J., Vernon, F. L. and Thomson, D. J., 1998: Detection of dispersive signals using multitaper dual-frequency coherence, *Geophys. J. Int.*, 135, 146–154.

Miller, M. S., Levander, A., Niu, F. and Li, A., 2009: Upper mantle structure beneath the Caribbean-South American plate boundary from surface wave tomography, *J. Geophys. Res.*, 114, B01312, doi: 10.1029/2007JB005507.

Mitra, S., Priestley, K., Gaur, V. K. and Rai, S. S., 2006: Shear-Wave Structure of the South Indian lithosphere from Rayleigh wave phase-velocity measurements, *Bull. Seism. Soc. Am.*, 96, 1551–1559.

Miyazawa, M. and Brodsky, E. E., 2008: Deep low-frequency tremor that correlates witgh passing surface waves, *J. Geophys. Res.*, 113, B01307, doi: 10.1029/2006JB004890.

Mlčoch, B., Schulmann, K., Šrámek, J., Manová, M., Pokorný, L., Fiala, J. and Vejnar, Z., 1997: Geological interpretation of major regional units – the Saxothuringian zone, in: Vrána, S. and Štědrá, V. (eds):

Geological Model of Western Bohemia Related to the KTB Borehole in Germany, Czech Geological Survey, Prague, 51–61.

Montagner, J.-P. and Jobert, N., 1983: Variation with age of the deep structure of the Pacific Ocean inferred from very long-period Rayleigh wave dispersion, *Geophys. Res. Lett.*, 10, 273–276.

Montagner, J.-P. and Tanimoto, T., 1990: Global anisotropy in the upper mantle inferred from the regionalization of phase velocities, *J. Geophys. Res.*, 95, 4797–4819.

Montagner, J.-P. and Tanimoto, T., 1991: Global upper mantle tomography of seismic velocity and anisotropies, *J. Geophys. Res.*, 96, 20337–20351.

Moschetti, M. P., Ritzwoller, M. H. and Shapiro, N. M., 2007: Surface wave tomography of the western United States from ambient seismic noise: Rayleigh wave group velocity maps, *Geochemistry, Geophysics, Geosystems*, 8, Q08010, doi: 10.1029/2007GC001655, ISSN: 1525–2027.

Murphy, J. R. and Shan, H. K., 1988: An analysis of the effects of site geology on the characteristics of near-field Rayleigh waves, *Bull. Seism. Soc. Am*, 78, 64–82.

Muyzert, E. and Snieder, R., 1996: The influence of errors in source parameters on phase velocity measurements of surface waves, *Bull. Seism. Soc. Am.*, 86, 1863–1872.

Nafe, J. E. and Brune, J. N., 1960: Observations of phase velocity for Rayleigh waves in the period range 100 to 400 seconds, *Bull. Seism. Soc. Am.*, 50, 427–439.

Nakanishi, I. and Anderson, D. L., 1982: Worldwide distribution of group velocity of mantle Rayleigh waves as determined by spherical harmonic inversion, *Bull. Seism. Soc. Am.*, 72, 1185–1194.

Nakanishi, I. and Anderson, D. L., 1983: Measurements of mantle wave velocities and inversion for lateral heterogeneity and anisotropy, 1. Analysis of great circle phase velocities, *J. Geophys. Res.*, 88, 10267–10283.

Nehybka, V. and Skácelová, Z., 1997: Seismological Study of the Kraslice/Vogtland-Oberpfalz Region, in: Vrána, S. and Štědrá, V. (eds.): *Geological Model of Western Bohemia Related to the KTB Borehole in Germany*, Czech Geological Survey, Prague, 186–190.

NEIC (National Earthquake Information Center), 2006: PDE Catalog, Washington, US, neic.usgs.gov.

Nishida, K., Kawakatsu, H., Fukao, Y. and Obara, K., 2008: Background Love and Rayleigh waves simultaneously generated at the Pacific Ocean floors, *Geophys. Res. Lett.*, 35, L16307, doi: 10.1029/2008GL347753.

Novotný, M., 1997: The ray interpretation of DSS data from the VI/70 seismic transect across the Bohemian Massif, in: Vrána, S. and Štědrá, V. (eds): *Geological Model of Western Bohemia Related to the KTB Borehole in Germany*, Czech Geological Survey, Prague, 131–139.

Novotný, O., 1970: Partial derivatives of dispersion curves of Love waves in a layered medium, *Stud. Geophys. Geod.*, 14, 36–50.

Novotný, O., 1983: Theoretical dispersion curves for the seismic profile Kašperské hory (Czechoslovakia) – Ksiaz (Poland), *Stud. Geophys. Geod.*, 27, 157–163.

Novotný, O., Proskuryakova, T. A., Shilov, A. V., 1995: Dispersion of Rayleigh waves along the Prague-Warsaw profile, *Stud. Geophys. Geod.*, 39, 138–147.

Novotný, O., Burlako, L. V. and Proskuryakova, T. A., 1995: Modifications of the dispersion relations for surface waves in a layer on a half-space, *Stud. Geophys. Geod.*, 40, 166–177.

Novotný, O., 1996: A preliminary seismic model for the region of the West-Bohemian earthquake swarms, *Stud. Geophys. Geod.*, 40, 353–366.

Novotný, O., Grad, M., Lund, C. E. and Urban, L., 1997: Verification of the lithospheric structure along profile Uppsala-Prague using surface wave disperison, *Stud. Geophys. Geod.*, 41, 15–28.

Novotný, O. and Urban, L., 1988: Seismic models of the Bohemian Massif and some adjacent regions derived from deep seismic soundings and surface waves investigations: a review, in: Procházková, D. (ed): *Induced seismicity and associated phenomena*, Proceedings of conference in Liblice, Geophysical Institute, Czechoslovak Academy of Sciences, Prague, 227–249.

Novotný, O., 1999: Seismic surface waves, *Lecture notes for post-graduate studies*, Instituto de Física, Instituto de Geociências, Salvador, Bahia (textbook).

Novotný, O., 1999: A fast method of computing group-velocity partial derivatives for Love waves propagating in a layer on a half-space, *Stud. Geophys. Geodet.*, 43, 78–86.

Novotný, O., Zahradník, J. and Tselentis, G-A., 2001: Northwestern Turkey earthquakes and the crustal structure inferred from surface waves observed in western Greece, *Bull. Seism. Soc. Am.*, 91, 875–879.

Novotný, O., Málek, J., 2002: Note of the direct computation of geodetic distances and azimuths on an ellipsoid of revolution, *Acta Montana*, 22 (129), 75–78.

Novotný, O., Janský, J. and Málek, J., 2004: Some aspects of the application of the Wiechert-Herglotz method to refraction data from Western Bohemia, *Acta Geodyn. Geomater.*, 1 (134), 157–164.

Novotný, O., Mufti, I. and Vicentini, A. G., 2005: Analytical partial derivatives of the phase- and group velocities for Rayleigh waves propagating in a layer on a half-space, *Stud. Geophys. Geod.*, 49, 305–321.

Noponen, I., 1966: Surface wave phase velocities in Finland, *Bull. Seism. Soc. Am.*, 56, 1093–1104.

Nyman, D. C. and Landisman, M., 1977: The display-equalized filter for frequency-time analysis, *Bull. Seism. Soc. Am.*, 67, 393–404.

Okabe, A., Kaneshima, S., Kanjo, K., Ohtaki, T. and Purwana, I., 2004: Surface wave tomography for southeastern Asia using IRIS-FARM and JISNET data, *Phys. Earth Planet. Inter.*, 146, 101–112.

Oldham, R. D., 1900: On the propagation of earthquake motion to great distances, *Philosophical transactions of the Royal Society of London*, series A, Containing Papers of a Mathematical or Physical Character, 194, 135–174.

Oliver, J. and Ewing, M., 1957: Higher modes of continental Rayleigh waves, *Bull. Seism. Soc. Am.*, 47, 187–204.

Oliver, J., Kovach, R. and Dorman, J., 1961: Crustal structure of the New York-Pennsylvania area, *J. Geophys. Res.*, 66, 215–225.

Oliver, J. and Dorman, J., 1961: On the nature of oceanic seismic surface waves with predominant periods of 6 to 8 seconds, *Bull. Seism. Soc. Am.*, 51, 437–455.

Oliver, J., 1962: A summary of observed seismic surface wave dispersion, *Bull. Seism. Soc. Am.*, 52, 81–86.

Park, Ch. B., Miller, R. D. and Xia, J., 1998: Imaging dispersion curves of surface waves on multi-channel record, *68th SEG Annual Meeting, Expanded Abstracts*, Kansas Geological Survey.

Pěč, K., Novotný, O., 1977: Joint interpretation of L_g and S_a waves based on spectral amplitudes of higher Love wave modes, *Stud. Geophys. Geod.*, 21, 242–248.

Pettersen, O. and Maupin, V., 2002: Lithospheric anisotropy on the Kerguelen hot spot track inferred from Rayleigh wave polarisation anomalies, *Geophys. J. Int.*,149, 225–246.

Pilant, W. L. and Knopoff, L., 1964: Observations of multiple seismic events, *Bull. Seism. Soc. Am.*, 54, 19–39.

Plešinger, A., 1979: The FBV broadband seismograph station profile KHC-KSP, *Stud. Geophys. Geod.*, 23, 296–299.

Plešinger, A., Neunhöfer, H. and Wielandt, E., 1991: Crust and upper mantle structure of the Bohemian Massif from the dispersion of seismic surface waves, *Stud. Geophys. Geod.*, 35, 184–195.

Plomerová, J., Achauer, U., Babuška, Vl., Vecsey, L. and BOHEMA working group, 2007: Upper mantle beneath the Eger Rift (Central Europe): plume or asthenosphere upwelling?, *Geophys. J. Int.*, 169, 675–682.

Plomerová, J., Babuška, V., Janatková, Z. and Lokajíček, T., 1987: Directional dependence of seismic waves propagation of the 1985-86 earthquake swarm in Western Bohemia, in: Procházková, D. (ed.): *Earthquake swarm 1985/86 in Western Bohemia – proceedings of workshop in Mariánské Lázně*, Czechoslovak Academy of Sciences, Geophysical Institute, Prague, 197–204.

Pollitz, F. F., 1994: Surface wave scattering from sharp lateral discontinuities, *J. Geophys. Res.*, 99, 21891–21909.

Pollitz, F. F., 2008: Observations and interpretation of fundamental mode Rayleigh wavefields recorded by the Transportable Array (USArray), *J. Geophys. Res.*, 113, B10311, doi: 10.1029/2007JB005556.

Pontevivo, A. and Panza, G. F., 2002: Group velocity tomography and regionalization in Italy and bordering areas, *Phys. Earth Planet. Inter.*, 134, 1–15.

Press, F., Ewing, M. and Oliver, J., 1956: Crustal structure and surface-wave dispersion in Africa, *Bull. Seism. Soc. Am.*, 46, 97–103.

Press, F., 1957: Determination of crustal structure from phase velocity of Rayleigh waves, Part II: San Francisco Bay region, *Bull. Seism. Soc. Am.*, 47, 87–88.

Press, H.W., Teukolsky, S. A., Vetterling, W. T. and Flannery, B.P., 1992: Numerical recipes in fortran, *World wide web sample pages from ...*, Cambridge University Press, Cambridge, UK.

Proskuryakova, T.A., Novotný, O. and Voronina, E. V., 1981: Studies of the Earth's structure by the surface-wave method (Central Europe) (Izuchenie stroeniya Zemli metodom poverkhnostnykh voln (Tsentral'naya Evropa)), Nauka, Moscow, in Russian, 92 pp.

Raykova, R. B. and Nikolova, S. B., 2000: Shear wave velocity models of the Earth's crust and uppermost mantle in the Balkan Peninsula and adjacent areas from Rayleigh waves, *Bulgarian Geophysical Journal*, 26, 11–27.

Raykova, R. B. and Nikolova, S. B., 2003: Anisotropy in the Earth's crust an uppermost mantle in southeastern Europe obtained from Rayleigh and Love surface waves, *Journal of Applied Geophysics*, 54, 247–256.

Raykova, R., 2005: Structure of the Earth's crust and upper mantle in southeastern Europe from surface waves, *PhD thesis*, Geophysical Institute of Bulgarian Academy of Sciences, Sofia, pp. 292.

Raykova, R. B. and Panza, G. F., 2006: Surface waves tomography and non-linear inversion in the southeast Carpathians, *Phys. Earth Planet. Inter.*, 157, 164–180.

Raykova, R. and Nikolova, S., 2007: Tomography and velocity structure of the crust and uppermost mantle in Southeastern Europe obtained from surface wave analysis, *Stud. Geophys. Geod.*, 51, 165–184.

Rayleigh, J. W. S., 1885: On waves propagating along the plane surface of an elastic solid, *Proc. London Math. Soc.*, 17, 4–11.

Rayleigh, J. W. S., 1900: Scientific papers, *Cambridge University Press*, vol. II. 1881 – 1887, 626 pp.

Ritzwoller, H. M. and Levshin A. L., 1998: Eurasian surface wave tomography: group velocities, *J. Geophys. Res.*, 103, B3, 4839–4878.

Ritzwoller, M. H., Shapiro, N. M., Levshin, A. L. and Leahy, G. M., 2001: Crustal and upper mantle structure beneath Antarctica and surrounding oceans, *J. Geophys. Res.*, 106, 30645–30670.

Ritzwoller, M. H. and Levshin, A. L., 2002: Estimating shallow shear velocities with marine multicomponent seismic data, *Geophysics*, 67, 1991–2004.

Ritzwoller. M. H., Shapiro, N. M., Barmin, M. P. and Levshin, A. L., 2002: Global surface wave diffraction tomography, *J. Geophys. Res.*, 107, B12, 2335, doi: 10.1029/2002JB001777.

Romanowicz, B., 1981: Depth resolution of earthquakes in central Asia by moment tensor inversion of long-period Rayleigh waves: Effects of phase velocity variations across Eurasia and their calibration, *J. Geophys. Res.*, 86, 5963–5984.

Romanowicz, B., 1995: A global tomographic model of shear attenuation in the upper mantle, *J. Geophys. Res.*, 100, 12375–12394.

Russell, D. R., Herrmann, R. B. and Hwang, H.-J., 1988: Application of frequency variable filters to surface-wave amplitude analysis, *Bull. Seism. Soc. Am.*, 78, 339–354.

Růžek B., Hrubcová P., Novotný M., Špičák A., Karousová O., 2007: Inversion of travel times obtained during active seismic refraction experiments CELEBRATION 2000, ALP 2002 AND SUDETES 2003, *Stud. Geophys. Geod.*, 51, 141–164.

Sabadell, F. J., Serón, F. J., Badal, J., 1997: A proper methodology aimed at surface wave tomography, *Annali di Geofysica*, XL, 195–207.

Sabra, K. G., Gerstoft, P., Roux, P., Kuperman, W. A. and Fehler, M. C., 2005a: Extracting time-domain Green's function estimates from ambient seismic noise, *Geophys. Res. Lett.*, 32, L03310, doi: 10.1029/2004GL021862.

Sabra, K. G., Gerstoft, P., Roux, P., Kuperman, W. A. and Fehler, M. C., 2005b: Surface wave tomography from microseisms in Souther California, *Geophys. Res. Lett.*, 32, L14311, doi: 10.1029/2005GL023155.

Saltzer, R. L., 2002: Upper mantle structure of the Kaapvaal craton from surface wave analysis – a second look, *Geophys. Res. Lett.*, 29, doi: 10.1029/2001GL013702.

Satô, Y, 1960: Synthesis of dispersed surface waves by means of Fourier transform, *Bull. Seism. Soc. Am.*, 50, 417–426.

Savage, W. A., 2004: An exact solution for effects of topography on free Rayleigh waves, *Bull. Seism. Soc. Am.*, 94, 1706–1727.

Schwab, F., 1970: Surface-wave dispersion computations: Knopoff's method, *Bull. Seism. Soc. Am.*, 60, 1491–1520.

Sebe, O., Forbriger, T. and Ritter, J. R. R., 2009: The shear wave velocity underneath Bucharest city, Romania, from the analysis of Love waves, *Geophys. J. Int.*, 176, 965–979.

Sekereš, J., 1983: Frequency-time analysis, *Master thesis*, Department of Geophysics, Faculty of Mathematics and Physics, Charles University, Prague (Frekvenčne-časová analýza, *Diplomová práce*, KG MFF UK, Praha, in Slovak).

Snieder, R., 1988a: Large-scale waveform inversions of surface waves for lateral heterogeneity 1. Theory and numerical examples, *J. Geophys. Res.*, 93, B10, 12055–12065.

Snieder, R., 1988b: Large-scale waveform inversions of surface waves for lateral heterogeneity 2. Application to surface waves in Europe and the Mediterranean, *J. Geophys. Res.*, 93, B10, 12067–12080.

Shapiro, N. M. and Singh, S. K., 1999: A systematic error in estimating surface-wave group-velocity dispersion curves and a procedure for its corrections, *Bull. Seism. Soc. Am.*, 89, 1138–1142.

Shapiro, N. M. and Ritzwoller, M. H., 2002: Monte-Carlo inversion for a global shear-velocity model of the crust and upper mantle, *Geophys. J. Int.*, 151, 88–105.

Shapiro, N. M., Ritzwoller, M. H., Mareschal, J. C. and Jaupart, C., 2004: Lithospheric structure of the Canadian shield inferred from inversion of surface-wave dispersion with thermodynamic a priori constraints, *Geological Society, London, Special Publications*, 239, 175–194.

Shapiro, N. M. and Campillo, M., 2004: Emergence of broadband Rayleigh waves from correlations of the ambient seismic noise, *Geophys. Res. Let.*, 31, L07614.

Shapiro, N. M., Campillo, M., Stehly, L. and Ritzwoller, M. H., 2005: High resolution surface wave tomography from ambient seismic noise, *Science*, 307, 1615–1618.

Shapiro, N. M., Ritzwoller, M. H. and Bensen, G. D., 2006: Source location of the 26 sec microseism from cross-correlations of ambient seismic noise, *Geophys. Res. Lett.*, 33, L18310, doi: 10.1029/2006GL027010.

Sieminski, A., Lévêque, J.-J. and Debayle, E., 2004: Can finite-frequency effects be accounted for in ray theory surface wave tomography? *Geophys. Res. Lett.*, 31, L24614, doi: 10.1029/2004GL021402.

Silveira, G., Stutzmann, E., Griot, D.-A., Montagner, J.-P. and Victor, L. M., 1998: Anisotropic tomography of the Atlantic Ocean from Rayleigh surface waves, *Phys. Earth Planet. Inter.*, 106, 257–273.

Silveira, G. and Stutzmann, E., 2002: Anisotropic tomography of the Atlantic Ocean, *Phys. Earth Planet. Inter.*, 132, 237–248.

Snieder, R., 1986: Phase speed perturbations and three-dimensional scattering effects of surface waves due to topography, *Bull. Seism. Soc. Am.*, 76, 1385–1392.

Snieder, R., 1988: Large-scale waveform inversions of surface waves for lateral heterogeneity 1. Theory and numerical examples, *J. Geophys. Res.*, 93, 12055–12065.

Snieder, R., 1988: Large-scale waveform inversions of surface waves for lateral heterogeneity 2. Application to surface waves in Europe and the Mediterranean, *J. Geophys. Res.*, 93, 12067–12080.

Spetzler, J., Trampert, J. and Snieder, R., 2001: Are we exceeding the limits of the great circle approximation in global surface wave tomography? *Geophys. Res. Lett.*, 28, 2341–2344.

Spetzler, J., Trampert, J. and Snieder, R., 2002: The effect of scattering in surface wave tomography, *Geophys. J. Int.*, 149, 755–767.

Špičák, A., Horálek, J., Boušková, A., Tomek, Č. and Vaněk, J., 1999: Magma intrusions and earthquake swarm occurrence in the western part of the Bohemian Massif, *Stud. Geophys. Geod.*, 43, 87–106.

Stange, S. and Friederich, W., 1993: Surface wave dispersion and upper mantle structure beneath southern Germany from joint inversion of network recorded teleseismic events, *Geophys. Res. Lett.*, 20 (21), 2375–2378.

Stephens, Ch. and Isacks, B. L., 1977: Toward an understanding of S_n: normal modes of Love waves in an oceanic structure, *Bull. Seism. Soc. Am.*, 67, 69–78.

Švancara, J. and Chlupáčová, M, 1997: Gravimetry – Density model of geological structure along the profile 9HR, in: Vrána, S. and Štědrá, V. (eds): *Geological model of Western Bohemia related to the KTB borehole in Germany*, Czech Geological Survey, Prague, 32–35.

Tanimoto, T. and Anderson, D. L., 1985: Lateral heterogeneity and azimuthal anisotropy of the upper mantle: Love and Rayleigh waves 100 – 250 s, *J. Geophys. Res.*, 90, 1842–1858.

Tanimoto, T., 2003: Geometrical approach to surface wave finite frequency effects, *Geophys. Res. Lett.*, 30, doi: 10.1029/2003GL017475.

Tape, C., Liu, Q. and Tromp, J., 2007: Finite-frequency tomography using adjoint methods – methodology

and examples using membrane surface waves, *Geophys. J. Int.*, 168, 1105–1129, doi: 10.1111/j.1365-246X.2006.03191.x.

Tarantola, A., 1987: Inverse problem theory: methods for data fitting and model parameter estimation, *Elsevier Science B.V.*, Amsterdam, Netherlands.

Thatcher, W. and Brune, J. N., 1969: Higher mode interference and observed anomalous apparent Love wave phase velocities, *J. Geophys. Res.*, 74, 6603–6611.

Thomson, W. T., 1950: Transmission of elastic waves through a stratified solid medium, *J. Appl. Phys.*, 21, 89–93.

Tibuleac, I. M. and Britton, J. M., 2006: An automated short-period surface-wave detection algorithm, *Bull. Seism. Soc. Am.*, 96, 334–343.

Toksöz, M. N. and Ben-Menahem, A., 1963: Velocities of mantle Love and Rayleigh waves over multiple paths, *Bull. Seism. Soc. Am.*, 53, 741–764.

Toksöz, M. N. and Anderson, D. L., 1966: Phase velocities of long-period surface waves and structure of the upper mantle, *J. Geophys. Res.*, 71, 1649–1658.

Tomek, Č., Dvořáková, V. and Vrána, S., 1997: Geological interpretation of the 9HR and 503M seismic profiles in Western Bohemia, in: Vrána, S. and Štědrá, V. (eds): *Geological model of Western Bohemia related to the KTB borehole in Germany*, Czech Geological Survey, Prague, 43–50.

Trampert, J. and Woodhouse, J., 1996: High resolution global phase velocity distribution, *Geophys. Res. Lett.*, 23, 21–24.

USGS/NEIC, 2003: United States Geological Survey / National Earthquake Information Center (Earthquake Hazards Program), http://neic.usgs.gov/neis/bulletin.

Vdovin, O., Rial, J. A., Levshin, A. L. and Ritzwoller, M. H., 1999: Group-velocity tomography of South America and the surrounding oceans, *Geophys. J. Int.*, 136, 324–340.

Velasco, A. A., Ammon, C. J., Farrell, J. and Pankow. K., 2004: Rupture directivity of the 3 November 2002 Denali Fault earthquake determined from surface waves, *Bull. Seism. Soc. Am.*, 94, 293–299.

Veselý, M., 1997: Frequency-time analysis and its use, *Master thesis*, Department of Geophysics, Faculty of Mathematics and Physics, Charles University, Prague (Frekvenčně-časová analýza a její použití, *Diplomová práce*, KG MFF UK, Praha, in Czech).

Villagómez, D. R., Toomey, D. R., Hooft. E. E. E. and Solomon, S. C., 2007: Upper mantle structure beneath the Galápagos Archipelago from surface wave tomography, *J. Geophys. Res.*, 112, B07303, doi: 10.1029/2006JB004672.

Villaseñor, A., Ritzwoller, M. H., Levshin, A. L.,, Barmin, M. P., Engdahl, E. R., Spakman, W. and Trampert, J., 2001: Shear velocity structure of Central Eurasia from inversion of surface wave velocities, *Phys. Earth Planet. Inter.*, 123, 169–184.

Villaseñor, A., Yang, Y., Ritzwoller, M. H. and Gallart, J., 2007: Ambient noise surface wave tomography of the Iberian Peninsula: implications for shallow seismic structure, *Geophys. Res. Lett.*, 34, L11304, doi: 10.1029/2007GL030164.

Vrána, S., Šrámek, J., Pokorný, L., Manová, M., Chlupáčová, M., 1997: Geological interpretation of major regional units – the Moldanubian Zone, in: Vrána, S. and Štědrá, V. (eds): *Geological model of Western Bohemia related to the KTB borehole in Germany*, Czech Geological Survey, Prague, 104–123.

Vuan, A., Robertson Maurice, S. D., Wiens, D. A., Panza, G. F., 2005: Crustal and upper mantle S-wave velocity structure beneath the Bransfield Strait (West Antarctica) from regional surface wave tomography, *Tectonophysics*, 397, 241–259.

Weeraratne, D. S., Forsyth, D. W., Yang, Y. and Webb, S. C., 2007: Rayleigh wave tomography beneath intraplate volcanic ridges in the South Pacific, *J. Geophys. Res.*, 112, B06303, doi: 10.1029/2006JB004403.

Wessel, P., and Smith, W. H. F., 1991: Free software helps map and display data, *Eos Trans. AGU*, 72, 441.

Wessel, P., and Smith, W. H. F., 1998: New, improved version of generic mapping tools released, *Eos Trans. AGU*, 79, 579.

Widmer-Schnidrig, R. and Laske, G., 2007: Theory and observations – Normal modes and surface wave measurements, in Romanowicz, B. A. and Dziewonski, A. M (eds.): *Vol. 1 – Seismology and structure of the Earth*; in Schubert, G. (ed.): *Treatise on Geophysics*, Elsevier, Amsterdam, pp 67–125.

Wielandt, E., Sigg, A., Plešinger, A. and Horálek, J., 1987: Deep structure of the Bohemian Massif from phase velocities of Rayleigh and Love waves, *Stud. Geophys. Geod.*, 31, 1–7.

Wielandt, E. and Schenk, H., 1983: On systematic errors in phase-velocity analysis, *J. Geophys.*, 52, 1–6.

Wielandt, E., 1993: Propagation and structural interpretation of non-plane waves, *Geophys. J. Int.*, 113, 45–53.

Wijk, K. and Levshin, A. L., 2004: Surface wave dispersion from small vertical scatterers, *Geophys. Res. Lett.*, 31, L20602, doi: 10.1029/2004GL021007.

Wilde-Piórko, M., Saul, J. and Grad, M., 2005: Differences in the crustal and uppermost mantle structure of the Bohemian Massif from teleseismic receiver functions, *Stud. Geophys. Geod.*, 49, 85–107.

Wilde-Piórko, M., Geissler, W. H., Plomerová, J., Grad, M., Babuška, V., Brückl, E., Cyziene, J., Czuba, W., England, R., Gaczyński, E., Gaždová, R., Gregersen, S., Guterch, A., Hanka, W., Hegedüs, E., Heuer, B., Jedlička, P., Lazauskiene, J., Keller, G. R., Kind, R., Klinge, K., Kolínský, P., Komminaho, K., Kozlovskaya, E., Krüger, F., Larsen, T., Majdański, M., Málek, J., Motuza, G., Novotný, O., Pietrasiak, R., Plenefisch, T., Růžek, B., Sliaupa, S., Środa, P., Świeczak, M., Tiira, T., Voss, P., Wiejacz, P., 2008: PASSEQ 2006 – 2008: Passive Seismic Experiment in Trans-Europe Suture Zone, *Stud. Geophys. Geod.*, 52, 439–448.

Wilson, J. T., 1940: The Love waves of the South Atlantic earthquake of August 28, 1933, *Bull. Seism. Soc.*

Am., 30, 237–301.

Wilson, J. T. and Baykal, O., 1948: Crustal structure of the North Atlantic basin as determined from Rayleigh-wave dispersion, *Bull. Seism. Soc. Am.*, 38, 41–53.

Wang, G. Q., Tang, G. Q.,Boore, D. M., Burbach, G. v. N., Jackson, C. R., Zhou, X. Y. and Lin, Q. L., 2006: Surface waves in the western Taiwan coastal plain from an aftershock of the 1999 Chi-Chi, Taiwan, earthquake, *Bull. Seism. Soc. Am.*, 96, 821–845.

Wang, C.-Y., Chia, Y., Wang, P.-L. and Dreger, D., 2009: Role of S waves and Love waves in coseismic permeability enhancement, *Geophys. Res. Lett.*, 36, L09404, doi: 10.1029/2009GL037330.

West, M., Gao, W. and Grand, S., 2004: A simple approach to the joint inversion of seismic body and surface waves applied to the southwest U.S., *Geophys. Res. Lett.*, 31, L15615, doi: 10.1029/ /2004GL020373.

Woodhouse, J. H. and Dziewonski, A. M., 1984: Mapping the upper mantle: Three dimensional modeling of Earth structure by inversion of seismic waveforms, *J. Geophys. Res.*, 89, 5953–5986.

Woods, M. T., Lévêque, J.-J. and Okal, E. A., 1991: Two-station measurements of Rayleigh wave group velocity along the Hawai'ian swell, *Geophys. Res. Lett.*, 18, 105–108.

Wong, H. L., 1982: Effect of surface topography on the diffraction of P, SV and Rayleigh waves, *Bull. Seism. Soc. Am.*, 72, 1167–1183.

Xia, J., Miller, R. D., Park, Ch. B. and Ivanov, J., 2004: Utilization of High-frequency Rayleigh Waves in Near-surface Geophysics, *The Leading Edge*, 23, 753–759.

Yamanaka, H., Kazuoh, S. and Samano, T., 1989: Effects of sedimentary layers on surface wave propagation, *Bull. Seism. Soc. Am.*, 79, 631–644.

Yang, Y., Ritzwoller, M. H., Levshin, A. L. and Shapiro, N. M., 2007: Ambient noise Rayleigh wave tomography across Europe, *Geophys. J. Int.*, 168, 259–274.

Yang, Y., Ritzwoller, M. H., Lin, F.-C., Moschetti, M. P. and Shapiro, N. M., 2008: Structure of the crust and uppermost mantle beneath the western United States revealed by ambient noise and earthquake tomography, *J. Geophys. Res.*, 113, B12310, doi: 10.1029/2008JB005833.

Yang, Y. and Ritzwoller, M. H., 2008: Characteristic of ambient seismic noise as a source for surface wave tomography, *Geochemistry, Geophysics, Geosystems*, 9, Q02008, doi: 10.1029/2007GC001814.

Yang, Y., Li, A. and Ritzwoller, M. H., 2008: Crustal and uppermost mantle structure in southern Africa revealed from ambient noise and teleseismic tomography, *Geophys. J. Int.*, doi: 10.1111/j.1365-246X.2008.03779.x.

Yang, Y. and Ritzwoller, M. H., 2008: Teleseismic surface wave tomography in the western U.S. using the Transportable Array component of USArray, *Geophys. Res. Lett.*, 35, doi: 10.1029/2007GL032278.

Yanovskaya, T. B. and Ditmar, P. G., 1990: Smoothness criteria in surface wave tomography, *Geophys. J. Int.*, 102, 63–72.

Yanovskaya, T. B., Kizima, E. S. and Antonova, L. M., 1998: Structure of the Black Sea and adjoining regions from surface wave data, *Journal of Seismology*, 2, 303–316.

Yanovskaya, T. B., Antonova, L. M. and Kozhevnikov, V. M., 2000: Lateral variations of the upper mantle structure in Eurasia from group velocities of surface waves, *Phys. Earth Planet. Inter.*, 122, 19–32.

Yanovskaya, T. B. and Kozhevnikov, V. M., 2003: 3D S-wave velocity pattern in the upper mantle beneath the continent of Asia from Rayleigh wave data, *Phys. Earth Planet. Inter.*, 138, 263–278.

Yao, H., Xu, G., Zhu, L., Xiao, X., 2005: Mantle structure from inter-station Rayleigh wave dispersion and its tectonic implication in western China and neighboring regions, *Phys. Earth Planet. Inter.*, 148, 39–54.

Yomogida, K. and Aki, K., 1985: Waveform synthesis of surface waves in a laterally heterogeneous Earth by the Gaussian beam method, *J. Geophys Res.*, 90, 7665–7688.

Yoshida, Y. and Suetsugu, D., 2004: Lithospheric thickness beneath the Pitcairn hot spot trail as inferred from Rayleigh wave dispersion, *Phys. Earth Planet. Inter.*, 146, 75–85.

Yoshizawa, K., Yomogida, K. and Tsuboi, S., 1999: Resolving power of surface wave polarization data for higher-order heterogeneities, *Geophys. J. Int.*, 138, 205–220.

Yoshizawa, K. and Kennett, B. L. N., 2002a: Non-linear waveform inversion for surface waves with a neighbourhood algorithm – application to multimode dispersion measurements, *Geophys. J. Int.*, 149, 118–133.

Yoshizawa, K. and Kennett, B. L. N., 2002b: Determination of the influence zone for surface wave paths, *Geophys. J. Int.*, 149, 440–453.

Yoshizawa, K., 2002: Development and application of new techniques for surface wave tomography, *PhD. thesis*, The Australian National University, 204 pp.

Yoshizawa, K. and Kennett, B. L. N., 2004: Multimode surface wave tomography for the Australian region using a three-stage approach incorporating finite frequency effects, *J. Geophys. Res.*, 109, B02310.

Zhang, S. X. and Chan, L. S., 2003: Possible effects of misidentified mode number on Rayleigh wave inversion, *Journal of Applied Geophysics*, 53, 17–29.

Zhang, X., Paulssen, H., Lebedev, S. and Meier, T., 2007: Surface wave tomography of the Gulf of California, *Geophys. Res. Lett.*, 34, L15305, doi: 10.1029/2007GL030631.

Zhang, Y.-S. and Lay, T., 1996: Global surface wave phase velocity variations, *J. Geophys. Res.*, 101 (B4), 8415–8436.

Zheng, S., Sun, X., Song, X., Yang, Y. and Ritzwoller, M. H., 2008: Surface wave tomography of China from ambient seismic noise correlation, *Geochemistry, Geophysics, Geosystems*, 9, Q05020, doi: 10.1029/2008GC001981.

Zhou, Y., Nolet, G., Dahlen, F. A. and Laske, G., 2006: Global upper-mantle structure from finite-frequency surface-wave tomography, *J. Geophys. Res.*, 111, B04304, doi: 10.1029/2005JB003677.



© Petr Kolínský 2010

Typeset by LaTeX

